The use of low molecular weight organic receptors for the development of novel detection, capture, and remediation technologies.

Thesis for the degree of Doctor of Philosophy.

By Rebecca Jane Ellaby

University of Kent

School of Physical Sciences

September 2022

UNIVERSITY OF KENT

SCHOOL OF PHYSICAL SCIENCES

Doctor of Philosophy

The use of low molecular weight organic receptors for the development of novel detection, capture, and remediation technologies.

By Rebecca Jane Ellaby

Abstract

This thesis reports the synthesis of a series of organophosphorus and organosulfur molecules designed to mimic the hydrogen bond accepting capacity of the P=O moiety common within all organophosphorus chemical warfare agents. The association of these molecules towards a series of non-specific low molecular weight hydrogen bond donating receptors and their hydrolysis in the presence of a base is investigated. The development of predictive methodologies for both hydrogen bond accepting simulants and for the reactivity of these molecules for the development of novel detection and remediation technologies; through the combination of low-level computational modelling, experimentally derived values, and exhaustive parameter searches. Here, it is also shown how that association constants derived from these non-specific hydrogen bonded complexes can be used as a parameter within predictive models for simulant reactivity. Finally, this thesis also reports the synthesis of a series of hydrogen bond donor-acceptor amphiphilic salts and their co-formulation with a series of organic molecules. The self-associative and physical chemical properties of these compounds are investigated in the solid and solution state. The potential for these amphiphilic salts to uptake their co-formulants is also investigated to assess their potential as environmental pollutant capture agents.

Publications relating to work presented within this thesis

1. **Identification of organophosphorus simulants for the development of next-generation detection technologies**. R. J. Ellaby, E. R. Clark, N. Allen, F. R. Taylor, K. K. L. Ng, M. Dimitrovski, D. F. Chu, D. P. Mulvihill and J. R. Hiscock, *Org. Biomol. Chem.*, 2021, **19**, 2008–2014.[1]
2. **Predicting the hydrolytic breakdown rates of organophosphorus chemical warfare agent simulans using association constants derived from hydrogen bonded complex formation events**. R. J. Ellaby, D. F. Chu, A. Pépés, E. R. Clark and J. Hiscock, *Supramol. Chem.*, 2021, 1–9.[2]
3. **Towards the application of supramolecular self-associating Amphiphiles as next-genration delivery vehicles**. L. J. White, J. E. Boles, K. L. F. Hilton, R. J. Ellaby and J. R. Hiscock, *Molecules*, 2020, **25**, 4126.[3]
4. **Supramolecular self-associating amphilies as aqueous pollutant scavangers.** R. J. Ellaby, L. J. White, J. E. Boles, S. Ozturk and J. R. Hiscock, *Org. Biomol. Chem.,* 2022, Advance article.

Acknowledgments

Firstly, I would like to express thanks to my supervisor Dr Jennifer R. Hiscock for allowing me to undertake this research as a member of her research group, and the guidance she has provided over the duration of this PhD.

I would like to thank all the members of the Hiscock group both past (Nyasha, Stella, Milan, Kendrick, Gina, Faith, Liam, Oni, Nova, Sena, Angelica, and George), and present (Kira and Jack). A particular thank you goes to Jess and Lisa, whom without I wouldn't have made it this far, with your assistance, support, input and most importantly with your friendship, you both have made this research journey truly amazing and couldn't imagine doing it without you.

Last but not least I would like to thank my amazing family who have been by my side, supporting me throughout this entire journey, my sisters Charlotte, Elizabeth, and Emily but especially my parents, Stephen and Terry, their endless support throughout this whole journey I will be forever grateful for, their encouragement when times were tough and being there to celebrate the good times. My fiancé Tomos, who has been my absolute rock throughout the period of this PhD, without his tremendous support and understanding, it would have been impossible to complete my studies.

Finally, I would like to dedicate this thesis to my grandfather, the gentle giant, Albert Ellaby, who always supported me and was there to offer his squeezes when I needed them, he taught me how to value what is truly important in life, until his death in December 2021. His strength was truly admirable, and I can only wish I can be as strong as he was.

RIP Grandad miss you more and more every day.

Table of Contents

Abstract i

Publications relating to work presented within this thesis ii

Acknowledgments iii

Declaration of Authorship vi

Abbreviations vii

Chapter 1 – Introduction 1

1.1 Supramolecular Chemistry 1

1.2 Non-covalent interactions 5

1.3 Non-covalent interactions found within nature 10

1.4 Supramolecular complex formation 13

1.4.1 Cation coordination 14

1.4.2 Anion coordination 16

1.4.3 Neutral guest coordination 25

1.5 PhD aim and objectives 28

1.5.1 PhD aim 28

1.5.2 PhD objectives 29

Chapter 2 – Development of chemical warfare agent simulants using association constant prediction. 30

2.1 Introduction 30

2.2 Synthesis 43

2.3 Association constant determination 44

2.4 *In-silico* modelling 51

2.5 Development of a single parameter predictive model 58

2.6 Exhaustive parameter search 60

2.7 Toxicity considerations 64

2.7 Conclusions 66

Chapter 3 – The development of predictive models for OP simulant reactivity 68

3.1 Introduction 68

3.2 Synthesis 80

3.3 Assessing the reactivity of simulants 80

3.4 Predicting simulant reactivity 84

3.5 Physical property considerations 96

3.6 Conclusions 98

Chapter 4 – The use of supramolecular self-associating amphiphiles (SSAs) as molecular capture agents in solution. 100

4.1 Introduction 100
4.2 Synthesis 114
4.3 Solid state: single crystal X-ray diffraction 115
4.4 Solution state studies 118
4.4.1 Quantitative ^{1}H NMR studies 119
4.4.2 Proton DOSY NMR studies 126
4.4.3 ^{1}H NMR self-association studies 133
4.4.4 Dynamic light scattering studies 137
4.4.5 Surface tension and critical micelle concentration studies 143
4.4.6 Zeta potential Studies 147
4.5 Co-formulant uptake studies 149
4.5.1 ^{1}H NMR studies 151
4.5.2 Dynamic light scattering and Zeta potential studies 155
4.6 Conclusions 158
Chapter 5 – Final Conclusions 160
Chapter 6 – Experimental procedures 162
6.1 General information 162
6.1.1 General information Chapter 2 163
6.1.1.1 Biological experimental 165
6.1.2 General information Chapter 3 166
6.1.3 General information Chapter 4 167
6.2 Synthetic procedures 168
References 182

Declaration of Authorship

I, Rebecca Jane Ellaby, declare that the thesis entitled The use of low molecular weight organic receptors for the development of novel detection, capture and remediation technologies and the work presented in this thesis are both my own and have been generated by me as the result of my original research.

I confirm that:

- this work was done wholly or mainly while in candidature for a research degree at this university.
- where any part of this thesis has previously been submitted for a degree or any other qualification at this university or any other institution, this has been clearly stated.
- where I have consulted the published work of others, this is always clearly attributed.
- where I have quoted from the work of others, the source is always given. With the exception of such quotations, this thesis is entirely my own work.
- I have acknowledged all main sources of help.
- where the thesis is based on work done by myself jointly with others, I have made clear exactly what was done by others and what I have contributed myself.
- parts of this work have been published as:

Identification of organophosphorus simulants for the development of next-generation detection technologies. R. J. Ellaby, E. R. Clark, N. Allen, F. R. Taylor, K. K. L. Ng, M. Dimitrovski, D. F. Chu, D. P. Mulvihill and J. R. Hiscock, *Org. Biomol. Chem.*, 2021, **19**, 2008–2014 (Chapter 2).

Predicting the hydrolytic breakdown rates of organophosphorus chemical warfare agent simulans using association constants derived from hydrogen bonded complex formation events. R. J. Ellaby, D. F. Chu, A. Pépés, E. R. Clark and J. Hiscock, *Supramol. Chem.*, 2021, **33**, 309–317. (Chapter 3).

Towards the application of supramolecular self-associating Amphiphiles as next-genration delivery vehicles. L. J. White, J. E. Boles, K. L. F. Hilton, R. J. Ellaby and J. R. Hiscock, *Molecules*, 2020, **25**, 4126 (Chapter 4).

Supramolecular self-associating amphililes as aqeous polluant scavangers. R. J. Ellaby, L. J. White, J. E. Boles, S. Ozturk and J. R. Hiscock, *Org. Biomol. Chem.,* 2022, Advance article (Chapter 4).

Signed: 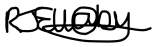

Abbreviations

2-NDP	2-nitrophenyl dimethyl phosphate
4-NDP	4-nitrophenyl dimethyl phosphate
A	Adenosine
Å	angstrom
AChE	acetylcholinesterase
AMS	aminomethane sulfonic acid
β-CD	Beta-cyclodextrin
bis-tris	2,2-bis(hydroxymethyl)-2,2’,2”-nitrilotriethanol
BNPP	bis(4-nitrophenyl) phosphate
C	cytosine
CD	cyclodextrin
CD_3Cl	Deuterated chloroform
CD_3CN	Deuterated acetonitrile
CMC	critical micelle concentration
CoEK	cooperative equal K
conc	concentration
CWA	Chemical warfare agent
CWC	chemical weapons convention
d	doublet (NMR)
D	Diffusion coefficient
DB-18-C-6	dibenzo-18-crown-6
DCM	Dichloromethane
DCP	Diethylchlorophosphate
DEEP	Diethyl ethylphosphate

DEMP	Diethyl methylphosphate
DFP	Diisopropyl fluorophosphate
DFT	Density functional theory
d_H	Hydrodynamic Diameter
DIAZ	N,N-diisopropylaziridium ion
DICP	Di(isopropyl)chlorophosphite
DIMP	Di(isopropyl) methylphosphate
DLS	Dynamic Light Scattering
DMF	Dimethylformamide
DMMP	Dimethyl methylphosphonate
DMNP	Dimethyl *p*-nitrophenyl phosphate
DMP	Dimethyl phosphoric acid
DMSO	Dimethyl sulfoxide
DNA	Deoxyribonucleic acid
DOSY	Diffusion-Ordered Spectroscopy
DVMP	Dichlorovinylmethyl phosphoric acid
E_{max}	Electrostatic maximum
E_{min}	Electrostatic minimum
EMMG	Edinburgh Minimal Media Glutamate
EMPT	O-Ethyl methyl phosphonothioate anion
ESI-MS	Electron Spray Ionisation Mass Spectrometry
ESPMs	Electrostatic potential maps
EtOH	Ethanol
FTIR	Fourier Transform infrared spectroscopy
G	Guanine

GA	Tabun
GB	Sarin
GD	Soman
GF	Cyclosarin
HBA	Hydrogen Bond Acceptor
HBD	Hydrogen Bond Donor
HD	Sulphur mustard
HOMO	Highest Occupied Molecular Orbital
HPTS	8-Hydroxypyrene-1,3,6-trisulfonic acid trisodium salt
IMP	Isopropyl methyl phosphonate
IMPA	Isopropyl methylphosphonic acid
ITC	Isothermal Titration Calorimetry
J	Coupling constant (NMR)
K_a/K_{ass}	Association constant
K_d	Dissociation constant
K_{dim}	Dimerisation constant
LD50	Lethal Dose
LDA	Linear Discriminant Analysis
LED	Light Emitting Diode
LUMO	Lowest Unoccupied Molecular Orbital
m	Multiplet (NMR)
mg	Milligram
MIPs	Molecularly Imprinted Polymers
mM	Milli molar
mN/m	Milli newton per meter

MOF	Metal-organic framework
MP	Melting point
mPa	Milli pascal
mV	Millivolts
m/z	Mass to charge ratio (mass spectroscopy)
NA	Not applicable
NaOH	Sodium hydroxide
NAs	Nerve agents
NEM	N-ethylmaleimide
nM	Nano Molar
NMR	Nuclear magnetic resonance
No.	Number
OD	Optical Density
OP	Organophosphorus
P	Parameter
PDI	Polydispersity index
pHIPEs	Poly high internal phase emulsions
pKa	Acid dissociation constant
PMP	Pinacolyl methylphosphonate
ppm	Parts per million
qNMR	Quantitative nuclear magnetic resonance
q	Quartet (NMR)
QSAR	Quantitative Structure Activity Relationship
S.pombe	Schizosaccharomyces pombe
SAF	Steric accessibility factor

SARs	Structure Activity Relationships
SCX-n	*p*-Sulfonatocalix[n]arenes
SI	The International System of units
S_N2	Substitution Nucleophilic Bimolecular
SSA	Supramolecular Self-associating Amphiphiles
SWF	Steric weighting factor
t	Triplet (NMR)
T	Thymine
TBA	Tetrabutyl ammonium
TBAOH	Tetrabutyl ammonium hydroxide
TFA	Trifluoroacetic acid
THF	Tetrahydrofuran
UK	United Kingdom
µL	Micro litre
UV-Vis	Ultraviolet-visible
vdW	van der Waals
wt.%	Weight percentage
WW2	World War 2
XRD	X-ray Diffraction
YES	Yeast Extract with Supplements
YFP	Yellow Fluorescent Protein

Chapter 1 – Introduction

1.1 Supramolecular Chemistry

Supramolecular chemistry is a fast-growing interdisciplinary field of research that in comparison to other branches of chemistry is still relatively young.[4] Supramolecular chemistry investigates "chemistry beyond the covalent bond", and has the objective of reproducing complex systems such as those found in nature.[5] Jean-Marie-Lehn first coined the term 'supramolecular' in 1969 and defining supramolecular chemistry as "*chemistry beyond the molecule*" through "*highly complex chemical systems interacting by non-covalent intermolecular forces*".[6] As a result of these early investigations Charles Pedersen,[7] Donald Cram,[8] and Jean-Marie Lehn[9] were awarded the Nobel Prize in 1987 for their investigation and development of molecules which exhibit structure-specific interactions of high selectivity.

Research into to molecular chemistry has undergone substantial development since its initiation in 1828 by Friedrich Wöhler, who contributed to the foundation of modern chemistry through the successful synthesis of urea using ammonium cyanate, displacing vital force theory (Scheme 1.1).[10,11] At the time this was ground breaking due to the belief that it was not possible to synthesise organic molecules from inorganic materials, thus disproving vitalism and consequently led the way for the development of other organic molecules in a similar way.

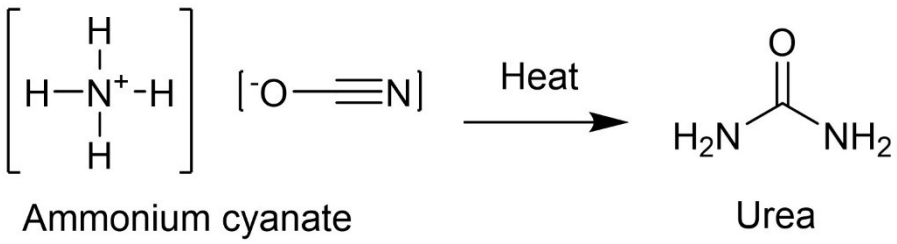

Scheme 1.1 – The synthesis of urea by Friedrich Wöhler's using ammonium cyanate.[10]

It was in 1913, that the American chemist Gilbert Newton Lewis formulated the idea of covalent bonding through the theory of 'valence', whereby 'the chemical bond consists of a pair of electrons held jointly by two atoms'[12,13] Here Lewis used dot and cross diagrams (Figure 1.1.1) to explain this theory.[12] The term covalent bond was later introduced by Irving Langmuir in 1919.[14]

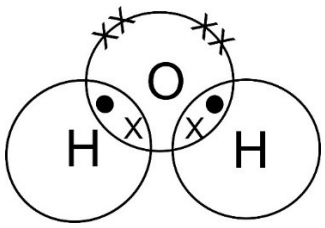

Figure 1.1.1 – An example of a dot and cross diagram using a water molecule depicting the theory of valence proposed by Gilbert Newton Lewis.

Supramolecular chemistry is centered around the investigation of non-covalent interactions between molecules. Examples of these non-covalent interactions are electrostatic interactions (such as hydrogen bonds), van der Waals forces (vdW), and π-π interactions (Figure 1.1.2) and further discussed in section 1.2. These reversible forces facilitate the production of self-assembling systems,[15] biological processes,[16] such as DNA, as well as the construction of complex materials and molecular machines (an area which won the Nobel prize in Chemistry in 2016).[17]

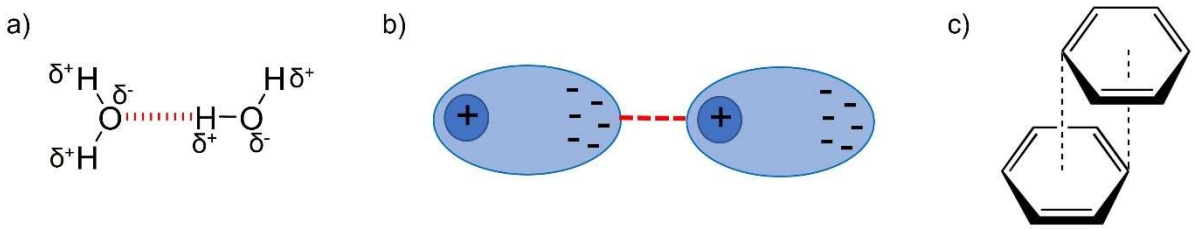

Figure 1.1.2 – Examples of non-covalent interactions. a) hydrogen bonding between two water molecules – red dashed line represents the hydrogen bond, b) cartoon representation of van der Waals forces – red dashed line represents van der Waals forces and c) examples of one type of π-π interactions (displaced conformation shown).

These fundamental principles of supramolecular chemistry were recognised long before the term was first coined.[6] In 1873 when Johannes Diderik van der Waals introduced the idea of intermolecular bonds;[18] he was developing a theory that accounted for the properties demonstrated by real gases. It was from this work that the idea of supramolecular chemistry began, although it would not be named this until 1969. Following van der Waals theory, Emil Fisher in 1894 proposed the lock and key principle to understand the interactions between enzymes and substrates,[19] where it was stated that a substrate of a specific shape would fit into a cavity of enzymes using non-covalent interactions through complimentary geometries and resultant interactions, in the same way a specific key fits into a lock. This principle became the fundamental basis for understanding the design of pharmaceuticals[20] and is now more commonly referred to as host guest chemistry (Figure 1.1.3).[21]

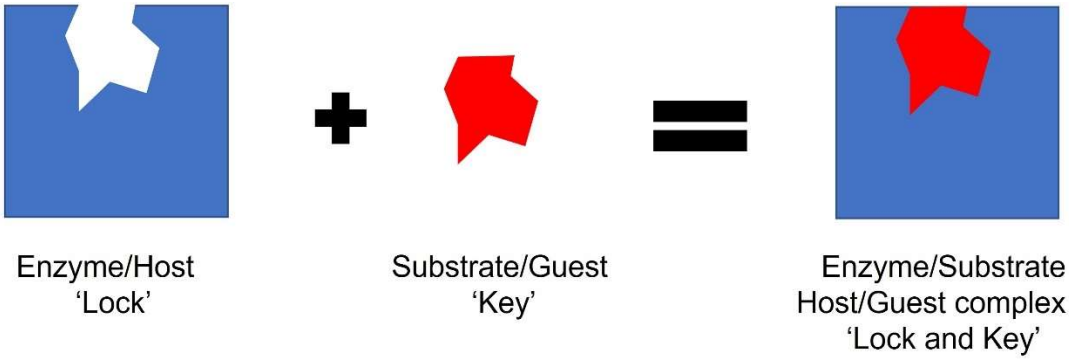

Figure 1.1.3 – An illustration of the "lock and key" principle used by Emil Fisher for the understanding of enzyme and substrate interactions, more commonly known as host guest complexes.

Following the work by Fisher and van der Waals, research into understanding non-covalent bonds was pursued, and in 1961 Charles Pedersen discovered the first crown ether, dibenzo-18-crown-6 (DB-18-C-6 - Figure 1.1.4 a)[22] which he found to solubilise sodium and potassium salts in aprotic solvents, he followed this up by publishing articles discussing to the design and development of a further 50 crown ethers containing between 9 and 60 atoms.[23,24] Subsequently, James Christensen used Pedersen's crown ethers to study the thermodynamics

of cation macrocyclic interactions, which further influenced their later work on molecular recognition.[25,26]

Jean-Marie Lehn[6] and Donald Cram[27] continued to build upon this ground breaking discovery with the development of more sophisticated novel macrocyclic molecules displaying cavities which were able to bind low molecular weight organic molecules, primarily alkali metal cations where the size of the cavity reflected its selectivity for certain alkali metal cations, where the cryptate shown in Figure 1.1.4 c had better selectivity for K^+ ions over Li^+ and Na^+.[4] Although, Lehn and Crams research concentrated on alkali metal cation co-ordination, Jean-Marie Lehn, when giving his Nobel prize lecture, brought the scientific communities attention to the unexplored area of anion coordination chemistry, indicating its relevance from both a chemical and biological standpoint. This work also contributed to the understanding of ion transport within biological membranes.[6]

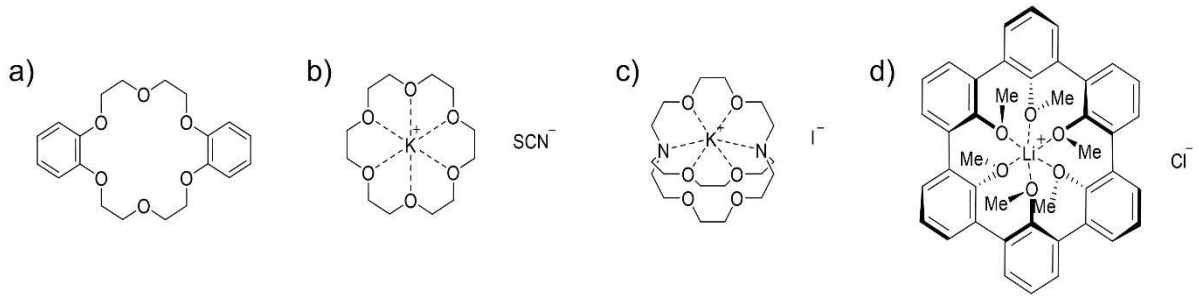

Figure 1.1.4 – Evolution of crown ethers following Charles Pedersen's discovery, **a**) DB-18-C-6,[22] **b**) Charles Pedersen's crown ether complex with K^+ cation,[3] **c**) A cryptate developed by Jean-Marie Lehn[4] and **d**) a spherand developed by Donald Cram.[24]

The area of supramolecular chemistry received further global recognition in 2016 with the Nobel prize in chemistry being awarded to Sir J. Fraser Stoddart, Jean-Pierre Sauvage and Bernard L. Feringa for their design and synthesis of molecular machines. Molecular machines have the potential to be used in the development of new materials, sensors, and energy storage systems. The first step towards these molecular machines was by Jean-Pierre Sauvage in 1983, who successfully designed and synthesised what is now called a catenane, where two

macrocycles are linked together to form an interlocked ring (Figure 1.1.5 a).[28,29] Following Sauvage's success, in 1991 Sir Fraser Stoddart developed a rotaxane. Here he threaded a molecular ring onto a thin molecular axle with stoppers on each end, and demonstrated that the ring was able to move along the axle when an external stimulus was applied such as changes in pH, solvent, and light (Figure 1.1.5 b).[30,31] Finally, in 1999 Bernard Feringa became in the first person to develop a molecular motor (a single molecule with paddle units that are connected by a carbon-carbon double bond), which utilised molecular rotor blades that spin continuously in the same direction which resulted in the development of a nano-car (Figure 1.1.5 c).[32] The Nobel prize committee commented that molecular machinery is now at the same stage that electric motors were in the 1830s, where scientists developed spinning wheels and cranks, which led on to the invention of washing machines and fans. This shows the potential for these molecular machines to be the start of a new generation of inventions.

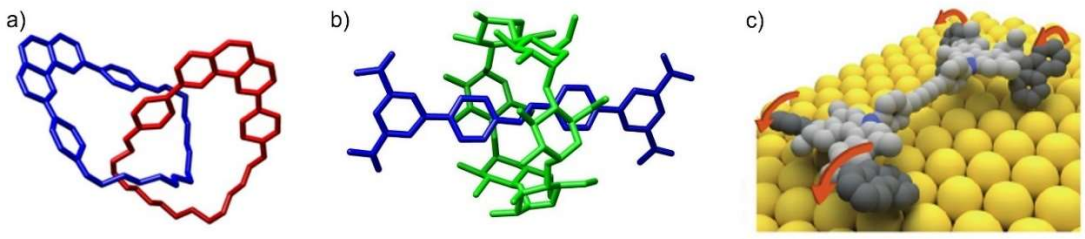

Figure 1.1.5 – Examples of the molecular structures produced by Sir J. Fraser Stoddart, Jean-Pierre Sauvage and Bernard L. Feringa. a) catenane,[30] b) rotaxane[33] and c) a nano-car.[32] a and b reproduced from ref. 27 and 30 with permission from Royal Society of Chemistry. c reproduced from ref. 32 with permission from Wiley.

1.2 Non-covalent interactions

Covalent and non-covalent interactions differ considerably. Covalent bonds are formed when partially occupied orbitals of interacting atoms overlap, and a pair of electrons are shared by these atoms and determine the primary structure of a given molecule.[34] Non-covalent interactions are formed as a result of the electron distribution between two or more molecules.

Intermolecular interactions promote the process of self-association which results in extended structure formation such as dimers, trimers or polymers etc.[35] Intramolecular interactions are interactions between different functional groups within a singular molecule.

There are many different types of non-covalent interactions, examples of which include: ion-ion interactions, vwD forces, dipole-dipole interaction, halogen bonding, π-π interaction, and lastly the hydrogen bond, which can be considered a combination of both electrostatic and covalent due to the partial covalent nature of these bonds.[36] Ion-ion interactions are an attractive force of two ions of opposite charges, as shown with sodium chloride for example where the attraction is between Na^+ ion and the Cl^- ion; this interaction is the strongest, exhibiting energies to that of weak covalent bonds in a range of 100 to 350 kJ mol^{-1} (Figure 1.2.1 a).[37] vdW forces are some of the weakest non-covalent interactions with bond energies < 5 kJ mol^{-1},[38] vdW forces are caused by the fluctuating polarizations of nearby particles resulting in a temporary shift in electron density, these fluctuations may cause the electron density to temporarily shift to one side of the nucleus. This shift then creates a transient charge whereby a nearby atom can be attracted or repelled (Figure 1.1.2 b); dipole-dipole interactions are formed between two permanent dipoles, with interactions that have the tendency to align molecules in such a way that it increases attraction with an exhibited energy range between 5 and 50 kJ mol^{-1} (Figure 1.2.1 b)[39]; ion-dipole interactions form as a result of the electrostatic attraction between an ion and neutral molecule that has a dipole, for example the interaction between Na^+ and a water molecule, where the sodium ion and oxygen atom are attracted to each other and the sodium ion and hydrogen are repelled, the energy range for this type of interaction is typically between 50 and 200 kJ mol^{-1} (Figure 1.2.1 c).[40] Halogen bonding is a non-covalent interaction where the halogen atom is acting as the electron acceptor. This interaction geometrically is similar to that of a hydrogen bond; however, it is affected more by steric due to the larger size of halogens. These bonds exhibit a bond energy with a range between 1-45 kJ mol^{-1}.

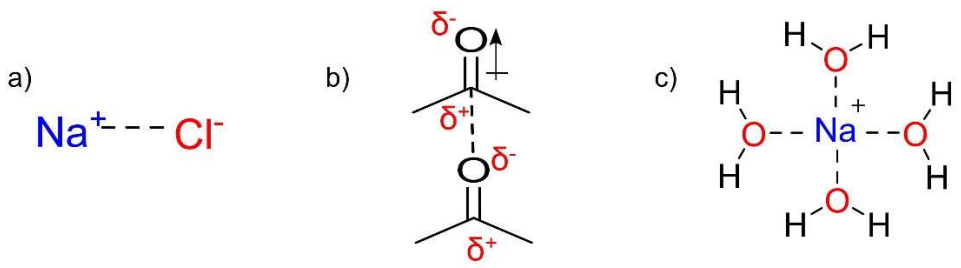

Figure 1.2.1 – Examples of non-covalent interactions. a) ion-ion interactions using sodium chloride as an example, b) dipole-dipole interactions using acetone as an example and c) ion-dipole interactions using the interaction between Na^+ and water as an example. Dashed line represents non-covalent interaction.

When considering the non-covalent interactions between aromatic units' π-π interactions come into effect, these interactions can be further broken down into more specific categories: π - π, cation/anion- π and polar- π interactions. π-π interactions occur between aromatic ring systems through the electropositive and electronegative regions that are generated due to the lateral overlapping of p-orbitals in π-conjugated systems. This type of interaction is weaker than those previously mentioned with typical energies between 5 and 40 kJ mol^{-1}. The alignment of these aromatic rings is relative to the π electron density, with partial positive charges around the periphery, and partial negative charges above both aromatic faces.[41,42] Between these ring systems there are known to be three ways that the ring systems stack: displaced (slip-stacked) (Figure 1.2.2 a), edge to face (Figure 1.2.2 b) or sandwich (Figure 1.2.2 c).[43] The sandwich conformation is the least favourable of the three due to the high electrostatic repulsion from the electrons within the π-orbitals. Cation-π interactions involve the positive charge of a cation interacting with the electrons within the π system (Figure 1.2.2 d), and can result in a very strong interaction (bond energy between 1 and 20 kJ mol^{-1}),[44] this type of interaction has potential applications in areas such as chemical sensors, and is of great interest within biological systems. Anion- π interactions are very similar to cation- π interactions, whereby the anion sits above an electron poor π system usually due to the presence of electron

withdrawing substituents on the π-conjugated system this type of interaction has a bond energy of around 5-10 kJ mol^{-1} (Figure 1.2.2 e).[44] The final non-covalent π interaction is polar- π interactions where molecules with permanent dipoles, such as water, interact with the quadrupole moment of a π system (Figure 1.2.2 f). These interactions are weaker than a conventional hydrogen bond and are commonly involved in protein folding and crystallinity of solids with both hydrogen bonding and π systems. Any molecule that contains a hydrogen bond donor (HBD) will favourably interact with electron rich π-conjugated systems.

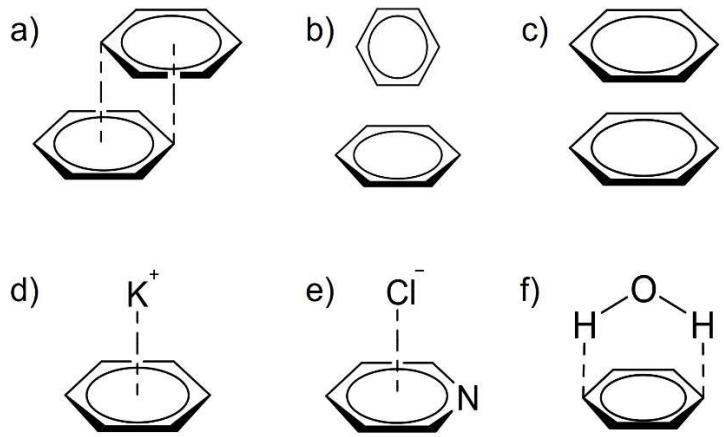

Figure 1.2.2 - Representation of π-π interactions: a) displaced (slip stacked); b) edge to face; c) sandwich; d) cation-π interactions using benzene and a potassium ion as an example; e) anion-π interactions using pyridine and a chloride ion as an example, and f) polar-π interactions using benzene and water as an example.

The final type of non-covalent interactions is the hydrogen bond, which has been studied in great depth since its discovery,[45–47] and is at the centre of a lot of research within supramolecular chemistry. Hydrogen bonds are formed between an electropositive hydrogen atom and an electronegative atom. Hydrogen bonds typically have bond lengths ranging between 1.2-4.0 Å (strong to weak)[39] with a broad energy range of between 4-165 kJ mol^{-1} and can have covalent character as well as electrostatic.[48] In comparison to a covalent bond, non-covalent interactions are significantly weaker. However, with non-covalent interactions there is

an additive effect of all interactions, which can be strong enough to stabilise larger structures and complexes. Hydrogen bonds can be influenced by a multitude of factors, which include: i) the electron-withdrawing/donating properties of any functional groups associated with the principle hydrogen bond donating or accepting site; ii) bond angle; iii) reactant concentrations;[49] iv) temperature;[50] iii) chemical environment;[51] and v) pressure.[52] Host/guest complexes form predominantly due to intermolecular hydrogen bonds, containing a complementary range of hydrogen bond donor (HBD) and acceptor groups (HBA). The HBDs are primarily an electronegative element such as nitrogen, oxygen or sulphur with a hydrogen atom attached. This bond therefore becomes polarised resulting in a partial negative charge on the atom bound to the hydrogen and a positively charged hydrogen atom. Hydrogen bonds can be formed between a HBD and HBA on the same molecule (intramolecular) or between HBD and HBA on different molecules (intermolecular). The geometry of hydrogen bonded complexes traditionally known to adopt one of the following six and are illustrated in Figure 1.2.3: a) linear; b) bent; c) donating bifuricated; d) accepting bifuricated; e) trifuricated and e) three centred bifuricated.[53]

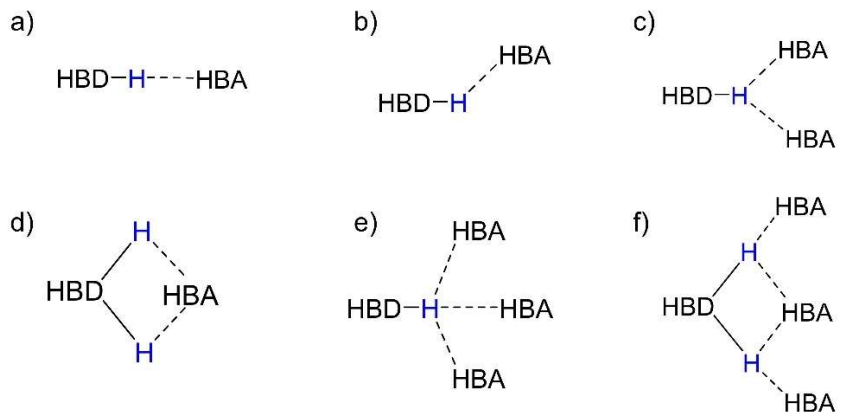

Figure 1.2.3 – Hydrogen bond complex geometries. a) linear; b) bent; c) donating bifuricated; d) accepting bifuricated; e) trifuricated and f) three-centred bifuricated.[53]

The hydrogen bond angle is optimised at 180° when considering single donor-acceptor complexes (Figure 1.2.3 a).[54] It was suggested by Pimentel and McClellan the even small deviations from linearity will result in an approximate 10 % decrease in binding energy.[55]

However, when considering double acceptor systems, bifurcated angles are of preference (Figure 1.2.3 c),[56] as this is more energetically stable than a linear conformations.[57] On the other hand, the more molecular species that are involved within the self-assembly process there are more variables to consider, such as the formation of the thermodynamically more favoured six-membered ring as there is the least amount of strain on the hydrogen bond angles in this conformation versus smaller membered rings.[58] The geometry of a hydrogen bond isn't the only contributor to its strength, there needs to also be consideration for what functional groups are attached to the HBD and HBA, as they can result in a decrease in strength due to partial charge repulsion of increase the binding strength due to attraction of partial charges of the opposite sign.[53] These are classed as secondary interactions and either decrease the binding strength due to repulsions from partial charges of the same sign (Figure 1.2.4 - Examples of secondary hydrogen bond interactions between two neighbouring groups a) repulsions (↔) from a mixed donor/acceptor arrangement and b) attractive interactions (-----) between an all donor and all acceptor arrangement.[53]Figure 1.2.4) or increase by virtue of attraction between opposite charges, as shown in Figure 1.2.4.[53]

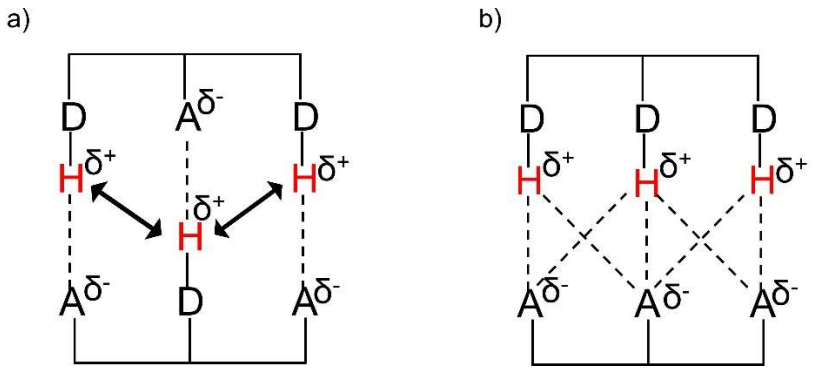

Figure 1.2.4 - Examples of secondary hydrogen bond interactions between two neighbouring groups a) repulsions (↔) from a mixed donor/acceptor arrangement and b) attractive interactions (-----) between an all donor and all acceptor arrangement.[53]

1.3 Non-covalent interactions found within nature

Supramolecular architectures take inspiration from nature where non-covalent interactions are fundamental for the stabilisation of three-dimensional structure of large molecules such as the secondary, tertiary and quaternary structures of proteins[59] and nucleic acids and the formation of the DNA double helix.[60] These are often complex 3D structures formed by non-covalent interactions that catalyse chemical reactions within the body.[61]

There are four different classifications of protein structure; the primary structure of a protein consists of a chain of amino acids which are held together by peptide bonds. The specific property of each amino acid is determined by the presence of differing R groups, these R groups vary and can be hydrophobic or hydrophilic and charged or neutral.[62] The hydrophobic effect provides the primary thermodynamic drive for the overall structure of proteins in water, however, between side groups within this chain of amino acids, hydrogen bonding can occur, here the hydrogen bonds role is to provide the majority of the directional interactions, which underpin the rigidity of the structure and provide specificity in both molecular recognition and protein folding. Proteins contain many sites capable of being a HBD and a HBA, with groups such as the carbonyl and amide groups on the peptide backbone,[63] as well as polar functional groups (hydroxyls, acids, amides, and amines) found on several of the amino acid side chains.[64] These primary structures undergo a self-assembly process forming secondary structures, such as α-helixes, β-sheets and β-coils (Figure 1.3.1 b) these structures are stabilised by hydrogen bonds between the carbonyl oxygen on the peptide backbone and the amide nitrogen contained in the hydrophobic core.[65,66]

Tertiary structures are the general three-dimensional organisation of a polypeptide chain in space, formed through the self-assembly of secondary structures through non-covalent interactions, such as hydrogen bonding, ionic interactions, sulfonate bridges and hydrophobic interactions, and are stabilised by the internal hydrophobic interactions between the non-polar amino acid side chains and external hydrogen bond and ionic bond interactions[67] The final protein structure is the quaternary structure, assembled via either multiple folded protein

subunits or co-factors, this structure is predominantly driven by the hydrophobic effect, and further stabilised by a range of non-covalent and covalent interactions such as hydrogen bonds, vdW, and disulphide bridges and can be driven by the hydrophobic effect (Figure 1.3.1 d).[68–73] An example of a quaternary structure is an antibody; an intrinsic structure designed to detect foreign particles within the body and defend against them.[74]

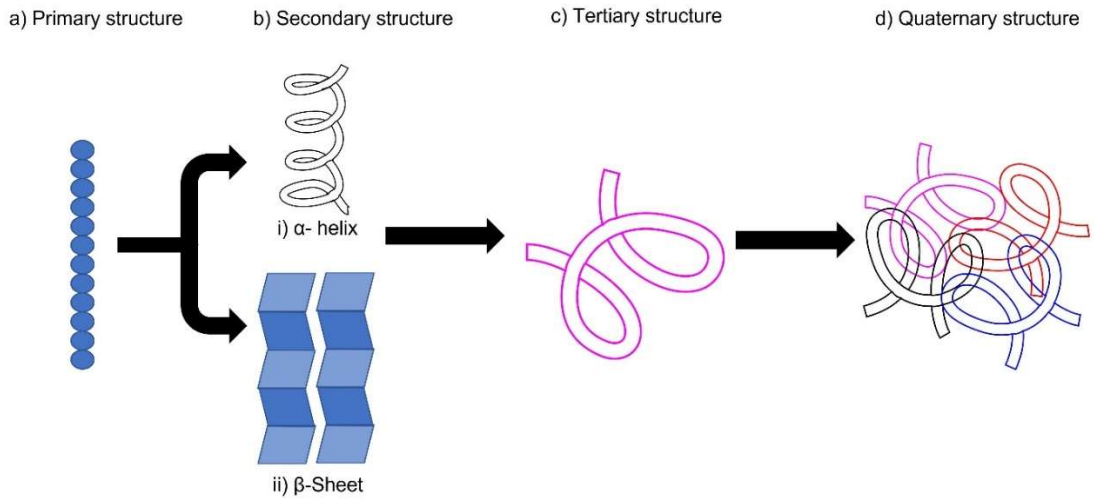

Figure 1.3.1 - Cartoon representations of the different protein structures. a) the primary structure – a chain of amino acids; b) the two secondary structures i) alpha helices and ii) beta sheets; c) tertiary structure formed from the self-assembly of secondary structures and d) the quaternary structure, assembled via either multiple folded protein subunits or co-factors.

One of the most well studied examples of non-covalent interactions found naturally, is the double helix structure of deoxyribonucleic acid (DNA), whose structure was discovered by Rosalind Franklin, James Watson, and Francis Crick in 1953. Here, two antiparallel repeating strands of nucleotides interact to form a double helix (Figure 1.3.2 c);[75] held together through the formation of hydrogen bonds between complimentary bases such as adenosine (A) and thymine (T) forming one base pairing through the formation of two hydrogen bonds (Figure 1.3.2 a) and cytosine (C) and guanine (G) forming another base pair with three hydrogen bonds - commonly known as Watson-Crick base pairing (Figure 1.3.2 b).[75,76] The number of hydrogen bonds between base pairs can have a large effect on the DNAs stability, as there is an additive

strength of hydrogen bonds which therefore means DNA with a higher GC content than AT results in a higher stability due to the strength provided from the one extra hydrogen bond within the base pair.[77] However, it is not solely down to hydrogen bonding that provides structural stability to DNA, the hydrophobic nitrogenous bases that are located on the interior on the helix are sequestered away from the aqueous and polar environment within cells. This also allows for the hydrophilic phosphate head groups to be exposed and interact with water increasing the solubility within aqueous and polar environments. Furthermore, the negatively charged phosphate head groups can also ionically interact with cations found within the cellular environment such as Na^{+}, Ca^{2+} and Mg^{2+} which also increased structural stability.

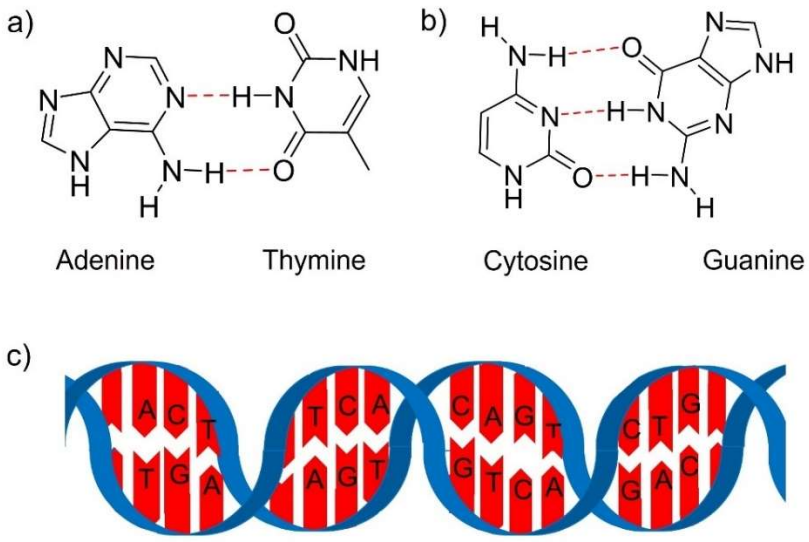

Figure 1.3.2 – Hydrogen bond complexes found within DNA. a) Adenine and thymine complex through the formation of two hydrogen bonds; b) cytosine and guanine complex through the formation of three hydrogen bonds and c) a cartoon representation of DNA showing antiparallel base pairing base pairs shown in a and b.

1.4 Supramolecular complex formation

A supramolecular complex (or host/guest complex) is composed of two or more molecules or ions that are held together using non-covalent interactions as previously discussed, but the

principal non-covalent interaction is hydrogen bonding. The binding between a host and a guest molecule is usually specific to two molecules concerned, and it is the formation of these complexes that is at the centre of molecular recognition.

The selective recognition and sensing by selective coordination via hydrogen bond donating receptors has attracted considerable research interest within the supramolecular community for its importance within both biological and environmental areas.[78–82] This area of research can be broken down into three areas cation coordination and anion coordination and neutral guest coordination. The premise of this thesis is around anion and neutral guest coordination and will be covered in more depth in sections 1.4.2 and 1.4.3.

1.4.1 Cation coordination

The sensing of cations has gained the attention of many scientists, not just chemists, but also biologists and environmental scientists. There are several metal ions that play a vital role in our daily physiological life. These include but are not limited to sodium (Na^+) potassium (K^+), calcium (Ca^{2+}), copper (Cu^+ and Cu^{2+}) and zinc (Zn^{2+}). However, some metal ions such as lead (Pb^{2+}), cadmium (Cd^{2+}) and mercury (Hg^{2+}) are toxic and cause serious health and environmental problems.[44] Therefore, detection of these cations is highly desirable. There are numerous analytical methods that can detect cations; however, they are expensive, and some equipment does not allow for remote testing. Methods for cation recognition based on fluorescent sensors offers the advantage of sensitivity and selectivity, and you can use these sensors remotely using optical fibres with the sensor at the tip of the fibre.[83,84]

Sousa and co-workers reported two naphthalene-based chemosensors for the detection of alkali metal ions (Figure 1.4.1.1), where the orientation of the attached naphthalene changed the fluorescence upon complexation of alkali metal halides, **1** resulted in a decrease in fluorescence quantum yield, whereas **2** resulted in an increase in quantum yield.[85] Subsequently, fluorescent chemosensor design based on macrocycles has attracted a lot of attention from

scientists. Pillararenes have gathered much attention due to their broad applications such as artificial transmembrane channels,[86] controlled delivery systems[87] and the extraction and absorption of materials.[88] Thus, pillararene-based fluorescent chemosensors for cations also achieved a rapid development.[89,90] Huang and co-worked designed and synthesised an anthracene appended 2:3 copillar[5]arene in 2015, which was used as a selective fluorescent chemosensor for Fe^{3+}, as it was found that only this cation quenched the fluorescence in DMSO and other cations tested had no effect on the fluorescence.[89]

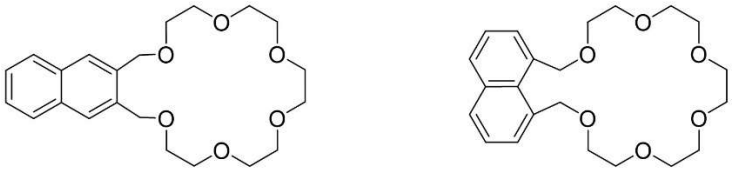

1 **2**

Figure 1.4.1.1 – Chemdraw structures of the naphthalene based sensors **1** and **2** synthesised by Sousa and co-workers for sensing alkali earth metals.

More recently, Pinkesh and co-workers developed a novel calix[4]arene with a lower rim linked 1-aminoanthracene unit through an amide linkage (**3**, Figure 1.4.1.2).[91] This compound was found to bind two cations (La^{3+} and Cu^{2+}) as well as the anion Br^-, the fluorescence of this compound was not found to significantly change upon the addition of multiple other cations and anions. They demonstrated that **3** could be used as a paper based fluorescent sensor for these ions with detection limits of 0.88 nM, 0.19 nM and 0.15 nM for La^{3+}, Cu^{2+} and Br^- respectively. Their binding constants were also determined using fluorescent emission titration data and reported binding constants of 10.21 x 10^8 M^{-1} for La^{3+}, 7.04 x 10^8 M^{-1} for Cu^{2+} and 7.96 x 10^8 M^{-1} for Br^-.[91] Highlighting that this compound could be used as a selective fluorescent probe.

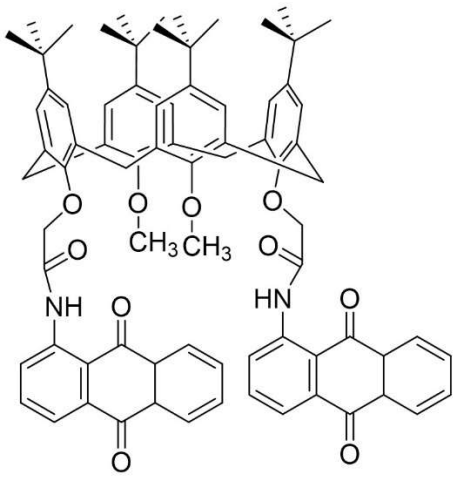

3

Figure 1.4.1.2 – Lower rim modified calix[4]arene reported by Pinkesh and co-workers.[91]

1.4.2 Anion coordination

Anion receptor chemistry is an area within supramolecular chemistry that involves the design of molecules that can recognise, respond to and/or sense a species that carries a negative charge.[92] Anions are fundamental in most processes that occur naturally. Chloride anions are important for the control of water within mucus membranes, it is a lack of this anion within mucus that results in the genetic disease cystic fibrosis.[93] Anions also play an integral part of enzyme substrate complexes as well as forming the phosphate backbone of DNA. Anions can also be found within ground water and soils which provide information on their quality and anthropogenic pollution. This is particularly true for nitrates and phosphates which are integral for plant growth, but they can also cause damage through their widespread use in fertilisers and pesticides, which can poison organisms in both contaminated earth and from surface run offs into water systems. There are two types of synthetic anion receptor, charged and neutral, with the latter being the inspiration for the receptors used within this thesis and will primarily be discussed.

This area of research currently receives a vast amount of research interest due to the importance of anion transport within biological systems such as transport across cell membranes and lipid bilayers,[93–96] but also for their potential use for therapeutics in treating diseases caused my dysregulation of anions such as chloride with cystic fibrosis[93] and iodide thyroid cancer.[96,97] This area of supramolecular chemistry has several applications, such as: the separation of anion mixtures;[98–100] organocatalysis[100,101] and for the production of anion sensors (Figure 1.4.2.1).[94,102]

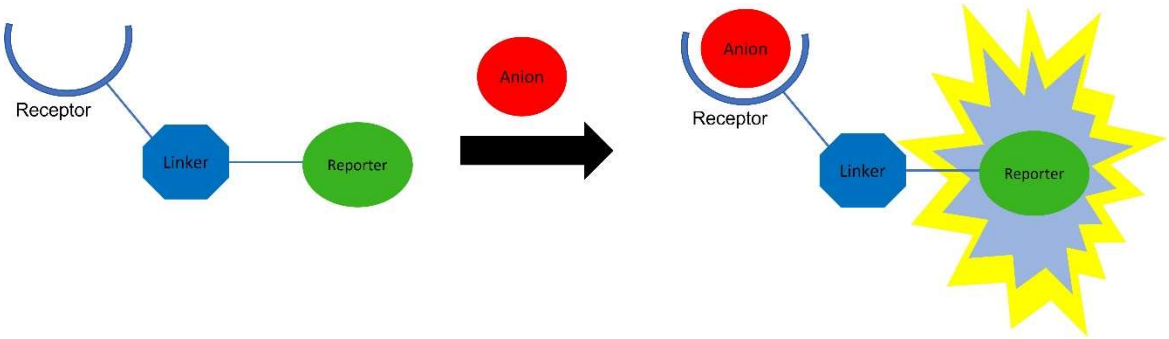

Figure 1.4.2.1 – Cartoon representation of an anion sensor. Indicating the complementary interaction between an anion analyte and a receptor binding pocket. The linker which is capable of reporting this binding event converts the receptor into a sensor. In this cartoon, an ''off-on'' response is depicted from binding an anion.

To develop a receptor that is selective towards a specific analyte, multiple interactions between a host and a guest in a complementary manner must be considered. There are several strategies that can be followed in the design of artificial receptors with optimal selectivity toward a particular ion when considering neutral, hydrogen bond receptors. The receptor may contain a variety of functionalities, such as amides, ureas, and hydroxyl groups, which must be organised to complement the size and shape of the analyte.[103] The topology of the receptor is of importance in determining the overall receptor-ion interactions, here intramolecular

hydrogen bonding can play a key role in the stabilisation of structures and also in modulating the receptor-anion binding affinity.[104] This effect explained the higher affinity for pyridine-2,6-dicarboxamide based receptors compared to their isophthaloyldiaminde congeners (**4** and **5**, Figure 1.4.2.2).[104,105] This is due to the intramolecular amide proton to pyridine nitrogen hydrogen bonding locks the molecule into a 'pocketlike' structure, forcing all HBD and HBA to face inwards, resulting in optimised anion binding; this theory was supported by solid state structural analysis by Gale and co-workers.[104,106–108]

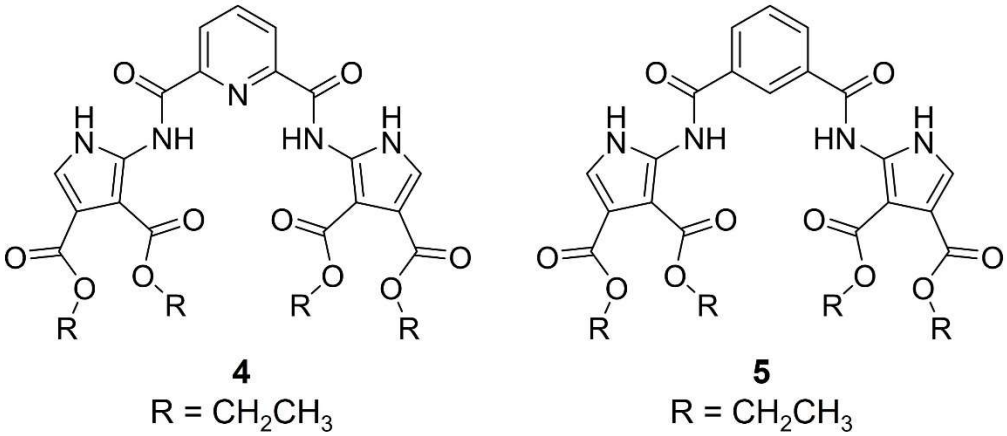

Figure 1.4.2.2 – Structures of compounds **4** and **5** reported be Sessler and co-workers.[104,105]

1.4.2.1 Charged receptors for anion binding

Simmons and Park in 1968 reported the first example of a synthetic anion receptor (**6,** Figure 1.4.2.3) binding an anion.[109] This was a charged receptor and was designed around a tripodal ammonium bridge. This receptor was shown to favourably bind chloride anions over bromide and showed no indication of binding with iodide anions in a 50% TFA solution.[109] This work is also an early example of using nuclear magnetic resonance (NMR) to monitor binding events. X-ray crystallography by Marsh and co-workers in 1975 showed that the protons on the ammoniums NHs faced inwards towards the chloride anion, although full elucidation of the structure was not complete.[110]

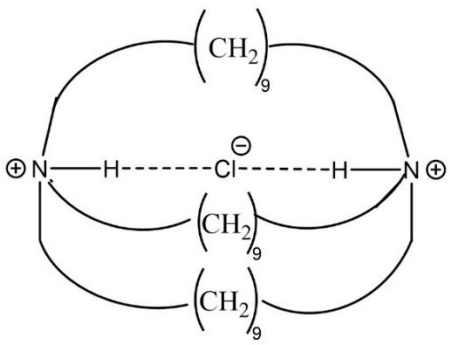

Figure 1.4.2.3 – The first synthetic anion receptor **6**, synthesised by Simmons and Park.[109]

Additional molecular receptor designs include the tripodal, this model exhibits three arms to which ligating groups can be attached and tailored, it is because of this that this design provides control of binding properties such as complex stability and its selectivity. The selectivity of these receptors are greatly related to the rigidity of its arms and its cavity size.[111–114] Tripodal topologies have been shown to demonstrate some advantages over monopodal and bipodal: (i) tripodal ligands often bind metal ions very strongly due to the enhanced chelating effects; and (ii) the steric bulkiness of tripodal ligands is highly tuneable which allows for controlled reactivity to metal ions. As a result of these benefits, the design and development of artificial tripodal receptor system represent an active area in supramolecular chemistry.[114–116]

Lehn and co-workers subsequently designed variety of macro bicyclic and macro tricyclic ammonium based receptors (cryptands) which optimized the anion fit within the charged cavity for stronger binding (Figure 1.4.2.4).[117] Scmidtchen and co-workers then designed and synthesised a series of cages with quaternary ammonium groups that were capable of binding anions within the cage through electrostatic interactions; the selectivity towards an anion was increased by altering the alkyl chain length between the ammonium centres (Figure 1.4.2.4).[118] The disadvantage to using a charged receptor is that any anion will have to compete with counter ions of the receptor, and it is for this reason that zwitterionic or neutral anion receptors started to be developed.

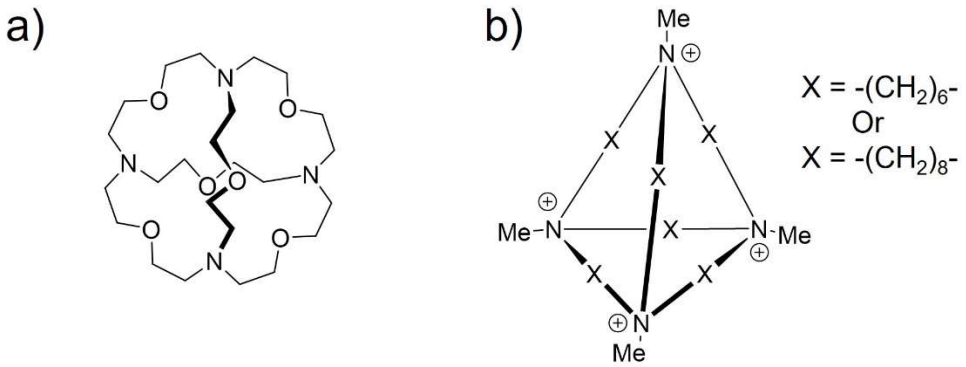

Figure 1.4.2.4 – Examples of macrocyclic anion receptors. a) amine based cryptand produced by Lehn and co-workers[117] and b) ammonium cage produced by Scmidtchen and co-workers.[118]

1.4.2.2 Neutral receptors for anion binding.

The first neutral hydrogen bonding anion receptor (**7,** Figure 1.4.2.5) was reported in 1986 by Pascal and co-workers.[119] This receptor utilises the previously discussed tripodal capsule design, binding an anion through the formation of three hydrogen bonds from the amide NHs. This receptor was found to bind fluoride in a DMSO-d_6 solution using tetrabutylammonium fluoride. Anion binding was determined by ^{1}H and ^{19}F NMR spectroscopic studies.[119] This early work was then followed by polyamine macrocycles[120,121] (**8**, Figure 1.4.2.5) and cages,[122–124] whereby the protonated forms can act as anion receptors in both organic and aqueous media.

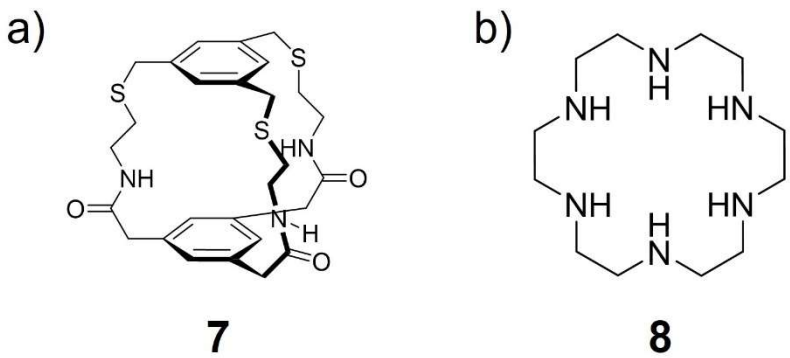

Figure 1.4.2.5 – Early neutral anion receptors. a) The first reported neutral receptor by Pascal and co-workers[119] and b) an example of a polyamine macrocycle reported by Lehn and co-workers.[124]

Urea and thiourea units are currently used within anion receptor design due to their ability to act as hydrogen bond donors.[125,126] They became more prevalent in this area following work on urea-anion interactions by Wilcock and Hamilton, with a variety of receptors reported using one or more urea units.[127,128] Anion receptors containing these groups have been shown to act as selective receptors in both polar and non-polar solvents.[113,128–130] The hydrogen atoms on the nitrogen atoms within the urea or thiourea binding site are capable of forming parallel orientated hydrogen bonds, this enables complementarity with oxygen atoms within oxo anions molecular structure, thus resulting in the formation of an eight-membered ring (Figure 1.4.2.6 a). Bifurcated hydrogen bonds between these units and a spherical anion can form six membered rings upon complexation (Figure 1.4.2.6 b).[103]

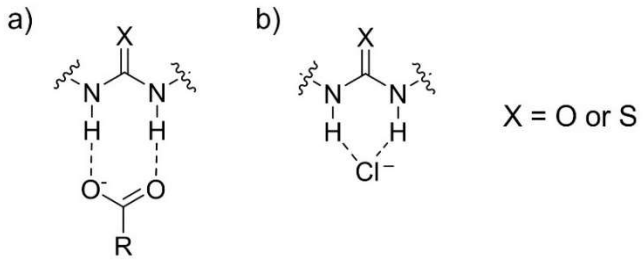

Figure 1.4.2.6 – Hydrogen bonding motifs of urea and thiourea units, a) parallel orientated forming an eight membered ring with oxo anions and b) bifurcated hydrogen bonds forming a six-membered ring with spherical anions.

The first urea receptors reported within literature were simple diphenyl ureas (**9**-**11** Figure 1.4.2.7).[103,131] These receptors are planar, and the size of the substituent directly attached to the aromatic unit does not induce any steric hindrance for hydrogen bond formation. However, the electron withdrawing NO_2 substituent increased the acidity of the urea group and as a result its hydrogen bond donating properties.[103,131,132] There are numerous articles of anion binding using a diphenylurea[133,134] or a diphenylthiourea[135,136] as they are the simplest symmetrical receptor, with the parent structure being modified through different R groups on the aromatic ring.[103] The strength and the stability of the hydrogen bonds formed are heavily

influenced by the acidity of the receptor (HBD) and the basicity of the anion (HBA), therefore, the most electronegative anions such as fluorine and oxygen form the strongest hydrogen bonds compared to carboxylates and oxoanions.[103] However, with sufficiently basic anions, deprotonation of the urea/thiourea NH can occur, and in the case of fluoride the deprotonation will result in the formation of the stable HF_2^- anion, which could then be bound by the deprotonated receptor.[131,137,138]

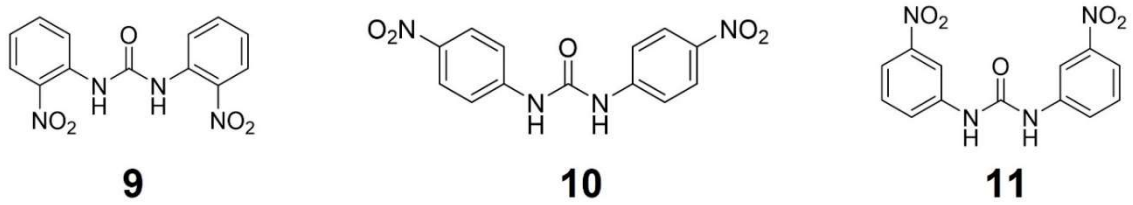

Figure 1.4.2.7 – The first urea anion receptors reported, **9** = bis(2-nitrophenyl)urea, **10** = bis(4-nitrophenyl)urea and **11** = bis(5-nitrophenyl)urea, as reported by Panunto and co-workers.[131]

Gunnlaugasson and co-workers also observed that the addition of a highly basic anion in a polar solvent induced complete thiourea deprotonation.[139] Fabbrizzi and co-workers reported a detailed study of this proton transfer from the urea group to F^- through a series of spectrophotometric titrations with oxoanions and halides in acetonitrile, their published results detailed that the decrease in anion basicity is also the resulting decrease in stability constant observed.[132] The acidity of the thiourea or urea group is influenced by the directly attached substituents, resulting in those receptors with aromatic substituents forming stronger complexes than those receptors with alkyl groups on either both sides of the urea or one due to the increased NH acidity. The use of a thiourea over a urea group results in a higher acidity as thiourea is more acidic than urea (thiourea pK_a = 21.1, urea pK_a = 26.9 in DMSO).[140] This enables thioureas to form a stronger hydrogen bond, however, this also enables these receptors to be more easily deprotonated, which further increased with increasing receptor acidity.

Wu and co-workers have reported a tetra-urea receptor (**12**, Figure 1.4.2.8 **a**) which in the solid state was found to coordinate with phosphate anions. Intriguingly, in the solid state this compound was shown to form a triple helix like structure, where three ligands enfold around two PO_4^{3-} anions (Figure 1.4.2.8 b and c); here six urea groups bind to the phosphate anion through the formation of twelve hydrogen bonds. This complex was also studied in the solution state through ^{1}H NMR titrations in a DMSO-d_6 solution and also found that the most prevalent species was a 3:2 host:guest aggregate.[141]

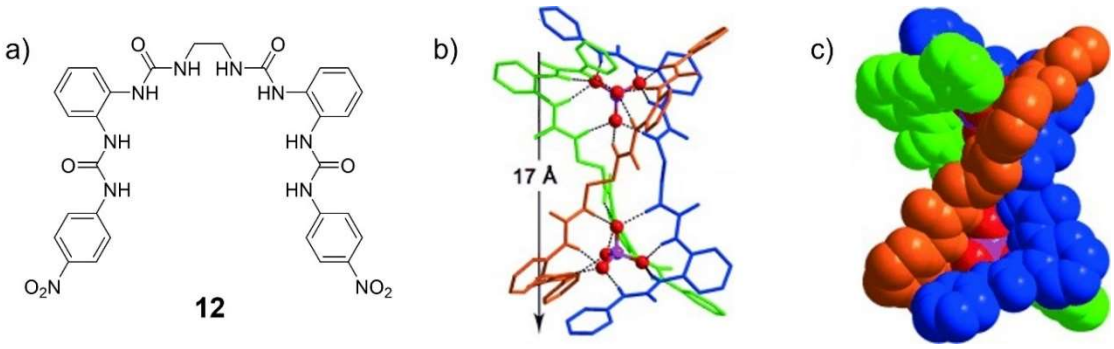

Figure 1.4.2.8 – Tetra urea receptor **12** produced by Wu and co-workers. a) chemdraw structure of receptor **12**, b) side view of x-ray single crystal structure of triple helical phosphate anion complex – grey dashed line represents hydrogen bonding. Hydrogens and nitro groups omitted for clarity and c) space filling representation of the complex.[141] b and c reproduced from ref. 141 with permission from Wiley, copyright 2011.

The inclusion of additional hydrogen bonding groups to a receptor, in theory should increase the stability of any complexes formed, work by Gale and co-workers studied diindolylurea and thiourea receptors (**13** and **14**, Figure 1.4.2.9) in a DMSO-d_6 and water solution with anions using NMR. They concluded that these receptors were selective towards oxo-anions, and in particular $H_2PO_4^-$ with similar observations for the carbazolylurea analogue.[142]

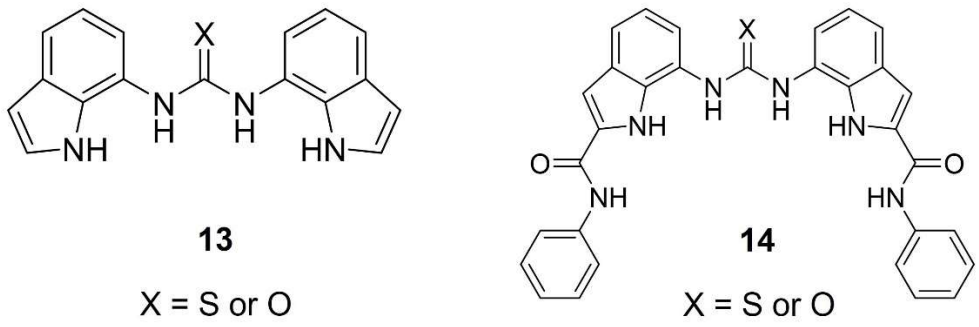

Figure 1.4.2.9 - Diindolylurea and thiourea receptors produced by Gale and co-workers.[142]

In a further body of work by Gale and co-workers, utilising a urea moiety to design transmembrane anionphores, the ortho-phenylene bis ureas **15a-c** and **16a-d (**Figure 1.4.2.10) were used. These compounds (**15a-c** and **16a-d)** displayed high intrinsic anionphoric activity at low transporter loading, with **15a** and **15b** being the most active when based on halogenated scaffolds. All compounds were found to mediate chloride-iodide exchange in Fisher rat thyroid cells when tested with the halide sensor YFP=H148Q/I152L (YFP-FRT cells), which resulted in a decay of YFP fluorescence.[143]

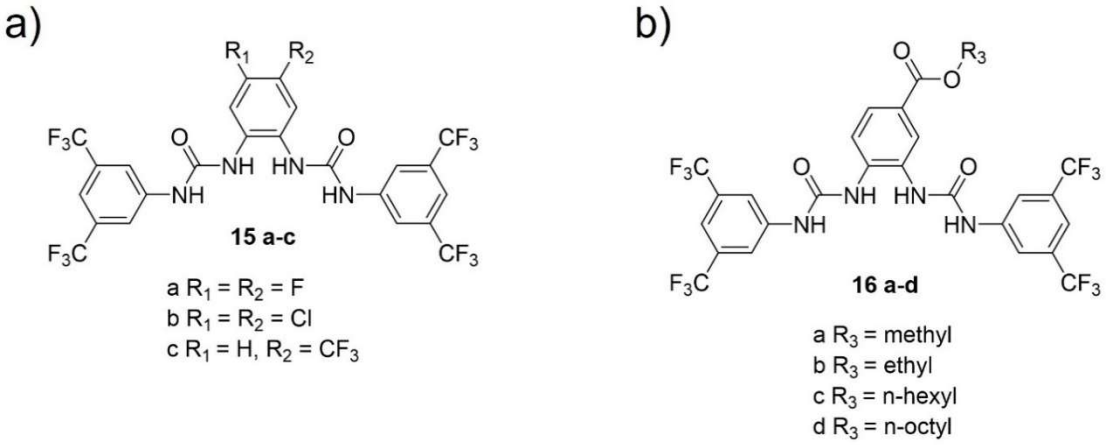

Figure 1.4.2.10 – Structures of bis urea transmembrane anionphores by Gale and co-workers a) compounds **15a-c** and b) compounds **16a-d**.[143]

Anion receptors typically use NH and OH groups as their principal hydrogen bond donor groups, although the focus of the work discussed here has been NH groups. More recently new

motifs and scaffolds for anion binding have been developed, arylboronic acids and phosphazanes[144] are emerging inorganic anion receptors. Arylboronic acids have demonstrated their ability to form covalent adducts with basic anions such as fluoride and hydroxide with the acidic boron centre. Work by Martinez and Yatsimirsky[145] showed that not only do arylboronic acids form covalent adducts but they also interact with anions through hydrogen bonding via the $B(OH)_2$ hydroxyl groups; using both ^1H and ^{11}B NMR binding studies in both DMSO-d_6 and CD_3CN solutions they found that less basic anions such as chloride, bromide, hydrogen sulphate and acetate hydrogen bonded complexes were found to dominate in a DMSO solution compared to a covalent adduct dominating in the same solvent for fluoride and dihydrogen phosphate.[145]

1.4.3 Neutral guest coordination

The ability to design molecular receptors that can recognise neutral or charged species with a high selectivity is one of the main aims within supramolecular chemistry.[146,147] Such a binding between uncharged host and uncharged guests is especially interesting, this is because there are no strong binding forces such as full positive or negative charges involved. Host/guest binding must therefore be due to several (multiple) weak attractive interactions of the hydrogen bond, dipole-dipole or hydrophobic type.[148] Utilization of hydrogen bonding groups in the scaffold of a receptor to complex neutral molecules requires precise design. This is in comparison to the molecular structures used for cation or anion recognition where ionic forces are sometimes included to make a strong and stable complex. Recognition of neutral molecules with biological significance such as urea (and its derivatives),[149,150] biotin,[151] carboxylic acids[152] and amino acids[153] have potential biomedical and clinical applications.[154]

Calix[4]pyrroles are readily used as receptors for anions, however, in 1996 work by Sessler and co-workers demonstrated that this macrocycle was not only able to bind anionic substrates such as chloride and fluoride but also neutral substrates. They studied the binding of a range of alcohols and amines with calix[4]pyrrole using ^1H NMR in benzene-d_6.[155] They

observed that when increasing the bulk around the HBA oxygen atom there was a decrease in binding constant, with methanol displaying the strongest binding with a K_a of 12.7 ± 1.0 M^{-1} with ethanol and benzyl alcohol displaying K_a values around 10 M^{-1}. For amide substrates they demonstrated higher association for secondary formamide (N-formyl glycine ethyl ester, K_a = 13.3 ± 1.0 M^{-1}) than for tertiary amines such as DMF (K_a = 11.3 ± 0.8 M^{-1}), DMF was also shown to bind more strongly than N,N-dimethylacetamide (K_a = 9.0 ± 0.9 M^{-1}).[155]

Calixarenes are known for inclusion properties of neutral molecules due to their unique three-dimensional shapes.[156,157] Lhoták and co-workers noted that during their complexation studies of bis(N'-p-nitrophenylureido)calix[4]arenes (**18**) and bis(ureido)calix[4]arenes (**19**) that the binding of anions in more polar solvents, such as DMSO-d_6, is diminished and the interactions with DMSO were observed instead of the intended anion binding.[156] NMR titration studies conducted in CD_3Cl showed that **18** would bind DMSO with an association constant of 33 M^{-1} whereas, **19** bound DMSO with a binding constant of 5 M^{-1}.[156]

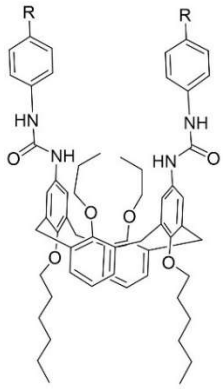

18 R = NO_2
19 R = H

Figure 1.4.3.1 – Structure of compounds **18** and **19** as synthesised by Lhoták and co-workers.[156]

Goswami and co-workers developed a fluorescent macrocycle (**17**, Figure 1.4.3.2) as an artificial receptor for urea, with a potential use for clinical identification of diabetes, kidney or thyroid diseases.[158] Urea is typically a difficult to recognise by synthetic receptors due to weak

intermolecular forces of attraction and weak solubility in organic solvents such as chloroform. However, urea does contain both hydrogen bond donor and acceptor sites which can be utilised in the formation of supramolecular complexes. This receptor was shown to encircle a urea molecule, which formed a 1:1 complex in $CDCl_3$ that was monitored through the downfield change in chemical shift of the urea NHs. Goswami and co-workers also observed a noticeable quenching of fluorescence (approximately 50%) of the macrocycle upon the addition of urea.[158]

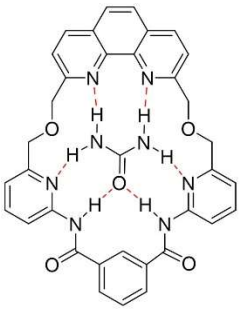

17

Figure 1.4.3.2 – The structure of the 1:1 macrocycle:urea complex (**17**) synthesised by Goswami and co-workers.[158]

A lot of studies involving hydrogen bonding are typically conducted in an organic solvent, this in part is due to the scaffolds used which are easier to handle in this media, but it is also because hydrogen bonds in water are generally weaker as both the donor and acceptor are solvated, thus the water must be displaced from both components and therefore, binding affinities are usually small.[159] A supramolecular chemistry aim is to mimic biological recognition not only to gain further insights and understanding, but also for biomedical applications. To develop molecular recognition for biomedical applications, the solvent of choice needs to water. However, the design and synthesis of water soluble systems can be challenging but is becoming more recognised.[159–161]

A bicyclic hexaurea (**20**) synthesised by Davies and co-workers, has proved to be successful in the binding of glucose – a biologically important target with the potential for applications within diabetes management, a current health crisis.[162] This bicyclic structure is very

complimentary to glucose and modelling has shown that it binds to glucose through 10 hydrogen bonds as well as CH-π interactions with a binding affinity of approximately 18600 M^{-1} in D_2O using ^1H NMR titration techniques, and further confirmed using isothermal titration calorimetry (ITC). Not only did this compound show high binding but also selectivity for glucose and closely related substrates (Methyl β-D-glucoside, glucuronic acid and xylose with K_a values of 7,900, 5,300 and 5,800 M^{-1} respectively).[162] This compound showed such promise, the rights to this glucose receptor were bought by a pharmaceutical company, Novo Nordisk, who specialise in diabetes.[162]

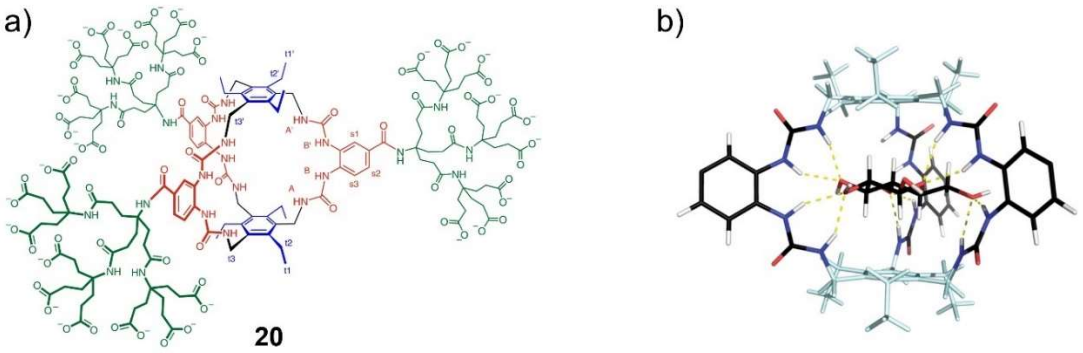

Figure 1.4.3.3 - a) Chemical structure of glucose receptor **20**, polar groups are displayed in red, hydrophobic groups in blue and water solubilising groups in green. b) the molecular modelling structure of **20** showing the hexaurea binding site (side-chains omitted for clarity) and hydrogen bonding depicted as yellow dashed lines.[162] Reproduced from ref. 162 with permission from Nature Research, Copyright 2019.

1.5 PhD aim and objectives.

1.5.1 PhD aim

To be able to use low molecular weight organic receptors to develop novel technologies for chemical detection, capture and remediation.

1.5.2 PhD objectives

Chapter 2 aims to use association constants derived from non-specific hydrogen bonded complexes and computationally determined parameters to produce a predictive model for improved chemical warfare agent simulant selection. Chapter 3 aims to investigate the hydrolytic breakdown of potential chemical warfare agent simulants o produce predictive models for the hydrolytic breakdown of chemical warfare agents using exhaustive parameter searches. Finally, chapter 4 aims to synthesise and elucidate the physicochemical properties of supramolecular self-associating amphiphiles (SSAs) and their ability to uptake and capture environmental pollutants.

Chapter 2 – Development of chemical warfare agent simulants using association constant prediction.

2.1 Introduction

Chemical warfare agents (CWAs) are extremely toxic synthetic chemicals that can be dispersed as a gas, liquid, or an aerosol.[163] They have a lethal or incapacitating effect on humans and other organisms. Compounds are categorised as CWAs based on their properties, high toxicity, imperceptibility to senses, their rapidity of action after dissemination and their persistency. These CWAs are usually used during periods of conflict to indiscriminately incapacitate the opposition and are listed in the Chemical Weapons Convention (CWC).[163] Poisonous compounds have been integral parts of human evolution, with some of the earliest mention of chemical weapons being part of the Greek myth of Hercules, who poisoned his arrows with venom from hydra monster as well as in the Iliad and the odyssey it was alluded to the use of poisoned arrows.[164] During the Peloponnesian war between Athens and Sparta, Spartan forces placed a lighted mixture of wood, pitch, and sulphur under the walls hoping that the noxious smoke would incapacitate the Athenians.[165]

The use of poisonous chemicals from plants is also widely documented throughout the Middle Ages, although it wasn't until the 19th century that mass production and deployment of chemical agents in warfare started.[166] World War 1 saw the beginning of the modern era of chemical warfare,[166] with the use of gases such as chlorine and phosgene, and most notably bis(2-chloroethyl) sulphide, commonly known as sulphur mustard or HD (Figure 2.1.1), which caused over 100,000 deaths and 1.2 million casualties.[166] During World War 2, Zyklon B (hydrogen cyanide gas) was used by the Nazis to kill millions of Jews in concentration camps.[167] Since then, there have been several chemicals designed and synthesised for the purpose of chemical warfare with the development of the organophosphorus (OP) G-series (German-type) nerve agents (NAs),[166] the V-series,[168] and the Russian series of nerve agents, Novicok.[169]

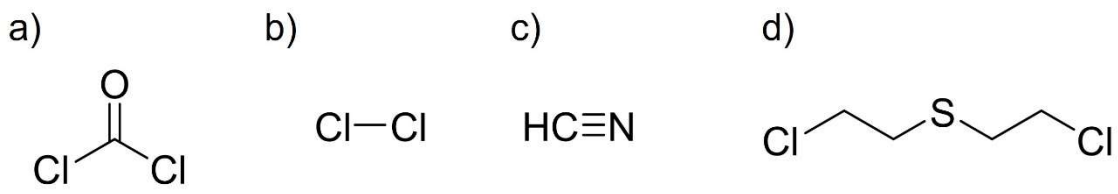

Figure 2.1.1 – Structures of some modern era CWAs, a) phosgene, b) chlorine, c) hydrogen cyanide and d) sulphur mustard (HD).

There are various classes of these compounds with pronounced physicochemical, physiological, and chemical properties, they can be classified by their volatility, chemical structure, and their use. When classifying based on volatility, CWAs can be deemed to be persistent or non-persistent. Volatile agents such as phosgene and chlorine are non-persistent, whereas the less volatile agents such as sulphur mustard are considered persistent. Non-persistent CWAs are those that when released disperse quickly leaving no liquid contamination; persistent CWAs are those which evaporate slowly, and give off a vapour, which results in the agent being dangerous until all the agent has been evaporated or decontaminated to render it ineffective. Most CWAs can be classified as follows: organophosphorus (OP), organosulfur, organofluoride, and arsenicals. Although the most common classification is based on their use and physiological effects as follows: Nerve agents (these agents vary from non-persistent agents like sarin to persistent agents such as VX), vesicants (also called blistering agents- these agents are classified as persistent), blood agents or cyanogenic agents (non-persistent), choking agents/pulmonary agents (non-persistent), riot control agents (such as tear gas – which are non-persistent), and psychomimetic agents. The focus of some of the work within this thesis is based around nerve agents (chapter 2 and 3) so only they will be discussed further.

In 1936, G. Schrader and co-workers associated with I. G. Farbenindustrie (Leverkusen, Germany) prepared tabun (GA), closely followed by sarin (GB) in 1938 and then soman (GD) in 1944, with cyclosarin (GF) being later developed in 1948. These compounds then became open knowledge to the world after WW2 (Figure 2.1.2).[170] During the 1950s, VX was first prepared

whilst trying to synthesise new insecticides. VX is more potent and stable than sarin, with a lethal dose (LD_{50}) in the ranges from as little as 10 mg in dermal exposure cases to 25-30 mg through inhalation.[171] Whereas, sarin has an LD_{50} of 1700 mg.[172] The low volatility of VX makes it more stable than other nerve agents like sarin that are quite volatile.

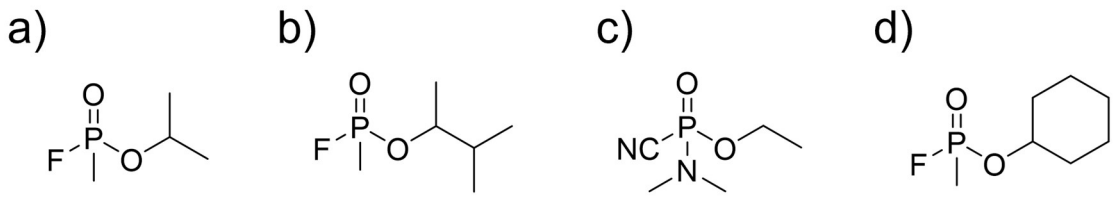

Figure 2.1.2 – Structures of the G series of nerve agents, a) sarin (GB), b) soman (GD), c) tabun (GA) and d) cyclosarin (GF).

Nerve agents (NAs) represent one of the most lethal classes of CWAs, with the lethal dose of sarin at approximately 28-35 mg/m^3/min, which is around 43 times more lethal than phosgene with a lethal dose around 1,500 mg/m^3/min.[173] NAs have rapid and severe effects on both humans and animals, they can cause death within minutes up to a few hours depending on the concentration of exposure.[174] This is due to their ability to block the action of the critical central nervous system enzyme, acetylcholinesterase (AChE), this enzyme is responsible for the breakdown of the neuron transmitter acetylcholine which is found in post-synaptic membranes and neuromuscular junctions.[170,175] NAs are a class of OP compounds, it is this phosphoryl unit that can irreversibly bind to the catalytic site of AChE, followed by a dealkylation step known as 'aging', resulting in the loss of enzyme function and a build-up of acetylcholine (scheme 1).[173,176–178] Acute cholinergic syndrome associated with sarin occurs when AChE is inhibited by 75-80%,[179] the symptoms include: constriction of pupils, involuntary urination and defecation and most critically is paralysis of respiratory muscles which leads to death by asphyxiation.[163]

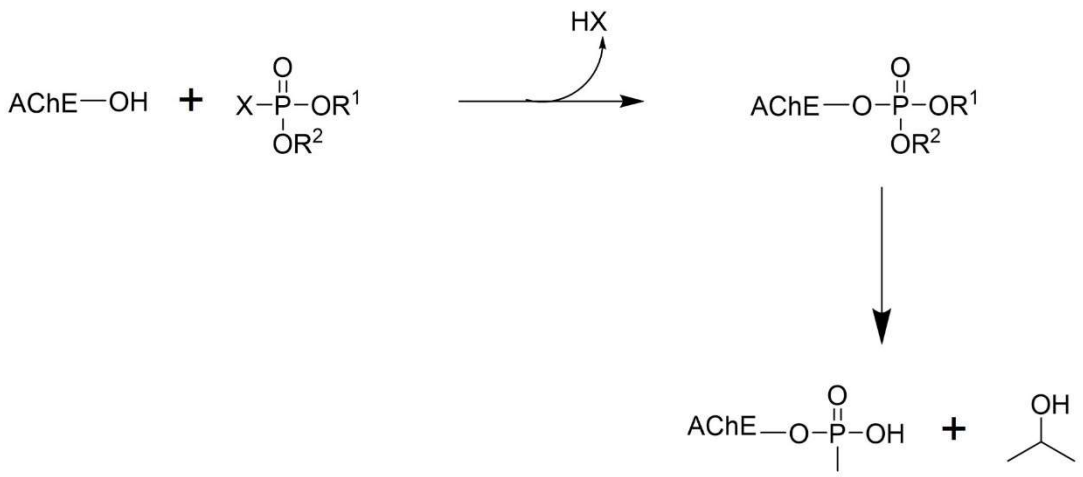

Scheme 1 – Binding and subsequent aging of an OP CWA to the enzyme AChE, resulting in the loss enzyme function.[174] The leaving group of the CWA is represented as X, in the case of GB, GD and GF X is fluorine, in the case of GA this leaving group is CN.

The simplicity of their production makes this type of CWA very attractive as a weapon for terrorists. This has been highlighted through the Tokyo subway attacks in 1995,[180] where 5,500 people were injured with remarkably only 14 fatalities. However, this number is dramatically lower than what could have been due to the inefficient dispersal method (pouches placed on the subway and pierced with the end of an umbrella),[181] with the same perpetrators behind a sarin attack nine months prior killing 8 people and injuring 500 people in Matsumoto. More recently, there have been large scale attacks using sarin in Syria in 2013,[182] with further small scale uses within Malaysia in 2017 with the assassination of Kim Jong-nam with the nerve agent VX,[183] and the UK in 2018 with the poisoning of Sergei Skripal in Salisbury with a Russian nerve agent Novicok,[169,184] with the same agent being used again in 2020 in Germany on the Russian opposition leader, Alexei Navalny.[185]

In response to the serious national and global threats that CWAs pose, intense efforts into research for novel sensitive and selective detection methods is of high global importance.[1,166,174,186–188] Due to the nature of nerve agents, there are very strict legal restrictions placed upon their access, therefore, comparatively innocuous, and readily available molecules

are used within research, as simulants. It is these OP simulants (some commonly used simulants are presented in Figure 2.1.3) that are typically the only option for developing novel detection methodologies to help combat OP CWA release. However, no single simulant can mimic all properties of an OP CWA without inheriting the undesirable toxicity of the live agent itself, therefore, simulants can only provide an estimate measure of a CWAs behaviour in the conditions measured, as they are unable to provide the exact behaviour.[1,163,166,173,174] Therefore, it is vital to consider the properties of any chosen simulant when developing novel OP CWA detection, decontamination or remediation technologies.[189–192]

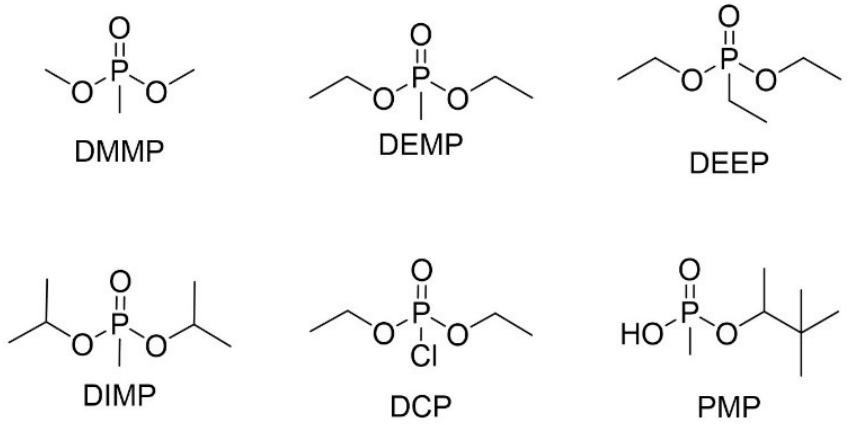

Figure 2.1.3 – Structures of some of the most commonly used OP CWA simulants.

In order to detect the presence of an OP CWA there are a range of commercially available detection equipment, such as the handheld detector AP2C, individual chemical agent detectors and automatic chemical agent detection alarms are capable of accomplishing diverse detection tasks. However, these techniques possess several limitations, such as low specificity, poor sensitivity, and inability to detect and differentiate all CWAs. Therefore, new technologies are needed.[193] Recently, supramolecular chemistry has demonstrated it could fill this role with many exciting reports and applications for chemical sensing.[1,166,193] These results strongly suggest that these sophisticated approaches may generally become more appropriate alternatives for existing detection systems for chemical agents. This has included the

development of fluorescent[194] and luminescent sensors,[195–197] as well as supramolecular organogels capable of acting as both as a sensor and a decontamination method.[198–200]

Anzenbacher and co-workers reported the first example of a fluorescent chemosensor for phosphate recognition.[201] This sensor was able to give a fluorescent turn on response in the presence of the hydrolysis products of sarin, isopropyl methyl phosphonate (IMP) and methyl phosphonate (MP). Seven fluorescent tripodal sensors with a 1,3,5-triethylbenzene core (**21**-**27**, Figure 2.1.4) were found to form 1:1 complexes in DMSO-d_6 10% water with anions through Job plot analysis.[201] They also reported that when conducting fluorescent titrations that the sensors had a dramatic increase in fluorescence when in the presence of strongly bound anions such as, MP, IMP, fluoride, and dihydrogen phosphate, with K_a values ranging from 1.7 x 10^3 to 4.3 x 10^5 M^{-1}. The ability of these sensors to distinguish MP and IMP over other anions were analysed through linear discriminate analysis (LDA) and reported that the sensors gave a fingerprinted response for IMP and MP over anions tested.[201,202]

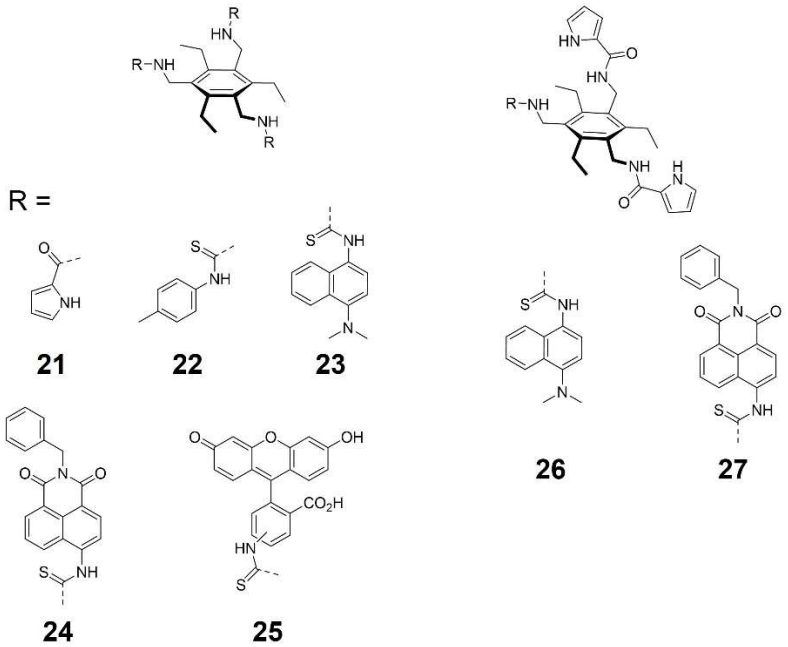

Figure 2.1.4 – Structures of **21**-**27**, synthesised by Anzenbacher and co-workers.[201]

Lanthanide ions have been previously shown to bind organophosphates.[201,203,204] Lanthanide complexes are suited for use as chemical sensors due to their characteristically narrow excitation and emission bands and their intense fluorescence. Jenkins and co-workers used Eu^{3+} ions in combination with molecularly imprinted polymers (MIPs) to create a soman sensor.[205,206] They reported that when the sensor was exposed to pinacolyl methylphosphonate (PMP - soman hydrolysis product, see Figure 2.1.3) there was a significant increase of one of the Eu fluorescence bands (609 nm). Although the response time was limited to the diffusion of the analyte into the MIP, which in this study was reported to be 30 minutes.[201,205,206]

Sfrazzetto and co-workers obtained the first fluorescent uranyl-receptor for the supramolecular recognition of DMMP, through the functionalisation of a uranyl-salen backbone with bodipy (Figure 2.1.5 inset), a strong fluorophore.[207,208] Binding constants were measured through fluorescence titrations and demonstrated a K_a value of 1.86 M^{-1}.[208] This receptor demonstrated a strong *turn-on* fluorescence response (Figure 2.1.5), showing selectivity even when in the presence of acetone and other analytes[207,208]

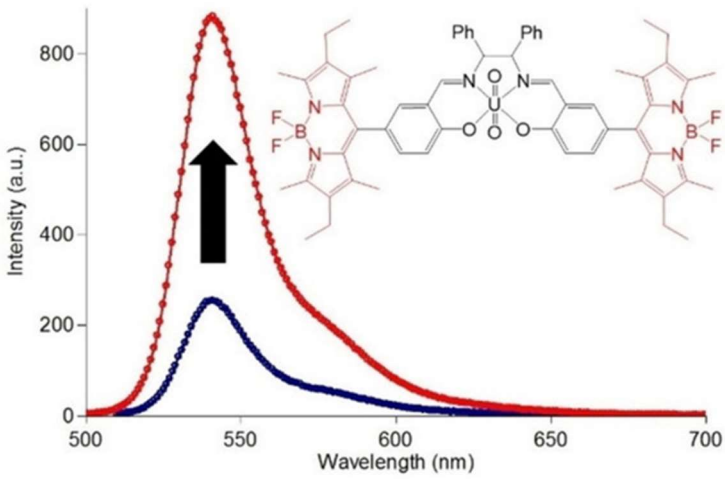

Figure 2.1.5 – Fluorescence response of the bodipy uranyl-salen complex (shown inset) to DMMP.[208] Reproduced from ref. 208 with permission from Bentham Science.

In a large body of work, Gale and co-workers reported several neutral ureas/thioureas[209–211] or polyureas that are capable of recognising the CWA soman and other

OP species. The recognition of these species is related to the formation of hydrogen bonds between the urea/thiourea host and the OP guests. They utilised the 1,3-diindolylureas and thioureas (compounds **28**-**32**, Figure 2.1.6) based on their ability to selectively coordinate to phosphate anions in polar conditions, through hydrogen bonding interactions.[209] Job plot analysis of **28** with GD demonstrated 1:1 complex stoichiometry, and rather unexpectedly **30** with GD resulted in the formation of a 2:1 (host:guest) complex. DFT modelling of **31** with GD indicated the formation of a 1:1 complex through the formation of four hydrogen bonds between the receptor and GD (Figure 2.1.6); three to the P=O oxygen and one from an indole NH to the fluorine atom. It was also noted that this modelling was conducted using gas phase measurements and may not be representative of solution state binding, highlighting that the NH-F hydrogen bond was not noted from their experimental data.[209]

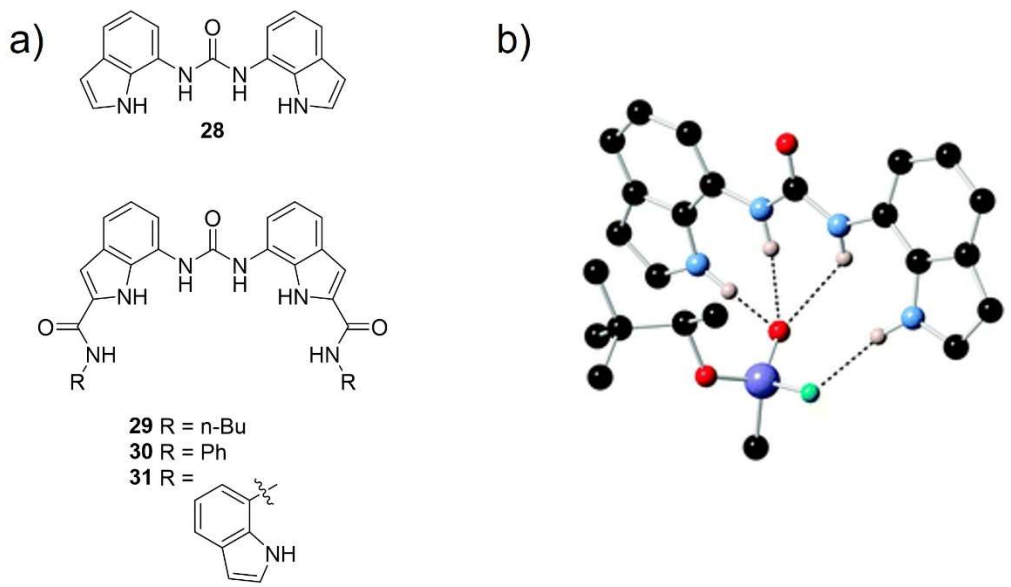

Figure 2.1.6 – a) structures of **28**-**31** as reported by Gale and co-workers, b) DFT modelling of **28** with soman.[209] Reproduced from ref. 209 with permission from the Royal Society of Chemistry, copyright 2012.

Supramolecular gels are a class of gels that are able to form a gel through the formation of non-covalent interactions between monomeric units resulting in fibre formation.[212] Stimuli-responsive supramolecular gels have potential applications as sensors, due to their ability to change physical properties in the presence of specific analytes.[213,214] The sensing of OP CWAs by

these systems is due to the possibility of the CWA or simulant to form or disrupt hydrogen bonds, which leads to the disassembly of the gel structure, this is due to the CWA or simulant being able to disrupt the self-association processes that form the gel fibre network. Following their work on OP CWA recognition through hydrogen bond formation, Gale and co-workers developed a new OP CWA sensing system using a supramolecular gel formed from bis and tris ureas (Figure 2.1.7) that had previously been shown to gelate in organic solvents. They reported that the gel formation of **35** was perturbed by the greatest extent to the presence of the OP CWA simulant, DMMP, with the gel formation delayed by four minutes upon DMMP addition. Analogous experiments were conducted utilising the NA, soman. The results from these studies showed that soman behaved in a similar way to that of DMMP, however, lower concentrations of soman were needed to completely stop gel formation.[215]

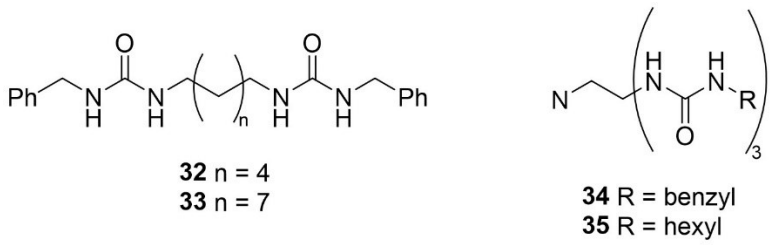

Figure 2.1.7 – Bis and tris ureas **32**-**35** synthesised by Gale and co-workers.[215]

Further work led to the production of a simple electrical sensing system, where the disruption of the organogels in the presence of the CWA soman, and simulants dimethyl methyl phosphonate (DMMP) and diethyl chlorophosphate (DCP) resulted in the completion of a simple electrical circuit switching on a LED. This study also highlighted the importance of simulant choice, and that not all simulants are appropriate for all studies. They noted that the simulant DCP didn't result in the most comparable results to that of the live agent itself, due to the enhanced reactivity of chloride leaving group of DCP.[200]

In addition, the same group developed a further series of responsive supramolecular organogels, that not only disclose the presence of CWA liquid and vapours through a naked eye,

observable colour change of red to yellow (Figure 2.1.8) but also as the potential use as a decontamination tool. The gels red colour came from the use of an oximate decontaminate which reacts with the CWA as it diffuses through the gel. When the decontaminate is loaded in high concentrations it has the potential to give local decontaminate release when the adsorption limits are reached and oximate is released from the organogels matrix.[198]

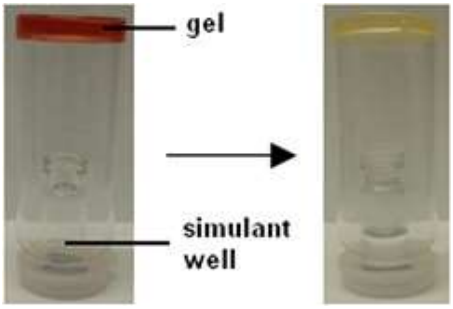

Figure 2.1.8 – Experimental set up of Gale and co-workers responsive supramolecular organogels, highlighting the colour change from red (left) to yellow after being exposed to a simulants vapour (right) from the well placed within the vial.[198] Reproduced from ref. 198 with permission from the Royal Society of Chemistry.

A number of macrocycles have been synthesised that contain a hydrophobic cavity that are able to coordinate non-polar cargo molecules, which has the potential to be compared to the active site of enzymes, and in the area of CWA detection partially inspired by AChE.[207] Recognition of CWAs by cyclodextrins (CDs) has been demonstrated by a few research groups, with α-CDs binding sarin and β-CD binding soman.[216,217] Work by Cragg and co-workers combined both experimental and computational methods to study the inclusion of soman within the hydrophobic cavity of β-CDs and made comparisons to the binding behaviour of other commonly used OP CWA simulants.[191] The authors presented an experimentally derived association constant of 2075 ± 75 M^{-1} in D_2O for GD with a β-CD and confirmed a 1:1 complex stoichiometry through Job plot analysis. A combination of semi-empirical and DFT modelling methods were carried out to further study the inclusion of soman within the cavity, these

researchers confirmed soman recognition in this instance occurred through both hydrophobic effects and the formation of hydrogen bonds (Figure 2.1.9) However, they also reported that the closest structural simulant PMP (hydrolysis product of soman) having a binding constant of 230 ± 26 M^{-1}. Further highlighting the importance of simulant choice within studies, with other simulants tested showing binding constants of values less than 120 M^{-1}.[191] The discrepancy of binding constants determined for GD and simulants highlight the importance of appropriate simulant selection and also the need for more effective simulants for development of new CWA recognition technologies

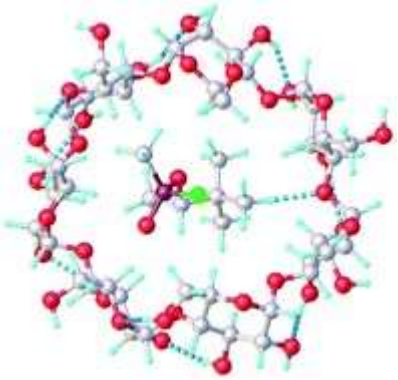

Figure 2.1.9 – Computational model of the inclusion of soman into a β-CD cavity. Dashed lines represent hydrogen bonds.[191] Reproduced from ref. 191 with permission from the Royal Society of Chemistry.

Sambrook and co-workers also demonstrated the inclusion of soman into water soluble p-sulfonatocalix[n]arenes (SCX-n) where n = 4 or 6.[189] Here they compared the binding behaviour of soman and OP simulants with both SCX-4 and SCX-6. The formation of 1:1 complexes were confirmed through Job plot analysis and association constants determined through ^{1}H NMR titrations. The binding of soman within SCX-6 was weaker than that of SCX-4 (<10 M^{-1} compared to 75 M^{-1} ± 2) hypothesised to be due to non-optimal size match between SCX-6 and soman. They also reported that there is little difference between the binding affinity of the cavity for OP simulants versus soman.[189]

In addition, Ward and co-workers have recently reported the use of coordination cages to act as hosts for a range of OP CWA simulants and providing a luminescent response.[218] For these studies they utilised a cage with a bis(pyrazolyl-pyridine) ligand along each edge and a M(II) ion at each vertex, where M = Co or Cd (Figure 2.1.10). The central cavity of these cages had a volume of approximately 400 Å^3, therefore, using Rebeks 55% rule[219] the optimal guest size is expected to be around 220 Å^3.

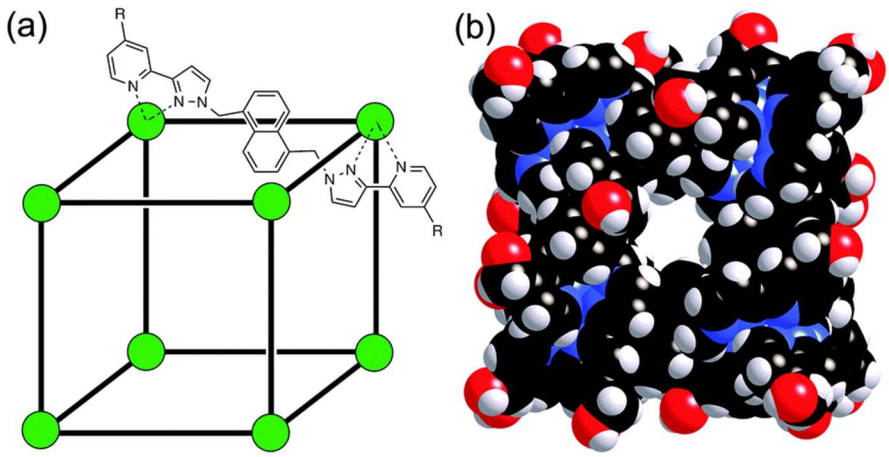

Figure 2.1.10 - An image to illustrate the structure of the cage by Ward and co-workers. a) a sketch showing the ligand arrangement along the cage edges, and b) a space-filling view of the cage. [218] Image is reproduced from ref 218 from the Royal Society of Chemistry.

Association constants were determined using conventional ^{1}H NMR titration techniques in CD_3CN, D_2O and H_2O; The highest K_a value reported was for the OP simulant DIMP in D_2O with a value of 390 ± 80 M^{-1} (Figure 2.1.11).[218] DIMP has a volume of 193 Å^3, which out of all the simulants used has a volume nearest to the 220 Å^3 using Rebeks 55% rule,[219] indicating this is the most optimal guest. For luminescence studies, the Co(II) ions were replaced for Cd(II) due it its non-quenching properties of the luminescence of the naphthyl groups of the cage, this is due to the d^{10} configuration of Cd(II), enabling for a water soluble isostructural cage that could provide a luminescent response upon binding of OP CWA simulants. They reported that upon titration of the phosphate guest there was a steady decrease in luminescence, which demonstrated the

potential for the use of such supramolecular technologies as luminescent CWA sensing systems.[218]

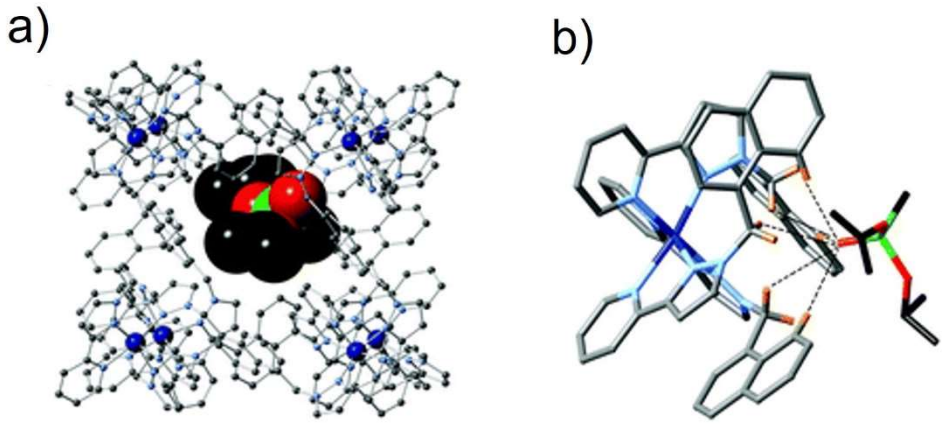

Figure 2.1.11 – Crystal structure of the Co(II) cage host with DIMP guest. a) the host cage showing the DIMP guest (space-filling) and b) showing how the DIMP P═O group interacts with the H-bond donor pockets at the *fac* tris-chelate vertices. Colour code P = green, O = red, N = blue and C = grey.[218] Reproduced from ref. 218 with permission from the Royal Society of Chemistry.

The work in this chapter aims to utilise the experimentally determined association constants (K_{ass}) derived from neutral hydrogen bond thioureas **36**-**39** (Figure 2.1.12) with a range of potential OP CWA simulants **40**-**61** (Figure 2.1.12). It is hypothesised that these values will allow insight into a simulant's principal hydrogen bonding site. This work also looks to determine whether these experimentally derived K_{ass} values can be correlated with values attained from computational modeling for to develop a predictive model for appropriate CWA simulant selection.

The work detailed in this chapter has been published within the following peer-reviewed journal article:

1. R. J. Ellaby, E. R. Clark, N. Allen, F. R. Taylor, K. K. L. Ng, M. Dimitrovski, D. F. Chu, D. P. Mulvihill and J. R. Hiscock, *Org. Biomol. Chem.*, 2021, **19**, 2008–2014.

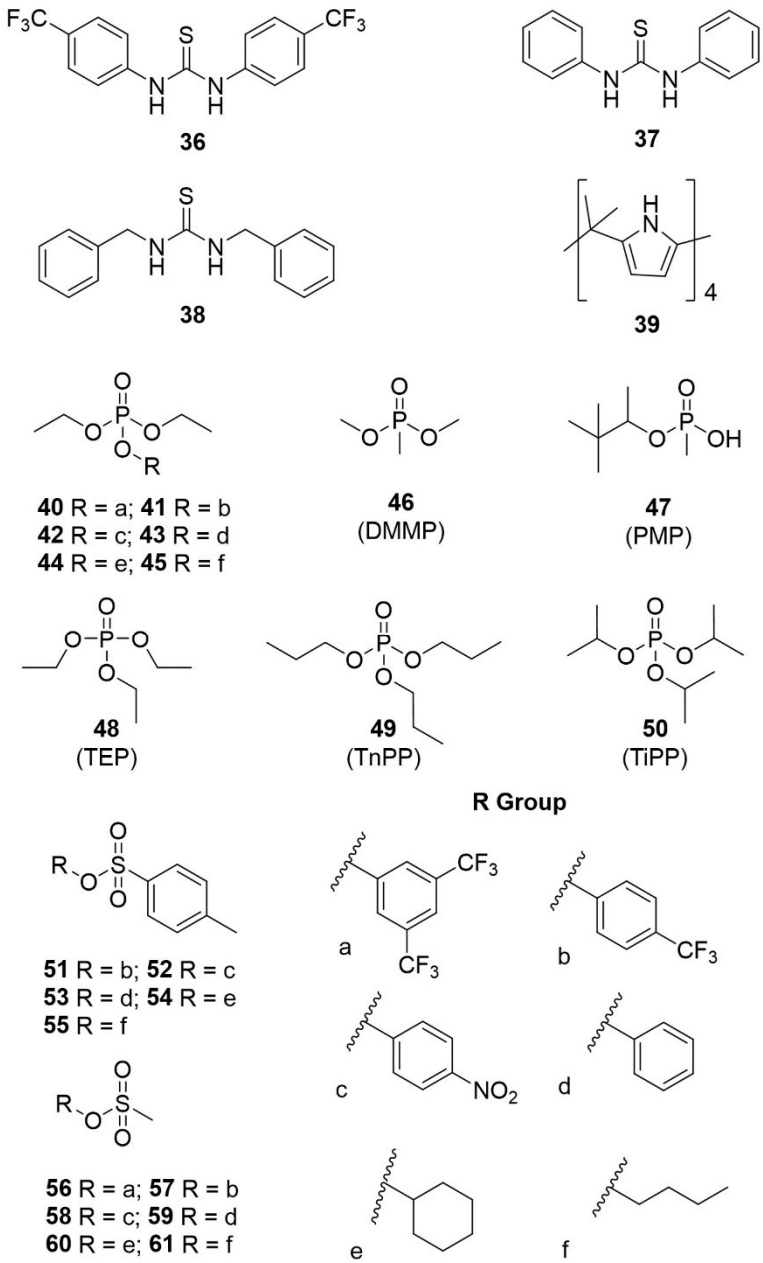

Figure 2.1.12 – Chemical structures of the 23 compounds discussed in this chapter. Compounds **36**-**39** are the non-specific hydrogen bond donating receptors and compounds **40**-**61** are the potentially OP CWA simulants studied.

2.2 Synthesis

Compounds **36**-**38** were synthesised through the reaction of the appropriate isothiocyanate with the corresponding amine. After purification the pure products were obtained as white solids in yields of 74%, 84%, and 73%. Compound **39** was synthesised through

the reaction of acetone with pyrrole. After purification the pure product was obtained as a white solid in a yield of 57%.

The compounds **40**-**45** were synthesised by the reaction of diethylchlorophosphate with the appropriate alcohol in chloroform at room temperature. After purification the pure products of **40**, **41**, **43**-**45** were obtained as colourless oils in yields of 65%, 90%, 64%, 82% and 85% respectively, the pure product of **42** was obtained as a yellow oil in a yield of 80%.

The compounds **51**-**55** were synthesised by the reaction of *p*-toluene sulfonylchloride with the appropriate alcohol in chloroform at room temperature. After purification the pure products of **51**, **53**-**55** were obtained as white solids in yields of 59%, 96%, 72%, 86% respectively. the pure product of **52** was obtained as a pale-yellow solid in a yield of 80%.

The compounds **56**-**61** were synthesised by the reaction of methylsulfonyl chloride with the appropriate alcohol in chloroform at room temperature. After purification the pure products **56, 58**, **59** were obtained as pale white solids in yields of 99%, 61% and 52% respectively. Pure product of **57** was obtained as a pale-yellow solid in a yield of 91%. Pure products of **60** and **61** were obtained as yellow oils in yields of 94% and 70% respectively.

2.3 Association constant determination

It was hypothesised that neutral HBD receptors **36**–**39** (Figure 2.1.12) would form a hydrogen bonded complex with potential OP CWA simulants (**40**–**61**) and because of the designed structural simplicity of **36**-**39**, the strength of the resulting complex formed would depend on the properties relating to the principal HBA group. The experimentally derived association constants (K_{ass}) relating to these hydrogen bonded complexation events could potentially provide information relating to the simulants' **40**-**61** principal HBA site, which corresponds to the unit mimicking the P=O group of a specific OP CWA. As simulants **51**-**61**

contain two HBA units (S=O), there is the potential for two 1:1 complex binding modes, whereas as simulants **40**-**50** only contain one HBA unit (P=O) as illustrated in Figure 2.3.1.

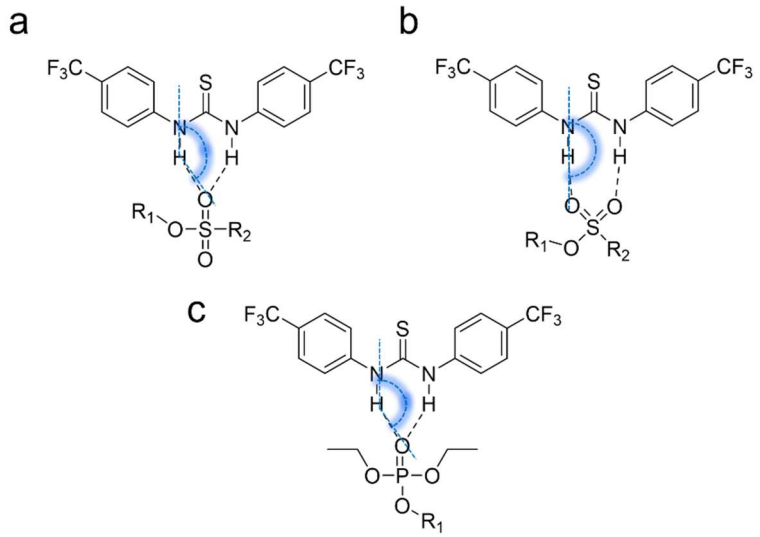

Figure 2.3.1 - Possible binding modes hypothesised for the 1:1 complexes formed between **36** with a) **51**–**61**, b) **51**–**61**, c) **40**–**45.** Hydrogen bonding angles for these binding modes are shown in blue.

A single crystal X-ray structure was obtained and refined by Dr Jennifer Ruth Hiscock for receptor **36** in DMSO and demonstrates the formation of a 1:1 complex with DMSO (Figure 2.3.2).[1] The complex consists of one hydrogen bond from each of the thiourea NH groups to the S=O HBA group of the DMSO solvent molecule. It is therefore logical to hypothesise that analogous hydrogen bonded complexes may be formed between **36**-**39** and simulants **40**–**50**, which contain a single oxygen atom acting as the principal HBA. However, as shown in Figure 2.3.1 when considering simulants **51**–**61**, the formation of hydrogen bonds may be permitted to one (Figure 2.3.1 a) or both atoms (Figure 2.3.1 b).

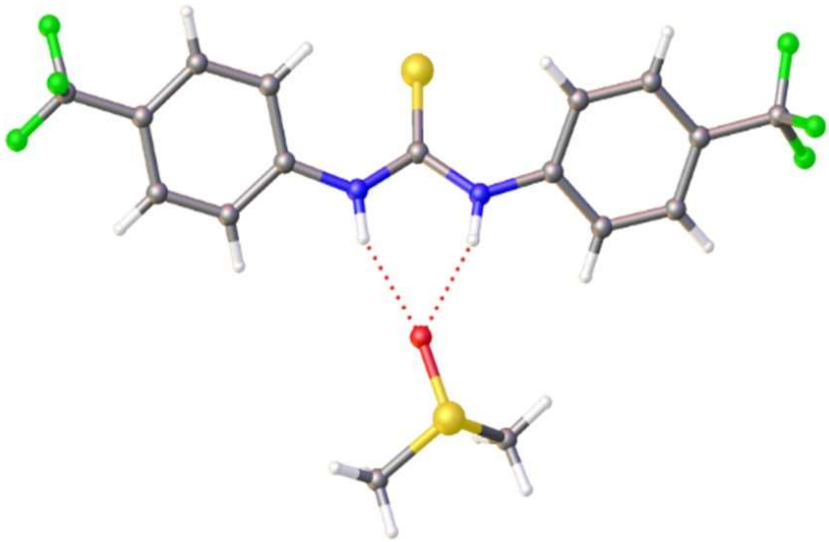

Figure 2.3.2 - Single crystal X-ray structure of 1 binding a single DMSO solvent molecule through the formation of two hydrogen bonds. Disorder associated relating to the DMSO molecule and CF_3 moiety have been omitted for clarity. Colour scheme: grey = carbon; white = hydrogen; green = fluorine; blue = nitrogen; yellow = sulfur.[1]

NMR spectroscopy is an important tool that has been routinely used to characterise non-covalent interactions within the solution state. Examples of these interactions characterised using this method include halogen bonding,[220] π- π stacking[221] and hydrogen bonding.[222–224] To gain an understanding of strength of the receptor:simulant interaction, a series of ^{1}H NMR titration studies were conducted in a CD_3CN solution, following the downfield change in chemical shift of the thiourea/pyrrole NH upon the increasing concentration of the simulant with respect to the receptor **38**-**39**, an example of the change in NH chemical shift demonstrated in Figure 2.3.3. These solvent conditions allowed for the direct observation of the HBD N-H resonances in a non-competitive solvent environment and to maximise any complexation events. All experimental data attained were fitted to a 1:1, 2:1 and 1:2 host:guest binding isotherm using Bindfit v0.5,[225,226] the errors associated with these fittings were compared and supported the formation of a 1:1 host:guest complex formation.

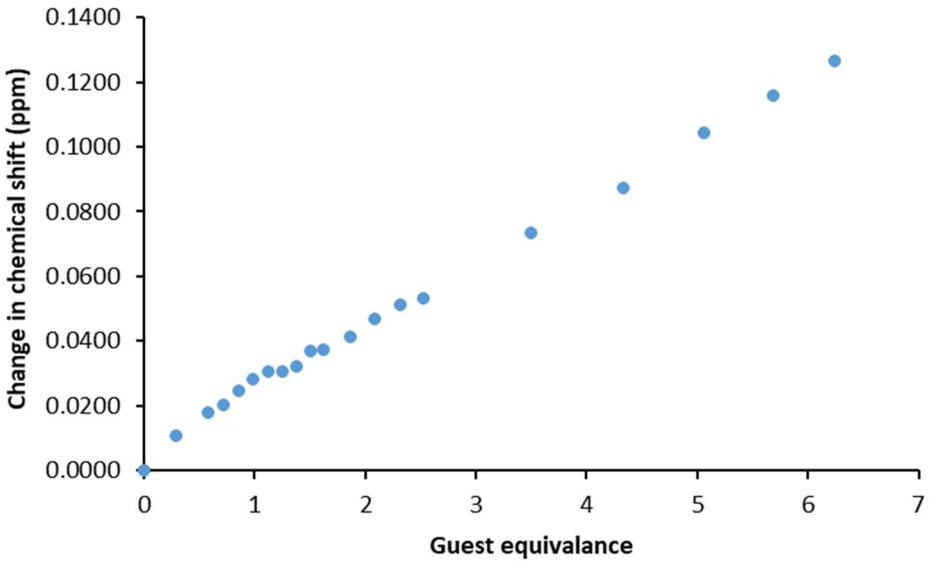

Figure 2.3.3 – Change in chemical shift of NH resonances of **37** (host) upon the addition of compound **45** (guest).

Job plots were also conducted to confirm the stoichiometry of the formed host:guest complex, however, these data gave inconclusive results, with a typical example of these data illustrated in Figure 2.3.4. Although this is in line with an article published by Thordarson and Hibbert stating how that Job plots may not always be suitable for supramolecular host:guest systems.[227] Concerns over the validity of the Job plot had previously been raised by Connors,[228] Thordarson[225] and Schneider and Yatsimirsky[229], it was only work that work by Jurczak and co-workers[230] which in the words of Thordarson and Hibbert "*spelled the death of the Job plot as a useful tool in the analysis of supramolecular complexation events*".[227] Jurczak and co-workers demonstrated through a series of simulations of various 1:2 equilibria cases that the observed maxima (χ_{max}) may or may not result in the expected maxima around 0.33; indicating that the χ_{max} can be misleading.[230] The message that they put across from these studies was that "*Job plots are exceptionally poor indicators of stoichiometry in supramolecular host-guest chemistry*" It was also noted that this method still has valid use in the study of inorganic complexes.[230]

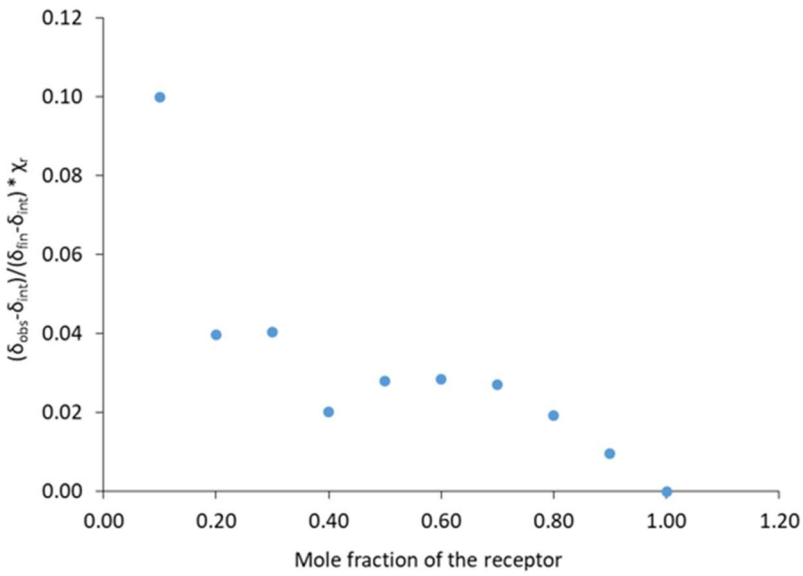

Figure 2.3.4 – Example of job plot analysis conducted, here showing the results of receptor **36** and simulant **55**.

Initially, ^{1}H NMR titrations were conducted with a small percentage of simulants, this was to identify a lead receptor with the results detailed in Table 2.1. These results demonstrate the most acidic thiourea receptor **36** to be the lead receptor, as it was the only receptor found to produce association constants that span the ≥ two orders of magnitude necessary to validate our hypothesis. As the receptor acidity decreases, the ability to determine an association constant using this method also decreases, with no association constants able to be determined with the macrocyclic **39**. This is because as the substitution onto the benzene ring of the receptor goes from electron withdrawing to electron donating, the acidity of the thiourea NHs become less acidic, and therefore the hydrogen bonding strength is diminished. Association constants with values less than 10 have not been included as these values are too small to accurately be quantified.

Table 2.1 - Association constants (M^{-1}) calculated for **36**–**39** with potential simulants in a CD_3CN solution at 298 K, obtained through the fitting of ^1H NMR titration data to a 1:1 host: guest binding isotherm using Bindfit v0.5.[225226]

No.	36	37	38	39
40	36 (± 6 %)	< 10	19 (± 11 %)	< 10
41	17 (± 1 %)	20 (± 5 %)	27 (± 9 %)	*b*
43	< 10	24 (± 4 %)	< 10	*b*
45	< 10	32 (± 7 %)	< 10	*a*
51	22 (± 6 %)	*a*	*a*	*a*
53	< 10	19 (± 6 %)	*b*	*a*
55	106 (± 8 %)	*a*	*b*	*a*

a - Data could not be fitted to either a 1:1, 2:1 or 1:2 binding isotherm. b - Peak overlap prevented binding constant determination.

Using the lead receptor **36**, the data set was expanded for all simulants and the results of these are summarised in Table 2.2. Having achieved a full data set for **36**, we can see that there are a range of K_{ass} values, ranging from 11 M^{-1} to 106 M^{-1}, with 11 of the 22 simulants demonstrating a K_{ass} of 10 or less, these values will be excluded from further work (as these values are too small to state these constants with accuracy), with the dataset now being reduced to a total of 10 potential simulants.

Table 2.2 - Association constants (M^{-1}) calculated for **36** with **40**–**61** in a CD_3CN solution at 298 K, obtained through the fitting of ^1H NMR titration data to a 1:1 host: guest binding isotherm using Bindfit v0.5.[225,226]

No.	K (M^{-1})	No.	K (M^{-1})
40	36 (± 6 %)	**51**	22 (± 6 %)
41	17 (± 1 %)	**52**	< 10
42	< 10	**53**	< 10
43	< 10	**54**	48 (± 11 %)
44	< 10	**55**	106 (± 8 %)
45	< 10	**56**	41 (± 8 %)
46	11 (± 1 %)	**57**	64 (± 5 %)
47	52 (± 6 %)	**58**	46 (± 9 %)
48	< 10	**59**	76 (± 6 %)
49	< 10	**60**	< 10
50	< 10	**61**	< 10

In summary, it has been shown that the use of simple neutral thioureas can be used to determine a range of K_{ass} values in the non-competitive solvent system CD_3CN, and that the initial hypothesis of the most acidic thiourea allowing for the determination of a complete data set was true, with **36** producing the final data set over the less acidic, **37**-**39**. It has also been demonstrated the potential binding modes expected for these simulants as **51**-**61** have two HBA acceptor sites there is the potential for hydrogen bonding to occur between the HBD NHs and either one or two of the HBA oxygen atoms. A single crystal of **36** with DMSO demonstrated the predicted binding modes between receptor and simulants.

2.4 *In-silico* modelling

Computational modelling has previously been used to model and predict the properties and 3D conformation of compounds and allows for the study of hydrogen bonded complexes through the prediction of hydrogen bond formation. One method for visualising whether a molecular interaction will occur is through the use of electrostatic potential analysis, mapping the electronegative and electropositive areas across a molecule.[231] Electrostatic potential analyses are essential theoretical tools for deriving non-covalent interactions.[232] In 2004, work conducted by Hunter showed that low level theoretically derived electrostatic potential maps (ESPMs Figure 2.4.1), using energy minimised semi-empirical AM1 modelling methods found that E_{max} (most electropositive) and E_{min} (most electronegative) surface values that correlate well with experimentally derived data.[233] Where the E_{max} represents the principle HBD group and E_{min} represents the principle HBA group. Further work by Sathyamurthy and co-workers investigated the concept of intramolecular interactions in the form of hydrogen bonding, using the topological properties of electron density.[234] The results from their studies demonstrated that the electron density at the hydrogen bond critical point increases linearly with increasing stabilisation energy, from weak to strong hydrogen bonds.[234]

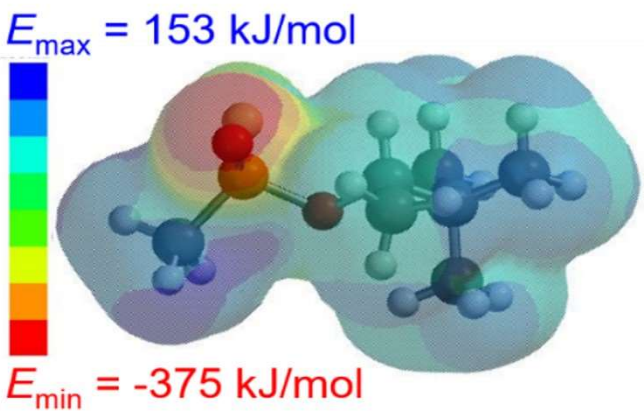

Figure 2.4.1 – An electrostatic potential map calculated for the CWA soman, using energy minimised semi-empirical PM6 modelling methods.

ESPMs were calculated for compounds **36**-**61**, and the CWAs sarin and soman using energy minimised semi-empirical PM6 calculations using Spartan'16 software (Figure 2.4.1). AM1 modelling methods previously used by Hunter were substituted for PM6 modelling methods in line with work by Stewart.[235] The results from these studies demonstrate that the calculated E_{max} values of the receptors **36-38** correspond to the HBD NHs, and E_{min} values of the simulants **40**-**61** correlate with their principle HBA site. This corresponds with the fact that hydrogen bonds are mainly electrostatic interactions, and therefore, we would expect to see a HBA site to be the most negative surface point and the HBD site to be the most positive. These values are overviewed in Table 2.3.

Table 2.3 - E_{max} and E_{min} values (kJ mol^{-1}) calculated for **40**-**61** using energy minimised semi-empirical PM6 modelling methods with Spartan '16 software.

No.	E_{max} (kJmol^{-1})	E_{min} (kJmol^{-1})	**No.**	E_{max} (kJmol^{-1})	E_{min} (kJmol^{-1})
40	195.91	-323.65	**52**	329.31	-290.66
41	159.77	-322.43	**53**	262.22	-336.50
42	170.70	-320.59	**54**	223.55	-360.05
43	120.71	-356.94	**55**	235.78	-357.85
44	81.05	-385.97	**56**	371.31	-281.06
45	77.78	-389.84	**57**	355.94	-292.00
46	110.29	-383.65	**58**	304.57	-320.56
47	173.87	-385.75	**59**	386.40	-277.91
48	84.88	-374.75	**60**	272.44	-350.32
49	100.74	-378.20	**61**	267.26	-343.14
50	72.83	-389.35	sarin	154.00	-373.00
51	316.35	-311.10	soman	153.00	-375.00

As it is possible that **51**–**61** could adopt one of two 1:1 binding modes with **36** (Figure 2.3.1), the potential for one of these binding modes prevailing within the solution state was

further explored computationally using higher level DFT (M06-2X/6-311 g(d,p)) calculations (PCM = acetonitrile, Gaussian16) by Dr Ewan Clark and are summarised in Table 2.4.[236–238] The geometries of **41**, **44**, **45**, **46**, **51**–**56**, **60**, **61**, sarin and soman with receptor **36**, were optimised individually and as interacting pairs in both 1 oxygen binding (O1) and 2 oxygen binding (O2) configurations. These calculations confirmed the possibility of both binding modes for the sulfonyl species (Figure 2.4.2). However, as was expected no stable two oxygen binding modes were found for the phosphonyl species (Figure 2.4.2).

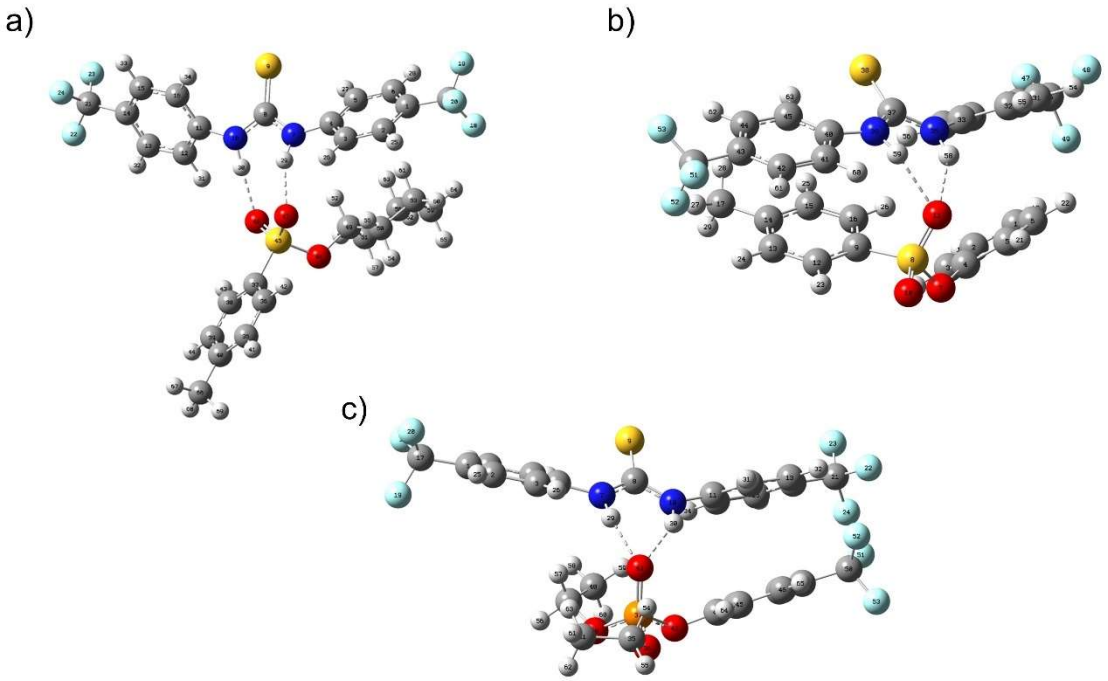

Figure 2.4.2 - Possible 1:1 binding modes found by DFT (M06-2X/6-311 g(d,p)) calculations for: a) **36**:**54** where a single hydrogen bond is formed to each of the S=O HBA groups and; a) **36**:**53** where two hydrogen bonds are formed to one the S=O HBA groups and c) **36**:**41** where the complex formed is stabilised not only through the formation of two hydrogen bonds to the central P=O accepting group but also through π-π stacking interaction between the aromatic ring systems of both the host and guest. Colour code: grey = carbon; white = hydrogen; turquoise = fluorine; blue = nitrogen; yellow = sulphur. Grey dashed line indicates hydrogen bonding.

Table 2.4- Relative energies of binding modes compared to free species. Mode 1 is binding through the single, primary H-bond acceptor atom. Mode 2 is bonding through two O acceptor atoms. Mode 3 is binding via fluoride. Mode 4 binding through the nitro functionality. a - Oxygen except where otherwise specified b - Fluorine, c - Sulfur.

Guest species	Binding Mode	Total Energy Binding ($kJmol^{-1}$)	NBO Charges on H-Bond Acceptors[a]				
			1	2	3	4	5
sarin	1	-51.2	-1.107	-0.876	-0.582[b]		
	2	-56.3					
	3	-57.9					
soman	1	-53.0	-1.109	-0.878	-0.582[c]		
	2	-58.0					
	3	-62.8					
41	1	-58.0	-1.116	-0.860	-0.859	-0.823	
	2	-84.6					
44	1	-67.8	-1.138	-0.880	-0.866		
45	1	-59.6	-1.130	-0.862	-0.862	-0.858	
	2	-53.7					
46	1	-63.0	-1.127	-0.860	-0.848		
	2	-59.0					
51	1	-81.5	-0.939	-0.939	-0.735		
	2	-69.2					
52	1	-74.4	-0.937	-0.936	-0.734	-0.413	-0.413
	2	-70.5					
	4	-37.1					
53	1	-84.2	-0.942	-0.942	-0.737		
	2	-65.8					
54	1	-57.8	-0.962	-0.961	-0.767		
	2	-59.0					
55	1	-49.2	-0.959	-0.959	-0.755		
	2	-52.8					
60	1	-41.1	-0.962	-0.961	-0.771		
	2	-61.0					
61	1	-58.9	-0.959	-0.958	-0.759		
	2	-55.5					

The binding energies calculated are significant (−41.1 to −84.6 kJ mol^{-1}) for both sulfonyl and phosphonyl species, however, no clear preference for O1 or O2 binding was found for the

sulfonyls. These calculations did confirm the viability of both O1' and O2' binding modes for the sulfonyl species. However, as expected no stable O2' binding modes were found for the phosphonyl species (see Figure 2.3.1 d). From the binding energies calculated, it can be hypothesised that the binding mode with the lowest energy will be the most preferable, although both binding modes are possible, for the purposes of these studies, the binding mode for any further studies was taken as the one with the lowest energy.

Having confirmed the binding modes for a selection of compounds, we then sought to expand the data for the remaining compounds. However, even though DFT (M06-2X/6-311 g(d,p)) is a proficient computational model for systems such as these as it can account for non-covalent interactions but is quite computationally expensive.[239] It has been shown previously that low-level calculations such as those previously mentioned can supply useful guest-only parameters for predicting trends in K_{ass} without substantial computational overhead. Reducing the size of the calculations requires far less computational time; additionally, Spartan '16 can run on a conventional desktop making this approach accessible to a wider chemical audience. The range of parameters output by default for PM6 calculations is limited, and therefore to expand the scope of searchable parameter space, DFT (B3LYP/6-3G1*) calculations were also performed using Spartan '16.[233,235,240] These analogous parameters obtained were found to be consistent with those values produced from both the PM6 and M06-2X/6-311 g(d,p) calculations, for full parameter comparisons see appendix figures S126-S138. As a result, a list of 19 computationally derived parameters (*P*), which are detailed in Table 2.5, were derived for each potential simulant/OP CWA as well as when in a 1:1 complex with **36**.

The computational method chosen for each parameter was justified based on the comparisons made between both low level methods and the high level DFT calculations, and where a low level method gave a better comparative value it was that method that was selected for that parameter determination. In order to estimate the accessibility of the principle HBA site

towards supramolecular coordination, the area of the ESPM within 1/8th of the E_{min} for the principle HBA group was used as a weighting factor for the E_{min}. This area is displayed in red on the ESPMs and is hereafter termed the 'steric weighting factor' (SWF) for ease of reference. The SWF was considered for either one or two sulfonate oxygen atoms of **51**-**61**, in line with the DFT modelling results. A second weighting factor was also derived which is in relation to how electropositive the P or S atom is, where the area of the ESPM within 1/8th of the E_{max} was used as a weighting factor for the E_{max}. This area is displayed as blue on the ESPMs and has been termed the 'steric accessibility factor' (SAF) for ease of reference. This list comprises of easily accessible parameters, which also haven't been filtered, this is to avoid assuming a parameters relevance and for the potential to bias certain parameters in exhaustive parameter searches (discussed in section 2.6). These parameters were then combined and used along the experimentally derived association constant data (Table 2.2) to produce initial predictive models for the determination of association constants.

Table 2.5 - List of parameters (P) used to produce association constant predictive models and computational method used to derive each parameter.

Parameter	Parameter description	SI Unit	Derivation method	
			PM6	B3LYP – 6-31G*
P_1	E_{min}	kJ/mol		×
P_2	E_{max}	kJ/mol		×
P_3	Molecular volume	$Å^3$	×	
P_4	Molecular area	$Å^2$	×	
P_5	Solvent accessible area	$Å^2$	×	
P_6	Polar surface area	$Å^2$	×	
P_7	% Polar surface area	$Å^2$	×	
P_8	Polarizability	$C\ m^{-2}$	×	
P_9	Steric weighting factor (SWF)	$Å^2$	×	
P_{10}	Steric accessibility factor (SAF)	$Å^2$	×	
P_{11}	HOMO	eV		×
P_{12}	LUMO	eV		×
P_{13}	Energy	kJ		×
P_{14}	Electrostatic charge	C		×
P_{15}	Additive N···O Bond length	Å		×
P_{16}	Log P	N/A	×	
P_{17}	Dipole moment	D		×
P_{18}	Additive NH···O bond length	$Å^2$		×
P_{19}	Bond angle difference from optimal 180°	°		×

N/A = non-applicable. '×' identifies the computational modelling method used to generate the values for a particular parameter (*P*).

In summary, it was shown that the E_{max} and E_{min} values on a ESPM correlate well with the HBD/HBA sites and have used computational modelling methods to derive a list of 19 parameters for each simulant to be used for the development of predictive models. It was also shown that lower level computationally modelling using Spartan'16 software could be used to create similar outputs to that of more computationally extensive methods such as DFT M06-2X/6-311 g(d,p). This will allow for a more accessible approach for a wider chemical audience to use similar methods for further development of predictive models.

2.5 Development of a single parameter predictive model

Comparisons between the parameters detailed in Table 2.5 and the experimentally derived association constants found in Table 2.2 were initially conducted manually, here it was found that a correlation between the hydrogen bond angle between **36** and the simulants **40**-**61** and K_{ass} values. This correlation is illustrated in Figure 2.5.1. These parameters were chosen initially as the hydrogen bonding angles can be correlated to hydrogen bonding strength, with the optimal hydrogen bonding angle being 180°. To aid interpretation of the correlation, the hydrogen bond angles have been represented as the sum of the difference from the optimal 180° hydrogen bonding angle; as there are two HBD NHs the hydrogen bond angle from both NHs were considered, and noted as hydrogen bond angle 1 and 2 to distinguish between each NH.[241,242] From Figure 2.5.1, there are three trends established, one for the phosphoryl species and two for the sulfonyl species. The two trends found for the sulfonyl species correspond with the two different classes of sulfonate molecules used within this study, those that contain a substituted toluene group (**51**-**55**) and those that contain a substituted methyl group (**56**-**61**).

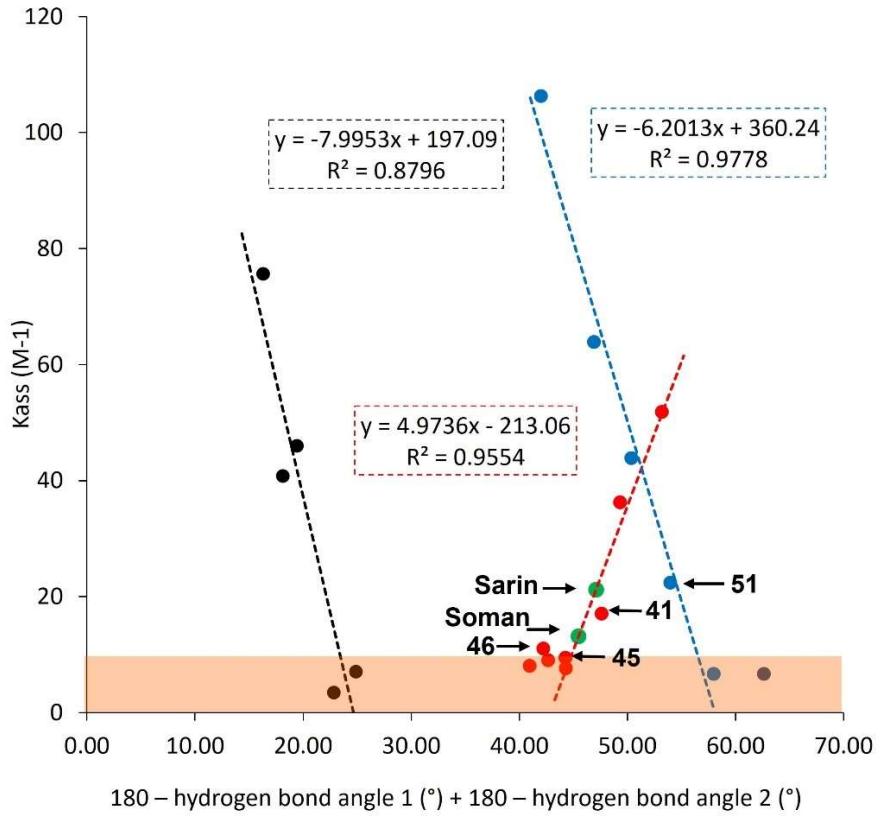

Figure 2.5.1 - One parameter association constant (K_{ass}) prediction. Red = phosphoryl species; blue = toluene substituted sulfonyl species; black = methyl substituted sulfonyl species; green = predicted OP CWAs; orange shaded section = $K_{ass} \leq 10\ M^{-1}$.

The limitation of the experimental association constant determination methodology used is ≈10 M^{-1}, therefore those K_{ass} values that fall within this limitations were considered unsuitable when included into a model such as this and should be treated with caution. It was hypothesised that when a complex is formed that incorporates a single HBA atom, that a decrease in the hydrogen bonding angle away from the optimal 180°, the hydrogen bonding strength will increase, this is as the host (**36**) and the guest (**40**-**61**) move closer together; this results in a correlation with a positive gradient, as demonstrated for the phosphoryl species as shown in red in Figure 2.5.1. This hypothesis is supported also by the predicted binding modes as illustrated previously in Figure 2.3.1, where the phosphoryl species will have a more trigonal pyramidal bonding angle, moving more towards angles around 120°, which is further highlighted

by the highest K_{ass} value for a phosphoryl species was 51.82 M^{-1} with hydrogen bonding angles of 126.8°.

However, for those complexes formed where there are two HBA oxygen atoms, the hydrogen bonding angles will more towards the optimal 180° into a more linear geometry, this will in turn result in a correlation with a negative gradient, which was observed for both sulfonyl species (black and blue trends, Figure 2.5.1). It is hypothesised that we observe two trends for the sulfonyl species due to the additional R-group specific interactions of the toluene and methyl substituted compounds. Where the toluene substituted compounds demonstrating an overall larger deviation away from 180° when compared to the methyl substituted sulfonyls, which resulted in the splitting of the two species when correlated with association constants, although both display the same trend. To identify any lead simulants for OP CWAs, the K_{ass} values for sarin and soman were predicted (green, Figure 2.5.1), these values were predicted using the trend shown for the phosphoryl species, the prediction resulted in K_{ass} values of 22 and 13 M^{-1} for sarin and soman respectively. Comparison of these values identified that the most appropriate simulants for sarin are **41** and **51**, with **45** and **46** being identified as the most appropriate simulants for soman.

In summary, here we have shown that the hydrogen bonding angle of complexes formed between **36** and **40**-**61** determined using easily accessible computational modelling; resulting in three trends that correspond to the species of compounds studied. Further to this, using this model four lead simulants have been identified for sarin and soman.

2.6 Exhaustive parameter search

To enable to elucidate further predictive models for association constant that contains more than one parameter, as the energetics relating to association vary rarely depend on one molecular property. It has been shown that an exhaustive, high throughput parameter search can allow for the identification of predictive models, through using this methodology it also

eliminates the data set being swayed by human preference as it is a build study, whereby each parameter is assigned a number.[243] R data analysis software[244] was used to complete an exhaustive search of all potential parameter combinations for direct and inverse correlations of up to three parameters (equations (1) and (2)) where P_0 is the experimentally derived association constants. These searches were limited to compounds that have a $K_{ass} > 10$, this was to be able to identify a single linear correlation. The use of the multiplication operator was chosen in line with previous work conducted by Hiscock and co-workers[243] to enable the weighting of specific parameters within the output. The script used for this work was written by Dr Dominique Chu, with execution of the script and data analysis conducted by me.

$$P_0 = P_x^a \times P_y^b$$
$$|a| + |b| = 2 \qquad \text{Equation 1}$$

$$P_0 = P_x^a \times P_y^b \times P_z^c$$
$$|a| + |b| + |c| = 3 \qquad \text{Equation 2}$$

Using these equations all possible combinations of parameters were explored and ranked through R^2 analysis. This allows for a complete unbiased approach to model development as no parameter favoured over another. The top 10 fits from these data from each equation was ranked and those models can be found within the appendix (Figures S189-S208). This approach unfortunately did not result in the identification of any viable predictive models, with the highest ranked three parameter combination model returning a R^2 value of 0.6002, and the highest ranked two parameter combination model returning a R^2 value of 0.4715. However, this method did allow for insight into which parameters appeared most often in these models and are therefore likely to be the most influential in these binding events and should consequently be considered for future model development (see Table 2.6) into binding which could be utilised for other predictive model development. It also allowed for the conclusion that three parameter combinations allow for the identification of more appropriate models than two parameters.

The occurrence of each parameter within the top fits for both two and three parameter combinations indicated that there are some parameters that indicate energetic significance towards binding. The total occurrences have been summarised and can be found in Table 2.6. From this analysis it was found that the three parameters that occur the most are P_{10} (SAF), P_{14} (electrostatic charge at the HBA), and P_{11} (HOMO energy), appearing a total of 17, 9 and 8 times across the 20 fits examined. The predominant occurrence of P_{14} is not too surprising as it would be expected that the electrostatic charge on the HBA atoms would contribute to the electrostatic component of hydrogen bonding, the same argument can be applied to the occurrence of P_{11} (HOMO), as the HOMO is associated with the lone pairs on the HBA oxygen atom, and as hydrogen bonding can have covalent character it could potentially be involved in the covalent contribution to hydrogen bonding. The most interesting result is that of P_{10} and how frequently it appears within these top fits, as P_{10} describes the area surrounding the exposed electrophilic site and not the HBA oxygen atom. However, upon further investigation of these trends, it showed an inverse trend with P_{10} whereby the larger the exposed electrophilic site the smaller the resulting binding constant. Therefore, this parameter is reporting about the steric bulk surrounding the P or S atom, and subsequently are the attached substituents are folded towards the HBA oxygen atom. From this we can deduce that in this case that P_{10} is acting as a proxy for the steric bulk surrounding the HBA atoms.

Table 2.6 - The total number of occurrences by a single parameter appears in the top 10 models, as identified through comparative R^2 analysis, obtained from an exhaustive search of P_1–P_{19} with equation (1) and (2).

P	Equation 1	Equation 2	Total
P_1	1	2	3
P_2	0	0	0
P_3	0	0	0
P_4	0	0	0
P_5	0	0	0
P_6	0	1	1
P_7	0	0	0
P_8	0	0	0
P_9	0	0	0
P_{10}	8	9	17
P_{11}	4	4	8
P_{12}	0	0	0
P_{13}	0	0	0
P_{14}	4	5	9
P_{15}	2	2	4
P_{16}	0	0	0
P_{17}	0	3	3
P_{18}	1	4	5
P_{19}	0	0	0

In summary, it has been shown that exhaustive parameter searches can be used to determine relevant parameters for the development of predictive models, however in this case it did not result in the identification of an appropriate model, and that the use of simple

electrostatic models for hydrogen bonding are not sufficient in this instance; it is hypothesised that models that focus on the parameters highlighted here to be more influential on association constant will allow for the elucidation of a model for the prediction of association constants of OP simulants and CWAs in the future.

2.7 Toxicity considerations

Work conducted in this section was collected in collaboration with Dr Nyasha Allen and Dr Daniel Mulvihill, with Dr Nyasha Allen conducting the biological experiments.

It is vital that any potential simulants do not replicate the toxicity demonstrated of OP CWAs, therefore the potential simulants **40**-**61** were screened against a commonly used model species *Schizosaccharomyces pombe* (*S. pombe*) was used to gain an insight into the potential toxicity of **40**-**61** towards eukaryotic cells within a biological environment.[245,246] *S. pombe* was used as it is a unicellular yeast cell which has many genes orthologous to human genes (~ 70%).[247] It has become a model system for the study of basic cell principles for the understanding of more complex organisms such as humans.[248] *S. pombe* is non-pathogenic and can be easily grown within a laboratory setting.[249]

The growth of S. pombe was monitored using optical density measurements at 600 nm (OD_{600}) both in the presence of **40**-**61** and without over the course of 45 hours. The compounds and the controls were added as an aqueous 5% ethanol solution to a suspension of cells (density = 0.5×10^6 cells/mL) in EMMG media, this was done to aid the solubility of compounds **40**-**61**. The growth curves can be found in the appendix, The percentage inhibition of growth for **40**-**61** has been illustrated in Figure 2.7.1, here for simplicity the rate of growth when compared to the aqueous 5% ethanol solution control was split into three zones, less than 16% inhibition of growth (shown in green), between 16% and 50% inhibition of growth (shown in blue) and greater than 50% inhibition of growth shown in red.

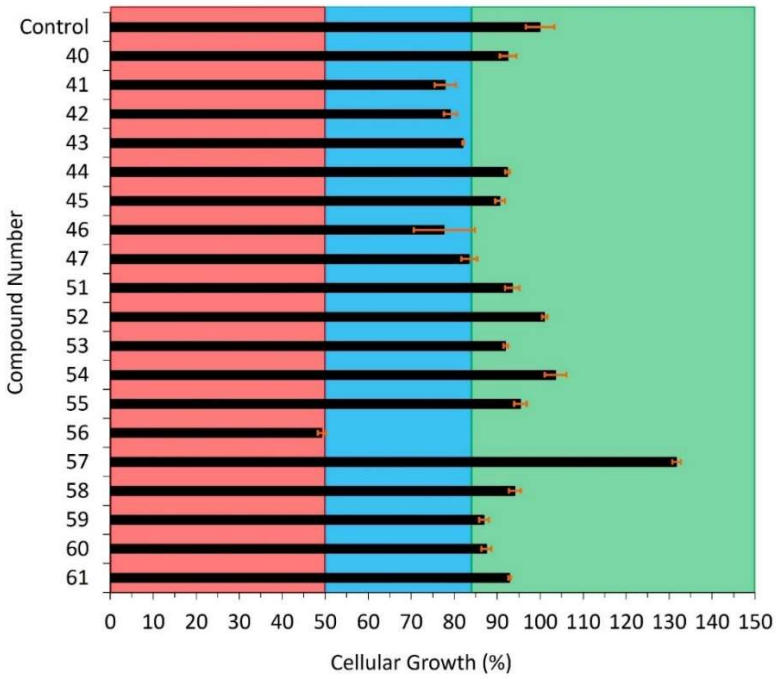

Figure 2.7.1 - *S. pombe* toxicity screening % cellular growth (recorded as maximum OD_{600}) reached at stationary phase in the presence of 5–12, 16–26 (3.3 mM) relative to controls after 45 hours. Data shown represents an average of three experiments. Green – cell growth impeded by <16% over the course of 45 hours; Blue - cell growth impeded by 16–50% over the course of 45 hours; Red – cell growth impeded by 50% over the course of 45 hours. Control = 5% aqueous ethanol solution. Error = standard error of the mean.

These screening results show that, at 3.3 mM the simulants **40**, **44**, **45**, **51**–**55**, **57**, **60** and **61** have no significant impact on cell growth, and therefore demonstrating little/no toxic effects, while simulants **41**, **42**, **44**, **46**, **47**, **56**, **58** and **59** show a degree of toxicity that will warrant further investigation prior to any use as a simulant for testing outside of a laboratory setting. The lead simulants that were identified to mimic complex formation for soman and sarin were shown to reduce the growth of *S. pombe* by 22.1%, 17.8%, 7.6%, 9.3%, 22.3% and 6.5% for **41**, **43**–**46**, and **51** respectively over the period of 45 hours relative to control samples. This indicates that the lead simulants **43**, **45** and **51** potentially pose no significant toxicity risk to eukaryotic organisms (although this would require further testing to confirm these preliminary screening result), while the simulants **41**, **44** and **46** would require further investigation to

determine their toxicity risks. It is worth noting that simulants **52**, **54** and **57** showed growths of greater than 100% when compared to the controls, this is hypothesised to be either because the *s. pombe* cells were able to utilise the compounds to grow better or as bacteria can rapidly adapt to different environments and utilise their environment to improve growth.[250,251] A further hypothesis is that it has been shown that exposing bacteria to sublethal concentrations of antimicrobials can improve growth which may be due to the development of resistance and increased nutrient uptake, leading to increased growth and reach higher ODs than the control sample, therefore, in this case the compounds could have been dosed at a concentration whereby there was an initial affect, however, the *S.pombe* cells were able to bypass these effects and overcompensate in growth. However, to confirm either hypothesis further tests would be needed that go beyond the scope of the screening study. Nevertheless, full pharmacodynamic and pharmacokinetic studies should be undertaken before these simulants are considered safe to handle without the use of personal protective equipment.

2.7 Conclusions

In this chapter, the association constants for a series of hydrogen bonded complexes have been experimentally determined and modelled using a range of computational methods. Through the combination of low-level computational modelling and exhaustive parameter searches it has allowed for the production of a first-generation predictive model with the hope to aid with OP CWA simulant selection, for use in the development of defensive technologies relating to OP CWA sensing through complexation. This first generation model identified four lead simulants for sarin and soman: **41** and **51** (for sarin), and **45** and **46** (for soman). We have also screened all compounds **40**-**61** for any toxic effects against *S. pombe*, with lead simulants **43**, **45** and **51** posing no significant toxicity risk to eukaryotic organisms but would need more in depth testing before being deemed non-toxic to these organisms. Additionally, we hypothesise

that the single parameter relationships identified here maybe developed in the future towards the identification of binding modes in solution.

Chapter 3 – The development of predictive models for OP simulant reactivity

3.1 Introduction

As discussed in the previous chapter chemical warfare agents (CWAs) are extremely toxic synthetic chemicals that can be dispersed as a gas, liquid, or an aerosol.[163] They have a lethal or incapacitating effect on humans and other organisms.[95,252] In the event of their release, decontamination methods are important for the elimination or reduction of the health hazards posed by these substances on people.[95,252] Decontamination is defined as the process of removing or neutralising chemical agents from people, equipment and the environment.[253]

Prior to 1969, sea-dumping was a simple approach to "destroy" munitions and materials that remained after the First and Second World Wars.[253] Waste burning in open pits and burying were also pursued as alternative disposal methods.[253] In the case of burying, the very slow corrosion of containments led to the subsequent slow release of toxic compounds which resulted in localised contamination of soil and groundwater, and therefore, it represents long-term environmental threat. Both sunken and buried munitions might explode which would cause a sudden release of nerve agents.[253] The standard methods of decontamination are either high temperature incineration (an example is shown in Scheme 3.1) or chemical hydrolysis with high concentrations of base or sodium hypochlorite, all of which are destructive and can potentially result in the release of hazardous by-products such as HF as demonstrated in Scheme 3.1.[95,252–254] The release of these hazardous by-products can be also be very damaging to the environment.

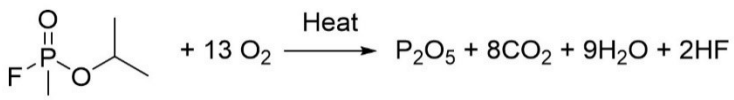

Scheme 3.1 – A scheme demonstrating the incineration of sarin.

While incineration is attractive as an approach for the destruction of CWAs, there were concerns from the possible dangers from emissions of incineration facilities.[255,256] This led to the examination of alternative technologies for nerve agent destruction. NAs can react with water, and therefore hydrolysis is an alternative method of detoxification.[257] Soman and sarin are soluble in water and their hydrolysis under different pH conditions have been carefully studied.[253,258–260] Hydrolysis of these agents proceeds by a nucleophilic SN2 attack on the P atom (Scheme 3.2 a); the hydrolysis rate is both temperature and pH-dependent,[253,259] A decrease in temperature has also facilitated in the persistency of NAs, through slowing down the rate of hydrolysis.[256] This reaction gives the nontoxic products isopropyl methylphosphonic acid (IMPA) in the case of sarin and pinacolyl methylphosphonic acid in the case of soman (Scheme 3.2 b).[253] The hydrolysis of tabun gives phosphoric acid as a final product; under both neutral and basic conditions, hydrolysis occurs through the formation of O-ethyl-N,N-dimethylamidophosphoric acid and cyanide; under an acidic environment hydrolysis gives ethylphosphoryl cyanidate and dimethylamine (Scheme 3.2 c).[253]

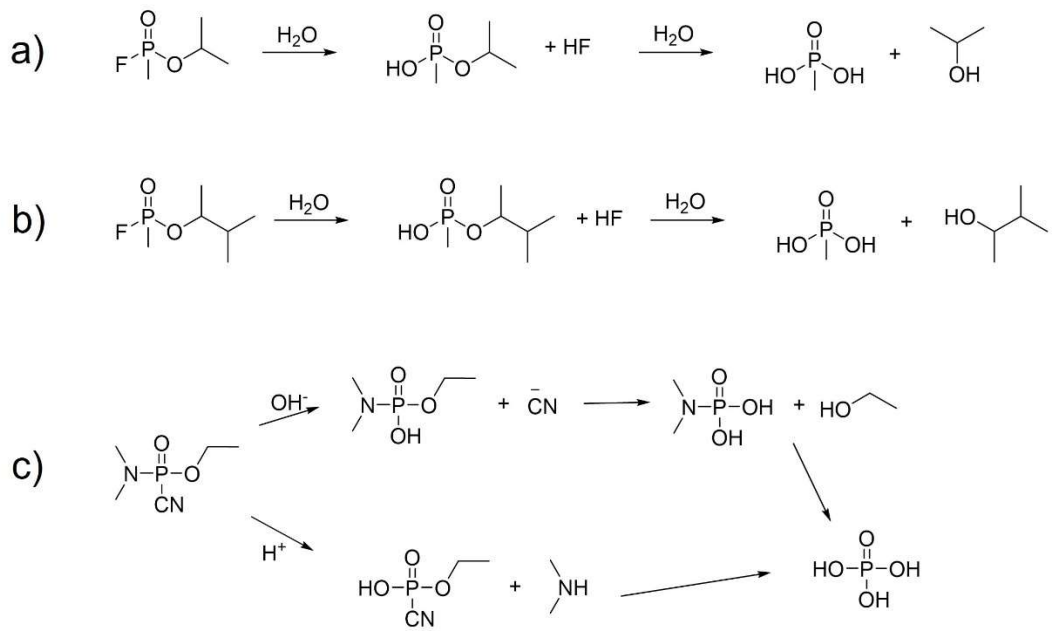

Scheme 3.2 – Hydrolysis schemes of a) sarin, b) soman and c) the basic and acidic hydrolysis routes of tabun.

The neutralisation of NAs through base hydrolysis is currently a method used for NA decontamination, with sodium hydroxide (NaOH) added to facilitate the neutralisation.[261] The hydrolysis of soman at room temperature and in neutral conditions (pH 6) is slow, it can take up to 60 hours to completely hydrolyse; however, when at pH 10.8 it has been shown to completely hydrolyse in 1.8 minutes.[261,262] As an acid product is formed, the pH decreases, and the rate of hydrolysis is also subsequently decreased; therefore, excess base is required to maintain the same reaction rate.[253,261]

To avoid the use of excess base or other reagents,[253] catalysis underpinned by molecular recognition strategies has been investigated as a route to promote the hydrolysis of bound OPs to safe products. However, investigating strategies to remediate or sense live CWAs is extremely challenging due to the acute toxicity of these species. While significant progress has been made using simulants of lower toxicity and greater ease of handling, their behaviour invariably differs from that of live agents.[202,253] Work conducted by Snurr and Mendonca, has demonstrated that density functional theory (DFT) can be used to study the mechanism of OP hydrolysis. This work resulted in the development of a quantitative structure activity relationship (QSAR) model that enables the identification of appropriate OP CWA simulants for decontamination purposes.[263]

Within the field of supramolecular chemistry, the use of CWA simulants to develop technologies is well documented and the use of supramolecular chemistry for detection purposes also were discussed in Chapter 2.[166,202] The use of supramolecular chemistry for decontamination and remediation purposes has focussed on strategies to both immobilise the agent and subsequently trigger its breakdown.[202] In the 1980s, Desire and Saint-Andre reported the catalysed hydrolysis of soman by a β-CD.[264] They postulated the following mechanism: formation of the β-CD:soman complex, followed by phosphonylation of the CD and subsequent hydrolysis and dephosphonylation (Scheme 3.3).[264] The breakdown of GD appears to be effectively catalysed by the presence of β-CD, and a strong complex is suggested with a

dissociation constant (K_d) = 5.3 x 10^{-4} M for the S enantiomer of soman. However, they did note that when the CD was fully phosphonylated it no longer accelerates agent breakdown and therefore, it is not truly catalytic.

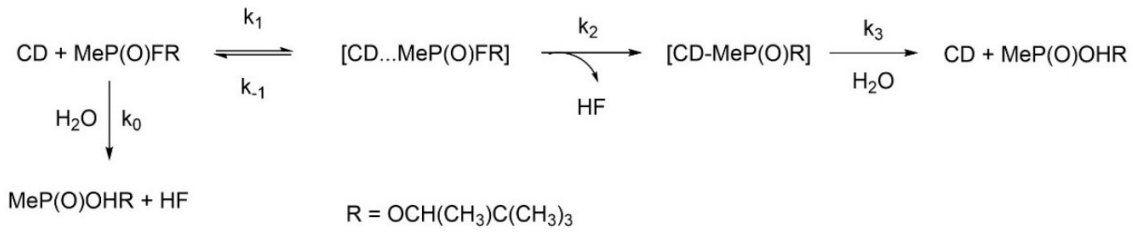

Scheme 3.3 – The mechanism postulated by Desire and Saint-Andre for the β-CD catalysed hydrolysis of soman.

Work by Costero, Martinez-Máñez, Gale and co-workers utilised hydrogen bond donor molecules (**13**, **62** and **63**, Figure 3.1.1) that have been previously described by Gale and co-workers and reported them as organocatalysts for the increased hydrolysis rate of the NA simulants diisopropyl fluorophosphate (DFP) and diethyl cyanophosphate (DCNP).[166,209] They confirmed the formation of hydrogen bonded complexes in an acetone-d_6 solution using both Job plot and ^{1}H NMR titration methods.[209]

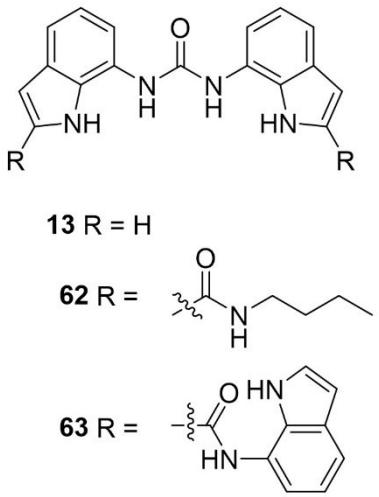

Figure 3.1.1 – Structures of the diindolylureas used by Costero, Martinez-Máñez, Gale and co-workers.[209]

To screen the receptors for their ability to catalyse hydrolysis of CWA simulants, an acetone:water solution (80:20) was used, and while rate constants for the reactions were not reported, they reported the change in hydrolysis rate, and in all cases the hydrolysis rate was found to be greater in the presence of a receptor than without.[209] Whereby some of the receptors reported a 50% enhancement of hydrolysis rate with only a 0.001 molar equivalent of catalyst.[209] They hypothesised that the binding of the simulant resulted in the increased electrophilicity of the phosphorus centre, thus making it more susceptible to nucleophilic attack (Figure 3.1.2).[209] They also reported that there were greater catalytic effects with those receptors that contain a greater number of HBD groups (**62** and **63**).[209] This further supported their hypothesis that the catalytic mechanism includes simulant complexation.

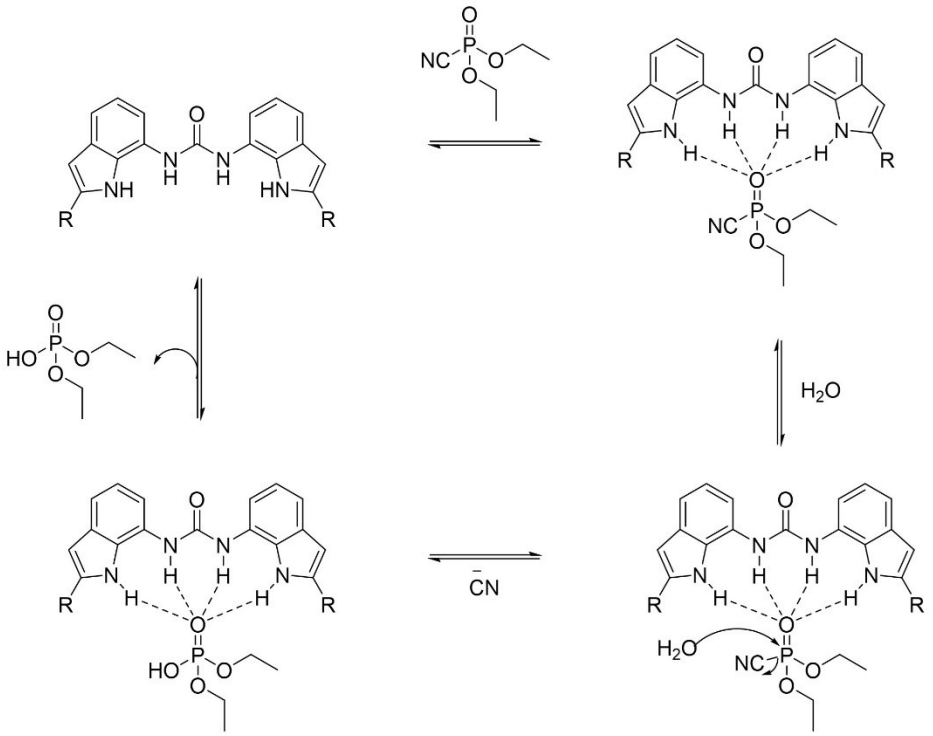

Figure 3.1.2 – Catalytic cycle proposed involving **13**, **62** and **63** with DCNP. The cycle involves 1) complexation of DCNP with **13**, **62** and **63**, 2) enhancement of the electrophilic character of the P atom due to coordination, 3) nucleophilic attack of water, and 4) formation of the corresponding less toxic organophosphate hydrolysis product.

In addition, work by Gale and co-workers[265] have shown that simple tripodal compounds (**64**-**66**, Figure 3.1.3) containing amino acids can not only bind to OP CWA agents, but also enhance the rate of their hydrolysis.[265] Using buffered stock solutions of 2,2-bis(hydroxymethyl)-2,2',2"-nitrilotriethanol (bis-tris) at pH 6.1 or 7.1 and 21-23 °C, the hydrolysis of bis(4-nitrophenyl) phosphate (BNPP) was monitored through UV-Vis spectroscopy.[265] They reported that the presence of **64**-**66** increased the formation of hydrolysis product *p*-nitrophenolate compared to the absence of **64**-**66**. Compound **64** was shown to be the most active and was subsequently tested for its effectiveness against GD, with GD hydrolysis monitored through both ^{1}H and ^{31}P NMR under the same conditions used to test **64** with BNPP. They reported that after 16 hours, approximately 50% of GD remained with 100 mol% of **64**.[265] Association constants could only be reported for **66** with PMP and DMMP with a K_{ass} of 14 M^{-1} reported for PMP, and DMMP showing no interactions.[265] Complexes incorporating **64**, **65** or BNPP couldn't be determined due to compound solubility and protonation issues.[265]

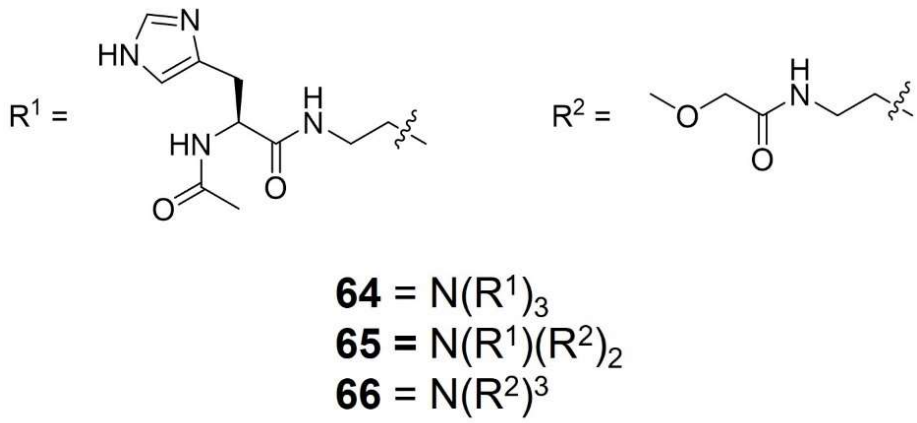

Figure 3.1.3 – Chemical structures of the tripodal compounds synthesised by Gale and co-workers.[265]

In further work, this research group also demonstrated the use of responsive supramolecular organogels for not only sensing the presence of OP CWAs, but also CWA encapsulation and decontamination.[266–268] These responsive supramolecular gels were

previously discussed in Chapter 2.1, page 39 and therefore, will not be discussed in further detail here. While organogels formed from gelators that can act as destructive agents to trigger the decomposition of the CWA are known, it is also possible to immobilise reactive decontaminants within an organogel matrix to form a multicomponent material from simple precursors.[268]

Further to this, work by Holder, Blight and co-workers examined the immobilisation of the nerve agent VX using a composite material made from a catalytical metal organic framework (MOF) within a polymer sponge network (Figure 3.1.4).[269] Here the authors combined a previously reported styrene based poly high internal phase emulsions (pHIPEs) capable of swelling and trapping a range of OP NA and mustard CWAs,[270] with the tendency of zirconium MOFs to function as catalysts for OP CWA hydrolysis.[271] In this work, they prepared a composite material made from a styrene or vinyl based pHIPE and a zirconium-808 MOF, with a 25 wt.% loading of MOF relative to the monomer weight. The authors chose this MOF due to both its activity for OP hydrolysis but also because it contains a commercially available linker, which makes this a more cost effective MOF for scale up. It was reported that the hydrolysis of the OP simulant dimethyl *p*-nitrophenyl phosphate (DMNP) was significantly increased when in the presence of the composite material in a 0.45 M N-ethylmaleimide (NEM) buffer and THF/H_2O/D_2O (2:1:1) solution.[269]

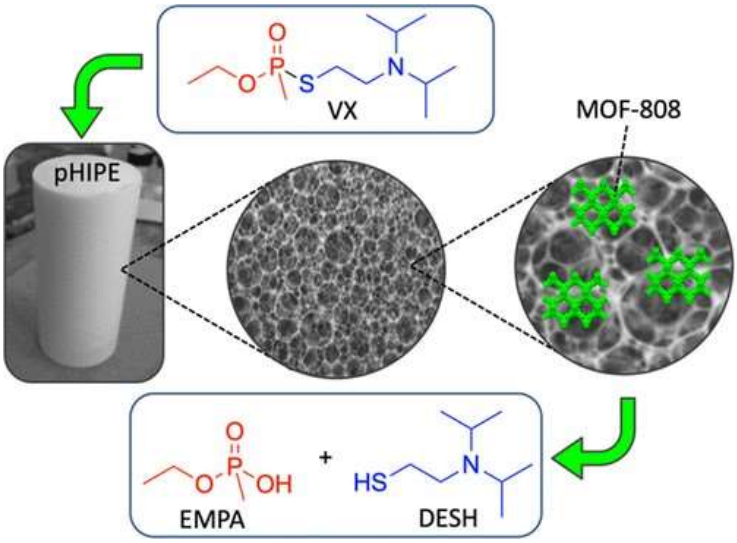

Figure 3.1.4 – Graphical abstract of the design of the composite materials reported by Holder, Blight and co-workers for the catalytic degradation of VX.[269] Reprinted with permission from ref. 268 Copyright 2020 American Chemical Society

They also noted that the MOF performed better when it was added as a powder, allowing for more optimal dispersion, and also that there was minimal hydrolysis of the simulant in the absence of the composite material. Hydrolysis data for the live agent VX was obtained, with the composite material triggering hydrolysis with a one hour half-life in a THF/H_2O solution, VX could also be degraded neat with a catalyst loading of 0.18% relative to VX; with nearly 100% hydrolysis of VX reported after two weeks at an ambient humidity, compared to only 50% without the catalyst.[269] It was noted that potentially the contents of a standard barrel (208 L) of VX could be absorbed, immobilised, and degraded by 4.5 kg of composite material.[269]

Nitschke and co-workers demonstrated the capability of a M_4L_6 cage to catalytically accelerate the hydrolysis of the CWA simulant and pesticide, dichlorvos.[272] Control experiments and experiments containing other binding guests, such as cyclooctane, were shown to not accelerate hydrolysis, this was believed to be because the other guest blocked the cavity within the cage.[272] Using NMR, a host:guest complex between the cage and dichlorvos was found, although on the NMR timescale it was observed to undergo rapid exchange between bound and

unbound states. The hydrolysis products, dimethyl phosphoric acid (DMP) and dichlorovinylmethyl phosphoric acid (DVMP) are hypothesised not to be bound within the cage due to there being no change in chemical shift when in the presence of the cage.[272]

Furthermore, Ward and co-workers have demonstrated that supramolecular cages can be used for catalysing the hydrolysis of organophosphates upon binding within the cage cavity and on the exterior surface of the cage.[273,274] Here the authors used OP CWA simulants, dichlorvos, di(isopropyl)chlorophosphate (DICP), 4-nitrophenyl dimethyl phosphate (4-NDP) and its isomer 2-nitrophenyl dimethyl phosphate (2-NDP) and a M_8L_{12} cage (Figure 3.1.5), that contains a Co(II) ion at each vertex and a bis(pyrazolyl-pyridine) bridging ligand on each edge.[274] Association constants between the simulants and the cage were attempted, but there were clear signs of breakdown during the ^{1}H NMR experiment, with estimated K_{ass} values to be of the order of 10 M^{-1} at 298 K for dichlorvos with a 1:1 binding isotherm.[274] Due to the issues with the ^{1}H NMR titration method, estimate binding constants using a molecular docking program GOLD was used, which provides a quantitative prediction of guest binding within the cavity of the cage in water.[275,276] This produced the predicted binding constants of 31 M^{-1}, 14 M^{-1}, and 310 M^{-1} for dichlorvos, 2-NDP and DICP respectively.[274] The crystal structure of the inclusion of dichlorvos into the cage cavity is illustrated in Figure 3.1.5. The hydrolysis of these simulants was measured using ^{31}P NMR in D_2O at 298 K buffered to a pD in a range of 7.7-9.0 using borate buffer, in the presence and absence of the cage.[274] The observed hydrolysis rate constant for dichlorvos in the absence of the cage was found to be 1.0 x 10^{-6} s^{-1} at a pD of 7.7 at 298 K, under the same conditions and with the presence of 0.68 mM of cage as a catalyst, the formation of hydrolysis product was found to be an order of magnitude faster at a rate of 1.4 x 10^{-5} s^{-1}, with similar behaviour observed for the other simulants tested, with the exception of DICP which proved more difficult to analyse, this is due to the generation of chloride which has an inhibiting effect on cage-based hydrolysis,[277] and therefore this was not pursued further.[274] To confirm whether the guests need to be bound within the cavity of the cage for catalysis to occur, a control

experiment where the cavity was blocked by a strongly binding but unreactive guest; within this study the authors used cycloundecanone.[274] The authors reported no significant change in reaction rate for dichlorvos and 2-NDP, demonstrating that binding of the guests within the internal cavity is therefore not necessary for hydrolysis catalysis.[274] This is hypothesised to be because the exterior of the cage also displays the same hydrophobic components as the interior, therefore even at the exterior of the cage there is a higher local concentration of hydroxide ions.[274]

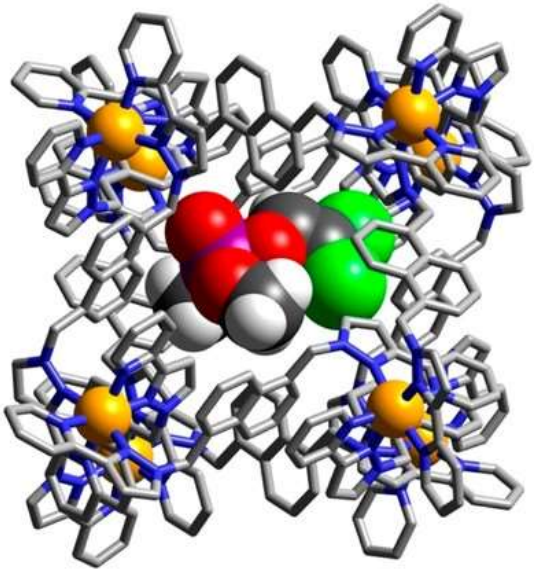

Figure 3.1.5 – Crystal structure of dichlorvos encapsulated with a M_8L_{12} cage (in wireframe, with Co(II) ions shown as orange spheres) containing a molecule of dichlorvos in the cavity (shown as space filled). Colour code: Co = orange, Cl = green, P = purple, O = red, C = black, N = blue).[274]

The use of cyclodextrins,[191,217,278,279] calixarenes,[189,280] molecular baskets,[281–283] tubes,[284] MOFs[285,286] and cages[272–274] as well as anion receptors[209,211,265] have been shown to bind and detoxify NAs. Cavitands have also been shown to bind NAs. In these cases, the recognition of the NA followed by a reaction of a functional group close to the binding site is crucial for their mode of action. As VX has a pKa of 8.6 in water at 25°C, the use of cation receptors can be used to recognise the protonated amino groups. Isaacs[287,288] introduced cucurbiturils and acyclic analogues that could be used as VX scavengers. Kubik and co-workers then investigated their

effects on VX degradation.[289] This would typically proceed through the hydrolysis of either the P-S or P-O bond, through a slow reaction with a half-life of 31 minutes at pH 13 and 25°C.[289] They reported that the cucurbiturils resulted in a third reaction pathway; this pathway differs to the other pathways, as the hydroxide is added to the phosphorus atom and is followed by the release of thiolate or ethoxide (Scheme 3.4), with a C-S cleavage in one step.[289] Here the nitrogen atom attacks the carbon next to the sulphur atom and the nucleophilic substitution results in the formation of N,N-diisopropylaziridium ion (DIAZ) and the O-ethyl methyl phosphonothioate anion (EMPT).[289] The presence of these species was hypothesised using ^{31}P NMR and confirmed through ESI-MS.[289] Under basic conditions (pD ~ 10.0) the cucurbit[7]uril was shown to facilitate the complete hydrolysis of VX at room temperature in 30 minutes.[289] It was noted by the authors that these conditions and the alkylating properties of the DIAZ void its use for *in vivo* applications, however its applications could lie in the decontamination of exposed surfaces.[289]

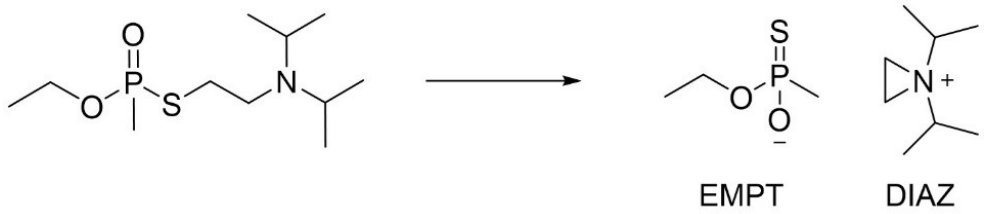

Scheme 3.4 – The third hydrolysis pathway of VX demonstrated by Kubik and co-workers.[289]

All the examples described here rely on access to the nerve agent itself or an appropriate simulant to enable effective development of new technologies. Therefore, the work in this chapter aims to assess the reactivity of potential OP CWA simulants (**40**-**61** Figure 3.1.6) in the presence of a base (NaOH) using ^{1}H NMR and to use that data to develop predictive models using the association constants (K_{ass}) derived in Chapter 2 between OP CWA simulants **40**-**61** with compound **36** and the values derived from computational modelling (also as detailed in Chapter 2) to determine whether K_{ass} can be used as a parameter to predict simulant reactivity. Other physical properties of these compounds are also investigated to help aid OP CWA simulant

selection. These models could then be used as an accessible method to initially develop new remediation technologies without the need to access the live agents and aid with appropriate simulant selection.

The work detailed in this chapter has been published in the following journal:

R. J. Ellaby, D. F. Chu, A. Pépés, E. R. Clark and J. Hiscock, *Supramol. Chem.*, 2021, **33**, 309–317.

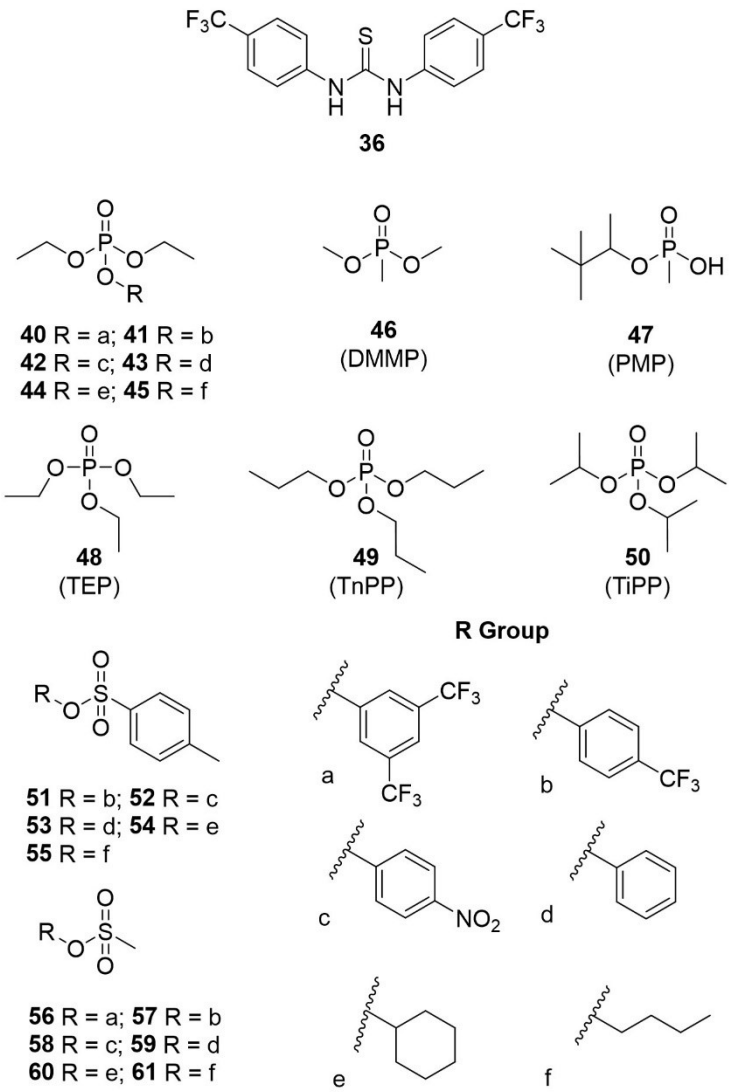

Figure 3.1.6 – Chemical structures of the 23 compounds discussed in this chapter.

3.2 Synthesis

The synthesis of compounds **36** and **40**-**61** are as detailed in Chapter 2 (2.2 synthesis, page 43)

3.3 Assessing the reactivity of simulants

The identification of simulants that effectively mimic the reactivity of OP CWAs to allow the development of more effective decontamination agents is also of high importance. There are several commercially available OP CWA decontamination solutions/systems, these include the US army developed skin decontamination M258 kit,[290] which is a two phase system that contains two packets to be used one after the other; Packet 1 contains a towelette impregnated with phenol (10 wt %), ethanol (72 wt %), NaOH (5 wt %), ammonia (≈1 wt %), and water (12 wt %), whilst Packet 2 contains a towelette impregnated with chloramine-B and a sealed glass ampoule filled with zinc chloride.[95,290] A second decontamination solution is DS2 which consists of diethylenetriamine (70 wt %), ethylene glycol monomethyl ether (28 wt %), and NaOH (2 wt %).[95,291] Super topical bleach (calcium hypochlorite (93 wt %) and NaOH (7 wt %)), when supplied as a solid or slurry with water is also deemed useful for OP CWA decontamination.[291,292] All of these systems/solutions (with the partial exception of super topical bleach) have in common the presence of an alcohol, NaOH, and H_2O. Here the hydroxide ion acts as a nucleophile which attacks the electrophilic phosphorus centre, which is common to all members of this class of OP CWAs, this neutralises/reduces the toxic effects of these agents.[173,257,293] When considering the library of potential simulants **40**-**61**, the electrophilic centre that is analogous to that of the OP CWA is either the comparable P=O phosphorus or O=S=O sulphur atom.

Initially a series of studies were conducted in DMSO-d_6 to assess compounds **40**-**61** hydrolytic stability upon the addition of D_2O. The proportion of D_2O added was calculated to be the maximum amount of water that could be added before any compound start to precipitate

out of solution, to ensure compound solubility throughout the duration of the studies but to also ensure there was the maximum amount of water to study a compound's stability in the presence of water. Even though some compounds could be studied with increased amounts of D_2O present, to ensure the same conditions for every compound, the amount was selected based on the least water soluble compound. The spectra from these results can be found in the appendix Figures S209-S225, and an example of the data collected is illustrated in Figure 3.3.1.

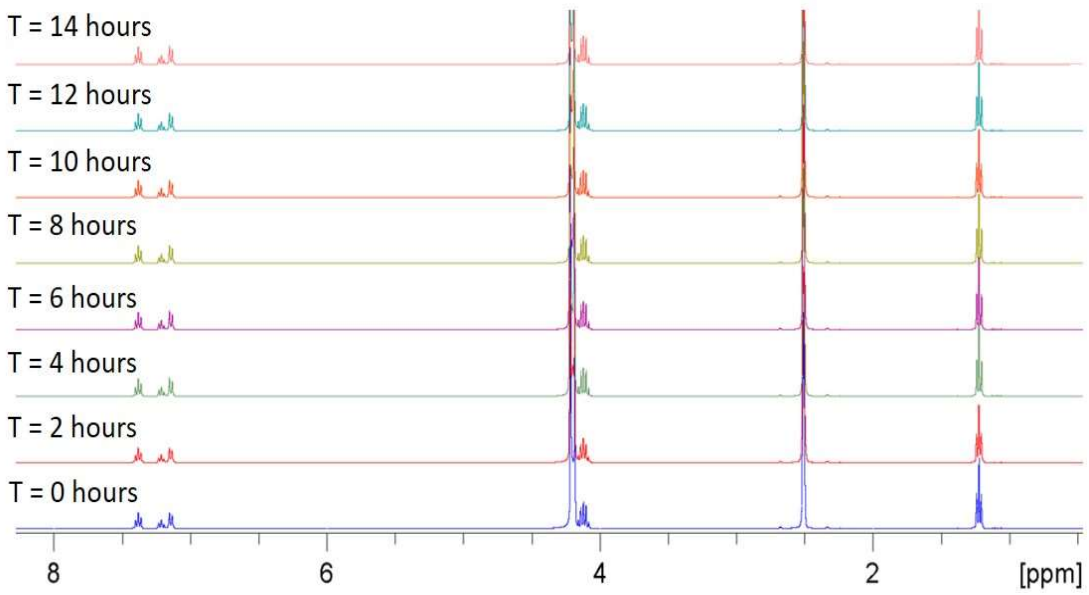

Figure 3.3.1 - Stacked ^{1}H NMR spectra (DMSO-d_6:D_2O (70:30)), showing the results of compound **43** hydrolysis over 14 hours. Results indicate 0 % breakdown.

In order to evaluate the reactivity of these potential OP CWA simulants **40**-**61** (see Scheme 3.5) in the presence of NaOH. A series of ^{1}H NMR spectroscopy studies (n=3) were conducted at 291 K in a methanol-d_4:D_2O 70:30 solution with either one or five equivalents of NaOH, whereby the relative proportions of simulant and hydrolysis product were monitored through integration with respect to time. These solvent conditions were chosen to allow for compound solubility throughout the duration of the study. The experimental conditions were optimised to consist of five equivalents of NaOH, which allowed for a more accurate study of the breakdown of these potential simulants under these conditions and a summary of those

results can be found in Table 3.1. The results of those reactions using one equivalent of NaOH are detailed within the appendix (see Figures S226-S235). As a range of reaction rates were observed for compounds **40-61** under these conditions, it was not possible to calculate an experimental hydrolysis rate constants for all the simulants tested. Therefore, the percentage (%) simulant breakdown after 6 hours has been used as a comparative simulant reactivity value in order to create this dataset. Through using this approach, it allowed for the inclusion of all values generated from these studies for all the potential simulants **40**-**61**. Additionally, where an experimental rate constant was able to be calculated (**40**-**43**, **46**, **51**-**55**, **57**, **59** and **60**) all reactions were found to follow first order kinetics apart from that of compound **57** which was found to obey second order kinetics (fit with R^2 = 0.9924) with respect to the simulant, however the fit for first order kinetics was 0.9218 and chemically is expected to be first order over second order kinetics.

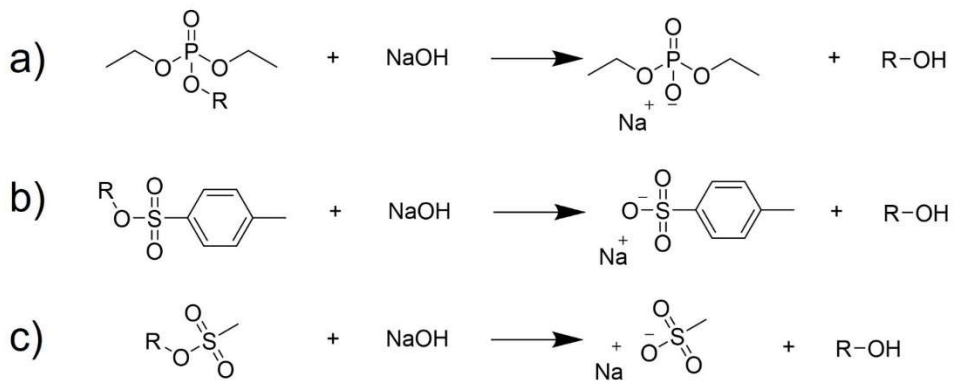

Scheme 3.5 Reaction of OP simulants a) **40**-**50**, b) **51**-**55**, c) **56**-**61** in the presence of the base NaOH.

Table 3.1 - Summary of average data (n=3) obtained from the reaction of potential OP CWA simulants **40** – **61** (10 mM) in the presence of 5 equivalence of NaOH (50 mM) in a methanol-d_4:D_2O 70:30 solution at 291 K. Error = standard error of the mean.

OP CWA simulant	Simulant breakdown after 6 hours (%)	Rate order	Experimental rate constant (s^{-1})
40	92.8 (± 2.19)	1st	0.42
41	47.9 (± 3.06)	1st	0.22
42	100 (± ≤ 0.01)	1st	0.46
43	17.6 (± 0.01)	1st	0.08
44	5.3 (± 0.23)	*a*	n/a
45	52.5 (± 0.01)	*a*	n/a
46	10.4 (± 0.01)	1st	0.05
47	0 (± ≤ 0.01)	-	-
49	0 (± ≤ 0.01)	-	-
49	0 (± ≤ 0.01)	-	-
50	0 (± ≤ 0.01)	-	-
51	55.7 (± 2.24)	1st	0.26
52	57.4 (± 0.06)	1st	0.27
53	1.5 (± 0.05)	1st	0.01
54	5.0 (± 0.36)	1st	0.02
55	8.2 (± 0.52)	1st	0.04
56	100 (± ≤ 0.01)	*b*	1.18
57	80.9 (± 0.16)	2nd	0.37[c]
58	100 (± ≤ 0.01)	*b*	n/a
59	2.1 (± 0.16)	*a*	n/a
60	66.5 (± 1.00)	1st	0.31
61	94.1 (± 1.28)	1st	0.44

a – Rate order could not be assigned. b – Rate of reaction could not be obtained due to speed of reaction. c – Reaction rate units = $M^{-1}.s^{-1}$, n/a – non applicable.

In summary, the reactivity of compounds **40**-**61** have been assessed using ^{1}H NMR in the presence of the base NaOH, with reaction conditions designed to mimic that of commercially available decontamination solutions and then optimised to allow for more accurate determination breakdown rates for this set of compounds. It was also determined that to allow for the inclusion of the whole data set that the use of the % breakdown after 6 hours would allow for this and could be used as a benchmark for the rate constant.

3.4 Predicting simulant reactivity

The script used within this section was written by Dr Dominique Chu, data collection and analysis were conducted by myself.

Organocatalysis by (thio)ureas is generally considered to arise from enhanced reactivity/electrophilicity of the substrate induced by hydrogen bonding with the catalyst, and the catalyst efficacy is typically correlated with hydrogen bonding complexation strength of the substrate with the (thio)urea moiety.[294–298] Therefore, it is plausible to hypothesise that the 1:1 association constants, derived using the non-specific hydrogen bond donating receptor **36** (results and experimental methods are detailed in Chapter 2.3 page 44 - however, for ease of reference are detailed in Table 3.2) could potentially be used as a predictor of reaction centre electrophilicity when the principal hydrogen bond accepting group is directly joined to the electrophilic centre. Thus, we further hypothesise these association constants could be used in the prediction of reaction rates.

Table 3.2 - Association constants (M^{-1}) calculated for **40–61** in a CD_3CN solution at 298 K,[1] obtained through the fitting of ^1H NMR titration data to a 1:1 host: guest binding isotherm using Bindfit v0.5.[225,299]

No.	K (M^{-1})	No.	K (M^{-1})
40	36 (± 6 %)	**51**	22 (± 6 %)
41	17 (± 1 %)	**52**	< 10
42	< 10	**53**	< 10
43	< 10	**54**	48 (± 11 %)
44	< 10	**55**	106 (± 8 %)
45	< 10	**56**	41 (± 8 %)
46	11 (± 1 %)	**57**	64 (± 5 %)
47	52 (± 6 %)	**58**	46 (± 9 %)
48	< 10	**59**	76 (± 6 %)
49	< 10	**60**	< 10
50	< 10	**61**	< 10

To investigate this hypothesis, an exhaustive parameter search was conducted for the parameters detailed in

Table 3.3.[1] Here the experimentally derived association constants of compounds **40**-**61** with receptor **36** (Table 3.2) were included as well as parameters derived using computational modelling (detailed in Chapter 2.4, page 51). This list of parameters includes a mix of both thermodynamic and kinetic parameters, with the results detailed within this chapter for rate constants being kinetic parameters and the parameters such as the HOMO and LUMO detailed in chapter 2 are thermodynamic, so caution when comparing the two is required. Here, we utilised R data analysis software[300] to determine both direct and inverse predictive models, using equations 1 and 2, applying the same methods as previously detailed in Chapter 2.6 page 60.

$$P_0 = P_x^a \times P_y^b$$
$$|a| + |b| = 2 \qquad \text{Equation 1}$$

$$P_0 = P_x^a \times P_y^b \times P_z^c$$
$$|a| + |b| + |c| = 3 \qquad \text{Equation 2}$$

Table 3.3 - List of parameters (*P*) used to produce potential simulant predictive models. P_1 – P_{20} are previously published data sets.[1]

P	Parameter description	SI Unit
P_0	Breakdown after 6 hours	%
P_1	Association constant	M^{-1}
P_2	E_{min}	kJ mol^{-1}
P_3	E_{max}	kJ mol^{-1}
P_4	Molecular Volume	$Å^3$
P_5	Molecular Area	$Å^2$
P_6	Solvent accessible area	$Å^2$
P_7	Polar surface area	$Å^2$
P_8	% Polar surface area	$Å^2$
P_9	Polarizability	
P_{10}	Steric weighting factor (SWF)	$Å^2$
P_{11}	Steric accessibility factor (SAF)	$Å^2$
P_{12}	HOMO	eV
P_{13}	LUMO	eV
P_{14}	Energy	kJ
P_{15}	Electrostatic charge	C
P_{16}	Additive N···O hydrogen bond length	Å
P_{17}	Log P	N/A
P_{18}	Dipole moment	D
P_{19}	Additive N-H···O hydrogen bond length	Å
P_{20}	Additive hydrogen bond angle difference from 180°	°

N/A – non-applicable

To take into account the limitations of the experimentally derived data (P_0 and P_1), five datasets were produced as follows: (1) all data generated for all parameters and potential simulants listed in Figure 3.1.6 and Table 3.3; (2) exclusion of association constant (P_1) from the complete data set (1); (3) exclusion of K_{ass} values less than 10 M^{-1} from the P_1 data set, because these values are known to fall outside of experimental limitations; (4) exclusion of percentage breakdown data from P_0, where potential simulant breakdown was found to be < 10 % over 6 hours, as these values are believed to fall outside of experimental limitations due to inherent integration errors; and (5) the exclusion of both P_1 < 10 M^{-1} and P_0 < 10 %.

This approach allowed for the determination of the importance of an experimental association constant value in the prediction of a simulant's reactivity. The models produced using these exhaustive search methods for datasets 1-5 and equations 1 and 2 were then ranked according to their R^2 values. From this ranking, the ten best fitting models from each equation were selected. This resulted in the production of 20 models of best fit for each dataset, creating a total of 100 models, which can be found within the appendix (see pages S282-S381). Using these 100 models, the frequency of each parameter was examined to identify those parameters that are the most relevant for the prediction of a simulants reactivity, the summary of these results of this are detailed in Figure 3.4.5 - Figure 3.4.5.

From data set one, the occurrence of each parameter for each equation was calculated and can be found in Figure 3.4.1. Here we observe that the parameter P_{13} (LUMO) appears the most frequently with 20 occurrences. The frequency of this parameter is not surprising given the partial covalency of a hydrogen bond, and how this orbital is directly involved in the reaction process. The second most occurring parameter is P_5 (molecular area), with a total of 7 occurrences. It is interesting to note, that without considering any experimental limitations that association constant appears in three of the top 20 models for this data set.

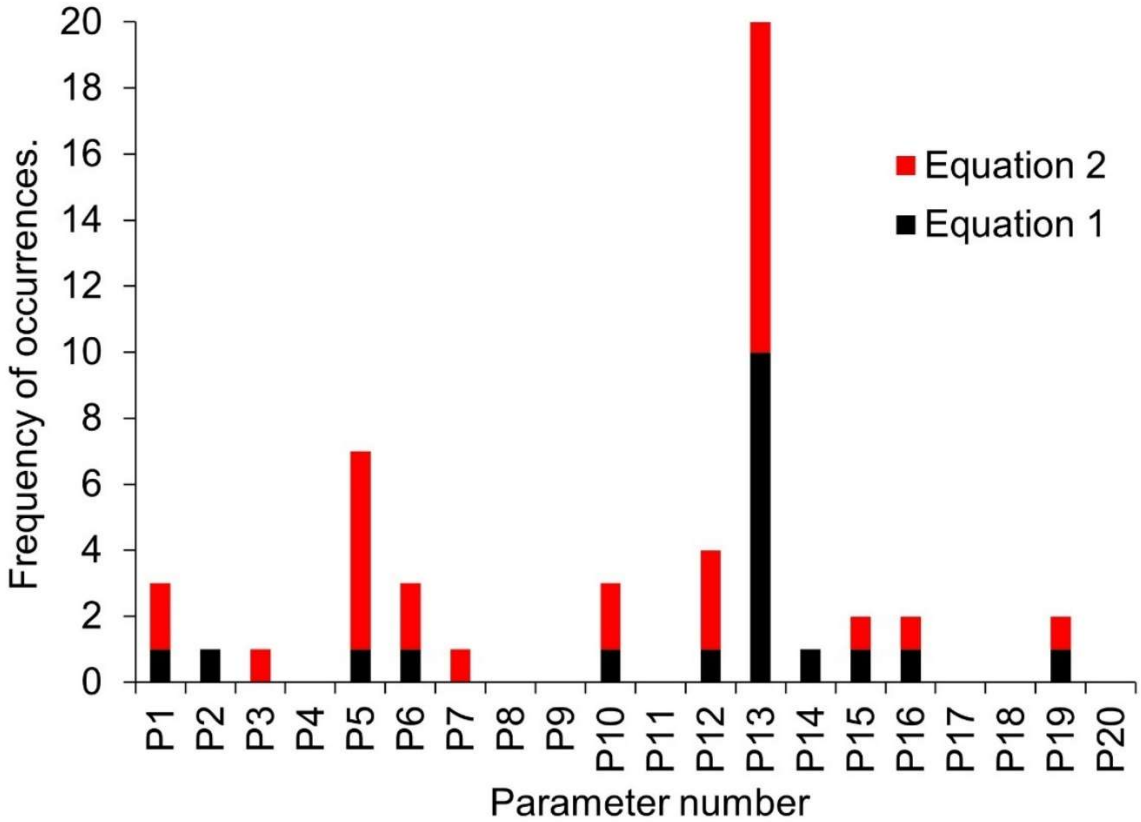

Figure 3.4.1 - The frequency of parameter occurrences in the top 10 models, produced by an exhaustive search of fits for data set 1, ranked by R^2 analysis for each parameter to: i) Equation 1 (black); and ii) Equation 2 (red).

In order to ascertain whether the experimentally derived K_{ass} values are an important parameter to consider for the development of these models, data set 2 was created to observe which parameters occur most frequently with the exclusion of K_{ass} values. From this data set (Figure 3.4.5) we observe that the same parameters appear in both data sets, with the exception of the P_3 no longer occurs. P_{13} is observed to still be the most frequent parameter, and P_5 the second most frequent. Three of the 11 parameters that appear in both models have an increase in occurrence, these parameters are P_2, P_5 and P_{19}. From this data set we observe no significant differences when excluding K_{ass} as a parameter.

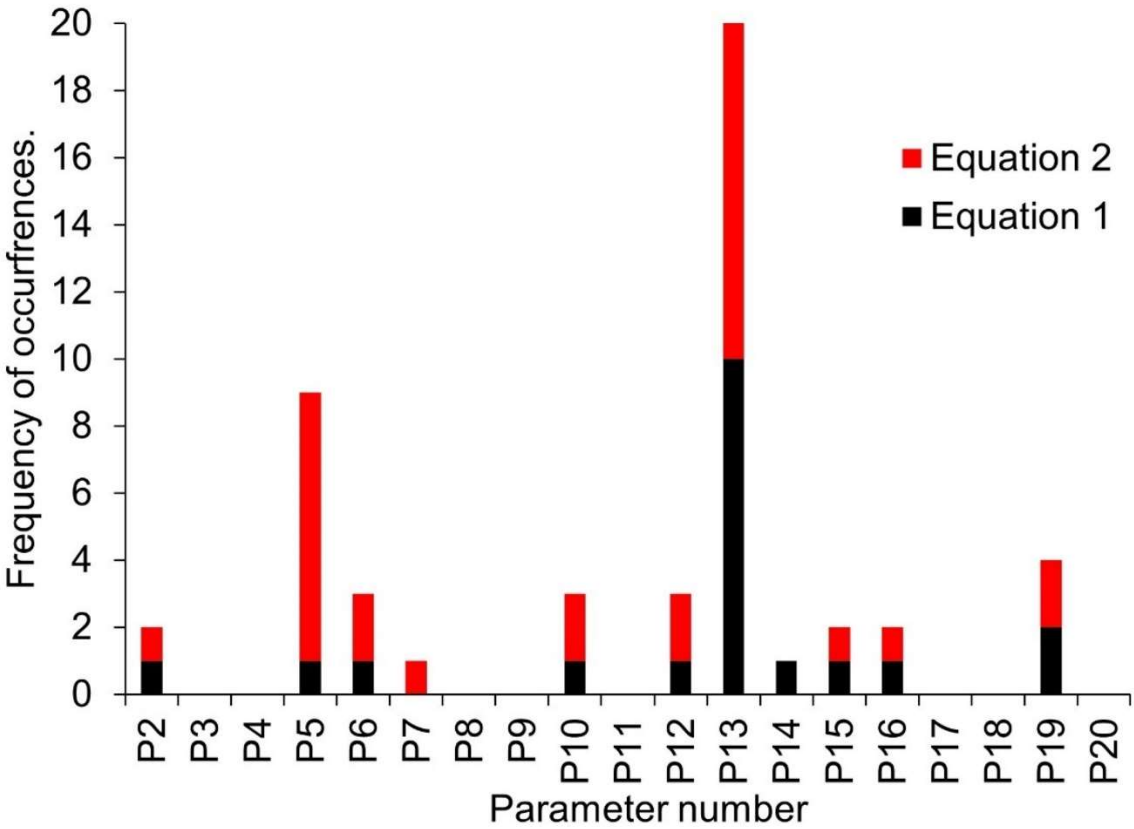

Figure 3.4.2 - The frequency of parameter occurrences in the top 10 models, produced by an exhaustive search of fits for data set 2, ranked by R^2 analysis for each parameter to: i) Equation 1 (black); and ii) Equation 2 (red).

It was due to these observations that data set 3 was created and studied, in order to consider the experimental limitations of the K_{ass} values (the exclusion of K_{ass} values <10 M^{-1}). From this data set we saw an overall increase in R^2 values (see appendix Figures S302 – S321). A summary of the parameter occurrences is summarised in Figure 3.4.5. From these models we observe the reappearance of P_1 (K_{ass}) with a total of 11 occurrences, an increase in 8 from data set 1. The parameter P_{13} is still the most frequent parameter, however, the total number of occurrences have dropped from 20 to 16 in this data set. We also observe that all but five parameters (P_{10}, P_{14}, P_{16}, P_{17} and P_{18}) occur at least once. Where we have previously seen P_5 as the second most frequent parameter in this data set this is no longer the case and the number of occurrences dropped to only the once across the 20 models studied from this data set. From

this data set we observe the importance of considering the limitations of experimentally derived data in the formation of these models.

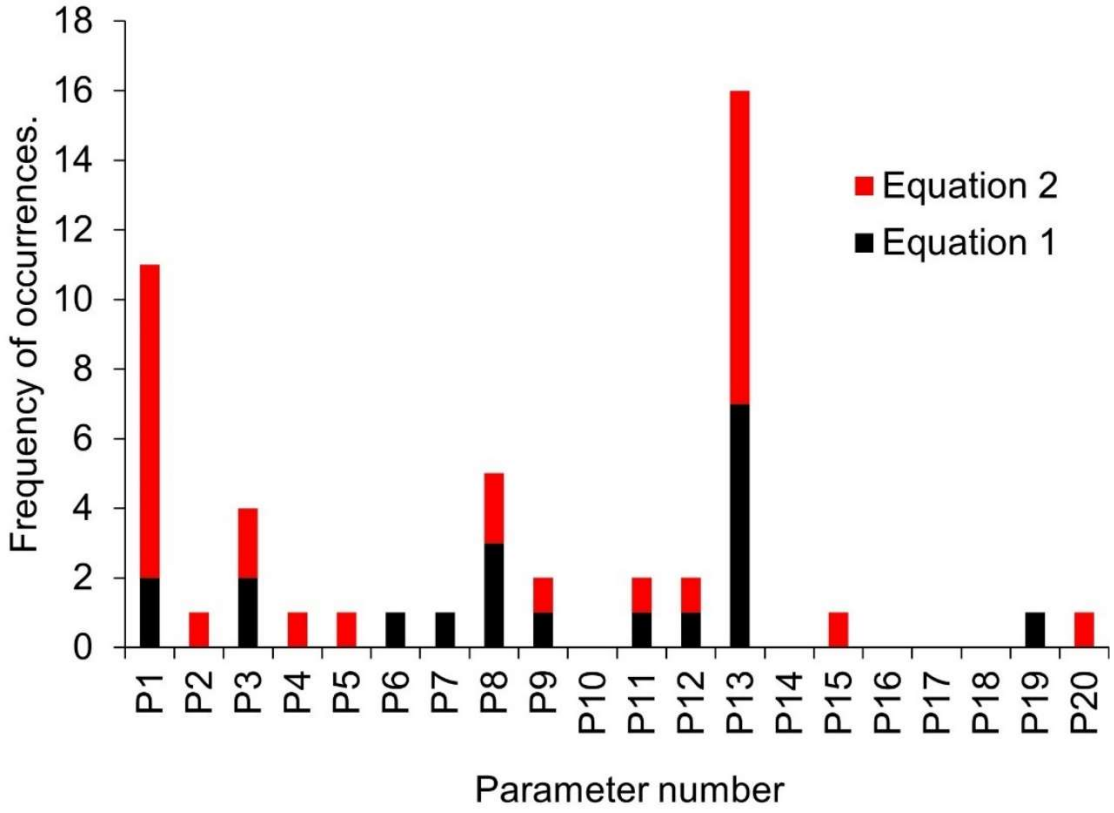

Figure 3.4.3 - The frequency of parameter occurrences in the top 10 models, produced by an exhaustive search of fits for data set 2, ranked by R^2 analysis for each parameter to: i) Equation 1 (black); and ii) Equation 2 (red).

Due to the observation of how important it is to consider experimental limitations; it was concluded that the limitations of the percentage breakdown of compounds in the presence of NaOH also be considered. Here those compounds which a percentage breakdown of 10% or less were excluded and these percentages are rather small takes into account the error found from the triplicate results, and integration of NMR spectra. This new data set forms data set 4 (Figure 3.4.4). From this data set we see a different picture to that previously seen, here P_1 appears a total of zero times, and no parameter appears more than 10 times across the 20

models examined in this data set. P_{13} is still the most frequent parameter with a total of 9 occurrences, with P_6 the second most frequent parameter with a total of 8 occurrences.

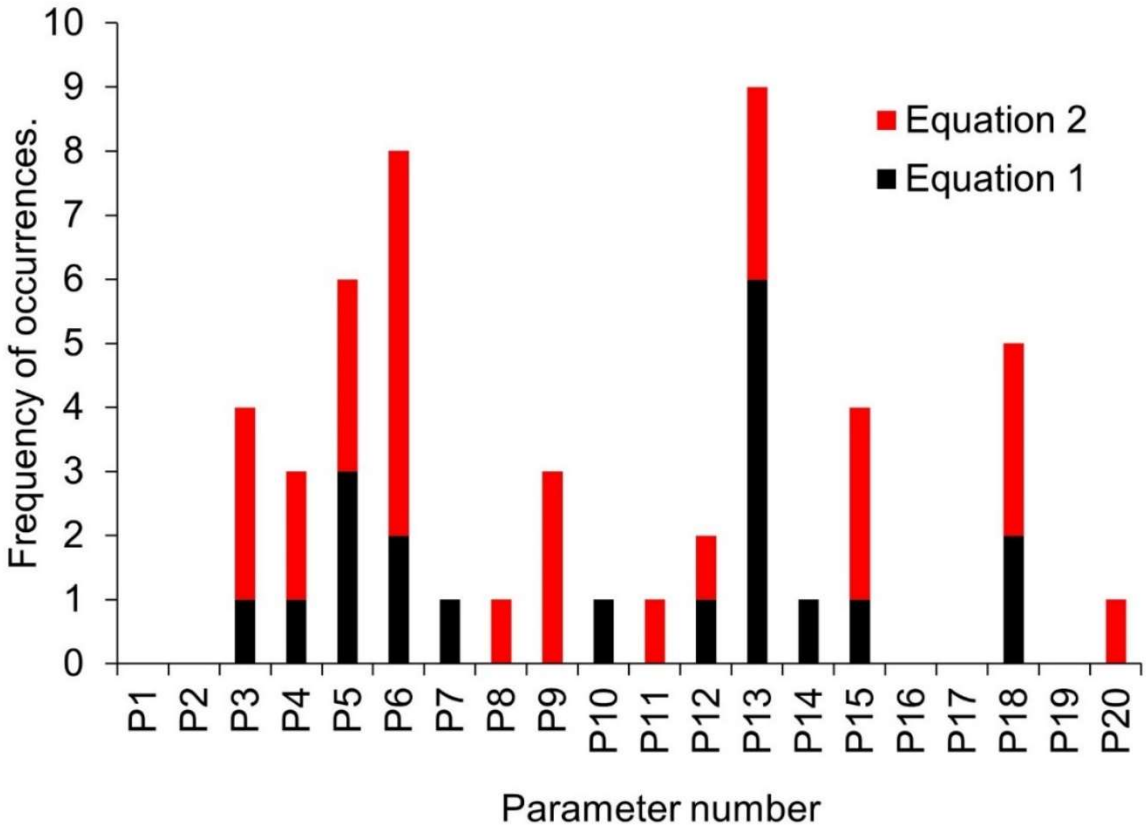

Figure 3.4.4 - The frequency of parameter occurrences in the top 10 models, produced by an exhaustive search of fits for data set 2, ranked by R^2 analysis for each parameter to: i) Equation 1 (black); and ii) Equation 2 (red).

Data set 4 further highlighted the importance of experimental limitation considerations, as when you compare data set 1 to data set 2, they tell a different story on which parameters are significant in the prediction of simulant reactivity. With this in mind, and the findings from data set 3, both experimental limitations were considered together to give data set 5, which excluded K_{ass} values <10 M^{-1} (data set 3) and percentage breakdown of <10 % (data set 4), the frequency of parameter occurrences for this data set are summarised in Figure 3.4.5, and the 20 models studied from this data set can be found in the appendix (Figures S362-S381). Here we

now observe that P_1 is the most significant parameter, with a total of 21 occurrences, with P_8 the second most observed parameter with a total of 5 occurrences, which is quite a large different in frequency in comparison to P_1. Interestingly, in this dataset, P_{13} only occurs twice and only in models from equation 2, whereas, in data sets 1-4 it was deemed a significant parameter with the most occurrences in each data set, so is curious that within this dataset it only occurs twice.

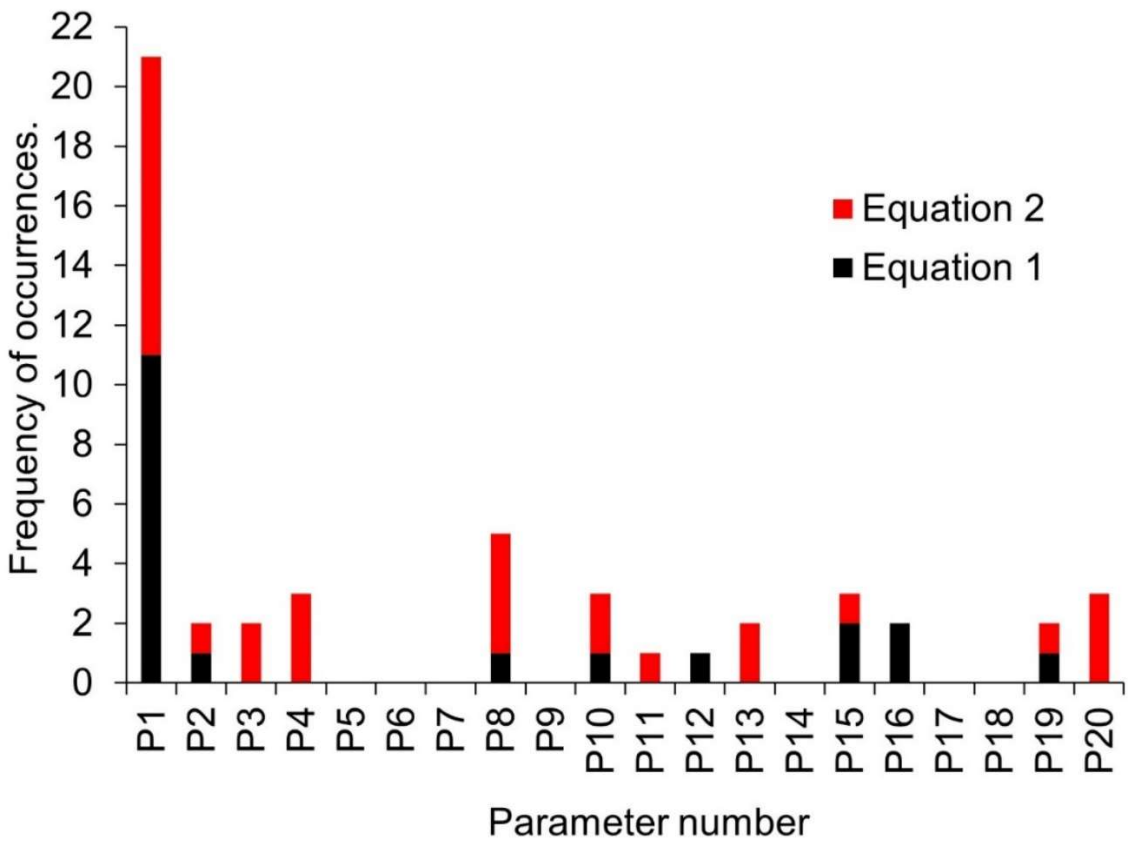

Figure 3.4.5 - The frequency of parameter occurrences in the top 10 models, produced by an exhaustive search of fits for data set 5, ranked by R^2 analysis for each parameter to: i) Equation 1 (black); and ii) Equation 2 (red).

When comparing all five data sets, the parameters P_2, P_3, P_4, P_7, P_8, P_9, P_{10}, P_{11}, P_{14}, P_{16}, P_{17}, P_{18}, P_{19} and P_{20} (see Table 3.3) all occur ≤ 10 times within the 100 models. Therefore, it is unlikely that these are significant parameters to include for the construction of a predictive OP CWA simulant breakdown model. These 100 models also indicate that P_{13} (LUMO) should be

considered a significant parameter with a total of 64 occurrences overall; although, this is not surprising as this orbital is directly involved within the reaction process. To our surprise, the parameter with the second highest number of occurrences is P_1 (the experimentally derived association constant), with a total of 35 occurrences over the 80 models where this parameter was included within the initial datasets (Figure 3.4.5 a, c, d, and e). Furthermore, the occurrences of this parameter were shown to increase when the experimental limitations of the K_{ass} determination are considered, with 3 occurrences with data set 1 (Figure 3.4.1) to 11 occurrences in data set 3 (Figure 3.4.3) and 21 occurrences in data set 5 (Figure 3.4.5). This highlights the importance of considering the experimental limitations of the data for the development of these predictive models.

In addition, where the experimental limitations are considered for the percentage simulant breakdown, but not for the association constant parameters, we see the occurrence of P_1 drop to zero as highlighted in Figure 3.4.5 d, this supports further the importance of including such limitations within these datasets. After screening, the 20 models with the highest R^2 values came from data set 5 (Figure 3.4.5 e) which considers the experimental limitations placed on both the reactivity and association constant data. Within these models, the association constant parameter (P_1) occurs a total of 21 times. Consequently, it is believed that this result confirms that experimental association constants for hydrogen bonded complex formation can be utilised in the construction of predictive reactivity models for the identification of OP simulants.

When assessing the top 20 models produced, as ranked by R^2 analysis (data set 5) those models produced that used Equation 2 reported higher R^2 values than those that used Equation 1. It was also noted that within the other data sets (1-4) that those models produced from Equation 2 ranked higher by R^2 than those from Equation 1. The three models that reported the highest R^2 values (R^2 = 0.9596, 0.9359 and 0.9204 respectively) have been identified as the current lead predictive models and are shown in Figure 3.4.6. The parameters that are included within these models are: i) Figure 3.4.6 a – P_1 (association constant), P_4 (molecular volume) and

P_8 (% polar surface area); ii) Figure 3.4.6 b – P_1 (association constant), P_4 (molecular volume) and P_{13} (LUMO); iii) Figure 3.4.6 c – P_1 (association constant), P_{11} (SAF) and P_{13} (LUMO). From these three models the deduction that P_1 and P_{13} are significant parameters to consider, P_1 appears in all three models and P_{13} in two of the three. We also observe that although P4, P8 and P11 occurred less than 10 times in total across the 100 models, it highlights than even those parameters not deemed significant can still have an overall impact in conjunction with these significant parameters. With the third model (Figure 3.4.*6* c) including P11 (SAF) this compares with P13, and this is the electrostatic surface potential of the molecule around where the LUMO orbital sits, therefore, these parameters are similar as they represent the same area of the compounds, just from different perspectives.

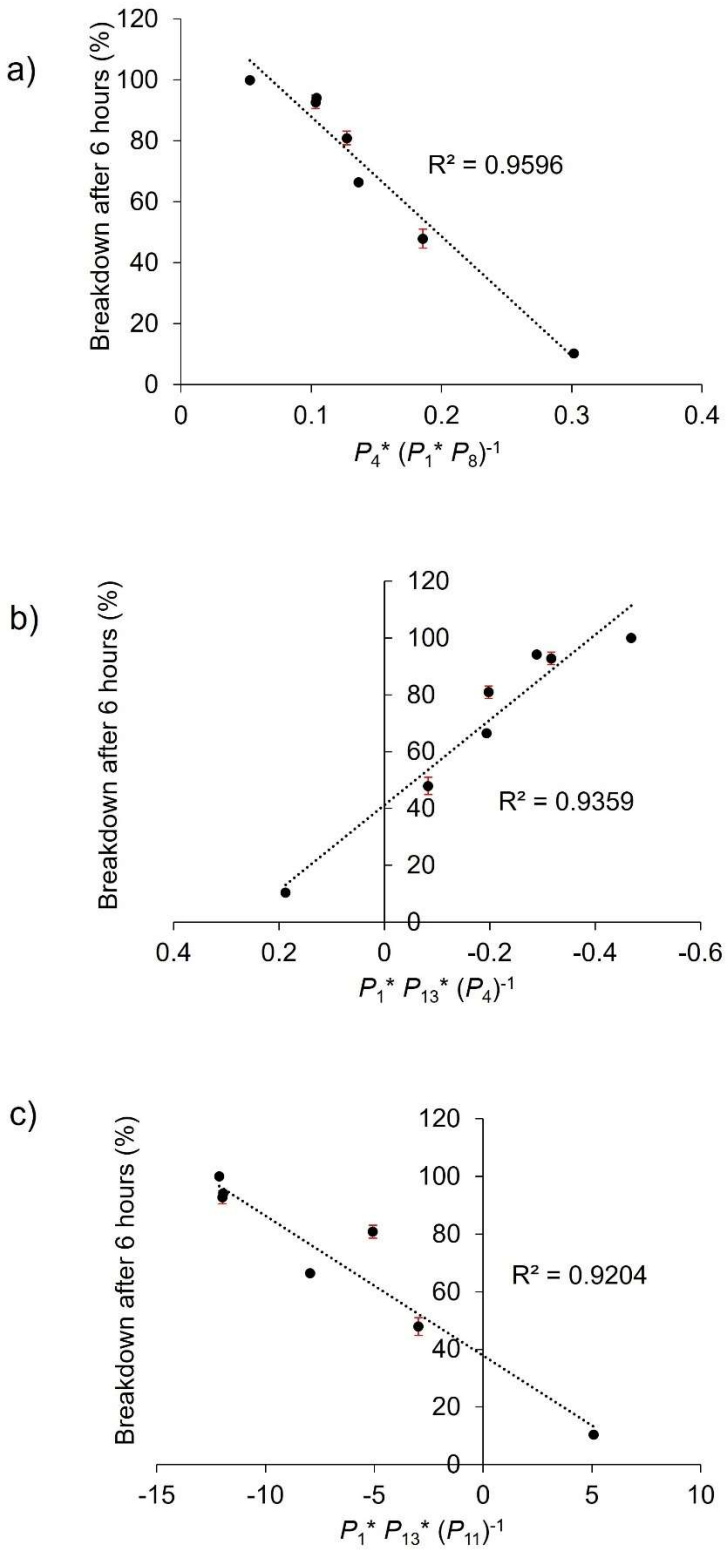

Figure 3.4.6 – The top three predictive models for simulant breakdown, defined through the ranking of R^2 values (from highest to lowest), obtained from fitting datasets 1-5 to Equations 1 and 2. The models shown in a-c were generated from dataset 5 and Equation 2.

In summary, it has been detailed how the use of exhaustive parameter searches can be utilised to not only identify what parameters could be significant to producing predictive models but also for producing a predictive model. In this case, we have found three predictive models for potential OP CWA simulant breakdown in the presence of five equivalents of NaOH, in a methanol-d_4:D_2O 70:30 solution at 291 K. It is hoped that the development of such predictive methodologies will enable the production of next-generation OP CWA decontamination technologies that rely on nucleophilic breakdown reaction mechanisms specifically. Additionally, the importance of considering experimental limitations on both association constant and reactivity datasets has been shown using these exhaustive search methods.

3.5 Physical property considerations

Further to a simulants breakdown rate, there may be other physical properties required to make its use practical in exercises such as live testing scenarios. The choice of simulant is therefore often a compromise between competing demands, for example the simulant might have to be readily available in advance of live experiment and thus require medium/long term storage. Considering possible practical requirements, we explored several physical properties for the simulants. In order to measure the stability of compounds **40**-**61**, a vial of each compound was left sealed on the bench and monitored over the period of one month using ^{1}H NMR, and the percentage breakdown of the compounds determined through comparative integration; for measuring the hydrolytic stability, the compounds were dissolved in DMSO-d_6:H_2O (70:30) solution and monitored over 14 hours at 291 K for any indication of breakdown. These solvent conditions were chosen to aid compound solubility. The results of these studies are detailed in Table 3.4. Compounds **46**-**50** were not studied as they are already commonly used simulants

Table 3.4 – A summary of the storage stability and the hydrolytic stability of compounds **40**-**61**.

No.	Storage breakdown (%)	Hydrolytic breakdown (%)	No.	Storage breakdown (%)	Hydrolytic breakdown (%)
40	0	0	**54**	2	0
41	0	0	**55**	0	0
42	0	0	**56**	0	0
43	0	0	**57**	0	0
44	0	0	**58**	0	0
45	0	0	**59**	0	0
51	0	0	**60**	0	0
52	0	0	**61**	0	0
53	0	0			

From the results detailed in Table 3.4, this shows that these compounds are stable under these experimental conditions, and as such could be prepared for testing in advance and stored at room temperature, removing the need for refrigerated storage, which can add extra costs when planning a decontamination method testing scenario. In addition, for those simulants that are liquid at room temperature, viscosity, density, and surface tension measurements were carried out, this was to give an indication as to how a simulant will behave on surfaces, these studies were conducted in triplicate (n=3) at 298 K, the average of these results are summarised in Table 3.5. These type of properties would be considered when investigating how a simulant would interact with different surfaces, how it could move across those surfaces which in turn would impact how you would treat a contaminated surface.

Table 3.5 – A summary of the average results (n=3) of density, surface tension and viscosity measurements for compounds **40**-**61**. All measurements were recorded at 298 K.

No.	Density ($g.cm^{-3}$)	Surface tension ($mN.m^{-1}$)	Viscosity (mPa)	No.	Density ($g.cm^{-3}$)	Surface tension ($mN.m^{-1}$)	Viscosity (mPa)
40	1.39	18.0	4.8	**54**	*a*	*a*	*a*
41	1.17	23.2	6.2	**55**	1.31	28.6	6.8
42	1.83	26.1	15.5	**56**	*a*	*a*	*a*
43	1.30	25.9	4.1	**57**	*a*	*a*	*a*
44	1.06	27.2	5.5	**58**	*a*	*a*	*a*
45	1.19	24.4	0.8	**59**	*a*	*a*	*a*
51	*a*	*a*	*a*	**60**	1.45	32.0	2.8
52	*a*	*a*	*a*	**61**	1.12	22.7	12.2
53	*a*	*a*	*a*				

a = not a liquid under experimental conditions.

3.6 Conclusions

In this chapter, the breakdown rates of potential OP CWA simulants **40**-**61** have been investigated in the presence of five equivalents of NaOH. Although rate constants were not able to be calculated for all compounds, comparative breakdown rates were used and resulted in the identification of three models for the prediction of OP CWA simulant reactivity, through the use of exhaustive parameter searches. It is hoped that in conjunction with the predictive model development demonstrated in Chapter 2 that it will allow for a more accessible approach to assessing a potential OP CWA simulants suitability. The importance of considering experimental limitations in the formation of predictive models was also investigated and it was demonstrated through the use of R^2 analysis that when these limitations are considered, the resulting models produced are of a better fit. It has also been demonstrated that the use of experimentally derived association constants can be used to predict a simulants reactivity. In addition, a variety

of the physicochemical properties of potential OP CWA simulants have been studied to support the breakdown data attained. It is hoped that this data will aid simulant selection for decontamination technology development. It is hoped that the use and development of structure activity relationships, achieved using similar, predictive methodologies to those detailed within, will allow for progressively more effective identification of appropriate simulants to aid in the development of novel decontamination technologies and combat the global threat posed by OP CWAs.

Chapter 4 – The use of supramolecular self-associating amphiphiles (SSAs) as molecular capture agents in solution.

4.1 Introduction

An amphiphile is a term to describe a chemical compound that possesses two distinctly covalently bound constituents, which demonstrate different affinities for a solvent within the same system, such as hydrophobic and hydrophilic components.[301] Depending on the nature of the hydrophilic group, amphiphiles can be categorised as anionic, cationic, zwitterionic or neutral (**67**-**70**, Figure 4.1.1).[302] Anionic amphiphiles contain a negative charge, with common head groups being carboxylates, sulphates, sulfonates and phosphates. An example of an anionic amphiphile is sodium dodecyl sulphate (**67**, Figure 4.1.1).[303] This is a water-soluble surfactant at room temperature and commonly used in medicated shampoos. This compound also exhibits antimicrobial activity against Gram-positive bacteria and is used as a preoperative skin cleanser.[304] Cationic amphiphiles contain a positively charged head group, common examples of cationic head groups are amines or ammonium ions,[305] such as benzalkonium chloride used as an antimicrobial preservative (**68**, Figure 4.1.1), due to its broad spectrum bactericidal activity.[306] It is worth noting here that the counter ions in both anionic and cationic amphiphiles are non-amphiphilic in nature. Zwitterionic amphiphiles exhibit high polarity and carry both a positive and negative charge on the same molecule that are bridged through alkyl chains or other spacers,[306] but overall are neutral molecules, cocamidopropyl betaine (**69**, Figure 4.1.1) is an example of a zwitterionic amphiphile that is used as a surfactant in bath products, or as an emulsifier in cosmetic products.[306] Neutral amphiphiles do not carry a charge, their amphiphilic nature is derived from the attached functional groups and its acidity, an example of a neutral amphiphile is sorbitan laurate which is used as a food additive/emulsifier (**70**, Figure 4.1.1).[306] The hydrophobic component usually consists of a hydrocarbon chain, however, there

are exceptions such as aromatic rings and trifluoromethyl functional groups,[307–309] these are sufficiently hydrophobic to act as a barrier against substances that are water soluble.[310,311]

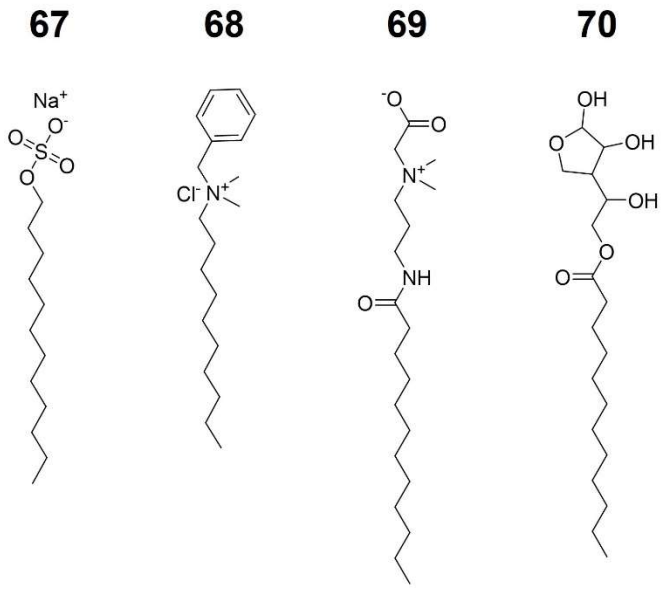

Figure 4.1.1 – Examples of amphiphiles; **67**) anionic (sodium dodecyl sulphate), **68**) cationic (benzalkonium chloride), **69**) zwitterionic (cocamidopropyl betaine) and **70**) neutral (sorbitan laurate).

One feature of amphiphiles is that while at a low concentration they will predominantly occur as monomers, when that concentration is increased, they can interact and start to self-assemble/aggregate, and depending on the solvent system, temperature, pressure, and the pH to form a variety of different aggregated species. The aggregates formed are restricted to maximise preferential intermolecular interactions and minimise non-preferential interactions with other species present within the solution. Examples of these structures include micelles, reverse micelles, lipid bilayers or vesicles as illustrated in Figure 4.1.2.[312,313] Micelles (Figure 4.1.2 a) form in polar solvents, here the hydrophilic head group interacts with the water molecules whilst the hydrophobic tails are sequestered away from the aqueous solvent creating a hydrophobic core. Reverse micelles (Figure 4.1.2 b) are the opposite to micelles, they form in non-polar solvents, where the hydrophobic tail interacts with the solvent and the polar head groups are oriented towards the centre, creating a hydrophilic core. The structure of the amphiphile itself directly affects the result of the aggregate produced; for examples

phospholipids with a single hydrocarbon chain will preferentially form micelles whereas, phospholipids that contain multiple hydrocarbon chains, preferentially form a bilayer (Figure 4.1.2 c)[314] or vesicles (Figure 4.1.2 d).[315] This is because of the increased steric hindrance which occurs with multiple alkyl chains attached to a single phosphate head group.[316]

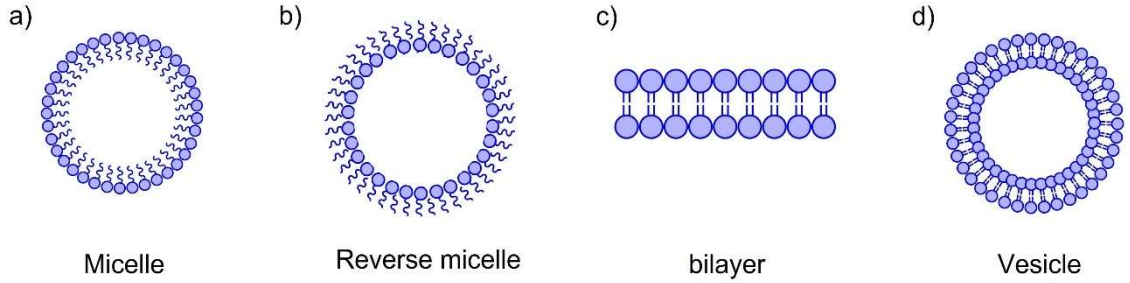

Figure 4.1.2 - Cartoon representation of possible amphiphilic aggregate formations. a) micelle, b) reverse micelle, c) bilayer and d) vesicle.

Supramolecular chemists have taken inspiration from nature and developed amphiphilic molecules that can form supramolecular complexes, termed supra-amphiphiles. These supra-amphiphiles are amphiphiles which are designed to incorporate intermolecular interactions within the self-association events of non-covalent interactions and dynamic covalent bonds.[317,318] The driving force that aids the complex formation are reversible non-covalent and dynamic covalent interactions such as: hydrogen bonds,[319] electrostatic interactions,[320] host guest recognition,[321] charge transfer interactions[322] and imine[323] and boronic ester bonds.[324] Alterations to these interactions alter the amphiphilicity of the molecules and as such can result in supra-amphiphiles with unique properties, including stimuli responsive and controllability of both the self-assembly and disassembly processes.[325]

An example includes work by Wang and co-workers studied the self-assembly of an amphiphilic zinc porphyrin derivative, which can be controlled to form spherical aggregates, upon the addition of different sized guests such as 4,4'- bipyridine and 2,4,6-tri(pyridin-4-yl)-1,3,5-triazine. These spherical aggregated were constructed through a combination of π-π

stacking interactions and hydrogen bonding.[326] Other work conducted by Zhang and co-workers utilised wedge shaped perylene bisimides that were able to form spherical aggregates in polar solvents.[327]

Klymchenko and co-workers designed a fluorescent nanoparticle based on cross linked calixarene micelles. These amphiphilic calixarenes (Figure 4.1.3) consisted of four alkyne groups and were found to self-assemble into micelles with a hydrodynamic diameter of 7 nm confirmed through dynamic light scattering (DLS), whereby the hydrophilic rim was turned towards the water and free to cross link with cyanine dyes. These structures were explored for applications in bioimaging, where it was found they were rapidly internalised into HeLa cells and shown as stable bright dots (Figure 4.1.3), and predominantly distributed in endosomes and lysosomes, whereas there was no fluorescence of these cells shown without these structures present.

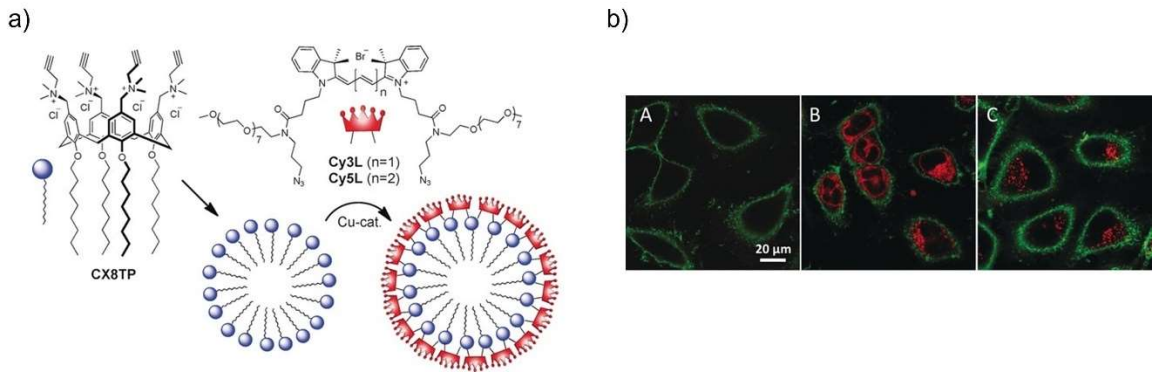

Figure 4.1.3 – Fluorescent amphiphilic calixarene produced by Klymchenko and co-workers. 1) Concept of calixarene micelles crosslinking cyanine dyes and 2) Fluorescence confocal imaging of HeLa cells incubated with fluorescent micelles. A) Control cells without micelles; B) cells incubated with non-cross-linked or C) cross-linked CX/Cy3L micelles. Green corresponds to plasma membrane staining with WGA-Alexa Fluor488 (50 nm), while red corresponds to the micelles.[328] Image reproduced from ref. 327 with permission from Wiley and Sons copyright 2016.

Kabanov and co-workers developed utilised the electrostatic interactions between a single-tail cation surfactant and an ionic head group (**71** Figure 4.1.4), which when combined they formed a micelle-like aggregations with low polydispersity under electroneutral

conditioins.[329] This unique self-assembly behaviour, combined with the wide variety of available surfactant components make these systems promising in addressing various theoretical and practical problems, particularly in pharmaceuticals, where block copolymers and polyelectrolyte complexes are already being intensively investigated as drug and gene delivery systems.[329] Kunitake and Kimizuka utilised melamines and isocyanuric acid derivatives as complimentary building blocks to form double and single chain supra-amphiphiles using extended hydrogen bonding arrays (**72** and **73**, Figure 4.1.4).[330–332]

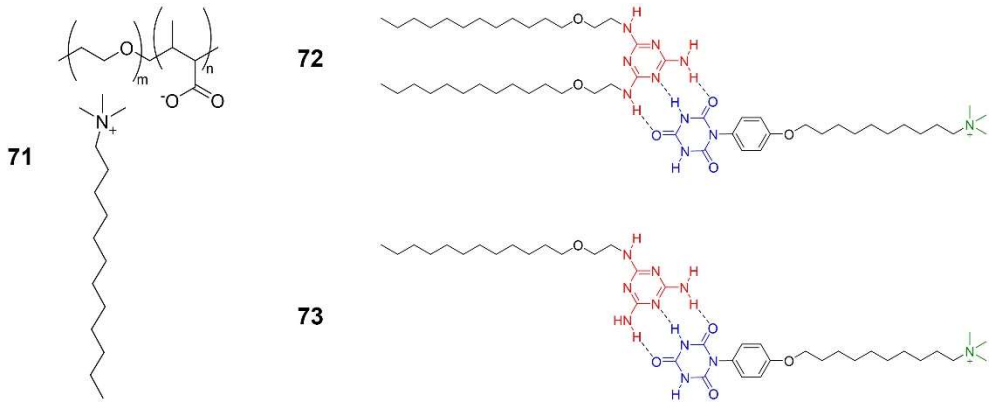

Figure 4.1.4 – Supra-amphiphiles **71**-**73**.

Supra-amphiphiles can be formed also through dynamic covalent bonds such as imine and disulphide bond formation, where these bonds are reversible under certain conditions,[333] which are comparable to non-covalent interactions.[334] The physicochemical properties and the applications of a supra-amphiphile are determined by topology. Apart from single-chain head-to-tail supra-amphiphiles, there are other forms: a) multi-chain head-to-tail, here there are multiple tails are present on either solely the hydrophilic, solely the hydrophobic or both components;[310] ii) bola-forms, where two hydrophilic headgroups can be covalently linked by one or two hydrophobic alkyl chains,[332,335] commonly utilised in solubilisation and drug or gene delivery vehicles;[302] and finally iii) polymeric supra-amphiphiles, which are constructed from

either non-covalent or dynamically covalent bound polymeric segments of two or more.[336] This type of supra-amphiphile is frequently used in cancer therapies and the formation of surfactants and nanocarriers.[337]

Finally, Faustino and co-workers investigated the surfactant properties of a series of hydrogen bond donating anions containing a urea-spacer-carboxylate/sulfonate motif (Figure 23).[338–340] Here the authors reported a correlation between the critical micelle concentration (CMC) and the amino acid residues **74**-**78**, whereby the CMC increased with increasing number of carbons on the side chain of the amino acid. It was also reported that the substitution of the carboxylate group for either a phosphate (**79**), sulfonate (**80**) or sulfate (**81**) group resulted in a decrease in CMC in the following order: $CO_2^- > PO_4^{2-} > SO_3^- > SO_4^-$. They hypothesised that this was due to the increased polarisation of the surfactants that contain sulphur or phosphorus atoms within their polar head groups. Faustino and co-workers also reported that compounds with increased (**82**) and branched (**83**) alkyl chains resulted in the lowest calculated CMC values of ≤ 3.04 x 10^{-2} mol dm^{-3}, this was attributed to the steric hindrance from the closely connected hydrocarbon chain, which prevented micellisation.

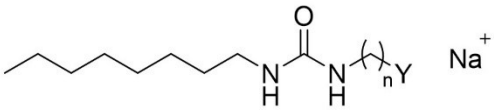

74-78 Y = CO_2^-, n = 1-5
79 Y = OPO_3^- n = 2
80 Y = SO_3^- n = 2
81 Y = OSO_3^- n = 2

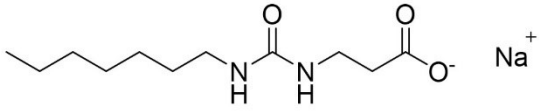

82

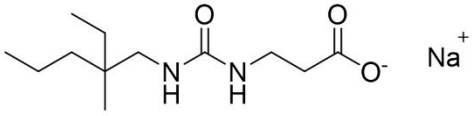

83

Figure 4.1.5 - The urea-spacer-carboxylate/sulfonate/phosphate motifs (**74**-**83**) synthesised by Faustino and co-workers.

Taking inspiration from Faustino's work, Hiscock and co-workers developed a series of novel 'Supramolecular Self-associating Amphiphiles' (SSAs), these SSAs incorporate the urea/thiourea spacer sulfonate motif with an alkyl ammonium counter cation. The general structure of these SSAs is shown in Figure 4.1.6 and it incorporates an anionic HBA group; a urea/thiourea HBD/HBA unit and a hydrophobic region. Through stepwise modifications of the R groups of the hydrophobic region they were able to alter the acidity of the urea/thiourea NHs.

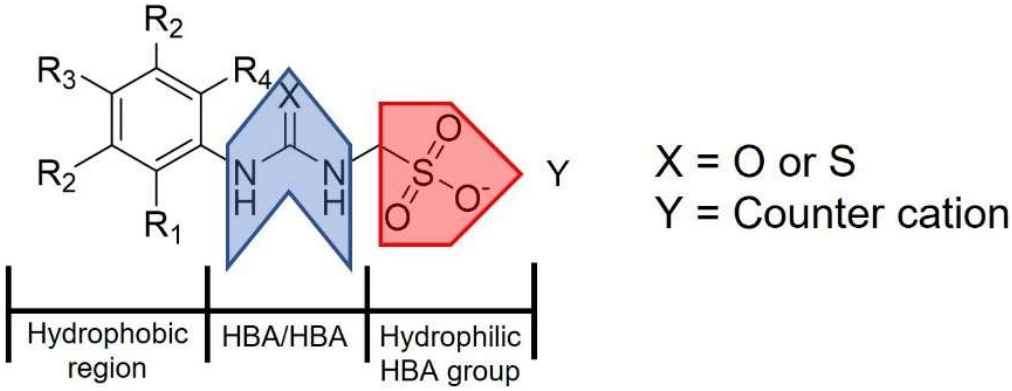

Figure 4.1.6 – The general structure of SSAs developed by Hiscock and co-workers.

As can be seen from the general structure in Figure 4.1.6, SSAs contain two possible HBA sites (the urea/thiourea moiety and the sulfonate moiety), but only contains one HBD site (the urea/thiourea unit), it is the competitive nature of these substituents that gives rise to a *'frustrated'* system. As a result of this there are at least four different self-associated hydrogen bonding motifs that can be adopted (Figure 4.1.7); a) (thio)urea-anion dimer; b) (thio)urea-anion stacking; c) anti-(thio)urea-(thio)urea stacking and d) *syn*-(thio)urea-(thio)urea stacking.[242] It has been shown that these binding motifs can be manipulated through alteration of the physical state, chemical composition, solvent environment and through changes of the cationic unit. Changes in the HBD acidity through modifications of the R and X groups resulted differing hydrogen bond lengths and angles, which in turn affected the angle of dimerisation.[341] In addition, the increased acidity of the NHs gave rise to the more optimal urea-anion hydrogen bond formation. Changes in the cationic unit also gives rise to differing binding modes; when in

the presence of a weakly coordinating cation such as tetrabutylammonium (TBA) it was found to predominantly form urea-anion dimers, however, when using more strongly coordinating cations such as potassium and sodium, the same binding mode was prevented, resulting in the urea-urea binding mode instead. Further to this, the self-association properties of these compounds were studied in the solid state, gas phase, solution state and *in silico*.[222]

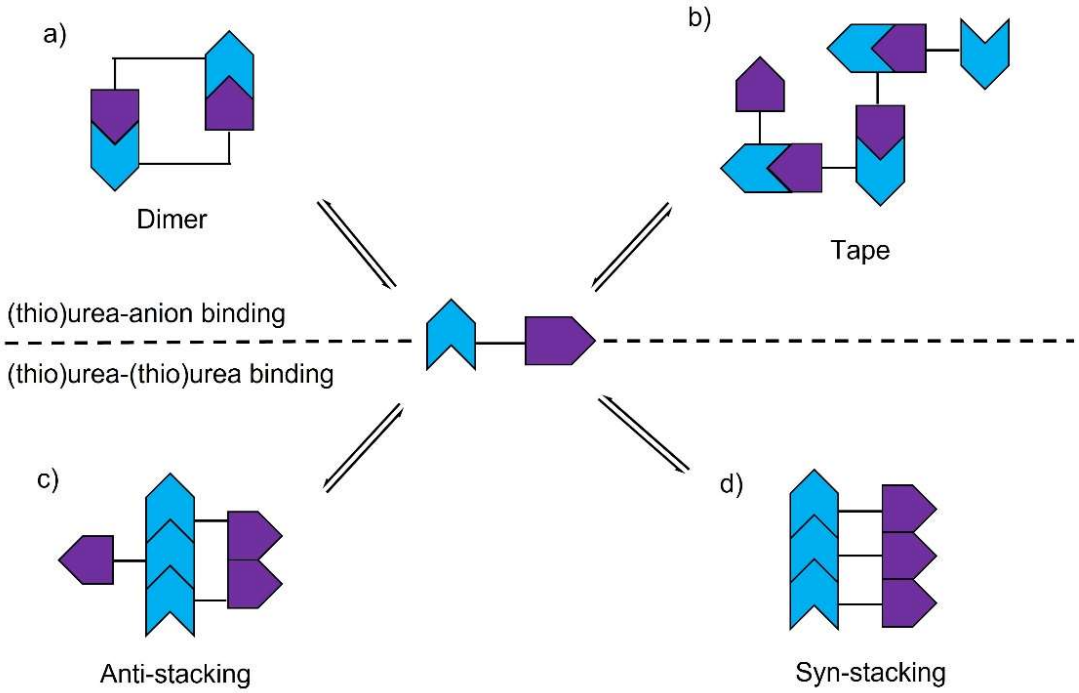

Figure 4.1.7 – Possible self-associated hydrogen bonded motifs for SSAs. a) dimer; b) tape; c) (thio)urea-(thio)urea anti-stacking; d) (thio)urea-(thio)urea syn-stacking.[242]

More recently Hiscock and co-workers focused on the synthesis and self-associated properties of a series of intrinsically fluorescent SSAs (Figure 4.1.8). Here they reported how the solvent environment played a vital role in the size of formed aggregate, with predominantly dimeric species observed in DMSO. However, when the percentage of water was increased, a greater percentage of larger aggregates were observed. These larger structures were studied through a combination of dynamic light scattering (DLS), ^{1}H NMR, tensiometry (to determine the CMC) and directly visualised through a combination of transmission and fluorescence microscopy.[342] These larger aggregates in aqueous solutions were shown to have a

hydrodynamic diameter of 100-550 nm.[243] In addition to dimeric species (< 10 nm) being present in the solution state (DMSO) they were also found to exist in both the gas phase and the solid state. These were identified through high-resolution electrospray ionisation mass spectrometry (ESI-MS) and single-crystal X-ray diffraction techniques (XRD) respectively. In order to elucidate structure-activity relationships (SARs) electrostatic potential maps were used to calculate surface energy maximum (E_{max}) and minimum (E_{min}) values using semi-empirical PM6 modelling methods. These calculated values were found to correlate well with both the dimerisation constants derived from the ^{1}H NMR studies and the CMC values.[222,341] Hiscock and co-workers concluded that it could be possible to predict the surfactant properties of this class of SSA (Figure 4.1.8) by measuring the dimerisation constant and using by simple computational techniques.[222] The SSAs have also been shown to have antimicrobial activity against clinically relevant gram-negative and gram-positive bacteria,[243,342,343] and further investigated the antimicrobial properties of their library of SSAs, and their potential to be used as drug delivery vehicles[3] and potential to enhance the efficacy of commonly used antimicrobials and anti-cancer agents.[344,345]

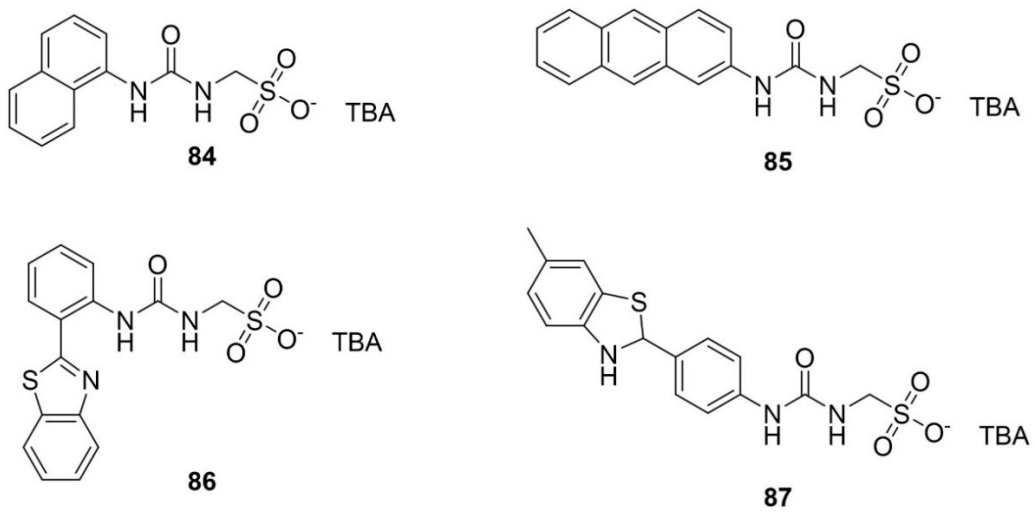

Figure 4.1.8 – Chemical structure of intrinsically fluorescent SSAs **84**-**87** synthesised by Hiscock and co-workers. TBA = Tetra butyl ammonium [222,243,341]

More recently, further work by Hiscock and co-workers have further illustrated the use of these amphiphilic molecules, whereby, it was demonstrated that when in a saline solution

SSAs can form gel fibres. This work shows how the solvent environment can be used to control self-association events and the resulting material formation. Here a para-substituted benzothiazole SSA **87** (Figure 4.1.8) , was shown to form a hydrogel in an aqueous salt solution, with both the physicochemical and morphological properties reliant on the salt present.[342] The stability of the of these gelated materials was found to be dependent on several salt solution-based factors such as pH, ionic strength, and cation size. Due to the intrinsic fluorescent nature of **87**, Hiscock and co-workers were able to visualise the fibrous networks formed (Figure 4.1.9).[342] These gels were further investigated to demonstrate whether they kept their antimicrobial properties against both model Gram-positive and Gram-negative bacteria. In addition to this, the hydrogel formed with **87** in aqueous NaCl was also found to support the incorporation of the antibiotic ampicillin, with the activity of the ampicillin shown to be conserved. The diffusive release of ampicillin was also achieved at concentrations that can inhibit the growth of both model bacteria.[342]

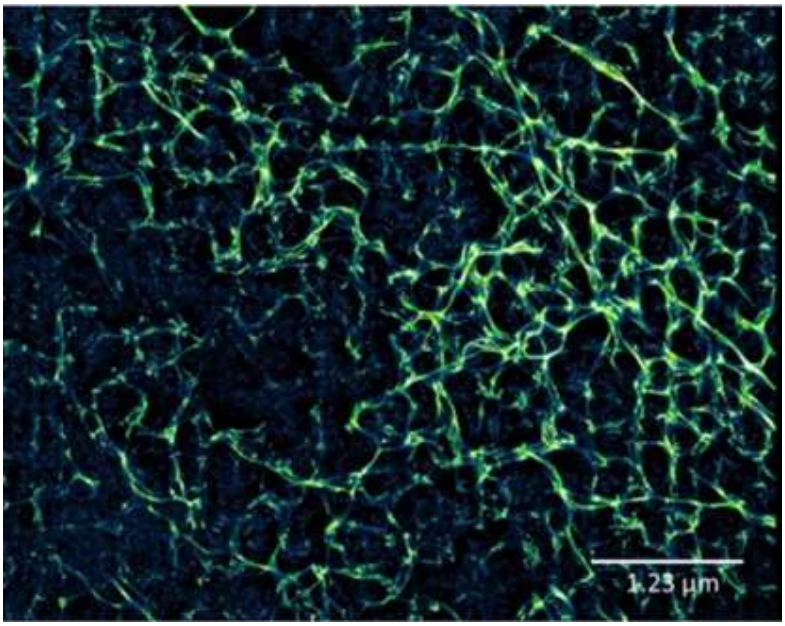

Figure 4.1.9 – Refined fluorescence microscopy image of the hydrogel observed for **87**. Image reproduced from reference 341, with permission from the Royal Society of Chemistry.[342]

The increasing global occurrence of organic micropollutants such as pesticides and pharmaceuticals in water resources has raised many concerns with regards to the potential negative effects on both aquatic ecosystems and human health.[202,346–349] The typical absorbent material used is activated charcoal, however, this suffers from slow uptake of pollutants[350,351] and it also isn't particularly very good for the uptake of hydrophilic pollutants.[352] To regenerate spent activated charcoal is also quite energy intensive and doesn't fully restore to 100 % performance.[353]

Supramolecular chemistry has been applied to this problem with work by Alsbaiee and co-workers utilised β-CD for their ability to encapsulate and form stable host:guest complexes. Here they cross linked β-CD with rigid aromatics (tetrafluoroterephthalonitrile) forming a mesoporous polymer of β--CD with a high surface area.[348] They found that this polymer was able to rapidly adsorb a variety of organic pollutants, which included plastic components, pharmaceuticals, pesticides, and aromatic carcinogens. This polymer was reported to have adsorption rate constant of 15-200 times greater than other non-porous β-CDs and activated charcoal, as well as the ability to be regenerated multiple times with mild washing with no loss of performance.[348]

More recently, work by Fernando, Mako and co-workers have reported a water-soluble pillar[5]arene with pendent cationic groups that was able to bind a variety of analytes within the pillararene core with K_{ass} values of 10^3-10^{10} M^{-1} reported (Figure 4.1.10).[354] These pillararenes were then able to be removed from the solution with their encapsulated guest using cationic exchange resins, allowing for pollutant removal from water.[354]

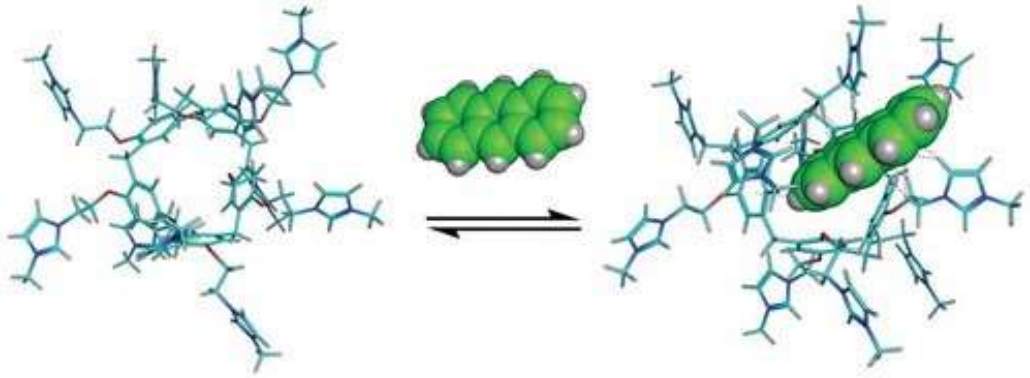

Figure 4.1.10 – Pillar[5]arene synthesised by Fernando, Mako and co-workers, showing the uptake of a pollutant into the hydrophobic core.[354] Image reproduced from ref. 353 with permission from Taylor and Francis.

The work in this chapter aims to build upon the current capabilities of the SSA technology investigating whether these agents can be used as environmental clean-up agents within aqueous systems. Here the physicochemical properties of three novel SSAs (**90**-**93**, Figure 4.1.11) and the generation of a new series of SSA co-formulations, using SSAs **88**-**93** and co-formulants **94**-**96** (**co-formulations *a*-*l***, Figure 4.1.12) are investigated following flow chart illustrated in Figure 4.1.13. Tetrabutyl ammonium (TBA) was used as the counter cation as it is weakly coordinating and therefore, won't be competitive when investigating any self-association events. It is hypothesised that the spherical aggregates formed by SSAs in aqueous conditions could capture pollutants within its core, the proof-of-concept of pollutant uptake is to be studied through a series of quantitative ^{1}H NMR, DLS and zeta potential studies, to investigate the self-associative processes by these SSAs and co-formulations.

The work detailed in this chapter has been published within the following peer-reviewed journal article:

1. L. J. White, J. E. Boles, K. L. F. Hilton, R. J. Ellaby and J. R. Hiscock, *Molecules*, 2020, **25**, 4126.
2. R. J. Ellaby, L. J. White, J. E. Boles, S. Ozturk and J. R. Hiscock, *Org. Biomol. Chem.,* 2022,

Advance article.

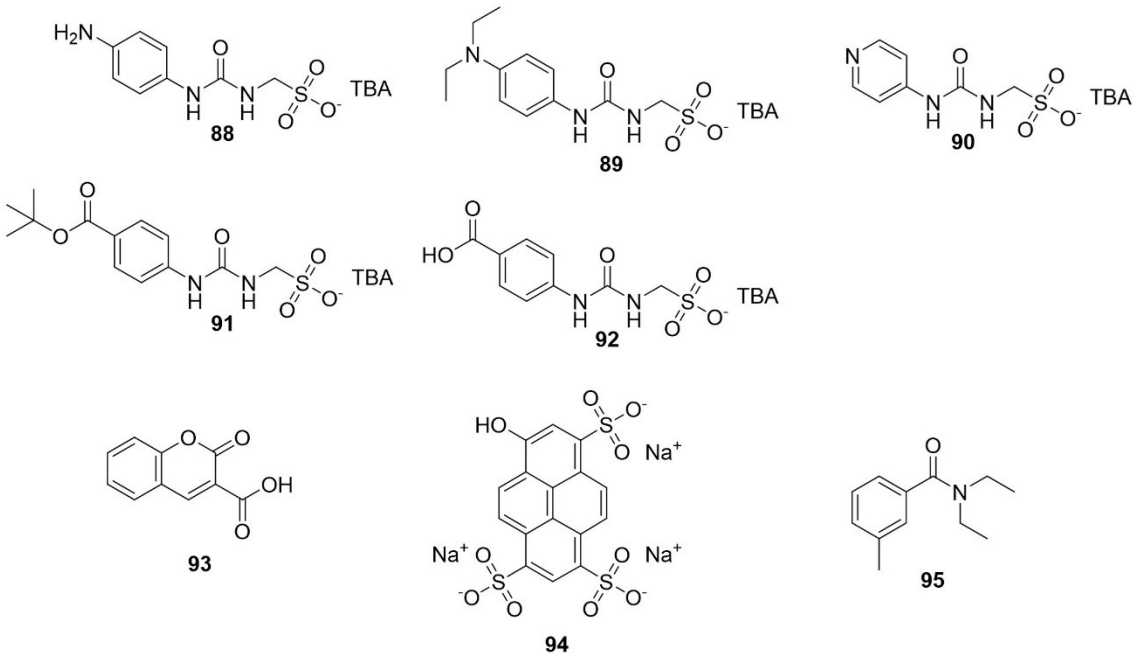

Figure 4.1.11 – Chemical structures of the 5 compounds (**88**-**92**) and 3 co-formulants (**93**-**95**) discussed in this chapter. TBA = tetrabutylammonium

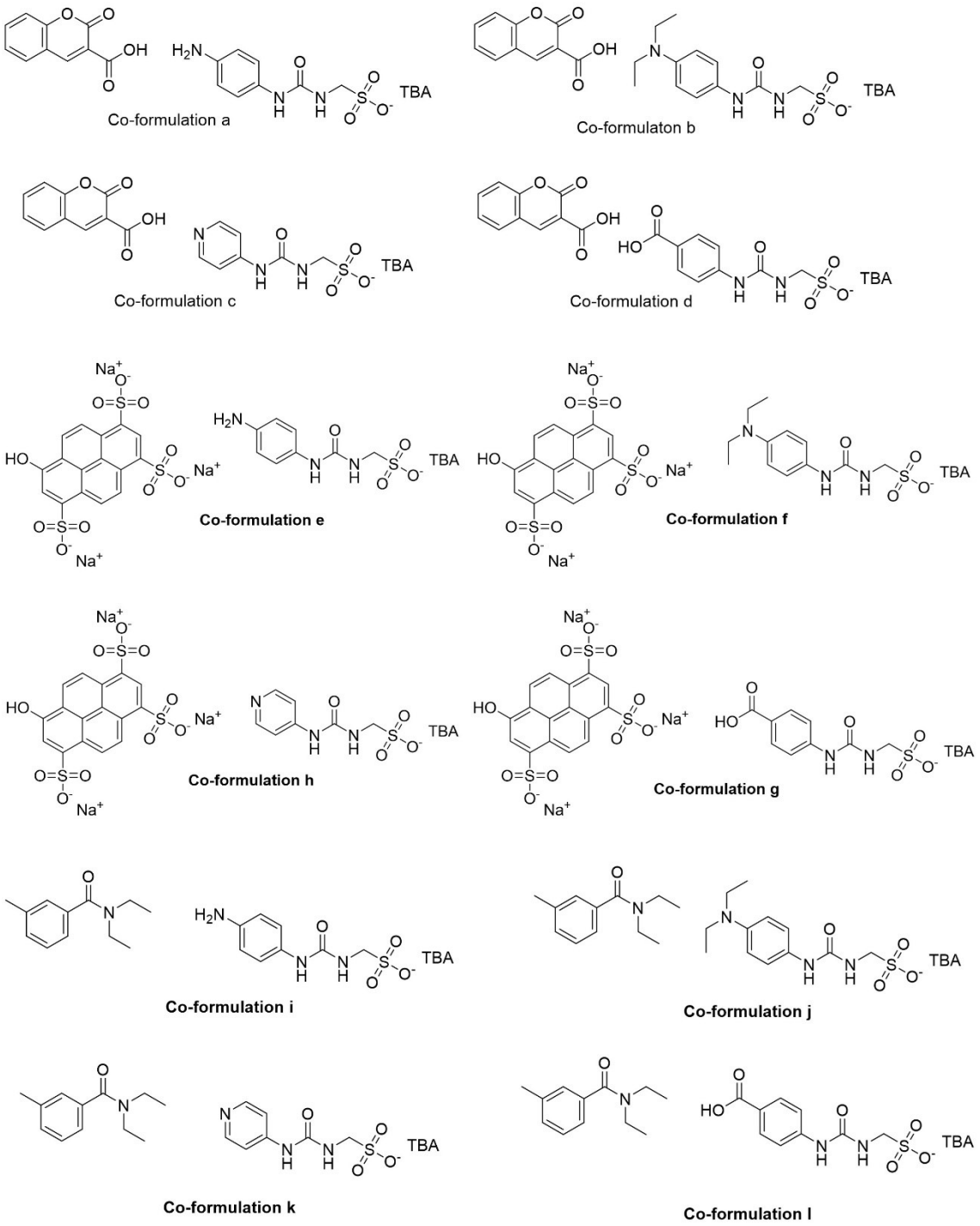

Figure 4.1.12 – Chemical structures of the 12 co-formulations (***a-l***) discussed in this chapter. TBA = tetrabutylammonium

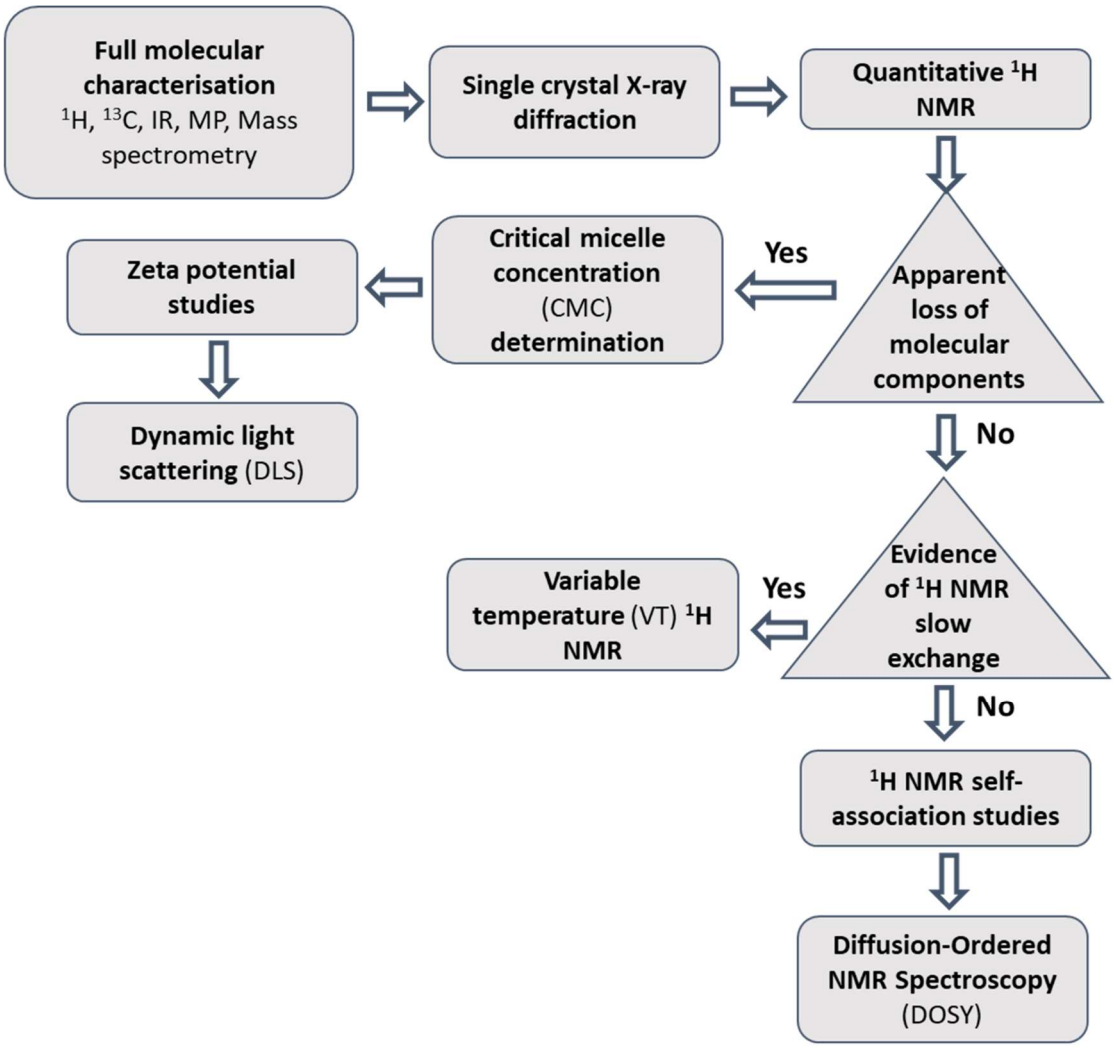

Figure 4.1.13 – Physicochemical property flow chart for the characterisation of SSAs.

4.2 Synthesis

Compound **88** synthesised through the reaction of 4-nitrophenylamine with triphosgene in ethyl acetate, followed by the addition of TBA aminomethane sulfonic acid ((AMS) Scheme 4.1 a). This was subsequently reduced with hydrazine hydrate and Pd/C in ethanol (Scheme 4.1 b) and the pure product was obtained as a brown solid in a yield of 84 %. Compound **89** was synthesised through the reaction of diethylphenyldiamine with triphosgene in chloroform. This was followed by the addition of TBA AMS (Scheme 4.1 a). After purification the pure product was obtained as a purple solid in a yield of 89%. Compounds **90** and **91** were synthesised through the reaction of the appropriate amine with triphosgene in ethyl acetate. This was followed by the addition of

TBA AMS. After purification the pure products were obtained as white solids in yields of 64 and 81 % (Scheme 4.1 a).

Compound **92** was synthesised through the deprotection of **91** in dichloromethane with trifluoroacetic acid. After purification the pure product was obtained as a white solid in a yield of 80 % (Scheme 4.1 c).

Co-formulations ***a***-***d*** were prepared by dissolving the appropriate SSA (**88**-**90**, **92**) in methanol, followed by the addition of one equivalence of **93**. Co-formulations ***e***-***g*** were prepared by dissolving the appropriate SSA (**88**-**90**, **92**) in methanol, followed by the addition of one equivalence of **94**. Co-formulations ***i***-***l*** were prepared by dissolving the appropriate SSA (**88**-**90**, **92**) in methanol, followed by the addition of one equivalence of **95**.

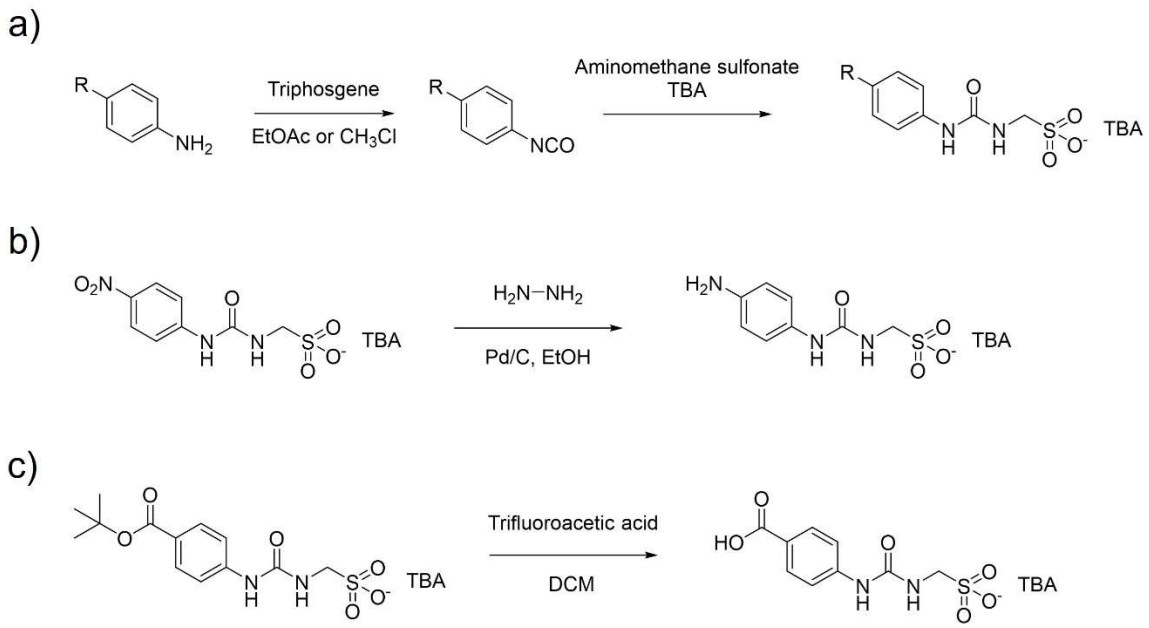

Scheme 4.1 – The synthesis of compounds **88**-**92**. a) compounds **89**-**91**, b) compound **88** and c) compound **92**.

4.3 Solid state: single crystal X-ray diffraction

Single-crystal XRD is routinely used as a non-destructive analytical technique in the field of supramolecular chemistry for the characterisation of crystalline materials. Crystal structures

have been previously obtained for **88** and **89**.[3,341] With SSAs **88** and **89** shown to dimerise through urea-anion hydrogen bond formation. Interestingly, SSA **89**, has also been shown to be present as a zwitterion when it was previously co-formulated with salicylic acid, where the tertiary amine group of SSA **89** was protonated (Figure 4.3.1 a).[3] This zwitterion was also found to dimerize in an identical fashion to the anion form of **89** (Figure 4.3.1 b).[3] It is reasonable to expect that there is a potential for SSAs **88** and **90** to also form a zwitterion when co-formulated with a species with functionalities capable of protonating the aromatic amino moiety such as carboxylic acids. However, to date we have been unable to attain single crystal X-ray structures to confirm this.

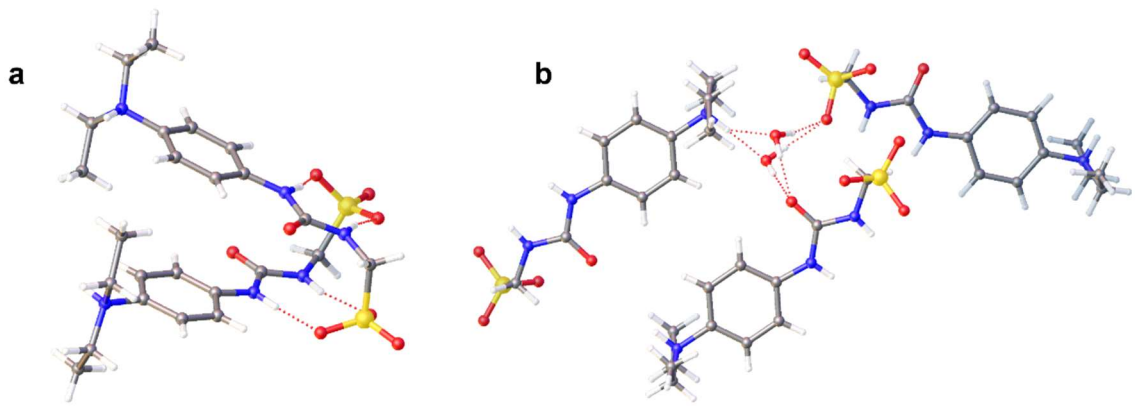

Figure 4.3.1 –Single crystal X-ray structure obtained by slow evaporation of a methanol solution containing co-formulation of SSA **89** and salicylic acid. Here SSA **89** was obtained as a zwitterion that is involved in a complex hydrogen-bonded network. This network includes (**a**) urea-anion dimer formation and (**b**) hydrogen-bonded network formed between the water molecules through the urea, anion, and amine functionalities of the SSA. Here, the TBA counter cation and salicylic acid has been omitted for clarity. Grey = carbon, blue = nitrogen, red = oxygen, yellow = sulfur, white = hydrogen, red dashed lines = hydrogen bonds Hydrogen bond lengths and angles are detailed in the appendix (Table S75).[3]

The crystallography data discussed in this chapter was obtained and refined by Dr Jennifer Ruth Hiscock. Novel single-crystal X-ray structures of **90** were obtained from a two-week crystallisation process through slow evaporation of ethyl acetate solutions containing the

compound **90**. The crystal structure obtained for **90** shows the formation of a urea-anion dimer. The structure is stabilised through the formation of four hydrogen bonds from each HBD urea NH to a different oxygen atom contained within the sulfonate moiety as illustrated in Figure 4.3.2. Hydrogen bond distances and angles observed for **90**, can be found within the appendix (Figure S572 - CCDC 2108071)

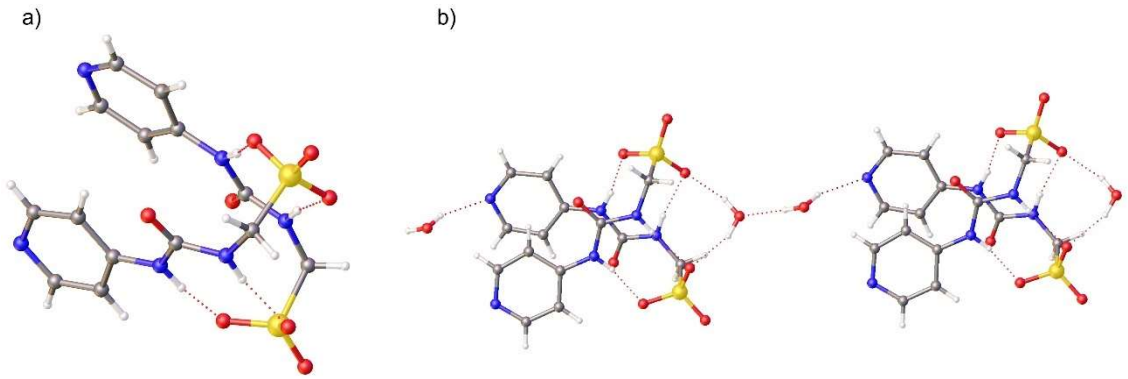

Figure 4.3.2 – Single crystal X-ray structure obtained for SSA **90**. a) showing the anionic dimer formed through the formation of four hydrogen bonds and b) two dimers of **90** bridged through water molecules. Here, the TBA counter cation have been omitted for clarity. Grey = carbon, blue = nitrogen, red = oxygen, yellow = sulfur, white = hydrogen, red dashed lines = hydrogen bonds.

This binding mode of **90** is in an identical fashion shown by previous SSAs **88** and **89**. The interior angle of dimerisation calculated for **90** was 22.9° and 21.9°. Surprisingly, this is rather different to the interior angle of dimerisation shown with both **88** (180°)[341] and **89** (180°), and quite far away from the optimal angle of 180°.[3] This difference in the interior angle of dimerisation is hypothesised to be due to a combination of crystal packing forces and the difference in solvent used for the crystallisation process, for **90** ethyl acetate was used whereas for **88** and **89** a 5% EtOH solution was used as the solvent. These self-associated complex formation events of **88**-**90** have shown that the resulting structures are planar in nature.

In summary, it has been shown that a novel single crystal X-ray structure for compound **90**, forms urea-anion dimers within the solid state similar to that of the previously published **88**

and **89**. The interior angles of dimerisation of these dimers do differ however, it is similar to angles exhibited by published *para*-nitro substituted SSAs. It is hoped that in the future that crystals of good enough quality for analysis for compounds **91** and **92** can be attained and analysed. It is hypothesised that **92** may form end-on urea-anion interactions, which has been previously demonstrated for SSAs that contain a carboxylate moiety, however, as **92** also contains a sulfonate group this could form more complex structures within the solid state, with a combination of binding modes.

4.4 Solution state studies

When investigating the self-association processes in solution, the solvent environment must be considered unlike the solid state. The solution state introduces solvent-solute interactions. These interactions apply influence on molecular self-association events and the resulting aggregate, micelle[355] or inverse micelle formation processes.[356] This is generally observed in solvents that contain HBD or HBA groups, for example water or DMSO, as they can form competitive interactions with the solvent molecules.[357] There is competition between the intermolecular forces between the solute and solvents and those between the solute molecules. Which must be disrupted to allow for the formation of any hydrogen bonded self-associated complexes. The solvent environment of the system can dictate the conformation of any extended aggregates formed.[222] Increasing the strength of the intermolecular interactions present between the molecular species will enhance the stabilisation of the extended aggregates.

4.4.1 Quantitative ^{1}H NMR studies

Solution state NMR spectroscopy has the following limitations: sensitivity, natural abundance of the isotope and the solubility of the molecule, if a molecule is not in solution, it cannot be seen using technique. These limitations of sensitivity and natural abundance can be averted through using a concentrated sample and a nucleus with a high natural abundance, such as using a proton NMR experiment versus a carbon NMR experiment.[358] Quantitative ^{1}H NMR (qNMR) is a technique which allows for the comparison of the compound with an internal standard in order to calculate the proportion of molecules within the solution. This technique utilises an inherent property of NMR; that the magnitude of each NMR signal is proportional to the number of nuclei responsible for that specific peak.[359] Therefore, by using an internal standard at a known concentration and a known concentration of the compound, it is then possible to calculate the percentage of molecules present the solvent. If the observed percentage is lower than 100%, they are categorised as being 'NMR silent' and it then becomes outside the limitations for this technique. Consequently, if the compound becomes 'NMR silent' it will be a results of the compound self-associating into an aggregate that adopts solid-like characteristics and can therefore, no longer be seen by solution state NMR due to the restriction in tumbling of the compound as it becomes larger and adopts more 'solid like properties', in order to observe these larger aggregates through ^{1}H NMR magic angle spinning or solid state NMR could be used. For the purposes of these studies, we are investigating the proportion of compound that are involved in the formation of these larger aggregates and is why these methods were not utilised here.

In order to gain an understanding of the self-associated interactions at the molecular level of **88**-**92** and **co-formulations *a*-*l***, a series of ^{1}H qNMR studies were utilised in either a DMSO-d_6 or D_2O solution. The internal standard chosen for the qNMR studies in DMSO-d_6 was dichloromethane in a 1 % w/v (5 µL). This was chosen due to the miscibility of DCM with DMSO

as well as the corresponding proton peak for DCM (5.76 ppm) does not overlap any of the peaks attributed to the compounds, which allows for effective signal integration. DCM is also not likely to get involved in any molecular self-association events, and therefore is a spectator molecule. For the D_2O qNMR studies, an internal standard of ethanol was chosen, in a 5% w/v (25 µL), again this solvent was chosen due to solvent miscibility and peak position allowing for effective integration. When studying **co-formulations *i-j*** an internal standard of acetonitrile in a 1 % w/v (5 µL) was chosen instead of ethanol, this was chosen as this will allow for effective integration of compound signals as ethanol (that is typically used as the internal standard for aqueous conditions), peaks overlap the peaks for **95.** These conditions will also replicate the solvent conditions for other studies carried out that will be discussed in this chapter.

To ensure that the entirety of the NMR signal was collected, the relaxation time was increased to 60 seconds as a shortened signal collection time can result in a percentage of the signal to be lost. The limitations of this experimental technique include i) the absence of any self-associated species at concentrations below the NMR spectrometer detection limits cannot be quantified; and ii) when performing this experiment in a D_2O solvent results in the absence of those signals attributed to the N-H groups due to proton exchange.

In a DMSO-d_6 solution, compounds **88** - **91**, **co-formulations *a***, ***b***, and ***i*** - ***k*** showed no discernible loss of signal from solution through comparative integration with the internal standard DCM signal, an example of this is illustrated in Figure 4.4.1.1 for compound **90**. As no loss was observed within this ^{1}H NMR experiment, this suggests that should there be any larger species present they are at concentrations too low to be detected using this method.

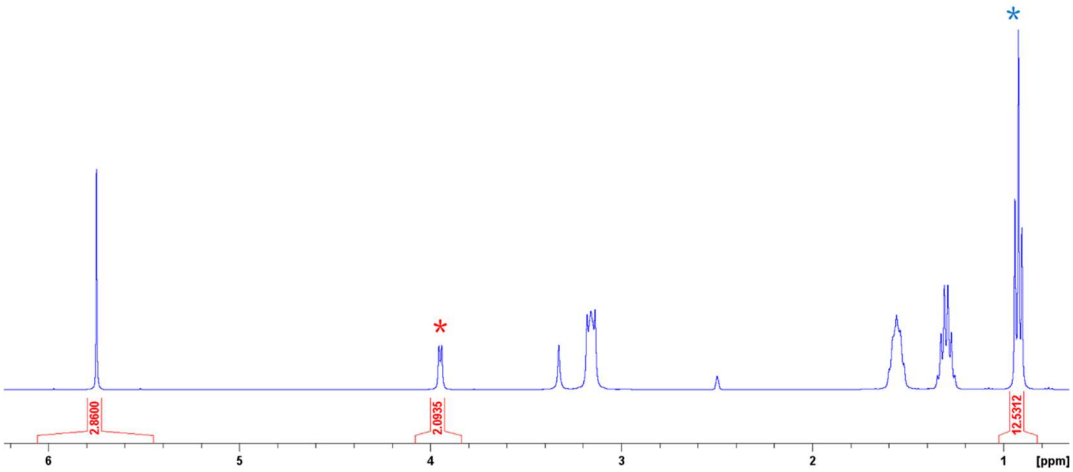

Figure 4.4.1.1 - ^{1}H NMR spectrum with a delay (d_1 = 60 s) of compound **90** (112 mM) in DMSO-d_6/ 1.0 % DCM. Comparative integration indicated 0 % of sample has become NMR silent (anionic component of SSA*, TBA*).

However, for compound **91** and **co-formulations *c* – *h*** and ***l*** in a DMSO-d_6 solution we observe a comparative loss of signal, which indicates the presence of larger self-associated species in solution which a representative spectrum of **92** demonstrating this 'loss' of compound is shown in Figure 4.4.1.2 where a loss of 33% and 28 % was demonstrated for the anionic component of SSA and the TBA respectively, demonstrating 1:1 loss ratio of anion and cation. A summary of the results from in a DMSO-d_6 solution can be found in Table 4.4.1.1.

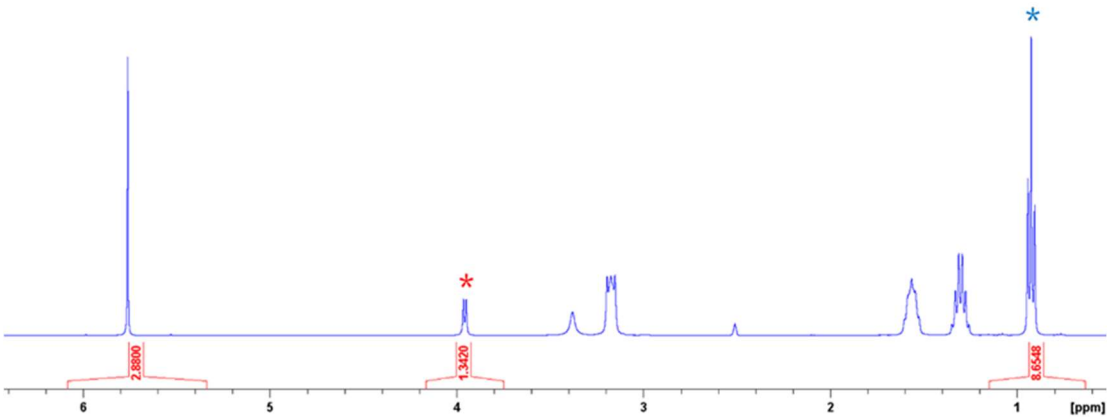

Figure 4.4.1.2 – A zoomed in ^{1}H NMR spectrum with a delay (d_1 = 60 s) of compound **92** (112mM) in DMSO-d_6/ 1.0 % DCM. Comparative integration indicated 33 % of the anionic component of SSA (*) and 28 % of the TBA (*) has become NMR silent.

From Table 4.4.1.1 we observe that for **92** and all co-formulations with this compound all exhibit a 'loss' in DMSO-d_6, this is hypothesised to be due to the addition of an extra HBD/HBA site added via the carboxylate moiety, which could allow for an increased propensity for extended aggregate formation. Furthermore, from **co-formulation *l*** we observe evidence of protonation events as the carboxylate moiety of **92** has the capacity to protonate co-formulant **95**, resulting in **co-formulation *l*** being the only co-formulation with **95** to show a 'loss' and therefore, the presence of larger self-associated aggregates, with a 1:1 loss ratio of **92**:**95**.

Table 4.4.1.1 - Overview of the results from quantitative ^{1}H NMR studies in a DMSO-d_6. Values given in % represent the observed proportion of compound that became NMR silent.

Compound/ Co-formulation	Loss of anion	Loss of cation	Loss of co-formulant
88[341]	0	0	N/A
89[3]	0	0	N/A
90	0	0	N/A
91	0	0	N/A
92	33	28	N/A
a[3]	0	0	0
b[3]	0	0	0
c	47	51	43
d	40	47	86
e	50	53	68
f	57	55	67
g	60	62	67
h	65	72	70

i	0	0	0
j	0	0	0
k	0	0	0
l	51	70	45

N/A – not applicable

In addition to this, we observe that all co-formulations that contain **94**, the only charged co-formulant studied, demonstrate an apparent loss, which all are around the same percentage (67-70% loss of 94 demonstrated). It is hypothesised that due this co-formulant containing three sulfonate moieties and a hydroxyl moiety, all of which are HBA/HBD groups which increases the ability of SSAs to form hydrogen bonded structures with this co-formulant.

Furthermore, for all co-formulations where a loss in DMSO-d_6 was identified, it was noted that the percentage loss of anion:cation:co-formulant was in a 1:1:1 ratio, with the exception of **co-formulation *d***, where a 1:1:2 ratio loss was observed, this is interesting and is hypothesised to demonstrate the capability of an SSA to uptake other molecules within their self-associated structures, which will be discussed in Chapter 4.5.1.

When we move into an aqueous solution, we observe that a greater proportion of compounds and co-formulations exhibit an apparent 'loss' of compound than was observed in DMSO, however, those that exhibited a loss in both solvent systems demonstrated a greater loss in DMSO when compared to D_2O (see Table 4.4.1.2). This is hypothesised to be attributed that for these cases a less polar organic solvent environment is required in order to stabilise these larger self-associated structure, which in comparison previous studies of SSAs, it is the more hydrophilic solvent systems that we primarily observe the presence of these larger structures.[3,222,243,341,343,345] However, with **co-formulations *e***, and ***i***, we observe no discernible loss of compound in D_2O, which when considering these SSAs by themselves (**89** and **90**) they show a loss, indicating that in this specific co-formulation the hydrophilic solvent environment

may be too competitive for the stabilisation of any larger self-associated structures. Therefore, compounds in this solvent system were further studied via ^{1}H DOSY NMR to establish the size of any structures in solution, and to observe how all three components diffuse through solution (see Chapter 4.4.2 Proton DOSY NMR studies for further details). A summary of the qNMR results obtained in D_2O can be found in Table 4.4.1.2.

Table 4.4.1.2 - Overview of the results from quantitative ^{1}H NMR studies in D_2O. Values given in % represent the observed proportion of compound that became NMR silent.

Compound	Loss of anion	Loss of cation	Loss of co-formulant
88[341]	0	0	N/A
89[3]	65	21	N/A
90	21	11	N/A
91	50	42	N/A
92	13.5	15.7	N/A
a[3]	52	55	86
b[3]	41	43	81
c	3	3	14
d	2	18	3
e	0	0	0
f	0	0	0
g	10	11	25
h	38	40	23
i	0	0	0
j	0	0	0

k	7	7	2
l	31	30	7

N/A – not applicable

Upon comparison of these data attained in D_2O with these data from studies in DMSO-d_6 for co-formulation d, we observe quite different results, whereby an almost 0% loss of anion and co-formulant was noted in D_2O in when compared to 40% and 86% loss observed in DMSO-d_6 for the anionic component and co-formulant respectively. This is hypothesised to be due to the D_2O solvent being too competitive and reduces the stability of the larger self-associated structures and therefore, the apparent loss seen is vastly reduced in D_2O. This hypothesis is further supported from the comparison of loss of anion in **co-formulation *e*-*h*** in DMSO-d_6 with the loss of anion of the same co-formulations in D_2O. Here we observe a similar drop in observed loss, as in D_2O we observe losses of between 0% and 38%, whereas in DMSO-d_6 the loss of anion is between 50% and 60%.

In contrast, for **co-formulations *a*** and ***b***, we observe a large proportion of co-formulant is NMR silent (86 and 81% respectively), here is it hypothesised that the larger self-associated aggregates formed by the SSAs have been able to uptake the co-formulant **93**, resulting in the 25-50% increase in loss of co-formulant to anion/cation. This property of SSAs is further investigated in Chapter 4.5.1.

In summary, a series of quantitative ^{1}H NMR studies were carried out in both an organic environment (DMSO-d_6) and aqueous environment (D_2O), in order to observe the presence of any larger self-associated species. It was observed that these species were present in both solvents however, although more compounds exhibited a loss in aqueous conditions, it was in DMSO-d_6 where the same compounds showed a greater proportion of compound involved in the formation of these self-associated species. It is hypothesised that this is due to the aqueous conditions may be to competitive for the stabilisation of these larger self-associated species for

the co-formulations. For **co-formulations *i*** and ***j*** they didn't demonstrate any observable presence of these species in either solvent and will be further discussed in the remainder of this chapter.

4.4.2 Proton DOSY NMR studies

Proton NMR DOSY studies are utilised in order to calculate the hydrodynamic radius of a complex in solution. The ^{1}H NMR DOSY experiment reports the diffusion coefficients for individual resonances in a ^{1}H NMR spectrum, the solvation sphere can then be calculated through using the Stokes-Einstein equation (Equation 3).

$$d_H = \frac{k_B T}{3\pi\eta D} \qquad (3)$$

d_H = Hydrodynamic diameter (m)
k_B = Boltzmann constant
T = Temperature (K)
η = Solvent viscosity ($kgm^{-1}s^{-1}$)
D = Diffusion coefficient (m^2s^{-1})

One limitation of this experiment is that this calculation assumes that the compound/particle are spherical in shape. However, this is not always the case as illustrated in Figure 4.4.2.1 and how their resulting d_H value would be calculated. It is because of this limitation that all sizes calculated using this method should be treated as an estimate and not an exact size. Furthermore, the hydrodynamic diameter can only be determined if the compounds are fully observable in the solution. Herein, the majority of the ^{1}H NMR DOSY experiments carried out are in a DMSO-d_6 solution, in line with the qNMR studies. In addition, where there was no apparent 'loss' of compound in the EtOH:D_2O (1:19) solution a ^{1}H NMR DOSY experiment was carried out to estimate the size of the structures in that solution.

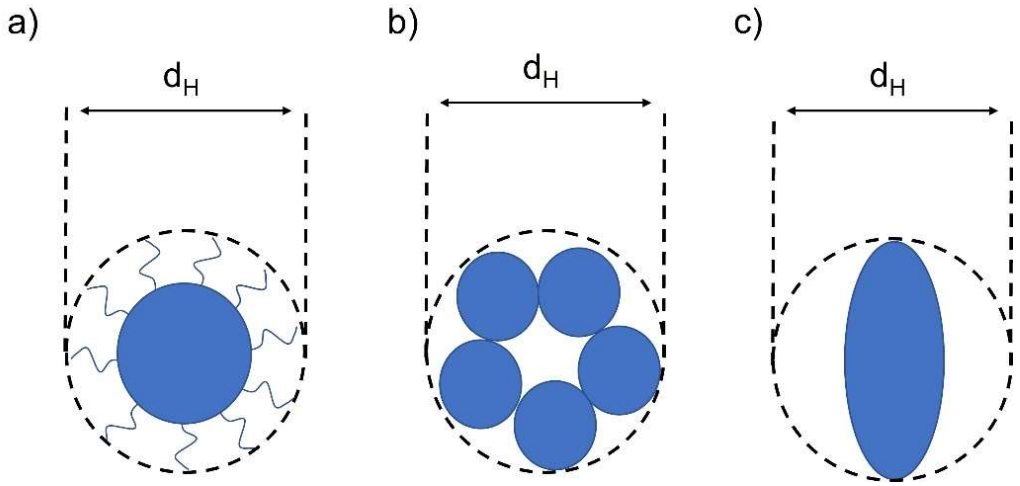

Figure 4.4.2.1 – Types of different aggregates and how their corresponding hydrodynamic diameter would be calculated, highlighting the limitation of the Stokes-Einstein equation. a) a spherical molecule with tails, showing how the tails are also included in the calculation of the d_H, b) multiple molecules, but the d_H is assumed to be the collective size rather than individual, c) a non-spherical molecule, but the d_H assumes it is spherical.

In order to establish the size of the particles for those compounds that did not exhibit a 'loss' within the qNMR (Chapter 4.4.1), whereby, there is no evidence of larger self-associated aggregates. Proton NMR DOSY experiments were conducted to calculate the hydrodynamic diameter of the anionic and cationic and co-formulant components as illustrated in Figure 4.4.2.2, a summary of the hydrodynamic diameters calculated can also be found in Table 4.4.2.1. When considering the size of the molecules in solution the hydrodynamic diameters for the SSAs are ≤ 1.62 nm which suggests the presence of monomeric or hydrogen bonded dimeric species only, as also observed in the solid state.

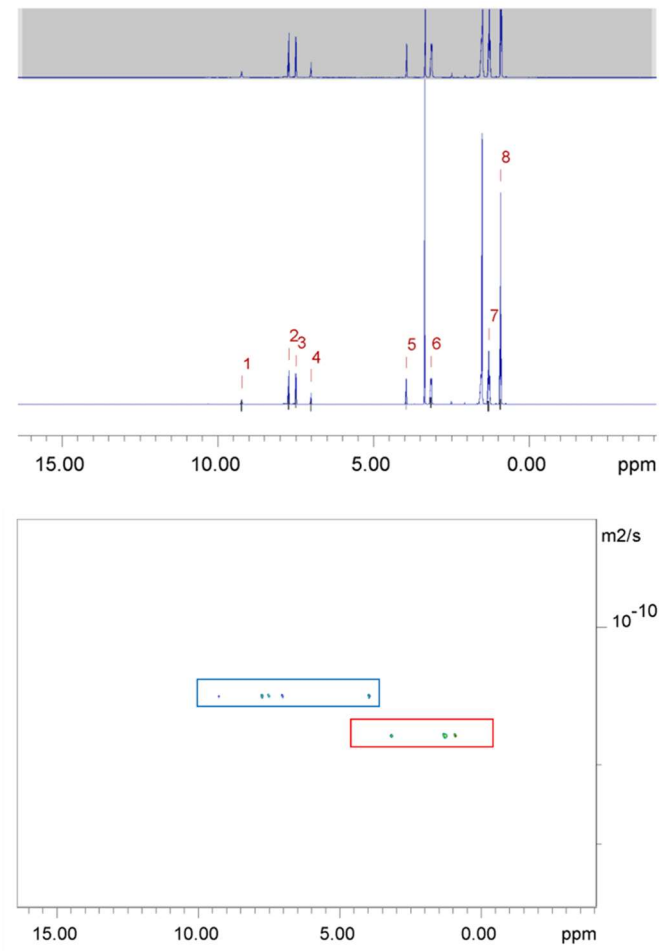

Figure 4.4.2.2 - ^{1}H NMR DOSY of compound **91** (112 mM) in DMSO-d_6 0.5 % H_2O, conducted at 298.15 K. The signals corresponding to the SSA anionic component are shown in blue, and the TBA counter cation are shown in red.

Table 4.4.2.1 – Summary of the hydrodynamic diameters calculated for compounds **88**-**92** and **co-formulations *a*-*l*** in DMSO-d_6 at 298 K. Hydrodynamic diameters suggest the presence of lower order dimeric species.

Compound/Co-formulation	Hydrodynamic diameter (nm)		
	Anion	TBA	Co-formulant
88[341]	1.15	1.08	N/A
89[3]	1.43	1.32	N/A
90	1.23	1.18	N/A
91	1.56	1.26	N/A
92	*a*	*a*	N/A
a[3]	1.59	1.43	1.15
b[3]	1.62	1.39	1.12
c	*a*	*a*	*a*
d	*a*	*a*	*a*
e [b]	0.78	1.20	1.24
f [b]	0.97	1.19	1.28
g	*a*	*a*	*a*
h	*a*	*a*	*a*
i	1.57	1.37	0.86
i [c]	0.11	0.14	0.11
j	1.45	1.25	0.81
j [c]	0.11	0.11	0.13
k	1.45	1.03	0.70
l	*a*	*a*	*a*

a – Experiment not conducted due to the presence of larger aggregates in DMSO-d_6 quantitative ^{1}H NMR studies, b – Experiment ran in a D_2O:EtOH (1:19) solution and c – Experiment ran in a D_2O solution.

The results generated from these studies support the theory that the TBA cation is not strongly coordinating to the SSA anion of coformulant (where applicable) in solution, as illustrated in Figure 4.4.2.2 the TBA cation diffuses at a different rate to that of the sulfonate-urea anionic moiety of **91**. As **88**-**90** and **92** all contain TBA as the counter cation within their molecular structure, the same trend is observed for these compounds, whereby the TBA is diffusing at a different rate to the anionic component of the SSA as detailed in Table 4.4.2.2 and Appendix Figures S445-S453. However, when we consider the co-formulations we generally see that the co-formulant also isn't strongly co-ordinating to the anion or cation of the SSA, as depicted in Figure 4.4.2.2, the exception to this has been displayed with **co-formulation *e*** in aqueous conditions, and **co-formulation *i*** in DMSO-d_6, where the co-formulant diffuses at a similar rate (~0.9 – 0.2 x 10^{10} difference) as either the cation or the anion respectively, as shown in Figure 4.4.2.3.

Table 4.4.2.2 - Overview of diffusion coefficients (m^2s^{-1}) for compounds **88**-**92** and **co-formulations a**-**l** DMSO-d_6 at 298 K. Errors for diffusion constants are no greater than ± 1 x 10^{-13} m^2s^{-1}.

Compound/Co-formulation	Diffusion Coefficient ($m^2 s^{-1}$)		
	Anion	TBA	Co-formulant
88[1]	1.53 x 10^{-10}	1.66 x 10^{-10}	N/A
89[2]	1.50 x 10^{-10}	1.71 x 10^{-10}	N/A
90	1.23 x 10^{-10}	1.86 x 10^{-10}	N/A
91	1.41 x 10^{-10}	1.74 x 10^{-10}	N/A
92	*A*	*a*	N/A
a[2]	1.38 x 10^{-10}	1.53 x 10^{-10}	1.91 x 10^{-10}
b[2]	1.36 x 10^{-10}	1.57 x 10^{-10}	1.95 x 10^{-10}
c	*a*	*a*	*a*
d	*a*	*a*	*a*
e[b]	4.00 x 10^{-10}	2.60 x 10^{-10}	2.51 x 10^{-10}
f[b]	3.21 x 10^{-10}	2.61 x 10^{-10}	2.42 x 10^{-10}
g	*a*	*a*	*a*
h	*a*	*a*	*a*
i	1.40 x 10^{-10}	1.59 x 10^{-10}	2.56 x 10^{-10}
i[c]	4.54 x 10^{-10}	3.48 x 10^{-10}	4.48 x 10^{-10}
j	1.51 x 10^{-10}	1.75 x 10^{-10}	2.70 x 10^{-10}
j[c]	4.45 x 10^{-10}	4.46 x 10^{-10}	3.72 x 10^{-10}
k	2.06 x 10^{-10}	2.12 x 10^{-10}	3.15 x 10^{-10}
l	*a*	*a*	*a*

a - experiment not conducted due to the presence of larger aggregates in DMSO-d_6 and D_2O quantitative ^{1}H NMR experiment, b – ran in a D_2O:EtOH (1:19) solution and c – ran in a D_2O solution.

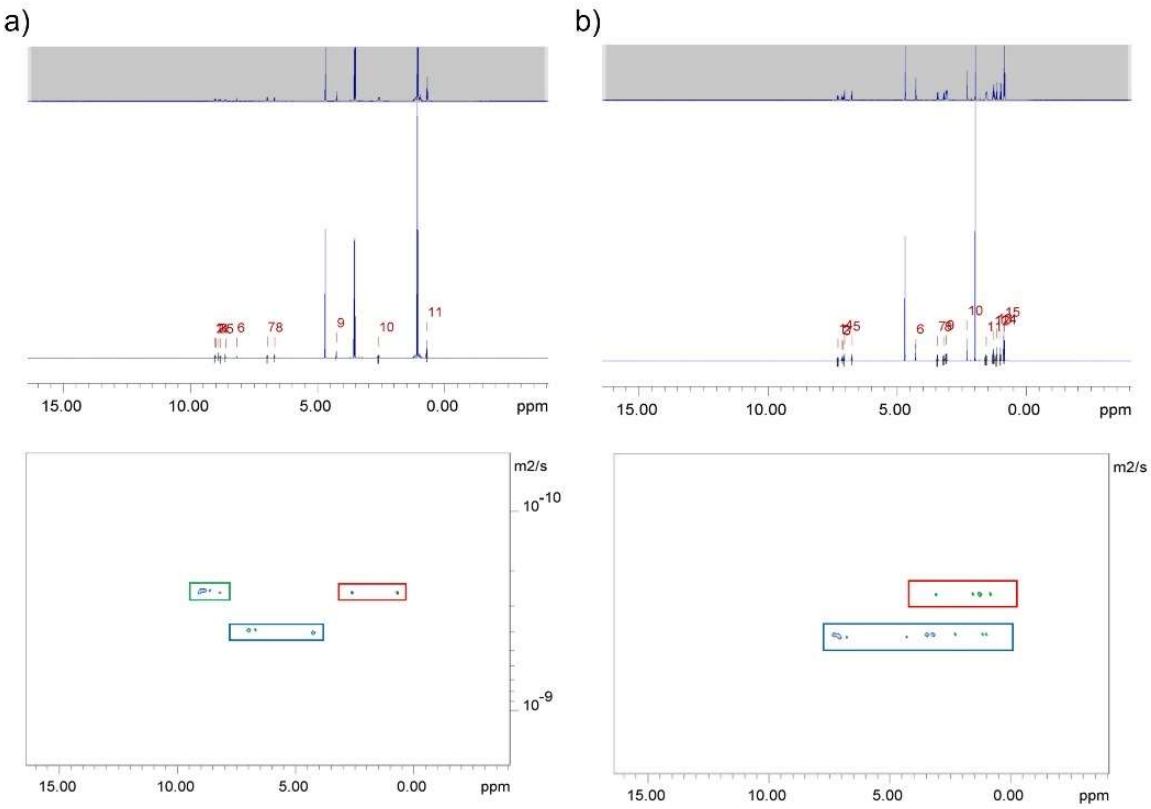

Figure 4.4.2.3 - ^{1}H NMR DOSY indicating examples of same diffusion rates of a) **co-formulation *e*** (11.2 mM) in D_2O/EtOH 19:1, conducted at 298.15 K and b) **co-formulation *l*** (11.2 mM) in D_2O at 298 K. Anionic component highlighted in blue, TBA counter cation highlighted in red, co-formulant in green, however, in the case of b) the co-formulant and anionic component are shown blue to avoid confusion as the peaks all appear at the same diffusion rate and there isn't a clear separation in the components as seen in a). Some peaks in each case have not been integrated due to peak overlap.

This could be hypothesised to be due to potential cation exchange, in the case of **co-formulation *e*** for example, HPTS dye (compound **94**) is a sodium salt, and as it has been previously reported that sodium has a stronger coordination than TBA with SSAs and other hosts,[341,360] the sodium and TBA could undergo cation exchange resulting in the sodium salt of the SSA and the HPTS TBA salt, although it has not been shown with other co-formulations with compound **94**. In the case of **co-formulation *i*** where the anion and the co-formulant (compound **95**) diffuse at the similar rates, this indicates that there potentially a strong co-ordination between the two constituents or they are of the same size. However, as we can see from Table

4.4.2.1, the size of the anionic component and co-formulant are of the same size, therefore it is more plausible to be due to this than a strong coordination between the two constituents. This hypothesised to be because when you consider the polar environment of this particular experiment (D_2O), there is the potential for both the SSA anion and compound **95** to be protonated, giving rise to either an SSA zwitterion or where the protonated form of the co-formulant becomes the counter cation, with all of these potential combinations in equilibrium with each other in the solution. This hypothesis is under investigation in order to determine what interactions are observed between all constituents of the SSA in these conditions.

In summary, DOSY ^{1}H NMR studies of solutions containing **89**-**91**, and **co-formulations *a***, ***b***, ***i***, ***j*** and ***k*** at 298 K are indicative of small low-order dimeric species with a d_H < 1.7 nm to be present for all compounds in a solution of DMSO-d_6 0.5 % H_2O and also for **co-formulations *e***, ***f***, ***i*** and ***j*** in aqueous conditions. There is also evidence to confirm this hypothesis that for **co-formulations *e*** and ***i*** there is exchange of cations within the system, whether that be through the formation of a SSA sodium salt, or through protonation events, of which further investigation to confirm this hypothesis is required. These investigations could include observations within the solid state such as using single crystal XRD (although with considerations to crystal packing forces) will offer some insight as to whether cation exchange has occurred within these systems.

4.4.3 ^{1}H NMR self-association studies

A series of ^{1}H NMR dilution studies were performed in order to explore the strength of the hydrogen bonded self-associative interactions. For these studies only those compounds which did not indicate the presence of larger self-associated species were studied, this is because we have identified that all the compound is present under these solvent conditions.

The dilution studies were conducted for compounds **90** and **91** and **co-formulations *i*** and ***j*** in DMSO-d_6 with 0.5 % H_2O. The results of the dilution studies of compounds **88** and **89** have already been reported.[3,341] Samples of **90** and **91** and **co-formulations *i*** and ***j*** were prepared

in series, with an aliquot of the most concentrated (≈ 112 mM – exception of **co-formulation *j***, the most concentrated ≈ 11.2 mM) undergoing serial dilution. This solvent system allowed for the observation and characterisation of the self-associative complexation events. The downfield change in chemical shift of the corresponding HBD NH resonances of **90** and **91** and **co-formulations *i*** and ***j*** with increasing compound concentration was monitored. The data obtained from the ^{1}H NMR self-association studies performed with **90** and **91**, and **co-formulations *i*** and ***j*** were fitted to mathematical binding isotherm models using BindFit v0.5, quantifying the strength of the hydrogen bonded self-association complexes formed.[226] The data was processed under the assumption of the compounds forming low order complex species as evidenced from the ^{1}H NMR DOSY results. Here, the data was fitted to both dimerization/equal K (EK) and cooperative equal K (CoEK) models. Both of these models assume one component, one-dimensional homogenous aggregation.[361] The EK model assumes all sell-association constants are identical for subsequent events, whereas the CoEK model assumes the first association event is different from all of the subsequent association events.[362] These binding isotherms were first explored by Meijer and co-workers who investigated the effect that temperature and concentration had on the binding strength of self-assembled arrangements, presenting quantitative information about cooperative and isodesmic self-assembly systems.[363,364]

Here as SSAs are not one component, we are able to use the results from the ^{1}H NMR DOSY studies which indicate that the TBA counter cation is weakly co-ordinating and therefore, the interactions by the anionic component are one component investigations. This is also true for **co-formulations *i*** and ***j***, whereby here we have three components in solution, however, as noted from the ^{1}H NMR DOSY studies in DMSO-d_6 this also indicates that there are no competitive interactions between all three components, allowing for the elucidation of self-association constants. However, these data obtained for **co-formulations *i*** and ***j*** must be treated with caution as there could be additional molecular host guest interactions which would cause

these data not to meet the criteria needed to conform to these binding isotherms. An example of the data obtained for **90** is illustrated in Figure 4.4.3.1.

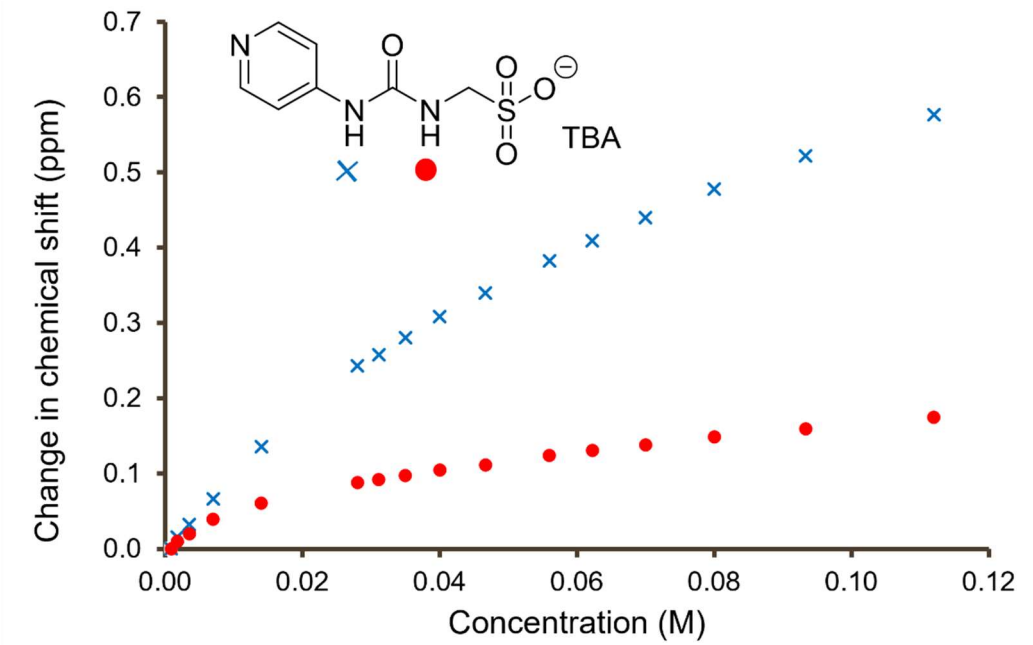

Figure 4.4.3.1 - Graph illustrating the ^{1}H NMR down-field change in chemical shift of urea N-H resonances with increasing concentration of compound **90** in DMSO-d_6 0.5 % H_2O (298 K).

The association constants of **90** and **91**, and **co-formulations *i*** and ***j*** calculated by fitting these dilution data to both the CoEK and EK binding isotherms are overviewed in Table 4.4.2.1. The associated errors of these derived values suggest these compounds best fit the (dimerisation) EK binding isotherm (K_{dim}) in preference to the CoEK binding isotherm. This adds further validates the presence of lower-order anionic dimers in a DMSO-d_6 0.5 % H_2O solution (Chapters 4.4.1 Quantitative ^{1}H NMR studiesand 4.4.2 Proton DOSY NMR studies).

Table 4.4.3.1 - Self-association constants (M^{-1}) calculated for **90** and **91**, and **co-formulations *i*** and ***j*** in a DMSO-d_6 0.5 % H_2O solution at 298 K. These constants were obtained from the fitting of ^{1}H NMR dilution data and refined to EK and CoEK models using Bindfit v0.5.[226]

Compound/ Co-formulation	Model				
	EK (M^{-1})		CoEK (M^{-1})		
	K_e	K_{dim}	K_e	K_{dim}	ρ
88[a 341]	3.6 (± 1.5 %)	1.8 (± 0.7 %)	4.6 (± 8.3 %)	2.3 (± 4.1 %)	0.9 (± 13.4 %)
89[3]	1.19 (± 0.99 %)	0.59 (± 0.50 %)	8.93 (± 2.12 %)	4.46 (± 1.06 %)	0.33 (± 5.69 %)
90	7.28 (± 1.21 %)	3.64 (± 0.61 %)	3.20 (± 9.46 %)	1.60 (± 4.73 %)	1.77 (± 12.97 %)
91	3.16×10^{-3} (± 0.66 %)	1.58×10^{-3} (± 0.33 %)	-1.71×10^{-3} (± -7.40 %)	-8.55×10^{-4} (± -3.70 %)	-0.23 (± -5.81 %)
i[a]	32.01×10^{-2} (± 0.83 %)	1.00×10^{-2} (± 0.42 %)	-3.53 (± -3.42 %)	-1.76 (± -1.71 %)	0.68 (± 1.58 %)
j[a]	1.81×10^{-2} (± 4.02×10^{-3}%)	9.05×10^{-3} (± 2.01×10^{-3}%)	17.83 (± 8.91 %)	8.92 (± 4.46 %)	0.38 (± 11.74 %)

a - Possibility of more complex binding events than are being modelled.

When comparing the fit of ^{1}H NMR dilution data for SSAs **89** – **91** to both the EK and CoEK binding isotherms, lower fitting errors were observed consistently for the (dimerization) EK over the CoEK model. This is consistent with previous observations made for >80 SSAs studied to date.[3,222,243,341] The appropriateness of the EK model is further highlighted with compound **91** and ***co-formulation i*** as the CoEK model cannot fit the data suitably, resulting in an output of negative values, which for the study of binding events the appearance of a negative value indicates inappropriate model choice. The binding events for these compounds and co-formulations studied are relatively low (< 10 M^{-1}), and when we compare the addition of the

carboxylate, which increasing the number of HBD/HBA sites of the SSA, we actually see a decrease in dimerisation constant, ~4 M^{-1} to < 0.1 M^{-1}, which indicates that the addition of this extra functionality has decreased the likelihood of lower order self-associated species formation. When considering compounds **89** – **91**, we can see that the pyridine functionality of **91** allows for the highest dimerisation constant, followed by the primary amine functionality of **89** with a dimerisation constant roughly half of that demonstrated with **91**, and with the increased steric bulk of the diethyl groups of **90** resulting in the lowest dimerisation constant of these three SSAs.

In summary, in order to quantify the strength of the hydrogen bonded self-associated complexation events undertaken by the anionic component of an SSA, a series of ^{1}H NMR dilution experiments were performed. Upon comparison of the errors relating to the derived association constants, it was concluded that all compounds best fit to the EK binding isotherm. The results from this study show **89** - **91** and **co-formulations *i*** and ***j*** produce a value that is indicative of lower-order anionic dimeric formation (K_{dim} < 10 M^{-1}). These observations are in agreement with the interpretations of the previously discussed ^{1}H NMR DOSY studies (Chapter 4.4.2 Proton DOSY NMR studies)

4.4.4 Dynamic light scattering studies

Dynamic light scattering (DLS) analyses are routinely used in chemical and biological laboratories for the detection of aggregates in solutions of macromolecules.[365] This well-established, non-invasive standardised technique is based on the Brownian motion of dispersed particles, the principle that particles are constantly colliding with solvent molecules. Such collisions produce a constant amount of transferable energy, which in turn induces the movement of a particle. This energy transfer has a greater effect on particles smaller in size than those that are larger.[366] When these particles are irradiated with visible monochromatic light, the intensities of the then scattered light fluctuates in a time-dependent manner due to the

continuously changing distances between the particles, analyses of these intensities allow for the determination of the diffusion coefficient (D). The hydrodynamic diameter can be calculated using the Stokes-Einstein equation (Equation 3) as discussed in Chapter 4.4.2 when relating to the calculation of the hydrodynamic diameter within DOSY NMR experiments.

There are limitations of this technique to be considered when acquiring particle measurements which include: i) a lower size limit of 1 nm in diameter, this value is defined by the signal-to-noise ratio as small particles do not scatter a sufficient amount of light, which results in a poor measurement signal; ii) an upper size limit of 1000 nm in diameter, whereby particles larger than this can be attributed to the onset of sedimentation or consolidation of smaller aggregates iii) the d_H is the calculated on the assumption that particles are spherical.[367] However, as discussed in Chapter 4.4.2, dispersed particles can be non-spherical, dynamic and solvated/hydrated, therefore DLS can only provide an indicative size of a particle, colloid or aggregated species.[368] Furthermore, the data produced within this study are intensity distributions, weighted by size. This is because the compounds discussed within this chapter are novel, refractive index calculations have yet to be investigated, therefore, number or volume distribution information could not be attained.

In this study the average intensity particle size distribution for compounds **90**-**92**, and co-formulations ***a***-***l*** was investigated in a solution of EtOH:H_2O (1:19) and DMSO using DLS and compared with previously published results for **88**, **89** and co-formulations ***a*** and ***b***.[3,341] These solvent systems were chosen as the monomeric units of SSAs have previously been shown to self-associate to form either spherical aggregates or dimeric species under these conditions.[3,243,341] Here the addition of the EtOH in the aqueous system was required to aid compound solubility and allow effective measurement comparison for the entire SSA library to date. These studies were only carried out for those compounds and co-formulations where a '*loss*' of

compound was observed through the qNMR studies as previously discussed (Chapter 4.4.1) giving the evidence for the presence of larger self-associated species in solution.

Extended self-associated aggregates (peak maxima > 50 nm in diameter) were all shown to form with compounds **88**-**92** and co-formulation ***α-l*** at a concentration of 5.56 mM in an aqueous solution of EtOH:H2O (1:19) and also in DMSO. At concentrations of 0.56 mM and 5.56 mM, a broad range of aggregate sizes with a peak maxima from 105 nm – 5339 nm were observed, as overviewed in Table 4.4.1 and Table 4.4.2, with a polydispersity index (PDI %) range of 3.94 – 40.5 %. Prior to these DLS studies being undertaken, the samples underwent an annealing process (heating to 40 °C and cooling back to 25 °C) to ensure any self-associated aggregates present had achieved a thermodynamic minimum.

Table 4.4.1 Peak maxima obtained from an average intensity particle size distribution of **88**-**92** and **co-formulations *a*-*l*** obtained at 0.56 mM and 5.56 mM in an H_2O:EtOH (19:1) system by DLS. An annealing process was applied in which the samples were heated to approximately 40 °C before being allowed to cool to a measurement temperature of 25 °C. Conc = concentration.

Compound/ Co-formulation	Concentration (mM)	Peak Maxima (nm)	Polydispersity (%)	Compound/ Co-formulation	Concentration (mM)	Peak Maxima (nm)	Polydispersity (%)
88[341]	5.56	342	-	***c***	5.56	301.00 (± 45.51)	31.49 (± 0.99)
	0.56	459	-		0.56	208.90 (± 3.29)	25.36 (± 0.41)
89[3]	5.56	159 (± 5.37)	26 (± 1.06)	***d***	5.56	543.82 (± 25.82)	28.09 (± 0.72)
	0.56	129 (± 2.43)	24 (± 0.25)		0.56	379.05 (± 30.41)	27.79 (± 0.90)
90	5.56	178.85 (± 3.41)	26.92 (± 1.01)	***g***	5.56	302.91 (± 8.79)	26.63 (± 0.47)
	0.56	202.32 (± 1.67)	23.28 (± 0.79)		0.56	312.79 (± 24.85)	27.36 (± 0.57)
91	5.56	189.07 (± 1.06)	12.61 (± 0.34)	***h***	5.56	358.15 (± 7.48)	25.26 (± 0.83)
	0.56	151.13 (± 1.22)	24.41 (± 0.72)		0.56	301 (± 10.12)	26.27 (± 0.63)
92	5.56	323.30 (± 9.06)	25.13 (± 0.27)	***k***	5.56	336.81 (± 10.96)	26.13 (± 0.26)
	0.56	272.45 (± 5.40)	25.50 (± 0.30)		0.56	695.33 (± 52.30)	37.94 (± 0.78)
a[3]	5.56	1317 (± 82.37)	29 (± 0.88)	***l***	*a*	*a*	*a*
	0.56	226 (± 17.18)	28 (± 0.65)		0.56	696 (± 54.93)	25.55 (± 1.32)
b[3]	5.56	768 (± 23.23)	27 (± 0.72)				
	0.56	105 (± 6.19)	28 (± 1.14)				

a – result not reported due to poor correlation function.

As discussed in Chapter 4.4.2 some of the SSAs and coformulations studied here exhibited a '*loss*' in DMSO-d_6, in order to determine the size of these aggregates in solution, DLS studies were carried out in filtered DMSO. Some SSAs exhibit structures that exceed the limitations of the experiment d_H > 1000 nm. These structures are attributed to amalgamations of smaller structures.

Some of the DLS studies carried out, the average peak maxima have not been determined due to a poor correlation function, these correlation functions can be found within the appendix (pages 315-346). As these studies were conducted at concentrations that match the qNMR studies in order to investigate the size of particles at that concentration, it is worth noting that it becomes difficult to therefore compare **88** and **92**, however, we can compare all the co-formulations studied as they are the same concentration (11.2 mM and 1.12 mM). For **co-formulations *a*-*l*** we can see that they all form extended self-associated aggregates (peak maxima > 50 nm in diameter), with the greatest peak maxima value of 5339.09 (**co-formulation *f***), however, this value should be treated with caution as with any value greater than 1000 nm as this exceeds the limits of the experiment conducted. The peak maxima observed for the co-formulations studied are observed to be larger than what was observed in H_2O, it is hypothesised that these larger structures are in part due to the amalgamation of aggregates and not the true size of an aggregate.

Table 4.4.2 - Peak maxima obtained from an average intensity particle size distribution of **88**-**92** and **co-formulations a**-**l** obtained at 11.2 mM and 1.12 mM in an DMSO solution by DLS (**88** and **92** were ran at a different concentration to match the concentration of samples used in the qNMR studies. An annealing process was applied in which the samples were heated to approximately 40 °C before being allowed to cool to a measurement temperature of 25 °C. Conc = concentration.

Compound/ Co-formulation	Concentration (mM)	Peak Maxima (nm)	Polydispersity (%)	Compound/ Co-formulation	Concentration (mM)	Peak Maxima (nm)	Polydispersity (%)
88[341]	5.56	396	-	***f***	11.2	5339.09 (±1206.18)	25.08 (± 0.77)
	0.56	342	-		1.12	221.28 (± 26.24)	27.25 (± 1.02)
92	112.0	454.67 (±15.44)	26.45 (± 1.29)	***g***	11.2	708.49 (± 16.02)	20.51 (± 0.86)
	11.2	171.15 (± 8.91)	25.34 (± 1.14)		1.12	600.15 (± 29.72)	24.71 (± 1.27)
c	11.2	*a*	*a*	***h***	11.2	501.48 (± 21.09)	
	1.12	*a*	*a*		1.12	*a*	*a*
d	11.2	*a*	*a*	***i***	112	965.76 (± 21.09)	26,25 (± 2.61)
	1.12	*a*	*a*		*a*	*a*	*a*
e	11.2	*a*	*a*	***l***	112	2113.14 (± 277.68)	34.55 (± 1.23)
	1.12	*a*	*a*		11.2	*a*	*a*

a – result not reported due to poor correlation function.

In summary, DLS studies conducted at concentrations of 0.56 mM and 5.56 mM show a broad range of aggregate sizes from 105 nm – 1317 nm were observed in an aqueous solution of EtOH:H2O (1:19). With extended self-associated aggregates (> 50 nm) shown to be present for all compounds at a concentration of 5.56 mM. Within an aqueous environment at 5.56 mM, all compounds have a prevalence to form higher-order self-associated aggregates with a d_H between 100-550 nm. Finally, in a DMSO solution a broad range of aggregate sizes from 171 nm – 5339 nm were observed, with all compounds and coformulations studied showing a

prevalence of higher-order self-associated species at the concentrations the qNMR studies conducted (1.12 mM – 112 mM). These results have also demonstrated that there are self-associated species that are larger in size formed in a DMSO solution than in aqueous conditions.

4.4.5 Surface tension and critical micelle concentration studies

The amphiphilic nature of surfactant molecules is responsible for their self-association properties. It is the balance of hydrophobic and hydrophilic effects that drives the monomers to self-assemble, resulting in the formation of energetically favourable structures. A common example of these aggregate formations are micelles, where a polar head group seeks to interact with an aqueous medium, and the hydrophobic tail is sequestered internally to the structure.[369] Here critical micelle concentration (CMC) is calculated by determining the surface tension of a compound in solution through serial dilutions. At low concentrations, the presence of molecules at the surface disrupts the cohesive energy of the solvent and consequently lowers the surface tension (Figure 4.4.5.1). As the molecular concentration increases, the surface interface then becomes saturated by these surface active molecules (Figure 4.4.5.1 b), the surface tension is found to then no longer decrease with increasing molecular concentration.[370] The CMC is determined to be the concentration above which any extra addition of compound will form larger self-associated structures within the bulk of the solution (micelles, reverse micelles, vesicles, aggregations) as shown in Figure 4.4.5.1 c.[371,372]

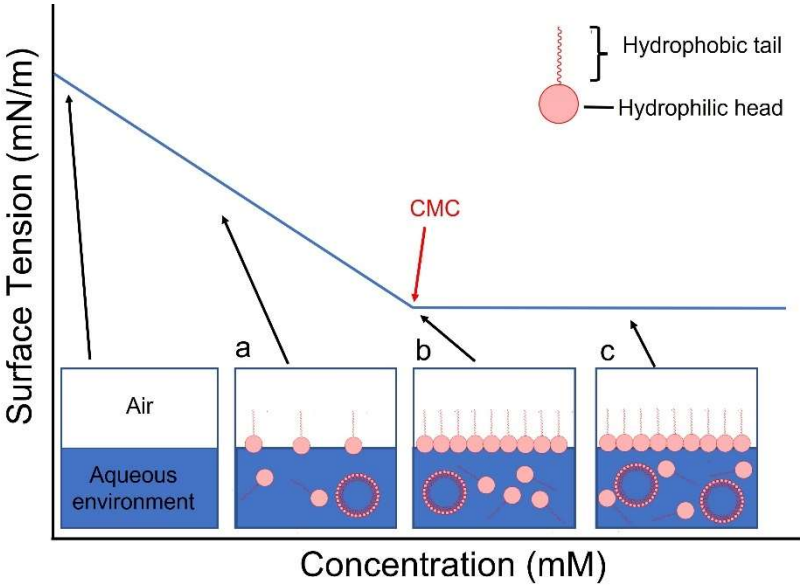

Figure 4.4.5.1 – A cartoon representation of CMC determination. a) Surfactant gathers at the surface, b) surface becomes saturated and c) proposed aggregate formation. [372]

Williams and co-workers in 1955 determined that within dilute solutions only small particles were present however, at higher concentration, both small and large colloidal structures present were in equilibrium.[372] Self-associated aggregates are now known to be present in dilute solutions below the CMC value as they are in a dynamic equilibrium with the structures at the unsaturated surface.[373] It is only with the further addition of solute molecules that we can recognise and detect the aggregation of spherical units by measuring surface tension against concentration.[222,374] There are several factors that affect the reproducibility of CMC determination which includes the presence of other surface-active substances,[375] the presence of electrolytes[376] and any variation of temperature[377] or pressure.[378]

The CMC and corresponding surfactant properties for **88**-**92** and **co-formulations *α*-*l*** in an EtOH:H_2O (1:19) solution were observed using the methods analogous with those reported by Costas and co-workers (Chapter 6 page 160).[370] The CMC and surface tension (obtained at CMC) values were calculated using a plot of surface tension versus concentration and taken at the point of which the surface tension is found to no longer decrease with the further addition of compound,[370] as shown in the example tensiometric profiles in Figure 4.4.5.2, with the results

overviewed in Table 4.4.5.1. All compounds and co-formulations exhibit a CMC above 5.56 mM the concentration that was used for the DLS studies and observed the presence of larger structures. This confirms the previous statement that self-associated aggregates of > 10 nm in diameter are present in dilute solutions before the CMC is reached.[222] Some compounds and co-formulations CMC could not be determined due to compound solubility (**88**, co-formulations ***a***, ***b***, ***d***, ***e***, ***f,*** and ***h***).

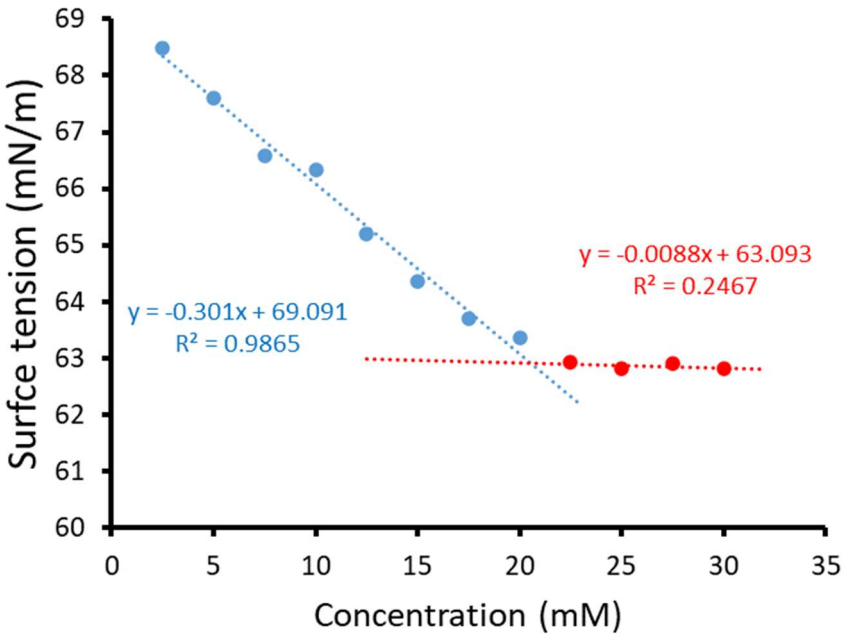

Figure 4.4.5.2 - Calculation of CMC (20.53 mM) for compound **92** in an EtOH:H_2O 1:19 mixture using surface tension measurements. Linear relationship between concentration and surface tension. Red points indicate where the CMC has been reached as there is no longer a change in surface tension with increasing concentration.

Table 4.4.5.1 – A summary of the CMC and surface tension (obtained at CMC) measurements for compounds **88**-**92** and **co-formulations *a*-*l*** in a solution of EtOH:H2O (1:19) at 25 °C.

Compound/ Co-formulation	CMC (mM)	Surface tension at CMC (mN/m)	Compound/ Co-formulation	CMC (mM)	Surface tension at CMC (mN/m)
88[341]	*a*	N/A	***e***	*a*	N/A
89[3]	35.27	32.21	***f***	*a*	N/A
90	14.55	58.92	***g***	44.13	51.60
91	17.64	35.72	***h***	*a*	N/A
92	20.53	62.91	***i***	21.38	44.69
a[3]	*a*	N/A	***j***	22.30	44.90
b[3]	19.87	37.95	***k***	22.04	44.83
c	16.10	56.89	***l***	22.45	51.63
d	*a*	N/A			

a – could not be determined, N/A – not applicable.

Compound **90** was the only compound where a CMC was able to be calculated for all corresponding co-formulations and displayed an increase in CMC when co-formulated with **93**-**95**, the addition of **94** to **90** displaying the largest increase in CMC, from 14.55 mM to 44.13 mM, with a decrease in surface tension at the CMC. Here this illustrates that the presence of a coformulant is disrupting the surfactant properties of the amphiphile.

In summary, it has been shown that compounds **88**-**92** have surfactant properties, with compound **90** displaying the lowest CMC value indicating that this would be the best surfactant. Upon co-formulation with compounds **93**-**95** the trend in data differs for each compound, there appears to be a difference in whether it displays an increase or decrease in CMC, for example co-formulations made with **90**, show an increase in CMC when co-formulated, decreasing the

surfactant properties of the SSA. However, when we compare this to the values obtained for **89** and its corresponding co-formulations, we see a decrease in CMC.

4.4.6 Zeta potential Studies

Zeta potential, which is also termed the 'electrokinetic potential' is a frequently used technique to define the stability of colloid particles or aggregates within a solution.[368] Guidelines for the classification zeta potential values for colloidal are common in literature, especially within pharmaceutical journals when investigating drug delivery systems.[368] It is noted that a measurement more positive than +30 mV or more negative than -30 mV is considered stable, a value smaller than this suggests aggregate instability and an inclination for the particles to flocculate.[379] However, although these values can provide a good indication of colloid/aggregate stability, there are occasions, where this isn't the case, such as with liposomes, where a zeta potential value of between -10 to -40 mV are considered stable,[379] therefore, this highlights how environmental conditions are an important factor for this technique.

In order to elucidate the stability of the larger higher-order self-associated aggregates observed at by DLS (Chapter 4.4.4), present at the CMC (Chapter 4.4.5) and those that became 'NMR silent' in the quantitative ^{1}H NMR studies (Chapter 4.4.1), zeta potential measurements were obtained for compounds **88**-**92** and **coformulations a**-**d**, **g**, **h**, **k**, and **l**. Table 4.4.6.1 gives an overview of the zeta potential results obtained.

Table 4.4.6.1 - Summary of zeta potential at 5.56 mM for compounds **88**-**92** and **co- formulations *a*-*l***. Data obtained in a 5% EtOH:H_2O solution at 298 K.

Compound/ Co-formulation	Zeta Potential (mV)	Compound/ Co-formulation	Zeta Potential (mV)
88[341]	-30.2	***e***	*a*
89[3]	-65.2	***f***	*a*
90	-0.95	***g***	-5.35
91	-68.16	***h***	-39.14
92	-45.45	***i***	*a*
a[3]	-51.8	***j***	*a*
b[3]	-42.7	***k***	-18.51
c	-11.15	***l***	-15.32
d	-7.42		

a- experiment not conducted due to the absence of larger self-associated species in qNMR studies.

The zeta potential measurements obtained from solutions containing **88**, **89**, **91**, **92** and **co-formulations *a***, ***b***, and ***h***, all showed evidence of stable aggregate formation with zeta potential values > ±30 mV. Compound **91** showed the formation of the most stable aggregate formation with a value of -68.16 mV, this compound is the protected carboxylate, and if we compare to compound **92** when the carboxylate is deprotected the compound becomes slightly less stable and the value drops to -45.45 mV, this could be due to the ability of this compound to have a different binding mode due to the carboxylate moiety, however, as we have currently been unable to achieve crystals of good enough quality for this compound to study how in the solid state how this extra functionality effects its binding mode. When compound **92** is co-

formulated, the aggregates formed become less stable, indicated that the co-formulations are destabilising the structures formed. When we compare this to compound **90**, we observe an increase in stability of aggregates, from -0.95 mV for 90, to -11.15 mV (**co-formulation *c***), -5.35 mV (**co-formulation *g***) and -18.51 mV (**co-formulation *k***), here the presence of a co-formulant is able to stabilise the structures formed, although these values still represent an unstable aggregate.

In summary, elucidation of the stability of those higher-order structures observed at 5.56 mM in the DLS studies; present at the CMC and those that became 'NMR silent' in the quantitative 1H NMR studies were conducted through measurement of the zeta potential value under analogous experimental conditions. All SSAs studied showed evidence of stable aggregate formation, and **co-formulations *a***, ***b*** and ***h*** also showed stable aggregate formation. Co-formulations formed with compound **95** only formed unstable aggregates.

4.5 Co-formulant uptake studies

The fluorescence microscopy images obtained of **co-formulations *a*** and ***b*** as shown in Figure 4.5.1, indicate the presence of intrinsically fluorescent aggregated species, thus leading us to form the following hypothesis that SSAs could be used to uptake other molecules, alongside the potential use as drug delivery vehicles[3] or themselves as an antimicrobial[243,343] or anti-cancer agents.[345] However, poor data quality resulting from the very nature of the system itself prevented any further analysis of this system using these microscopy methods, so with this in mind a combination of the following techniques were used to characterise the molecular association processes present within this and other systems to be discussed herein. The fluorescence microscopy imaging was conducted by Dr Lisa White and Professor Dan Mulvihill in a 5% EtOH solution at 298 K. To test this hypothesis, **co-formulations *a*-*l*** were studied further, however, rather than as previous where the co-formulant was added to a solution of SSA and dried down to form one solid mixture, here the SSA and co-formulant were kept separate and

added together prior to conducting ^{1}H qNMR, DLS and Zeta potential measurements which were taken 20 minutes after mixing 1 equivalent of co-formulant solution to an SSA solution. These studies were carried out in an aqueous environment, in order to observe the stability of any larger self-associated aggregates, as DMSO is not compatible with the Zeta potential cell. These studies in this solvent environment also lends itself to the potential end use of removal of pollutants from water, therefore, proof of concept in this environment is preferential over organic solvent systems.

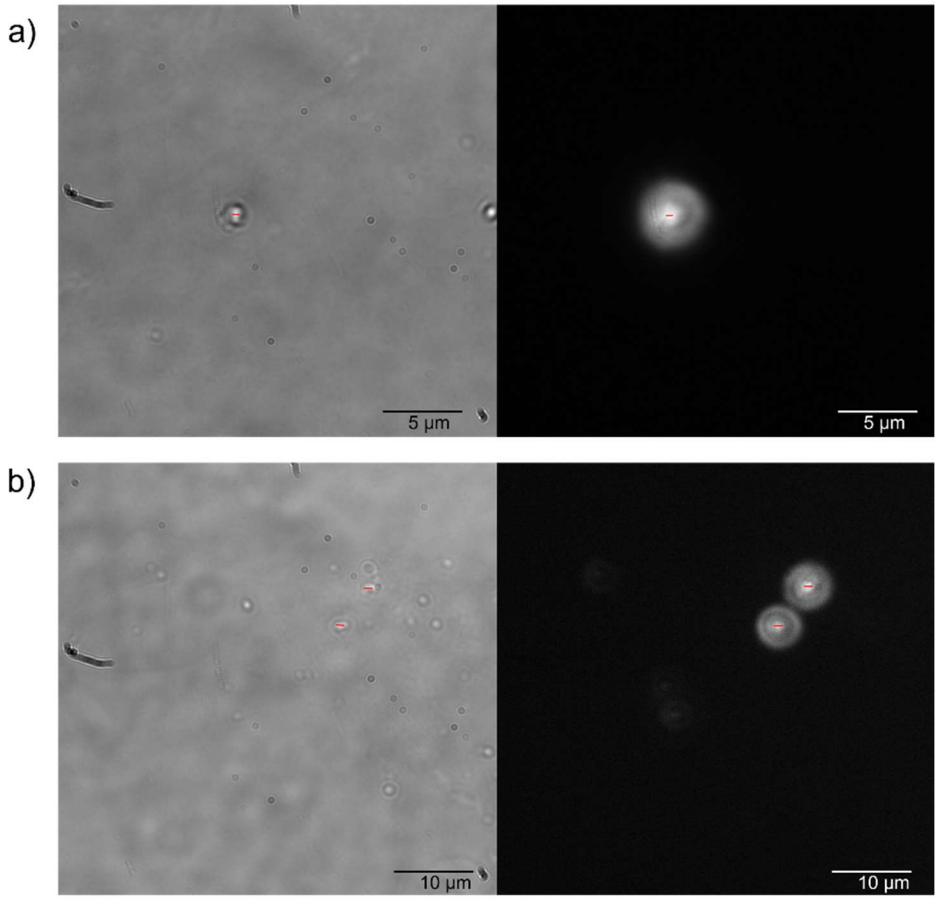

Figure 4.5.1 – Fluorescence microscopy images obtained of **co-formulations *a*** and ***b***, indicating fluorescent aggregated species. The samples were illuminated using LED light sources (Cairn Research Ltd, Faversham, UK) with DC/ET350/50x excitation and DC/457/50m emission filters (Chroma, Bellows Falls, VT). Images obtained by Dr Lisa White and Professor Dan Mulvihill.

4.5.1 ^{1}H NMR studies

A series of quantitative ^{1}H NMR studies were conducted over a time period of 24 hours after the addition of one equivalent of the co-formulant to the SSA, due to the time taken for the experiment the first time point is 20 minutes post the addition of the co-formulant solution, the subsequent time points are 12 hours and 24 hours to observe if over time the loss of signal relating to the co-formulant changes over time, which could indicate the uptake of the co-formulant by the SSAs into the larger self-associated aggregates they are known to form. These experiments were conducted in a 5% EtOH/D_2O solution, with the exception of **co-formulations *i-l*** which were conducted in a D_2O solution with the addition of 5 µL of acetonitrile, this was to allow for accurate comparative integration of both internal standard and compound peaks. This is the same internal standard used in previous qNMR studies (Chapter 4.4.1). All co-formulants were also studied individually in the same solvent system to ensure that they themselves do not exhibit the formation of larger self-associated species, and that any 'loss' of signal is due to the uptake of the co-formulant by the SSA, of which no co-formulant showed a loss of signal indicating that there are no larger aggregated species present in solution. A summary of the data collected using qNMR is summarised in Table 4.5.1. Here we can see that there is a loss of co-formulant in every experiment conducted. The results also show that the amount of co-formulant signal lost stays relatively the same from the first ^{1}H NMR to the ^{1}H NMR 24 hours after the solutions were mixed, this is indicative of co-formulant uptake by the SSAs.

Table 4.5.1 - Overview of the results from timed quantitative ^{1}H NMR studies. Values given as a percentage represent the observed proportion of co-formulant that became NMR silent.

Co-formulation	Percentage loss of co-formulant (%)		
	20 minutes	**12 hours**	**24 hours**
a	62	59	59
b	87	84	84
c	38	41	42
d	60	60	60
e	62	62	62
f	66	65	63
g	50	50	50
h	73	72	72
i	10	10	11
j	18	18	18
k	14	16	15
l	23	26	30

Interestingly, for **co-formulations *e*, *f*, *i*** and ***j*** they demonstrate a completely different result to that of previous qNMR studies, where they demonstrated a 0% loss, whereas, within these studies they exhibited a loss of 62%, 63%, 11% and 18% respectively after 24 hours. This difference shows that the mode of which the SSA is mixed (a 1:1 mixture dried down then studied or mixed as two separate solutions) with a co-formulant impacts the type of structures formed in aqueous conditions and provides a proof of concept that these SSAs could potentially uptake environmental pollutants. From these data we can also see that for nearly all compounds

there is also an increase of apparent 'loss' of compound within these studies compared to the original qNMR studies (for ease of reference a comparison of these values can be found in Table 4.5.2), this implies that even for those that previously showed formation of these larger species, a greater proportion of co-formulant is now involved and is hypothesised that the SSA has taken up the co-formulant within their self-associated aggregate. There was only one co-formulation which showed a loss less than the previous studies which was **co-formulation *a***, where the previous qNMR study indicated a 'loss' of 86% versus a 'loss' of only 59% in this study, the reasons for this difference has not yet been determined, but this warrants further investigation into why this difference is observed. It is also worth noting how these studies show that within 20 minutes the uptake processes are completed, as the proportion of loss doesn't largely change between the time points studied. Therefore, any future studies to further investigate SSAs could be contained to the initial 20-minute time period.

When investigating which SSA, on the whole is the better SSA for use as an uptake agent, although all SSAs show some form of uptake, it was noticed that **90** shows the lowest uptake of each co-formulant when comparing each set of co-formulant data, for example for the data with **93** as a co-formulant, we observe **co-formulation *c*** shows the lowest loss of co-formulant at 42% (**90** + **93**), when compared to the other values of 50% 60%, and 84% for **co-formulations *a***, ***b*** and ***d*** respectively. This trend is also seen when observing the loss of co-formulant **94**. Interestingly, when we consider co-formulant **95** we do observe some uptake, however, the proportion of co-formulant taken up by the SSAs are in proportion to the amount of SSA involved in the formation of larger self-associated aggregates (1:1 ratio of anion and co-formulant). From this we can deduce that this type of co-formulant, a neutral amine -which is more basic than the other two co-formulants studied here - is the least susceptible to SSA uptake, whereas, when we look at the co-formulants that contain a sulfonate or carboxylate moiety, we observe greater uptake. Therefore, those co-formulants with a more acidic moiety are ideal for this type of SSA technology. Further work to investigate this observation through the inclusion of more co-

formulants would be needed to verify this. It can be conducted that on the whole **89** and **92** are the best SSAs for co-formulant uptake, as for each co-formulant studied they demonstrate the largest loss.

Table 4.5.2 – A comparison of the observed percentage (%) 'loss' of co-formulant in qNMR studies conducted, and the difference between the qNMR studies conducted in Chapter 4.4.1 and the timed qNMR studies conducted within this section.

Co-formulation	qNMR	Uptake qNMR	Difference
a	86	59	-27
b	81	84	+3
c	14	42	+28
d	3	60	+57
e	0	62	+62
f	0	63	+63
g	25	50	+25
h	23	72	+19
i	0	11	+11
j	0	18	+18
k	2	15	+13
l	7	30	+23

In summary, through the use of quantitative ^{1}H NMR studies over a 24-hour period, it has been shown that SSAs can uptake other molecules within their self-associated aggregates, with the majority showing an increase in loss of the co-formulant used compared to the original qNMR studies in Chapter 4.4.1. It has also been shown that the amount of compound 'loss'

happens within the first 20 minutes of mixing the two solutions together, as the percentage 'loss' was consistent between all three time points. These studies also indicate that as a proof-of-concept SSAs can potentially be used as scavenger agents in aqueous conditions, as even when a solution of co-formulant (which was shown not to form larger self-associated species) is added to a solution of SSA, a proportion of the co-formulant after 20 minutes becomes NMR silent, which is indicative of uptake by the SSA self-associated structure.

4.5.2 Dynamic light scattering and Zeta potential studies

In order to determine the size and stability of those larger species that are NMR silent, DLS and Zeta potential studies were carried out as previously discussed in Chapter 4.4.4 and Chapter 4.4.6. However, where these studies differ to previous is that the co-formulant is kept in a separate solution to the SSA, here both solutions were annealed, allowed to cool, then mixed within the cuvette ensuring a 1:1 ratio of SSA and co-formulant and then allowed to equilibrate for 20 minutes prior to DLS/Zeta potential measurements in order to study the sizes seen at the first time point within the NMR studies. A summary of the DLS and Zeta potential measurements of **co-formulations *a-l*** can be found in Table 4.5.3.

Table 4.5.3 – A summary of DLS and Zeta potential measurements for **co-formulations *a*-*l*** conducted after 20 minutes after mixing the respective co-formulant with the appropriate SSA, giving a final concentration of 5.56 mM.

Co-formulation	Peak maxima (nm)	Polydispersity (%)	Zeta Potential (mV)
a	564.26 (± 17.04)	26.08 (± 0.76)	-17.69
b	1136.25 (± 176.29)	24.10 (± 4.04)	-16.11
c	281.04 (± 10.23)	26.78 (± 0.48)	-32.21
d	1063.01 (± 37.10)	36.63 (± 2.39)	-17.99
e	367.91 (± 20.78)	26.70 (± 0.79)	-23.20
f	1263.50 (± 65.32)	24.19 (± 0.78)	-46.86
g	246.05 (± 6.16)	24 (± 0.49)	-24.40
h	741.64 (± 161.55)	38.94 (± 9.32)	-32.99
i	585.26 (± 21.66)	25.69 (± 0.88)	-14.54
j	1676.44 (± 233.64)	24.52 (± 2.60)	-40.43
k	353.26 (± 13.40)	23.86 (± 0.42)	-27.90
l	623.21 (± 55.52)	26.85 (± 0.79)	-32.48

From Table 4.5.*3* it is observed that the sizes of the larger self-associated aggregates were found to correlate well with the size of aggregates observed within Chapter 4.4.4 Dynamic light scattering studies for **co-formulations *c*** and ***k.*** For **co-formulation *a***, where in the qNMR studies we saw a decrease in 'loss' of signal for, this is also mirrored within the DLS studies where the size of aggregates are around 564 nm compared to the amalgamation of aggregates at 1317 nm seen in Chapter 4.4.4. For **co-formulations *b, d, h***, the sizes observed here are larger than what

was previously seen, although with these sizes are indicative of amalgamations of the self-associated aggregates rather than the size of one aggregate. Due to a poor correlation function observed for ***l*** in previous studies the sizes can't be compared at this concentration, however, it can be noted that it was observed that the size of 623 nm within this study are within error to that observed for the same co-formulation at 0.56 mM previously. **Co-formulation *g*** shows sizes similar in both studies, however, fall outside the error of each other, but are shown to be within 50-60 nm between them, with an observed size of 246 nm observed in this study compared to 303 nm shown previously. No comparisons can be made for co-formulations ***e, f, i, j*** with previous data, as these co-formulations were not studied using this technique due to no apparent 'loss' in the qNMR discussed in Chapter 4.4.1. From these results it demonstrates that even when the co-formulant is added to a solution of annealed SSA that the aggregates are not disrupted, although it does demonstrate that the aggregates form more noticeable amalgamations that previously seen.

When we consider the stability of the aggregates seen within these uptake studies, it is observed that **co-formulations *c***, ***f***, ***h***, ***j*** and ***l*** formed stable aggregates (> ±30 mV), and **co-formulations *a***, ***b***, ***d***, ***e***, ***g***, ***i***, ***k*** didn't form stable aggregates. Comparison of these results with previously attained results (Chapter 4.4.6) shows that for those where a comparison can be made, it was observed that the aggregates were more stable (**co-formulations *b***, ***c***, ***d***, ***g***, ***k,*** and ***l***), however, it is worth noting that for **co-formulations *d***, ***g*** and ***l*** they are still deemed to be unstable. Co-formulation ***h*** demonstrated a stability comparable to previous studies with values of -33 mV and -39 mV respectively. Only one co-formulation demonstrated a stability less stable than what was previously observed which was **co-formulation *a***, although this may not be surprising given that the amount of SSA/Co-formulant involved in the formation of these aggregates is less and also the size of these aggregates are also smaller, so it could be expected for the aggregates to be less stable. As with the DLS data discussed, no comparisons can be made for co-formulations ***e***, ***f***, ***i*** and ***j*** as they were not previously studied using this technique.

In summary, it has been shown that the method by which an SSA is exposed to a co-formulant can give results that are comparable to previous studies or in the case of those co-formulations that showed larger sizes, as a result of the amalgamation of these aggregates. With the only exception being that of **co-formulation *a***, where the size was smaller than previously observed, but in line with qNMR studies where the observed 'loss' was less than previous. From the Zeta potential studies, these aggregates have been shown to produce more stable or just as stable aggregates, with **co-formulation *a*** again being the only exception.

4.6 Conclusions

In conclusion, the synthesis and characterisation of three novel SSAs (compounds **90-92**) and ten novel SSA co-formulations (**co-formulations *c-l***) have been discussed through the study in the solid and solution state. Solution state studies confirmed the presence of larger self-associated aggregates in aqueous conditions (5% EtOH) for all compounds and co-formulations, with the exceptions of compound **88**, co-formulations ***e***, ***f***, ***i*** and ***j***, which were further studied using DLS and zeta potential measurements. In the organic solvent DMSO compound ***88***, ***89***, ***90***, ***91*** and co-formulations ***a***, ***b***, ***i, j*** and ***k*** showed no 'loss' in qNMR studies and further studied using ^{1}H DOSY NMR to determine the size of the particles present in solution which the sizes observed were indicative of lower order species such as dimers. The strength of the association was then determined through a series of dilution studies. The surface tension and critical micelle concentration was determined for all compounds and co-formulations were solubility allowed.

In order to determine whether SSAs could be used as uptake agents, a series of timed qNMR, DLS and zeta potential measurements were carried out; to determine if whether over a timed period there is a difference in the observed amount of co-formulant signal 'lost' and therefore, deemed to have been taken up by the SSA into self-associated aggregates, with the size and stability of these aggregates also studied. The stability of the aggregates through this method were on the whole more stable using this method of combining SSA and co-formulant,

the sizes also reflected this as they either were larger (amalgamations of aggregates) or of similar in size that originally observed.

It is hoped that through this proof-of-concept study that SSAs can be used as uptake agents for other molecules, more specifically environmental pollutants from water. To further this work, the library of SSA co-formulations will be expanded to include more environmental pollutants and studied within the solution state as discussed here. Additional studies into whether an SSA can release the co-formulant after uptake would need to be studied which would further expand the use of SSAs into uptake and release agents.

Chapter 5 – Final Conclusions

This thesis has focused on the development of a range of OP CWA simulants and strategies for their detection and remediation, it has also focused on strategies that enable the cleanup of small molecules from an aqueous environment. The determination of association constants for a series of hydrogen bonded complexes experimentally and modelled using a range of computational methods. In addition, association constants were determined experimentally through a series of ^{1}H NMR titration studies at 298 K in CD_3CN. It was through the combination of these methods and exhaustive parameter searches that a predictive model to aid the choice of OP CWA simulant for novel detection technologies through complexation events was explored. Furthermore, a variety of physicochemical properties were investigated to further explore the properties of any potentially OP CWA simulant. Any biological toxicity of these compounds was considered and screened using *S. pombe.* It was found that the majority of the compounds discussed pose no significant toxicity to these eukaryotic organisms that these yeast cells are a model for.

Additionally, the breakdown of these compounds has been investigated in the presence of a base. Comparative breakdown rates determined and used in order to elucidate predictive models for OP CWA simulant reactivity, through the predictive methodologies developed for association constant determination. This will allow for a more accessible approach in the development of novel OP CWA remediation technologies, and through the development of these models the importance of considering experimental limitations was highlighted and allows for an improved predication of a potential simulants' reactivity.

Finally, the self-associative properties of five structurally related compounds and their co-formulations with three co-formulants were studied in organic and aqueous conditions and confirmed the presence of larger self-associated aggregates in both conditions. These aggregates were further investigated through a range of solution state methodologies such as

DLS, Zeta potential (aqueous conditions only) and CMC determination (aqueous conditions only). Lower order species such as dimers were also confirmed through a series of ^{1}H NMR DOSY studies, and self-association constants determined through a series of dilution studies. The potential for these molecules to be used as uptake agents was examined through a series of timed quantitative ^{1}H NMR, DLS and zeta potential studies, in order to observe whether not only could these aggregates be used to uptake other molecules but also over a time frame how this observed uptake may differ. These studies provided the proof-of-concept that these molecules can uptake other molecules and will provide a basis for further exploration into the area of SSAs as environmental organic pollutant uptake in aqueous systems.

Chapter 6 – Experimental procedures

6.1 General information

General remarks: A positive pressure of nitrogen and oven dried glassware were used for all reactions. All solvents and starting materials were purchased from known chemical suppliers or available stores and used without any further purification unless specifically stipulated. The NMR spectra were obtained using a Jeol ECS-400, Bruker AV2 400 MHz or AVNEO 400 MHz spectrometer. The data was processed using Topspin software. NMR Chemical shift values are reported in parts per million (ppm) and calibrated to the centre of the residual solvent peak set (s = singlet, br = broad, d = doublet, t = triplet, q = quartet, m = multiplet). Self-association constant calculation: Self-association constants were determined using Bindfit v0.5 (http://app.supramolecular.org/bindfit/). All the data can be accessed online using the hyperlinks provided.

Infrared spectra were obtained using a Shimadzu IR-Affinity-1 model Infrared spectrometer. The data are analysed in wavenumbers (cm -1) using IRsolution software. The melting point for each compound was measured using Stuart SMP10 melting point apparatus which has a temperature range from ambient to 200 °C, compounds which exhibit a melting point greater than 200 are displayed as > 200 °C.

High-resolution mass spectrometry was performed using a Bruker microTOF-Q mass spectrometer and spectra recorded and processed using Bruker's Compass Data Analysis software. Sample preparation: Approximately 1 mg of each compound was dissolved in 1 mL of methanol. This solution was further diluted 100-fold before undergoing analysis where 10 µL of each sample was then injected directly into a flow of 10 mM ammonium acetate in 95 % water (flow rate = 0.02 mL/min).

6.1.1 General information Chapter 2

Proton NMR titration studies: Firstly, a solution of the appropriate receptor (1.5 mL, 0.01 M) was prepared; of this solution 0.5 mL was placed in an NMR tube. The remaining 1 mL of the receptor solution was used to prepare a 0.15 M solution of the appropriate guest. The guest-receptor stock solution was titrated into the NMR tube and a ^{1}H NMR taken before/after each addition of the stock solution.

Job Plot analysis method: Two solutions were produced; the first solution was a 3 mL, 0.01 M solution of the receptor and the second was a 3 mL, 0.01 M solution of the simulant. Of the receptor solution 0.5 mL was added to an NMR tube. The amount of receptor solution was then decreased by 0.05 mL and the amount of simulant solution increased by 0.05 mL for each successive NMR tubes until a 9:1 simulant:receptor ratio was reached. A ^{1}H NMR spectra was taken for each of the ten NMR tubes and calibrated to the solvent peak. The data was then used to produce a job plot, in accordance with the methods described by Job.[380]

***Schizosaccharomyces* pombe studies:** Biological screening was carried out using 96 well plates and the Thermo Scientific™, Multiskan™ GO Microplate Spectrophotometer or CLARIOstar high performance plate reader with optical density reading taken at 600 nm every 15 minutes for 45 hours. A Neubauer Improved Bright-Line Cell Counting Chamber Hemocytometer was used in all cell density measurements.

Semi-empirical PM6 modelling methods: Computational calculations to identify primary hydrogen bond donating and accepting sites were conducted in line with studies reported by Hunter using Spartan 16'.[62] Calculations were performed using semi-empirical PM6 methods, after energy minimisation calculations, to identify E_{min} and polarizability values. PM6 was used over AM1 in line with research conducted by Stewart.[235] To estimate the accessibility of the principle HBA site towards supramolecular coordination, the area of the ESPM within 1/8th of the E_{min} for the principle HBA group, and has been termed the 'steric weighting factor' (SWF) for

ease of reference. The SWF was considered for either one or two sulfonate oxygen atoms for **51**-**61**.

Low level B3LYP/6-31-G* modelling methods: After energy minimisation calculations for compounds **40**-**61**, sarin and soman, along with complexes of **36** and compounds **40**-**61**, sarin and soman, in the gas phase using Spartan '16. Data from these calculations were compared to that of the semi-empirical PM6 calculations to determine which calculation method should be used for each parameter.

High Level DFT modelling methods: Each individual compound was pre-optimised in the gas phase at the PM6 level[381] using Spartan '16[18] before further geometry optimisation at the M06-2X level[382] and the 6-311g(d,p) basis set[381] using Gaussian16[383] with a PCM solvent model for acetonitrile. All structures were confirmed as energy minima by frequency analysis. Adducts were modelled by combining the appropriate M06-2X geometries. For each compound, initial geometries for appropriate coordination modes to **36** were chosen and allowed to freely optimise. Initial geometries for coordination via single oxygen atom (P=O or S=O), or via two oxygen atoms simultaneously (RO-P=O or O=S=O) were considered for **41**, **44**, **45**, **46**, **51-55**, **60**, **61**, sarin, soman; for **44**, the optimised geometry precluded a 2-oxygen coordination mode and so only the 1-oxygen mode was considered. Given the potential for the partial negative charge on fluorine in sarin and soman to engage in hydrogen bonding, an additional mode of association with the receptor via both the fluorine and P=O simultaneously (F-P=O association mode) was allowed to optimise for these systems. From these results, energies of complex formation could be determined by assessing the energy change for the reaction:

$$Receptor\ 36 + Binder \rightarrow Complex$$

6.1.1.1 Biological experimental

Preparation of amino acid solution: Adenine (5.63 g, 41.66 mmol), leucine (5.63 g, 41.00 mmol), histidine (5.63 g, 36.26 mmol) and uracil (5.63 g, 46.07 mmol) were dissolved into distilled H2O (500 mL), autoclaved then allowed to cool to room temperature.

Preparation of agar plates and initial cell growth: Yeast extract (10 g) and glucose (60.0 g, 333.03 mmol) were dissolved in distilled H_2O (2000 mL) to create a YES solution. This stock solution was then divided equally into five bottles. Agar (6 g) was then dissolved into each 400 mL YES media stock solution. The bottles were autoclaved then allowed to cool to room temperature and to each stock solution was added the pre-prepared amino acid solution (8 mL). This solution was then immediately poured into sterile Petri dishes under sterile conditions. The plates were then left to set and stored at 4 °C. Prototroph Schizosaccharomyces pombe cells were then streaked onto the agar plates under sterile conditions, sealed using Parafilm then grown at 25 °C for two days. EMMG (Edinburg minimal media with glutamic acid) media preparation: EMM powder without nitrogen (27.30 g) and L-glutamic acid monosodium salt hydrate (3.38 g, 19.99 mmol) were dissolved in distilled H2O (1000 mL). The EMMG media was then poured into bottles, autoclaved, and allowed to cool to room temperature before use. Preparation of 96 well plates for *S. pombe* toxicity screening: EMMG media (20 mL) was inoculated in a sterile Falcon using single colonies from the YES plate and incubated overnight at 25 °C with shaking. The cell density was calculated using a haemocytometer on the following day and the number of generation times were calculated using

Equation 6.1.1. The cell suspension was then diluted using Equation 6.1.2 to reach a cell density of $2x10^6$ cells/mL when grown for a further 20 hours. After 20 hours a final dilution with EMMG media was carried out to produce a cell suspension with a density of $0.5x10^6$ cells/mL when grown for a further 20 hours. Once the suspension had reached a cell density of $0.5x10^6$ cells/mL, an aliquot of the suspension (120 µL) was added to each well of the 96 well plate.

$$\text{Number of generation times} = \frac{\text{Incubation time}}{\text{Generation time}}$$

Equation 6.1.1 Equation to calculate the number of generation times, calculated by dividing the time the culture is growing in EMMG media by the number generation time. Our cell suspensions were grown over 20 hours (incubation time) and the generation time was 4.

$$\text{Volume of suspension needed or dilution} = 1000 \times \left[\left(\frac{\text{Desired volume (mL)} \times \text{Desired cell density (cells/mL)}}{2^{\text{number of generation times}}}\right) \div \text{Current density}\right]$$

Equation 6.1.2: The dilution equation to calculate the volume of suspension needed to inoculate a specific volume to a specific concentration after a specific period of time. The desired volume used was 20 mL, the desired cell density as stated in text and the number of generation times was calculated using

Equation 6.1.1.

A 10mM stock solution of each compound to be tested was prepared in a sterile 1:19 Ethanol: Distilled water mixture no longer than 2 hours before the start of the toxicity screening experiment. An aliquot (60 µL) of an appropriate compound stock solution was then added to a single well on the pre-prepared 96 well plate. Each experiment was repeated three times. A baseline for cell growth in the absence of compounds was obtained through the addition of an aliquot of a sterile 1:19 Ethanol:Distilled water mixture (60 µL) to twelve wells of the 96 well plate, to ensure stable growth. The 96 well plates were then sealed using Parafilm and incubated in a plate reader at 25°C with shaking. An absorbance reading at 600 nm was taken every 15 minutes for 45 hours.

6.1.2 General information Chapter 3

Hydrolytic stability studies: Stock solutions of the appropriate simulant (10 mM) were made up in DMSO-d_6:D_2O (70:30) at 291 K. With a reaction timer started upon the addition of D_2O. A ^1H NMR experiment was then completed for each sample every 2 hours thereafter. The mono hydrolysis product was the sole species observed as the result of simulant breakdown under these conditions.

Reactivity studies using sodium hydroxide: For the reactivity studies stock solutions of the appropriate simulants (10mM) were made up in MeOD-d_4:D_2O (70:30) at 291 K, one equivalent of NaOH (10 mM) or five equivalents of NaOH (50 mM) was added. A ^1H NMR experiment was

then completed for each sample every 2 hours thereafter. The mono hydrolysis product was the sole species observed as the result of simulant breakdown under these conditions.

Viscosity studies: Only simulants that are a liquid at 298 K were studied. Each simulant was loaded onto the base plate of a Anton Par modular compact rheometer (MCR302) and trimmed to the CP60-1 plate. Each experiment was run in triplicate, with three intervals within each run, at a d(gamma)/dt = 0-100 1/s logarithmic (sheer rate). The plateau of each viscosity measurement was used to calculate the average viscosity for each sample.

Surface tension studies: Measurements were undertaken using a Biolin Scientific Theta Attension optical tensiometer. The data was processed using Biolin OneAttension software. A Hamilton gas tight syringe was used for the measurements. A succession of 3 droplets were measured for each sample and an average for these measurements reported.

6.1.3 General information Chapter 4

DLS and zeta potential studies: DLS and Zeta Potential studies were carried out using a Malvern Zetasizer Nano ZS or Anton Paar LitesizerTM 500 and processed using KalliopeTM Professional.

DLS sample preparation: All vials used for preparing the samples were clean and dry. All solvents used were filtered to remove any particulates that can interfere with the results obtained. Samples of different concentrations were obtained through serial dilution of a concentrated solution. All samples underwent an annealing process, in which they were heated to 40 °C before being allowed to cool to 25 °C. A series of 9 or 10 runs were recorded at 25 °C.

Zeta potential sample preparation: All vials used for preparing the samples were clean and dry. All solvents used were filtered to remove any particulates that may interfere with the results obtained. All samples underwent an annealing process in which the various solutions were heated to approximately 40 °C before cooling to room temperature, allowing each sample to

reach a thermodynamic minimum. The final zeta potential value given is an average of the number of experiments conducted at 25 °C.

Single Crystal X-ray Studies: A suitable crystal of each compound was selected and mounted on a Rigaku Oxford Diffraction Supernova diffractometer. Data were collected using Cu Kα radiation at 100K or 293K as necessary due to crystal instability at lower temperatures. Structures were solved with the ShelXT or ShelXS structure solution programs via Direct Methods and refined with ShelXL by Least Squares minimisation. Olex2 was used as an interface to all ShelX programs.

Tensiometry Studies: Tensiometry measurements were undertaken using a Biolin Scientific Theta Attension optical tensiometer. The data was processed using Biolin OneAttension software. A Hamilton gas tight syringe was used for all measurements. **Sample preparation**: All the samples were prepared in an 5% EtOH solution. All samples underwent an annealing process in which the various solutions were heated to approximately 40 °C before being allowed to cool to room temperature, allowing each sample to reach a thermodynamic minimum. All samples were prepared through serial dilution of the most concentrated sample. Three surface tension measurements were obtained for each sample at a given concentration, using the pendant drop method. The average values were then used to calculate the critical micelle concentration (CMC).

6.2 Synthetic procedures

Compound 36: A solution of 4-(trifluoromethyl)phenyl isothiocyanate (1.57 g, 7.16 mmol) and 4-(trifluoromethyl)aniline (0.90 mL, 7.16 mmol) in pyridine (4 mL) was stirred at room temperature overnight. The pyridine solution was then added to water (30 mL) to precipitate a white solid. This solid was collected by filtration and washed with water and then dried to give the final product as a white solid (1.92 g, 5.26 mmol) in a yield of 73.5 %. ^{1}H NMR: (400 MHz, 298 K, DMSO-d_6): δ: 7.72 (dd, J_1= 8.80 Hz, J_2 = 16.40 Hz, 8H), 10.37 (s, 2NH). This compound has

been previously synthesised by Gale and co-workers.[384] The ^{1}H NMR data provided was found to match these previously published data.

Compound 37: A solution of phenyl isothiocyanate (1.45 g, 10.74 mmol) and aniline (0.98 mL, 10.74 mmol) in pyridine (4 mL) was stirred at room temperature overnight. The pyridine solution was then added to water (30 mL) to precipitate a white solid. This solid was collected by filtration and washed with water and dried to give the final product as a white solid (2.07 g, 9.06 mmol) in a yield of 84.4 %. ^{1}H NMR: (400 MHz, 298 K, DMSO-d_6): δ: 7.12 (t, J = 7.40 Hz, 2H), 7.33 (t, J = 8.28 Hz, 4H), 7.47 (d, J = 7.52 Hz, 4H), 9.80 (s, 2NH). This compound has been previously synthesised by Gale and co-workers.[384] The ^{1}H NMR data provided was found to match these previously published data.

Compound 38: A solution of benzyl isothiocyanate (1.24 mL, 9.33 mmol) and benzylamine (1 mL, 9.33 mmol) in pyridine (4 mL) was stirred at room temperature overnight. The pyridine solution was then added to water (30 mL) to precipitate a white solid. The white solid was then collected by filtration and washed with water and dried to give the pure product (1.74 g, 6.79 mmol) in a yield of 72.8 %. ^{1}H NMR: (400 MHz, 298 K, $CDCl_3$): δ: 4.66 (s, 4H), 7.25-7.34 (m, 12H). ^{1}H NMR: (400 MHz, 298 K, CD_3CN): δ: 4.69 (br s, 2H), 6.77 (br s, 2NH), 7.24-7.35 (m, 10H). This compound has been previously synthesised by Lui and co-workers.[385] The ^{1}H NMR data provided was found to match previously these published data. Proton NMR was also obtained in CD_3CN (Figure S4) to allow for accurate integration.

Compound 39: Acetone (5.00 mL, 67.15 mmol) was added to pyrrole (1.00 mL, 14.04 mmol), followed with a few drops of HCl. The solution was left to stir for 30 minutes. A yellow precipitate formed which was collected by filtration, washed with methanol and then dried to give the final product as a white solid (0.858 g, 2.00 mmol) in a yield of 57.1 %. ^{1}H NMR: (400 MHz, 298 K, $CDCl_3$): δ: 7.00 (s, 4NH), 5.90 (d, J = 2.72 Hz, 8H), 1.51 (s, 24H). This compound has been

previously synthesised by Chauhan and co-workers.[386] The ^{1}H NMR data provided was found to match these previously published data.

Compound 40: Diethyl chlorophosphate (0.45 mL, 3.08 mmol) was added to a stirring solution of 3,5-(trifluoromethyl)phenol (0.47 mL, 3.08 mmol) and triethylamine (0.43 mL, 3.08 mmol) in chloroform (10 mL). The mixture was then allowed to stir at room temperature overnight. The organic phase was then washed with an aqueous 0.3M NaOH solution (30 mL). The organic layer was then taken to dryness to give this final product as a colourless oil (0.73 g, 2.00 mmol) with a yield of 64.9 %. $^{1}H\{^{31}P\}$ NMR: (400 MHz, 298 K, CDCl3): δ: 1.32 (t, J= 7.08 Hz, 6H), 4.22 (q, J = 7.12 Hz, 4H), 7.64 (br s, 3H); $^{13}C\{^{1}H\}$ NMR: (100 MHz, 298 K, $CDCl_3$): δ: 16.0 (d, J = 6.49 Hz, CH_3), 65.3 (d, J = 6.12 Hz, CH_2), 118.7 (sept, J = 3.61 Hz, ArCH), 120.8 (m, ArCH), 122.6 (q, J = 271.42 Hz, CF_3), 133.3 (q, J = 33.94 Hz, ArC), 151.4 5 (d, J = 6.31 Hz, ArC). IR (film): ν = (cm^{-1}): 831 (P-O stretch), 1275 (P=O stretch); HRMS ($C_{12}H_{13}F_6O_4P$) (ESI+): m/z: act: 367.0652 $[M + H]^+$, cal: 367.0534 $[M + H]^+$.

Compound 41: Diethyl chlorophosphate (0.59 g, 3.08 mmol) was added to a stirring solution of 4-(trifluoromethyl)phenol (0.50 g, 3.08 mmol) and triethylamine (0.43 mL, 3.08 mmol) in chloroform (10 mL). The mixture was then allowed to stir at room temperature overnight. The organic phase was then washed with an aqueous 0.3M NaOH solution (30 mL). The organic layer was then taken to dryness to give the final product as a colourless oil (0.83 g, 2.78 mmol) in a yield of 90.3 %. $^{1}H\{^{31}P\}$ NMR: (400 MHz, 298 K, $CDCl_3$): δ: 1.39 (t, J= 7.08 Hz, 6H), 4.26 (q, J = 7.08 Hz, 4H), 7.36 (d, J = 8.56 Hz, 2H), 7.64 (d, J = 8.64 Hz, 2H); $^{13}C\{^{1}H\}$ NMR: (100 MHz, 298 K, $CDCl_3$): δ: 16.0 (d, J = 7.22 Hz, CH3), 64.9 (d, J = 5.77 Hz, CH2), 120.2 (d, J = 5.05, ArCH), 122.5 (q, J = 270.08 Hz, CF3), 127.1 (q, J = 3.61 Hz, ArCH), 127.2 (q, J = 33.22 Hz, ArC), 153.2 (dd, J1 = 1.59 Hz, J2 = 6.50 Hz, ArC); IR (film): ν = (cm-1): 820 (P-O stretch), 1277 (P=O stretch). HRMS ($C_{11}H_{14}F_3O_4P$) (ESI^+): m/z: act: 299.0762 $[M + H]^+$, cal: 299.0660 $[M + H]^+$.

Compound 42: Diethyl chlorophosphate (0.52 mL, 3.59 mmol) was added to a stirring solution of 4-nitrophenol (0.50 g, 3.59 mmol) and triethylamine (0.50 mL, 3.59 mmol) in chloroform (10 mL). This mixture was then allowed to stir at room temperature overnight. The organic phase was then washed with an aqueous 0.3M NaOH solution (30 mL). The organic layer was then taken to dryness to give the pure product as a clear yellow oil (0.86 g, 2.86 mmol) in a yield of 79.7 %. ^{1}H NMR: (400 MHz, 298 K, $CDCl_3$): δ: 1.31 (t, J = 7.08 Hz, 6H), 4.19 (q, J = 7.08, 4H), 7.31 (d, J = 9.20 Hz, 2H), 8.18 (d, J = 9.16, 2H). This compound has been previously synthesised by Kuei and co-workers.[387] The ^{1}H NMR data provided was found to match previously these published data.

Compound 43: Diethyl chlorophosphate (0.77 mL, 5.31 mmol) was added to a stirring solution of phenol (0.5 g, 5.31 mmol) and triethylamine (0.74 mL, 5.31 mmol) in chloroform (10 mL). The mixture was then allowed to stir at room temperature overnight. The mixture was then allowed to stir at room temperature overnight. The organic phase was then washed with an aqueous 0.3M NaOH solution (30 mL). The organic layer was then taken to dryness to give the pure product as a colourless oil (0.77 g, 3.37 mmol) with a yield of 63.5 %. ^{1}H{^{31}P} NMR: (400 MHz, 298 K, $CDCl_3$): δ: 1.34 (t, J = 7.08 Hz, 6H), 4.20 (q, J = 7.08 Hz, 4H), 7.14 – 7.22 (m, 3H), 7.33 (t, J = 8.58 Hz, 2H). This compound has been previously synthesised by Katritzky and co-workers.[388] The ^{1}H NMR data provided was found to match previously these published data.

Compound 44: Diethyl chlorophosphate (2.20 mL, 15.0 mmol) in pyridine (1.20 mL, 15.0 mmol) was added to a stirring solution of cyclohexanol (1.00 g, 9.98 mmol) in dichloromethane (10 mL).The solution was stirred at 0 °C then allowed to warm up to room temperature overnight. The reaction was then quenched with methanol (50 mL) and concentrated in vaccu. The resulting white solid was then dissolved in ethyl acetate (50 mL) and washed with 1M HCl (50 mL), saturated $NaHCO_3$ solution (50 mL). The organic layer was then taken to dryness to give a colourless oil (1.93 g, 8.17 mmol) with a yield of 81.7 %. ^{1}H{^{31}P} NMR (298 K, $CDCl_3$, 400 MHz): δ;

1.24-1.99 (m, 18H), 4.11 (q, J = 7.08, 4H), 4.34-4.41 (m, 1H). This compound has been previously synthesised by Kang et al.[389] The ^{1}H NMR data provided was found to match previously these published data.172

Compound 45: Diethyl chlorophosphate (0.97 mL, 6.74 mmol) was added to a stirring solution of butanol (0.50 g, 6.74 mmol) and triethylamine (0.94 mL, 6.74 mmol) in chloroform (10 mL). The mixture was then allowed to stir at room temperature overnight. The organic phase was then washed with an aqueous 0.3M NaOH solution (30 mL). The organic layer was then taken to dryness to give the pure product as a colourless oil (1.21 g, 5.74 mmol) in a yield of 85.2 %. ^{1}H{^{31}P} NMR: (400 MHz, 298 K, $CDCl_3$): δ: 0.93 (t, J = 7.36 Hz, 3H), 1.32 – 1.46 (m, 8H), 1.63 – 1.70 (m, 2H), 4.02 – 4.13 (m, 6H); ^{13}C{^{1}H} NMR: (100 MHz, 298 K, DMSO-d_6): δ: 13.9 (CH_3), 16.4 (CH_2), 18.6 (CH_2), 32.2 (d, J = 6.54 Hz, CH_3), 63.5 (d, J = 5.80 Hz, CH_2), 67.0 (d, J = 5.95 Hz, CH_2); IR (film): ν = (cm^{-1}): 802 (P-O stretch), 1275 (P=O stretch); HRMS ($C_8H_{19}O_4P$) (ESI$^+$): m/z: act: 211.1142 [M + H]$^+$, cal: 211.1099 [M + H]$^+$.

Compound 51: p-Toluene sulfonylchloride (0.588 g, 3.08 mmol) was added to a stirring solution of 4-(trifluoromethyl)phenol (0.75 g, 4.62 mmol) and triethylamine (0.43 mL, 4.62 mmol) in chloroform (10 mL). The mixture was then allowed to stir at room temperature overnight and then washed with an aqueous 0.3M NaOH solution (30 mL). The organic layer was then taken to dryness under reduced pressure to give the pure product as a white solid (0.58 g, 1.82 mmol) in a yield of 59.1 %. ^{1}H NMR: (400 MHz, 298 K, $CDCl_3$): δ: 2.44 (s, 3H), 7.10 (d, J = 8.36 Hz, 2H), 7.32 (d, J = 8.00 Hz, 2H), 7.55 (d, J = 8.52 Hz, 2H), 7.70 (d, J = 8.40 Hz, 2H). ^{13}C{^{1}H} NMR: (100 MHz, 298 K, $CDCl_3$): δ: 21.7 (CH3), 122.9 (ArCH), 122.2 (q, J = 270.81 Hz, CF_3), 127.0 (q, J = 3.61 Hz, ArCH), 128.5 (ArC), 129.2 (q, J = 33.22 Hz, ArC), 129.9 (ArCH), 132.0 (ArC), 145.8 (ArC), 151.9 (ArC); IR (film): ν = (cm^{-1}): 849 (S-O stretch), 1184 and 1352 (S=O stretch); HRMS ($C_{14}H_{11}F_3O_3S$) (ESI+): m/z: act: 339.0286 [M + Na]$^+$, cal: 339.0279 [M + Na]$^+$.

Compound 52: p-Toluene sulfonylchloride (0.69 g, 3.59 mmol) was added to a stirring solution of 4-nitrophenol (0.50 g, 3.59 mmol) and triethylamine (0.50 mL, 3.59 mmol) in chloroform (10 mL). This mixture was allowed to stir at room temperature overnight, then washed with an aqueous 0.3M NaOH solution (30 mL), and the organic layer was then taken to dryness to give the pure product as a pale yellow solid (0.84 g, 2.88 mmol) in a yield of 80.2 %. ^{1}H NMR: (400 MHz, 298 K, $CDCl_3$): δ: 2.50 (s, 3H), 7.21 (d, J = 9.20 Hz, 2H), 7.38 (d, J = 8.04 Hz, 2H), 7.76 (d, J = 8.40 Hz, 2H), 8.22 (d, J = 9.20 Hz, 2H). This compound has been previously synthesised by Wei and co-workers.[390] The ^{1}H NMR data provided was found to match these previously published data.

Compound 53: p-Toluene sulfonylchloride (1.01 g, 5.31 mmol) was added to a stirring solution of phenol (0.50 g, 5.31 mmol) and triethylamine (0.74 mL, 5.31 mmol) in chloroform (10 mL) and, stirred at room temperature overnight. The solution was then washed with an aqueous 0.3M NaOH solution (30 mL), and the organic layer was then taken to dryness to give the pure product as a white solid (1.27 g, 5.10 mmol) in a yield of 96.0 %. 1H NMR: (400 MHz, 298 K, CDCl3): δ: 2.42 (s, 3H), 7.00 (d, J = 8.16 Hz, 2H), 7.31 (t, J = 7.36 Hz, 1H), 7.38 (t, J = 7.12 Hz, 2H), 7.46 (d, J = 7.96 Hz, 2H), 7.72 (d, J = 8.32 Hz, 2H). This compound has been previously synthesised by Gibson and co-workers.[391] The ^{1}H NMR data provided was found to match these previously published data.

Compound 54: p-Toluenesulfonyl chloride (2.85 g, 15.00 mmol) in pyridine (1.20 mL, 15.00 mmol) was added to a stirring solution of cyclohexanol (1.00 g, 9.98 mmol) in dichloromethane (10 mL). The solution was stirred at 0 ℃ and allowed to warm to room temperature overnight. The reaction was then quenched with methanol (50 mL) and concentrated in vaccu. The resulting white solid was then dissolved in ethyl acetate (50 mL) and washed with 1M HCl (50 7 mL), saturated $NaHCO_3$ solution (50 mL). The organic layer was taken to dryness to give a colourless oil (1.82 g, 7.16 mmol) with a yield 71.6 %. ^{1}H NMR (298 K, $CDCl_3$, 400 MHz): δ; 0.85-

1.81 (m, 12H), 2.46 (s, 3H), 4.49 – 4.55 (m, 1H), 7.34 (d, J = 7.96 Hz, 2H), 7.34 (d, J = 8.32 Hz, 2H). This compound has been previously synthesised by Wei and co-workers.[390] The ^{1}H NMR data provided was found to match those previously published data.

Compound 55: p-Toluene sulfonylchloride (1.29 g, 6.74 mmol) was added to a stirring solution of butanol (0.62 mL, 6.74 mmol) and triethylamine (0.94 mL, 6.74 mmol) in chloroform (10 mL). This mixture was allowed to stir at room temperature overnight, then washed with an aqueous 0.3M NaOH solution (30 mL), and the organic layer was then taken to dryness to give the pure product as a colourless oil (1.32 g, 5.78 mmol) in a yield of 85.8 %. ^{1}H NMR: (400 MHz, 298 K, $CDCl_3$): δ: 0.85 (t, J = 7.40 Hz, 3H), 1.29-1.39 (m, 2H), 1.59-1.66 (m, 2H), 2.45 (s, CH3), 4.03 (t, J = 6.74 Hz, 2H), 7.35 (d, J = 8.00 Hz, 2H), 7.79 (d, J = 7.79 Hz, 2H). This compound has been previously synthesised by Wei and co-workers.[390] The ^{1}H NMR data provided was found to match these previously published data.

Compound 56: To a stirring solution of 3,5-bis(trifluoromethyl) phenol (1.00 g, 4.34 mmol) in chloroform (10 mL) and trimethylamine (0.86 ml, 6.17 mmol), was added methylsulfonyl chloride (0.34 mL, 4.34 mmol). The solution was stirred at room temperature for three hours, washed with an aqueous 0.3M NaOH solution (30 mL), and the organic layer taken to dryness to give a white solid (1.31 g, 4.25 mmol) with a yield of 98.5 % . ^{1}H NMR (298 K, $CDCl_3$, 400 MHz): δ; 3.31 (s, 3H), 7.79 (s, 2H), 7.89 (s, 2H). This compound has been previously synthesised by Seayad and co-workers.[392] The ^{1}H NMR data provided was found to match previously these published data.

Compound 57: Methylsulfonyl chloride (0.13 mL, 1.58 mmol) was added to a stirring solution of 4-trifluoromethyl phenol (0.26 g, 1.58 mmol) in chloroform (10 mL) and trimethylamine (0.22 ml, 1.58 mmol). The solution was stirred at room temperature for three hours, washed with an aqueous 0.3M NaOH solution (30 mL), and the organic layer taken to dryness to give a pale yellow solid (0.35 g, 1.44 mmol) with a yield of 91.2 %, melting point 49-51 °C. ^{1}H NMR (298 K,

$CDCl_3$, 400 MHz): δ; 3.23 (s, 3H), 7.44 (d, J = 8.52 Hz, 2H), 7.73 (d, J = 8.52 Hz, 2H); $^{13}C\{^1H\}$ NMR: (100 MHz, 298 K, $CDCl_3$): δ: 37.8 (CH_3), 122.2 (q, J = 270.84 Hz, CF_3), 122.6 (ArCH), 127.5 (q, J = 3.69 Hz, ArCH), 129.37 (q, J = 32.93 Hz, ArC), 151.3 (ArC). IR (film): ν = (cm^{-1}): 851 (S-O stretch), 1175 and 1364 (S=O stretch).

Compound 58: Methylsulfonyl chloride (0.56 mL, 7.19 mmol) was added to a stirring solution of 4-nitrophenol (1.00 g, 7.19 mmol) in chloroform (10 mL) and trimethylamine (0.50 ml, 3.56 mmol). The solution was stirred at room temperature for three hours, washed with an aqueous 0.3M NaOH solution (30 mL), and the organic layer taken to dryness to give a white solid (0.94 g, 4.35 mmol) with a yield of 60.5 %. ^1H NMR (298 K, $CDCl_3$, 400 MHz): δ; 3.23 (s, 3H), 7.50 (d, J = 9.20 Hz, 2H), 8.34 (d, J = 9.16 Hz, 2H). This compound has been previously synthesised by Tokuyama and co-workers.[393] The ^1H NMR data provided was found to match previously these published data.175

Compound 59: Methylsulfonyl chloride (0.82 mL, 10.63 mmol) was added to a stirring solution of phenol (1.00 g, 10.63 mmol) in chloroform (10 mL) and trimethylamine (0.50 ml, 3.56 mmol). The solution was stirred at room temperature for three hours, washed with an aqueous 0.3M NaOH solution (30 mL), and the organic layer taken to dryness to give a white solid (0.96 g, 5.56 mmol) with a yield of 52.3 %. ^1H NMR (298 K, $CDCl_3$, 400 MHz): δ; 3.16 (s, 3H), 7.31 – 7.38 (m, 3H), 7.45 (t, J = 7.28 Hz, 2H). This compound has been previously synthesised by Seayad and co-workers. [392] The ^1H NMR data provided was found to match previously these published data.

Compound 60: Methylsulfonyl chloride (0.78 mL, 10.10 mmol) in pyridine (0.82 mL, 10.10 mmol) was added to a stirring solution of cyclohexanol (1.00 g, 9.98 mmol) in dichloromethane (10 mL). The solution was stirred at 0 ℃ and allowed to warm to room temperature. The reaction was then quenched with methanol (50 mL) and concentrated in vaccu. The resulting white solid was then dissolved in ethyl acetate (50 mL) and washed with 1M HCl (50 mL), saturated NaHCO3 solution (50 mL). The organic layer was then taken to dryness to give a yellow oil (1.68 g, 9.42

mmol) with a yield of 94.4 %. ^{1}H NMR (298 K, $CDCl_3$, 400 MHz): δ; 1.29-2.03 (m, 10H), 3.02 (s, 3H), 4.72 (m, 1H). This compound has been previously synthesised by Martín and co-workers.[394] The ^{1}H NMR data provided was found to match previously these published data.

Compound 61: Methylsulfonyl chloride (1.56 mL, 20.20 mmol) in pyridine (1.64 mL, 20.20 mmol) was added to a stirring solution of butanol (1.00 g, 13.4 mmol) in dichloromethane (10 mL). The solution was stirred at 0 °C and allowed to warm to room temperature. The reaction was then quenched with methanol (50 mL) and concentrated in vaccu. The resulting white solid was then dissolved in ethyl acetate (50 mL) and washed with 1M HCl (50 mL), saturated NaHCO3 solution (50 mL) organic layer taken to dryness to give a yellow oil (1.43 g, 9.39 mmol) with a yield of 70.1 %. ^{1}H NMR (298 K, $CDCl_3$, 400 MHz): δ; 0.89 (t, J = 7.36 Hz, 3H), 1.37 (m, 2H), 1.67 (m, 2H), 2.93 (s, 3H), 4.17 (t, J = 6.56 Hz, 2H). This compound has been previously synthesised by Li and co-workers.[395] The ^{1}H NMR data provided was found to match previously these published data.

Compound 88: This compound was synthesised on a 2 mmol scale in line with our previously published method.[341] ^{1}H NMR (400 MHz, 298.15 K, DMSO-d_6): δ: 0.93 (t, J = 7.28 Hz, 12H), 1.26 - 1.35 (m, 8H), 1.52 - 1.60 (m, 8H), 3.14 - 3.18 (m, 8H), 3.81 (d, J = 5.80 Hz, 2H), 4.63 (s, 2H), 6.17 (t, J = 5.68 Hz, 1H), 6.45 (d, J = 8.68 Hz, 2H), 6.99 (d, J = 8.64 Hz, 2H), 8.22 (s, 1H).

Compound 89: This compound was synthesised on a 2 mmol scale in line with our previously published method.[15] ^{1}H NMR (400 MHz, 298.15 K, DMSO-d_6): δ: 0.92-1.06 (m, 18H), 1.29 - 1.35 (m, 8H), 1.56 - 1.59 (m, 8H), 3.15 - 3.27 (m, 12H), 3.84 (d, J = 5.80 Hz, 2H), 6.22 (t, J = 5.56 Hz, 1H), 6.59 (d, J = 9.00 Hz, 2H), 7.14 (d, J = 9.00 Hz, 2H), 8.34 (s, 1H).

Compound 90: Aminomethanesulfonic acid (0.22 g, 2.0 mM) was dissolved in tetrabutylammonium hydroxide in methanol (2.0 mL, 2.0 mM) and taken to dryness. Triphosgene (0.30 g, 1.0 mM) was added to 4-aminopyridine (0.39 g, 2.0 mM) and triethylamine (1.83 mL, 6.0 mM) in ethyl acetate (30 mL) and left to stir at RT under an inert atmosphere for 4 hours. Tetrabutylammonium aminomethanesulfonate (2.0 mM) was dissolved in ethyl acetate

(10 mL) and added to a stirring solution of the isocyanate in ethyl acetate (30 mL), refluxed at 60 °C under an inert atmosphere overnight. The resultant precipitate was recrystallised with ethyl acetate to give a white solid with a yield of 63.5 % (0.60 g, 1.27 mM). Melting point: > 200 °C ; ^{1}H NMR (400 MHz, 298.15 K, DMSO-d_6): δ: 0.93 (t, J = 7.28 Hz, 12H), 1.26 - 1.35 (m, 8H), 1.53 - 1.61 (m, 8H), 3.14 - 3.18 (m, 8H), 3.87 (d, J = 5.88 Hz, 2H), 6.67 (s, 1H), 7.33 (d, J = 6.36 Hz, 2H), 8.27 (d, J = 6.24 Hz, 2H), 9.22 (s, 1H); ^{13}C{^{1}H} NMR (100 MHz, 298.15 K, DMSO-d_6): δ: 13.6 (CH_3), 19.7 (CH_2), 23.5 (CH_2), 56.3 (CH_2), 58.0 (CH_2), 112.3 (ArCH), 147.9 (ArC), 150.0 (ArCH), 154.5 (C=O); IR (film): ν = 3275 (NH stretch), 1694, 1244, 1167, 878; HRMS for the sulfonate-urea ion ($C_7H_8N_3O_4S^-$) (ESI-): m/z: act: 230.8784 $[M]^-$ cal: 230.2185 $[M]^-$.

Compound 91: Aminomethanesulfonic acid (0.22 g, 2.0 mM) was dissolved in tetrabutylammonium hydroxide in methanol (2.0 mL, 2.0 mM) and taken to dryness. Triphosgene (0.30 g, 1.0 mM) was added to tert butyl-4-aminobenzoate (0.39 g, 2.0 mM) in ethyl acetate (30 mL) and left to stir at 60 °C under an inert atmosphere for 4 hours. Tetrabutylammonium aminomethanesulfonate (2.0 mM) was dissolved in ethyl acetate (10 mL) and added to a stirring solution of the isocyanate in ethyl acetate (30 mL), refluxed at 60 °C under an inert atmosphere overnight. The organic phase was then twice washed with H_2O (20 mL) and the organic layer taken to dryness to give a brown oil with a yield of 80.5 % (0.92 g, 1.60 mM). Melting Point: 68 °C; ^{1}H NMR (400 MHz, 298 K, DMSO-d_6): δ: 0.94 (t, J = 7.28 Hz, 12H), 1.26 - 1.34 (m, 8H), 1.50 - 1.61 (m, 17H), 3.15 - 3.19 (m, 8H), 3.88 (d, J = 5.84 Hz, 2H), 6.63 (s, 1H), 7.47 (d, J = 8.76 Hz, 2H), 7.76 (d, J = 8.76 Hz, 2H), 9.15 (s, 1H); ^{13}C{^{1}H} NMR (100 MHz, 298 K, DMSO-d_6): δ: 13.5 (CH_3), 19.2 (CH_2), 23.06 (CH_2), 27.9 (CH_3), 55.9 (CH_2), 57.5 (CH_2), 79.8 (C), 116.5 (ArCH), 123.4 (ArC), 130.0 (ArCH), 144.9 (ArC), 154.2 (C=O), 164.8 (C=O); IR (film): ν = 3280 (NH stretch), 1695, 1219, 1157, 858; HRMS for the sulfonate-urea ion ($C_{13}H_{15}N_2O_6S^-$) (ESI^-): m/z: act: 164.0026 $[M - H]^{2-}$, cal: 164.0107 $[M - H]^{2-}$.

Compound 92: Trifluoroacetic acid (2 mL) was added to a stirring solution of compound **3** (0.20 g, 0.39 mM) in dichloromethane (5 mL) and left at RT for 30 minutes. Sodium hydroxide (6 M) was added dropwise until a neutral pH was reached. The resultant precipitate removed by filtration to give the pure product as a white solid with a yield of 79.5 % (0.16 g, 0.31 mM). Melting point: 90 °C ; ^{1}H NMR (400 MHz, 298 K, DMSO-d_6): δ: 0.93 (t, J = 7.28 Hz, 12H), 1.26 - 1.35 (m, 8H), 1.53 - 1.60 (m, 8H), 3.14 - 3.18 (m, 8H), 3.87 (d, J = 5.84 Hz, 2H), 6.58 (s, 1H), 7.46 (d, J = 8.72 Hz, 2H), 7.80 (d, J = 8.76 Hz, 2H), 9.15 (s, 1H), 12.49 (s, 1H); ^{13}C{^{1}H} NMR (100 MHz, 298 K, DMSO-d_6): δ: 13.6 (CH_3), 19.2 (CH_2), 23.1 (CH_2), 56.2 (CH_2), 57.5 (CH_2), 115.9 (ArCH), 129.7 (ArCH), 133.2 (ArC), 141.4 (ArC), 157.8 (C=O), 170.0 (C=O); IR (film): ν = 3278 (NH stretch), 1697, 1220, 1163, 881; HRMS for the sulfonate-urea ion ($C_9H_7N_2O_6S^-$) (ESI$^-$): m/z: act: 164.0107 [M - H]$^{2-}$ cal: 164.0370 [M- H]$^{2-}$.

Co-formulation *a*: This compound was synthesized in line with our previously published method.[3] ^{1}H NMR (400 MHz, 298 K, DMSO-d_6): δ 0.93 (t, J = 7.28 Hz, 12H), 1.26-1.35 (m, 8H), 1.52-1.60 (m, 8H), 3.13-3.18 (m, 8H), 3.82 (d, J = 5.84 Hz, 2H), 6.21 (t, J = 5.52 Hz, 1H), 6.55 (d, J = 8.68 Hz, 2H), 7.05 (d, J = 8.72 Hz, 2H), 7.39-7.45 (m, 2H), 7.73 (t, J = 8.48 Hz, 1H), 7.90 (d, J = 9.28 Hz, 1H), 8.32 (s, 1H), 8.75 (s, 1H).

Co-formulation *b*: This compound was synthesized in line with our previously published method.[3] ^{1}H NMR (400 MHz, 298 K, DMSO-d_6): δ 0.94 (t, J = 7.28 Hz, 12H), 1.04 (t, J = 7.00 Hz, 6H), 1.26-1.36 (m, 8H), 1.53-1.61 (m, 8H), 3.14-3.27 (m), 3.82 (d, J = 5.80 Hz, 2H), 6.19 (t, J = 5.24 Hz, 1H), 6.58 (d, J = 8.96 Hz, 2H), 7.13 (d, J = 8.96 Hz, 2H), 7.35-7.41 (m, 2H), 7.66 (t, J = 8.20 Hz, 1H), 7.83 (d, J = 7.2 Hz, 1H), 8.32 (s, 1H), 8.45 (s, 1H).

Co-formulation *c*: Coumarin-3-carboxylic acid (0.08 g, 0.4 mM) was added to compound **90** (0.20 g, 0.4 mM) in methanol and taken to dryness to give a white solid with a yield of 100 % (0.27 g, 2.0 mM); ^{1}H NMR (400 MHz, 298 K, DMSO-d_6): δ: 0.94 (t, J = 7.32 Hz, 12H), 1.27 - 1.36 (m, 8H), 1.53 - 1.61 (m, 8H), 3.14 - 3.19 (m, 8H), 3.88 (d, J = 5.84 Hz, 2H), 6.79 (s, 1H), 7.35-7.45 (m, 4H),

7.73 (t, J = 8.48 Hz, 1H), 7.91 (d, J = 7.88 Hz, 1H), 8.28 (d, J = 6.32 Hz, 2H), 8.72 (s, 1H), 9.32 (s, 1H).

Co-formulation *d*: Coumarin-3-carboxylic acid (0.07 g, 0.38 mM) was added to compound **91** (0.2 g, 0.38 mM) in methanol and taken to dryness to give a white solid with a yield of 100 % (0.27 g, 0.38 mM); ^{1}H NMR (400 MHz, 298 K, DMSO-d_6): δ: 0.94 (t, J = 7.32 Hz, 12H), 1.27 - 1.36 (m, 8H), 1.53 - 1.61 (m, 8H), 3.14 - 3.89 (m, 8H), 3.87 (d, J = 5.80 Hz, 2H), 6.58 (s, 1H), 7.29-7.35 (m, 2H), 7.46 (d, J = 8.76 Hz, 2H), 7.55 (t, J = 7.12 Hz, 1H), 7.72 (d, J = 7.60 Hz, 1H), 7.81 (d, J = 8.84 Hz, 2H) 8.05 (s, 1H), 9.14 (s, 1H).

Co-formulation *e*: 8-Hydroxypyrene-1,3,6-trisulfonic acid trisodium salt (0.21 g, 0.4 mM) was added to compound **88** (0.20 g, 0.4 mM) in methanol and taken to dryness to give a brown solid with a yield of 100 % (0.40 g, 0.4 mM); ^{1}H NMR (400 MHz, 298 K, DMSO-d_6): δ: 0.95 (t, J = 7.28 Hz, 12H), 1.24 - 1.33 (m, 8H), 1.50 - 1.58 (m, 8H), 3.12 - 3.16 (m, 8H), 3.82 (d, J = 5.88 Hz, 2H), 4.69 (s, 1H) 6.20 (t, J = 5.16 Hz, 1H), 6.45 (d, J = 8.64 Hz, 2H), 6.80 (d, J = 8.64 Hz, 2H), 8.15 (s, 1H), 8.15-8.30 (m, 2H), 8.85 (d, J = 9.76 Hz, 1H), 8.95-9.02 (m, 2H), 10.67 (s, 1H).

Co-formulation *f*: 8-Hydroxypyrene-1,3,6-trisulfonic acid trisodium salt (0.19 g, 0.37 mM) was added to compound **89** (0.20 g, 0.37 mM) in methanol and taken to dryness to give a brown solid with a yield of 100 % (0.39 g, 0.37 mM); ^{1}H NMR (400 MHz, 298 K, DMSO-d_6): δ: 0.93 (t, J = 7.24 Hz, 12H), 1.01 (t, J = 6.96 Hz, 6H) 1.24 - 1.34 (m, 8H), 1.51 - 1.59 (m, 8H), 3.13 - 3.27 (m, 12H), 3.85 (d, J = 5.88 Hz, 2H), 6.24 (t, J = 5.64 Hz, 1H), 6.59 (d, J = 9.00 Hz, 2H), 7.14 (d, J = 9.00 Hz, 2H), 8.17 (s, 1H), 8.29-8.34 (m, 2H), 8.86 (d, J = 9.80 Hz, 1H), 8.97-9.03 (m, 2H), 10.68 (s, 1H).

Co-formulation *g:* 8-Hydroxypyrene-1,3,6-trisulfonic acid trisodium salt (0.17 g, 0.32 mM) was added to compound **90** (0.15 g, 0.32 mM) in methanol and taken to dryness to give a yellow solid with a yield of 100 % (0.32 g, 0.32 mM); ^{1}H NMR (400 MHz, 298 K, DMSO-d_6): δ: 0.92 (t, J = 7.32 Hz, 12H), 1.24 - 1.33 (m, 8H), 1.50 - 1.58 (m, 8H), 3.12 - 3.16 (m, 8H), 3.87 (d, J = 5.84 Hz,

2H), 6.69 (s, 1H), 7.33 (d, J = 6.44 Hz, 2H), 8.16 (s, 1H), 8.27-8.30 (m, 2H), 8.85 (d, J = 9.76, 1H), 8.96-9.02 (m, 2H), 9.23 (s, 1H). 10.68 (s, 1H).

Co-formulation *h*: 8-Hydroxypyrene-1,3,6-trisulfonic acid trisodium salt (0.10 g, 0.19 mM) was added to compound **92** (0.1 g, 0.19 mM) in methanol and taken to dryness to give a yellow solid with a yield of 100 % (0.20 g, 0.19 mM); ^{1}H NMR (400 MHz, 298 K, DMSO-d_6): δ: 0.93 (t, J = 7.36 Hz, 12H), 1.25 - 1.34 (m, 8H), 1.50-1.59 (m, 8H), 3.13 - 3.17 (m, 8H), 3.88 (d, J = 5.80 Hz, 2H), 6.54 (t, J = 4.16 Hz, 1H), 7.29 (d, J = 8.52 Hz, 1H), 7.48 (d, J = 8.80 Hz, 1H), 7.75-7.79 (m, 2H), 8.17 (s, 1H), 8.30 (d, J = 9.56 Hz, 1H), 8.85-9.03 (m, 3H), 9.28 (s, 1H), 10.74 (s, 1H).

Co-formulation *i:* N,N-Diethyl-m-toluamide (0.08 g, 0.4 mM) was added to compound **88** (0.20 g, 0.4 mM) in methanol and taken to dryness to give a purple solid with a yield of 100 % (0.27 g, 0.4 mM); ^{1}H NMR (400 MHz, 298 K, DMSO-d_6): δ: 0.92 (t, J = 7.24 Hz, 12H), 1.25 - 1.34 (m, 8H), 1.51 - 1.58 (m, 8H), 2.32 (s, 3H), 3.13 - 3.17 (m, 8H), 3.86 (d, J = 5.88 Hz, 2H), 4.65 (s, 2H), 6.38-6.46 (m, 3H), 7.01 (d, J = 8.64 Hz, 2H), 7.09-7.12 (m, 2H), 7.22-7.32 (m, 2H), 8.31 (s, 1H).

Co-formulation *j:* N,N-Diethyl-m-toluamide (0.07 g, 0.37 mM) was added to compound **89** (0.20 g, 0.37 mM) in methanol and taken to dryness to give a purple solid with a yield of 100 % (0.27 g, 0.37 mM); ^{1}H NMR (400 MHz, 298 K, DMSO-d_6): δ: 0.92 (t, J = 7.28 Hz, 12H), 1.00 - 1.12 (m, 12H), 1.25 - 1.34 (m, 8H), 1.51-1.59 (m, 8H), 2.32 (s, 3H), 3.13 - 3.25 (m, 16H), 3.87 (d, J = 5.92 Hz, 2H), 6.41 (t, J = 5.84 Hz, 1H), 6.56 (d, J = 8.96 Hz, 2H), 7.09-7.32 (m, 6H), 8.40 (s, 1H).

Co-formulation *k:* N,N-Diethyl-m-toluamide (0.08 g, 0.42 mM) was added to compound **90** (0.20 g, 0.42 mM) in methanol and taken to dryness to give a purple solid with a yield of 100 % (0.28 g, 0.42 mM); ^{1}H NMR (400 MHz, 298 K, DMSO-d_6): δ: 1.50 - 1.73 (m, 18H), 1.86 - 1.93 (m, 8H), 2.10-2.19 (m, 8H), 2.91 (s, 3H), 3.61 - 3.65 (m, 8H), 3.76 (s, 2H), 4.01 (s, 2H), 4.70 (d, J = 6.56 Hz, 2H), 7.66-7.70 (m, 2H), 7.79-7.94 (m, 4H), 8.47 (s, 1H), 8.68 (d, J = 5.80 Hz, 2H), 9.91 (s, 1H).

Co-formulation *l:* N,N-Diethyl-m-toluamide (0.07 g, 0.38 mM) was added to compound **92** (0.20 g, 0.38 mM) in methanol and taken to dryness to give a purple solid with a yield of 100 % (0.27 g, 0.38 mM); ^{1}H NMR (400 MHz, 298 K, DMSO-d_6): δ: 0.91 - 1.33 (m, 26H), 1.56 (s, 8H), 2.33 (m, 3H), 3.14 - 3.18 (m), 3.90 (d, J = 5.36 Hz, 2H), 6.72 (s, 1H), 7.10-7.16 (m, 6H), 7.78 (d, J = 8.04 Hz, 2H), 9.11 (s, 1H).

References

1 R. J. Ellaby, E. R. Clark, N. Allen, F. R. Taylor, K. K. L. Ng, M. Dimitrovski, D. F. Chu, D. P. Mulvihill and J. R. Hiscock, *Org. Biomol. Chem.*, 2021, **19**, 2008–2014.

2 R. J. Ellaby, D. F. Chu, A. Pépés, E. R. Clark and J. Hiscock, *Supramol. Chem.*, 2021, **00**, 1–9.

3 L. J. White, J. E. Boles, K. L. F. Hilton, R. J. Ellaby and J. R. Hiscock, *Molecules*, 2020, **25**, 4126.

4 B. Olenyuk, A. Fechtenkötter and P. J. Stang, *J. Chem. Soc. Dalt. Trans.*, 1998, 1707–1728.

5 J. Vicens and Q. Vicens, *J. Incl. Phenom. Macrocycl. Chem.*, 2009, **65**, 221–235.

6 J.-M. Lehn, *Angew. Chemie Int. Ed. English*, 1988, **27**, 89–112.

7 C. J. Pedersen, *Angew. Chemie Int. Ed. English*, 1988, **27**, 1021–1027.

8 D. J. Cram, *Angew. Chemie Int. Ed. English*, 1988, **27**, 1009–1020.

9 J. M. Lehn, *Acc. Chem. Res.*, 1978, **11**, 49–57.

10 P. S. Cohen and S. M. Cohen, *J. Chem. Educ.*, 1996, **73**, 883.

11 E. Kinne-Saffran and R. K. H. Kinne, *Am. J. Nephrol.*, 1999, **19**, 290–294.

12 G. N. Lewis, *J. Am. Chem. Soc.*, 1916, **38**, 762–785.

13 G. N. Lewis, *J. Am. Chem. Soc.*, 1913, **35**, 1448–1455.

14 I. Langmuir, *J. Am. Chem. Soc.*, 1919, **41**, 868–934.

15 G. M. Whitesides, *Science (80-.).*, 2002, **295**, 2418–2421.

16 D. Philp and J. F. Stoddart, *Angew. Chemie Int. Ed. English*, 1996, **35**, 1154–1196.

17 J. F. Stoddart, *Acc. Chem. Res.*, 2001, **34**, 410–411.

18 Johannes Diderik van der Waals - Biographical - NobelPrize.org.

19 D. E. Koshland, *Angew. Chemie Int. Ed. English*, 1995, **33**, 2375–2378.

20 U. Boas and P. M. H. Heegaard, *Chem. Soc. Rev.*, 2004, **33**, 43.

21 D. J. Cram and J. M. Cram, *Science (80-.).*, 1974, **183**, 803–809.

22 R. M. Izatt, *Chem. Soc. Rev.*, 2017, **46**, 2380–2384.

23 C. J. Pedersen, *J. Am. Chem. Soc.*, 2002, **92**, 391–394.

24 C. J. Pedersen, *J. Am. Chem. Soc.*, 1967, **89**, 2495–2496.

25 R. M. Izatt, J. H. Rytting, D. P. Nelson, B. L. Haymore and J. J. Christensen, *Science (80-.).*, 1969, **164**, 443–444.

26 R. M. Izatt, J. S. Bradshaw, S. R. Izatt and R. G. Harrison, *Macrocycl. Supramol. Chem.*, 2016, 1–9.

27 G. M. Lein and D. J. Cram, *J. Chem. Soc. Chem. Commun.*, 1982, 301–304.

28 C. Dietrich-Buchecker and J. P. Sauvage, *Tetrahedron*, 1990, **46**, 503–512.

29 J.-P. Sauvage, *Angew. Chemie Int. Ed.*, 2017, **56**, 11080–11093.

30 P. L. Anelli, S. Speciali, N. Spencer and J. F. Stoddart, *J. Am. Chem. Soc.*, 1991, **113**, 5131–5133.

31 C. J. Bruns and J. F. Stoddart, *Acc. Chem. Res.*, 2014, **47**, 2186–2199.

32 B. L. Feringa, *Angew. Chemie Int. Ed.*, 2017, **56**, 11060–11078.

33 C. A. Stanier, M. J. O'Connell, W. Clegg and H. L. Anderson, *Chem. Commun.*, 2001, 493–494.

34 K. Müller-Dethlefs and P. Hobza, *Chem. Rev.*, 2000, **100**, 143–167.

35 K. T. Mahmudov, M. N. Kopylovich, M. F. C. Guedes da Silva and A. J. L. Pombeiro, *Coord. Chem. Rev.*, 2017, 345, 54–72.

36 X. Lin and M. W. Grinstaff, *Isr. J. Chem.*, 2013, 53, 498–510.

37 R. L. Baldwin, *Biophys. J.*, 1996, **71**, 2056–2063.

38 I. E. Dzyaloshinskii, E. M. Lifshitz and L. P. Pitaevskii, *Adv. Phys.*, 1961, **10**, 165–209.

39 J. W. Steed and J. L. Atwood, *Supramolecular Chemistry*, John Wiley & Sons, Ltd, Chichester, UK, 2009.

40 K. H. Sippel and F. A. Quiocho, *Protein Sci.*, 2015, **24**, 1040–1046.

41 M. L. Waters, *Curr. Opin. Chem. Biol.*, 2002, 6, 736–741.

42 C. R. Martinez and B. L. Iverson, *Chem. Sci.*, 2012, **3**, 2191.

43 W. R. Zhuang, Y. Wang, P. F. Cui, L. Xing, J. Lee, D. Kim, H. L. Jiang and Y. K. Oh, *J. Control. Release*, 2019, 294, 311–326.

44 J. Sunner, K. Nishizawa and P. Kebarle, *J. Phys. Chem.*, 1981, **85**, 1814–1820.

45 M. M. Conn and J. Rebek, *Chem. Rev.*, 1997, **97**, 1647–1668.

46 S. Stončius, E. Butkus, A. Žilinskas, K. Larsson, L. Öhrström, U. Berg and K. Wärnmark, *J. Org. Chem.*, 2004, **69**, 5196–5203.

47 G. Ono, A. Izuoka, T. Sugawara and Y. Sugawara, *J. Mater. Chem.*, 1998, **8**, 1703–1709.

48 I. I. Cisse, H. Kim and T. Ha, *Nat. Struct. Mol. Biol.*, 2012, **19**, 623–627.

49 M. J. Mayoral, N. Bilbao and D. González-Rodríguez, *ChemistryOpen*, 2016, **5**, 10–32.

50 J. D. Smith, C. D. Cappa, K. R. Wilson, R. C. Cohen, P. L. Geissler and R. J. Saykally, *Proc.*

Natl. Acad. Sci., 2005, **102**, 14171–14174.

51 A. Gavezzotti, *New J. Chem.*, 2016, **40**, 6848–6853.

52 R. C. Dougherty, *J. Chem. Phys.*, 1998, **109**, 7372–7378.

53 J. W. Steed, D. R. Turner and K. Wallace, *Core Concepts in Supramolecular Chemistry and Nanochemistry: From Supramolecules to Nanotechnology*, 2007.

54 W. G. Schneider, *J. Chem. Phys.*, 1955, **23**, 26–30.

55 M. L. Huggins, *J. Chem. Educ.*, 1960, **37**, A754.

56 E. N. Baker and R. E. Hubbard, *Prog. Biophys. Mol. Biol.*, 1984, **44**, 97–179.

57 G. Alagona, C. Ghio and P. Kollman, *J. Am. Chem. Soc.*, 1983, **105**, 5226–5230.

58 R. D. Bach and O. Dmitrenko, *J. Am. Chem. Soc.*, 2004, **126**, 4444–4452.

59 F. Biedermann and H.-J. Schneider, *Chem. Rev.*, 2016, **116**, 5216–5300.

60 J. Černý and P. Hobza, *Phys. Chem. Chem. Phys.*, 2007, **9**, 5291.

61 R. Feyereisen, *Annu. Rev. Entomol.*, 1999, **44**, 507–533.

62 C. A. Hunter, *Angew. Chem. Int. Ed*, 2004, **43**, 5310–5324.

63 Y. Liu and D. W. Bolen, *Biochemistry*, 1995, **34**, 12884–12891.

64 M. A. Roseman, *J. Mol. Biol.*, 1988, **200**, 513–522.

65 M. Leippe, E. Tannich, R. Nickel, G. van der Goot, F. Pattus, R. D. Horstmann and H. J. Müller-Eberhard, *EMBO J.*, 1992, **11**, 3501–3506.

66 R. E. Hubbard and M. Kamran Haider, in *Encyclopedia of Life Sciences*, John Wiley & Sons, Ltd, Chichester, UK, 2010.

67 R. Fromme, Z. Katiliene, P. Fromme and G. Ghirlanda, *Protein Sci.*, 2008, **17**, 939–944.

68 J. M. Berg, J. L. Tymoczko and L. Stryer, *Biochemistry*, 2002, **262**, 159–173.

69 H. Lodish, A. Berk, S. L. Zupursky, D. B. Matsudaira and J. Darnell, *Molecular Cell Biology*, New York, 4th Editio., 2000.

70 B. A. Shirley, *Protein stability and folding: Theory and practice*, Springer, 1995, vol. 21.

71 N. Darby and T. E. Creighton, in *Protein Stability and Folding*, Springer, 1995, pp. 219–252.

72 K. P. Murphy, in *Protein Stability and Folding*, Springer, 1995, pp. 1–34.

73 S. C. Halls and N. G. Lewis, *Biochemistry*, 2002, **41**, 9455–9461.

74 B. H. Hahn, *N. Engl. J. Med.*, 1998, 338, 1359–1368.

75 J. D. Watson and F. H. C. Crick, *Nature*, 1953, **171**, 737–738.

76 A. Klug, *Nature*, 1968, **219**, 808–844.

77 P. Yakovchuk, E. Protozanova and M. D. Frank-Kamenetskii, *Nucleic Acids Res.*, 2006, **34**, 564–574.

78 R. Ludwig and N. T. K. Dzung, *Sensors*, 2002, 2, 397–416.

79 D. Diamond and K. Nolan, *Anal. Chem.*, 2001, 73.

80 M. M. G. Antonisse and D. N. Reinhoudt, *Electroanalysis*, 1999, **11**, 1035–1048.

81 P. D. Beer and P. A. Gale, *Angew. Chemie - Int. Ed.*, 2001, **40**, 486–516.

82 M. M. G. Antonisse and D. N. Reinhoudt, *Chem. Commun.*, 1998, **0**, 443–448.

83 B. Valeur and I. Leray, *Coord. Chem. Rev.*, 2000, **205**, 3–40.

84 O. S. Wolfbeis, *Anal. Chem.*, 2006, **78**, 3859–3874.

85 L. R. Sousa and J. M. Larson, *J. Am. Chem. Soc.*, 2002, **99**, 307–310.

86 W. Si, L. Chen, X. B. Hu, G. Tang, Z. Chen, J. L. Hou and Z. T. Li, *Angew. Chemie - Int. Ed.*, 2011, **50**, 12564–12568.

87 Y. L. Sun, Y. W. Yang, D. X. Chen, G. Wang, Y. Zhou, C. Y. Wang and J. F. Stoddart, *Small*, 2013, **9**, 3224–3229.

88 M. M. Tian, D. X. Chen, Y. L. Sun, Y. W. Yang and Q. Jia, *RSC Adv.*, 2013, **3**, 22111–22119.

89 K. Wang, C. Y. Wang, Y. Zhang, S. X. A. Zhang, B. Yang and Y. W. Yang, *Chem. Commun.*, 2014, **50**, 9458–9461.

90 N. Song and Y. W. Yang, *Sci. China Chem.*, 2014, **57**, 1185–1198.

91 P. G. Sutariya, H. Soni, S. A. Gandhi and A. Pandya, *J. Lumin.*, 2019, **212**, 171–179.

92 P. A. Gale, E. N. W. Howe and X. Wu, *Chem*, 2016, **1**, 351–422.

93 P. A. Gale, J. T. Davis and R. Quesada, *Chem. Soc. Rev.*, 2017, **46**, 2497–2519.

94 M. Wenzel and J. J. Weigand, *J. Incl. Phenom. Macrocycl. Chem.*, 2017, **89**, 247–251.

95 V. R. Singh Beer, Prasad G.K., Pandey K.S., Denikhel R.K., *Def. Sci. J.*, 2010, **60**, 428–441.

96 G. W. Gokel and I. A. Carasel, *Chem. Soc. Rev.*, 2007, **36**, 378–389.

97 N. Akhtar, O. Biswas and D. Manna, *Chem. Commun.*, 2020, **56**, 14137–14153.

98 K. Gloe, H. Stephan and M. Grotjahn, *Chem. Eng. Technol.*, 2003, **26**, 1107–1117.

99 I. Carreira-Barral, M. Mato-Iglesias, A. de Blas, C. Platas-Iglesias, P. A. Tasker and D. Esteban-Gómez, *Dalt. Trans.*, 2017, **46**, 3192–3206.

100 A. K. Sengupta, B. A. Moyer, J. A. Marinsky and Y. Marcus, .

101 A. Jeppesen, B. E. Nielsen, D. Larsen, O. M. Akselsen, T. I. Sølling, T. Brock-Nannestad and M. Pittelkow, *Org. Biomol. Chem.*, 2017, **15**, 2784–2790.

102 R. Tepper and U. S. Schubert, *Angew. Chemie Int. Ed.*, 2018, **57**, 6004–6016.

103 V. Blažek Bregović, N. Basarić and K. Mlinarić-Majerski, *Coord. Chem. Rev.*, 2015, 295, 80–124.

104 J. L. Sessler, N. M. Barkey, G. D. Pantos and V. M. Lynch, *New J. Chem.*, 2007, **31**, 646.

105 K. Kavallieratos, C. M. Bertao and R. H. Crabtree, *J. Org. Chem.*, 1999, **64**, 1675–1683.

106 P. A. Gale, *Coord. Chem. Rev.*, 2000, 199, 181–233.

107 P. A. Gale, *Coord. Chem. Rev.*, 2003, **240**, 191–221.

108 P. A. Gale, *Acc. Chem. Res.*, 2006, **39**, 465–475.

109 C. H. Park and H. E. Simmons, *J. Am. Chem. Soc.*, 1968, **90**, 2429–2431.

110 R. A. Bell, G. G. Christoph, F. R. Fronczek and R. E. Marsh, *Science (80-.).*, 1975, **190**, 151–152.

111 K. Sato, S. Arai and T. Yamagishi, *Tetrahedron Lett.*, 1999, **40**, 5219–5222.

112 P. Ballester, A. Costa, P. M. Deyà, M. Vega, J. Morey and G. Deslongchamps, *Tetrahedron Lett.*, 1999, **40**, 171–174.

113 A. Fan, H. K. Hong, S. Valiyaveettil and J. J. Vittal, *J. Supramol. Chem.*, 2002, **2**, 247–254.

114 B. Kuswandi, Nuriman, W. Verboom and D. N. Reinhoudt, *Sensors*, 2006, **6**, 978–1017.

115 M. M. Reinoso-García, A. Dijkman, W. Verboom, D. N. Reinhoudt, E. Malinowska, D. Wojciechowska, M. Pietrzak and P. Selucky, *European J. Org. Chem.*, 2005, **2005**, 2131–2138.

116 M. J. Berrocal, A. Cruz, I. H. A. Badr and L. G. Bachas, *Anal. Chem.*, 2000, **72**, 5295–5299.

117 E. Graf and J. M. Lehn, *J. Am. Chem. Soc.*, 1976, **98**, 6403–6405.

118 F. P. Schmidtchen, *Angew. Chemie Int. Ed. English*, 1977, **16**, 720–721.

119 R. A. Pascal, J. Spergel and D. Van Engen, *Tetrahedron Lett.*, 1986, **27**, 4099–4102.

120 J. Cullinane, R. I. Gelb, T. N. Margulis and L. J. Zompa, *J. Am. Chem. Soc.*, 1982, **104**, 3048–3053.

121 R. I. Gelb, L. M. Schwartz and L. J. Zompa, *Inorg. Chem.*, 1986, **25**, 1527–1535.

122 J. M. Lehn, *Cryptates: Inclusion Complexes of Macropolycyclic Receptor Molecules*, International Union of Pure and Applied Chemistry, 1979, vol. 50.

123 M. E. Jung and H. Xia, *Tetrahedron Lett.*, 1988, **29**, 297–300.

124 M. W. Hosseini and J. -M Lehn, *Helv. Chim. Acta*, 1988, **71**, 749–756.

125 B. H. M. Snellink-Ruël, M. M. G. Antonisse, J. F. J. Engbersen, P. Timmerman and D. N. Reinhoudt, *European J. Org. Chem.*, 2000, 165–170.

126 † Shin-ichi Sasaki, Masaaki Mizuno, and Koichiro Naemura and Y. Tobe*, *J. Org. Chem.*, 2000, **65**, 275–283.

127 P. J. Smith, M. V Reddington and C. S. Wilcox, *Tetrahedron Lett.*, 1992, **33**, 6085–6088.

128 E. Fan, S. A. Van Arman, S. Kincaid and A. D. Hamilton, *J. Am. Chem. Soc.*, 1993, **115**, 369–370.

129 Kwan Hee Lee and J. I. Hong, *Tetrahedron Lett.*, 2000, **41**, 6083–6087.

130 H. Boerrigter, L. Grave, J. W. M. Nissink, L. A. J. Chrisstoffels, J. H. Van der Maas, W. Verboom, F. De Jong and D. N. Reinhoudt, *J. Org. Chem.*, 1998, **63**, 4174–4180.

131 M. C. Etter, M. Zia-Ebrahimi, Z. Urbañczyk-Lipkowska and T. W. Panunto, *J. Am. Chem. Soc.*, 1990, **112**, 8415–8426.

132 M. Boiocchi, L. Del Boca, D. E. Gómez, L. Fabbrizzi, M. Licchelli and E. Monzani, *J. Am.*

Chem. Soc., 2004, **126**, 16507–16514.

133 M. J. Kim, H. W. Lee, D. Moon and K. S. Jeong, *Org. Lett.*, 2012, **14**, 5042–5045.

134 A. RoyChowdhury, P. Ghosh, S. K. Saha, P. Mitra and P. Banerjee, *Spectrochim. Acta Part A Mol. Biomol. Spectrosc.*, 2014, **124**, 492–499.

135 R. Kato, S. Nishizawa, T. Hayashita and N. Teramae, *Tetrahedron Lett.*, 2001, **42**, 5053–5056.

136 H. Valkenier, L. W. Judd, H. Li, S. Hussain, D. N. Sheppard and A. P. Davis, *J. Am. Chem. Soc.*, 2014, **136**, 12507–12512.

137 S. Camiolo, P. A. Gale, M. B. Hursthouse, M. E. Light and A. J. Shi, *Chem. Commun.*, 2002, **2**, 758–759.

138 Valeria Amendola, David Esteban-Gómez, * and Luigi Fabbrizzi and M. Licchelli, *Acc. Chem. Res.*, 2006, **39**, 343–353.

139 T. Gunnlaugsson, P. E. Kruger, P. Jensen, F. M. Pfeffer and G. M. Hussey, *Tetrahedron Lett.*, 2003, **44**, 8909–8913.

140 F. G. Bordwell, *Acc. Chem. Res.*, 1988, **21**, 456–463.

141 S. Li, C. Jia, B. Wu, Q. Luo, X. Huang, Z. Yang, Q. S. Li and X. J. Yang, *Angew. Chemie - Int. Ed.*, 2011, **50**, 5721–5724.

142 D. Makuc, J. R. Hiscock, M. E. Light, P. A. Gale and J. Plavec, *Beilstein J. Org. Chem.*, 2011, **7**, 1205–1214.

143 C. M. Dias, H. Li, H. Valkenier, L. E. Karagiannidis, P. A. Gale, D. N. Sheppard and A. P. Davis, *Org. Biomol. Chem.*, 2018, **16**, 1083–1087.

144 A. J. Plajer, J. Zhu, P. Proehm, A. D. Bond, U. F. Keyser and D. S. Wright, *J. Am. Chem.*

Soc., 2019, **141**, 8807–8815.

145 M. A. Martínez-Aguirre and A. K. Yatsimirsky, *J. Org. Chem.*, 2015, **80**, 4985–4993.

146 J. H. Hartley, T. D. James and C. J. Ward, *J. Chem. Soc. Perkin Trans. 1*, 2000, 3155–3184.

147 A. Lascaux, G. Delahousse, J. Ghostin, J. P. Bouillon and I. Jabin, *European J. Org. Chem.*, 2011, 5272–5278.

148 F. Vogtle and W. M. Muller, *J. Incl. Phenom.*, 1984, **1**, 369–386.

149 T. W. Bell and Z. Hou, *Angew. Chemie Int. Ed. English*, 1997, **36**, 1536–1538.

150 C. J. Pedersen, *J. Org. Chem.*, 2002, **36**, 1690–1693.

151 M. Á. Farrán, D. Santa María, M. Á. García, R. M. Claramunt and G. J. Clarkson, *J. Incl. Phenom. Macrocycl. Chem.*, 2015, **81**, 57–69.

152 S. Dey, D. Sain, A. Kumar and C. Kumari, *RSC Adv.*, 2014, **4**, 51486–51495.

153 H. Wang, W. H. Chan and A. W. M. Lee, *Org. Biomol. Chem.*, 2008, **6**, 929–934.

154 S. Adhikari, D. Kar, R. Fröhlich and K. Ghosh, *ChemistrySelect*, 2019, **4**, 12825–12831.

155 W. E. Allen, P. A. Gale, C. T. Brown, V. M. Lynch and J. L. Sessler, 1996, **2**, 12471–12472.

156 P. Cuřínová, M. Pojarová, J. Budka, K. Lang, I. Stibor and P. Lhoták, *Tetrahedron*, 2010, **66**, 8047–8050.

157 D. S. Guo, V. D. Uzunova, K. I. Assaf, A. I. Lazar, Y. Liu and W. M. Nau, *Supramol. Chem.*, 2016, **28**, 384–395.

158 S. Goswami, R. Mukherjee and J. Ray, *Org. Lett.*, 2005, **7**, 1283–1285.

159 J. Dong and A. P. Davis, *Angew. Chemie Int. Ed.*, 2021, **60**, 8035–8048.

160 P. S. Cremer, A. H. Flood, B. C. Gibb and D. L. Mobley, *Nat. Chem.*, 2017, **10**, 8–16.

161 G. V. Oshovsky, D. N. Reinhoudt and W. Verboom, *Angew. Chemie - Int. Ed.*, 2007, **46**, 2366–2393.

162 R. A. Tromans, T. S. Carter, L. Chabanne, M. P. Crump, H. Li, J. V. Matlock, M. G. Orchard and A. P. Davis, *Nat. Chem.*, 2019, **11**, 52–56.

163 K. Ganesan, S. K. Raza and R. Vijayaraghavan, *J. Pharm. Bioallied Sci.*, 2010, 2, 166–178.

164 A. Keaveney and A. Mayor, *Greek Fire, Poison Arrows & Scorpion Bombs: Biological and Chemical Warfare in the Ancient World*, Abrams Press, 2004, vol. 11.

165 B. J. Lukey, J. A. Romano Jr., J. A. Romano, H. Salem, B. J. Lukey and H. Salem, Eds., *Chemical Warfare Agents*, CRC Press, 2007.

166 M. R. Sambrook and S. Notman, *Chem. Soc. Rev.*, 2013, 42, 9251–9267.

167 P. Kenez, *Glob. War Stud.*, 2014, **11**, 85–87.

168 Y. C. Yang, *Acc. Chem. Res.*, 1999, 32, 109–115.

169 J. A. Vale, T. C. Marrs and R. L. Maynard, *Clin. Toxicol.*, 2018, **56**, 1093–1097.

170 Y. J. Jang, K. Kim, O. G. Tsay, D. A. Atwood and D. G. Churchill, *Chem. Rev.*, 2015, **115**, PR1–PR76.

171 P. R. Chai, E. W. Boyer, H. Al-Nahhas and T. B. Erickson, *Toxicol. Commun.*, 2017, **1**, 21–23.

172 S. Tang and J. Chan, *Hong Kong J. Emerg. Med.*, 2002, **9**, 83–89.

173 Y. J. Jang, K. Kim, O. G. Tsay, D. A. Atwood and D. G. Churchill, *Chem. Rev.*, 2015, **115**, PR1–PR76.

174 M. Burnworth, S. J. Rowan and C. Weder, *Chem. - Eur. J.*, 2007, **13**, 7828–7836.

175 M. B. Abou-Donia, B. Siracuse, N. Gupta and A. Sobel Sokol, *Crit. Rev. Toxicol.*, 2016, **46**,

845–875.

176 A. Friboulet, F. Rieger, D. Goudou, G. Amitai and P. Taylor, *Biochemistry*, 1990, **29**, 914–920.

177 C. Albaret, S. Lacoutière, W. P. Ashman, D. Froment and P. L. Fortier, *Proteins Struct. Funct. Genet.*, 1997, **28**, 543–555.

178 T. M. Shih, R. K. Kan and J. H. McDonough, *Chem. Biol. Interact.*, 2005, **157**–**158**, 293–303.

179 A. W. Abu-Qare and M. B. Abou-Donia, *Food Chem. Toxicol.*, 2002, **40**, 1327–1333.

180 T. Okumura, N. Takasu, S. Ishimatsu, S. Miyanoki, A. Mitsuhashi, K. Kumada, K. Tanaka and S. Hinohara, *Ann. Emerg. Med.*, 1996, **28**, 129–135.

181 R. C. Gupta, *Handbook of Toxicology of Chemical Warfare Agents*, 2009.

182 H. John, M. J. van der Schans, M. Koller, H. E. T. Spruit, F. Worek, H. Thiermann and D. Noort, *Forensic Toxicol.*, 2018, **36**, 61–71.

183 T. Nakagawa and A. T. Tu, *Forensic Toxicol.*, 2018, **36**, 542–544.

184 Mark Peplow, *C&EN Glob. Enterp.*, 2018, **96**, 3–3.

185 S. Seibert, Statement by the Federal Government on the Navalny Case, https://www.bundesregierung.de/breg-en/news/statement-by-the-federal-government-on-the-navalny-case-1781882, (accessed 24 September 2020).

186 L. R. EMBER, *Chem. Eng. News Arch.*, 1994, **72**, 26–32.

187 J. A. Ashley, C.-H. Lin, P. Wirsching and K. D. Janda, *Angew. Chemie*, 1999, **111**, 1909–1911.

188 D. Prosnitz, *Science (80-.).*, 2005, **310**, 978–978.

189 J. Ede, P. Cragg and M. Sambrook, *Molecules*, 2018, **23**, 207.

190 H. Cave, J. A. Ede, M. R. Sambrook, H. Dodd, F. Fucassi, A. S. Cragg, A. H. Lansley and P. J. Cragg, *Supramol. Chem.*, 2019, **31**, 703–712.

191 M. R. Sambrook, J. C. Vincent, J. A. Ede, I. A. Gass and P. J. Cragg, *RSC Adv.*, 2017, **7**, 38069–38076.

192 S. L. Bartelt-Hunt, D. R. U. Knappe and M. A. Barlaz, *Crit. Rev. Environ. Sci. Technol.*, 2008, **38**, 112–136.

193 V. Kumar, *Chem. Commun.*, 2021, **57**, 3430–3444.

194 B. Díaz de Greñu, D. Moreno, T. Torroba, A. Berg, J. Gunnars, T. Nilsson, R. Nyman, M. Persson, J. Pettersson, I. Eklind and P. Wästerby, *J. Am. Chem. Soc.*, 2014, **136**, 4125–4128.

195 G. H. Dennison, C. G. Bochet, C. Curty, J. Ducry, D. J. Nielsen, M. R. Sambrook, A. Zaugg and M. R. Johnston, *Eur. J. Inorg. Chem.*, 2016, **2016**, 1348–1358.

196 G. H. Dennison, M. R. Sambrook and M. R. Johnston, *RSC Adv.*, 2014, **4**, 55524–55528.

197 G. H. Dennison, R. Sambrook and M. R. Johnston, *ChemComm*, 2014, **50**, 195–197.

198 J. R. Hiscock, M. R. Sambrook, N. J. Wells and P. A. Gale, *Chem. Sci.*, 2015, **6**, 5680–5684.

199 J. R. Hiscock, I. L. Kirby, J. Herniman, G. John Langley, A. J. Clark and P. A. Gale, *RSC Adv.*, 2014, **4**, 45517–45521.

200 J. R. Hiscock, M. R. Sambrook, J. A. Ede, N. J. Wells and P. A. Gale, *J. Mater. Chem. A*, 2015, **3**, 1230–1234.

201 N. A. Esipenko, P. Koutnik, T. Minami, L. Mosca, V. M. Lynch, G. V. Zyryanov and P. Anzenbacher, *Chem. Sci.*, 2013, **4**, 3617–3623.

202 G. T. Williams, C. J. E. Haynes, M. Fares, C. Caltagirone, J. R. Hiscock and P. A. Gale, *Chem. Soc. Rev.*, 2021, **50**, 2737–2763.

203 M. Baaden, F. Berny, C. Boehme, N. Muzet, R. Schurhammer and G. Wipff, *J. Alloys Compd.*, 2000, **303**–**304**, 104–111.

204 P. Graham and M. Joesten, *J. Inorg. Nucl. Chem.*, 1970, **32**, 531–535.

205 A. L. Jenkins, O. M. Uy and G. M. Murray, 1997, **34**, 221–224.

206 A. L. Jenkins, O. M. Uy and G. M. Murray, *Anal. Chem.*, 1999, **71**, 373–378.

207 E. Butera, A. Zammataro, A. Pappalardo and G. T. Sfrazzetto, *Chempluschem*, 2021, **86**, 681–695.

208 A. Pappalardo, C. M. A. Gangemi, R. M. Toscano and G. T. Sfrazzetto, *Curr. Org. Chem.*, 2020, **24**, 2378–2382.

209 A. Barba-Bon, A. M. Costero, M. Parra, S. Gil, R. Martínez-Máñez, F. Sancenõn, P. A. Gale and J. R. Hiscock, *Chem. - Eur. J.*, 2013, **19**, 1586–1590.

210 J. R. Hiscock, N. J. Wells, J. A. Ede, P. A. Gale and M. R. Sambrook, *Org. Biomol. Chem.*, 2016, **14**, 9560–9567.

211 M. R. Sambrook, J. R. Hiscock, A. Cook, A. C. Green, I. Holden, C. Vincent and P. A. Gale, *ChemComm*, 2012, **48**, 5605–5607.

212 L. E. Buerkle and S. J. Rowan, *Chem. Soc. Rev.*, 2012, **41**, 6089–6102.

213 W. L. Guan, K. M. Adam, M. Qiu, Y. M. Zhang, H. Yao, T. B. Wei and Q. Lin, *Supramol. Chem.*, 2020, **32**, 578–596.

214 Y. F. Li, Z. Li, Q. Lin and Y. W. Yang, *Nanoscale*, 2020, **12**, 2180–2200.

215 J. R. Hiscock, F. Piana, M. R. Sambrook, N. J. Wells, A. J. Clark, J. C. Vincent, N.

Busschaert, R. C. D. Brown and P. A. Gale, *Chem. Commun.*, 2013, **49**, 9119–9121.

216 C. van Hooidonk and J. C. A. E. Breebaart-Hansen, *Recl. des Trav. Chim. des Pays-Bas*, 1971, **90**, 680–686.

217 S. Letort, S. Balieu, W. Erb, G. Gouhier and F. Estour, *Beilstein J. Org. Chem.*, 2016, **12**, 204–228.

218 C. G. P. Taylor, J. R. Piper and M. D. Ward, *Chem. Commun.*, 2016, **52**, 6225–6228.

219 S. Mecozzi and J. Rebek, *Chem. - A Eur. J.*, 1998, **4**, 1016–1022.

220 J. E. Del Bene, I. Alkorta and J. Elguero, *J. Phys. Chem. A*, 2008, **112**, 7925–7929.

221 Y. Xu, J. Yao, P. Yao, H. Li and S. Han, *Chinese J. Chem. Eng.*, 2010, **18**, 455–461.

222 L. J. White, N. J. Wells, L. R. Blackholly, H. J. Shepherd, B. Wilson, G. P. Bustone, T. J. Runacres and J. R. Hiscock, *Chem. Sci.*, 2017, **8**, 7620–7630.

223 G. A. Kumar and M. A. McAllister, *J. Org. Chem.*, 1998, **63**, 6968–6972.

224 J. E. Del Bene, S. A. Perera and R. J. Bartlett, *J. Phys. Chem. A*, 1999, **103**, 8121–8124.

225 P. Thordarson, *Chem. Soc. Rev.*, 2011, **40**, 1305–1323.

226 P. Thordarson, K. Sewell and V. Efremova, Bindfit v0.5, supramolecular.org.

227 D. Brynn Hibbert and P. Thordarson, *Chem. Commun.*, 2016, **52**, 12792–12805.

228 K. A. Connors, in *Comprehensive Supramolecular Chemistry*, ed. J. L. Atwood, 1996, pp. 205–241.

229 H.-J. Schneider and A. K. Yatsimirsky, *Principles and methods in supramolecular chemistry*, Wiley, 2000.

230 F. Ulatowski, K. Dabrowa, T. Bałakier and J. Jurczak, *J. Org. Chem.*, 2016, **81**, 1746–1756.

231 M. Schaefer and C. Froemmel, *J. Mol. Biol.*, 1990, **216**, 1045–1066.

232 N. Mohan and C. H. Suresh, *J. Phys. Chem. A*, 2014, **118**, 1697–1705.

233 C. A. Hunter, *Angew. Chemie - Int. Ed.*, 2004, **43**, 5310–5324.

234 R. Parthasarathi, V. Subramanian and N. Sathyamurthy, *J. Phys. Chem. A*, 2006, **110**, 3349–3351.

235 J. J. P. Stewart, *J Mol Model*, 2007, **13**, 1173–1213.

236 M. Walker, A. J. A. Harvey, A. Sen and C. E. H. Dessent, *J. Phys. Chem. A*, 2013, **117**, 12590–12600.

237 G. E. S. M. J. Frisch, G. W. Trucks, H. B. Schlegel, V. B. M. A. Robb, J. R. Cheeseman, G. Scalmani, M. C. G. A. Petersson, H. Nakatsuji, X. Li, R. G. A. V. Marenich, J. Bloino, B. G. Janesko, A. F. I. B. Mennucci, H. P. Hratchian, J. V. Ortiz, F. L. J. L. Sonnenberg, D. Williams-Young, F. Ding, T. H. F. Egidi, J. Goings, B. Peng, A. Petrone, G. Z. D. Ranasinghe, V. G. Zakrzewski, J. Gao, N. Rega, R. F. W. Liang, M. Hada, M. Ehara, K. Toyota, O. K. J. Hasegawa, M. Ishida, T. Nakajima, Y. Honda, J. A. M. J. H. Nakai, T. Vreven, K. Throssell, J. J. H. J. E. Peralta, F. Ogliaro, M. J. Bearpark, T. A. K. E. N. Brothers, K. N. Kudin, V. N. Staroverov, A. P. R. R. Kobayashi, J. Normand, K. Raghavachari, M. C. J. C. Burant, S. S. Iyengar, J. Tomasi, R. C. J. M. Millam, M. Klene, C. Adamo, O. F. J. W. Ochterski, R. L. Martin, K. Morokuma and J. B. Foresman and D. J. Fox, 2016.

238 A. D. McLean and G. S. Chandler, *J. Chem. Phys.*, 1980, **72**, 5639–5648.

239 A. F. Rodrigues-Oliveira, F. W. M. Ribeiro, G. Cervi and T. C. Correra, *ACS Omega*, 2018, **3**, 9075–9085.

240 Y. Shao, L. F. Molnar, Y. Jung, J. Kussmann, C. Ochsenfeld, S. T. Brown, A. T. B. Gilbert, L.

V. Slipchenko, S. V. Levchenko, D. P. O'Neill, R. A. DiStasio, R. C. Lochan, T. Wang, G. J. O. Beran, N. A. Besley, J. M. Herbert, C. Yeh Lin, T. Van Voorhis, S. Hung Chien, A. Sodt, R. P. Steele, V. A. Rassolov, P. E. Maslen, P. P. Korambath, R. D. Adamson, B. Austin, J. Baker, E. F. C. Byrd, H. Dachsel, R. J. Doerksen, A. Dreuw, B. D. Dunietz, A. D. Dutoi, T. R. Furlani, S. R. Gwaltney, A. Heyden, S. Hirata, C. P. Hsu, G. Kedziora, R. Z. Khalliulin, P. Klunzinger, A. M. Lee, M. S. Lee, W. Liang, I. Lotan, N. Nair, B. Peters, E. I. Proynov, P. A. Pieniazek, Y. Min Rhee, J. Ritchie, E. Rosta, C. David Sherrill, A. C. Simmonett, J. E. Subotnik, H. Lee Woodcock, W. Zhang, A. T. Bell, A. K. Chakraborty, D. M. Chipman, F. J. Keil, A. Warshel, W. J. Hehre, H. F. Schaefer, J. Kong, A. I. Krylov, P. M. W. Gill and M. Head-Gordon, *Phys. Chem. Chem. Phys.*, 2006, **8**, 3172–3191.

241 S. Thomas, *Angew. Chemie Int. Ed.*, 2002, **41**, 48–76.

242 L. R. Blackholly, H. J. Shepherd and J. R. Hiscock, *CrystEngComm*, 2016, **18**, 7021–7028.

243 N. Allen, L. J. White, J. E. Boles, G. T. Williams, D. F. Chu, R. J. Ellaby, H. J. Shepherd, K. K. L. Ng, L. R. Blackholly, B. Wilson, D. P. Mulvihill and J. R. Hiscock, *ChemMedChem*, 2020, **15**, 2193–2205.

244 R. Core Development Team, *R Found. Stat. Comput.*, 2020, **Vienna**, **Au**, https://www.R-project.org.

245 J. Hayles and P. Nurse, *Cold Spring Harb. Protoc.*, 2018, **2018**, pdb.top079749.

246 X. Gan, J. Yang, J. Li, H. Yu, H. Dai, J. Liu and Y. Huang, *Biochem. J.*, 2011, **435**, 103–111.

247 V. Wood, M. A. Harris, M. D. McDowall, K. Rutherford, B. W. Vaughan, D. M. Staines, M. Aslett, A. Lock, J. Bähler, P. J. Kersey and S. G. Oliver, *Nucleic Acids Res.*, 2012, **40**, 695–699.

248 S. L. Forsburg and N. Rhind, *Yeast*, 2006, **23**, 173–183.

249 J. Wixon, *Comp. Funct. Genomics*, 2002, **3**, 194–204.

250 H. Wang, S. Zhang, A. Pratush, X. Ye, J. Xie, H. Wei, C. Sun and Z. Hu, *Front. Microbiol.*, 2018, **9**, 225.

251 M. Fruci and K. Poole, in *Stress and Environmental Regulation of Gene Expression and Adaptation in Bacteria*, John Wiley & Sons, Inc., 2016, vol. 1, pp. 115–136.

252 A. W. Khan, S. Kotta, S. H. Ansari, J. Ali and R. K. Sharma, *Def. Sci. J.*, 2013, **63**, 487–496.

253 K. Kim, O. G. Tsay, D. A. Atwood and D. G. Churchill, *Chem. Rev.*, 2011, **111**, 5345–5403.

254 A. N. Bigley and F. M. Raushel, *Chem. Biol. Interact.*, 2019, **308**, 80–88.

255 N. B. Munro, S. S. Talmage, G. D. Griffin, L. C. Waters, A. P. Watson, J. F. King and V. Hauschild, *Environ. Health Perspect.*, 1999, 107, 933–974.

256 S. Vucinic, B. Antonijevic, A. M. Tsatsakis, L. Vassilopoulou, A. O. Docea, A. E. Nosyrev, B. N. Izotov, H. Thiermann, N. Drakoulis and D. Brkic, *Environ. Toxicol. Pharmacol.*, 2017, **56**, 163–171.

257 S. Farquharson, F. E. Inscore and S. Christesen, *Top. Appl. Phys.*, 2006, **103**, 447–461.

258 R. L. Gustafson and A. E. Martell, *J. Am. Chem. Soc.*, 1962, **84**, 2309–2316.

259 J. R. Ward, Y. C. Yang, R. B. Wilson, W. D. Burrows and L. L. Ackerman, *Bioorg. Chem.*, 1988, **16**, 12–16.

260 Y. C. Yang, J. A. Baker and J. R. Ward, *Chem. Rev.*, 1992, **92**, 1729–1743.

261 I. S. Che Sulaiman, B. W. Chieng, F. E. Pojol, K. K. Ong, J. I. Abdul Rashid, W. M. Z. Wan Yunus, N. A. Mohd Kasim, N. Abdul Halim, S. A. Mohd Noor and V. F. Knight, *Forensic Toxicol.*, 2020, **38**, 297–313.

262 S. Popiel and M. Sankowska, *J. Chromatogr. A*, 2011, **1218**, 8457–8479.

263 M. L. Mendonca and R. Q. Snurr, *Chem. - A Eur. J.*, 2019, 25, 9118–9118.

264 B. DESIRE and S. SAINT-ANDRE, *Toxicol. Sci.*, 1986, **7**, 646–657.

265 J. R. Hiscock, M. R. Sambrook, P. B. Cranwell, P. Watts, J. C. Vincent, D. J. Xuereb, N. J. Wells, R. Raja and P. A. Gale, *Chem. Commun.*, 2014, **50**, 6217–6220.

266 J. R. Hiscock, M. R. Sambrook, J. A. Ede, N. J. Wells and P. A. Gale, *J. Mater. Chem. A*, 2015, **3**, 1230–1234.

267 J. R. Hiscock, I. L. Kirby, J. Herniman, G. John Langley, A. J. Clark and P. A. Gale, *RSC Adv.*, 2014, **4**, 45517–45521.

268 J. R. Hiscock, M. R. Sambrook, N. J. Wells and P. A. Gale, *Chem. Sci.*, 2015, **6**, 5680–5684.

269 Y. Kalinovskyy, A. J. Wright, J. R. Hiscock, T. D. Watts, R. L. Williams, N. J. Cooper, M. J. Main, S. J. Holder and B. A. Blight, *ACS Appl. Mater. Interfaces*, 2020, **12**, 8634–8641.

270 A. J. Wright, M. J. Main, N. J. Cooper, B. A. Blight and S. J. Holder, *ACS Appl. Mater. Interfaces*, 2017, **9**, 31335–31339.

271 Y. Kalinovskyy, N. J. Cooper, M. J. Main, S. J. Holder and B. A. Blight, *Dalt. Trans.*, 2017, **46**, 15704–15709.

272 J. L. Bolliger, A. M. Belenguer and J. R. Nitschke, *Angew. Chemie - Int. Ed.*, 2013, **52**, 7958–7962.

273 C. G. P. Taylor, J. R. Piper and M. D. Ward, *Chem. Commun.*, 2016, **52**, 6225–6228.

274 C. G. P. Taylor, A. J. Metherell, S. P. Argent, F. M. Ashour, N. H. Williams and M. D. Ward, *Chem. - A Eur. J.*, 2020, **26**, 3065–3073.

275 W. Cullen, S. Turega, C. A. Hunter and M. D. Ward, *Chem. Sci.*, 2015, **6**, 2790–2794.

276 C. G. P. Taylor, W. Cullen, O. M. Collier and M. D. Ward, *Chem. - A Eur. J.*, 2017, **23**, 206–

213.

277 W. Cullen, A. J. Metherell, A. B. Wragg, C. G. P. Taylor, N. H. Williams and M. D. Ward, *J. Am. Chem. Soc.*, 2018, **140**, 2821–2828.

278 R. Le Provost, T. Wille, L. Louise, N. Masurier, S. Müller, G. Reiter, P. Y. Renard, O. Lafont, F. Worek and F. Estour, *Org. Biomol. Chem.*, 2011, **9**, 3026–3032.

279 F. Brandhuber, M. Zengerle, L. Porwol, A. Bierwisch, M. Koller, G. Reiter, F. Worek and S. Kubik, *Chem. Commun.*, 2013, **49**, 3425–3427.

280 C. Schneider, A. Bierwisch, M. Koller, F. Worek and S. Kubik, *Angew. Chemie - Int. Ed.*, 2016, **55**, 12668–12672.

281 S. E. Border, R. Z. Pavlović, L. Zhiquan and J. D. Badjić, *J. Am. Chem. Soc.*, 2017, **139**, 18496–18499.

282 Y. Ruan, P. W. Peterson, C. M. Hadad and J. D. Badjić, *Chem. Commun.*, 2014, **50**, 9086–9089.

283 S. Chen, Y. Ruan, J. D. Brown, J. Gallucci, V. Maslak, C. M. Hadad and J. D. Badjić, *J. Am. Chem. Soc.*, 2013, **135**, 14964–14967.

284 W. E. Liu, Z. Chen, L. P. Yang, H. Y. Au-Yeung and W. Jiang, *Chem. Commun.*, 2019, **55**, 9797–9800.

285 J. E. Mondloch, M. J. Katz, W. C. Isley, P. Ghosh, P. Liao, W. Bury, G. W. Wagner, M. G. Hall, J. B. Decoste, G. W. Peterson, R. Q. Snurr, C. J. Cramer, J. T. Hupp and O. K. Farha, *Nat. Mater.*, 2015, **14**, 512–516.

286 S. S. Mondal and H. J. Holdt, *Angew. Chemie - Int. Ed.*, 2016, **55**, 42–44.

287 J. Lagona, P. Mukhopadhyay, S. Chakrabarti and L. Isaacs, *Angew. Chemie - Int. Ed.*, 2005, **44**, 4844–4870.

288 S. Ganapati and L. Isaacs, *Isr. J. Chem.*, 2018, **58**, 250–263.

289 B. Andrae, D. Bauer, P. Gaß, M. Koller, F. Worek and S. Kubik, *Org. Biomol. Chem.*, 2020, **18**, 5218–5227.

290 M. A. Wartell, M. T. Kleinman, B. M. Huey and L. M. Duffy, *Strategies to Protect the Health of Deployed U.S. Forces*, National Academies Press, 1999.

291 H. J. Altmann and A. Richardt, in *Decontamination of Warfare Agents: Enzymatic Methods for the Removal of B/C Weapons*, John Wiley & Sons, Ltd, 2008, pp. 83–115.

292 J. A. Romano Jr, H. Salem, B. J. Lukey and B. J. Lukey, *Chemical warfare agents: chemistry, pharmacology, toxicology, and therapeutics*, CRC Press, 2nd edn., 2007.

293 C. Wilson, N. J. Cooper, M. E. Briggs, A. I. Cooper and D. J. Adams, *Org. Biomol. Chem.*, 2018, **16**, 9285–9291.

294 A. G. Doyle and E. N. Jacobsen, *Chem. Rev.*, 2007, 107, 5713–5743.

295 Á. Madarász, Z. Dósa, S. Varga, T. Soós, A. Csámpai and I. Pápai, *ACS Catal.*, 2016, **6**, 4379–4387.

296 O. V. Serdyuk, C. M. Heckel and S. B. Tsogoeva, *Org. Biomol. Chem.*, 2013, 11, 7051–7071.

297 M. D. Díaz de Villegas, J. A. Gálvez, P. Etayo, R. Badorrey and P. López-Ram-De-Víu, *Chem. Soc. Rev.*, 2011, **40**, 5564–5587.

298 M. S. Taylor and E. N. Jacobsen, *Angew. Chemie - Int. Ed.*, 2006, 45, 1520–1543.

299 D. Brynn Hibbert and P. Thordarson, *Chem. Commun.*, 2016, **52**, 12792–12805.

300 R: The R Project for Statistical Computing, https://www.r-project.org/, (accessed 24 May 2021).

301 P. A. Hassan, G. Verma and R. Ganguly, in *Functional Materials*, Elsevier, 2012, pp. 1–59.

302 D. Lombardo, M. A. Kiselev, S. Magazù and P. Calandra, *Adv. Condens. Matter Phys.*, 2015, 2015.

303 R. Azarmi and A. Ashjaran, *J. Chem. Pharm. Res*, 2015, **7**, 632–640.

304 V. A. Karetsi, C. N. Banti, N. Kourkoumelis, C. Papachristodoulou, C. D. Stalikas, C. P. Raptopoulou, V. Psycharis, P. Zoumpoulakis, T. Mavromoustakos, I. Sainis and S. K. Hadjikakou, *Antibiotics*, 2019, **8**, 213.

305 V. S. Kulkarni and C. Shaw, *Essential chemistry for formulators of semisolid and liquid dosages*, Academic Press, 2015.

306 Z. Ding and A. Hao, *J. Dispers. Sci. Technol.*, 2010, **31**, 338–342.

307 G. Graziano, *Biophys. Chem.*, 1999, **82**, 69–79.

308 R. Godawat, S. N. Jamadagni and S. Garde, *Proc. Natl. Acad. Sci.*, 2009, **106**, 15119–15124.

309 J. C. Biffinger, H. W. Kim and S. G. DiMagno, *ChemBioChem*, 2004, **5**, 622–627.

310 C. Wang, Z. Wang and X. Zhang, *Acc. Chem. Res.*, 2012, **45**, 608–618.

311 Y. Kang, K. Liu and X. Zhang, *Langmuir*, 2014, **30**, 5989–6001.

312 D. Bradburn and T. Bittinger, *Micelles: Structural biochemistry, formation and functions and usage*, Nova Science Publishers, 2013.

313 B. Alberts, A. Johnson, J. Lewis, M. Raff, K. Roberts and P. Walter, *Ann. Bot.*, 2003, **91**, 401.

314 W. Qiu, Z. Fu, G. G. Xu, R. A. Grassucci, Y. Zhang, J. Frank, W. A. Hendrickson and Y. Guo, *Proc. Natl. Acad. Sci. U. S. A.*, 2018, **115**, 12985–12990.

315 M. Doktorova, F. A. Heberle, B. Eicher, R. F. Standaert, J. Katsaras, E. London, G. Pabst and D. Marquardt, *Nat Protoc.*, 2018, **13**, 2086–2101.

316 J. M. Berg, J. L. Tymoczko and L. Stryer, *Biochemistry*, W.H. Freeman, 5th edn., 2002.

317 C. Wang, Z. Wang and X. Zhang, *Small*, 2011, **7**, 1379–1383.

318 X. Zhang and C. Wang, *Chem. Soc. Rev.*, 2011, **40**, 94–101.

319 C. Shan, X. Huang, H. Wei, W. Wei, H. Sun and X. Tang, *RSC Adv.*, 2014, **4**, 11216–11218.

320 C. Wang, Q. Chen, Z. Wang and X. Zhang, *Angew. Chemie - Int. Ed.*, 2010, **49**, 8612–8615.

321 G. Yu, K. Jie and F. Huang, *Chem. Rev.*, 2015, **115**, 7240–7303.

322 K. Liu, Y. Yao, Y. Liu, C. Wang, Z. Li and X. Zhang, *Langmuir*, 2012, **28**, 10697–10702.

323 C. B. Minkenberg, L. Florusse, R. Eelkema, G. J. M. Koper and J. H. Van Esch, *J. Am. Chem. Soc.*, 2009, **131**, 11274–11275.

324 X. Wu, X. X. Chen, M. Zhang, Z. Li, P. A. Gale and Y. B. Jiang, *Chem. Commun.*, 2016, **52**, 6981–6984.

325 F. Huang and X. Zhang, *Mater. Chem. Front.*, 2020, **4**, 11.

326 S. P. Wang, W. Lin, X. Wang, T. Y. Cen, H. Xie, J. Huang, B. Y. Zhu, Z. Zhang, A. Song, J. Hao, J. Wu and S. Li, *Nat. Commun.*, 2019, **10**, 2–13.

327 X. Zhang, Z. Chen and F. Würthner, *J. Am. Chem. Soc.*, 2007, **129**, 4886–4887.

328 I. Shulov, R. V. Rodik, Y. Arntz, A. Reisch, V. I. Kalchenko and A. S. Klymchenko, *Angew. Chemie - Int. Ed.*, 2016, **55**, 15884–15888.

329 A. V. Kabanov, T. K. Bronich, V. A. Kabanov, K. Yu and A. Eisenberg, *J. Am. Chem. Soc.*, 1998, 120, 9941–9942.

330 N. Kimizuka, T. Kawasaki, K. Hirata and T. Kunitake, *J. Am. Chem. Soc.*, 1995, **117**, 6360–6361.

331 N. Kimizuka, T. Kawasaki and T. Kunitake, *J. Am. Chem. Soc.*, 1993, **115**, 4387–4388.

332 X. Zhang and C. Wang, *Chem. Soc. Rev.*, 2011, **40**, 94–101.

333 A. Wilson, G. Gasparini and S. Matile, *Chem. Soc. Rev.*, 2014, **43**, 1948–1962.

334 Y. Kang, X. Tang, Z. Cai and X. Zhang, *Adv. Funct. Mater.*, 2016, **26**, 8920–8931.

335 Y. Kang and X. Zhang, in *Supramolecular Amphiphilies*, 2017, pp. 1–22.

336 J. Zou, F. Tao and M. Jiang, *Langmuir*, 2007, **23**, 12791–12794.

337 Y. Chang, Y. Jiao, H. E. Symons, J. F. Xu, C. F. J. Faul and X. Zhang, *Chem. Soc. Rev.*, 2019, **48**, 989–1003.

338 C. M. C. Faustino, A. R. T. Calado and L. Garcia-Rio, *J. Phys. Chem. B*, 2009, **113**, 977–982.

339 C. M. C. Faustino, A. R. T. Calado and L. Garcia-Rio, *J. Colloid Interface Sci.*, 2010, **351**, 472–477.

340 C. M. C. Faustino, A. R. T. Calado and L. Garcia-Rio, *J. Colloid Interface Sci.*, 2011, **359**, 493–498.

341 L. J. White, S. N. Tyuleva, B. Wilson, H. J. Shepherd, K. K. L. Ng, S. J. Holder, E. R. Clark and J. R. Hiscock, *Chem. - Eur. J.*, 2018, **24**, 7761–7773.

342 L. J. White, J. E. Boles, N. Allen, L. S. Alesbrook, J. M. Sutton, C. K. Hind, K. L. F. Hilton, L. R. Blackholly, R. J. Ellaby, G. T. Williams, D. P. Mulvihill and J. R. Hiscock, *J. Mater. Chem. B*, 2020, **8**, 4694–4700.

343 S. N. Tyuleva, N. Allen, L. J. White, A. Pépés, H. J. Shepherd, P. J. Saines, R. J. Ellaby, D. P.

Mulvihill and J. R. Hiscock, *Chem. Commun.*, 2019, **55**, 95–98.

344 J. E. Boles, R. J. Ellaby, H. J. Shepherd and J. R. Hiscock, *RSC Adv.*, 2021, **11**, 9550–9556.

345 N. O. Dora, E. Blackburn, J. E. Boles, G. T. Williams, L. J. White, S. E. G. Turner, J. D. Hothersall, T. Askwith, J. A. Doolan, D. P. Mulvihill, M. D. Garrett and J. R. Hiscock, *RSC Adv.*, 2021, **11**, 14213–14217.

346 J. Yeston, R. Coontz, J. Smith and C. Ash, *Science (80-.).*, 2006, **313**, 1067.

347 R. P. Schwarzenbach, B. I. Escher, K. Fenner, T. B. Hofstetter, C. A. Johnson, U. Von Gunten and B. Wehrli, *Science (80-.).*, 2006, **313**, 1072–1077.

348 A. Alsbaiee, B. J. Smith, L. Xiao, Y. Ling, D. E. Helbling and W. R. Dichtel, *Nature*, 2016, **529**, 190–194.

349 S. D. Richardson and S. Y. Kimura, *Anal. Chem.*, 2020, **92**, 473–505.

350 E. K. Putra, R. Pranowo, J. Sunarso, N. Indraswati and S. Ismadji, *Water Res.*, 2009, **43**, 2419–2430.

351 J. J. M. Órfão, A. I. M. Silva, J. C. V. Pereira, S. A. Barata, I. M. Fonseca, P. C. C. Faria and M. F. R. Pereira, *J. Colloid Interface Sci.*, 2006, **296**, 480–489.

352 L. Kovalova, D. R. U. Knappe, K. Lehnberg, C. Kazner and J. Hollender, *Environ. Sci. Pollut. Res.*, 2013, **20**, 3607–3615.

353 G. San Miguel, S. D. Lambert and N. J. D. Graham, *Water Res.*, 2001, **35**, 2740–2748.

354 A. Fernando, T. L. Mako, A. M. Levenson, P. T. Cesana, A. M. Mendieta, J. M. Racicot, B. DeBoef and M. Levine, *Supramol. Chem.*, 2019, **31**, 545–557.

355 C. A. Bunton and S. Barbara, 1996, **19**, 72–76.

356 J. L. Anderson, V. Pino, E. C. Hagberg, V. V. Sheares and D. W. Armstrong, *Chem.*

Commun., 2003, **3**, 2444–2445.

357 V. M. Wallace, N. R. Dhumal, F. M. Zehentbauer, H. J. Kim and J. Kiefer, *J. Phys. Chem. B*, 2015, **119**, 14780–14789.

358 M. C. Malet-Martino and R. Martino, *Clin. Pharmacokinet.*, 1991, **20**, 337–349.

359 R. F. Evilia, *Anal. Lett.*, 2001, **34**, 2227–2236.

360 R. Shukla, T. Kida and B. D. Smith, *Org. Lett.*, 2000, **2**, 3099–3102.

361 L. K. S. Von Krbek, C. A. Schalley and P. Thordarson, *Chem. Soc. Rev.*, 2017, **46**, 2622–2637.

362 T. Andrews, *J. Chem. Soc.*, 1870, **23**, 74–95.

363 D. E. Koshland, *Angew. Chemie Int. Ed. English*, 1995, **33**, 2375–2378.

364 M. M. J. Smulders, M. M. L. Nieuwenhuizen, T. F. A. De Greef, P. Van Der Schoot, A. P. H. J. Schenning and E. W. Meijer, *Chem. - A Eur. J.*, 2010, **16**, 362–367.

365 B. Lorber, F. Fischer, M. Bailly, H. Roy and D. Kern, *Biochem. Mol. Biol. Educ.*, 2012, **40**, 372–382.

366 W. I. Goldburg, *A Study Brownian Motion Using Light Scatt. Am. J. Phys.*, 1999, **67**, 1093.

367 P. M. Carvalho, M. R. Felício, N. C. Santos, S. Gonçalves and M. M. Domingues, *Front. Chem.*, 2018, **6**, 1–17.

368 S. Bhattacharjee, *J. Control. Release*, 2016, **235**, 337–351.

369 L. Maibaum, A. R. Dinner and D. Chandler, *J. Phys. Chem. B*, 2004, **108**, 6778–6781.

370 Á. Piñeiro, X. Banquy, S. Pérez-Casas, E. Tovar, A. García, A. Villa, A. Amigo, A. E. Mark and M. Costas, *J. Phys. Chem. B*, 2007, **111**, 4383–4392.

371 T. Tadros, *Encyclopedia of Colloid and Interface Science*, Springer, 2013.

372 R. J. Williams, J. N. Phillips and K. J. Mysels, *Trans. Faraday Soc.*, 1955, **51**, 728–737.

373 D. E. Kile and C. T. Chiou, *Environ. Sci. Technol.*, 1989, **23**, 832–838.

374 R. Nagarajan and E. Ruckenstein, *Langmuir*, 1991, **7**, 2934–2969.

375 K. Shinoda, *J. Phys. Chem.*, 1954, **58**, 541–544.

376 D. Attwood, *Kolloid-Zeitschrift Zeitschrift für Polym.*, 1969, **232**, 788–792.

377 S. K. Hait and S. P. Moulik, *J. Surfactants Deterg.*, 2001, **4**, 303–309.

378 M. Lesemann, K. Thirumoorthy, Y. J. Kim, J. Jonas and M. E. Paulaitis, *Langmuir*, 1998, **14**, 5339–5341.

379 J. D. Clogston and A. K. Patri, *Methods Mol. Biol.*, 2011, **697**, 63–70.

380 P. Job, *Anal. Chim. Appl.*, 1928, **9**, 113–203.

381 Y. Zhao and D. G. Truhlar, *Theor. Chem. Acc.*, 2008, **120**, 215–241.

382 A. D. McLean and G. S. Chandler, *J. Chem. Phys.*, 1980, **72**, 5639–5648.

383 M. J. Frisch, G. W. Trucks, H. B. Schlegel, G. E. Scuseria, M. A. Robb, J. R. Cheeseman, G. Scalmani, V. Barone, G. A. Petersson, H. Nakatsuji, X. Li, M. Caricato, A. V. Marenich, J. Bloino, B. G. Janesko, R. Gomperts, B. Mennucci, H. P. Hratchian, J. V. Ortiz, A. F. Izmaylov, J. L. Sonnenberg, Williams, F. Ding, F. Lipparini, F. Egidi, J. Goings, B. Peng, A. Petrone, T. Henderson, D. Ranasinghe, V. G. Zakrzewski, J. Gao, N. Rega, G. Zheng, W. Liang, M. Hada, M. Ehara, K. Toyota, R. Fukuda, J. Hasegawa, M. Ishida, T. Nakajima, Y. Honda, O. Kitao, H. Nakai, T. Vreven, K. Throssell, J. A. Montgomery Jr., J. E. Peralta, F. Ogliaro, M. J. Bearpark, J. J. Heyd, E. N. Brothers, K. N. Kudin, V. N. Staroverov, T. A. Keith, R. Kobayashi, J. Normand, K. Raghavachari, A. P. Rendell, J. C. Burant, S. S.

Iyengar, J. Tomasi, M. Cossi, J. M. Millam, M. Klene, C. Adamo, R. Cammi, J. W. Ochterski, R. L. Martin, K. Morokuma, O. Farkas, J. B. Foresman and D. J. Fox, .

384 N. Busschaert, I. L. Kirby, S. Young, S. J. Coles, P. N. Horton, M. E. Light and P. A. Gale, *Angew. Chemie - Int. Ed.*, 2012, **51**, 4426–4430.

385 C. M. Chau, T. J. Chuan and K. M. Liu, *RSC Adv.*, 2014, **4**, 1276–1282.

386 S. M. S. Chauhan, B. Garg and T. Bisht, *Molecules*, 2007, **12**, 2458–2466.

387 Y. F. Chen, C. L. Kao, W. K. Lee, P. C. Huang, C. Y. Hsu and C. H. Kuei, *J. Chinese Chem. Soc.*, 2016, **63**, 751–757.

388 D. S. Panmand, A. D. Tiwari, S. S. Panda, J. C. M. Monbaliu, L. K. Beagle, A. M. Asiri, C. V. Stevens, P. J. Steel, C. D. Hall and A. R. Katritzky, *Tetrahedron Lett.*, 2014, **55**, 5898–5901.

389 H. Huang, J. Ash and J. Y. Kang, *Org. Lett.*, 2018, **20**, 4938–4941.

390 S. Feng, J. Li and J. Wei, *New J. Chem.*, 2017, **41**, 4743–4746.

391 D. V. Schoonover and H. W. Gibson, *Tetrahedron Lett.*, 2017, **58**, 242–244.

392 J. W. W. Chang, E. Y. Chia, C. L. L. Chai and J. Seayad, *Org. Biomol. Chem.*, 2012, **10**, 2289–2299.

393 T. Noji, H. Fujiwara, K. Okano and H. Tokuyama, *Org. Lett.*, 2013, **15**, 1946–1949.

394 N. Ortega, A. Feher-Voelger, M. Brovetto, J. I. Padrón, V. S. Martín and T. Martín, *Adv. Synth. Catal.*, 2011, **353**, 963–972.

395 J. Wang, Y. Zhao, W. Zhao, P. Wang and J. Li, *J. Carbohydr. Chem.*, 2017, **35**, 445–454.

Table of Contents

Appendix 1: Chapter 2 218
1.1 Characterisation NMR 218
1.2 Single crystal X-ray structures 248
1.2.1 Hydrogen bonding tables from single crystal X-ray structure 254
1.3 Mass spectrometry data 255
1.3.1 Comparative overview 264
1.4 Dynamic light scattering data 264
1.4.1 Comparative overview 308
1.5 Surface tension measurements and CMC determination 309
1.5.1 Comparative overview 317
1.6 DOSY ^{1}H NMR experiments 318
1.6.1 Comparative overview 321
1.7 Quantitative ^{1}H NMR experiments 322
1.7.1 Comparative overview 325
1.8 Zeta potential 326
1.8.1 Comparative overview 336
1.9 ^{1}H NMR self-association studies 337
1.9.1 Comparative overview 371
1.10 Low-level computational modelling 372
1.10.1 Comparative overview 381
1.11 References 382
Appendix 2: Chapter 3 383
2.1 Characterisation NMR 383
2.2 Dynamic light scattering data 384
2.2.1 Comparative overview 386
2.3 Inversion test 387
2.3.1 Comparative overview 405
2.4 Rheological data 406
2.4.1 Amplitude sweep 406
2.4.2 Frequency sweep 412
2.4.3 Comparative overview 418
2.5 Microscopy and energy dispersive X-ray analysis 419
2.6 MIC_{50} Growth Curves 432
2.6.1 USA 300 Methicillin-resistant *Staphylococcus aureus* (MRSA) 432

2.6.2 *Escherichia coli* DH10β (*E. coli*) 435
2.6.3 Comparative overview 438
2.7 Hydrogel antimicrobial efficacy experiments 439
2.7.1 Disk diffusion assays *E. coli* DH5B 439
2.7.2 Disk diffusion assays MRSA USA300 442
2.7.3 Comparative overview 444
Appendix 3: Chapter 4 445
3.1 UV-Vis spectroscopy 445
3.1.1 Comparative overview 453
3.2 Spectral well-scans 454
3.3 Optical density intensity maps 468
3.3.1 Comparative overview 503
3.4 Fluorescence spectroscopy 504
3.5 Uniformity experiments 511

Appendix 1: Chapter 2

1.1 Characterisation NMR

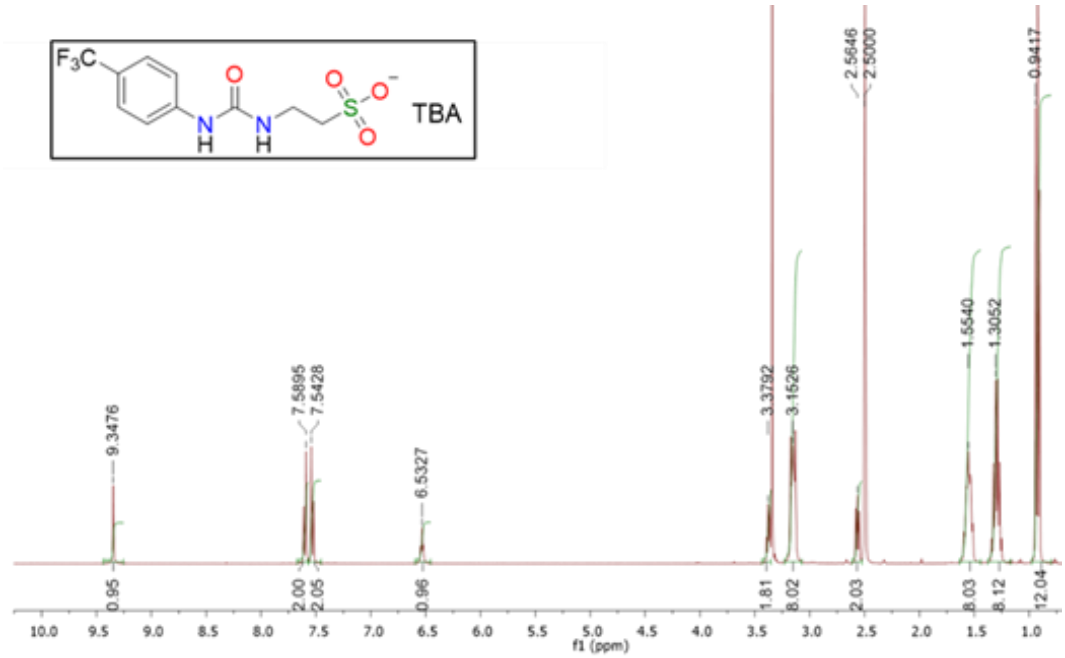

Figure S1 - ^{1}H NMR of compound **43** in DMSO-d_6 conducted at 298.15 K.

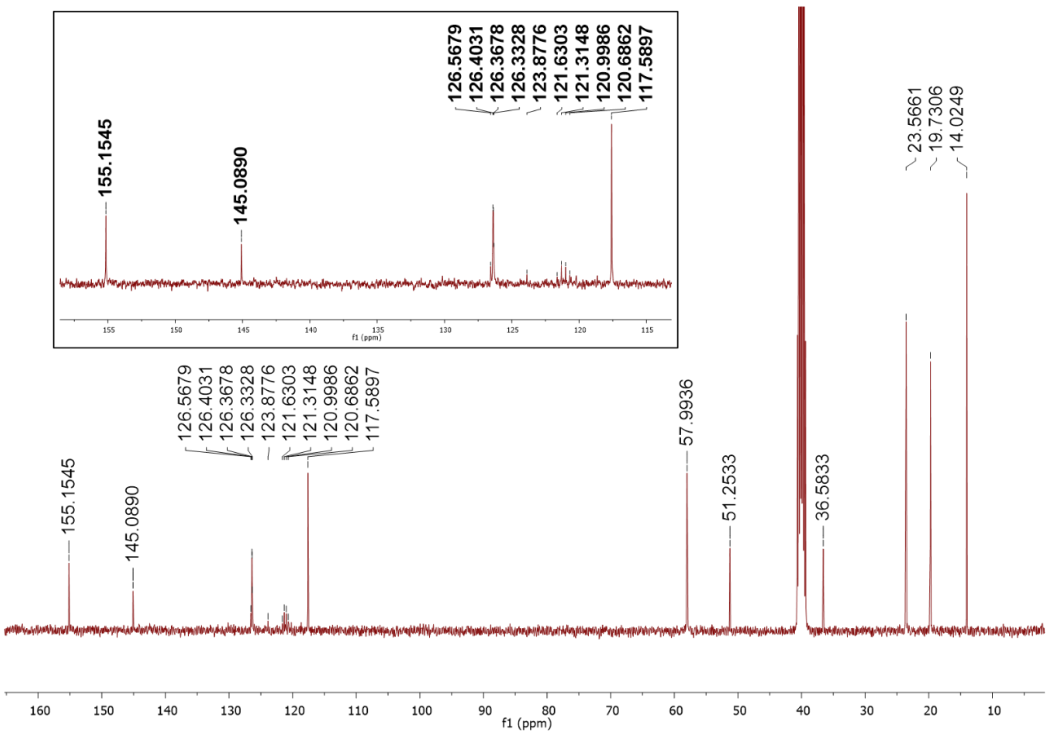

Figure S2 - ^{13}C NMR of compound **43** in DMSO-d_6 conducted at 298.15 K.

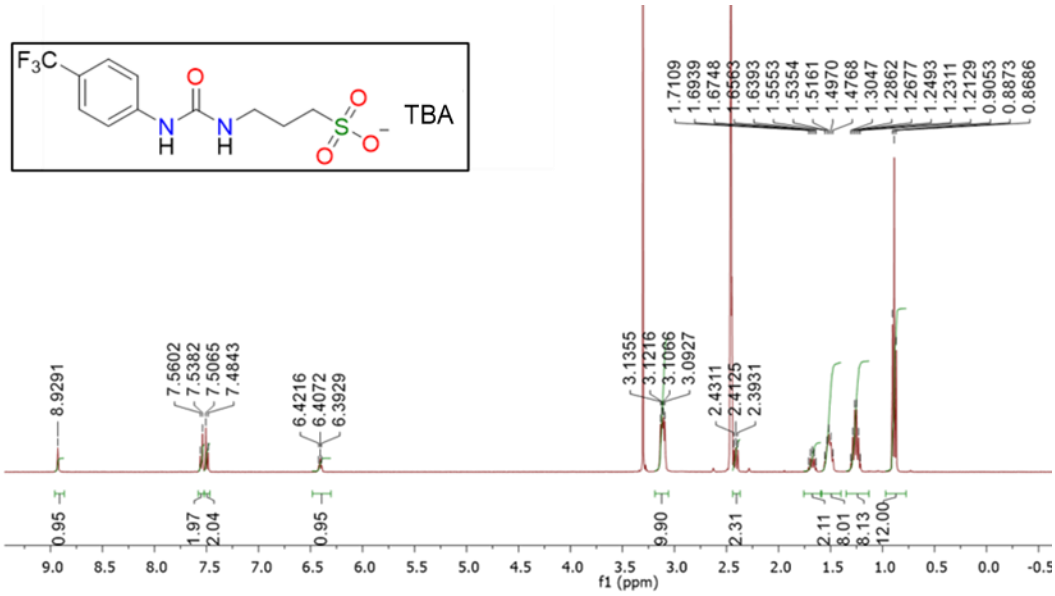

Figure S3 - ^{1}H NMR of compound **44** in DMSO-d_6 conducted at 298.15 K.

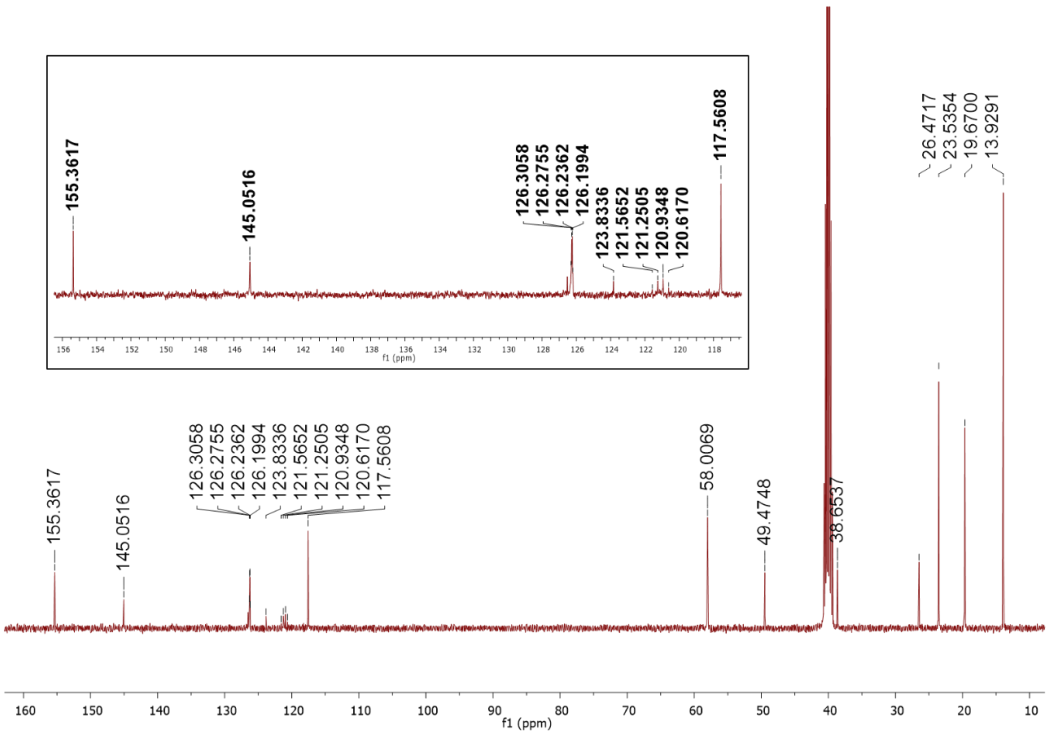

Figure S4 - ^{13}C NMR of compound **44** in DMSO-d_6 conducted at 298.15 K.

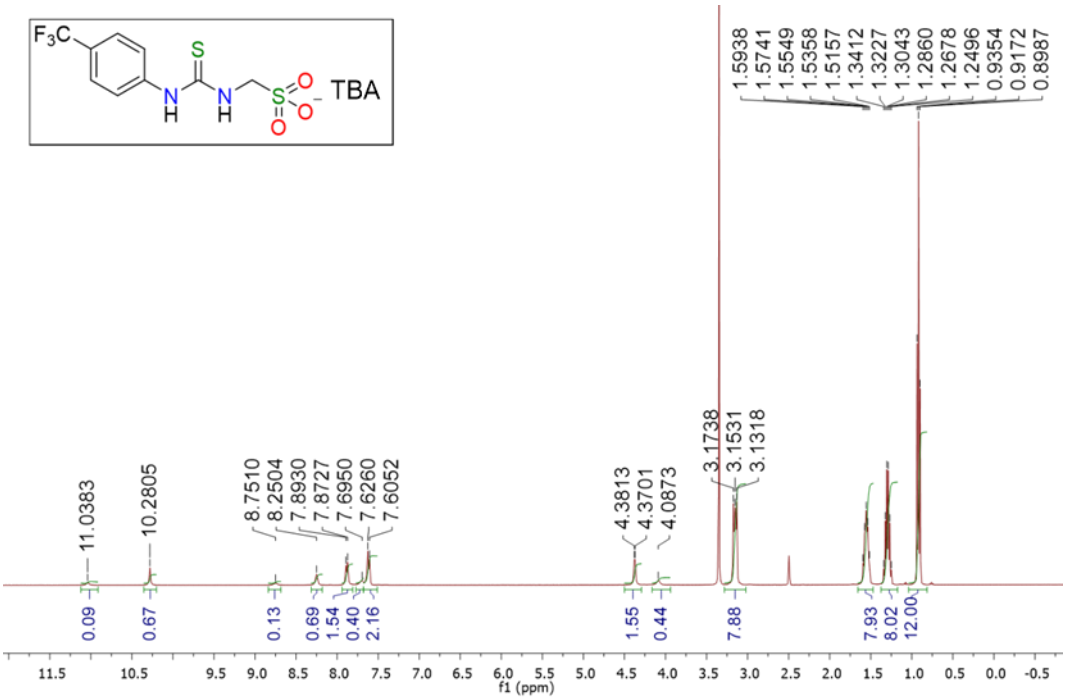

Figure S5 - ^{1}H NMR of compound **45** in DMSO-d_6 conducted at 298.15 K.

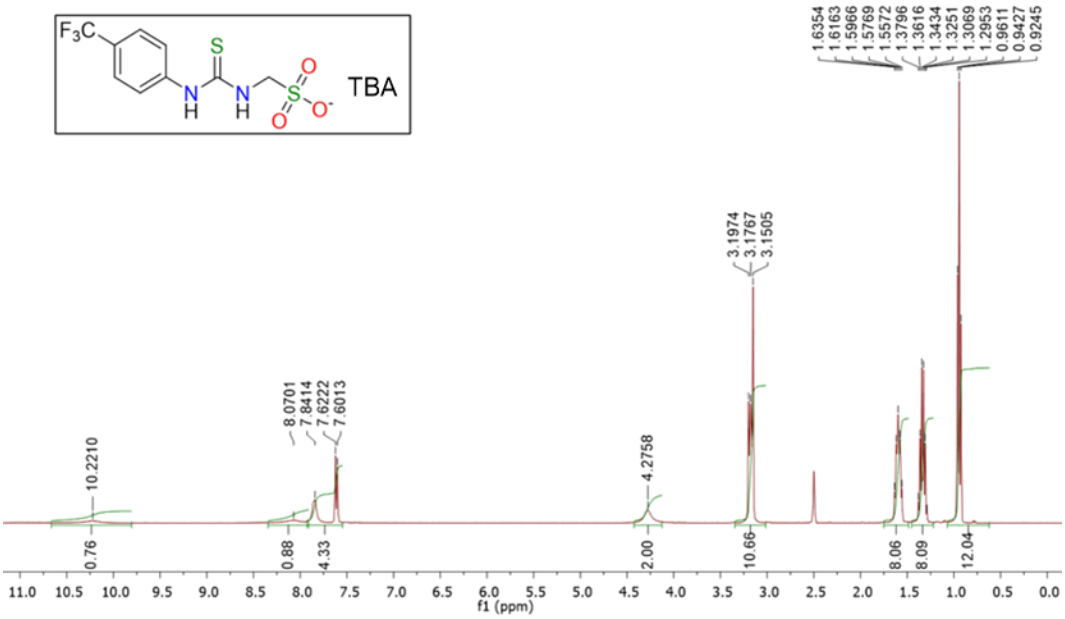

Figure S6 - ^{1}H NMR of compound **45** in DMSO-d_6 conducted at 333.15 K.

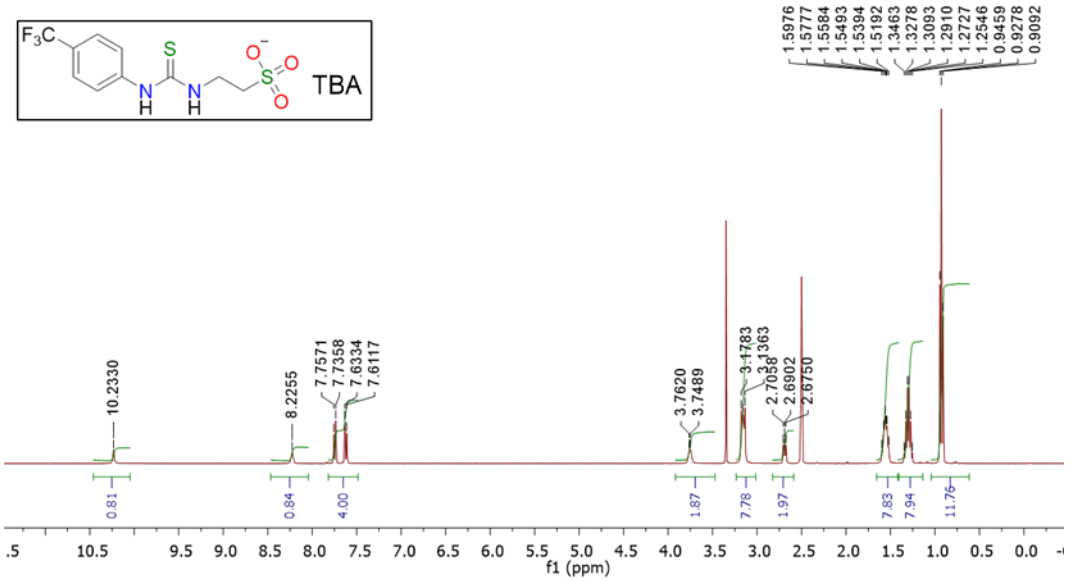

Figure S7 - ^{1}H NMR of compound **46** in DMSO-d_6 conducted at 298.15 K.

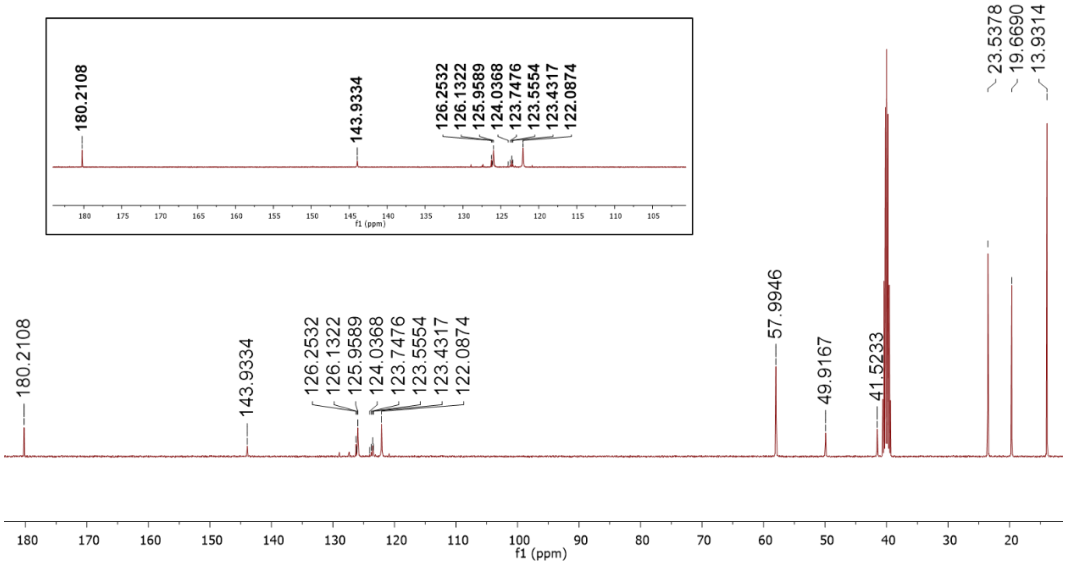

Figure S8 - ^{13}C NMR of compound **46** in DMSO-d_6 conducted at 298.15 K.

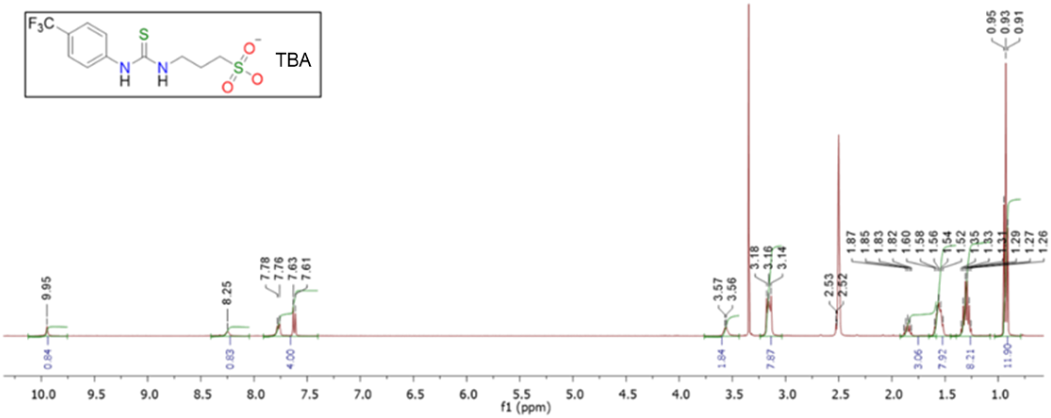

Figure S9 - ^{1}H NMR of compound **47** in DMSO-d_6 conducted at 298.15 K.

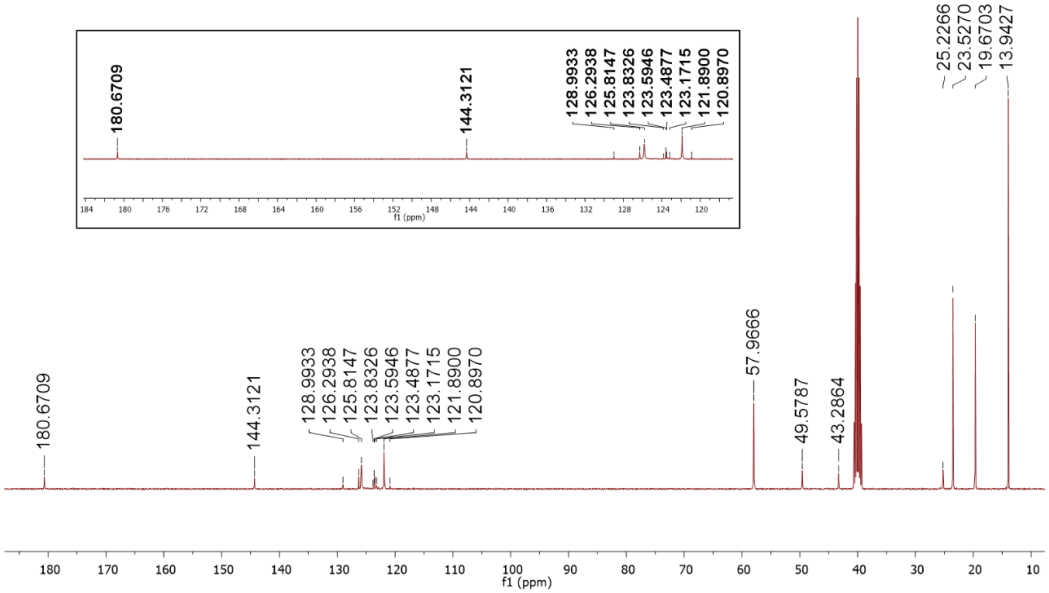

Figure S10 - ^{13}C NMR of compound **47** in DMSO-d_6 conducted at 298.15 K.

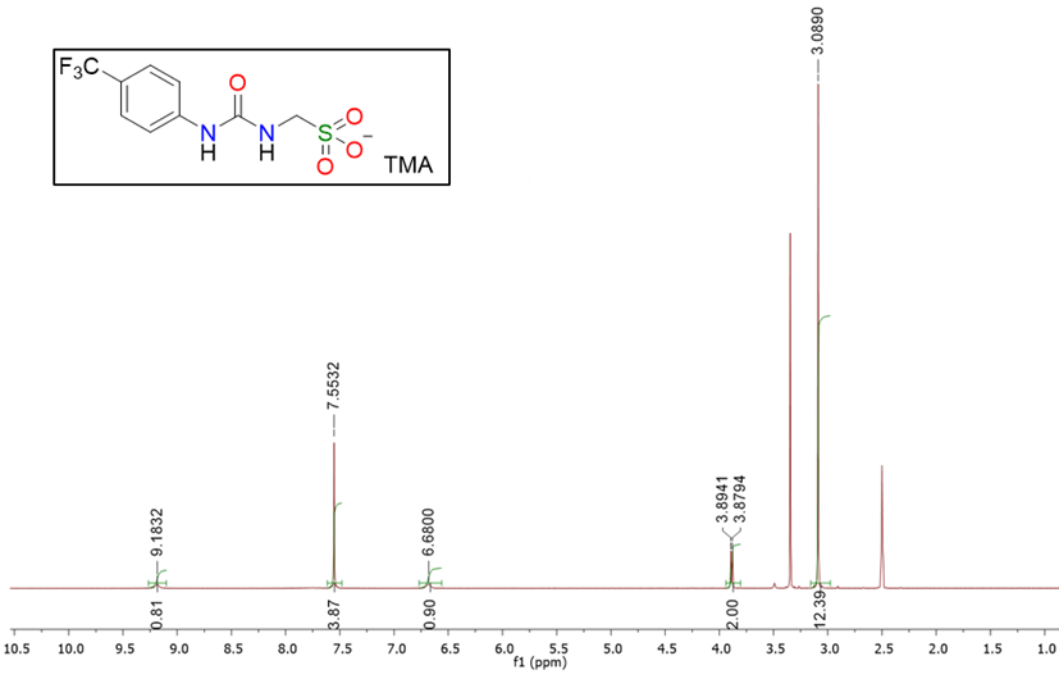

Figure S11 - ^{1}H NMR of compound **50** in DMSO-d_6 conducted at 298.15 K.

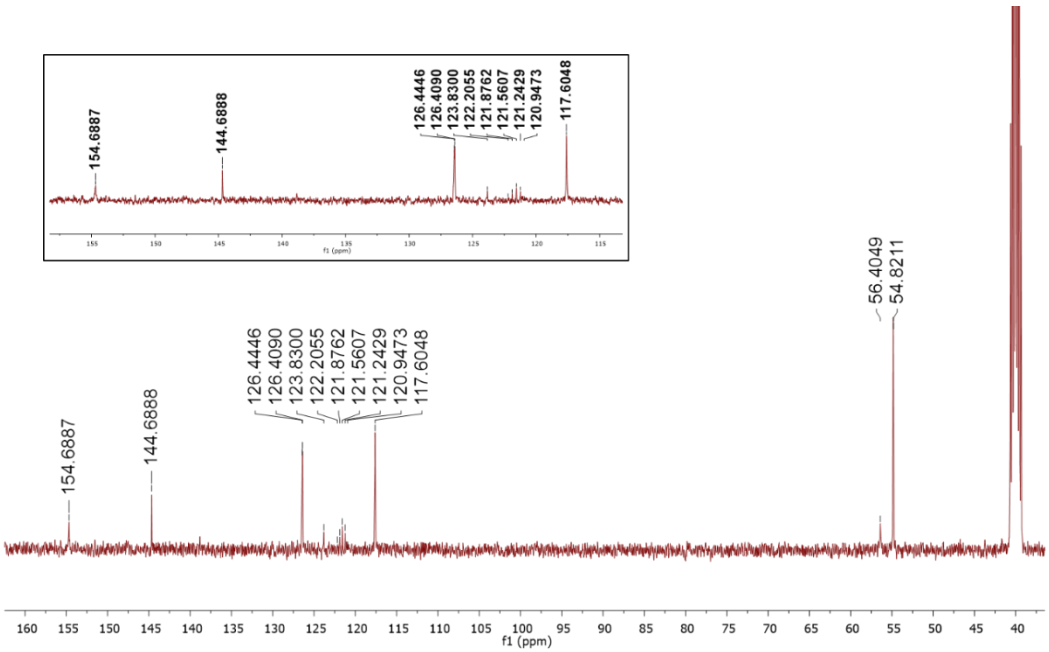

Figure S12 - ^{13}C NMR of compound **50** in DMSO-d_6 conducted at 298.15 K.

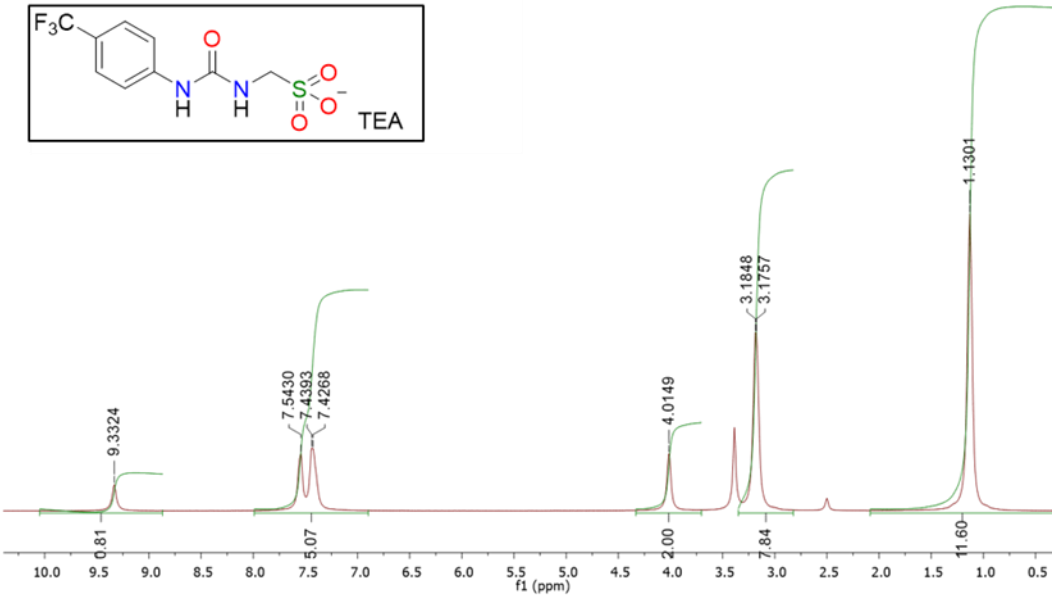

Figure S13 - ^{1}H NMR of compound **51** in DMSO-d_6 conducted at 298.15 K.

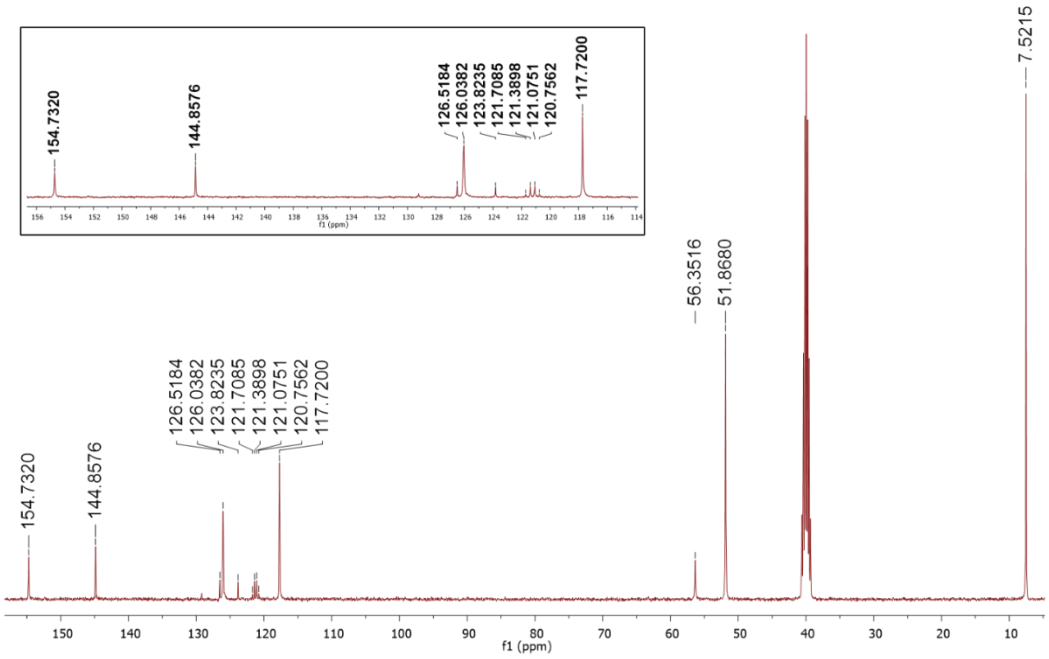

Figure S14 - ^{13}C NMR of compound **51** in DMSO-d_6 conducted at 298.15 K.

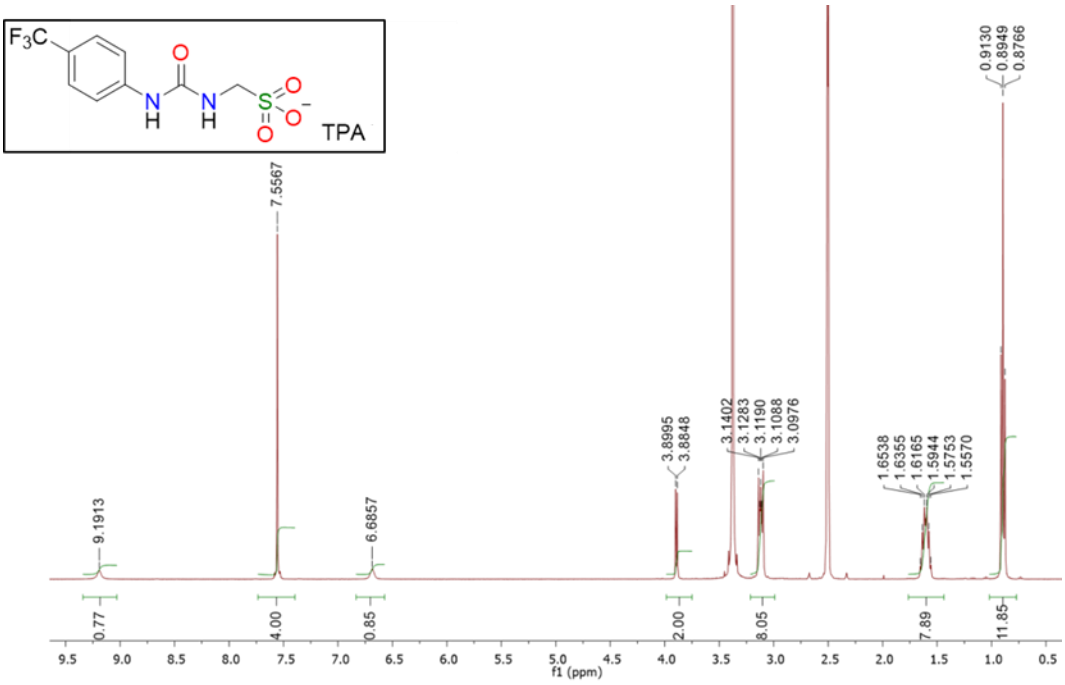

Figure S15 - ^{1}H NMR of compound **52** in DMSO-d_6 conducted at 298.15 K.

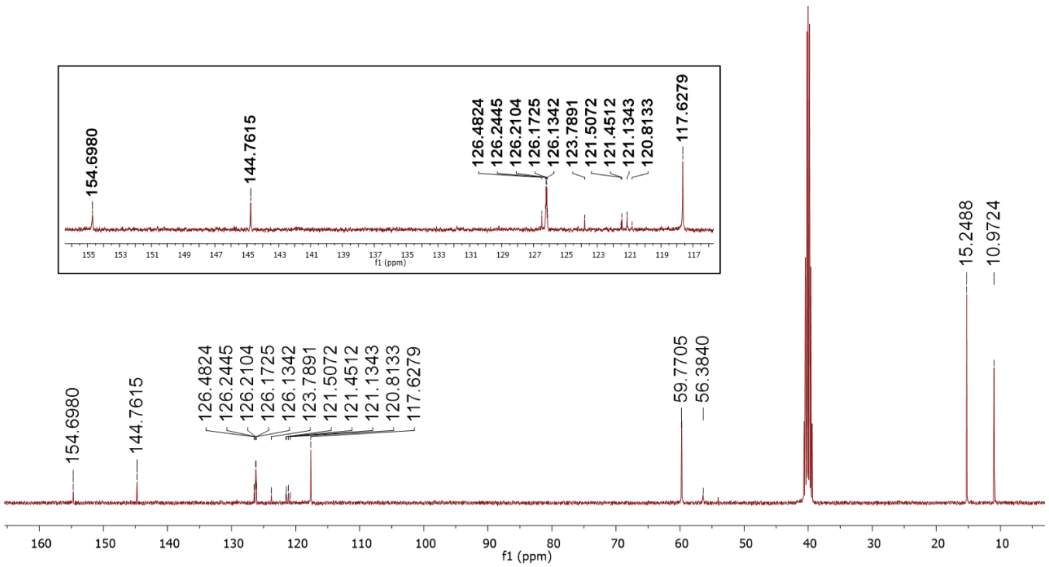

Figure S16 - ^{13}C NMR of compound **52** in DMSO-d_6 conducted at 298.15 K.

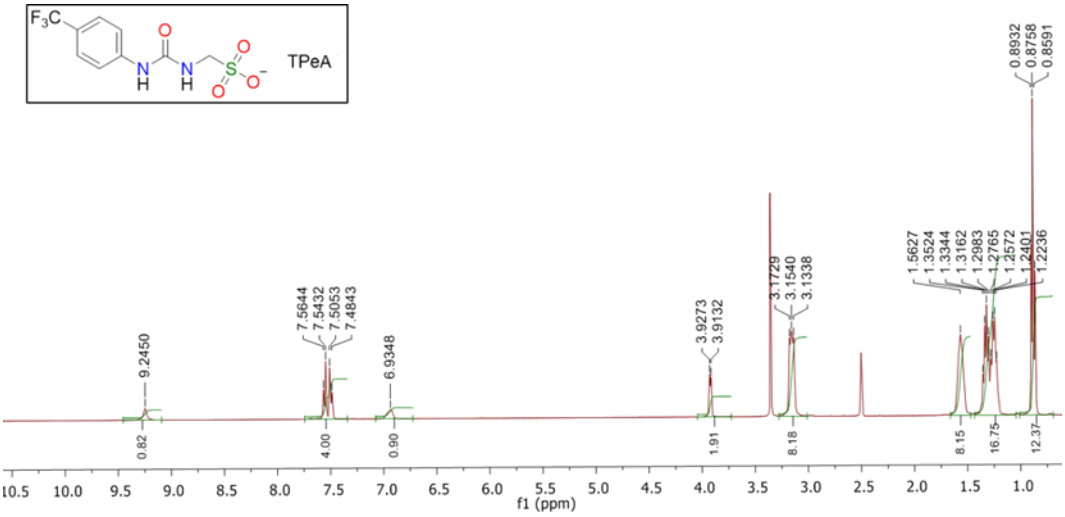

Figure S17 - ^{1}H NMR of compound **53** in DMSO-d_6 conducted at 298.15 K.

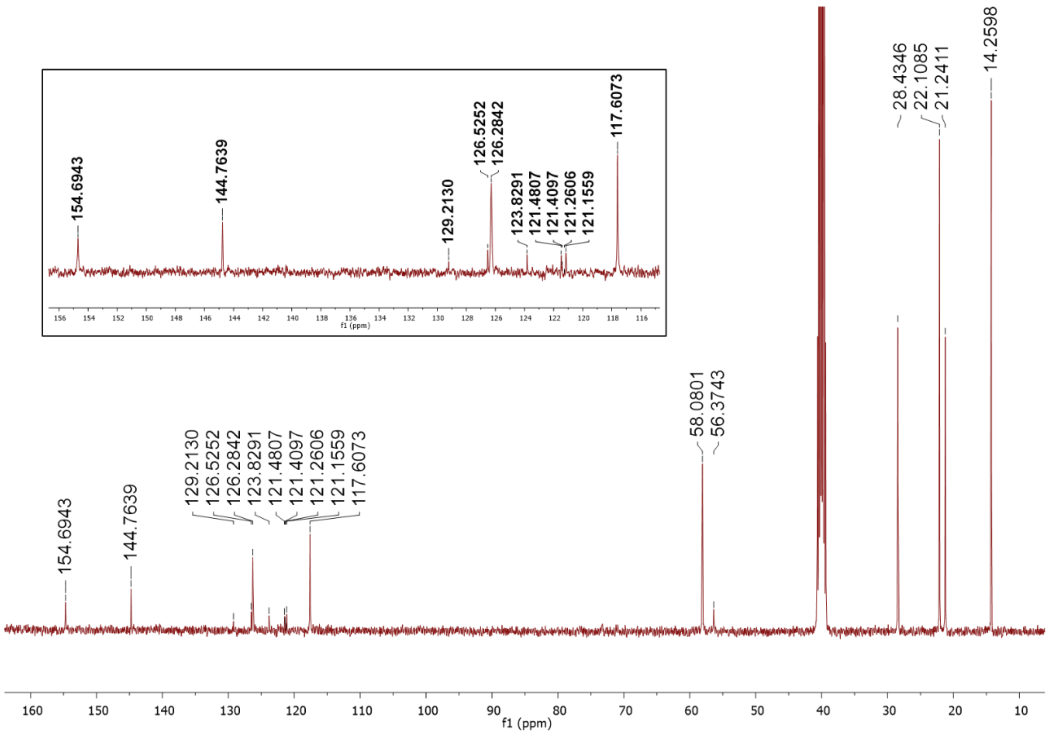

Figure S18 - ^{13}C NMR of compound **53** in DMSO-d_6 conducted at 298.15 K.

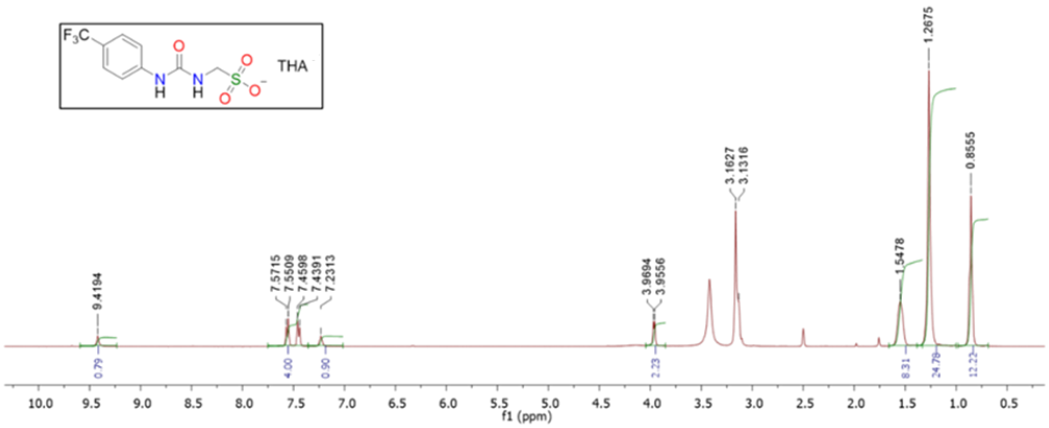

Figure S19 - ^{1}H NMR of compound **54** in DMSO-d_6 conducted at 298.15 K.

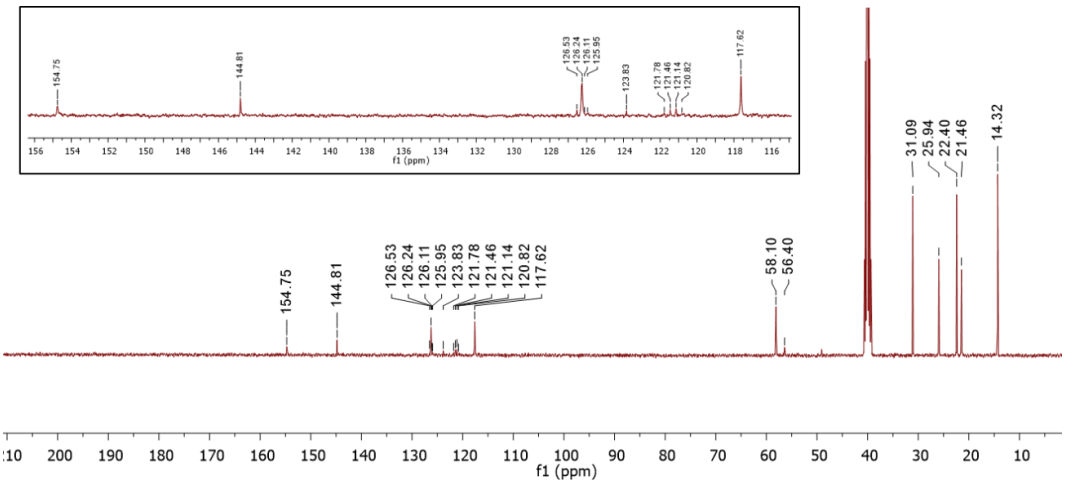

Figure S20 - ^{13}C NMR of compound **54** in DMSO-d_6 conducted at 298.15 K.

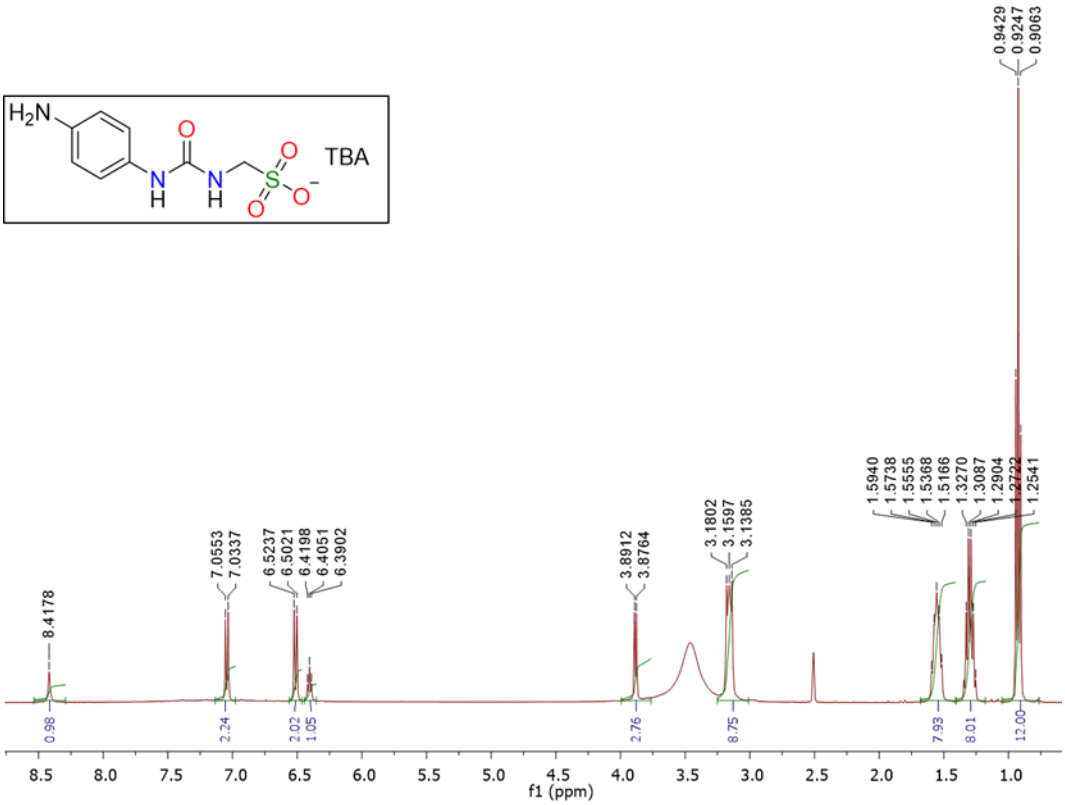

Figure S21 - ^{1}H NMR of compound **55** in DMSO-d_6 conducted at 298.15 K.

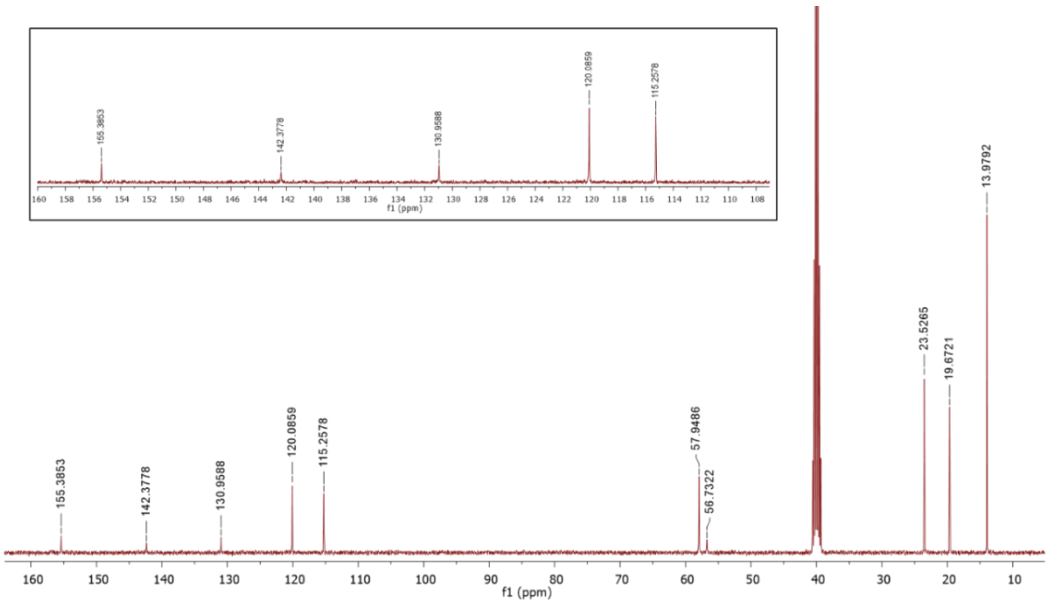

Figure S22 - ^{13}C NMR of compound **55** in DMSO-d_6 conducted at 298.15 K.

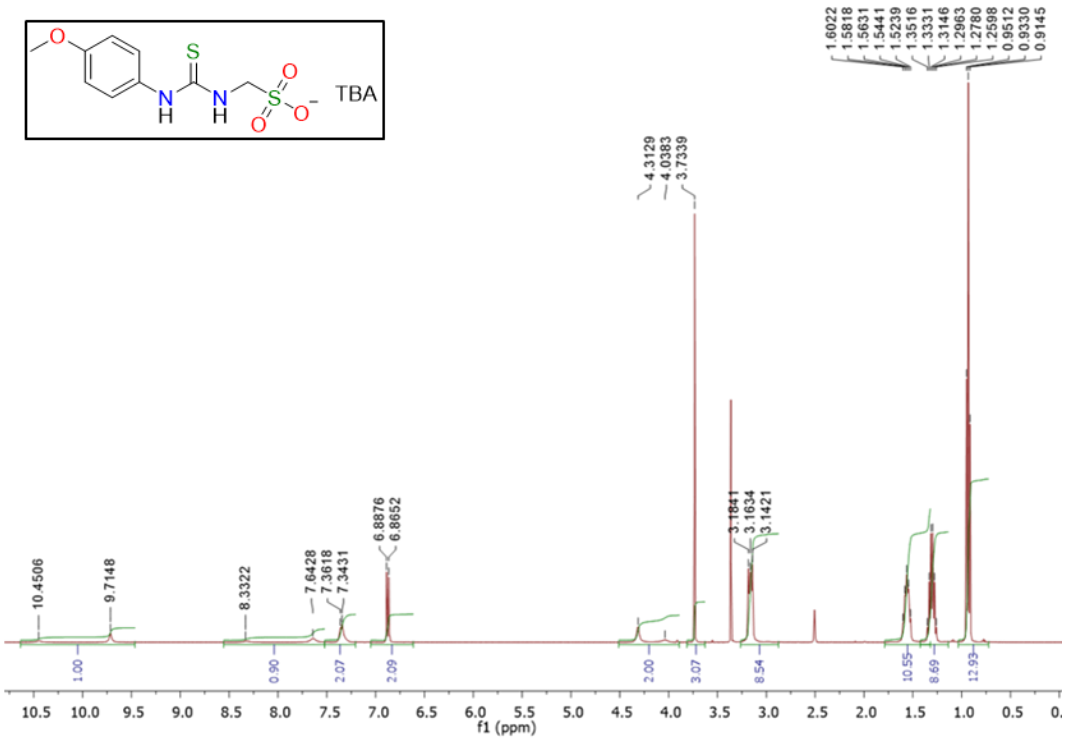

Figure S23 - ^{1}H NMR of compound **60** in DMSO-d_6 conducted at 298.15 K.

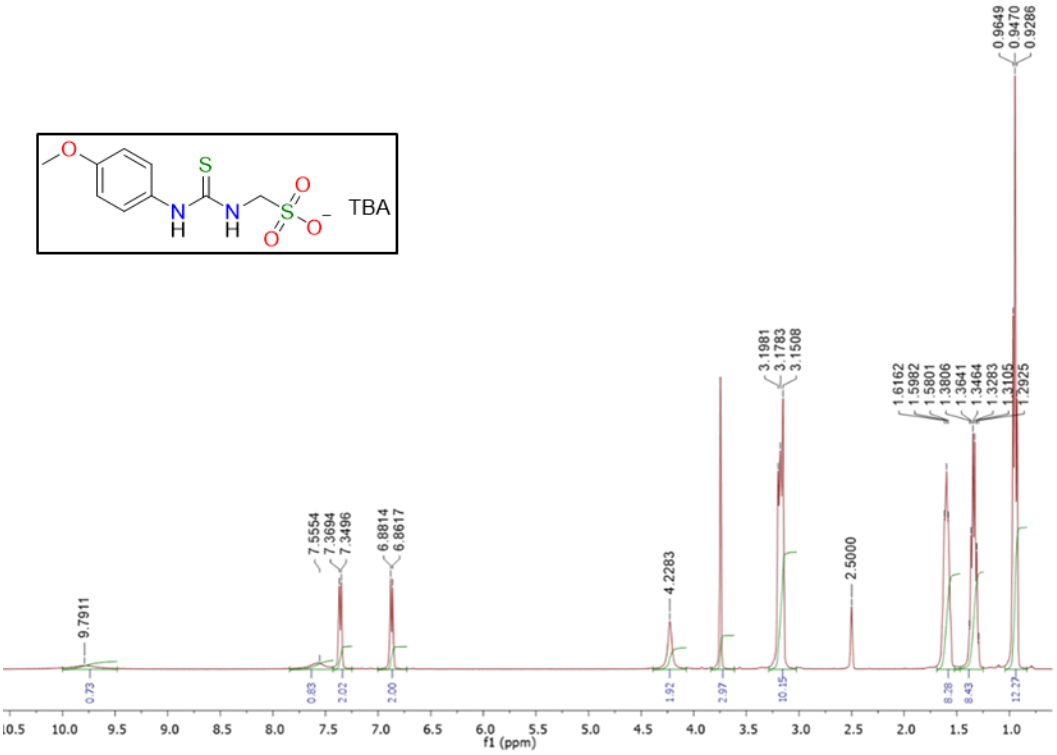

Figure S24 - ^{1}H NMR of compound **60** in DMSO-d_6 conducted at 333.15 K.

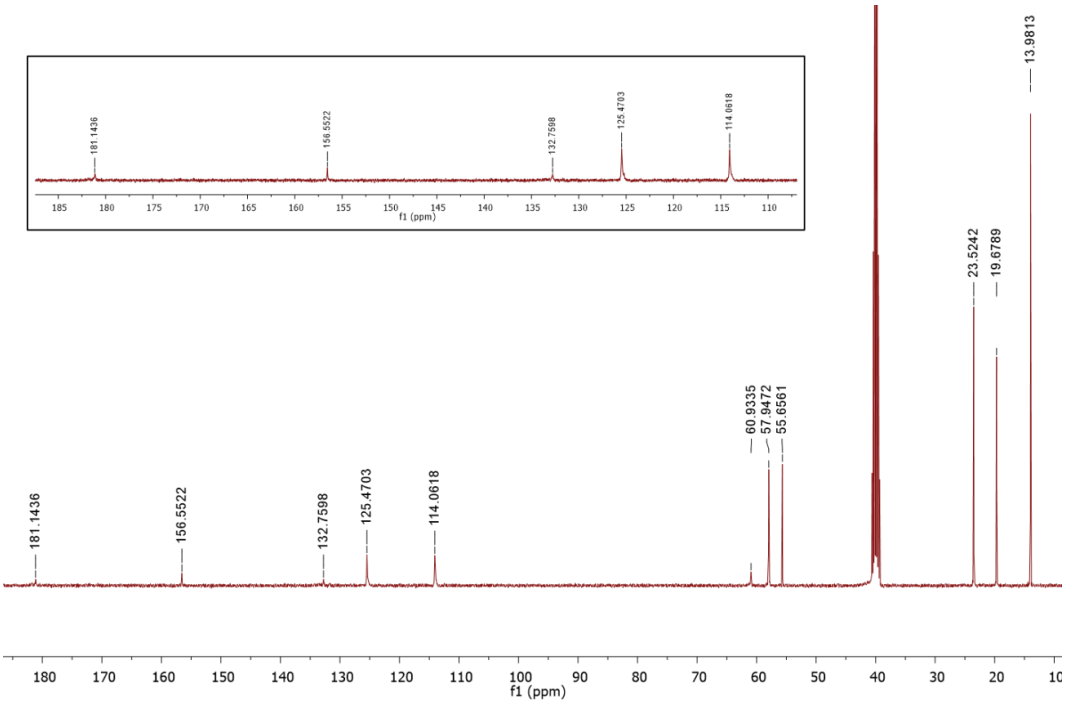

Figure S25 - ^{13}C NMR of compound **60** in DMSO-d_6 conducted at 298.15 K.

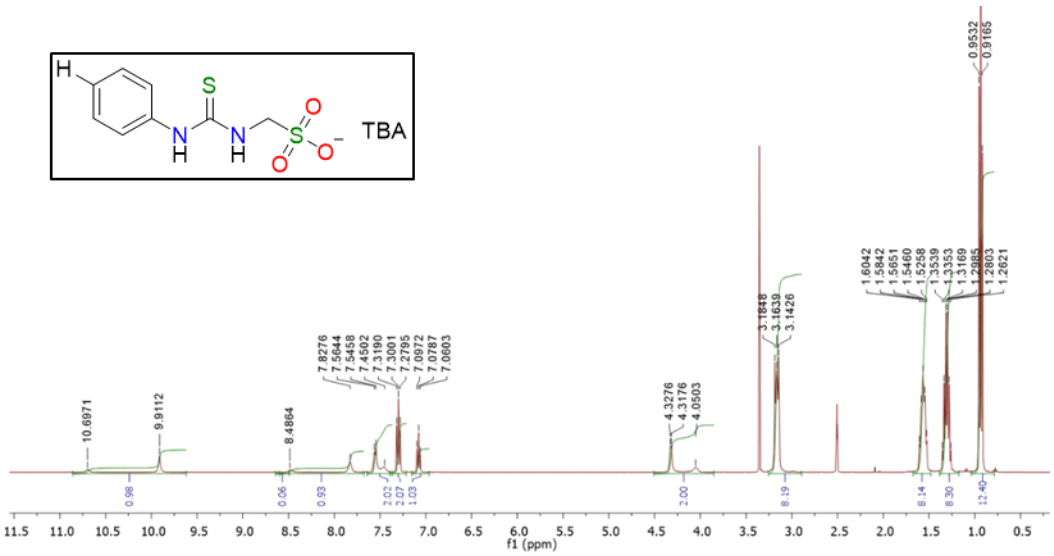

Figure S26 - ^{1}H NMR of compound **61** in DMSO-d_6 conducted at 298.15 K.

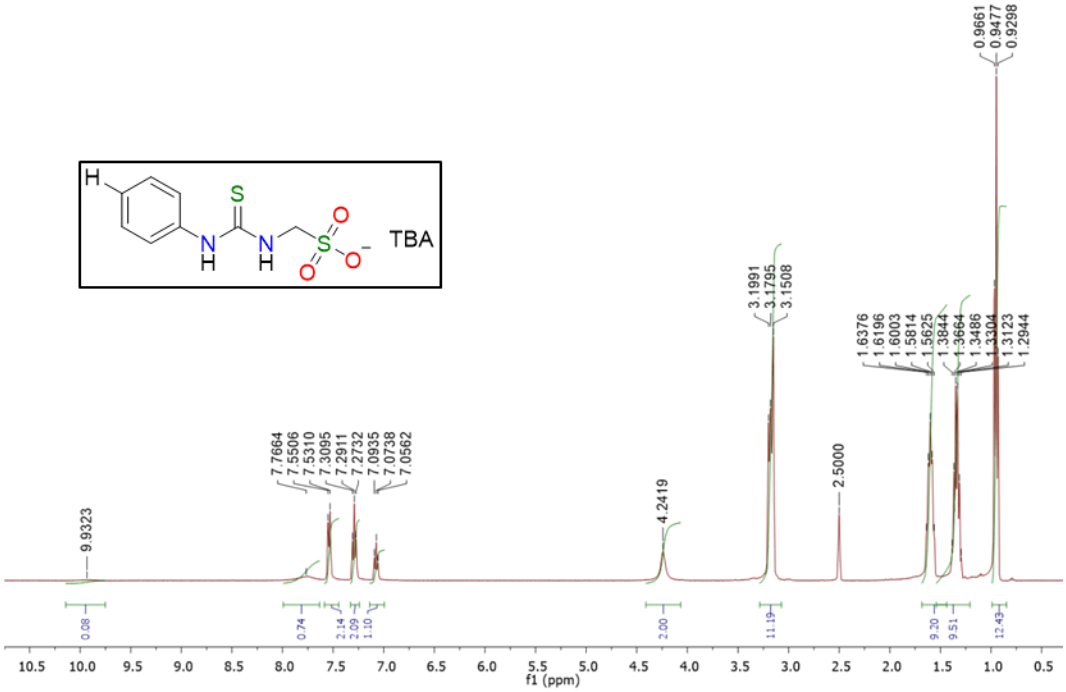

Figure S27 - ^{1}H NMR of compound **61** in DMSO-d_6 conducted at 333.15 K.

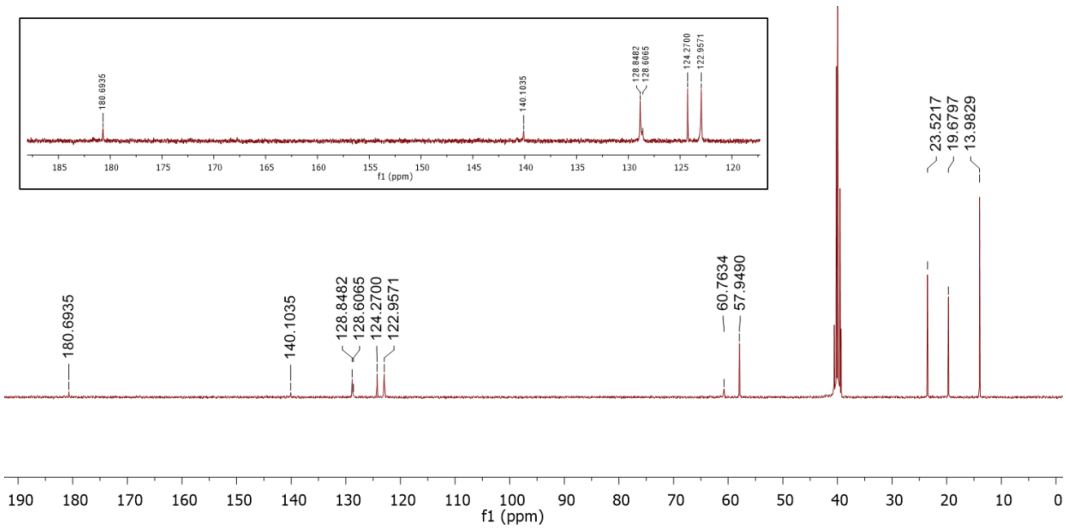

Figure S28 - ^{13}C NMR of compound **61** in DMSO-d_6 conducted at 298.15 K.

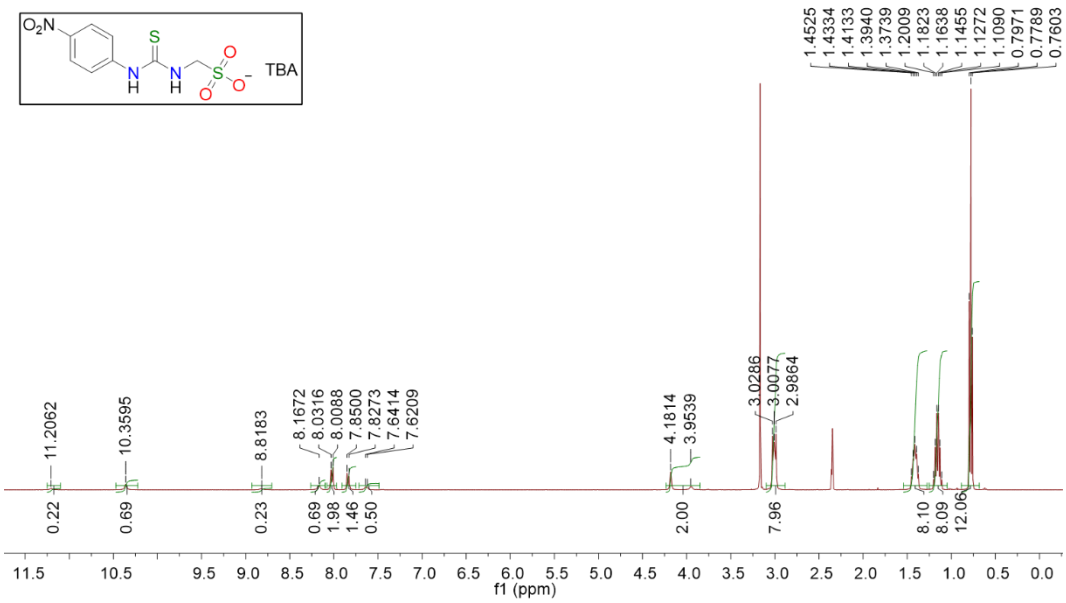

Figure S29 - ^{1}H NMR of compound **62** in DMSO-d_6 conducted at 298.15 K.

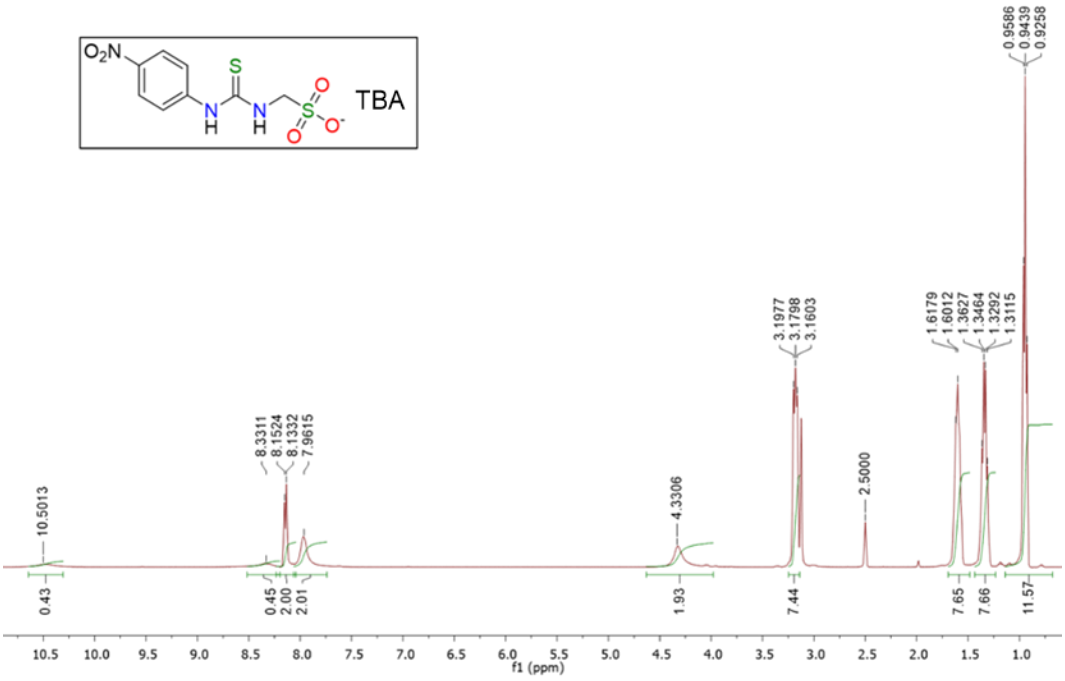

Figure S30 - ^{1}H NMR of compound **62** in DMSO-d_6 conducted at 333.15 K.

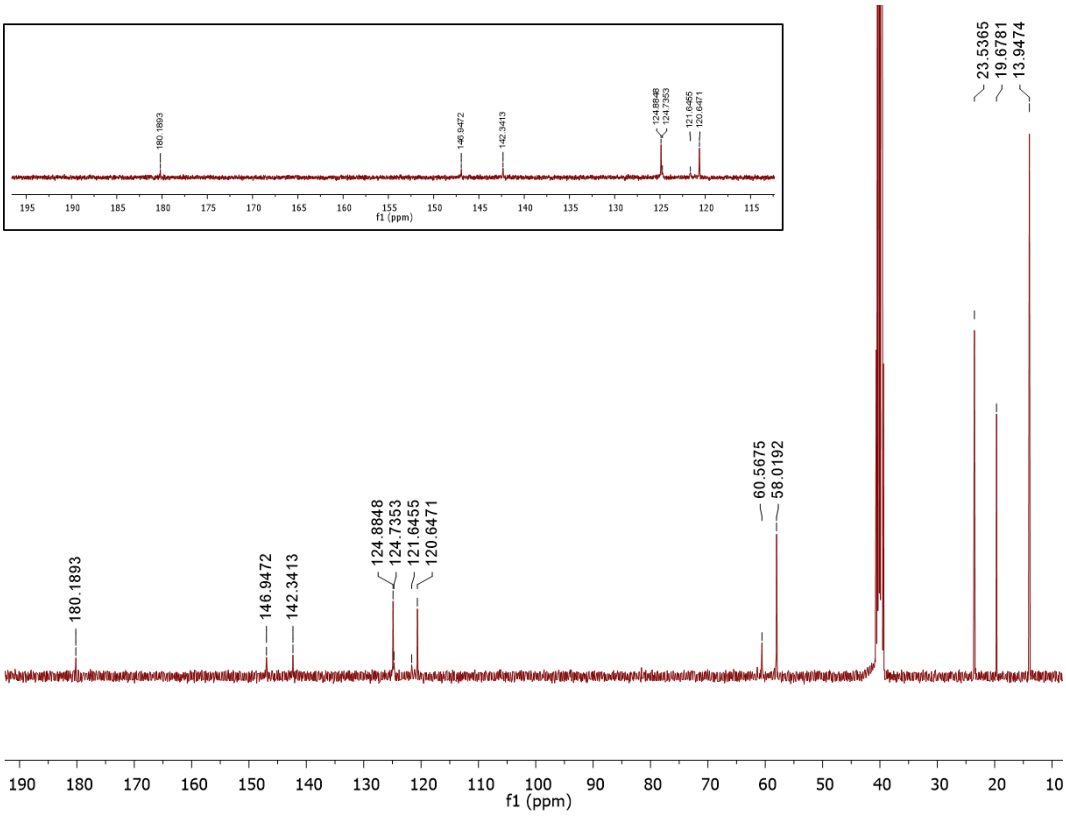

Figure S31 - ^{13}C NMR of compound **62** in DMSO-d_6 conducted at 298.15 K.

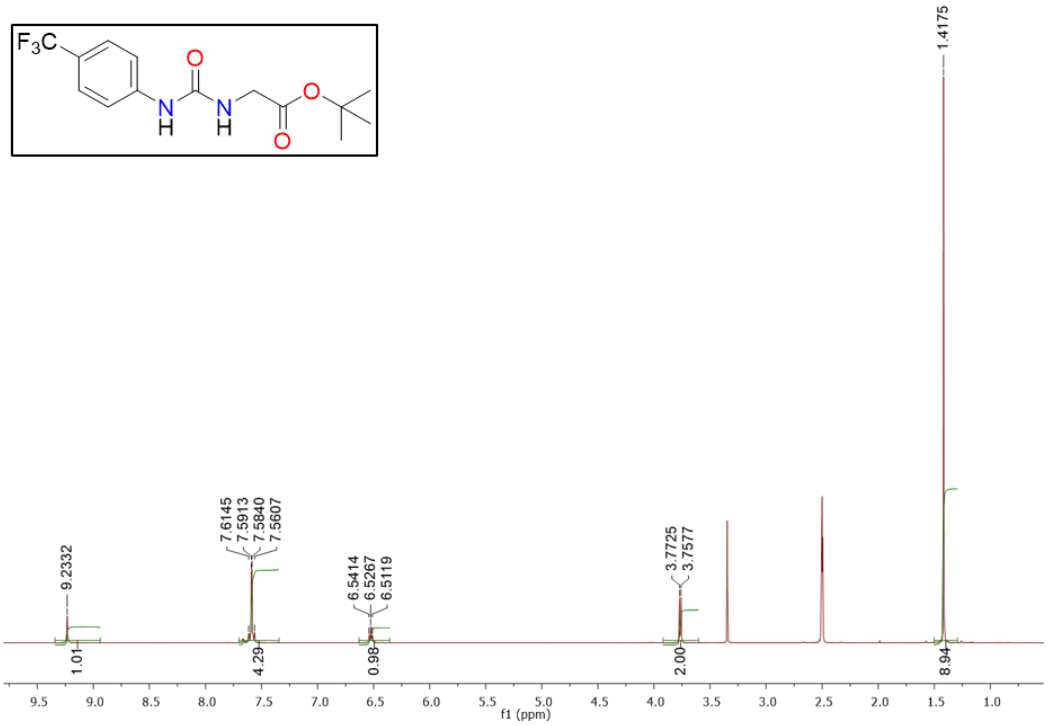

Figure S32 - ^{1}H NMR of compound **63** in DMSO-d_6 conducted at 298.15 K.

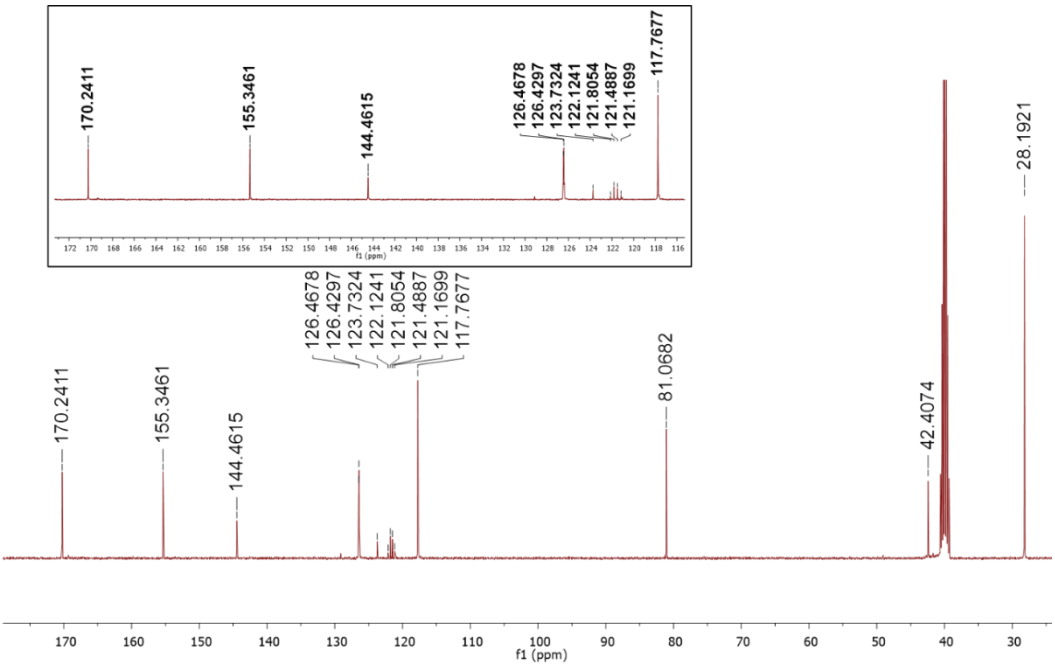

Figure S33 - ^{13}C NMR of compound **63** in DMSO-d_6 conducted at 298.15 K.

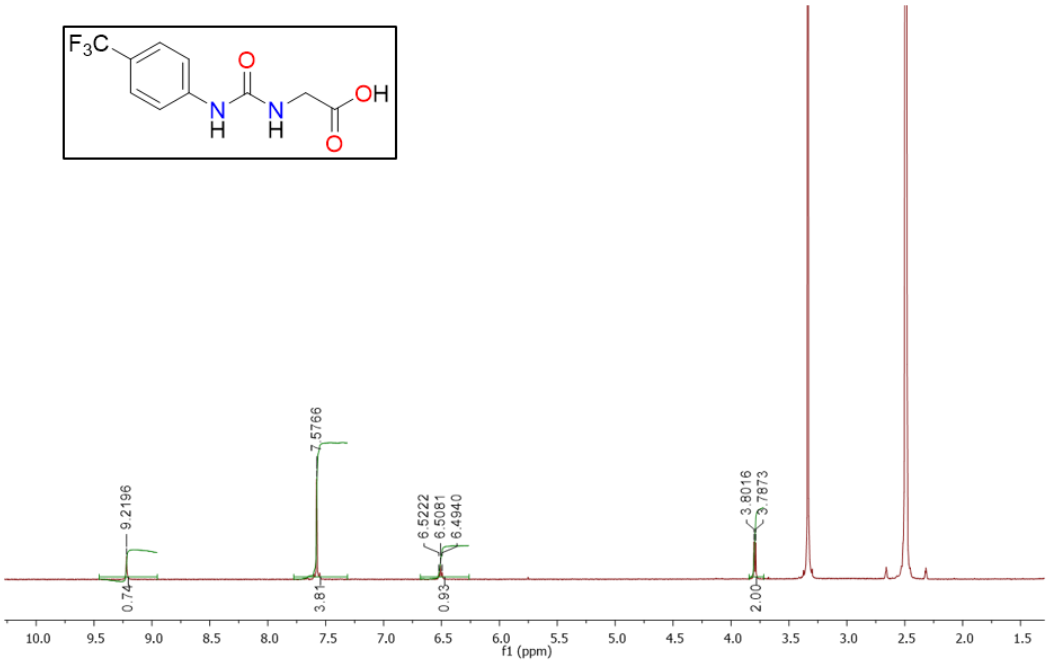

Figure S34 - ^{1}H NMR of compound **64** in DMSO-d_6 conducted at 298.15 K.

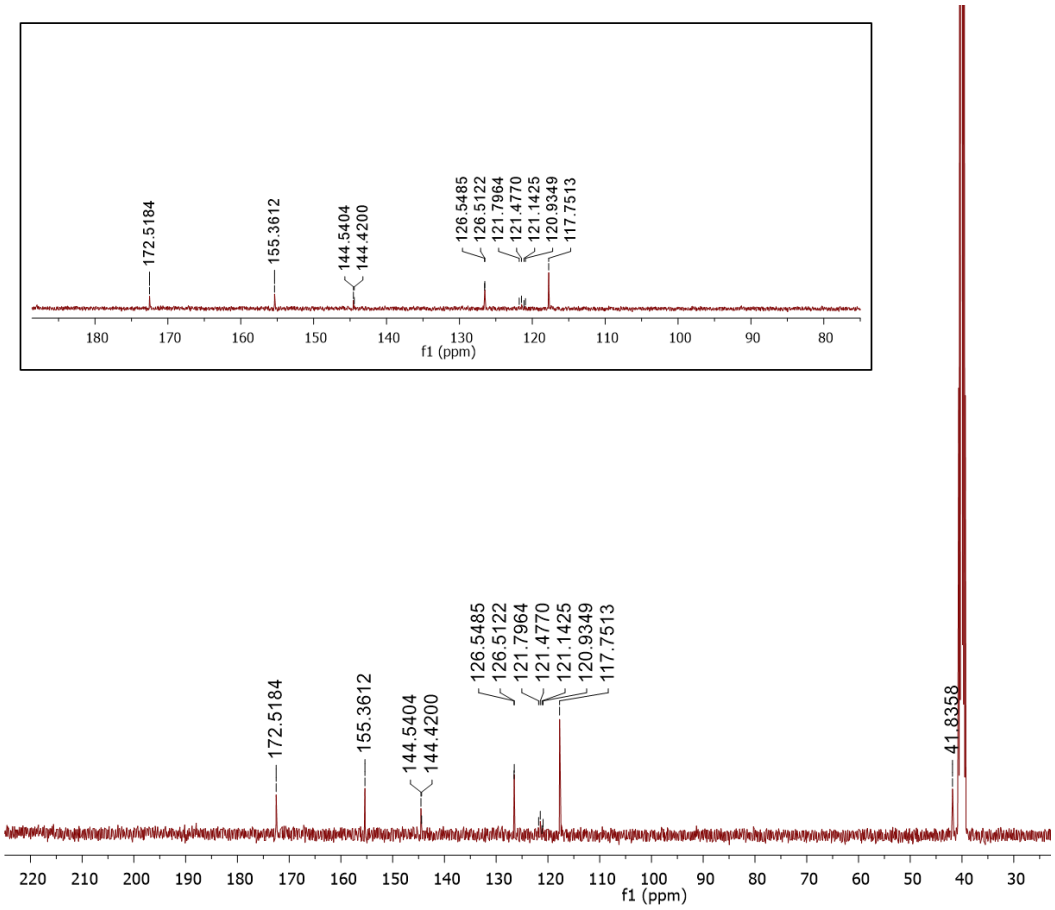

Figure S35 - ^{13}C NMR of compound **64** in DMSO-d_6 conducted at 298.15 K.

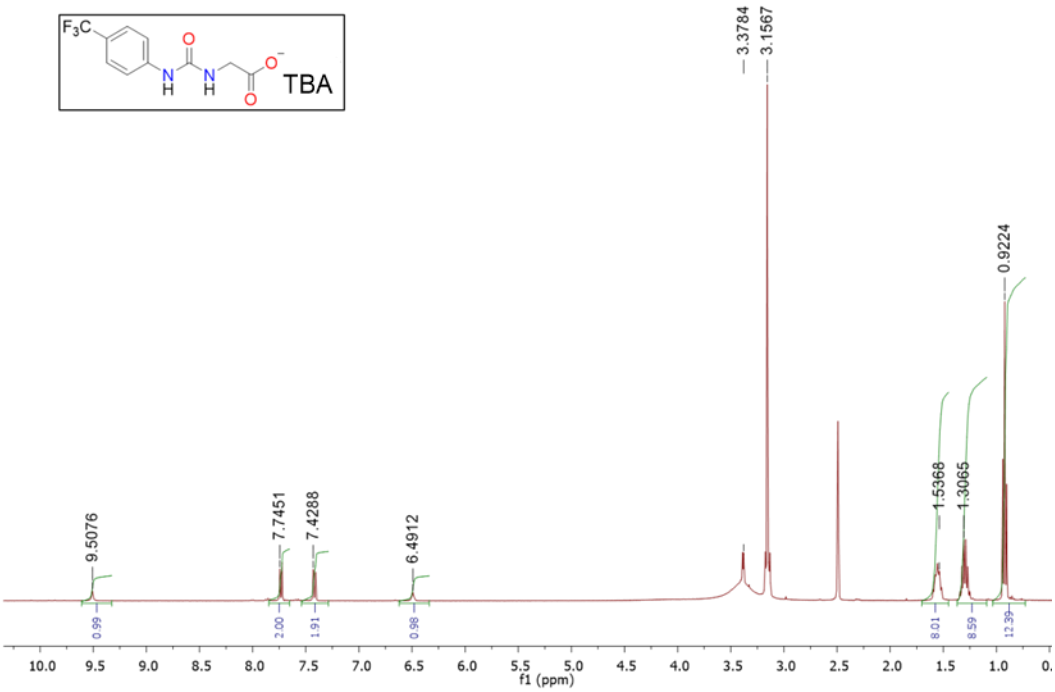

Figure S36 - ^{1}H NMR of compound **65** in DMSO-d_6 conducted at 298.15 K.

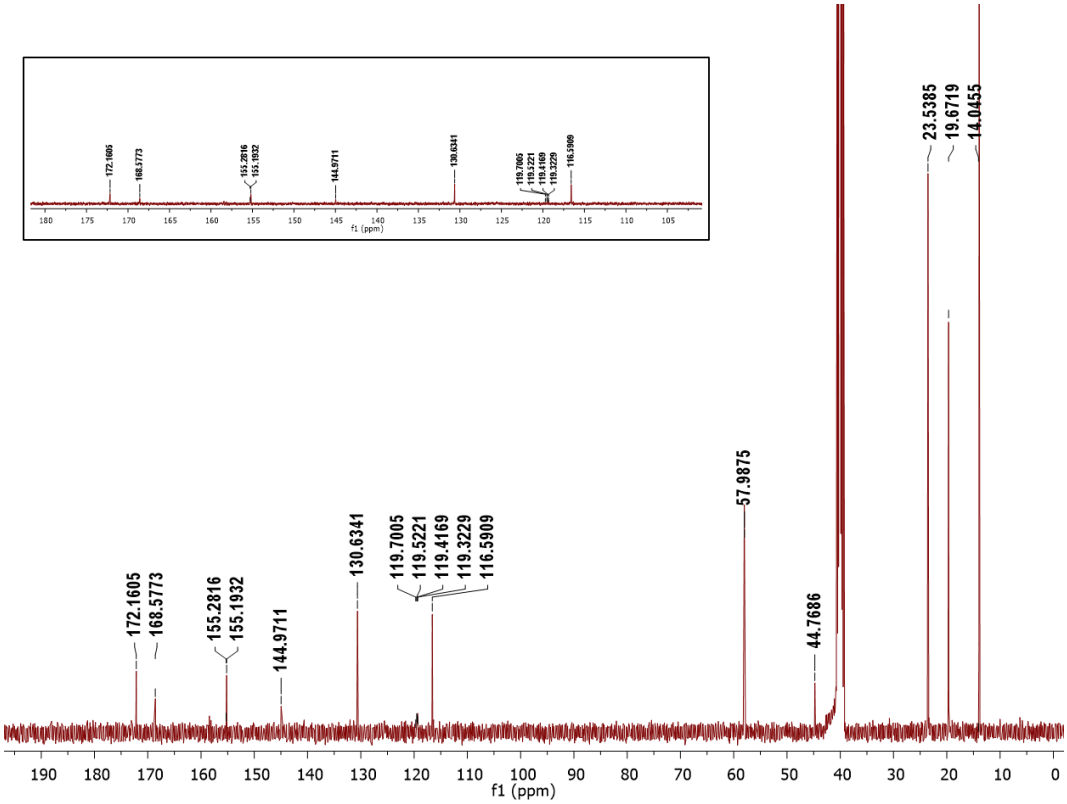

Figure S37 - ^{13}C NMR of compound **65** in DMSO-d_6 conducted at 298.15 K.

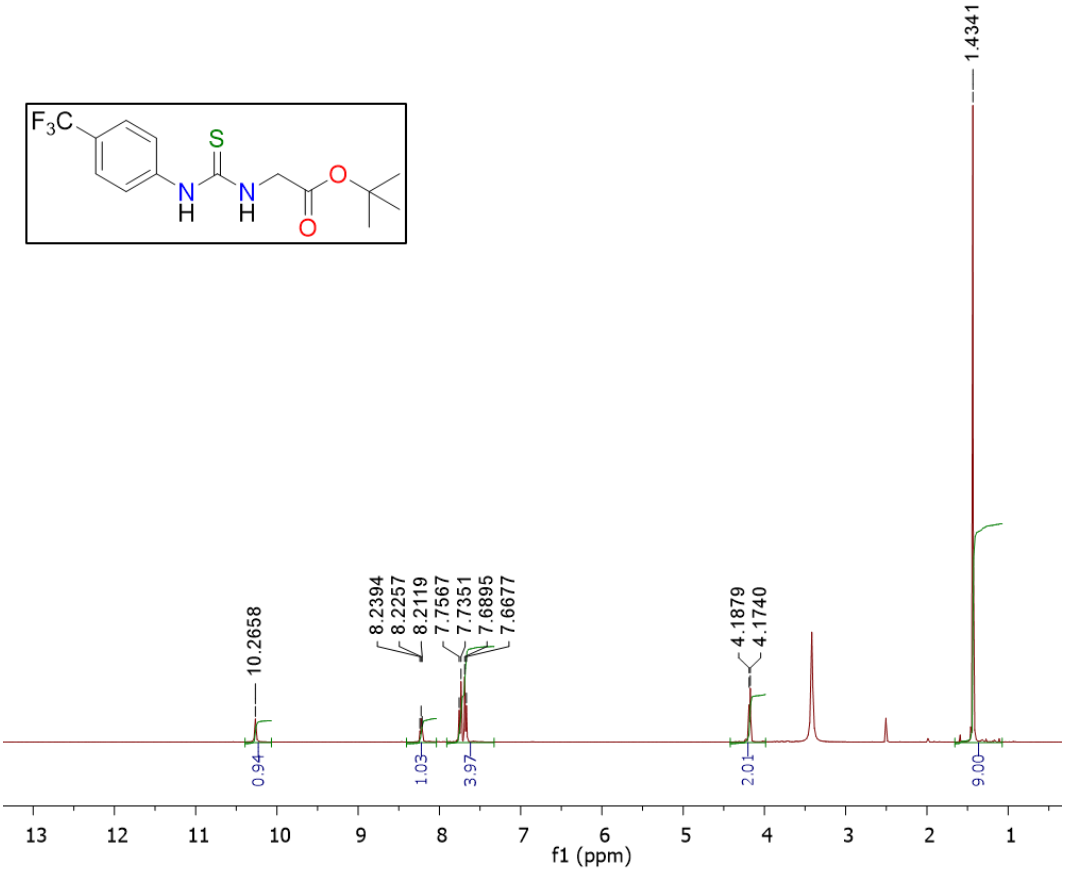

Figure S38 - ^{1}H NMR of compound **66** in DMSO-d_6 conducted at 298.15 K.

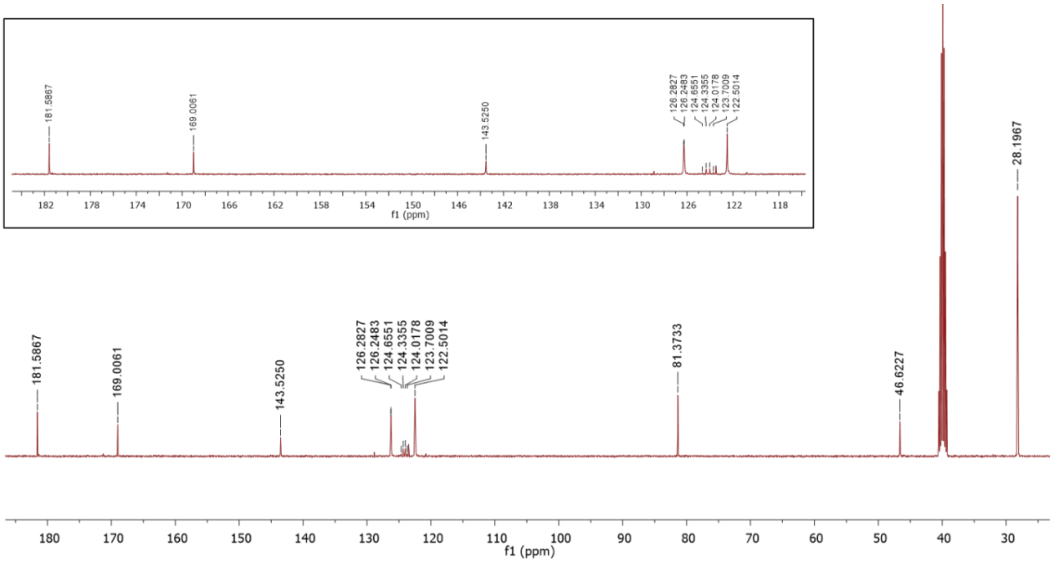

Figure S39 - ^{13}C NMR of compound **66** in DMSO-d_6 conducted at 298.15 K.

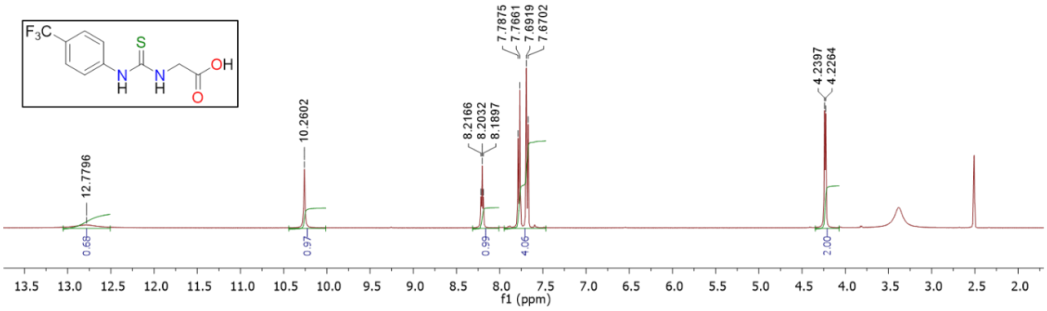

Figure S40 - ^{1}H NMR of compound **67** in DMSO-d_6 conducted at 298.15 K.

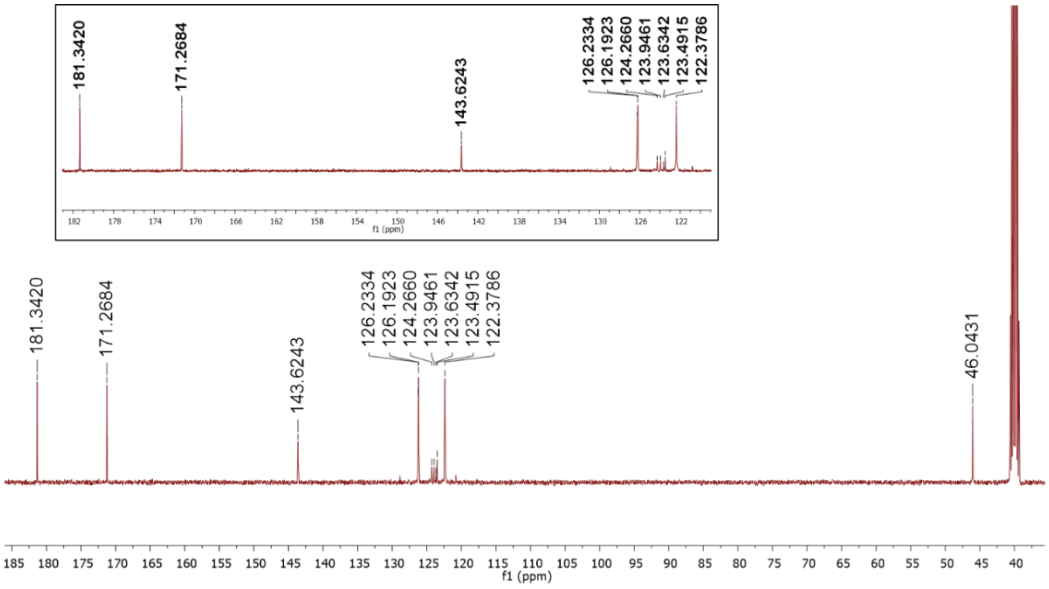

Figure S41 - ^{13}C NMR of compound **67** in DMSO-d_6 conducted at 298.15 K.

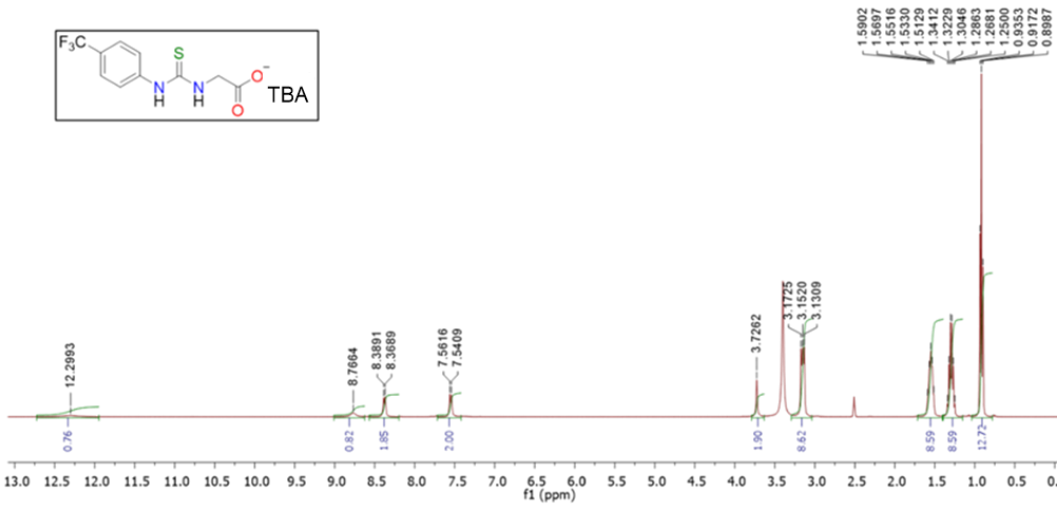

Figure S42 - ^{1}H NMR of compound **68** in DMSO-d_6 conducted at 298.15 K.

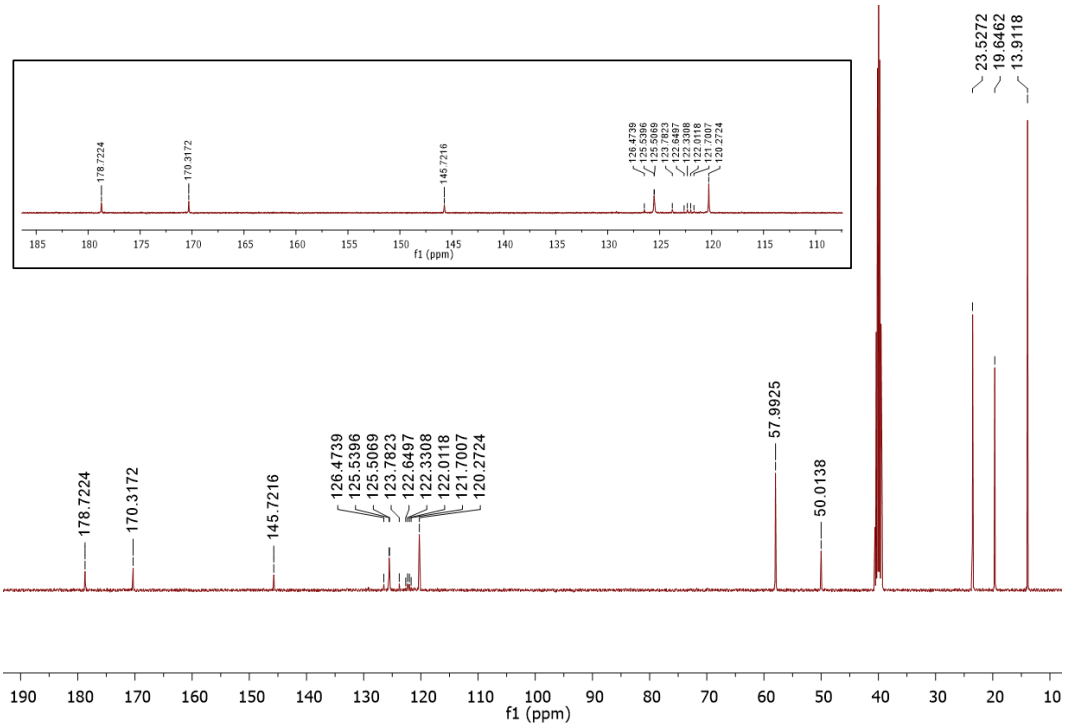

Figure S43 - ^{13}C NMR of compound **68** in DMSO-d_6 conducted at 298.15 K.

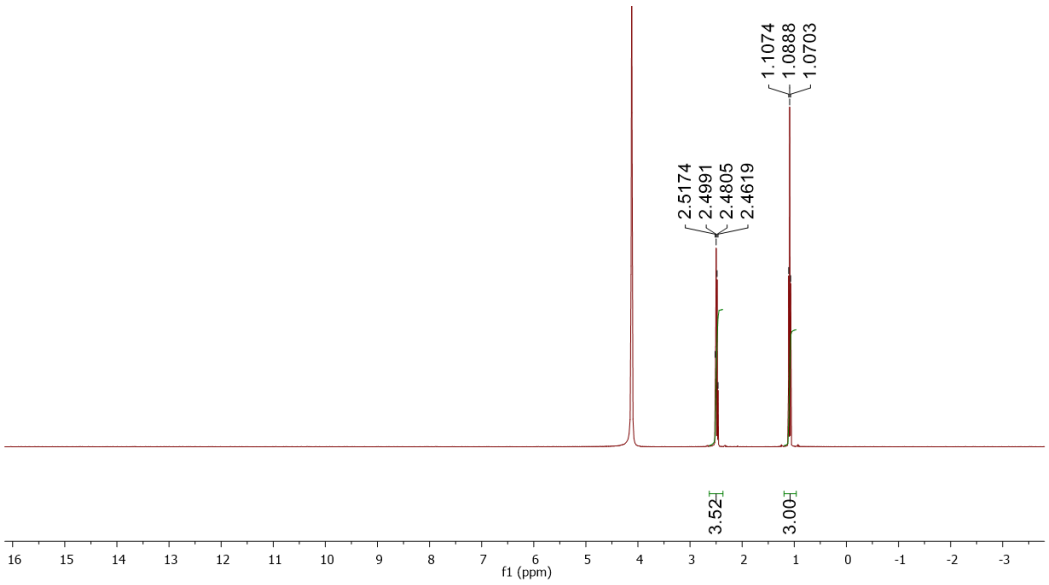

Figure S44 - ^{1}H NMR of compound **73** (55.56 mM) in DMSO-d_6 conducted at 298.15 K.

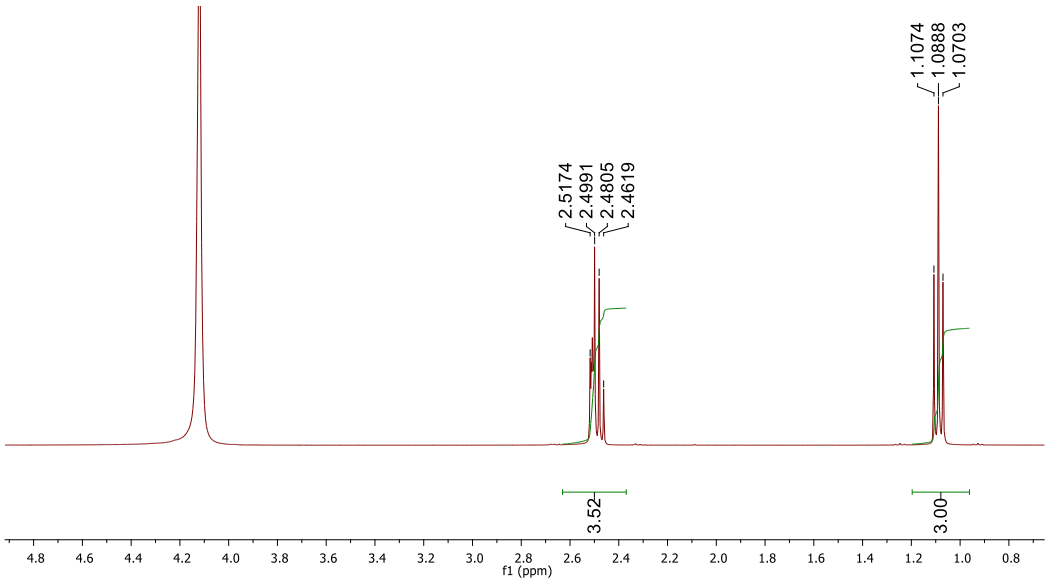

Figure S45 - Enlarged ^{1}H NMR of compound **73** (55.56 mM) in DMSO-d_6 conducted at 298.15 K.

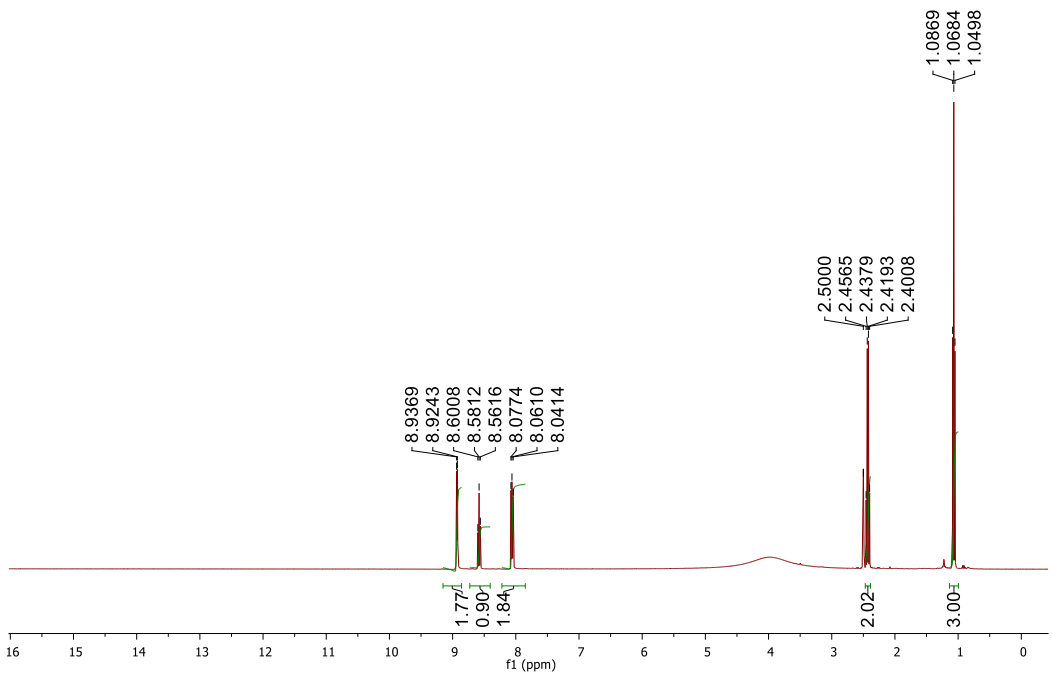

Figure S46 - ^{1}H NMR of compound **74** (55.56 mM) in DMSO-d_6 conducted at 298.15 K.

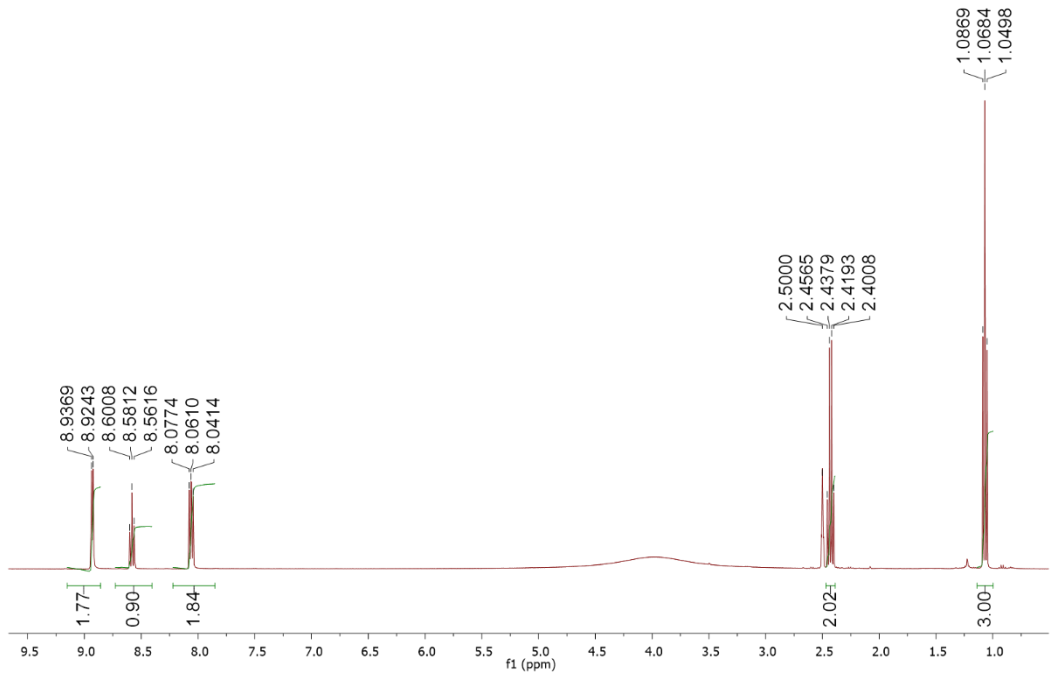

Figure S47 - Enlarged ^{1}H NMR of compound **74** (55.56 mM) in DMSO-d_6 conducted at 298.15 K.

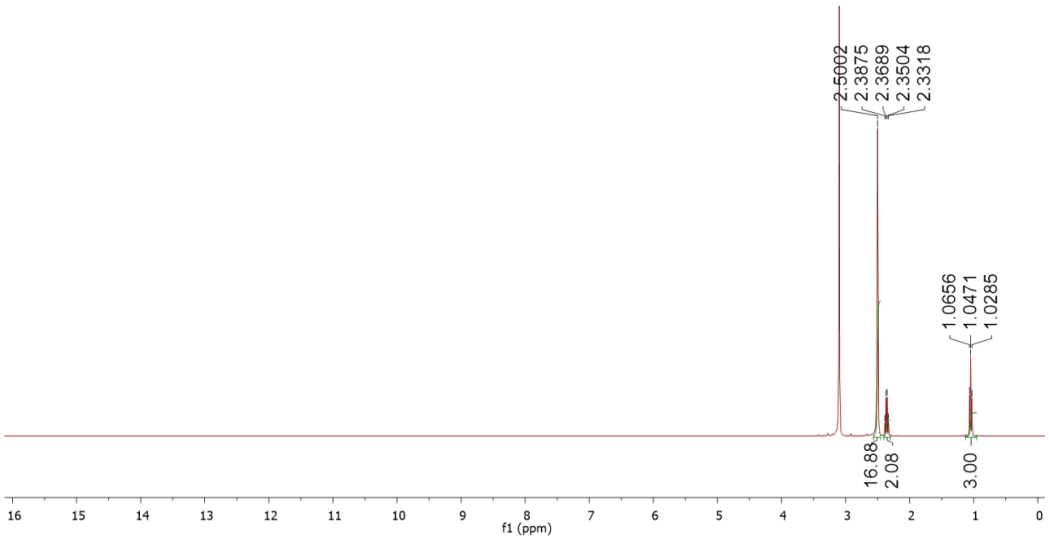

Figure S48 - ^{1}H NMR of compound **75** (55.56 mM) in DMSO-d_6 conducted at 298.15 K.

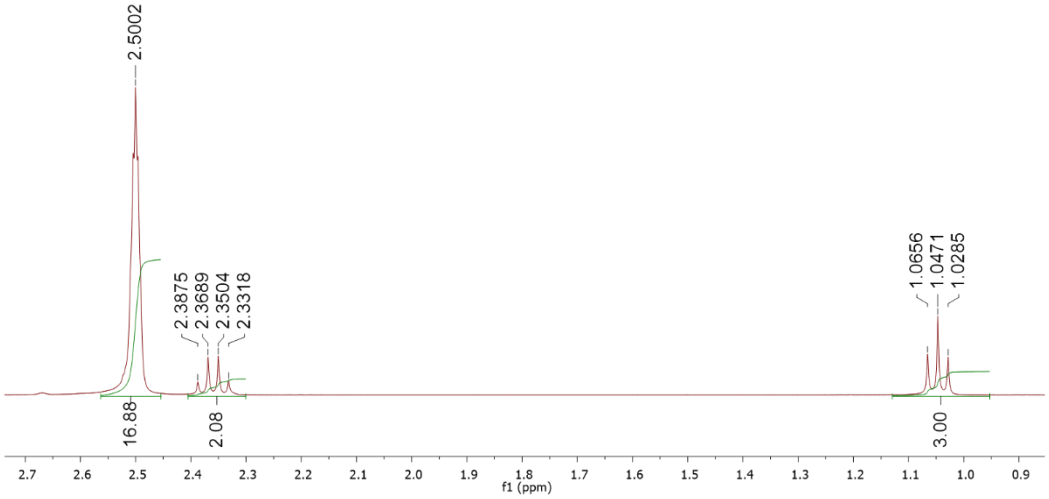

Figure S49 - Enlarged ^{1}H NMR of compound **75** (55.56 mM) in DMSO-d_6 conducted at 298.15 K.

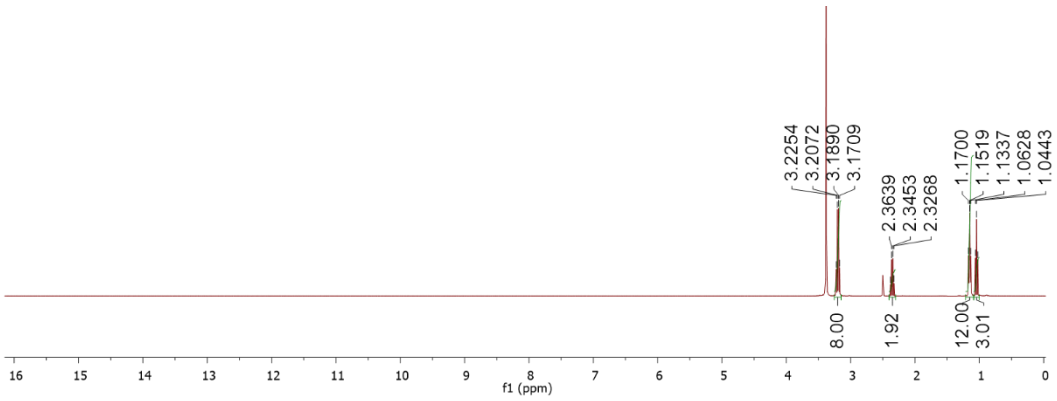

Figure S50 - ^{1}H NMR of compound **76** (55.56 mM) in DMSO-d_6 conducted at 298.15 K.

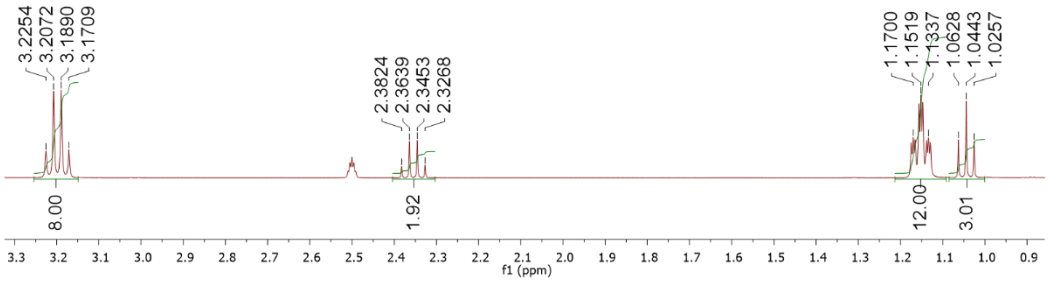

Figure S51 - Enlarged ^{1}H NMR of compound **76** (55.56 mM) in DMSO-d_6 conducted at 298.15 K.

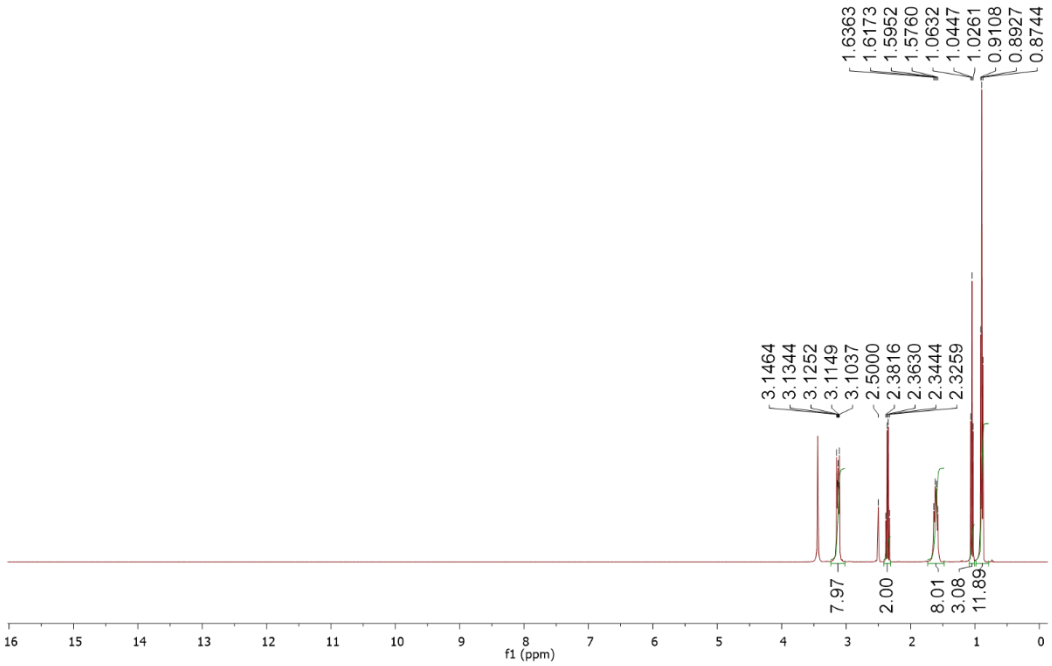

Figure S52 - ^{1}H NMR of compound **77** (55.56 mM) in DMSO-d_6 conducted at 298.15 K.

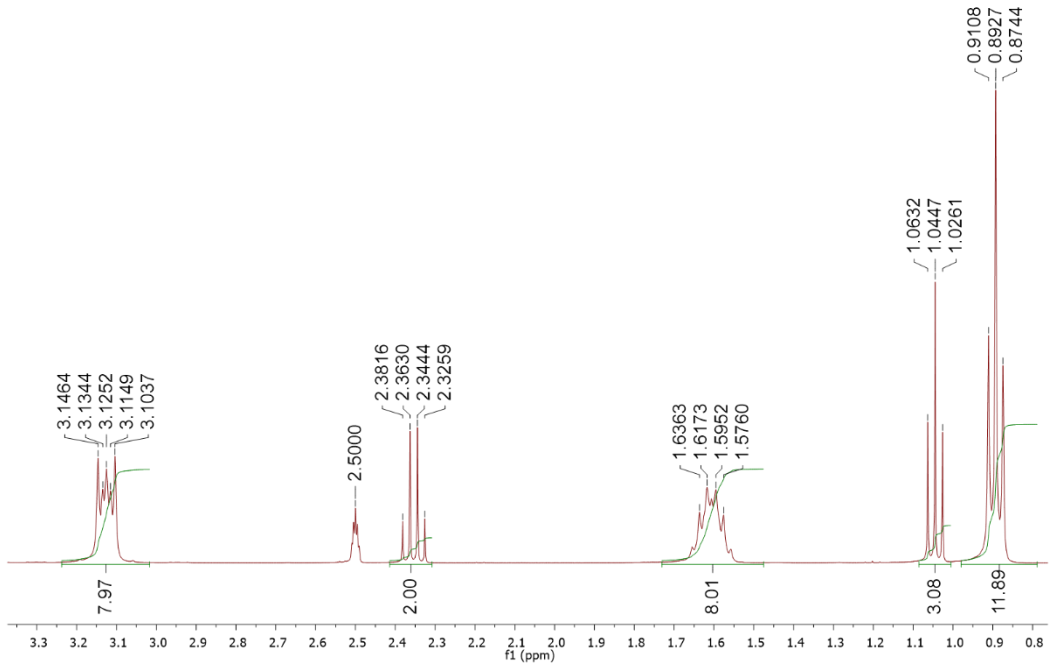

Figure S53 - Enlarged ^{1}H NMR of compound **77** (55.56 mM) in DMSO-d_6 conducted at 298.15 K.

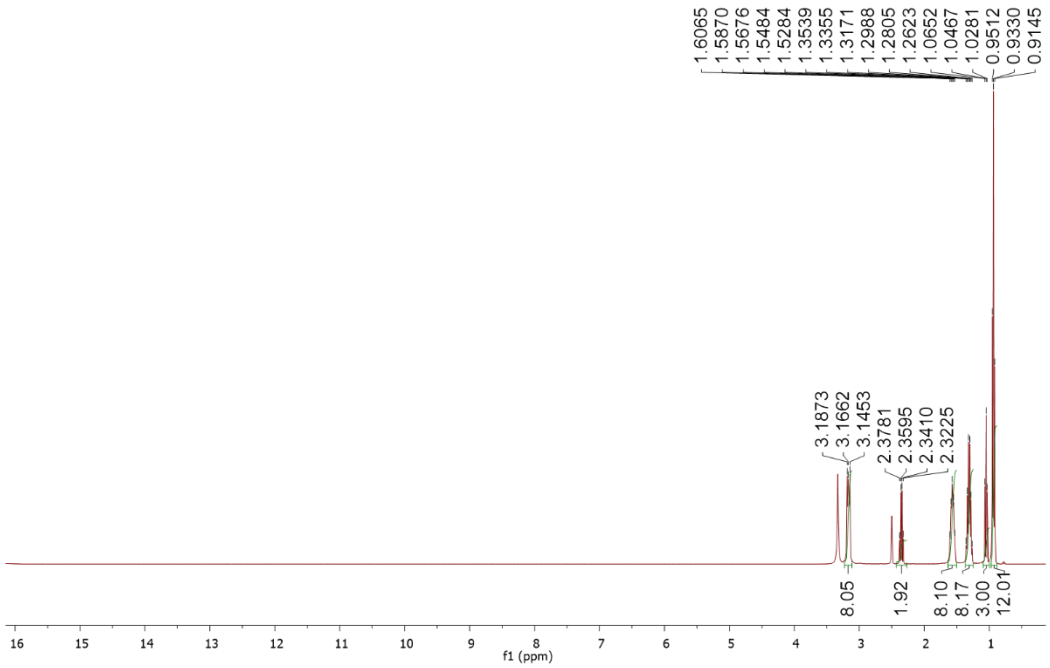

Figure S54 - ^{1}H NMR of compound **78** (55.56 mM) in DMSO-d_6 conducted at 298.15 K.

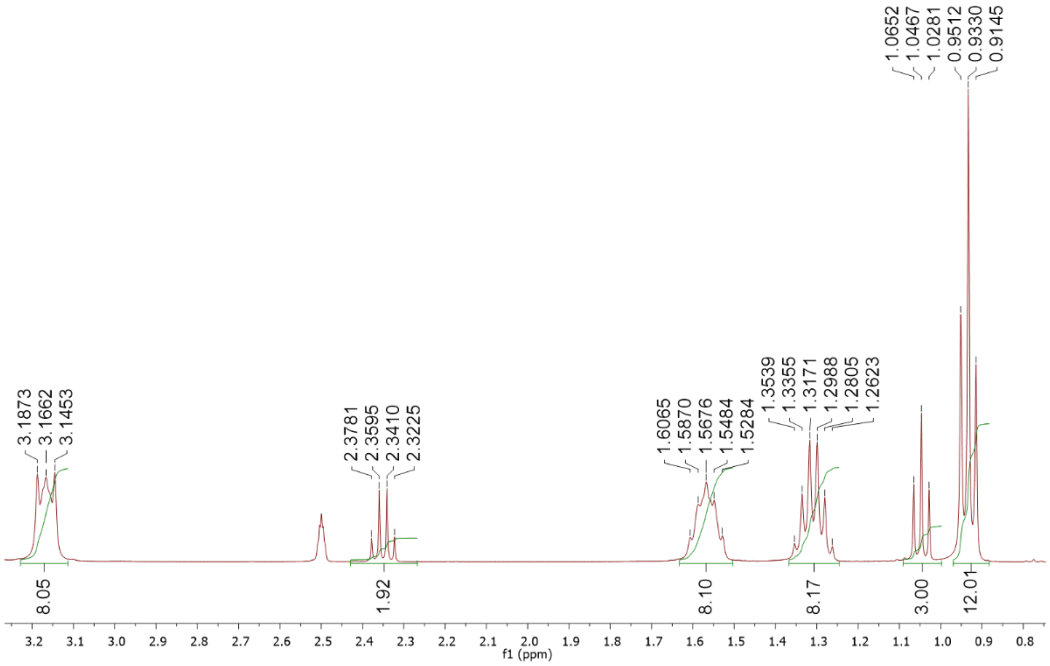

Figure S55 - Enlarged ^{1}H NMR of compound **78** (55.56 mM) in DMSO-d_6 conducted at 298.15 K.

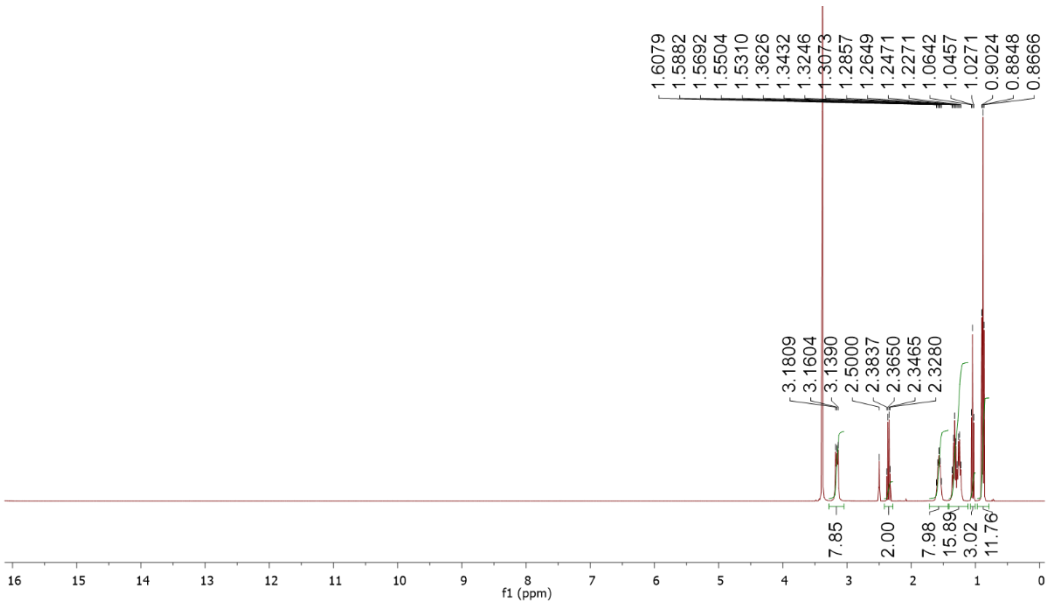

Figure S56 - ^{1}H NMR of compound **79** (55.56 mM) in DMSO-d_6 conducted at 298.15 K.

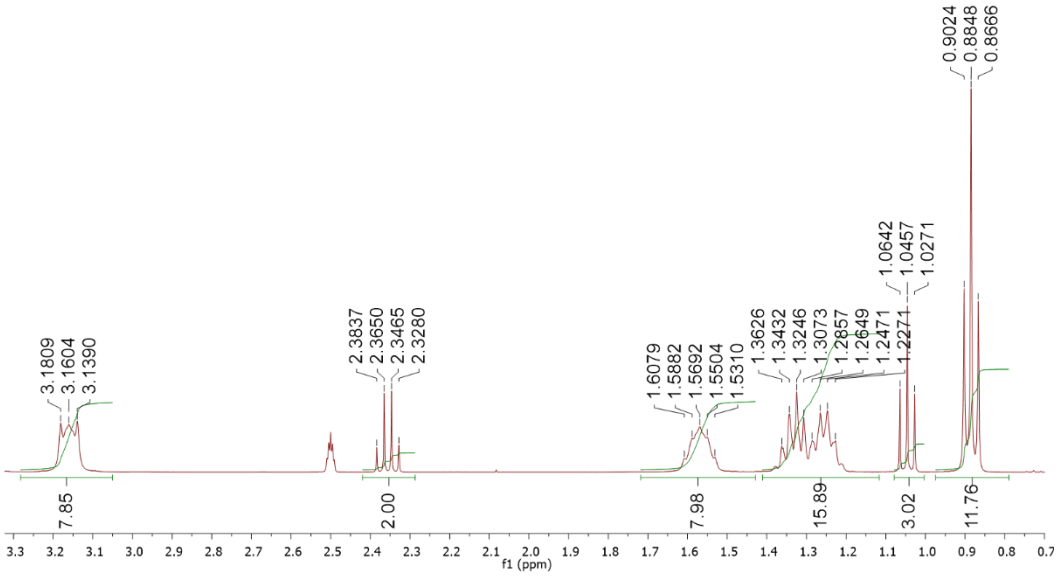

Figure S57 - Enlarged ^{1}H NMR of compound **79** (55.56 mM) in DMSO-d_6 conducted at 298.15 K.

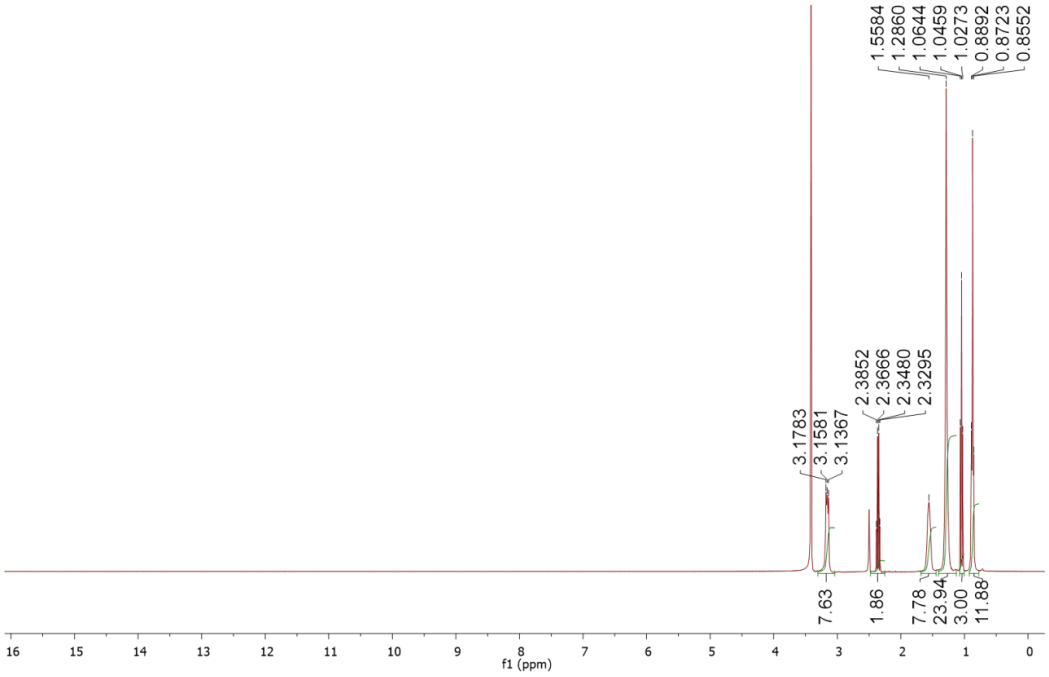

Figure S58 - ^{1}H NMR of compound **80** (55.56 mM) in DMSO-d_6 conducted at 298.15 K.

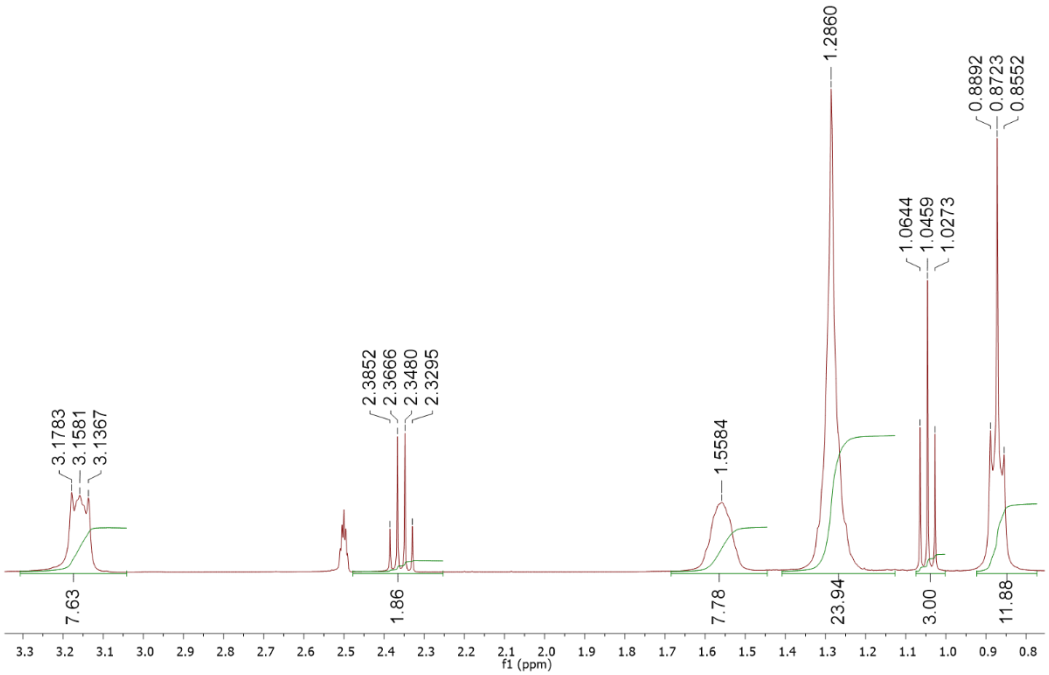

Figure S59 - Enlarged ^{1}H NMR of compound **80** (55.56 mM) in DMSO-d_6 conducted at 298.15 K.

1.2 Single crystal X-ray structures

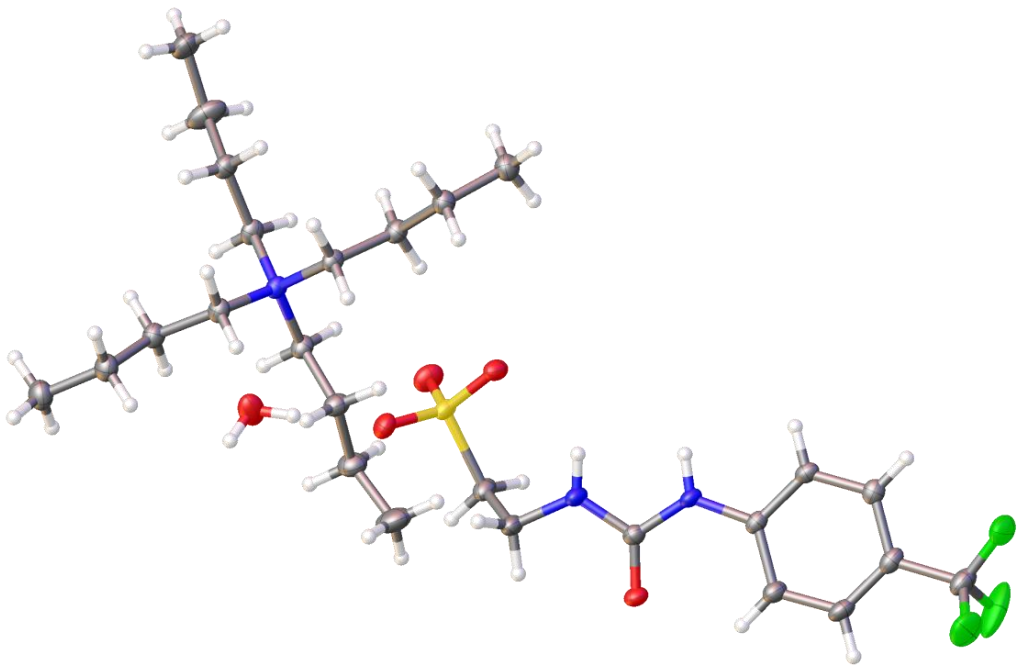

Figure S60 - Crystal data for compound **43**: red = oxygen; yellow = sulfur; blue = nitrogen; white = hydrogen; grey = carbon; green = fluorine. CCDC 1589886, $C_{26}H_{48}F_3N_3O_5S$ (M =571.73): monoclinic, space group P 21/c, a = 9.5166(2) Å, b = 20.0606(3) Å, c = 16.0871(3) Å, α = 90°, β = 95.510(2)°, γ = 90°, V = 3056.98(10) Å^3, Z = 4, T = 270(1) K, CuK\α = 1.5418 Å, Dcalc = 1.242 g/cm^3, 50907 reflections measured (7.064 ≤ 2Θ ≤ 133.188), 5404 unique (R_{int} = 0.0585, R_{sigma} = 0.0259) which were used in all calculations. The final R_1 was 0.0375 (I > 2σ(I)) and wR_2 was 0.0958 (all data).

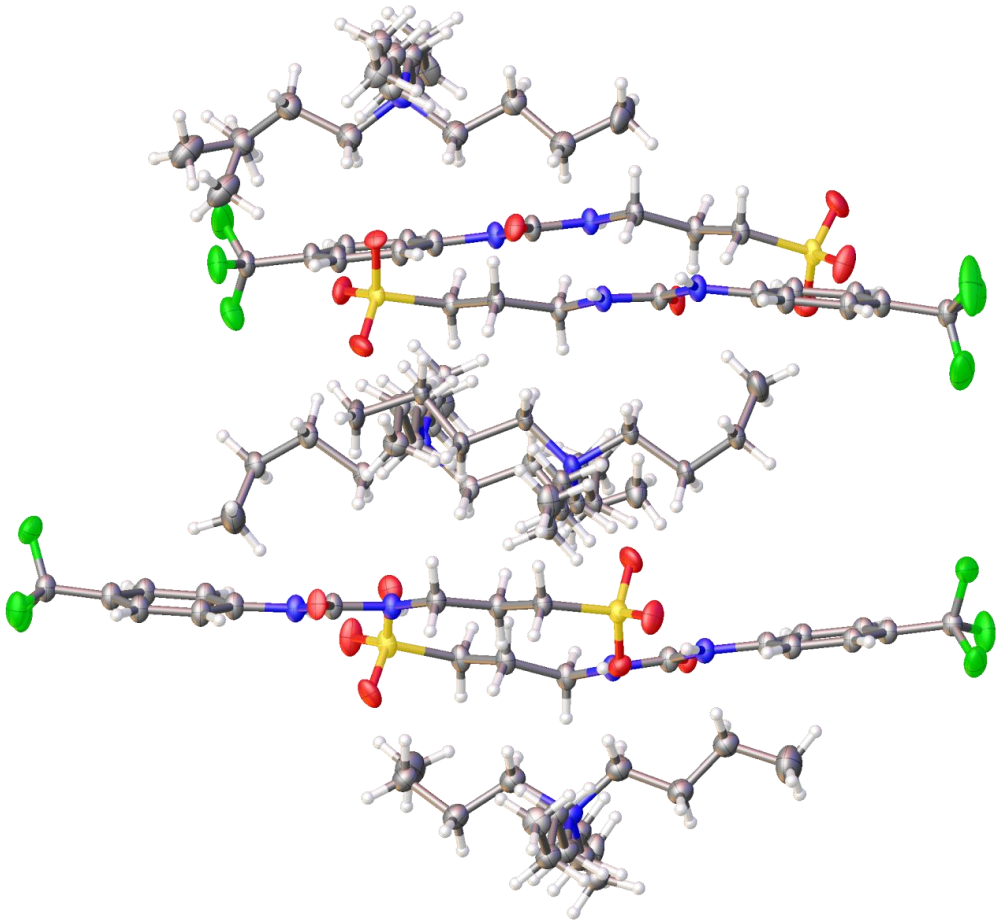

Figure S61 - Crystal data for compound **44**: red = oxygen; yellow = sulfur; blue = nitrogen; white = hydrogen; grey = carbon; green = fluorine. CCDC 1589882, $C_{27}H_{48}F_3N_3O_4S$ (M =567.74): monoclinic, space group P 21, a = 9.6443(3) Å, b = 31.9367(9) Å, c = 19.9817(6) Å, α = 90°, β = 101.941(3)°, γ = 90°, V = 6021.4(3) Å^3, Z = 8, T = 100(1) K, CuK\α = 1.5418 Å, Dcalc = 1.253 g/cm^3, 41806 reflections measured (5.300 ≤ 2Θ ≤ 133.198), 21243 unique (R_{int} = 0.0968, R_{sigma} = 0.1258) which were used in all calculations. The final R_1 was 0.1151 (I > 2σ(I)) and wR_2 was 0.3301 (all data).

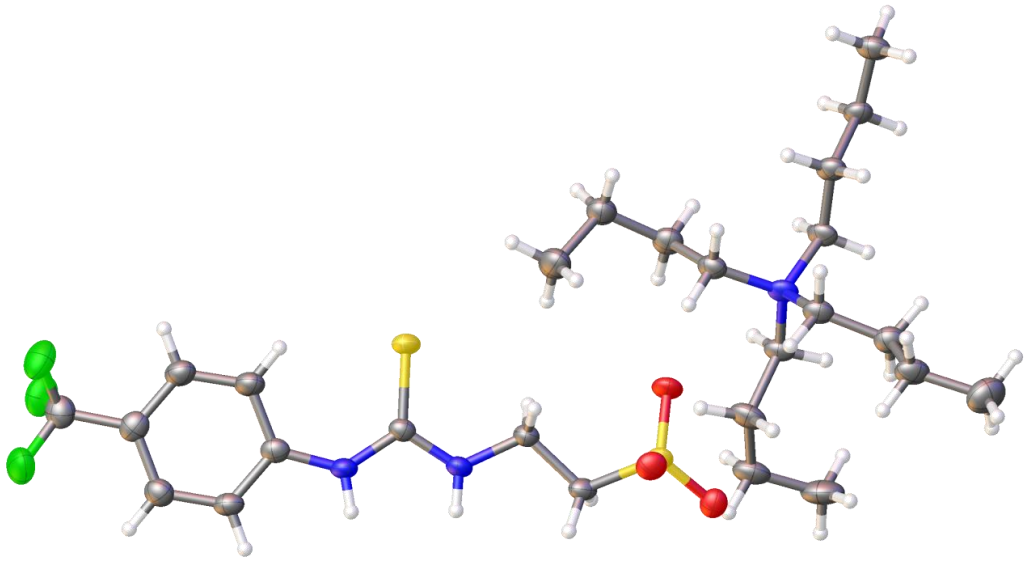

Figure S62 - Crystal data for compound **46**: red = oxygen; yellow = sulfur; blue = nitrogen; white = hydrogen; grey = carbon; green = fluorine. CCDC 1589887, $C_{26}H_{46}$ $F_3N_3O_3S_2$ (M =569.78): monoclinic, space group P 21/n, a = 17.8100(12) Å, b = 9.7869(7) Å, c = 19.6552(13) Å, α = 90°, β = 116.887(8)°, γ = 90°, V = 3055.6(4) Å^3, Z = 4, T = 270(1) K, CuK\α = 1.5418 Å, Dcalc = 1.239 g/cm^3, 47851 reflections measured (5.568 ≤ 2Θ ≤ 133.200), 5394 unique (R_{int} = 0.1287, R_{sigma} = 0.0656) which were used in all calculations. The final R_1 was 0.0713 (I > 2σ(I)) and wR_2 was 0.1864 (all data).

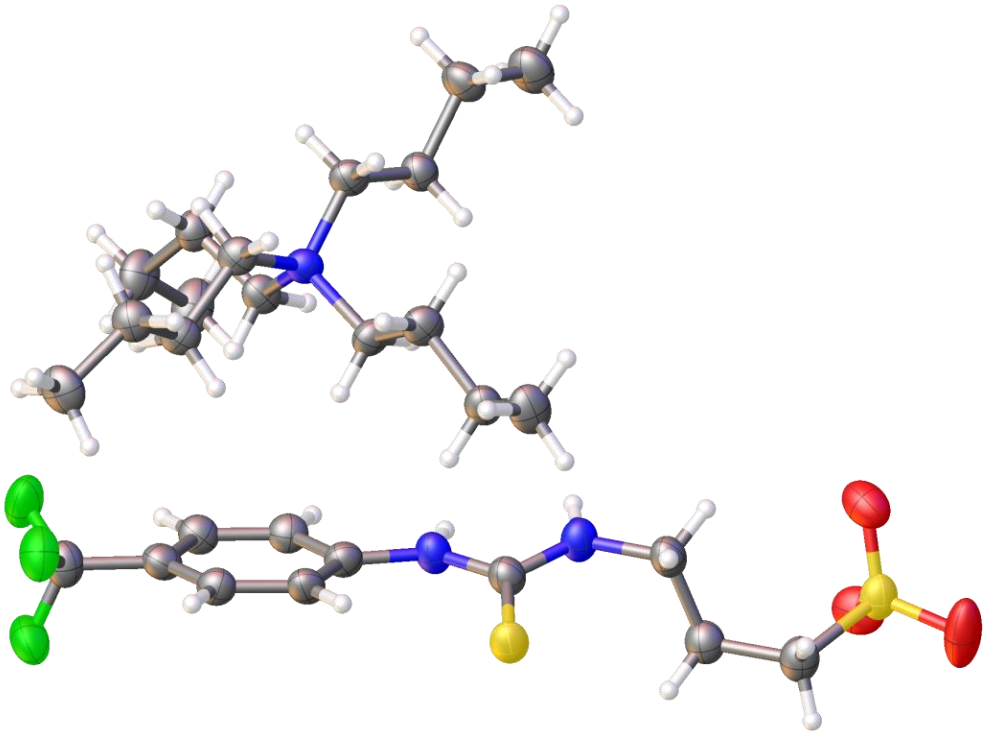

Figure S63 - Crystal data for compound **47**: red = oxygen; yellow = sulfur; blue = nitrogen; white = hydrogen; grey = carbon; green = fluorine. CCDC 1589888, $C_{27}H_{48}$ $F_3N_3O_3S_2$ (M =583.80): monoclinic, space group P 21/n, a = 9.6068(5) Å, b = 21.7563(9) Å, c = 14.6928(6) Å, α = 90°, β = 91.199(4)°, γ = 90°, V = 3070.2(2) Å^3, Z = 4, T = 270(1) K, CuK\α = 1.5418 Å, Dcalc = 1.263 g/cm^3, 47573 reflections measured (7.262 ≤ 2Θ ≤ 133.170), 5436 unique (R_{int} = 0.1816, R_{sigma} = 0.0773) which were used in all calculations. The final R_1 was 0.0946 (I > 2σ(I)) and wR_2 was 0.3041 (all data).

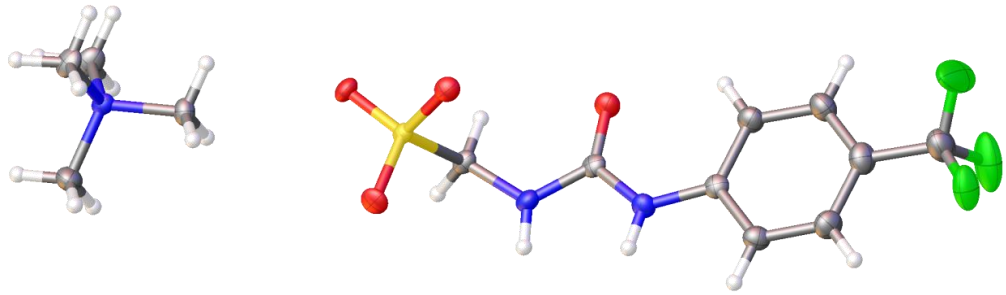

Figure S64 - Crystal data for compound **50**: red = oxygen; yellow = sulfur; blue = nitrogen; white = hydrogen; grey = carbon; green = fluorine. CCDC 1589880, $C_{13}H_{20}F_3N_3O_4S$ (M =371.38): monoclinic, space group C 2/c, a = 32.609(1) Å, b = 5.6739(2) Å, c = 19.0078(7) Å, α = 90°, β = 102.953(3)°, γ = 90°, V = 3427.3(2) Å^3, Z = 8, T = 100(1) K, CuK\α = 1.5418 Å, Dcalc = 1.439 g/cm^3, 13318 reflections measured (5.562 ≤ 2Θ ≤ 133.186), 3036 unique (R_{int} = 0.0627, R_{sigma} = 0.0523) which were used in all calculations. The final R_1 was 0.0604 (I > 2σ(I)) and wR_2 was 0.1718 (all data).

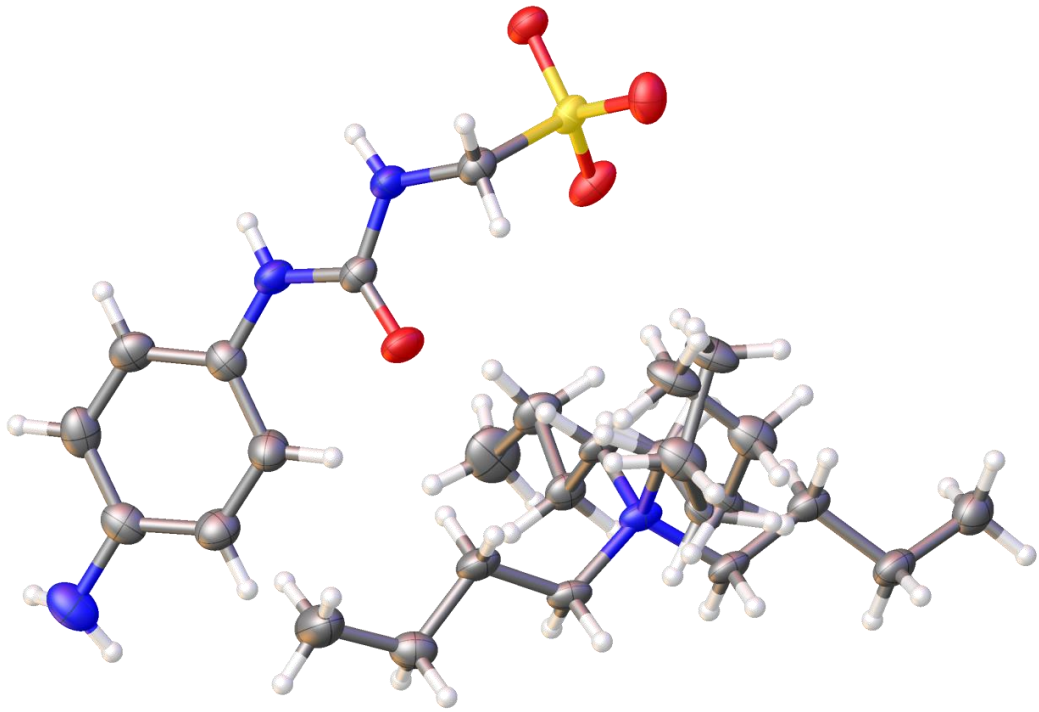

Figure S65 - Crystal data for compound **55**: red = oxygen; yellow = sulfur; blue = nitrogen; white = hydrogen; grey = carbon. CCDC 1589879, $C_{24}H_{46}N_4O_4S$ (M =486.71): monoclinic, space group P 21/n, a = 13.4243(13) Å, b = 14.8120(13) Å, c = 14.2467(16) Å, α = 90°, β = 106.523(11)°, γ = 90°, V = 2715.8(5) Å^3, Z = 4, T = 100(1) K, CuK\α = 1.5418 Å, Dcalc = 1.190 g/cm^3, 10406 reflections measured (7.998 ≤ 2Θ ≤ 133.176), 4796 unique (R_{int} = 0.0437, R_{sigma} = 0.0457) which were used in all calculations. The final R_1 was 0.0560 (I > 2σ(I)) and wR_2 was 0.1634 (all data).

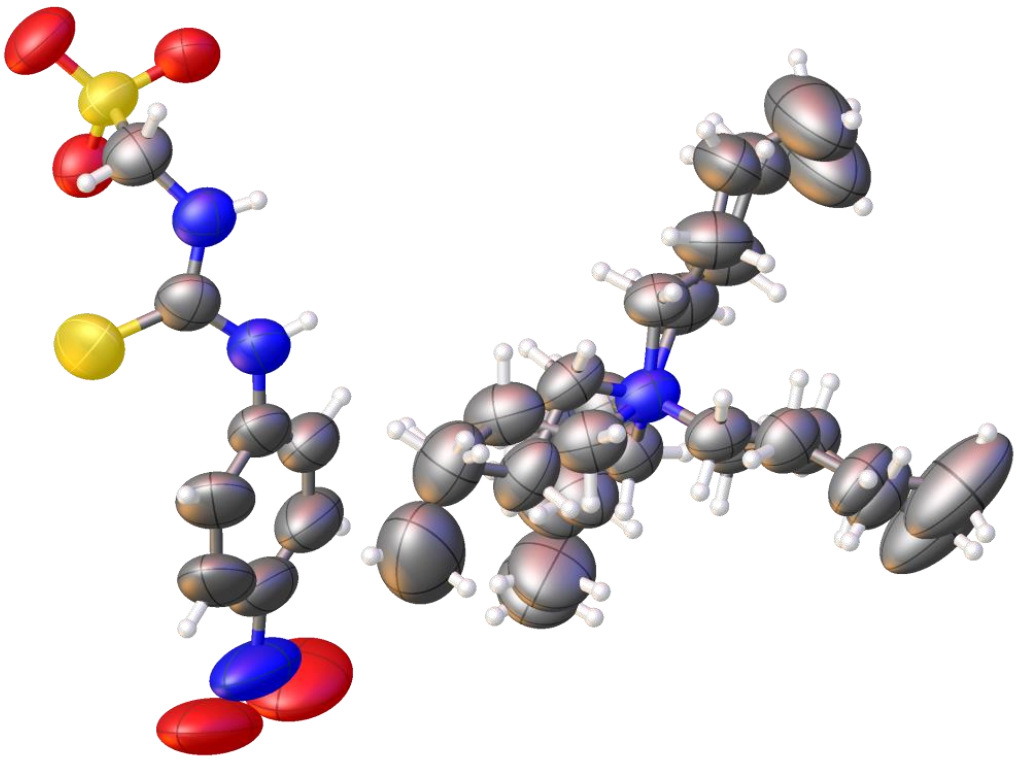

Figure S66 - Crystal data for compound **62**: red = oxygen; yellow = sulfur; blue = nitrogen; white = hydrogen; grey = carbon. CCDC 1589884, $C_{24}H_{44}N_4O_5S_2$ (M =532.75): monoclinic, space group C 2/c, a = 18.7541(18) Å, b = 16.1936(18) Å, c = 20.683(2) Å, α = 90°, β = 105.841(11)°, γ = 90°, V = 6042.7(11) Å^3, Z = 8, T = 290(1) K, CuK\α = 1.5418 Å, Dcalc = 1.171 g/cm^3, 26997 reflections measured (7.336 ≤ 2Θ ≤ 133.198), 5339 unique (R_{int} = 0.0422, R_{sigma} = 0.0246) which were used in all calculations. The final R_1 was 0.0706 (I > 2σ(I)) and wR_2 was 0.2426 (all data).

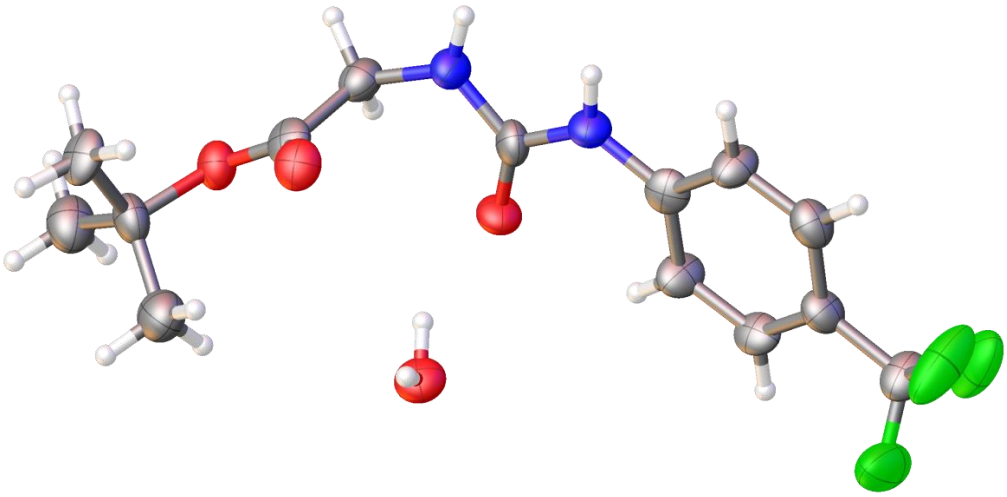

Figure S67 - Crystal data for compound **63**: red = oxygen; blue = nitrogen; white = hydrogen; grey = carbon; green = fluorine. CCDC 1589885, $C_{14}H_{19}F_3N_2O_4$ (M =336.31): triclinic, space group P -1, a = 6.4011(16) Å, b = 10.811(3) Å, c = 11.967(3) Å, α = 84.334(18)°, β = 88.945(19)°, γ = 81.70(2)°, V = 815(5) Å^3, Z = 2, T = 343(1) K, CuK\α = 1.5418 Å, Dcalc = 1.370 g/cm^3, 9213 reflections measured (7.422 ≤ 2Θ ≤ 108.462), 1970 unique (R_{int} = 0.1551, R_{sigma} = 0.1299) which were used in all calculations. The final R_1 was 0.1167 (I > 2σ(I)) and wR_2 was 0.2891 (all data).

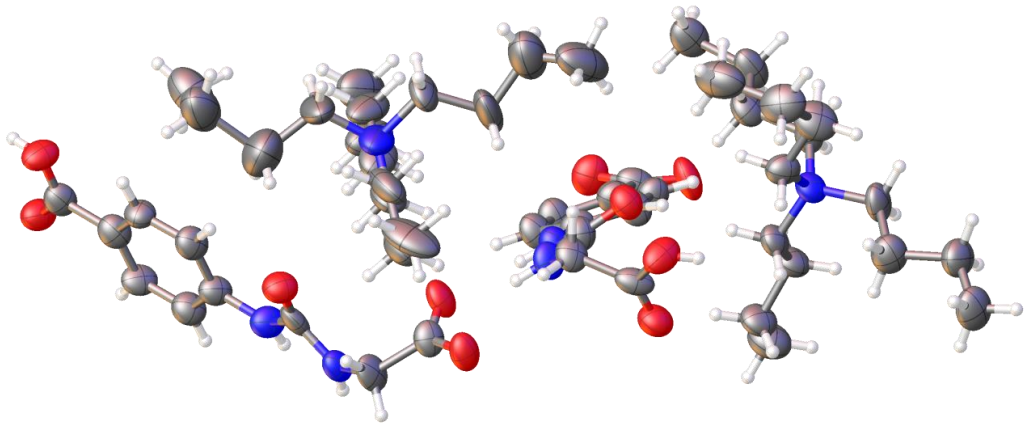

Figure S68 - Crystal data for a single crystal obtained from a solution of compound **65**: red = oxygen; blue = nitrogen; white = hydrogen; grey = carbon. CCDC 1589881, $C_{26}H_{45}N_3O_5$ (M =476.65): monoclinic, space group P n, a = 14.226(4) Å, b = 14.602(3) Å, c = 14.483(4) Å, α = 90°, β = 112.91(3)°, γ = 90°, V = 2771.0(13) Å^3, Z = 4, T = 100(1) K, CuK\α = 1.5418 Å, Dcalc = 1.150 g/cm^3, 15432 reflections measured (7.390 ≤ 2Θ ≤ 117.842), 6338 unique (R_{int} = 0.1754, R_{sigma} = 0.1246) which were used in all calculations. The final R_1 was 0.0865 (I > 2σ(I)) and wR_2 was 0.2092 (all data).

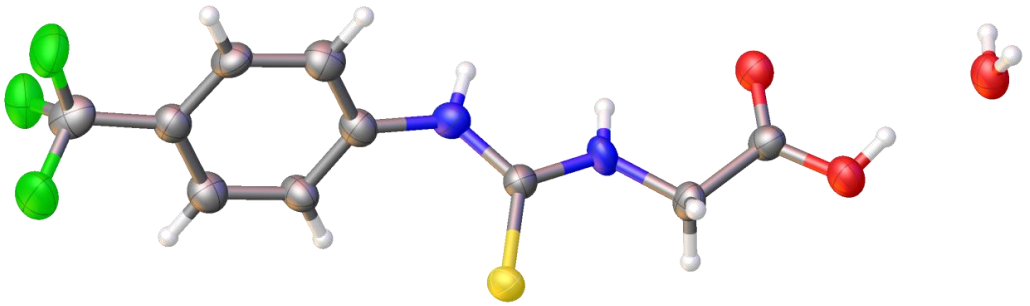

Figure S69 - Crystal data for compound **67**: red = oxygen; yellow = sulfur; blue = nitrogen; white = hydrogen; grey = carbon; green = fluorine. CCDC 1589883, $C_{10}H_{11}$ $F_3N_2O_3S$ (M =296.27): monoclinic, space group P 21/c, a = 20.786(10) Å, b = 6.941(2) Å, c = 8.610(2) Å, α = 90°, β = 100.49(4)°, γ = 90°, V = 1221.5(8) Å^3, Z = 4, T = 100(1) K, CuK\α = 1.5418 Å, Dcalc = 1.611 g/cm^3, 2649 reflections measured (8.625 ≤ 2Θ ≤ 133.198), 1825 unique (R_{int} = 0.0845, R_{sigma} = 0.1183) which were used in all calculations. The final R_1 was 0.1124 (I > 2σ(I)) and wR_2 was 0.3217 (all data).

1.2.1 Hydrogen bonding tables from single crystal X-ray structure

Table S1- Hydrogen bond distances and angles involved in N-H anion hydrogen bonded self-association, calculated from single crystal X-ray structures.

Compound	Hydrogen bond donor	Hydrogen atom	Hydrogen bond acceptor	Hydrogen bond length (D•••A) (Å)	Hydrogen bond angle (D-H•••A) (°)
2	N1	H1	O2	2.8954 (18)	163.42 (10)
2	N2	H2	O2	3.0960 (17)	149.23 (10)
2	N2	H2	O2	2.9813 (18)	122.31 (16)
3	N1	H1	O7	2.889 (13)	156.9 (7)
3	N2	H2	O7	2.917 (16)	154.0 (7)
3	N3	H3	O1	3.105 (15)	150.4 (7)
3	N4	H4	O1	2.967 (16)	151.7 (7)
3	N5	H5	O15	3.096 (15)	158.1 (7)
3	N6	H6	O14	2.980 (16)	148.1 (7)
3	N7	H7A	O9	2.909 (13)	157.5 (7)
3	N8	H8A	O9	2.916 (15)	152.4 (7)
5	N1	H1	O2	2.829 (4)	159.1 (2)
5	N2	H2	O1	2.918 (4)	159.9 (3)
6	N1	H1	O1	3.149 (5)	169.4 (3)
6	N2	H2	O3	3.013 (4)	141.7 (3)
9	N1	H1	O2	2.987 (3)	169.32 (18)
9	N2	H2	O3	2.862 (3)	172.3 (2)
14	N1	H1A	O3	3.094 (3)	154.41 (16)
14	N1	H1B	O3	3.423 (3)	153.24 (17)
14	N2	H2	O4	2.927 (2)	155.24 (15)
14	N3	H3	O4	2.903 (3)	152.77 (15)
21	N1	H1	O3	2.860 (3)	161.71 (16)
21	N2	H2	O1	2.897 (3)	154.17 (17)
23	N1	H1	O10	2.831 (13)	174.1 (10)
23	N2	H2	O9	2.828 (12)	159.9 (9)
23	N3	H3A	O1	2.884 (15)	155.2 (9)
23	N4	H4B	O1	2.812 (16)	152.2 (9)

1.3 Mass spectrometry data

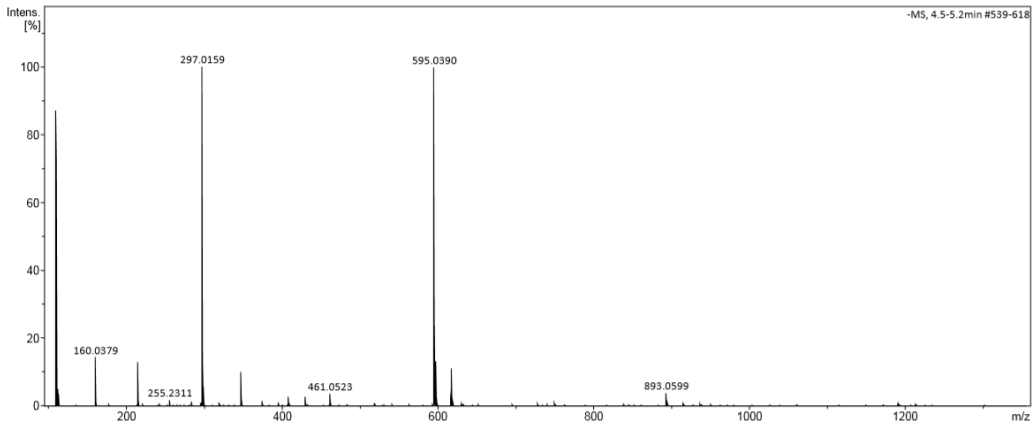

Figure S70 - ESI$^-$ mass spectrum collected for compound **42**.

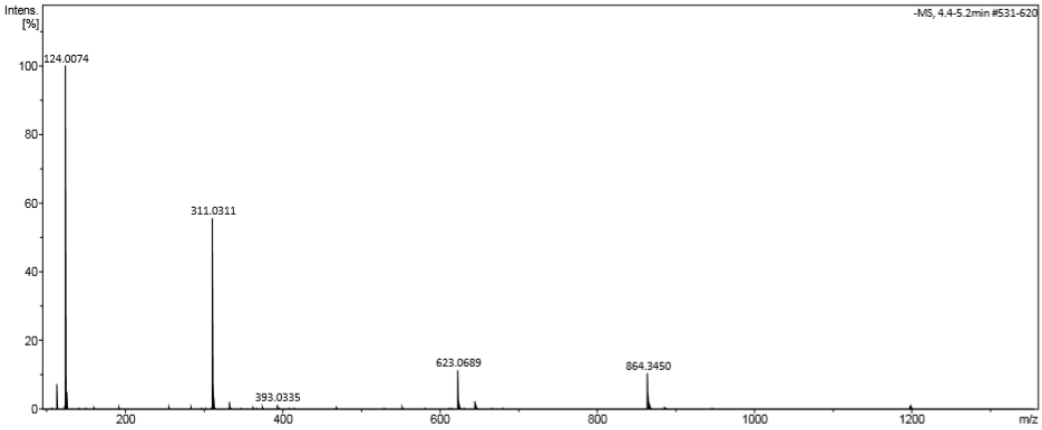

Figure S71 - ESI$^-$ mass spectrum collected for compound **43**.

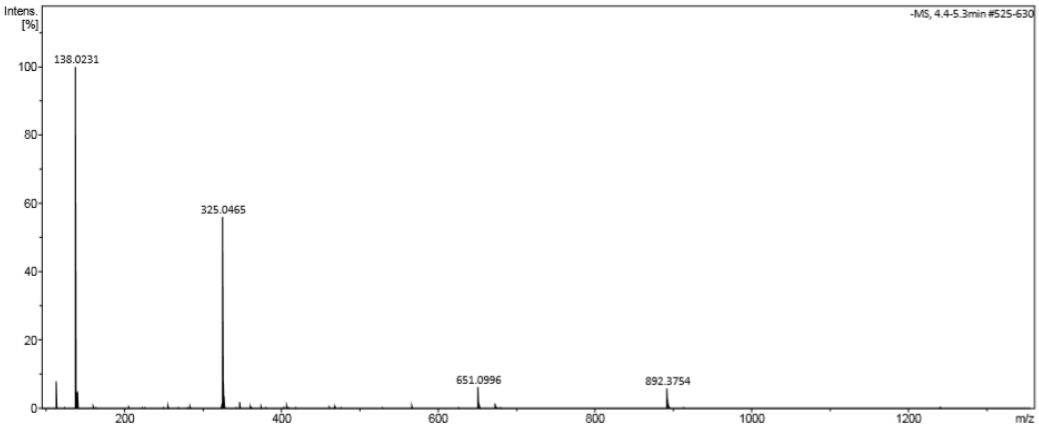

Figure S72 - ESI$^-$ mass spectrum collected for compound **44**.

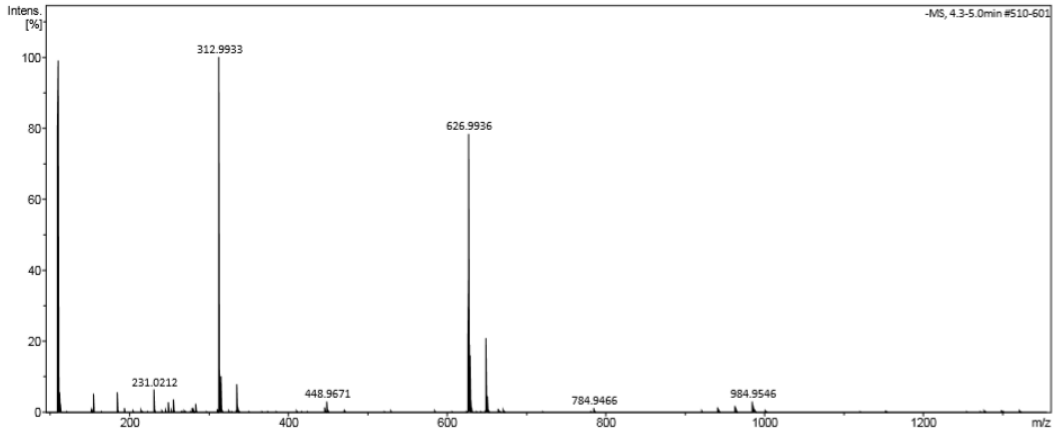

Figure S73 - ESI$^-$ mass spectrum collected for compound **45**.

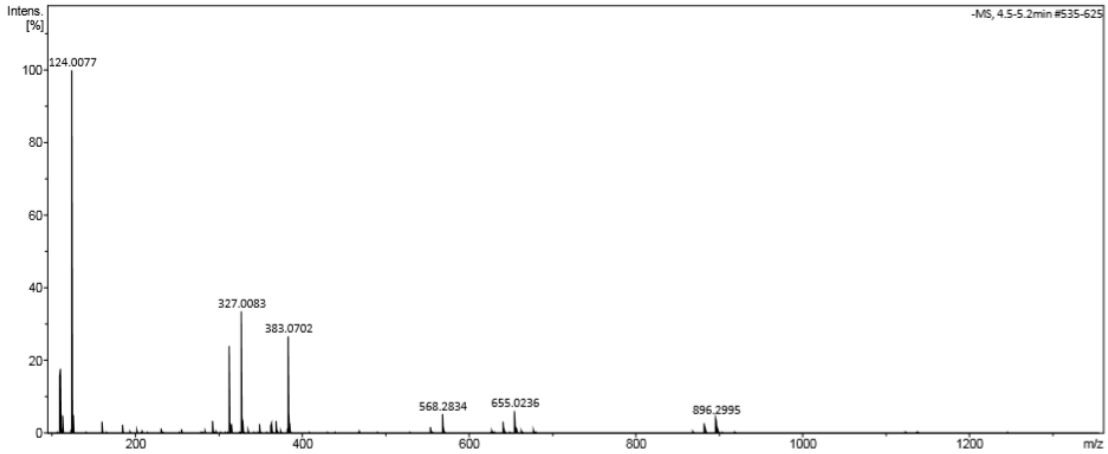

Figure S74 - ESI$^-$ mass spectrum collected for compound **46**.

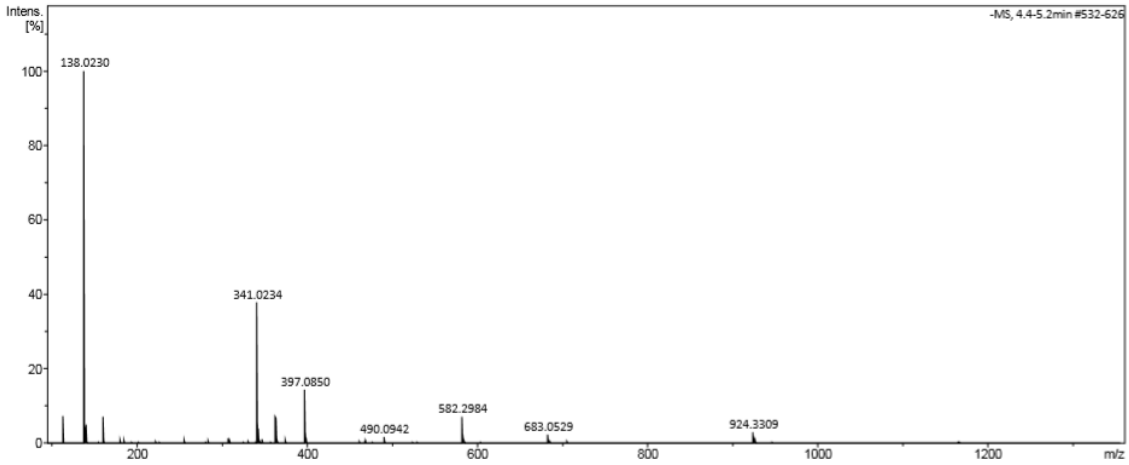

Figure S75 - ESI$^-$ mass spectrum collected for compound **47**.

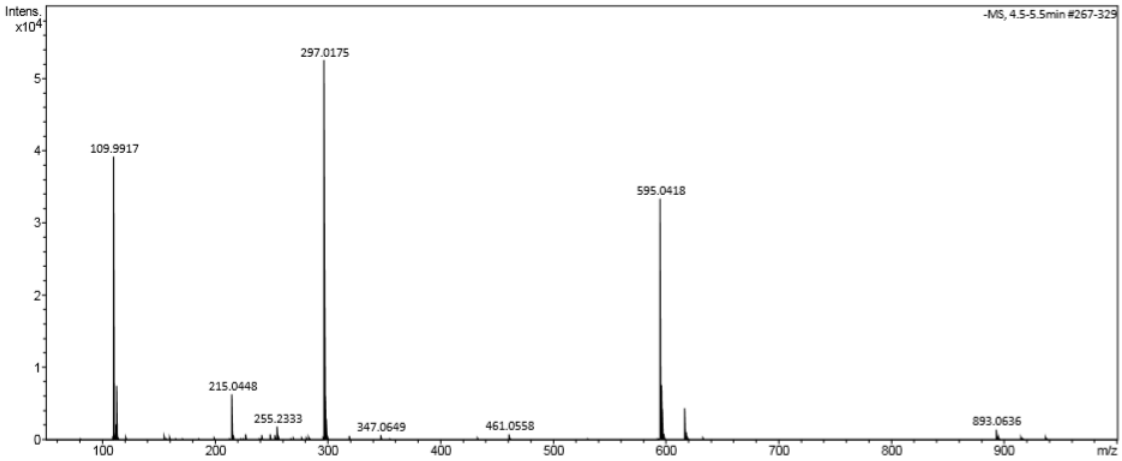

Figure S76 - ESI$^-$ mass spectrum collected for compound **48**.

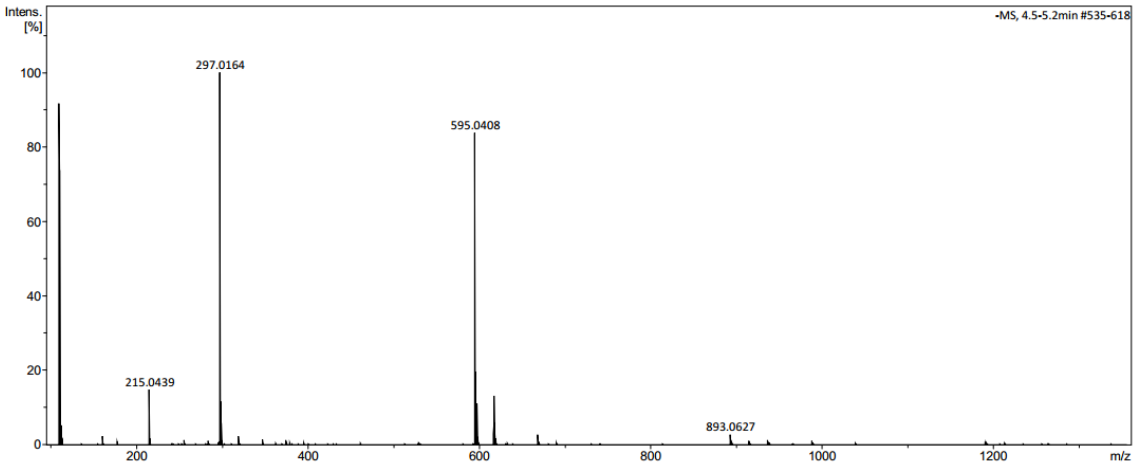

Figure S288 - ESI$^-$ mass spectrum collected for compound **49**.

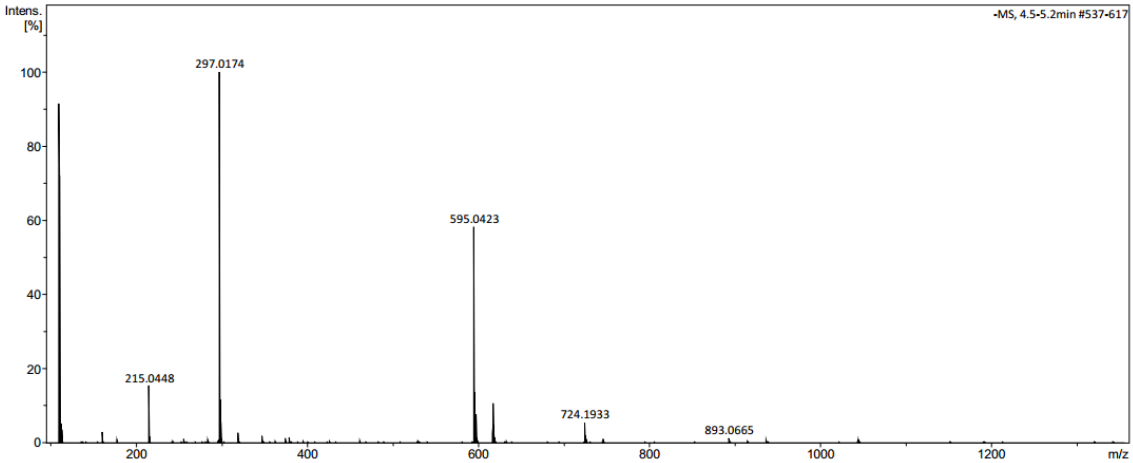

Figure S77 - ESI$^-$ mass spectrum collected for compound **50**.

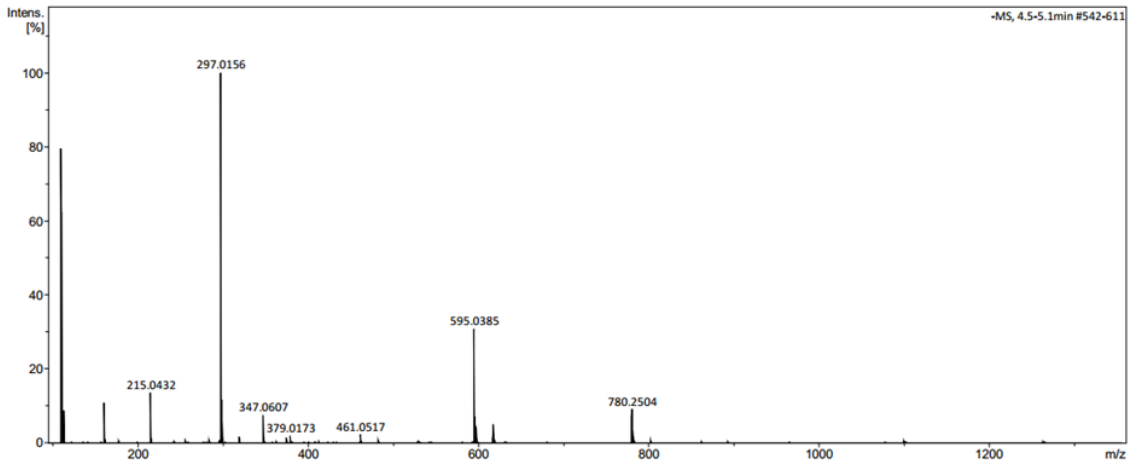

Figure S78 - ESI⁻ mass spectrum collected for compound **51**.

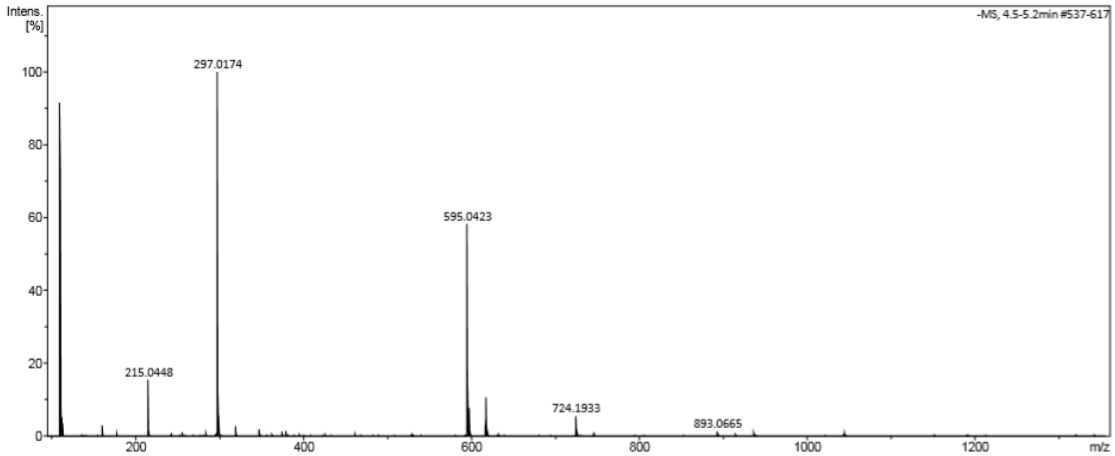

Figure S79 - ESI⁻ mass spectrum collected for compound **52**.

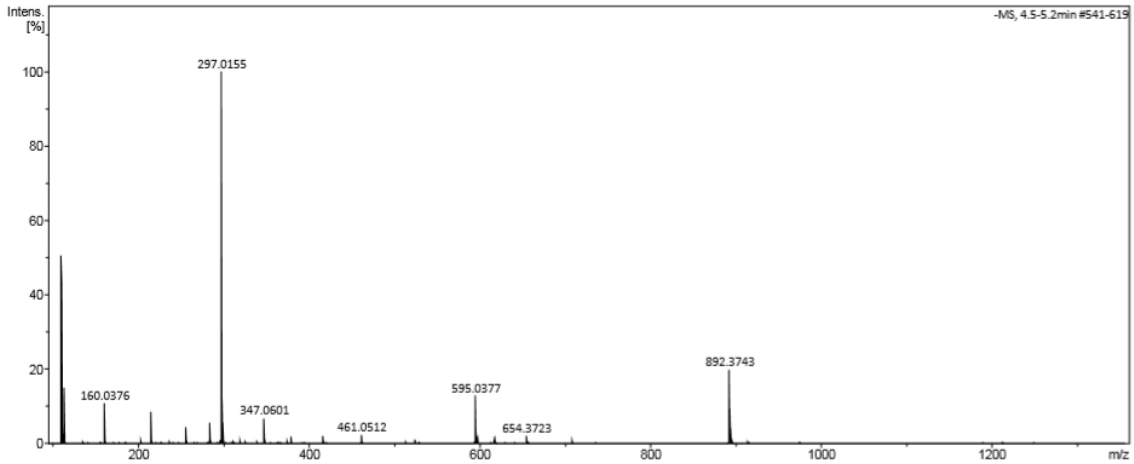

Figure S80 - ESI⁻ mass spectrum collected for compound **53**.

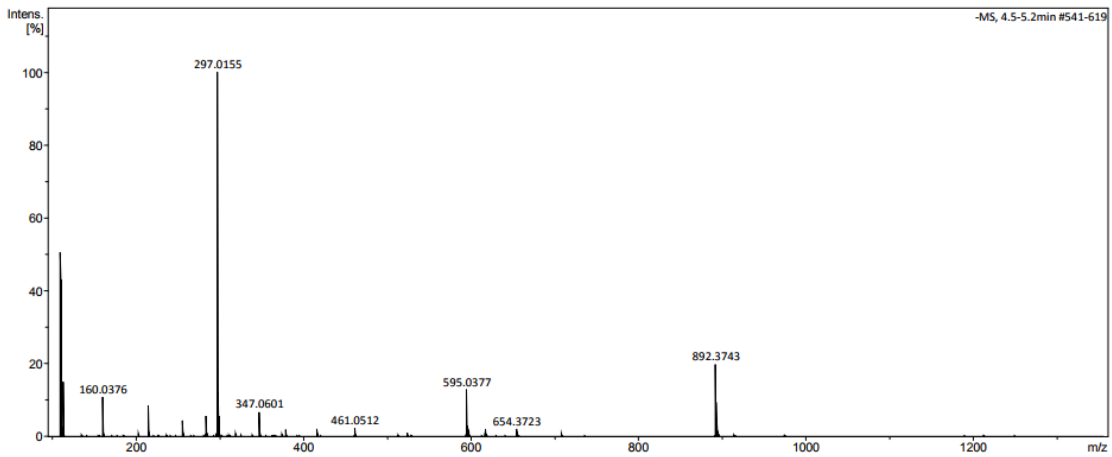

Figure S81 - ESI$^-$ mass spectrum collected for compound **54.**

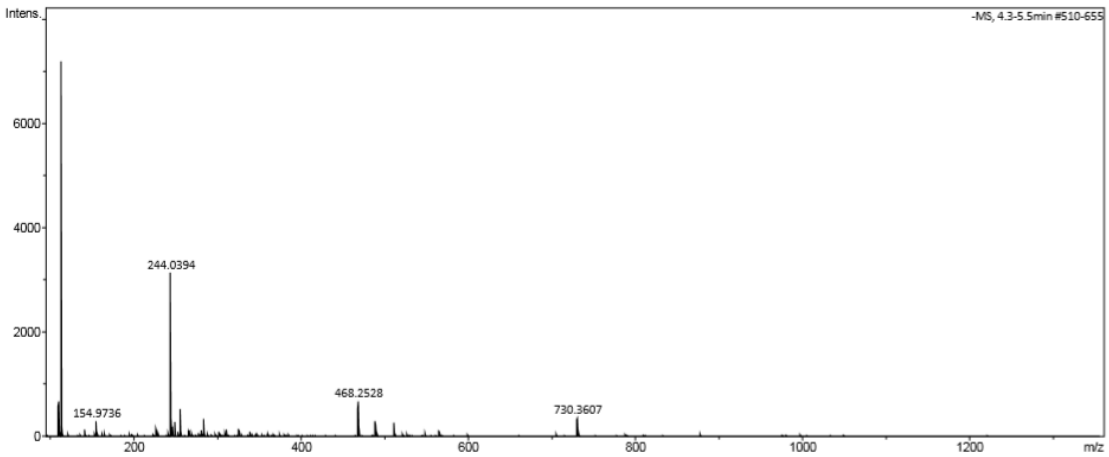

Figure S82 - ESI$^-$ mass spectrum collected for compound **55.**

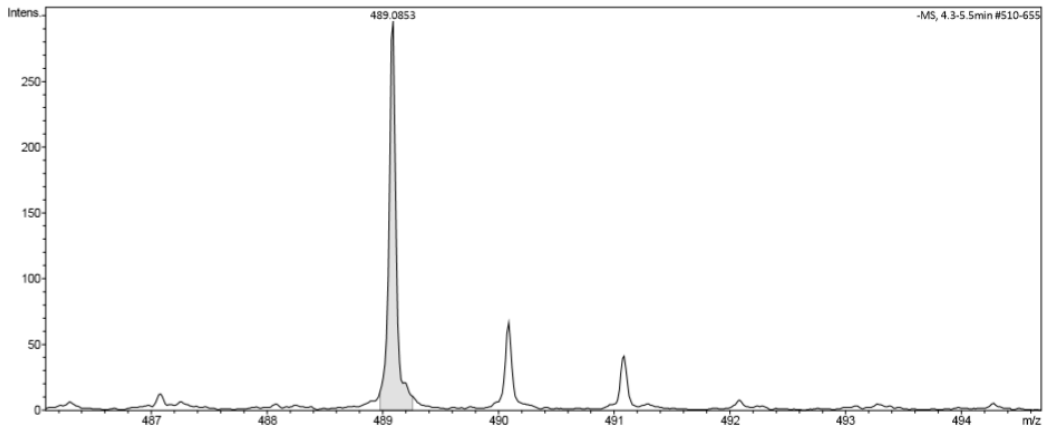

Figure S83 – Enlarged ESI$^-$ mass spectrum collected for compound **55.**

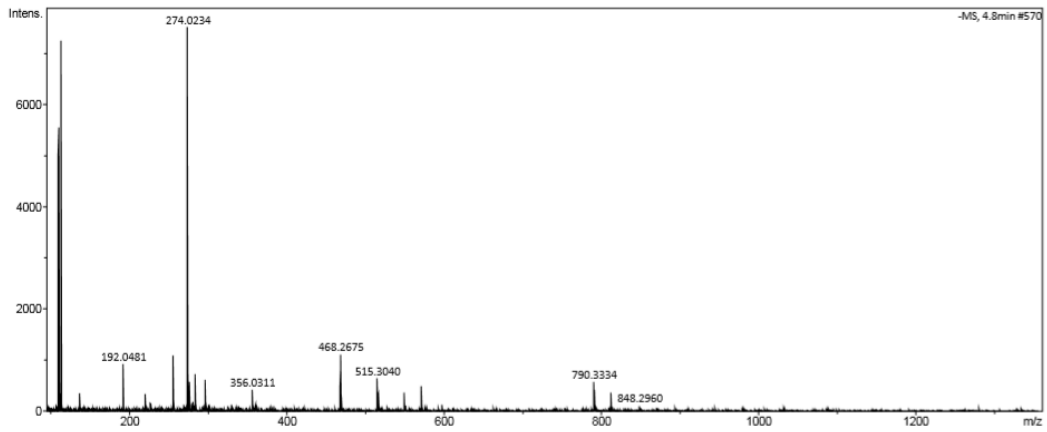

Figure S84 - ESI$^-$ mass spectrum collected for compound **58**.

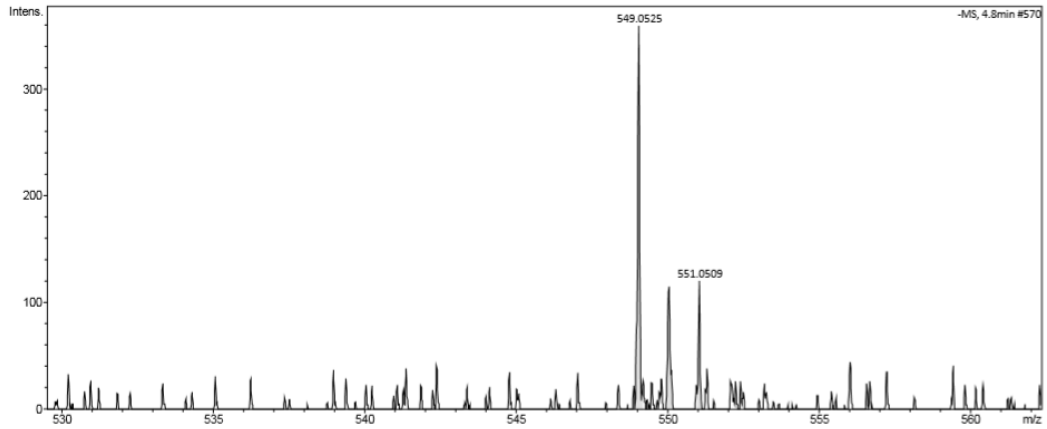

Figure S85 – Enlarged ESI$^-$ mass spectrum collected for compound **58**.

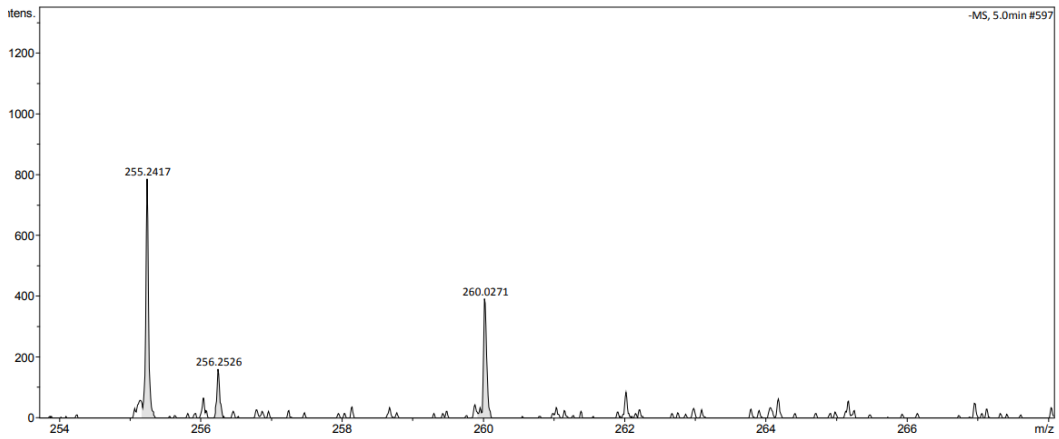

Figure S86 – ESI$^-$ mass spectrum collected for compound **59**.

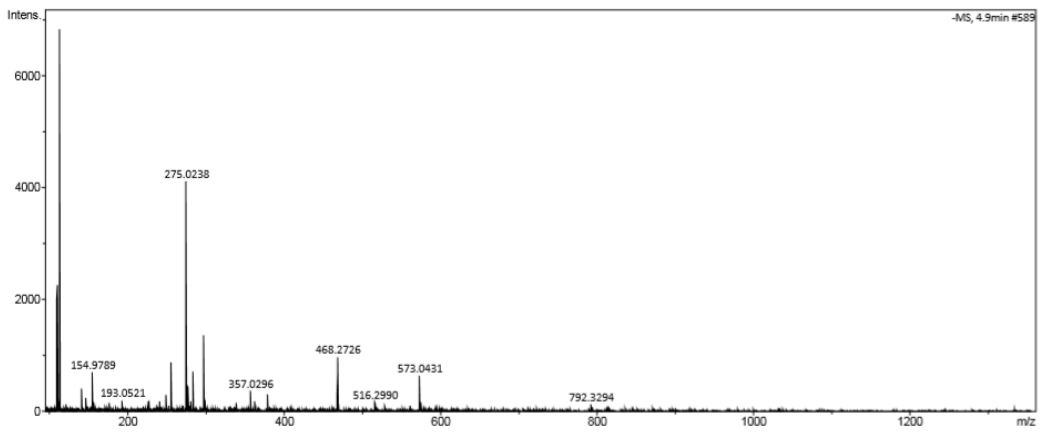

Figure S87 - ESI$^-$ mass spectrum collected for compound **60**.

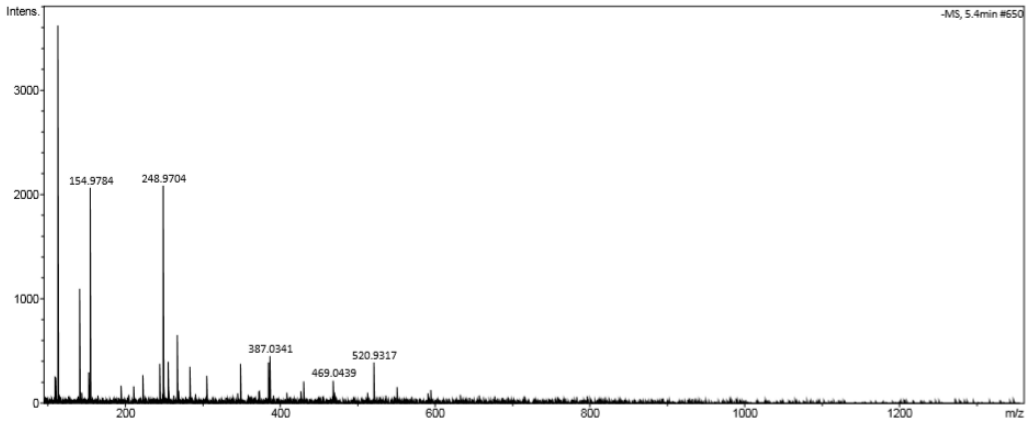

Figure S88 - ESI$^-$ mass spectrum collected for compound **61**.

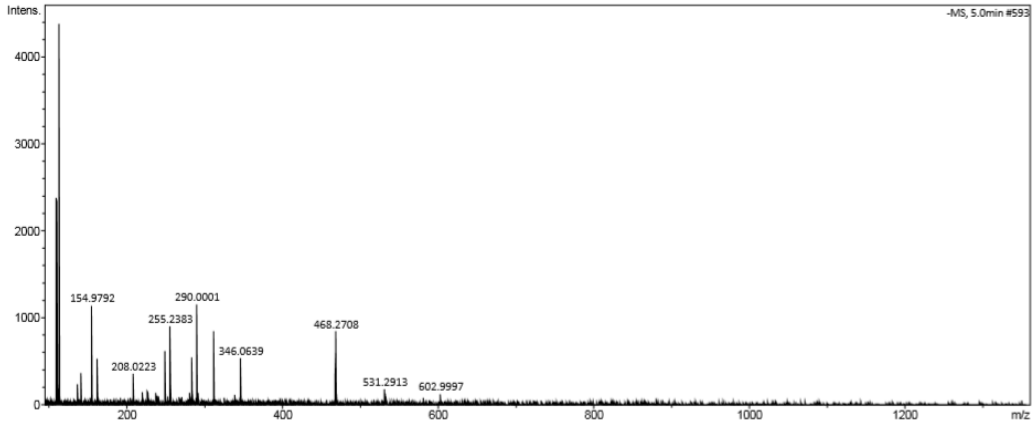

Figure S89 - ESI$^-$ mass spectrum collected for compound **62**.

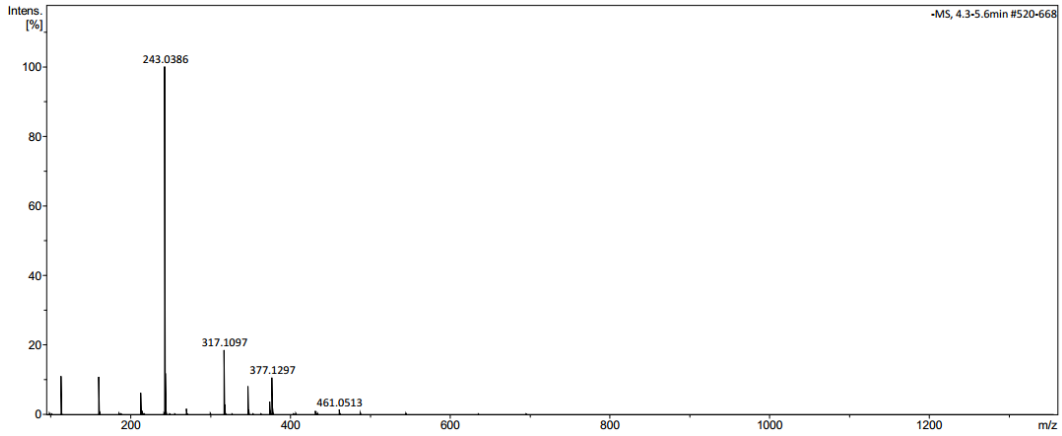

Figure S90 - ESI$^-$ mass spectrum collected for compound **63**.

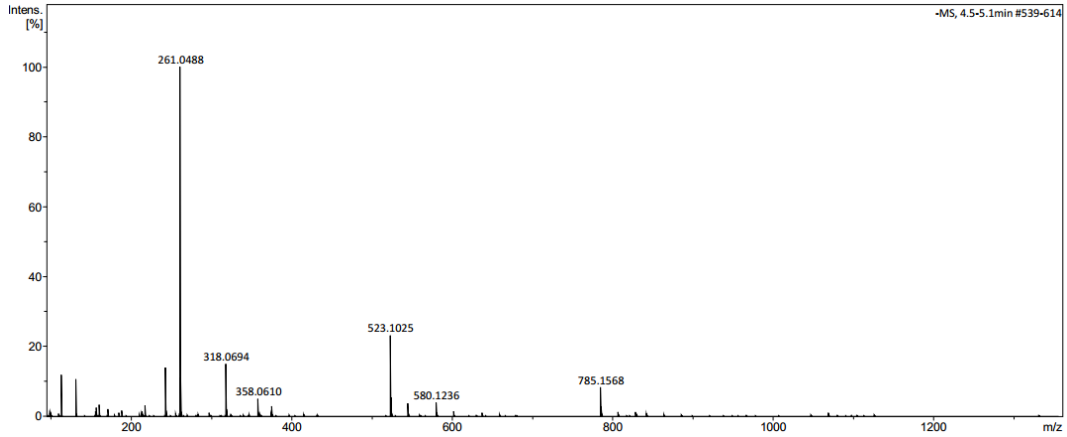

Figure S91 - ESI$^-$ mass spectrum collected for compound **64**.

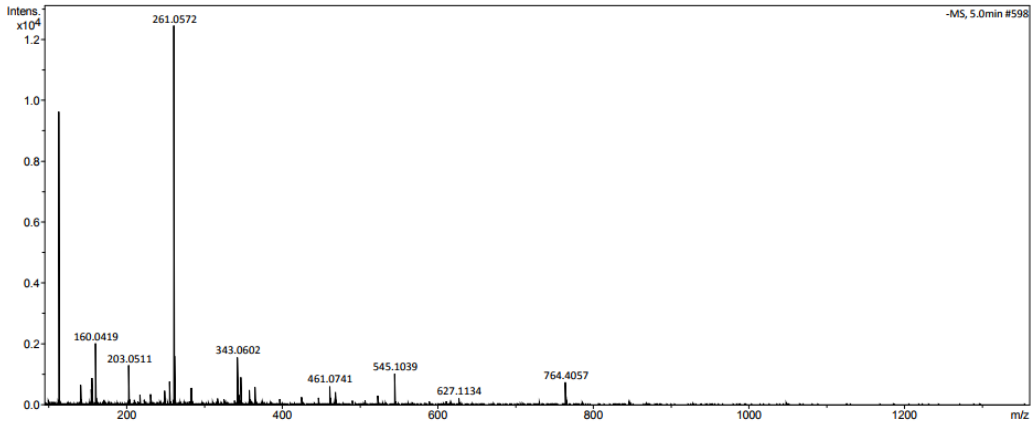

Figure S92 - ESI$^-$ mass spectrum collected for compound **65**.

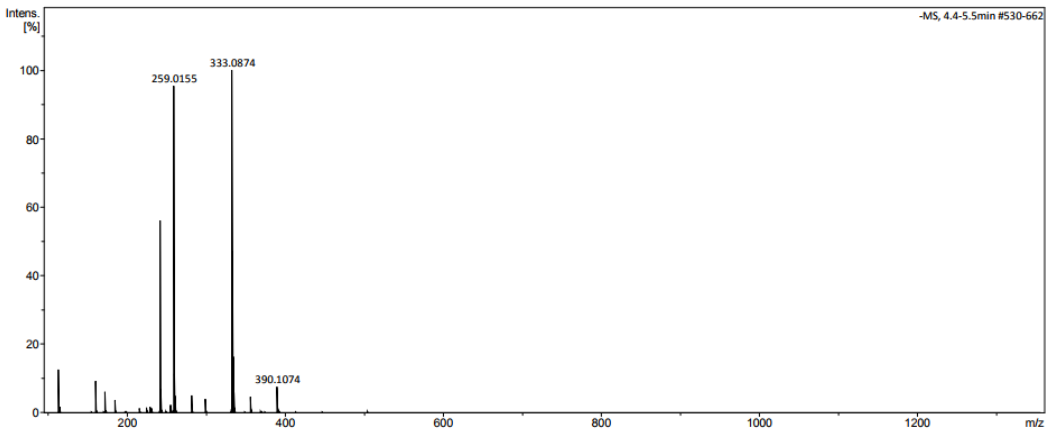

Figure S93 - ESI⁻ mass spectrum collected for compound **66**.

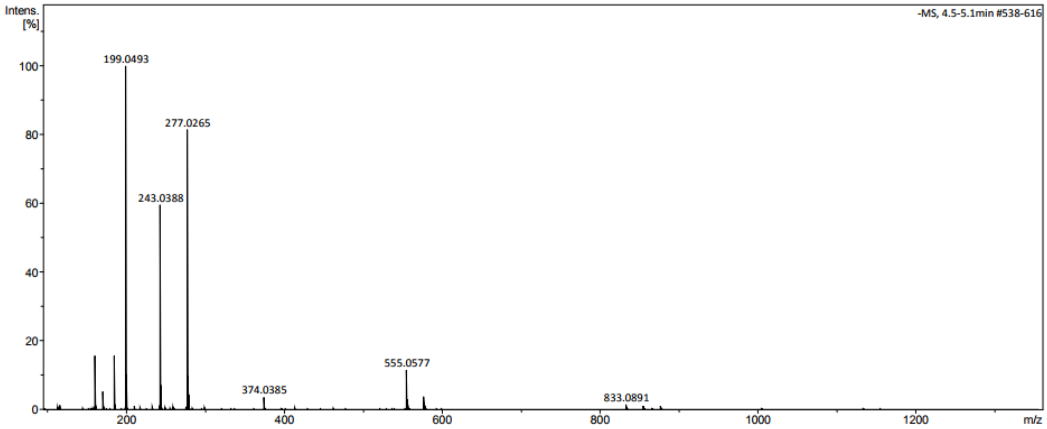

Figure S94 - ESI⁻ mass spectrum collected for compound **67**.

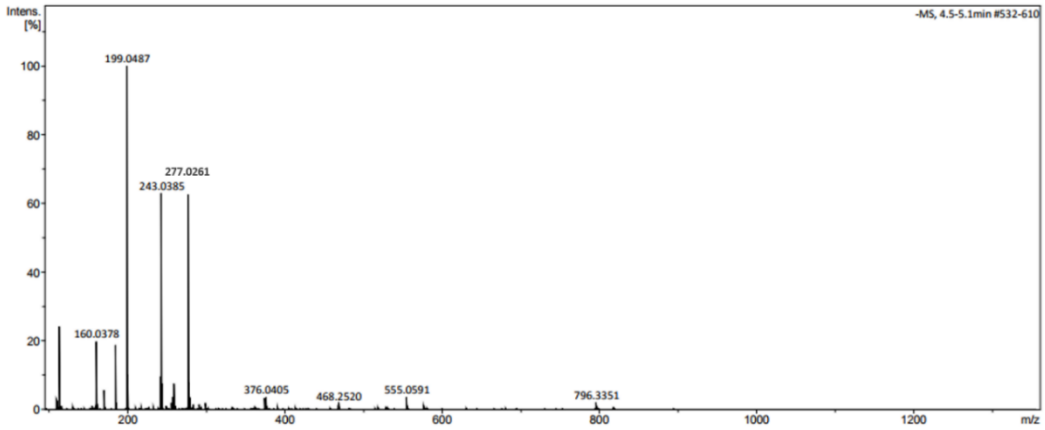

Figure S95 - ESI⁻ mass spectrum collected for compound **68**.

1.3.1 Comparative overview

Table S2 - High-resolution ESI$^-$ mass spectrometry theoretical and experimentally derived values.

Compound no.	*m/z* [M+M+H]$^-$ Theoretical	Actual	Compound no.	*m/z* [M+M+H]$^-$ Theoretical	Actual
42	595.0397	595.0390	**57**[a]	459.0578	459.0649
43	623.0710	623.0689	**58**	549.0351	549.0525
44	651.1023	651.0996	**60**[b]	573.0224	573.0431
45	626.9941	626.9936	**61**[b]	513.0012	512.9840
46	655.0254	655.0236	**62**[b]	602.9714	602.9997
47	683.0567	683.0529	**63**	Not observed	
48	595.0397	595.0418	**64**	523.1058	523.1025
49	595.0397	595.0408	**65b**	545.0877	545.1039
50	595.0397	595.0423	**66**	Not observed	
51	595.0397	595.0385	**67**	555.0601	555.0577
52	595.0397	595.0423	**68**	555.0601	555.0591
53	595.0397	595.0377	**69**[a]	559.0890	558.9373
54	595.0397	595.0347	**70**[a]	659.1204	659.1210
55	489.0868	489.0853	**71**[a]	Not observed	
56	519.0861	519.0867	**72**[a]	752.0862	753.0864

[*a*] Previously published results.[1] [*b*] Obtained as the [M+M+Na]$^-$ ion.

1.4 Dynamic light scattering data

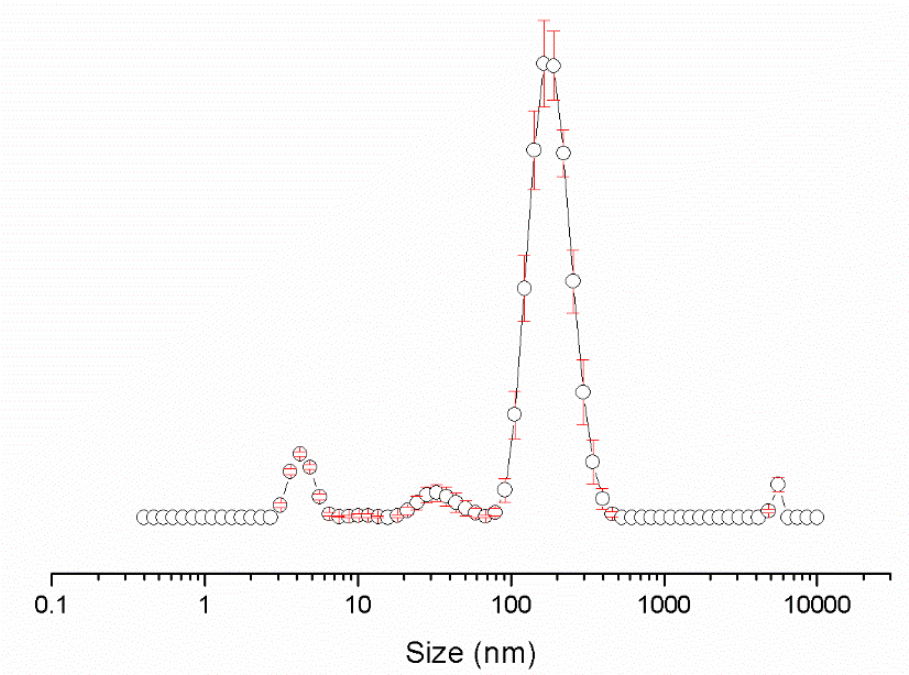

Figure S96 - The average intensity particle size distribution calculated using 9 DLS runs for compound **42** (5.56 mM) in an EtOH:H_2O (1:19) solution at 298.15 K.

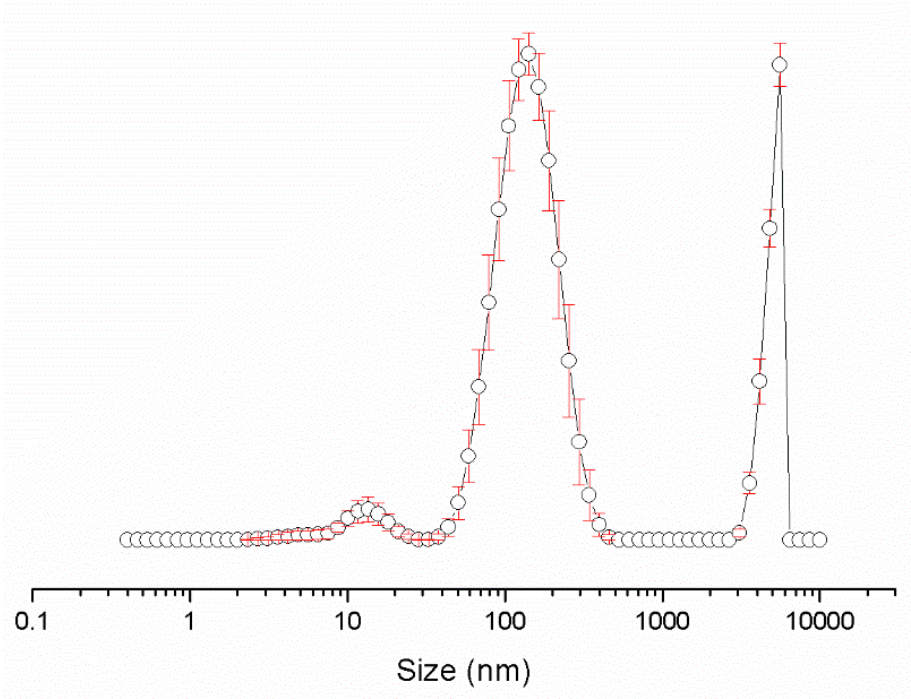

Figure S97 - The average intensity particle size distribution calculated using 9 DLS runs for compound **42** (0.56 mM) in an EtOH:H_2O (1:19) solution at 298.15 K.

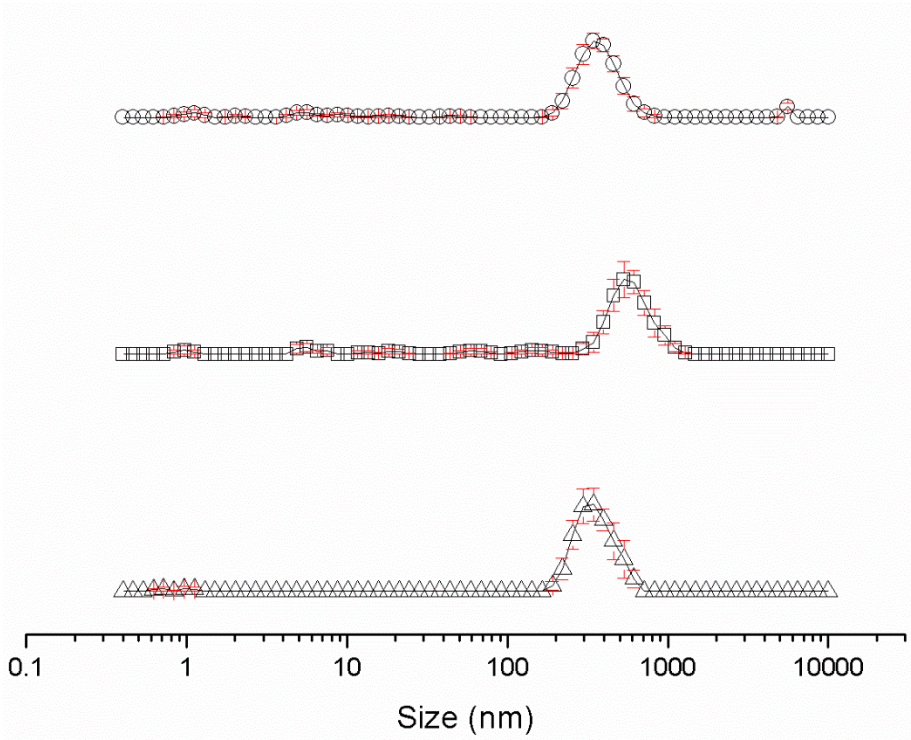

Figure S98 - Average intensity particle size distribution, calculated from 9 DLS runs, of aggregates formed by dissolving compound **43** at a concentration of 5.56 mM in DMSO at Δ) 25 °C, □) heating to 40 °C and ○) cooling to 25 °C. Only 9 of the available 10 DLS runs were used as in some cases, due to the heating and cooling processes there were some obvious temperature equilibration issues for the first run.

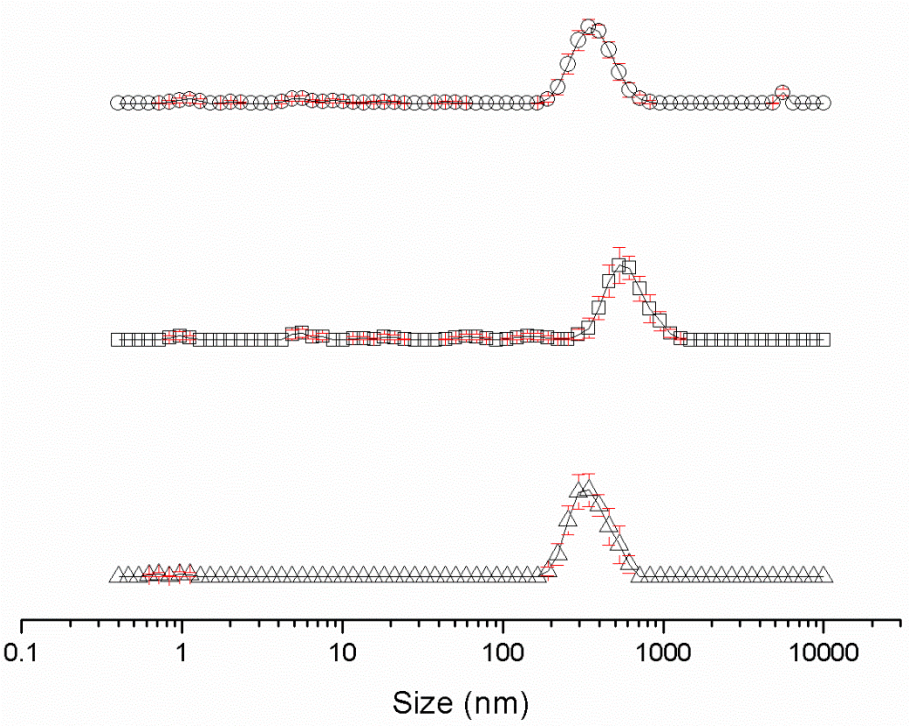

Figure S99 - Average intensity particle size distribution, calculated from 9 DLS runs, of aggregates formed by dissolving compound **43** at a concentration of 0.56 mM in DMSO at Δ) 25 °C, □) heating to 40 °C and ○) cooling to 25 °C. Only 9 of the available 10 DLS runs were used as in some cases, due to the heating and cooling processes there were some obvious temperature equilibration issues for the first run.

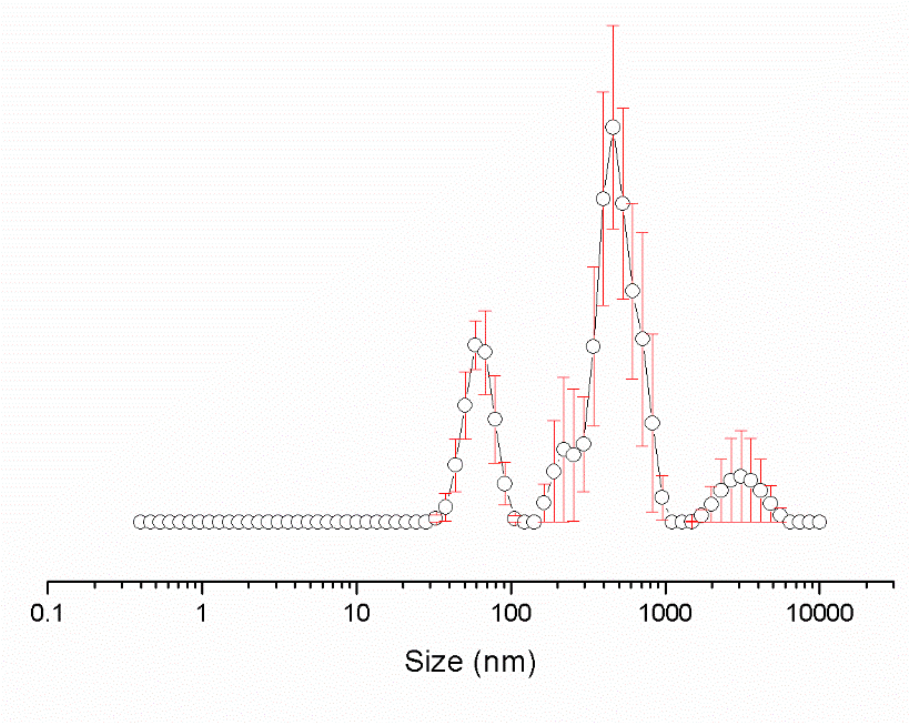

Figure S100 - The average intensity particle size distribution calculated using 9 DLS runs for compound **43** (5.56 mM) in an EtOH:H_2O (1:19) solution at 298.15 K.

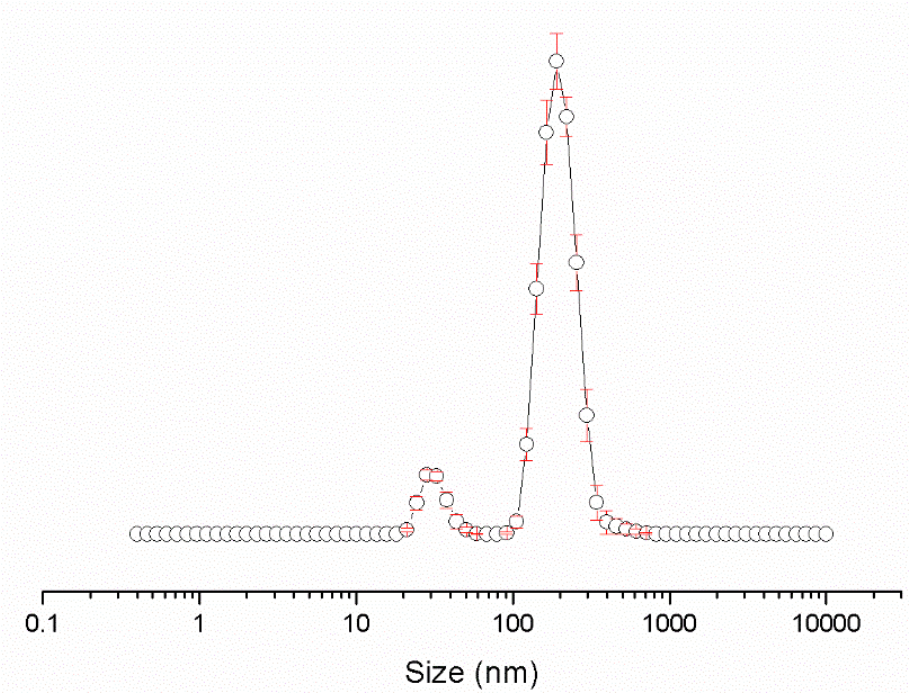

Figure S101 - The average intensity particle size distribution calculated using 9 DLS runs for compound **43** (0.56 mM) in an EtOH:H_2O (1:19) solution at 298.15 K.

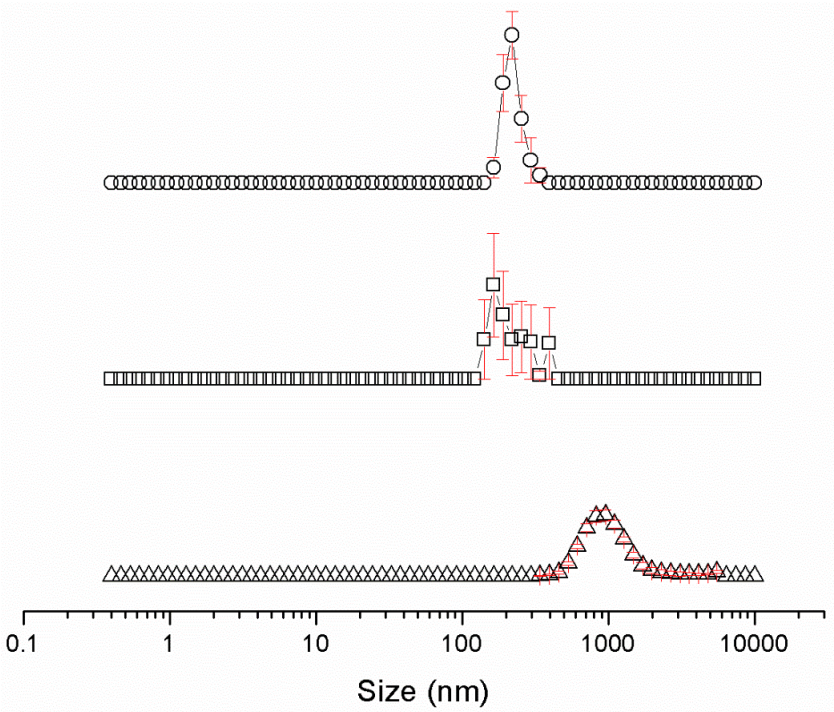

Figure S102 - Average intensity particle size distribution, calculated from 9 DLS runs, of aggregates formed by dissolving compound **44** at a concentration of 5.56 mM in DMSO at Δ) 25 °C, □) heating to 40 °C and ○) cooling to 25 °C. Only 9 of the available 10 DLS runs were used as in some cases, due to the heating and cooling processes there were some obvious temperature equilibration issues for the first run.

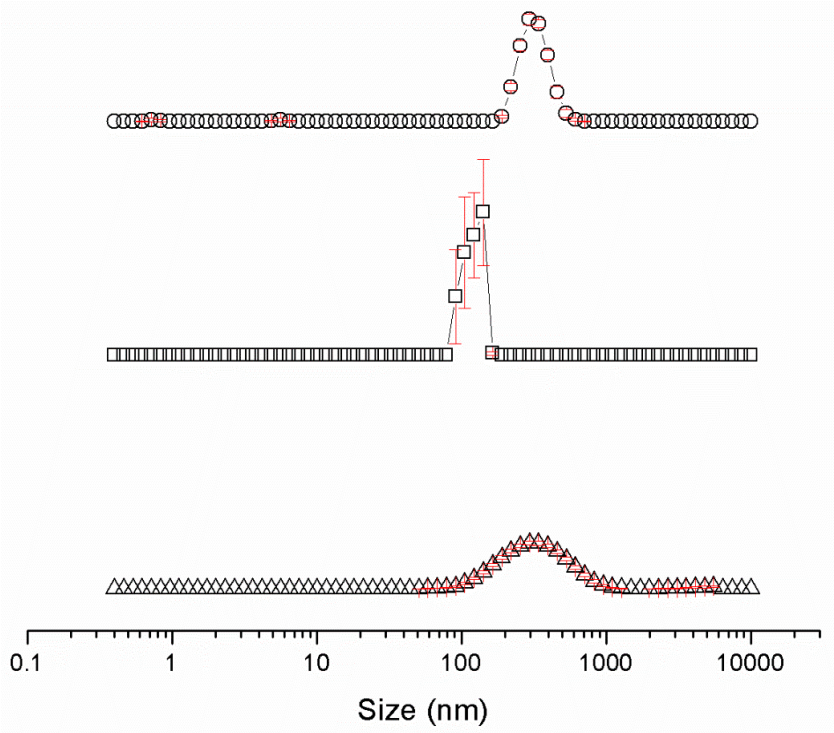

Figure S103 - Average intensity particle size distribution, calculated from 9 DLS runs, of aggregates formed by dissolving compound **44** at a concentration of 0.56 mM in DMSO at Δ) 25 °C, □) heating to 40 °C and ○) cooling to 25 °C. Only 9 of the available 10 DLS runs were used as in some cases, due to the heating and cooling processes there were some obvious temperature equilibration issues for the first run.

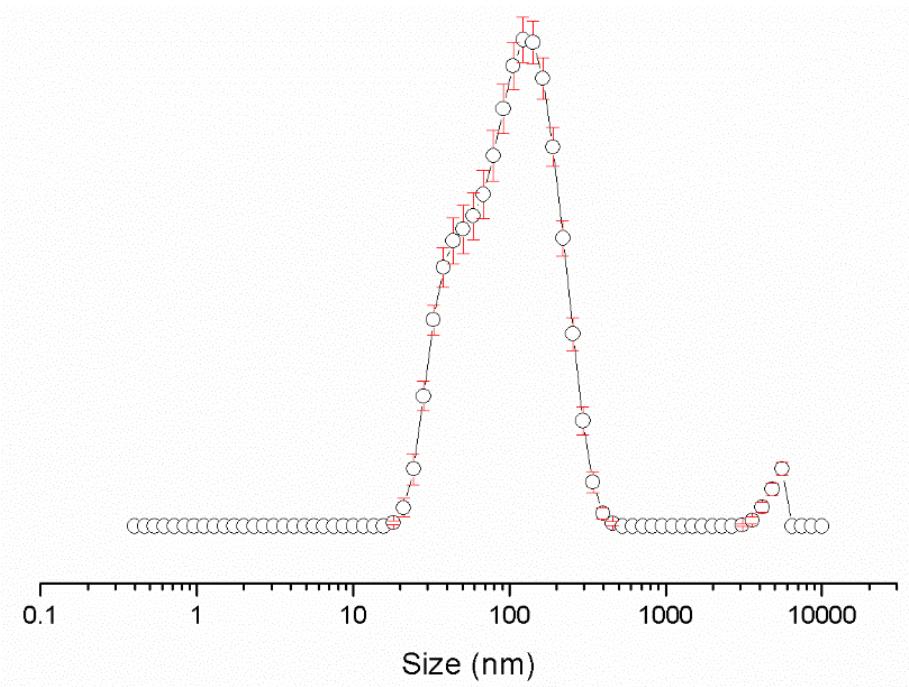

Figure S104 - The average intensity particle size distribution calculated using 9 DLS runs for compound **44** (5.56 mM) in an EtOH:H_2O (1:19) solution at 298.15 K.

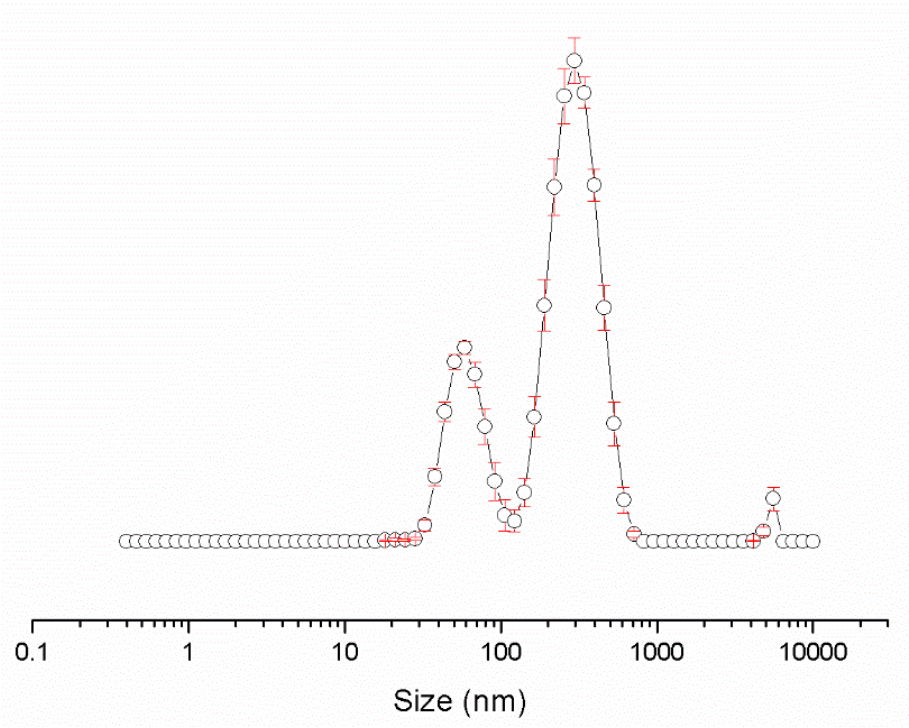

Figure S105 - The average intensity particle size distribution calculated using 9 DLS runs for compound **44** (0.56 mM) in an EtOH:H_2O (1:19) solution at 298.15 K.

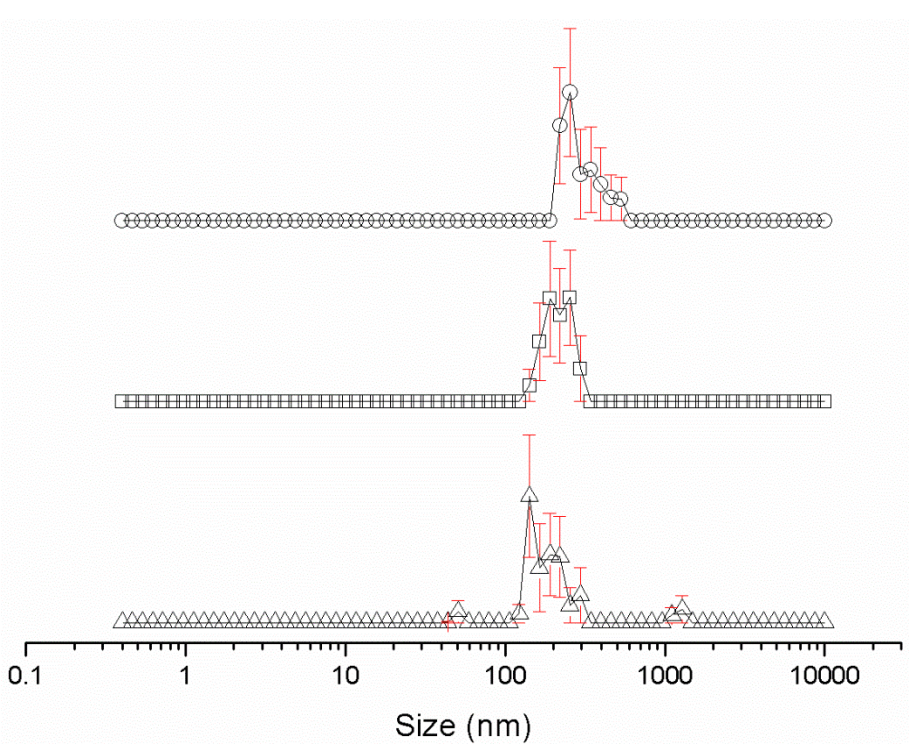

Figure S106 - Average intensity particle size distribution, calculated from 9 DLS runs, of aggregates formed by dissolving compound **46** at a concentration of 5.56 mM in DMSO at Δ) 25 °C, □) heating to 40 °C and ○) cooling to 25 °C. Only 9 of the available 10 DLS runs were used as in some cases, due to the heating and cooling processes there were some obvious temperature equilibration issues for the first run.

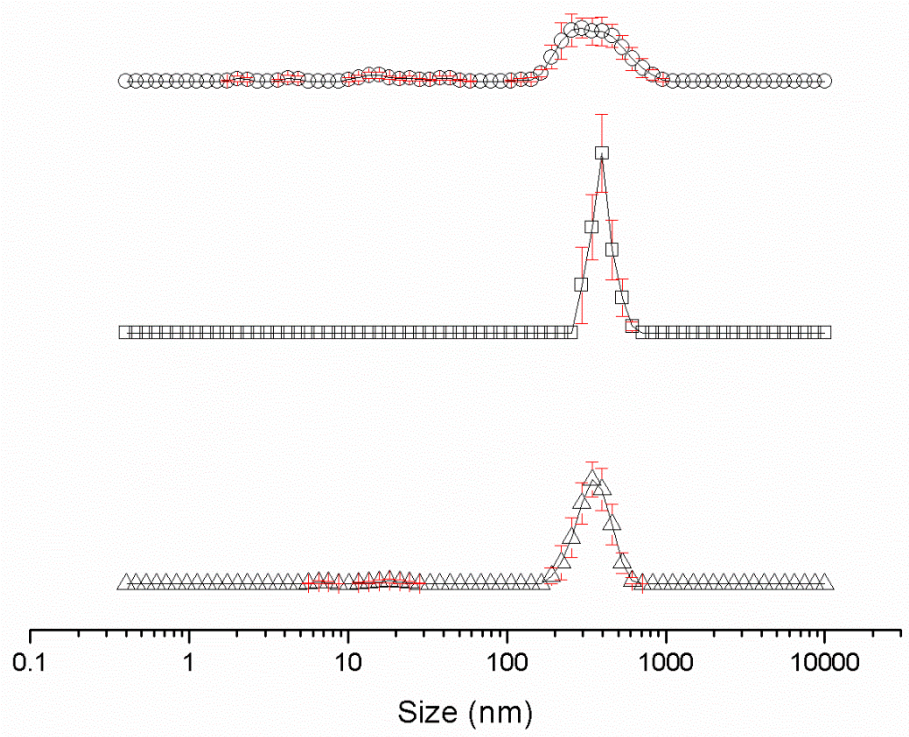

Figure S107 - Average intensity particle size distribution, calculated from 9 DLS runs, of aggregates formed by dissolving compound **46** at a concentration of 0.56 mM in DMSO at Δ) 25 °C, □) heating to 40 °C and ○) cooling to 25 °C. Only 9 of the available 10 DLS runs were used as in some cases, due to the heating and cooling processes there were some obvious temperature equilibration issues for the first run.

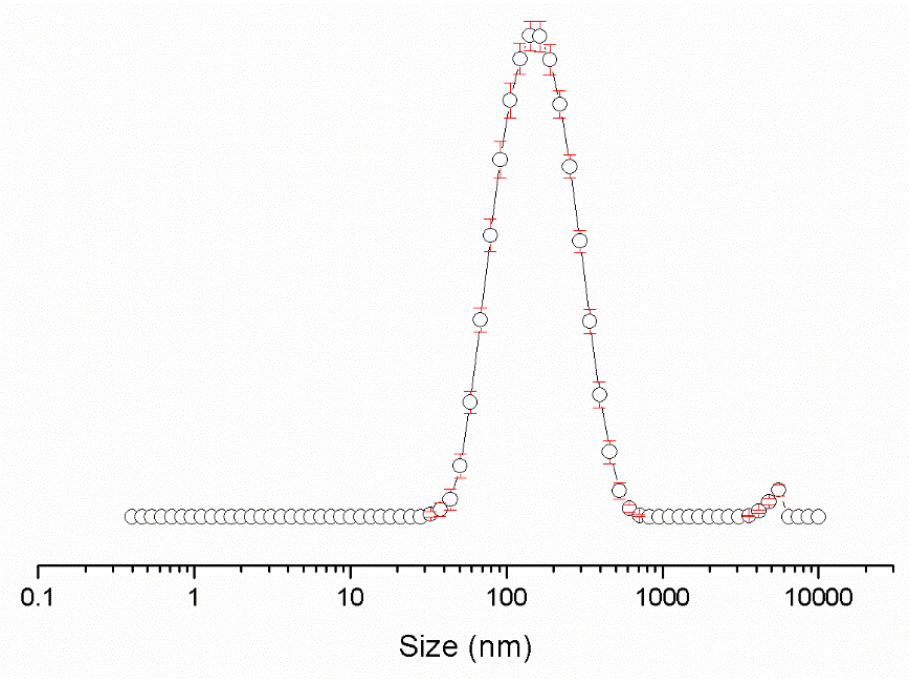

Figure S108 - The average intensity particle size distribution calculated using 9 DLS runs for compound **46** (5.56 mM) in an EtOH:H_2O (1:19) solution at 298.15 K.

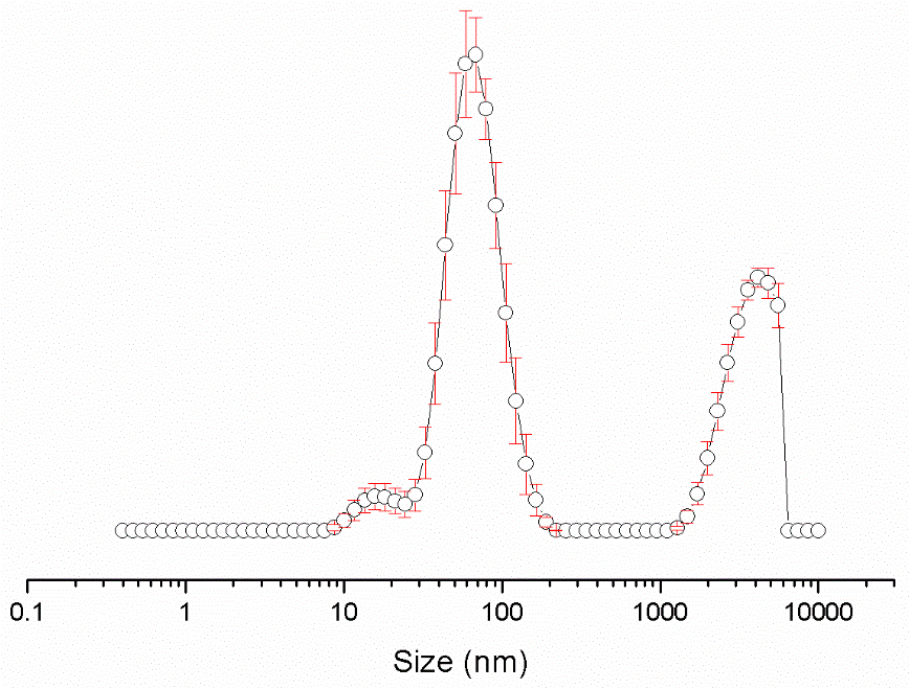

Figure S109 - The average intensity particle size distribution calculated using 9 DLS runs for compound **46** (0.56 mM) in an EtOH:H_2O (1:19) solution at 298.15 K.

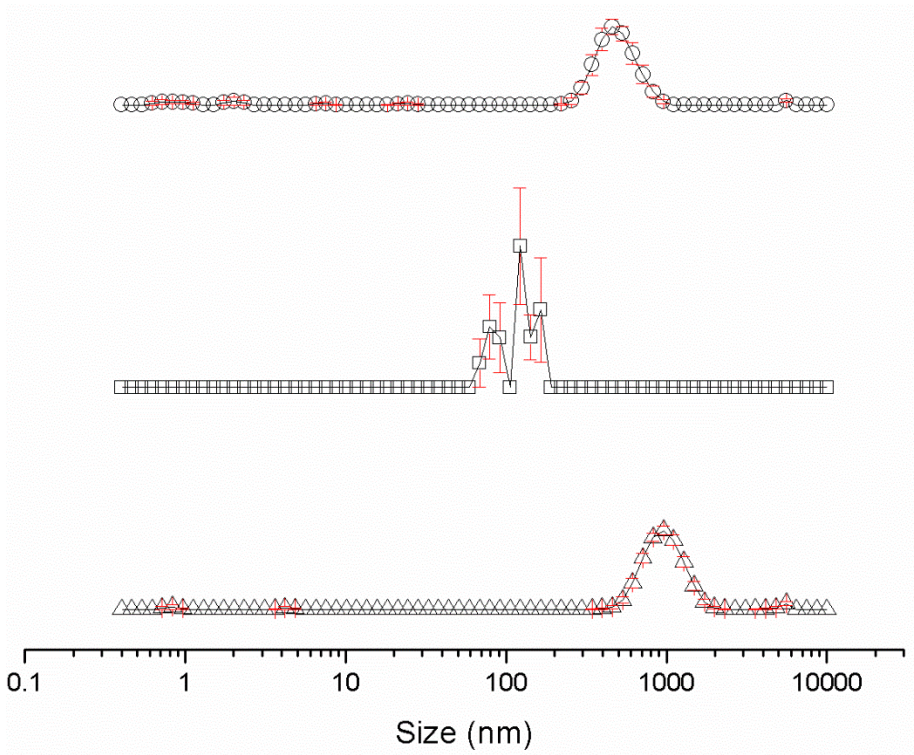

Figure S110 - Average intensity particle size distribution, calculated from 9 DLS runs, of aggregates formed by dissolving compound **47** at a concentration of 5.56 mM in DMSO at Δ) 25 °C, □) heating to 40 °C and ○) cooling to 25 °C. Only 9 of the available 10 DLS runs were used as in some cases, due to the heating and cooling processes there were some obvious temperature equilibration issues for the first run.

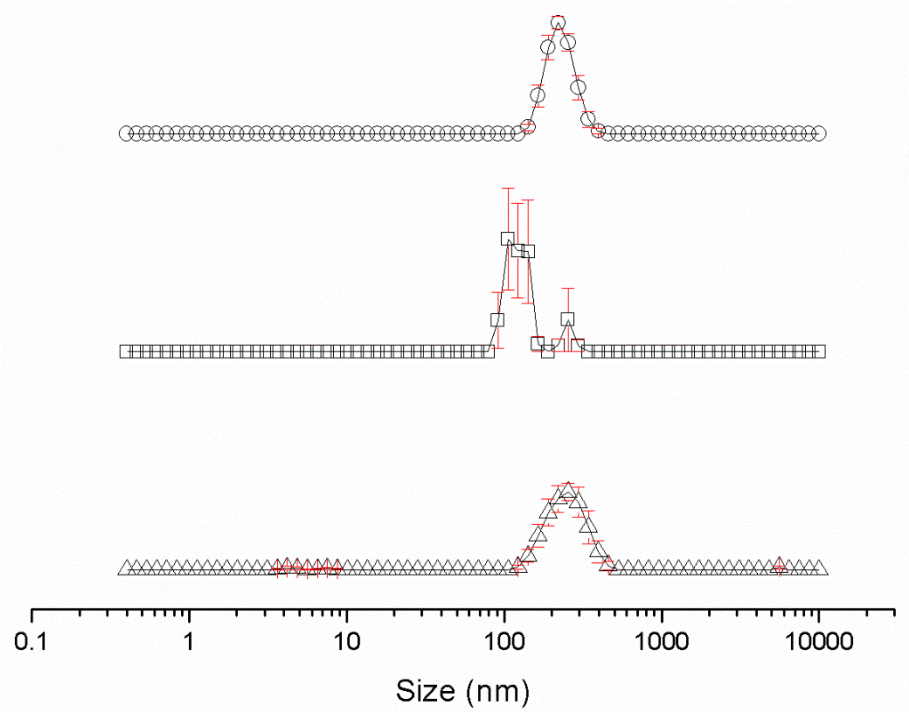

Figure S111 - Average intensity particle size distribution, calculated from 9 DLS runs, of aggregates formed by dissolving compound **47** at a concentration of 0.56 mM in DMSO at Δ) 25 °C, □) heating to 40 °C and ○) cooling to 25 °C. Only 9 of the available 10 DLS runs were used as in some cases, due to the heating and cooling processes there were some obvious temperature equilibration issues for the first run.

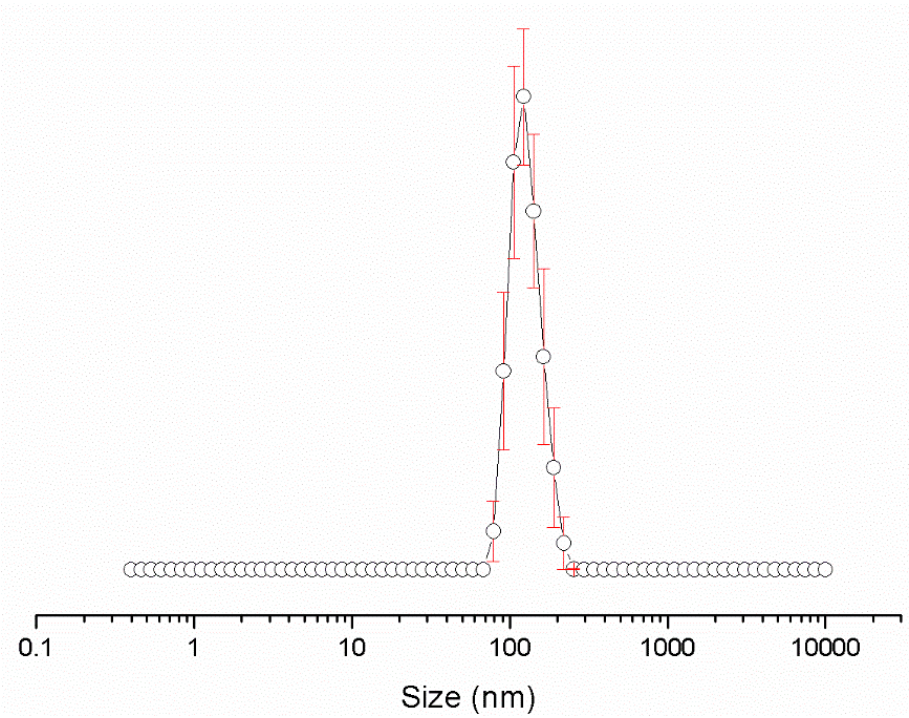

Figure S112 - The average intensity particle size distribution calculated using 9 DLS runs for compound **47** (5.56 mM) in an EtOH:H_2O (1:19) solution at 298.15 K.

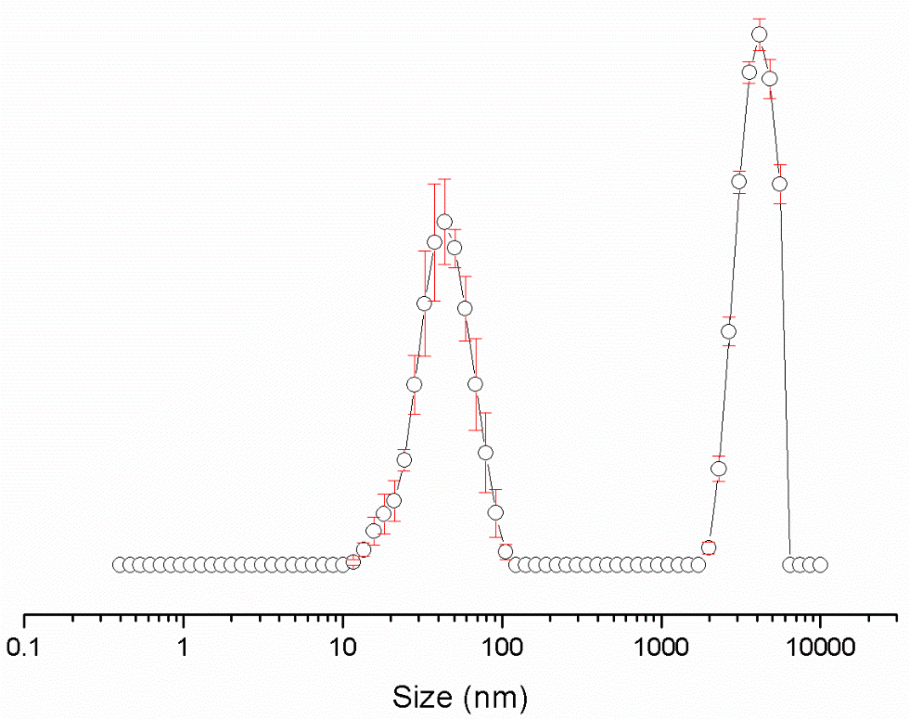

Figure S113 - The average intensity particle size distribution calculated using 9 DLS runs for compound **47** (0.56 mM) in an EtOH:H_2O (1:19) solution at 298.15 K.

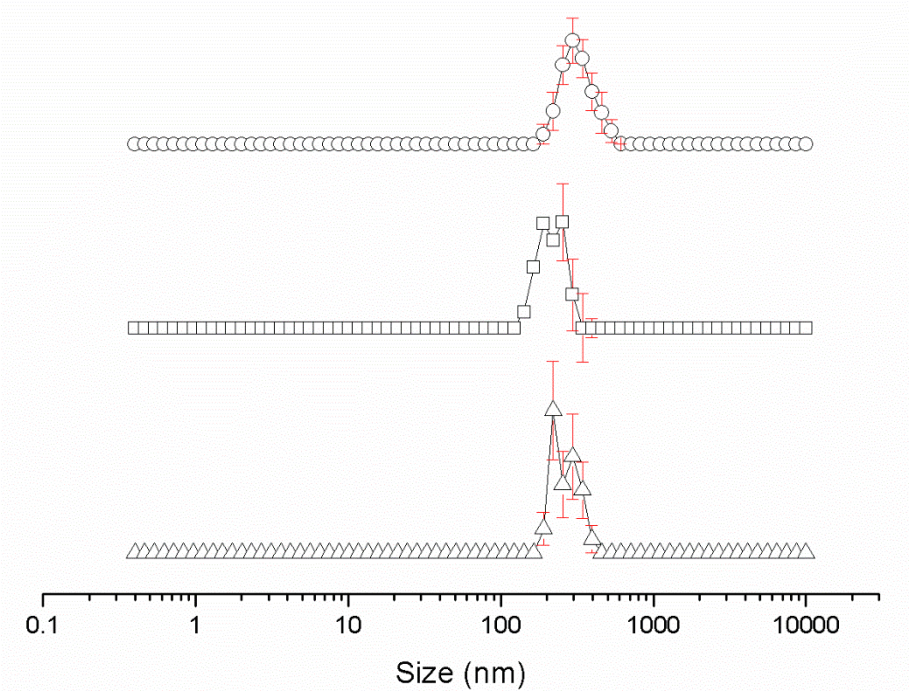

Figure S114 - Average intensity particle size distribution, calculated from 9 DLS runs, of aggregates formed by dissolving compound **48** at a concentration of 5.56 mM in DMSO at Δ) 25 °C, □) heating to 40 °C and ○) cooling to 25 °C. Only 9 of the available 10 DLS runs were used as in some cases, due to the heating and cooling processes there were some obvious temperature equilibration issues for the first run.

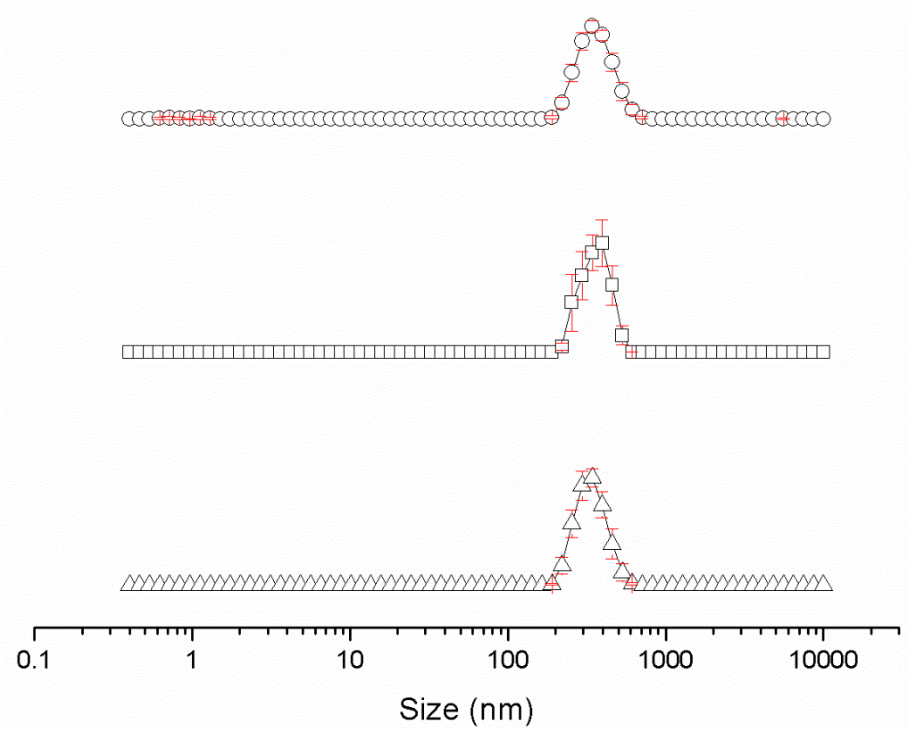

Figure S115 - Average intensity particle size distribution, calculated from 9 DLS runs, of aggregates formed by dissolving compound **48** at a concentration of 0.56 mM in DMSO at Δ) 25 °C, □) heating to 40 °C and ○) cooling to 25 °C. Only 9 of the available 10 DLS runs were used as in some cases, due to the heating and cooling processes there were some obvious temperature equilibration issues for the first run.

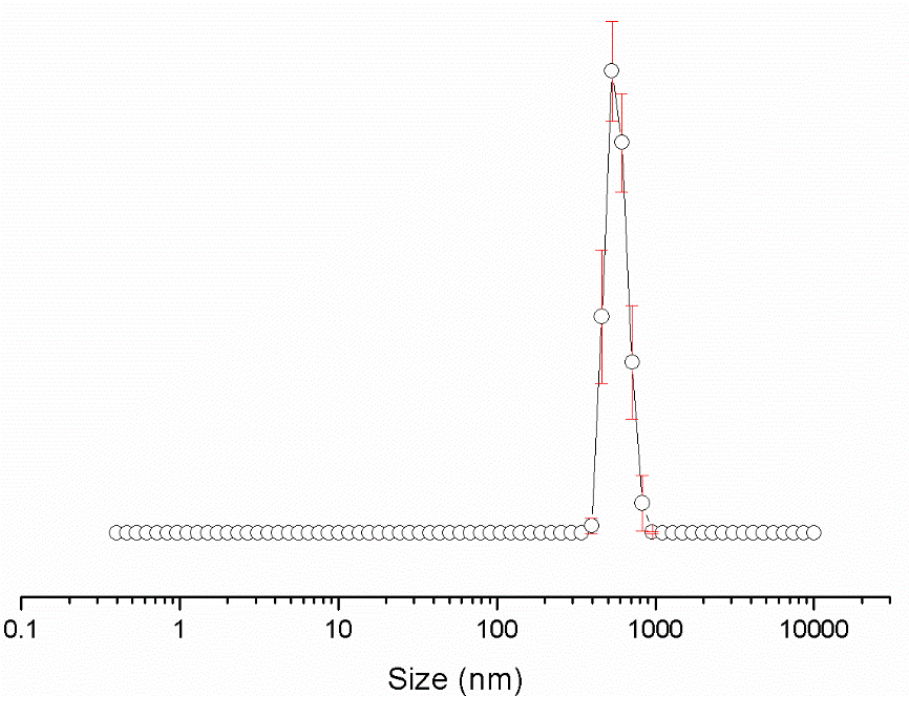

Figure S116 - The average intensity particle size distribution calculated using 9 DLS runs for compound **48** (5.56 mM) in an EtOH:H_2O (1:19) solution at 298.15 K.

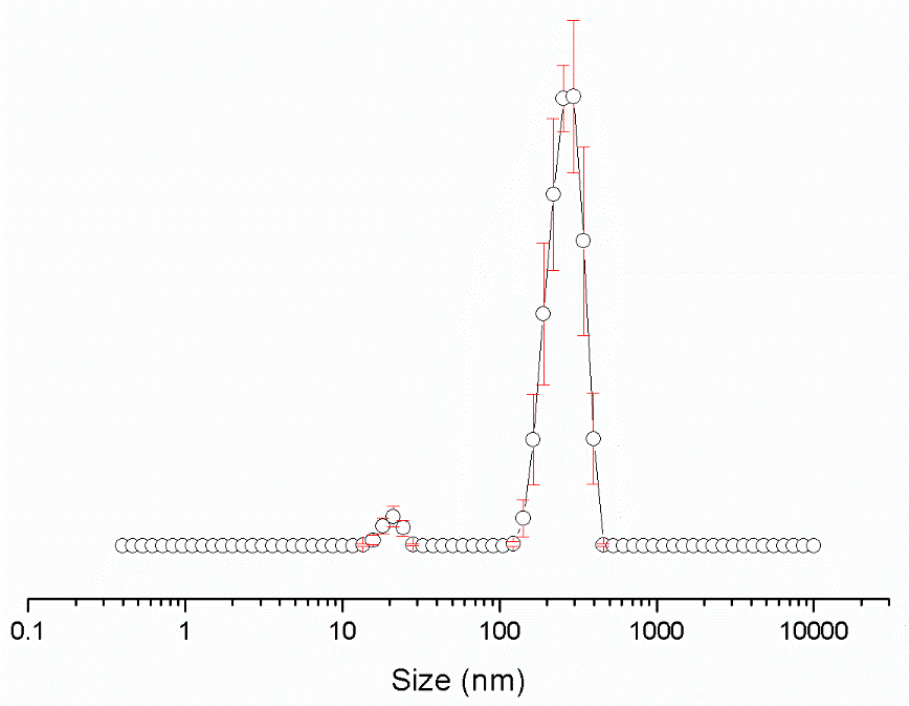

Figure S117 - The average intensity particle size distribution calculated using 9 DLS runs for compound **48** (0.56 mM) in an EtOH:H_2O (1:19) solution at 298.15 K.

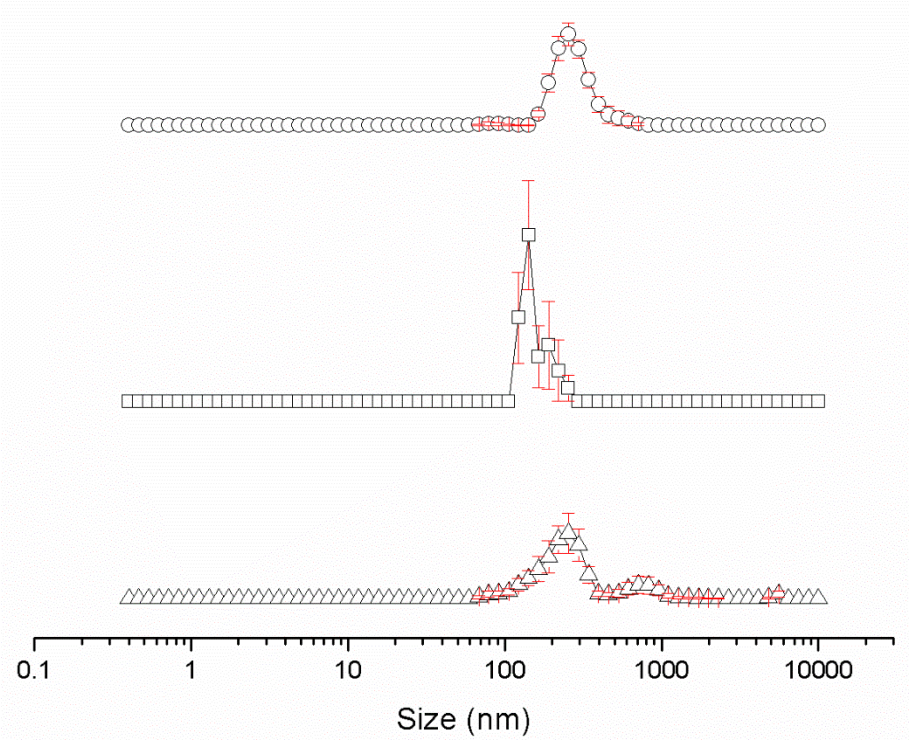

Figure S118 - Average intensity particle size distribution, calculated from 9 DLS runs, of aggregates formed by dissolving compound **49** at a concentration of 5.56 mM in DMSO at Δ) 25 °C, □) heating to 40 °C and ○) cooling to 25 °C. Only 9 of the available 10 DLS runs were used as in some cases, due to the heating and cooling processes there were some obvious temperature equilibration issues for the first run.

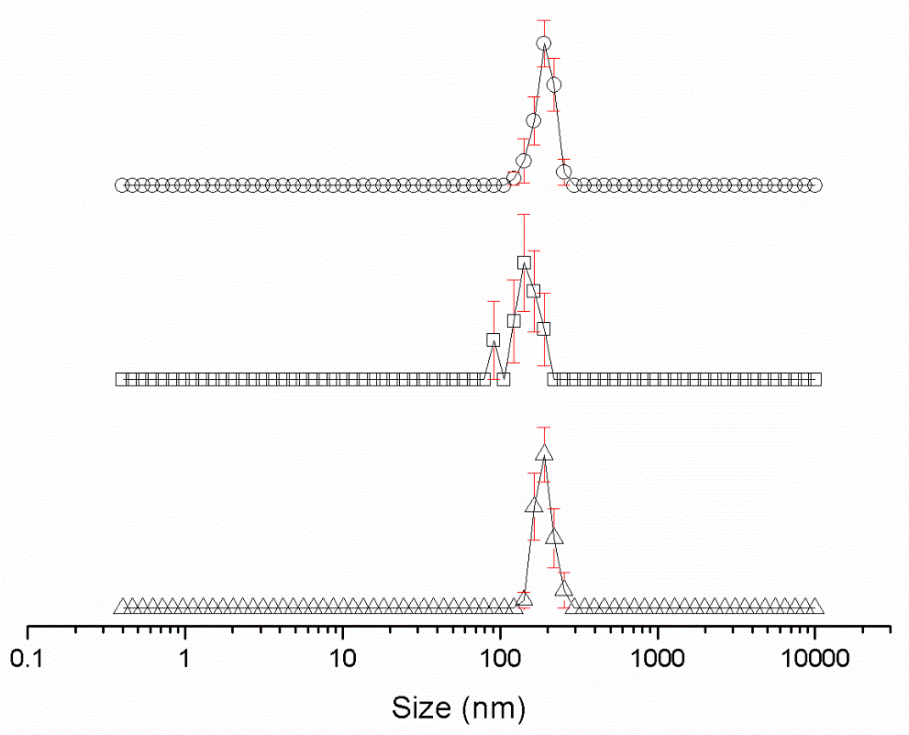

Figure S119 - Average intensity particle size distribution, calculated from 9 DLS runs, of aggregates formed by dissolving compound **49** at a concentration of 0.56 mM in DMSO at Δ) 25 °C, □) heating to 40 °C and ○) cooling to 25 °C. Only 9 of the available 10 DLS runs were used as in some cases, due to the heating and cooling processes there were some obvious temperature equilibration issues for the first run.

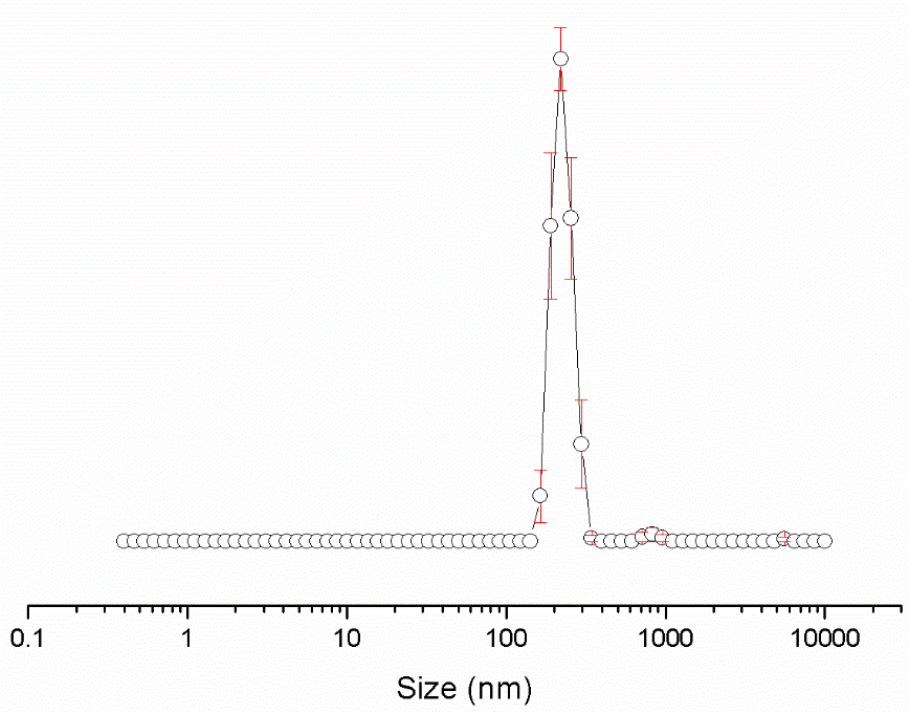

Figure S120 - The average intensity particle size distribution calculated using 9 DLS runs for compound **49** (5.56 mM) in an EtOH:H_2O (1:19) solution at 298.15 K.

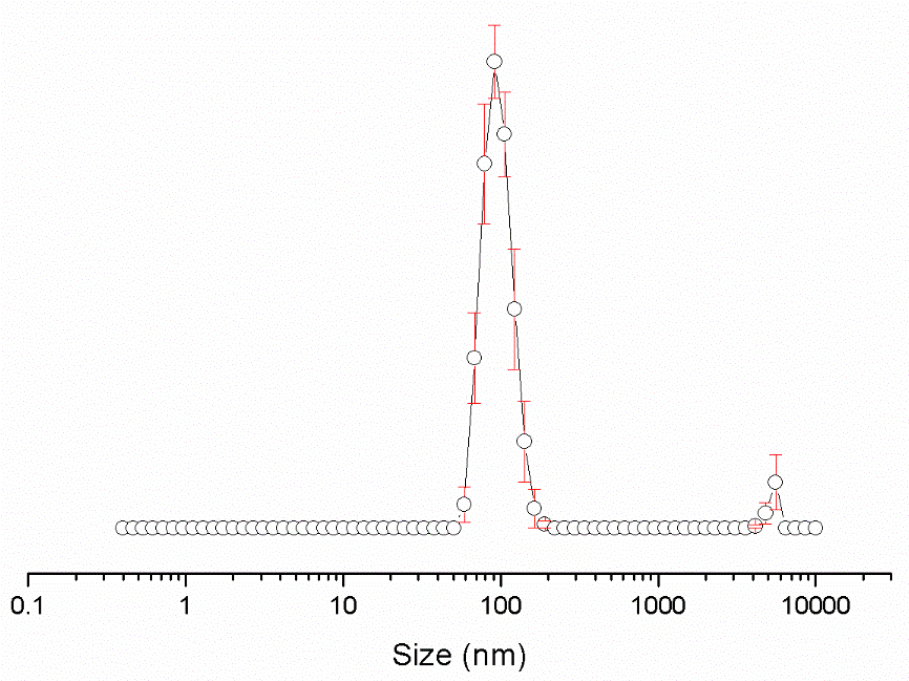

Figure S121 - The average intensity particle size distribution calculated using 9 DLS runs for compound **49** (0.56 mM) in an EtOH:H_2O (1:19) solution at 298.15 K.

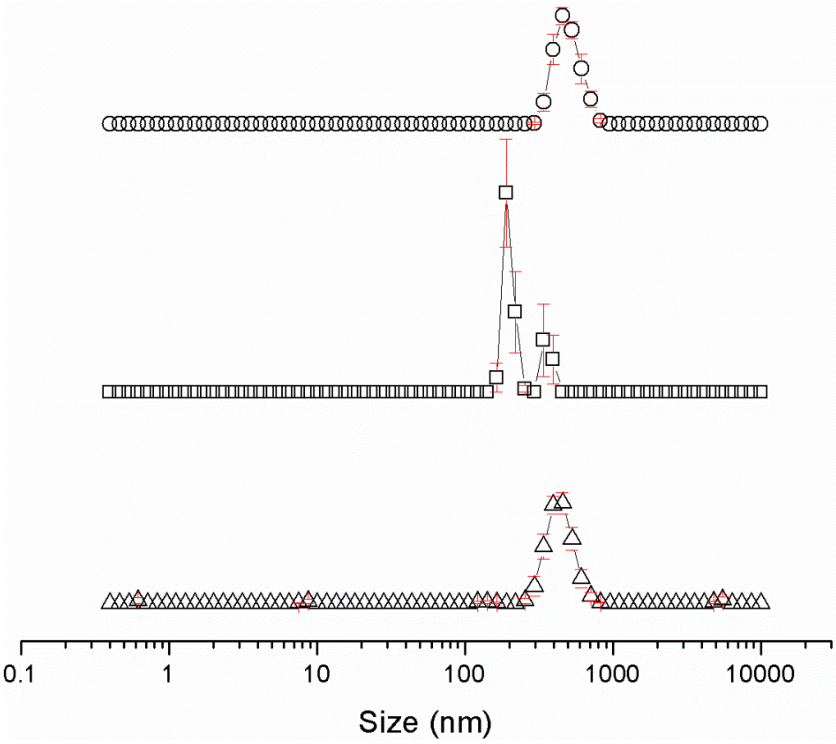

Figure S122 - Average intensity particle size distribution, calculated from 9 DLS runs, of aggregates formed by dissolving compound **50** at a concentration of 5.56 mM in DMSO at Δ) 25 °C, □) heating to 40 °C and ○) cooling to 25 °C. Only 9 of the available 10 DLS runs were used as in some cases, due to the heating and cooling processes there were some obvious temperature equilibration issues for the first run.

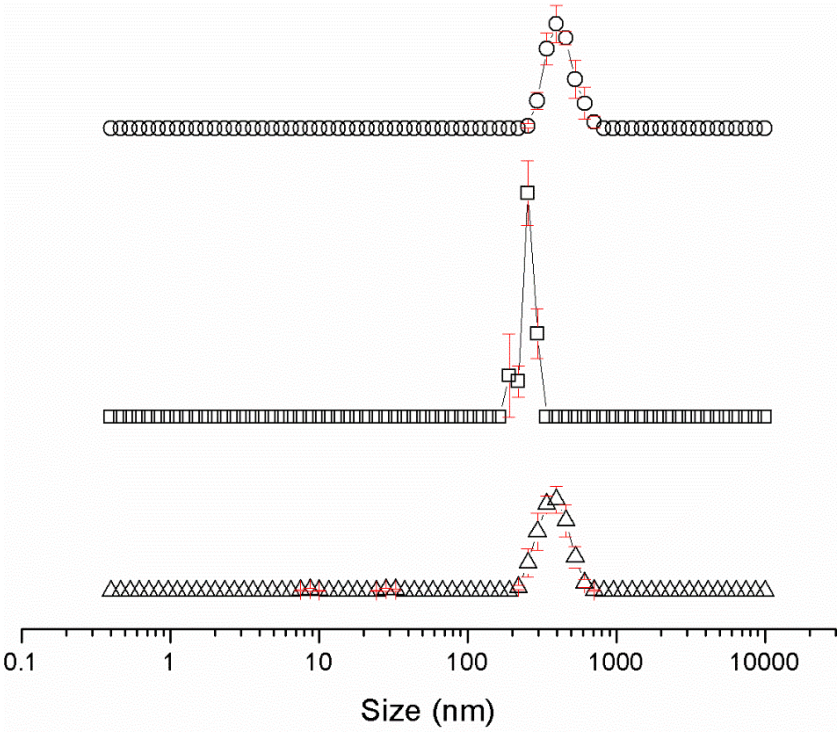

Figure S123 - Average intensity particle size distribution, calculated from 9 DLS runs, of aggregates formed by dissolving compound **50** at a concentration of 0.56 mM in DMSO at Δ) 25 °C, □) heating to 40 °C and ○) cooling to 25 °C. Only 9 of the available 10 DLS runs were used as in some cases, due to the heating and cooling processes there were some obvious temperature equilibration issues for the first run.

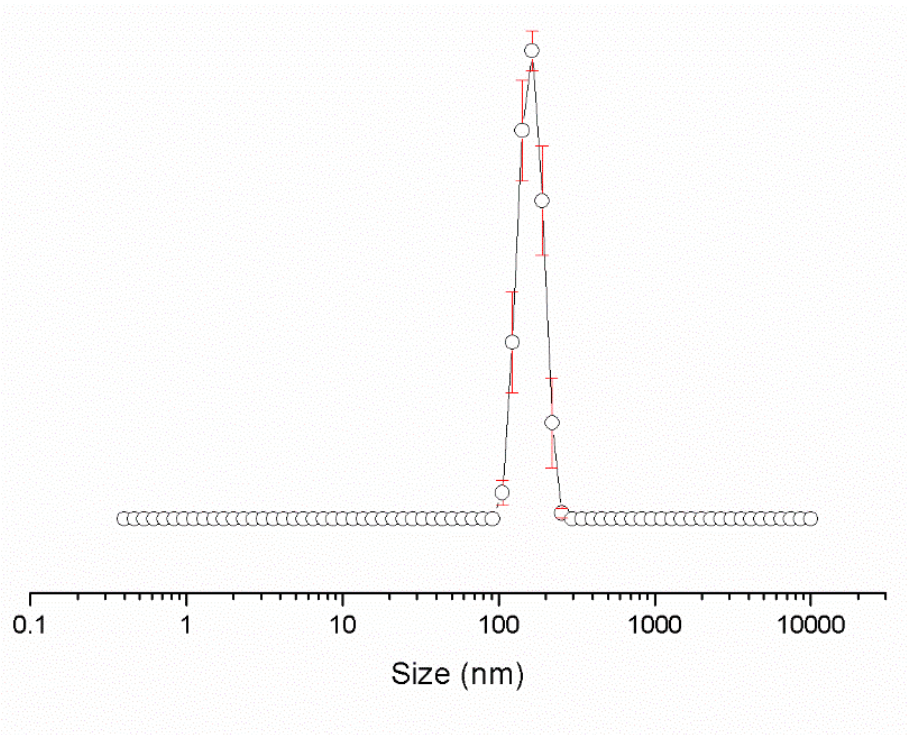

Figure S124 - The average intensity particle size distribution calculated using 9 DLS runs for compound **50** (5.56 mM) in an EtOH:H_2O (1:19) solution at 298.15 K.

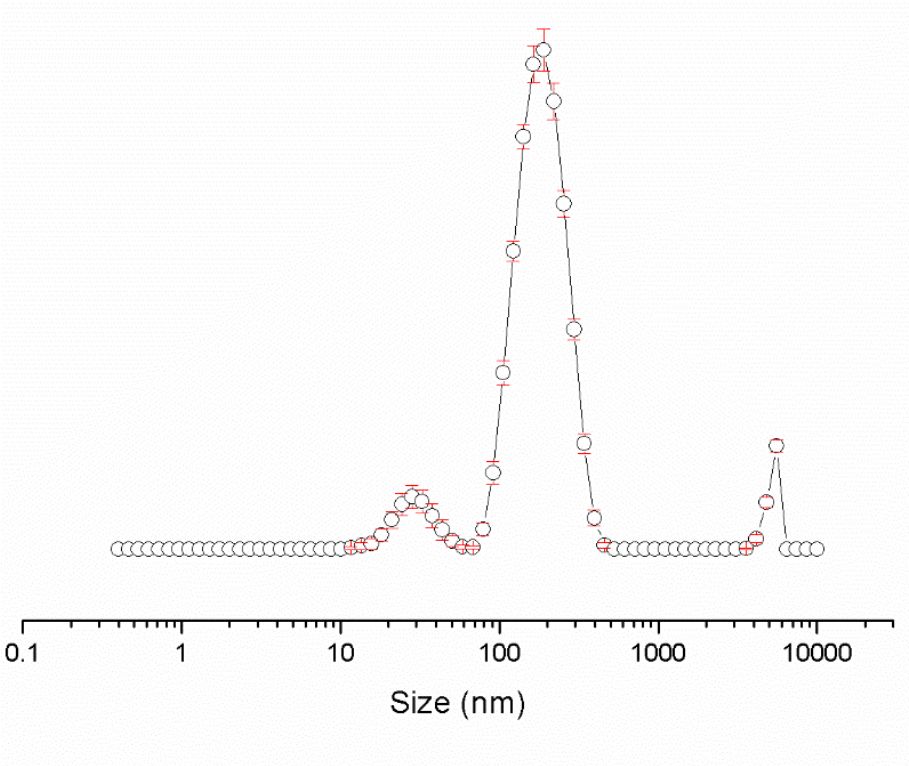

Figure S125 - The average intensity particle size distribution calculated using 9 DLS runs for compound **50** (0.56 mM) in an EtOH:H_2O (1:19) solution at 298.15 K.

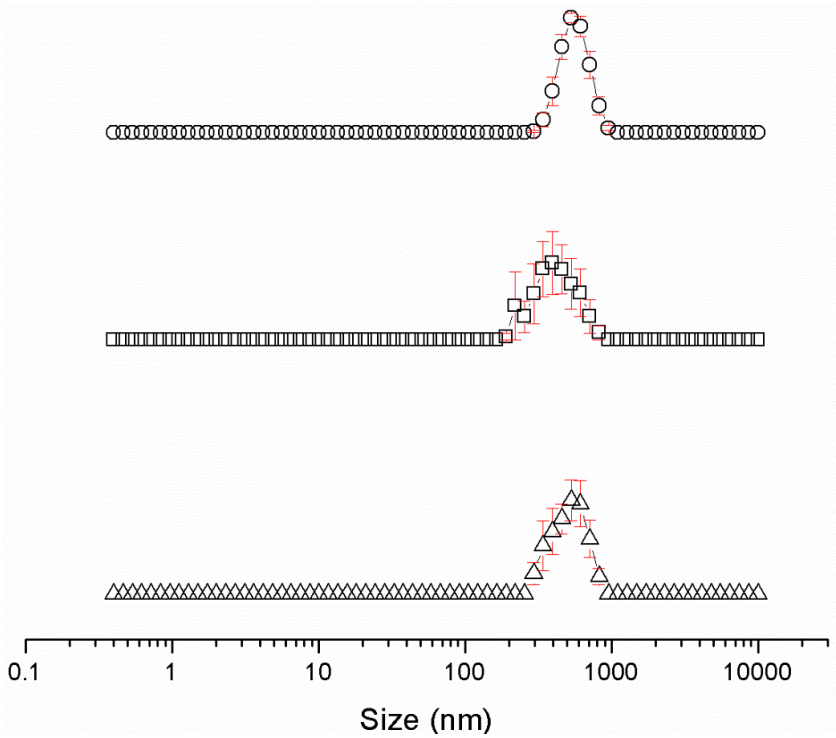

Figure S126 - Average intensity particle size distribution, calculated from 9 DLS runs, of aggregates formed by dissolving compound **51** at a concentration of 5.56 mM in DMSO at Δ) 25 °C, □) heating to 40 °C and ○) cooling to 25 °C. Only 9 of the available 10 DLS runs were used as in some cases, due to the heating and cooling processes there were some obvious temperature equilibration issues for the first run.

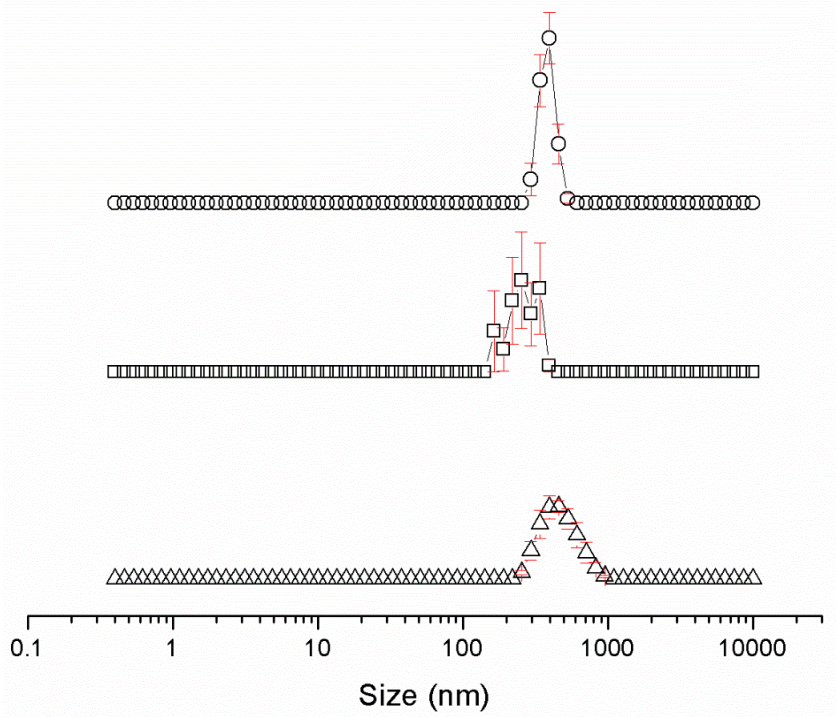

Figure S127 - Average intensity particle size distribution, calculated from 9 DLS runs, of aggregates formed by dissolving compound **51** at a concentration of 0.56 mM in DMSO at Δ) 25 °C, □) heating to 40 °C and ○) cooling to 25 °C. Only 9 of the available 10 DLS runs were used as in some cases, due to the heating and cooling processes there were some obvious temperature equilibration issues for the first run.

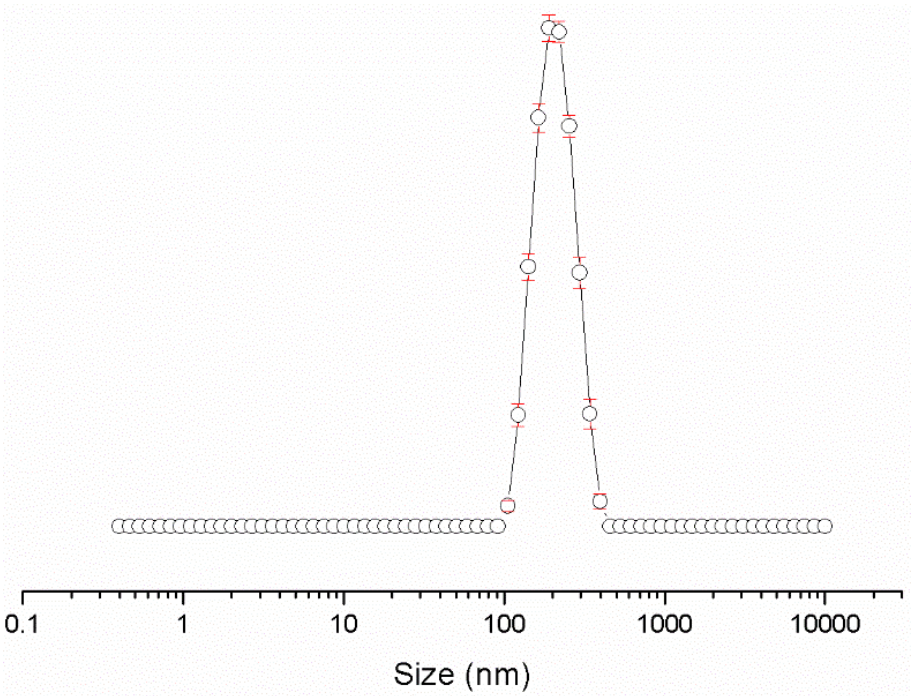

Figure S128 - The average intensity particle size distribution calculated using 9 DLS runs for compound **51** (5.56 mM) in an EtOH:H_2O (1:19) solution at 298.15 K.

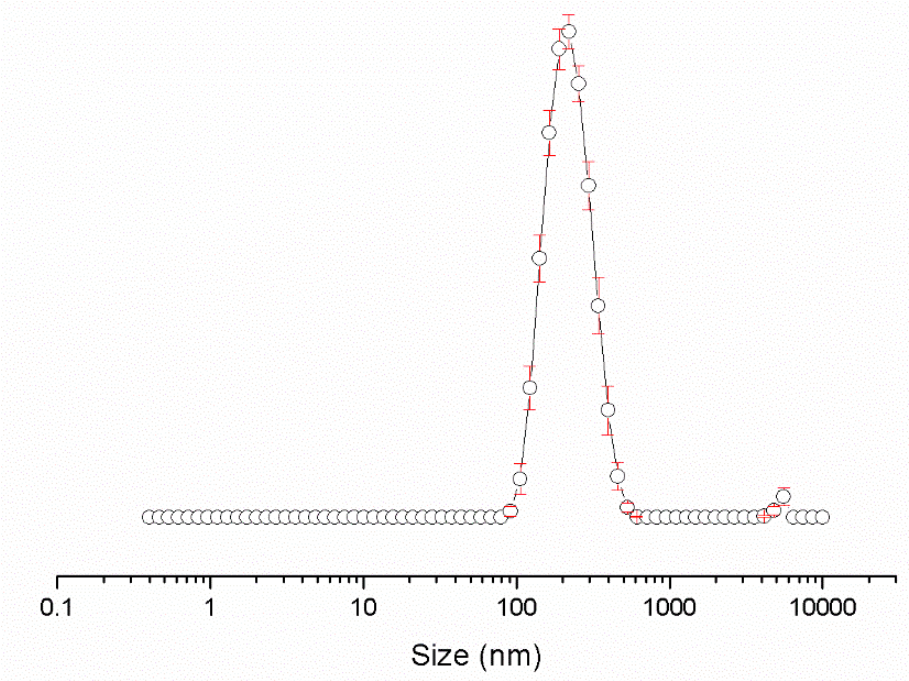

Figure S129 - The average intensity particle size distribution calculated using 9 DLS runs for compound **51** (0.56 mM) in an EtOH:H_2O (1:19) solution at 298.15 K.

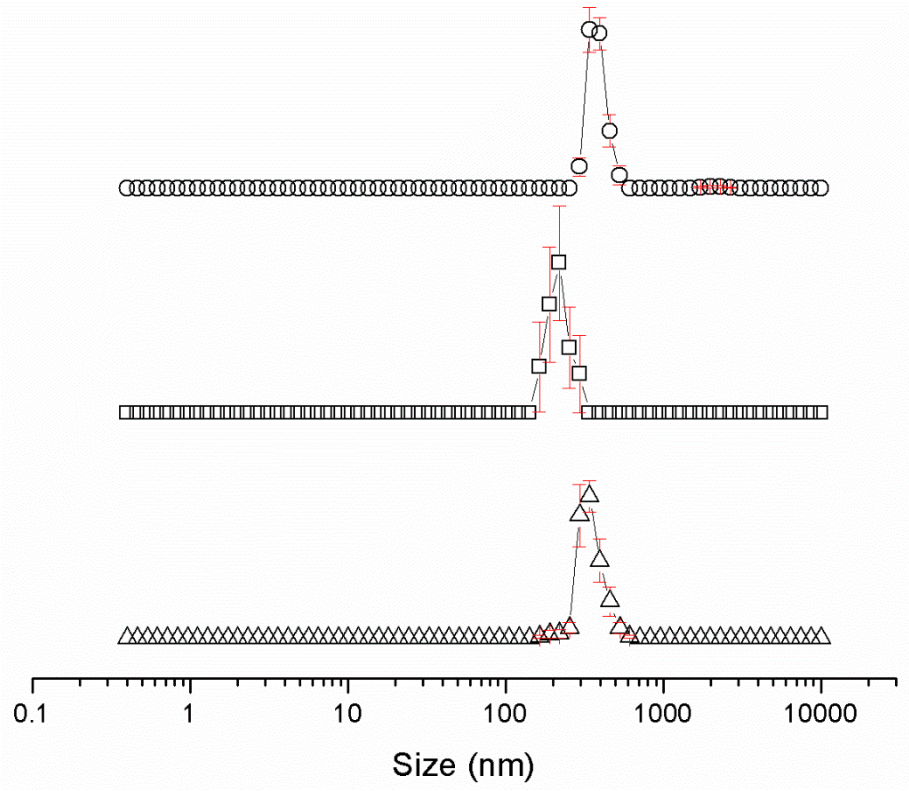

Figure S130 - Average intensity particle size distribution, calculated from 9 DLS runs, of aggregates formed by dissolving compound **52** at a concentration of 5.56 mM in DMSO at Δ) 25 °C, □) heating to 40 °C and ○) cooling to 25 °C. Only 9 of the available 10 DLS runs were used as in some cases, due to the heating and cooling processes there were some obvious temperature equilibration issues for the first run.

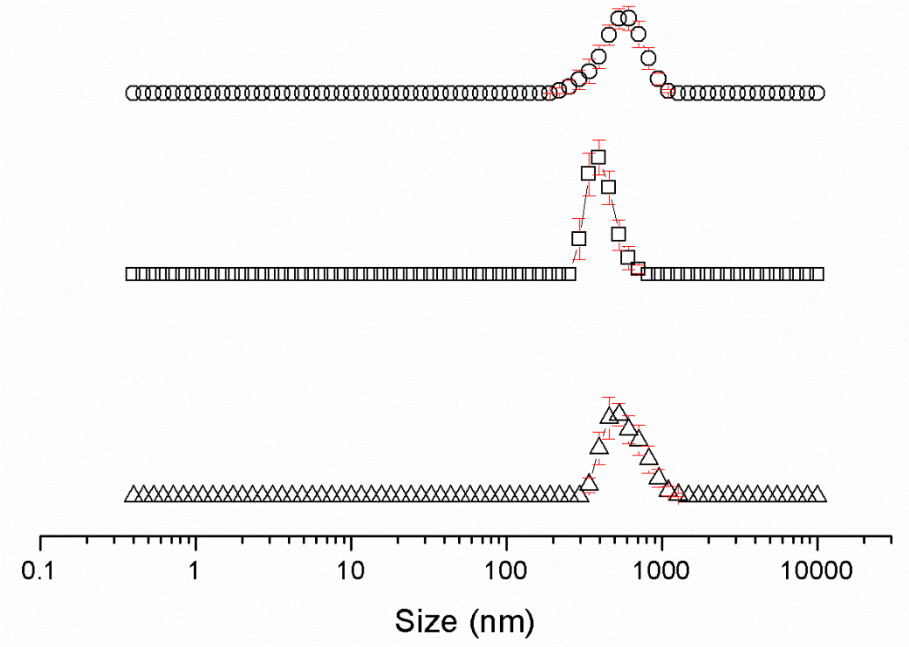

Figure S131 - Average intensity particle size distribution, calculated from 9 DLS runs, of aggregates formed by dissolving compound **52** at a concentration of 0.56 mM in DMSO at Δ) 25 °C, □) heating to 40 °C and ○) cooling to 25 °C. Only 9 of the available 10 DLS runs were used as in some cases, due to the heating and cooling processes there were some obvious temperature equilibration issues for the first run.

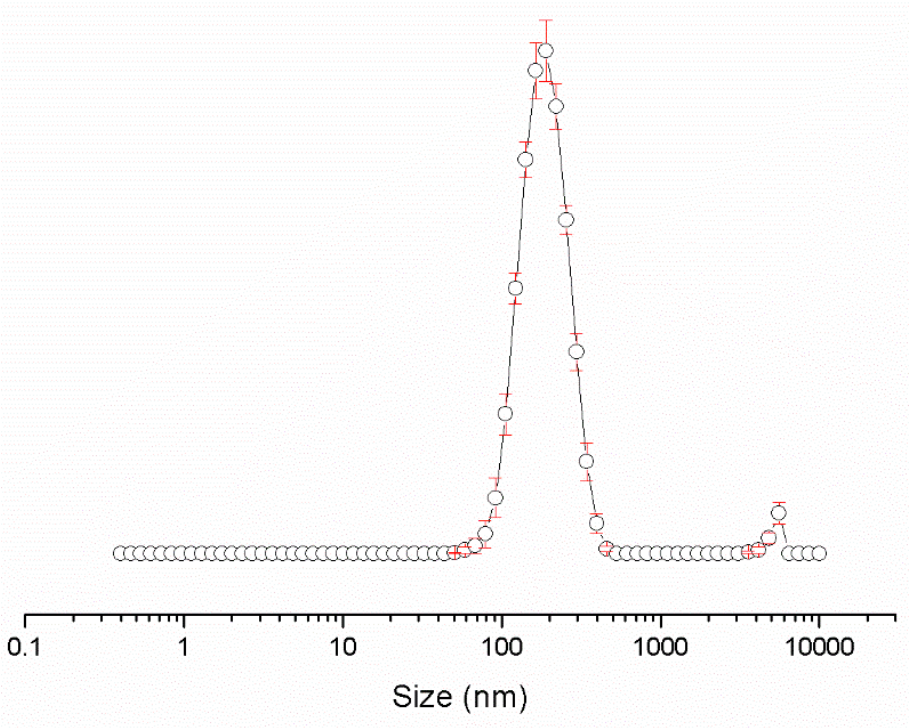

Figure S132 - The average intensity particle size distribution calculated using 9 DLS runs for compound **52** (5.56 mM) in an EtOH:H_2O (1:19) solution at 298.15 K.

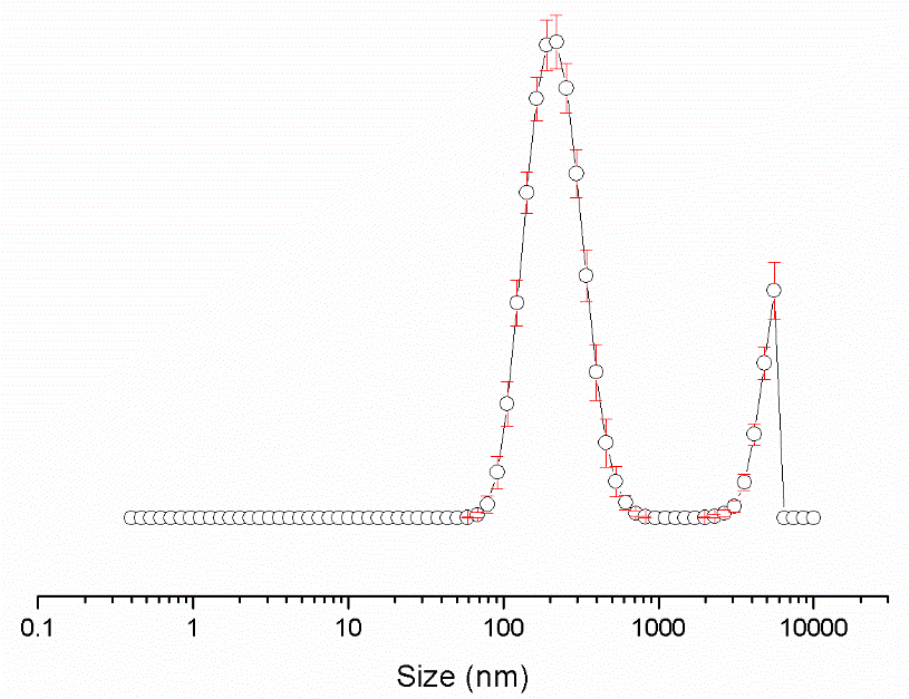

Figure S133 - The average intensity particle size distribution calculated using 9 DLS runs for compound **52** (0.56 mM) in an EtOH:H_2O (1:19) solution at 298.15 K.

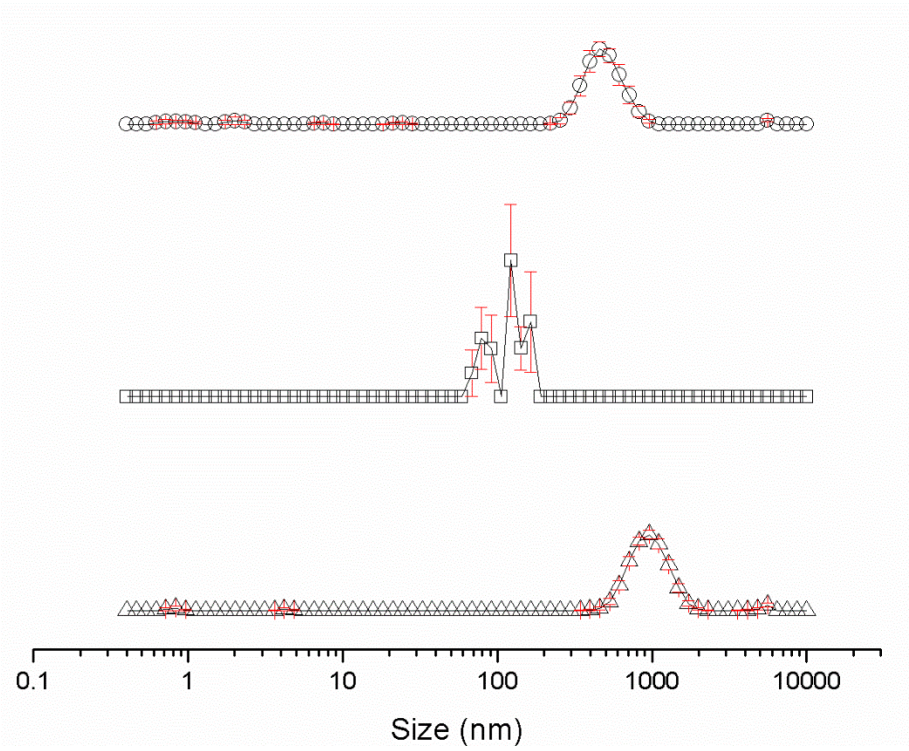

Figure S134 - Average intensity particle size distribution, calculated from 9 DLS runs, of aggregates formed by dissolving compound **53** at a concentration of 5.56 mM in DMSO at Δ) 25 °C, □) heating to 40 °C and ○) cooling to 25 °C. Only 9 of the available 10 DLS runs were used as in some cases, due to the heating and cooling processes there were some obvious temperature equilibration issues for the first run.

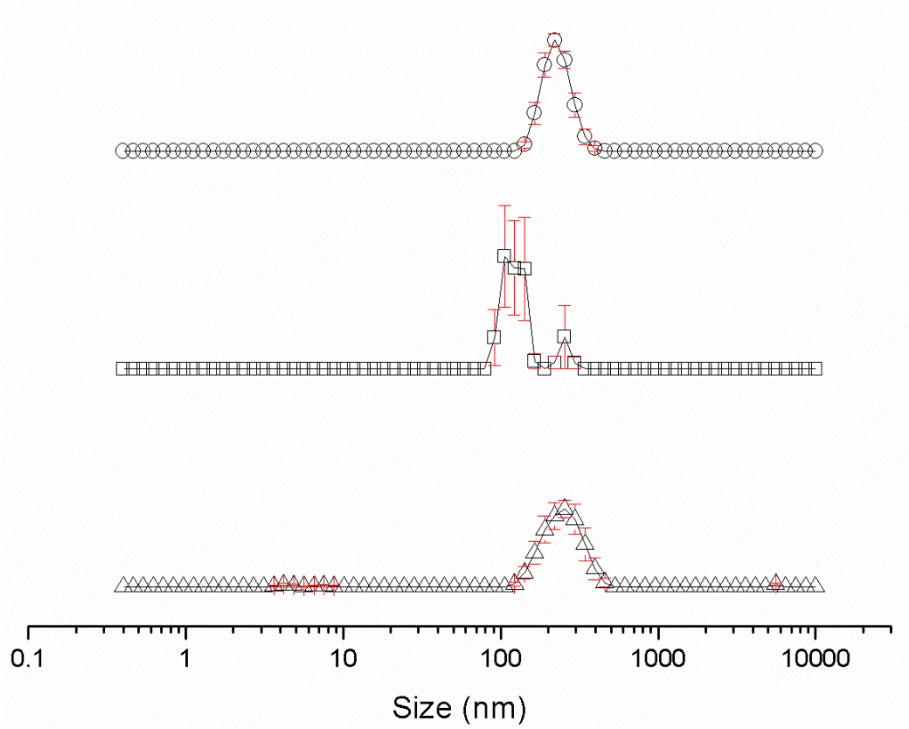

Figure S135 - Average intensity particle size distribution, calculated from 9 DLS runs, of aggregates formed by dissolving compound **53** at a concentration of 0.56 mM in DMSO at Δ) 25 °C, □) heating to 40 °C and ○) cooling to 25 °C. Only 9 of the available 10 DLS runs were used as in some cases, due to the heating and cooling processes there were some obvious temperature equilibration issues for the first run.

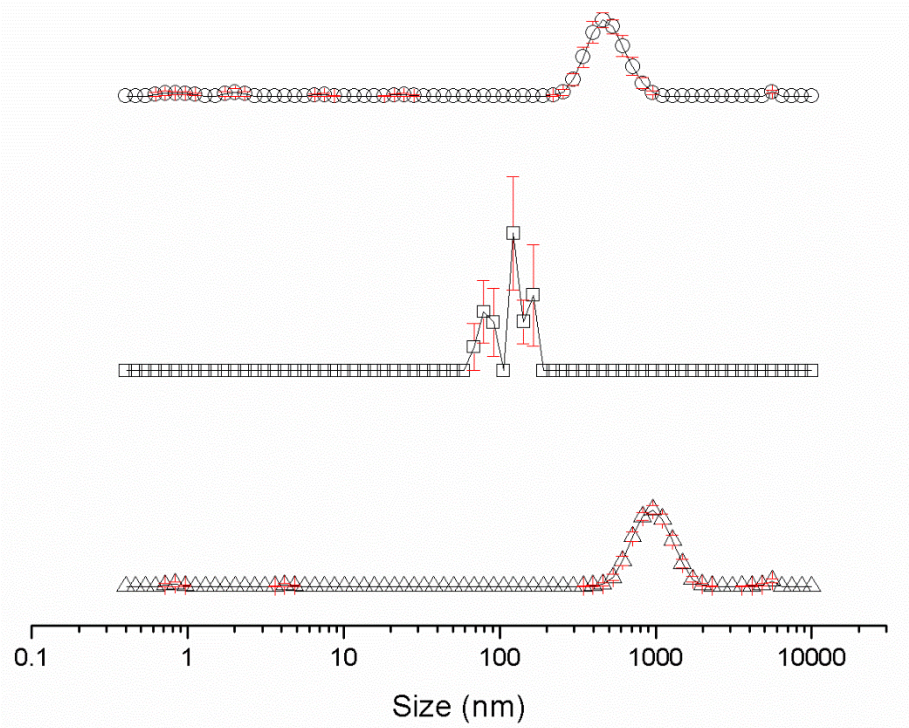

Figure S136 - Average intensity particle size distribution, calculated from 9 DLS runs, of aggregates formed by dissolving compound **54** at a concentration of 5.56 mM in DMSO at Δ) 25 °C, □) heating to 40 °C and ○) cooling to 25 °C. Only 9 of the available 10 DLS runs were used as in some cases, due to the heating and cooling processes there were some obvious temperature equilibration issues for the first run.

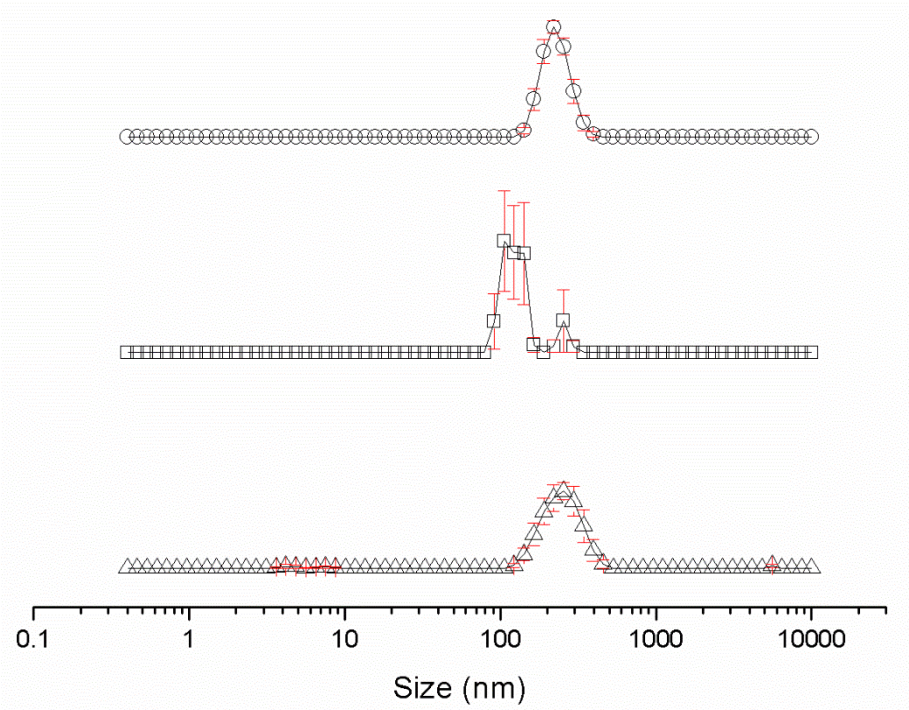

Figure S137 - Average intensity particle size distribution, calculated from 9 DLS runs, of aggregates formed by dissolving compound **54** at a concentration of 0.56 mM in DMSO at Δ) 25 °C, □) heating to 40 °C and ○) cooling to 25 °C. Only 9 of the available 10 DLS runs were used as in some cases, due to the heating and cooling processes there were some obvious temperature equilibration issues for the first run.

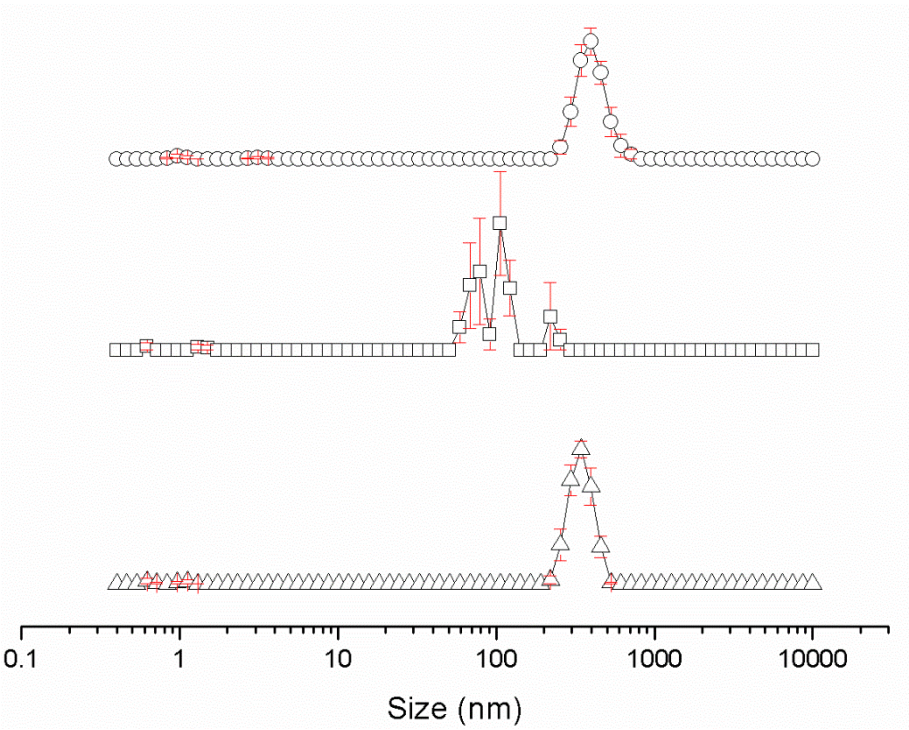

Figure S138 - Average intensity particle size distribution, calculated from 9 DLS runs, of aggregates formed by dissolving compound **55** at a concentration of 5.56 mM in DMSO at Δ) 25 °C, □) heating to 40 °C and ○) cooling to 25 °C. Only 9 of the available 10 DLS runs were used as in some cases, due to the heating and cooling processes there were some obvious temperature equilibration issues for the first run.

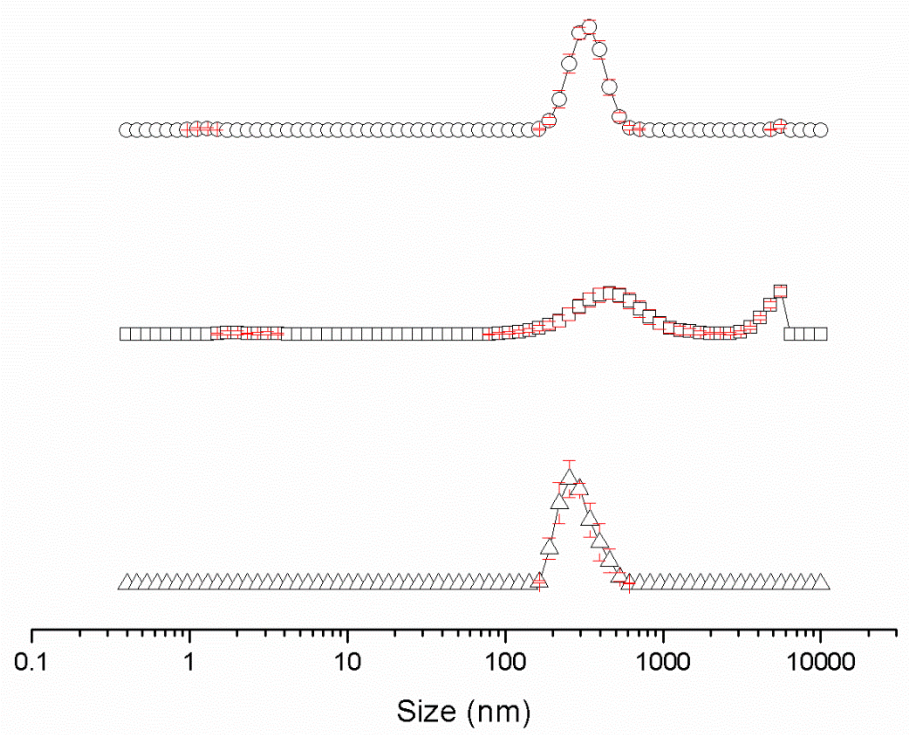

Figure S139 - Average intensity particle size distribution, calculated from 9 DLS runs, of aggregates formed by dissolving compound **55** at a concentration of 0.56 mM in DMSO at Δ) 25 °C, □) heating to 40 °C and ○) cooling to 25 °C. Only 9 of the available 10 DLS runs were used as in some cases, due to the heating and cooling processes there were some obvious temperature equilibration issues for the first run.

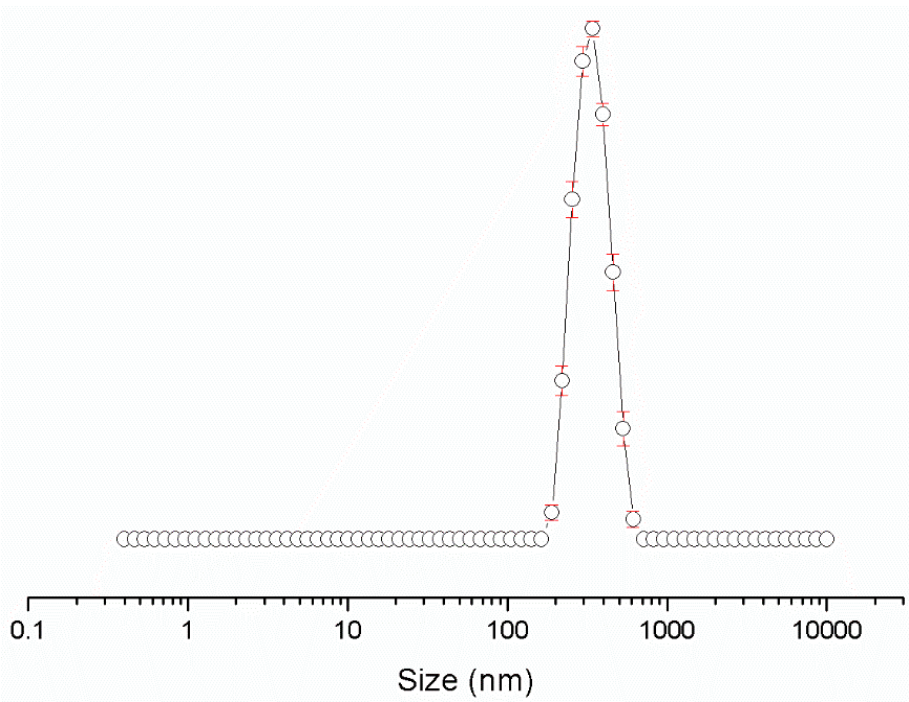

Figure S140 - The average intensity particle size distribution calculated using 9 DLS runs for compound **55** (5.56 mM) in an EtOH:H_2O (1:19) solution at 298.15 K.

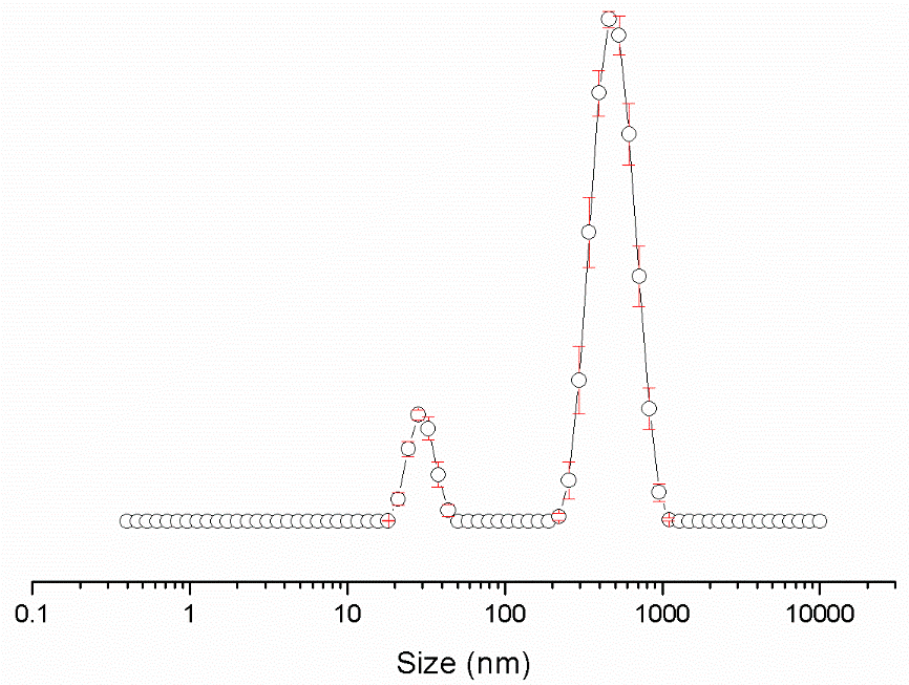

Figure S141 - The average intensity particle size distribution calculated using 9 DLS runs for compound **55** (0.56 mM) in an EtOH:H_2O (1:19) solution at 298.15 K.

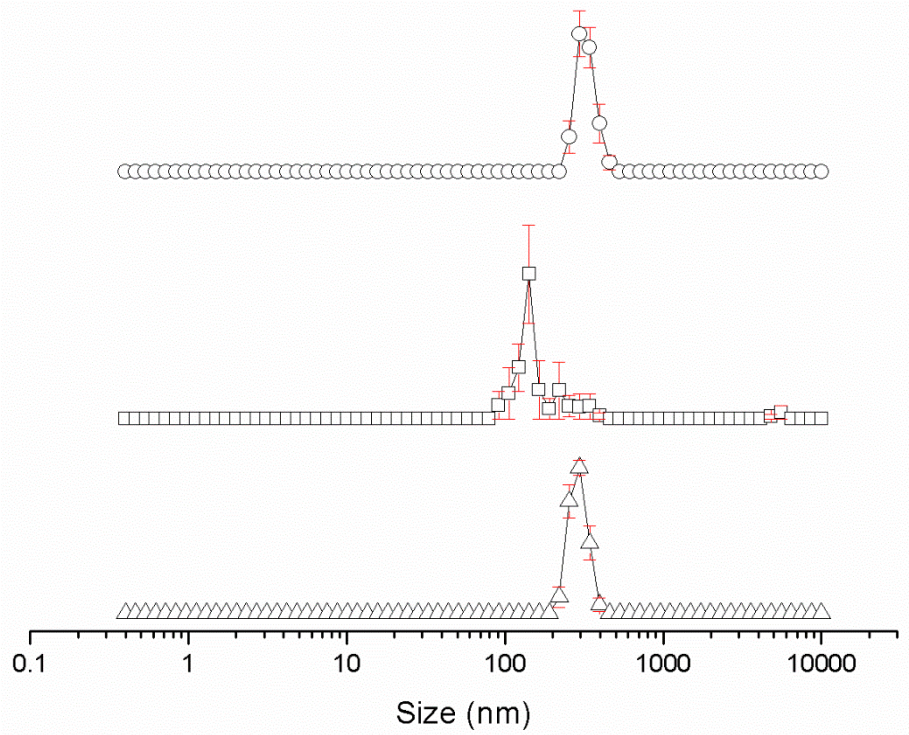

Figure S142 - Average intensity particle size distribution, calculated from 9 DLS runs, of aggregates formed by dissolving compound **56** at a concentration of 5.56 mM in DMSO at Δ) 25 °C, □) heating to 40 °C and ○) cooling to 25 °C. Only 9 of the available 10 DLS runs were used as in some cases, due to the heating and cooling processes there were some obvious temperature equilibration issues for the first run.

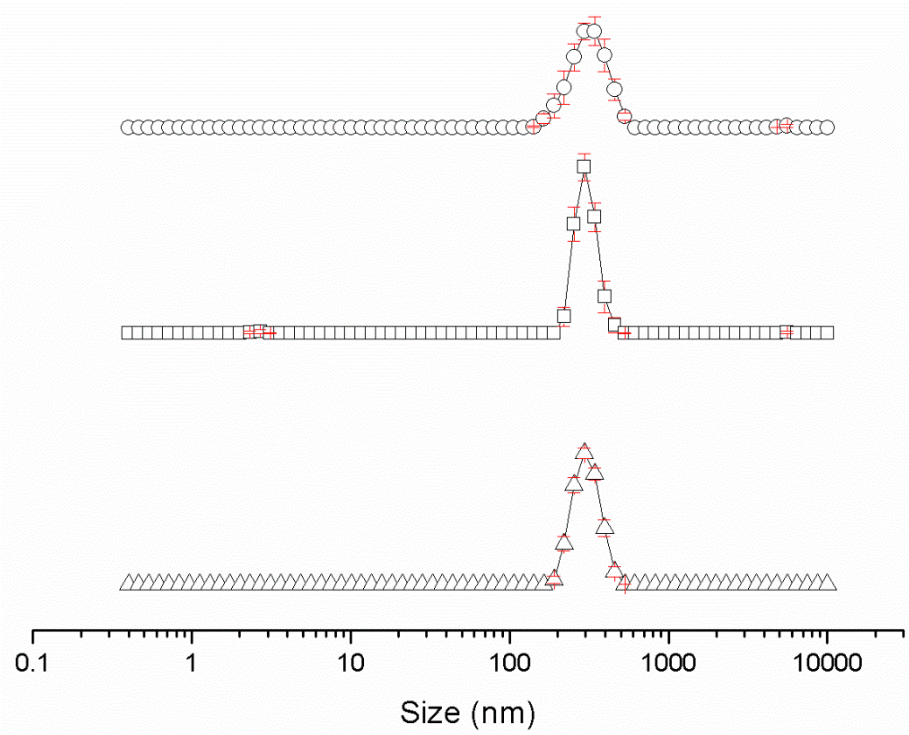

Figure S143 - Average intensity particle size distribution, calculated from 9 DLS runs, of aggregates formed by dissolving compound **56** at a concentration of 0.56 mM in DMSO at Δ) 25 °C, □) heating to 40 °C and ○) cooling to 25 °C. Only 9 of the available 10 DLS runs were used as in some cases, due to the heating and cooling processes there were some obvious temperature equilibration issues for the first run.

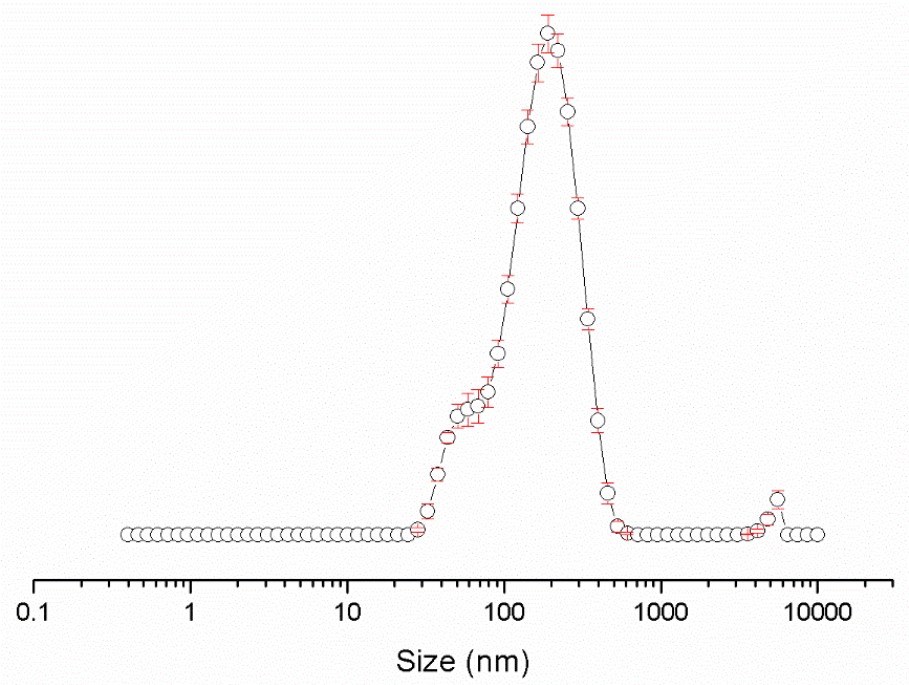

Figure S144 - The average intensity particle size distribution calculated using 9 DLS runs for compound **56** (5.56 mM) in an EtOH:H_2O (1:19) solution at 298.15 K.

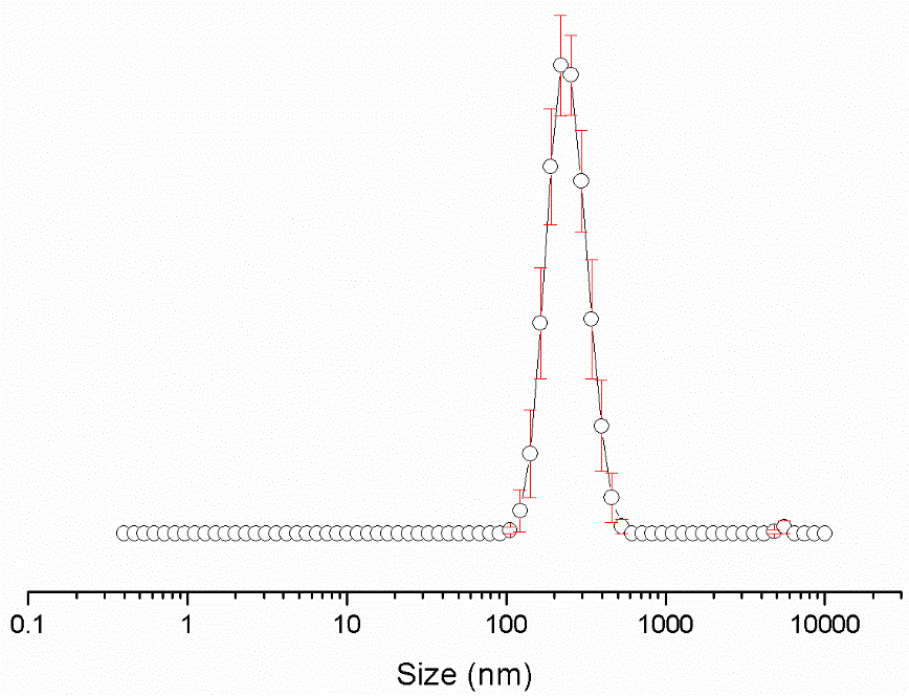

Figure S145 - The average intensity particle size distribution calculated using 9 DLS runs for compound **56** (0.56 mM) in an EtOH:H_2O (1:19) solution at 298.15 K.

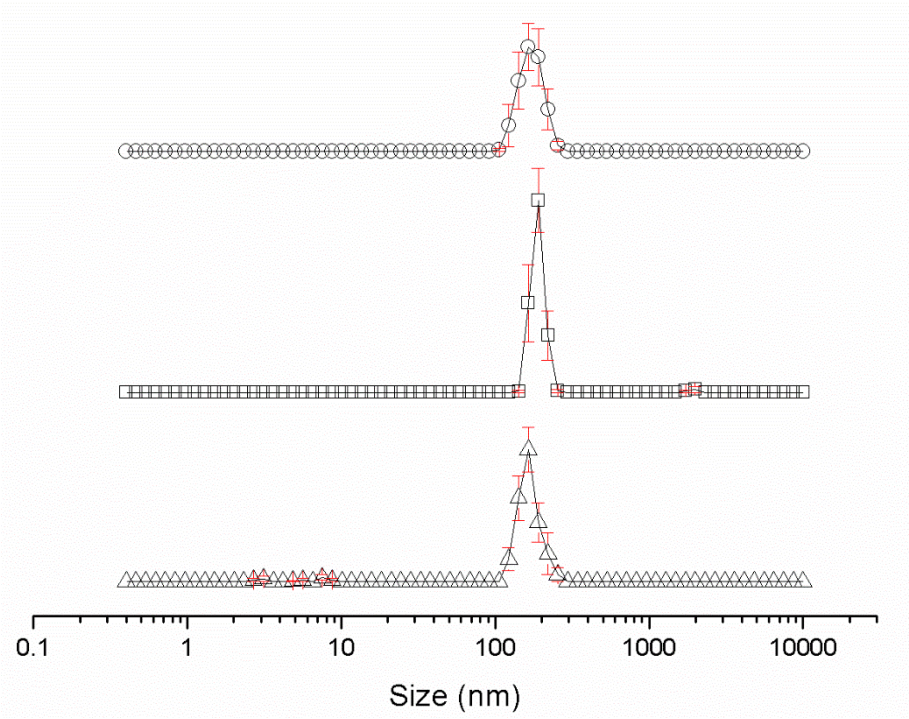

Figure S146 - Average intensity particle size distribution, calculated from 9 DLS runs, of aggregates formed by dissolving compound **58** at a concentration of 5.56 mM in DMSO at Δ) 25 °C, □) heating to 40 °C and ○) cooling to 25 °C. Only 9 of the available 10 DLS runs were used as in some cases, due to the heating and cooling processes there were some obvious temperature equilibration issues for the first run.

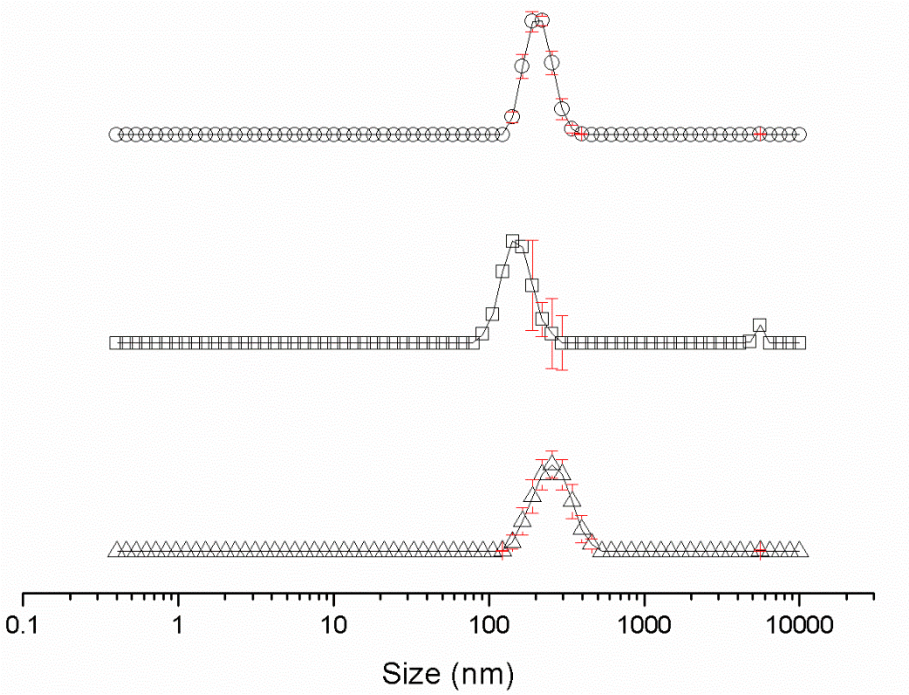

Figure S147 - Average intensity particle size distribution, calculated from 9 DLS runs, of aggregates formed by dissolving compound **58** at a concentration of 0.56 mM in DMSO at Δ) 25 °C, □) heating to 40 °C and ○) cooling to 25 °C. Only 9 of the available 10 DLS runs were used as in some cases, due to the heating and cooling processes there were some obvious temperature equilibration issues for the first run.

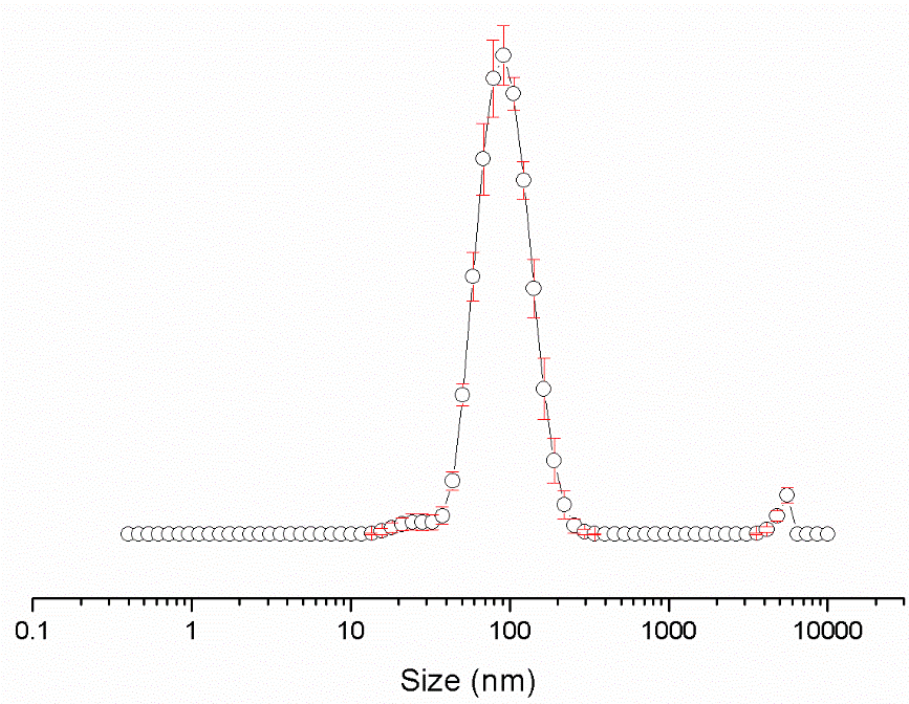

Figure S148 - The average intensity particle size distribution calculated using 9 DLS runs for compound **58** (5.56 mM) in an EtOH:H_2O (1:19) solution at 298.15 K.

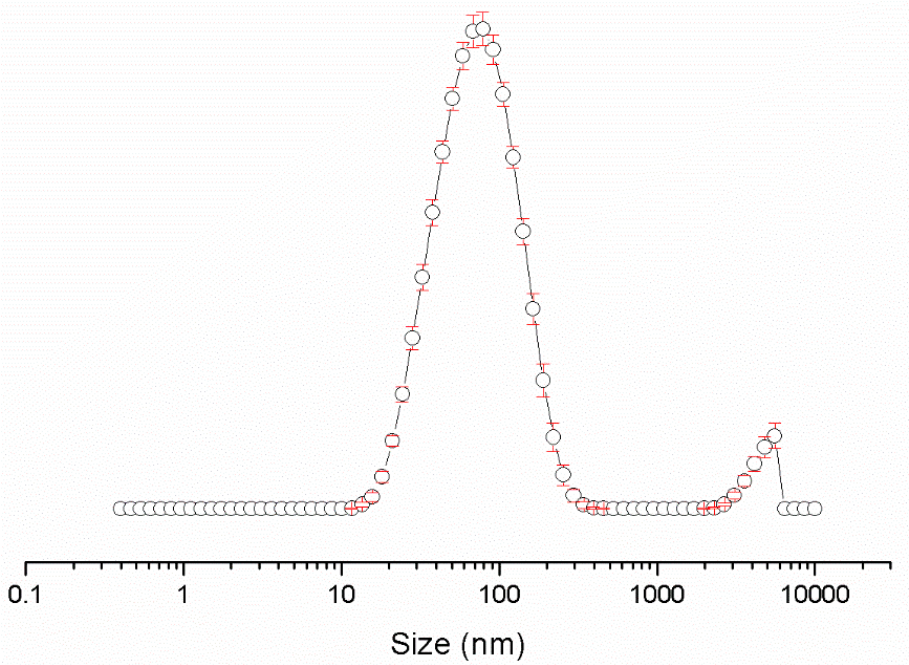

Figure S149 - The average intensity particle size distribution calculated using 9 DLS runs for compound **58** (0.56 mM) in an EtOH:H_2O (1:19) solution at 298.15 K.

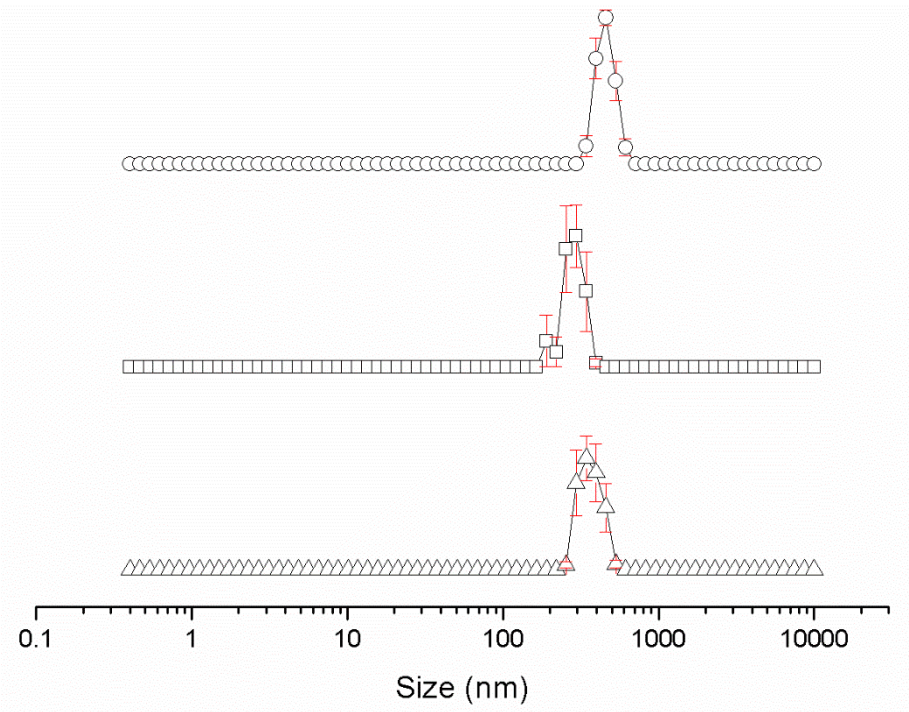

Figure S150 - Average intensity particle size distribution, calculated from 9 DLS runs, of aggregates formed by dissolving compound **60** at a concentration of 5.56 mM in DMSO at Δ) 25 °C, □) heating to 40 °C and ○) cooling to 25 °C. Only 9 of the available 10 DLS runs were used as in some cases, due to the heating and cooling processes there were some obvious temperature equilibration issues for the first run.

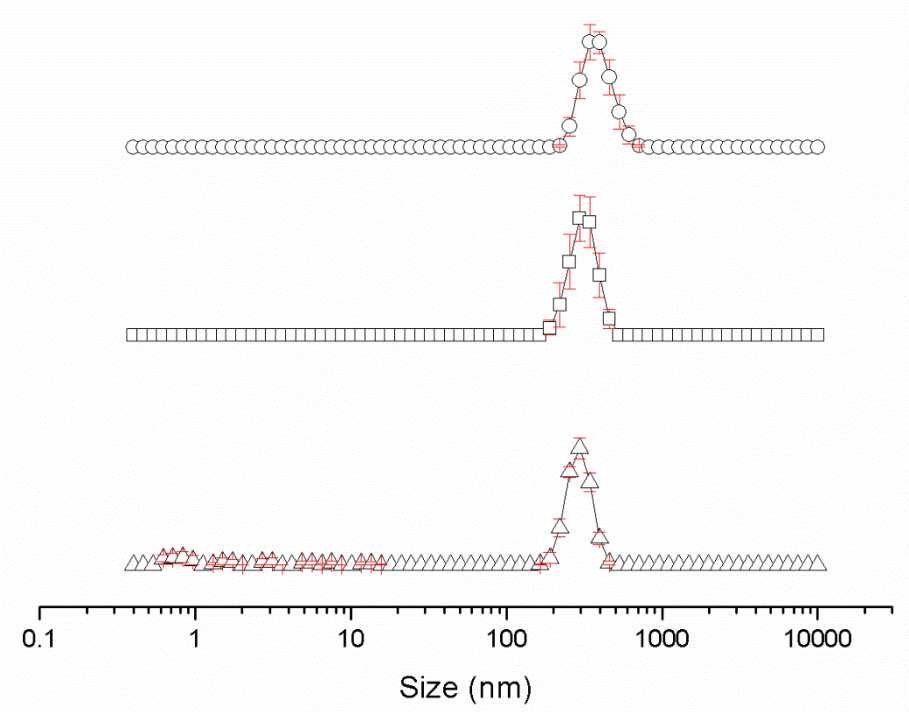

Figure S151 - Average intensity particle size distribution, calculated from 9 DLS runs, of aggregates formed by dissolving compound **60** at a concentration of 0.56 mM in DMSO at Δ) 25 °C, □) heating to 40 °C and ○) cooling to 25 °C. Only 9 of the available 10 DLS runs were used as in some cases, due to the heating and cooling processes there were some obvious temperature equilibration issues for the first run.

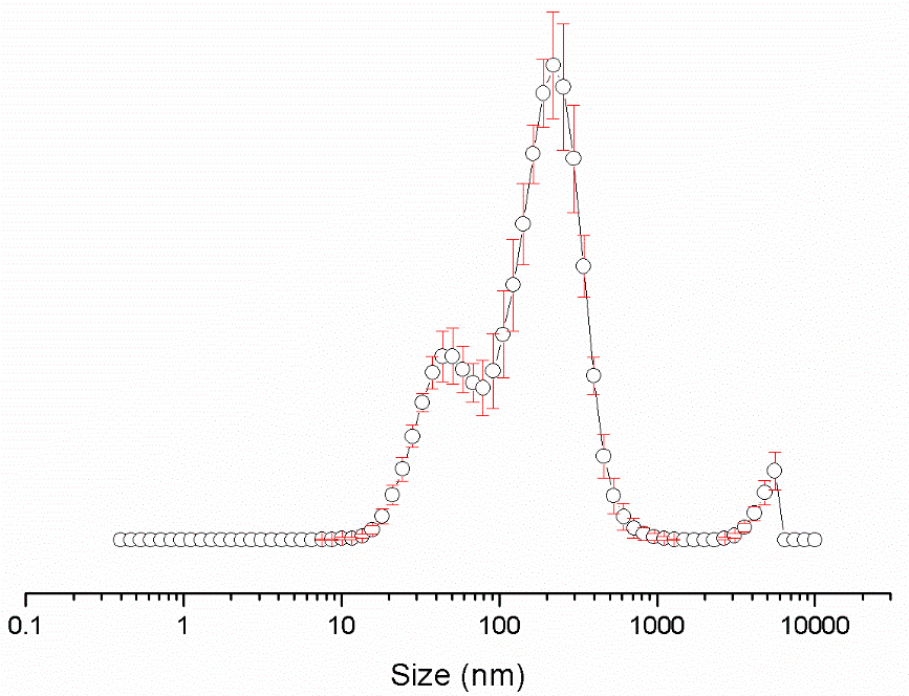

Figure S152 - The average intensity particle size distribution calculated using 9 DLS runs for compound **60** (5.56 mM) in an EtOH:H_2O (1:19) solution at 298.15 K.

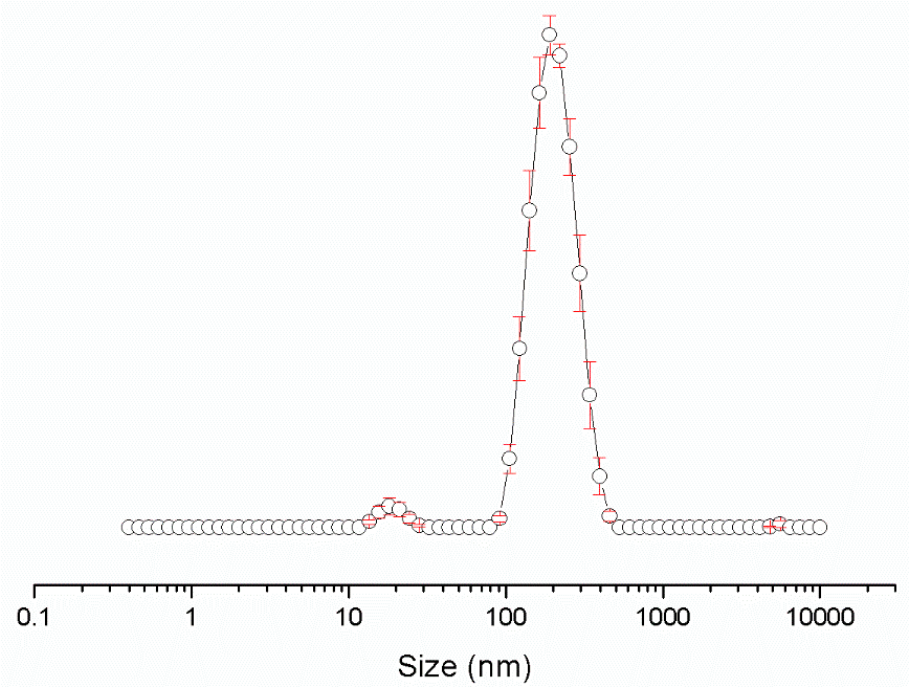

Figure S153 - The average intensity particle size distribution calculated using 9 DLS runs for compound **60** (0.56 mM) in an EtOH:H_2O (1:19) solution at 298.15 K.

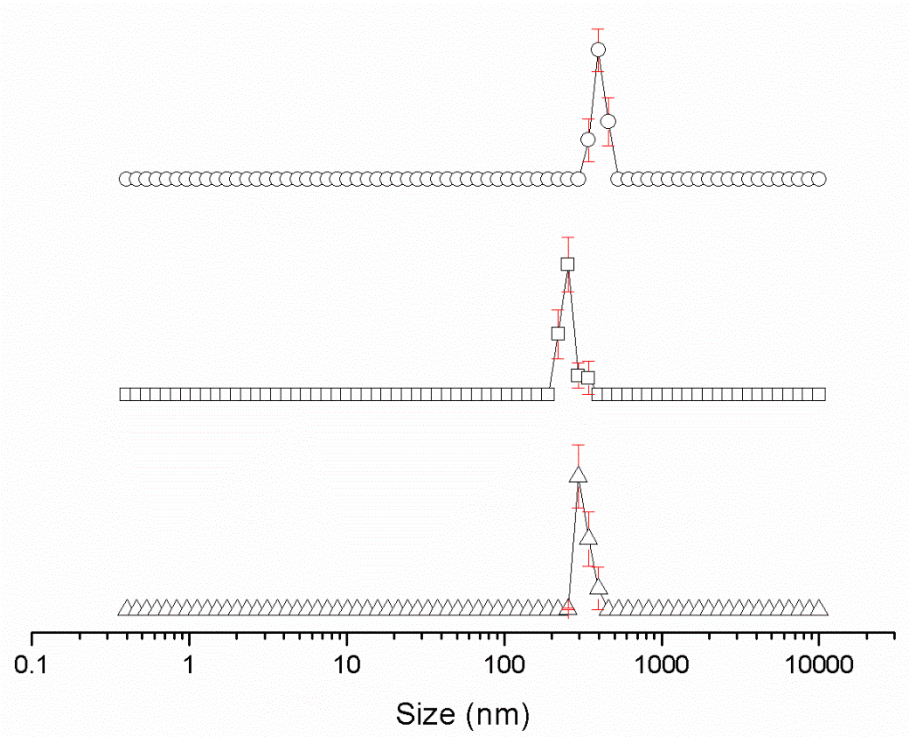

Figure S154 - Average intensity particle size distribution, calculated from 9 DLS runs, of aggregates formed by dissolving compound **61** at a concentration of 5.56 mM in DMSO at Δ) 25 °C, □) heating to 40 °C and ○) cooling to 25 °C. Only 9 of the available 10 DLS runs were used as in some cases, due to the heating and cooling processes there were some obvious temperature equilibration issues for the first run.

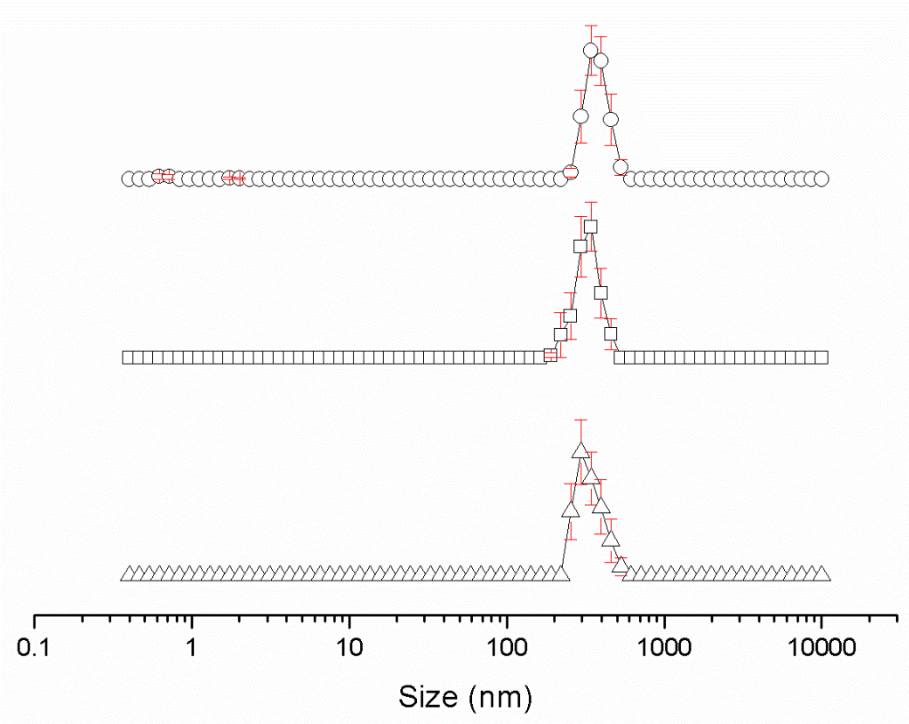

Figure S155 - Average intensity particle size distribution, calculated from 9 DLS runs, of aggregates formed by dissolving compound **61** at a concentration of 0.56 mM in DMSO at Δ) 25 °C, □) heating to 40 °C and ○) cooling to 25 °C. Only 9 of the available 10 DLS runs were used as in some cases, due to the heating and cooling processes there were some obvious temperature equilibration issues for the first run.

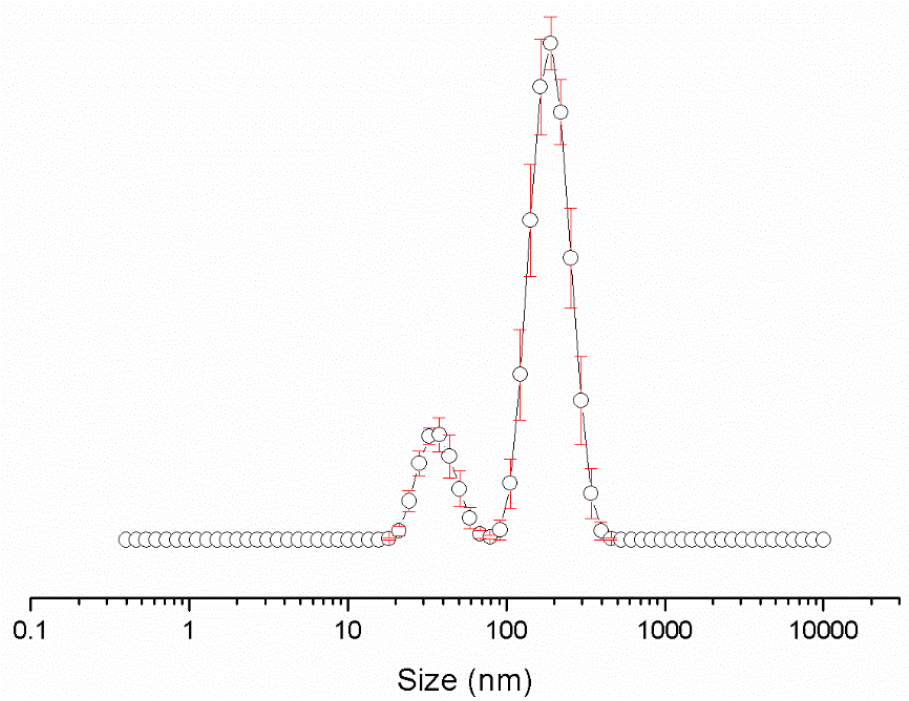

Figure S156 - The average intensity particle size distribution calculated using 9 DLS runs for compound **61** (5.56 mM) in an EtOH:H_2O (1:19) solution at 298.15 K.

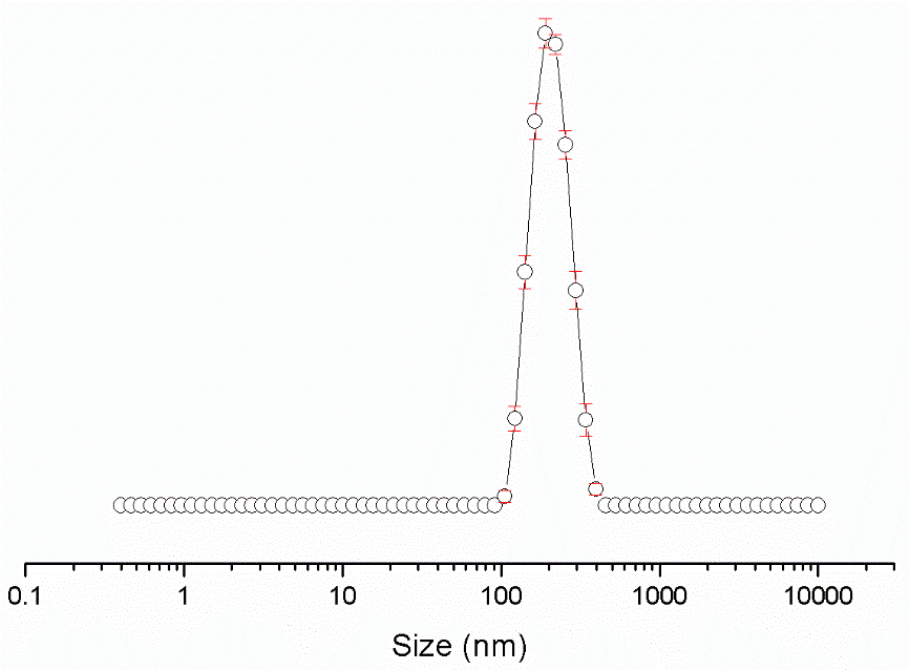

Figure S157 - The average intensity particle size distribution calculated using 9 DLS runs for compound **61** (0.56 mM) in an EtOH:H_2O (1:19) solution at 298.15 K.

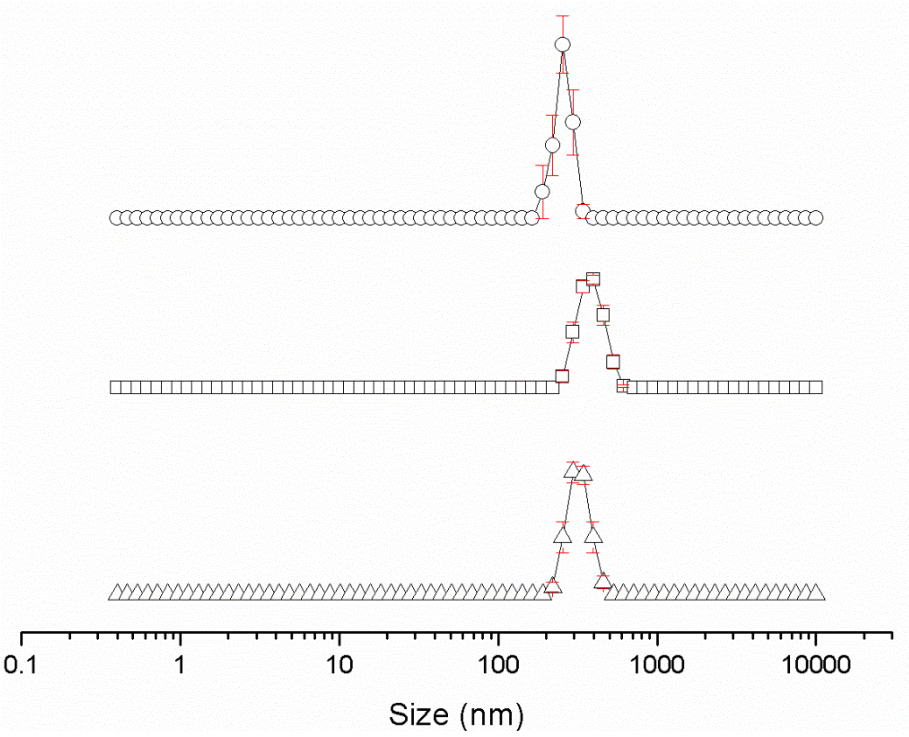

Figure S158 - Average intensity particle size distribution, calculated from 9 DLS runs, of aggregates formed by dissolving compound **62** at a concentration of 5.56 mM in DMSO at Δ) 25 °C, □) heating to 40 °C and ○) cooling to 25 °C. Only 9 of the available 10 DLS runs were used as in some cases, due to the heating and cooling processes there were some obvious temperature equilibration issues for the first run.

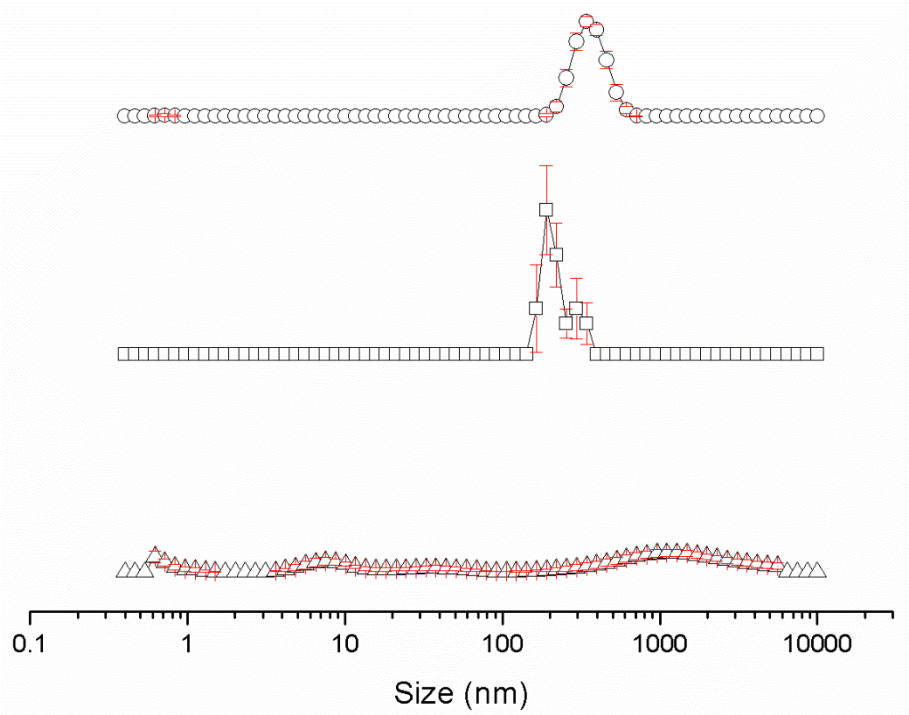

Figure S159 - Average intensity particle size distribution, calculated from 9 DLS runs, of aggregates formed by dissolving compound **62** at a concentration of 0.56 mM in DMSO at Δ) 25 °C, □) heating to 40 °C and ○) cooling to 25 °C. Only 9 of the available 10 DLS runs were used as in some cases, due to the heating and cooling processes there were some obvious temperature equilibration issues for the first run.

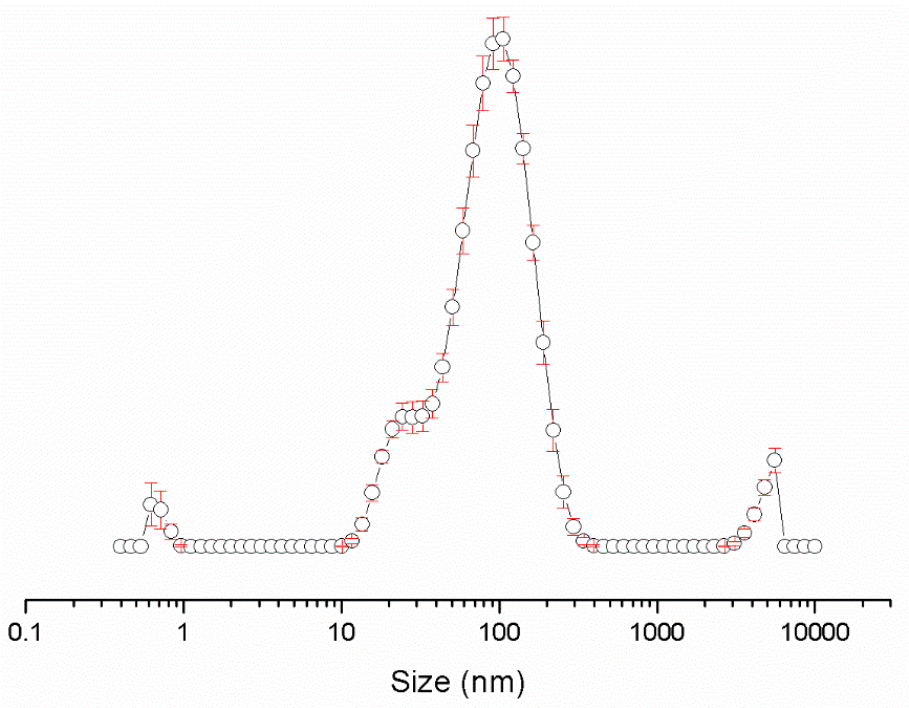

Figure S160 - The average intensity particle size distribution calculated using 9 DLS runs for compound **62** (5.56 mM) in an EtOH:H_2O (1:19) solution at 298.15 K.

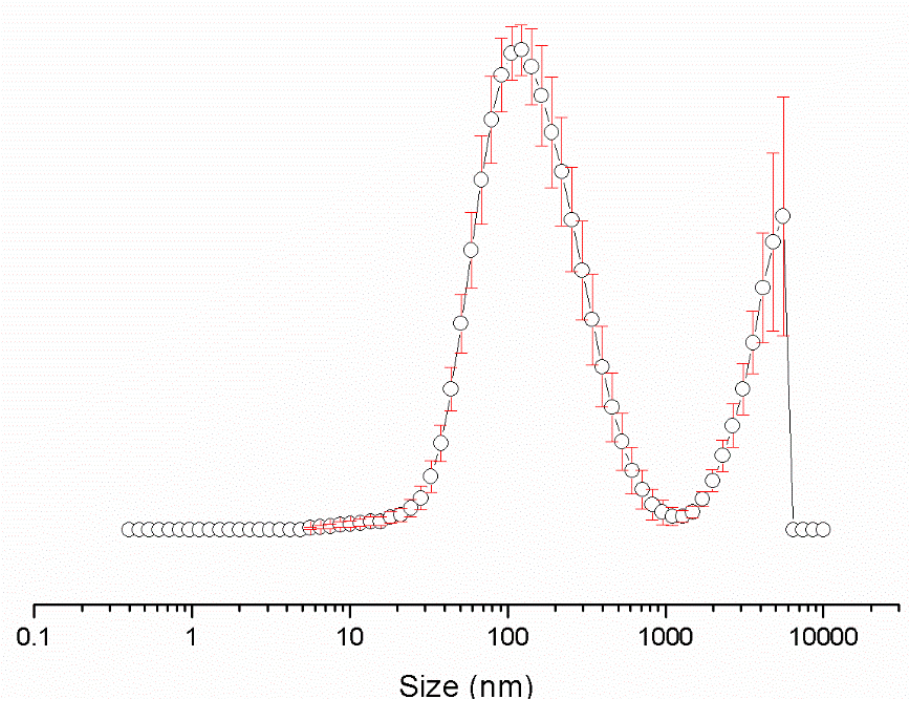

Figure S161 - The average intensity particle size distribution calculated using 9 DLS runs for compound **62** (0.56 mM) in an EtOH:H_2O (1:19) solution at 298.15 K.

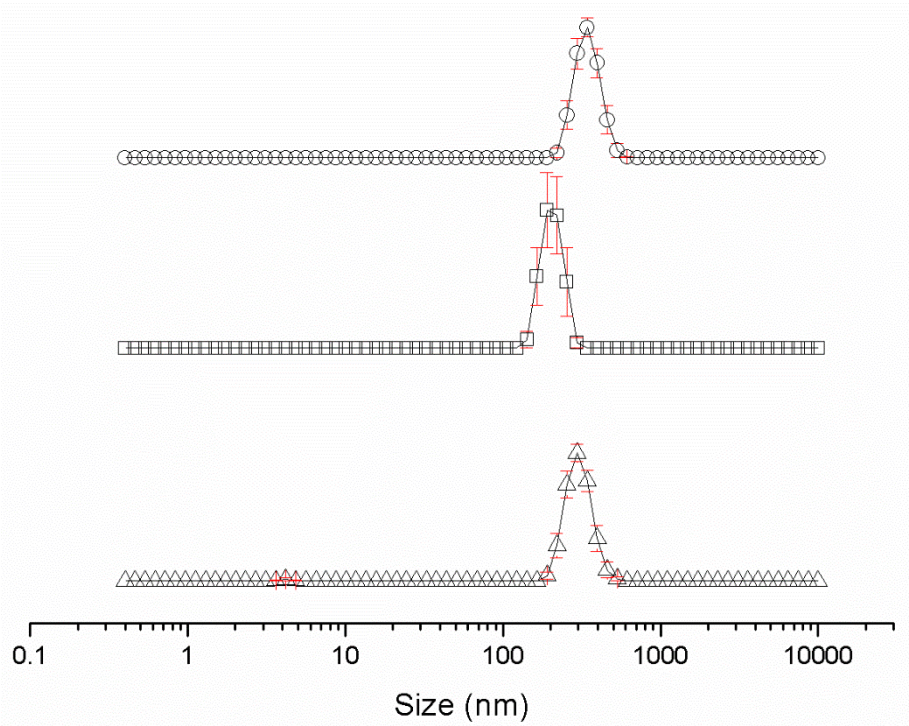

Figure S162 - Average intensity particle size distribution, calculated from 9 DLS runs, of aggregates formed by dissolving compound **63** at a concentration of 5.56 mM in DMSO at Δ) 25 °C, □) heating to 40 °C and ○) cooling to 25 °C. Only 9 of the available 10 DLS runs were used as in some cases, due to the heating and cooling processes there were some obvious temperature equilibration issues for the first run.

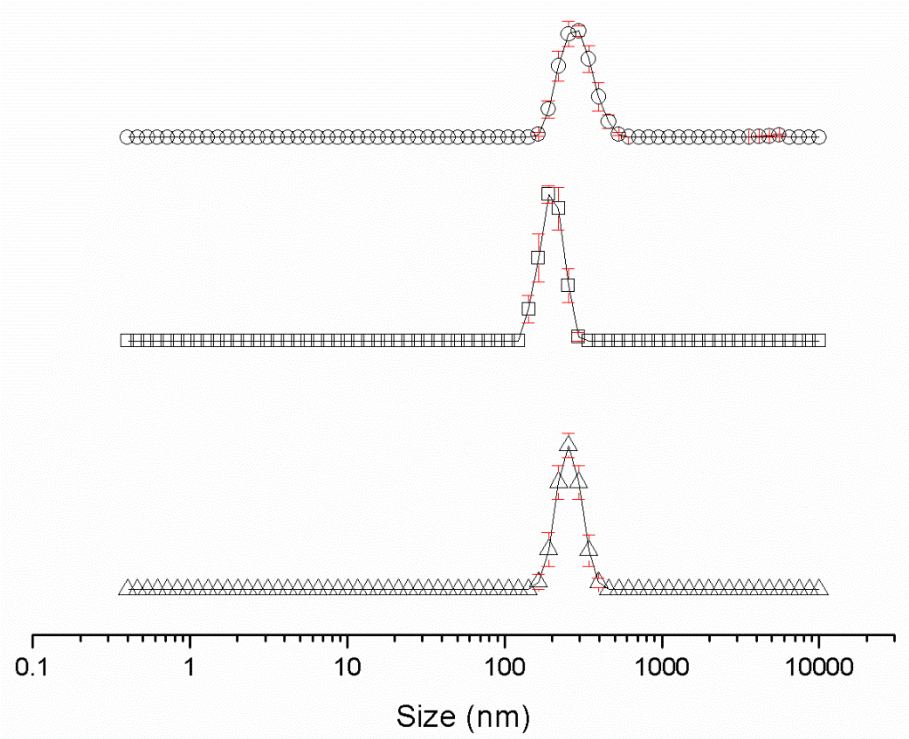

Figure S163 - Average intensity particle size distribution, calculated from 9 DLS runs, of aggregates formed by dissolving compound **63** at a concentration of 0.56 mM in DMSO at Δ) 25 °C, □) heating to 40 °C and ○) cooling to 25 °C. Only 9 of the available 10 DLS runs were used as in some cases, due to the heating and cooling processes there were some obvious temperature equilibration issues for the first run.

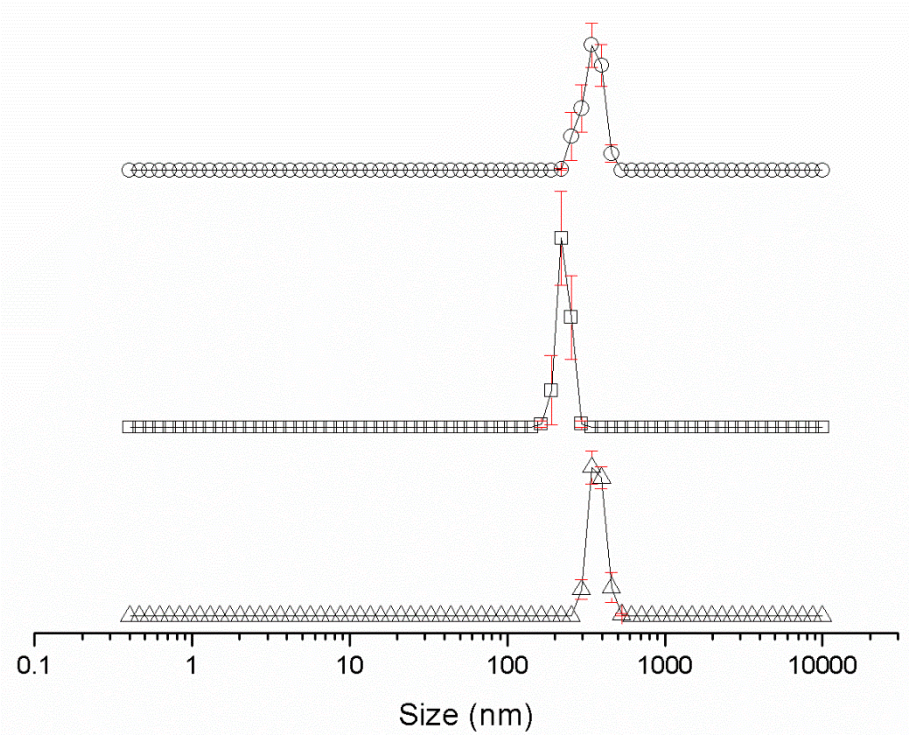

Figure S164 - Average intensity particle size distribution, calculated from 9 DLS runs, of aggregates formed by dissolving compound **64** at a concentration of 5.56 mM in DMSO at Δ) 25 °C, □) heating to 40 °C and ○) cooling to 25 °C. Only 9 of the available 10 DLS runs were used as in some cases, due to the heating and cooling processes there were some obvious temperature equilibration issues for the first run.

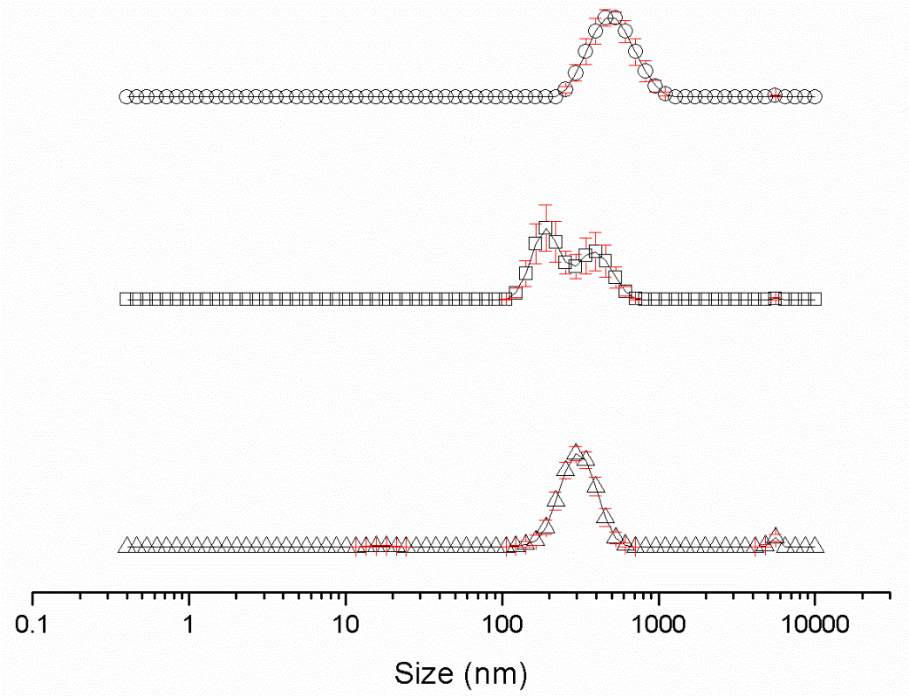

Figure S165 - Average intensity particle size distribution, calculated from 9 DLS runs, of aggregates formed by dissolving compound **64** at a concentration of 0.56 mM in DMSO at Δ) 25 °C, □) heating to 40 °C and ○) cooling to 25 °C. Only 9 of the available 10 DLS runs were used as in some cases, due to the heating and cooling processes there were some obvious temperature equilibration issues for the first run.

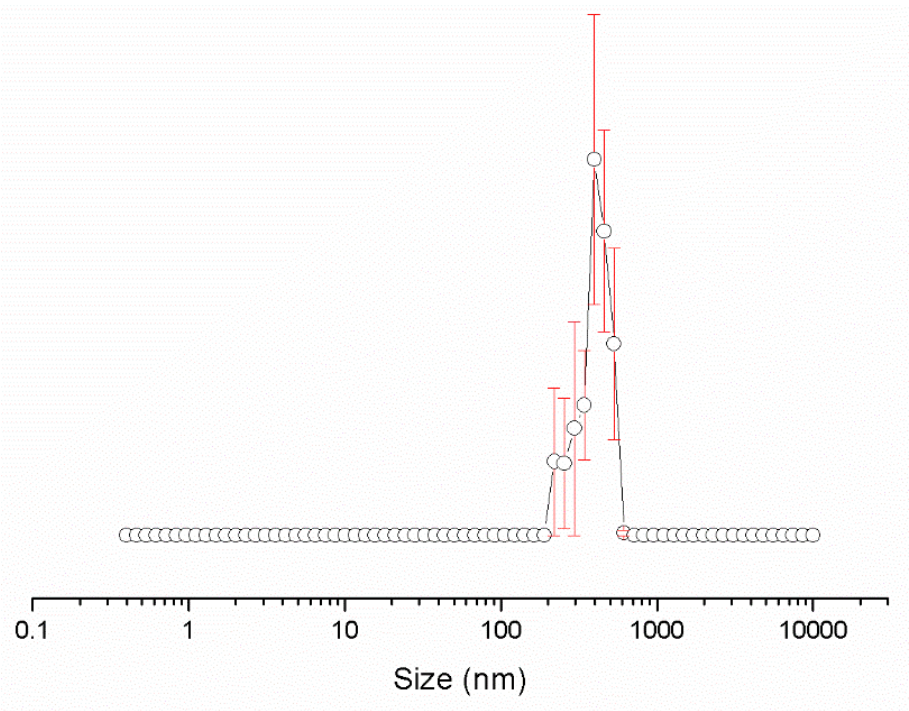

Figure S166 - The average intensity particle size distribution calculated using 9 DLS runs for compound **64** (5.56 mM) in an EtOH:H_2O (1:19) solution at 298.15 K.

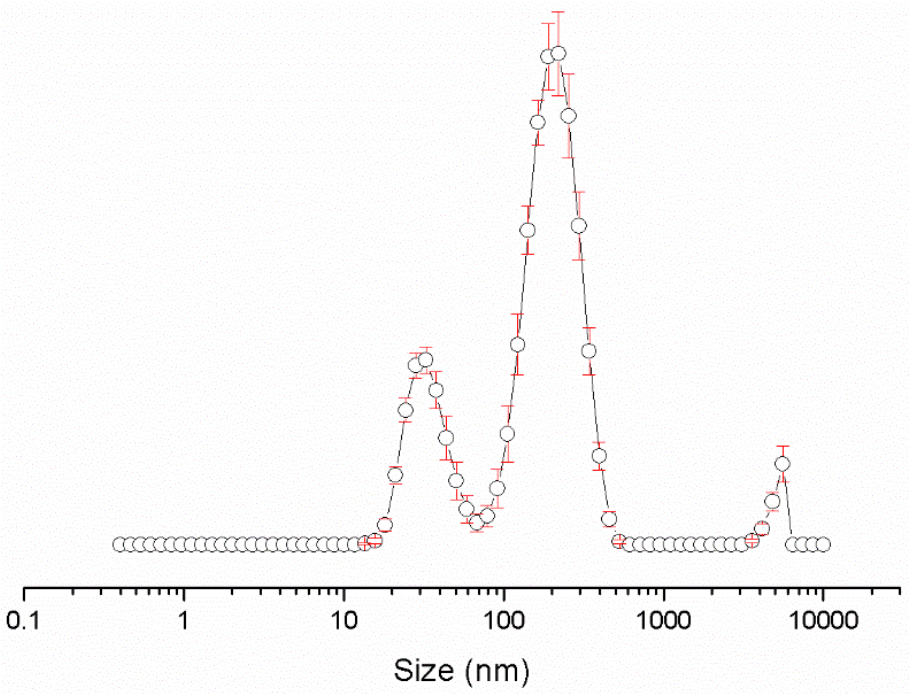

Figure S167 - The average intensity particle size distribution calculated using 9 DLS runs for compound **64** (0.56 mM) in an EtOH:H_2O (1:19) solution at 298.15 K.

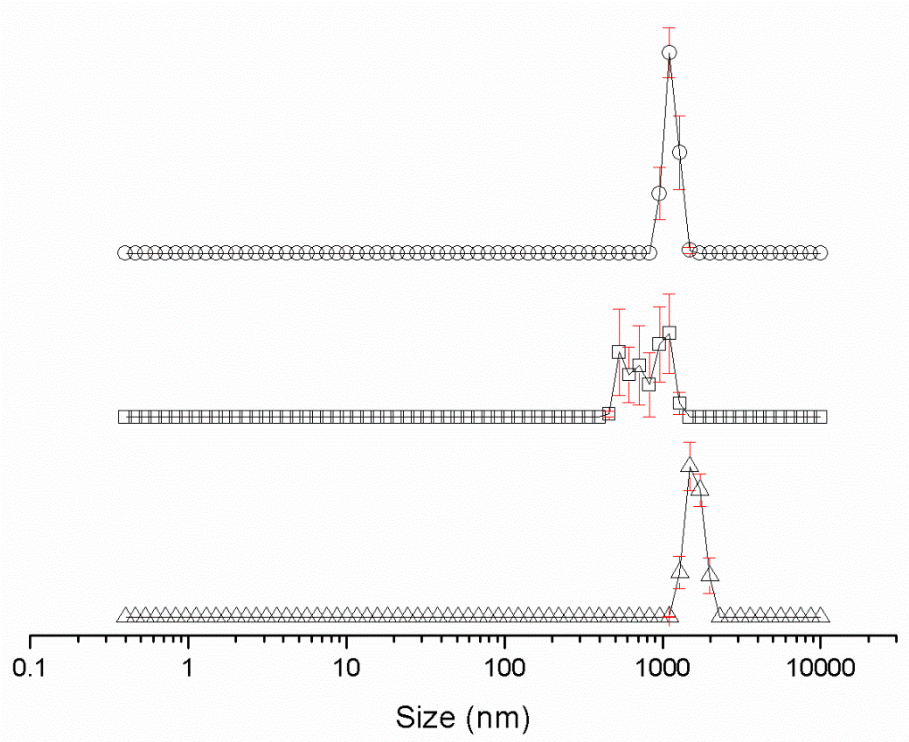

Figure S168 - Average intensity particle size distribution, calculated from 9 DLS runs, of aggregates formed by dissolving compound **65** at a concentration of 5.56 mM in DMSO at Δ) 25 °C, □) heating to 40 °C and ○) cooling to 25 °C. Only 9 of the available 10 DLS runs were used as in some cases, due to the heating and cooling processes there were some obvious temperature equilibration issues for the first run.

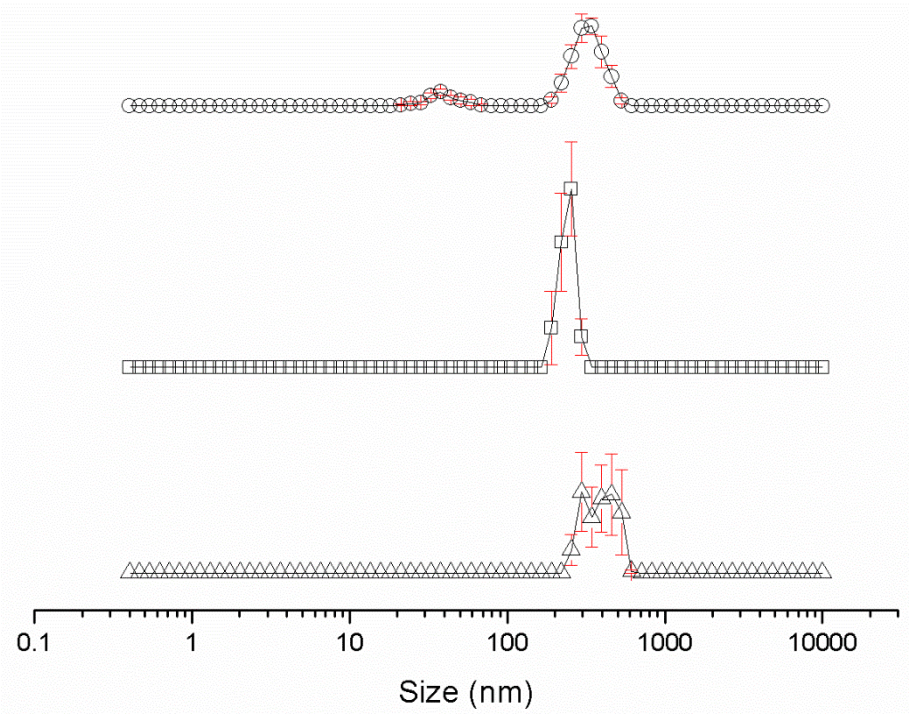

Figure S169 - Average intensity particle size distribution, calculated from 9 DLS runs, of aggregates formed by dissolving compound **65** at a concentration of 0.56 mM in DMSO at Δ) 25 °C, □) heating to 40 °C and ○) cooling to 25 °C. Only 9 of the available 10 DLS runs were used as in some cases, due to the heating and cooling processes there were some obvious temperature equilibration issues for the first run.

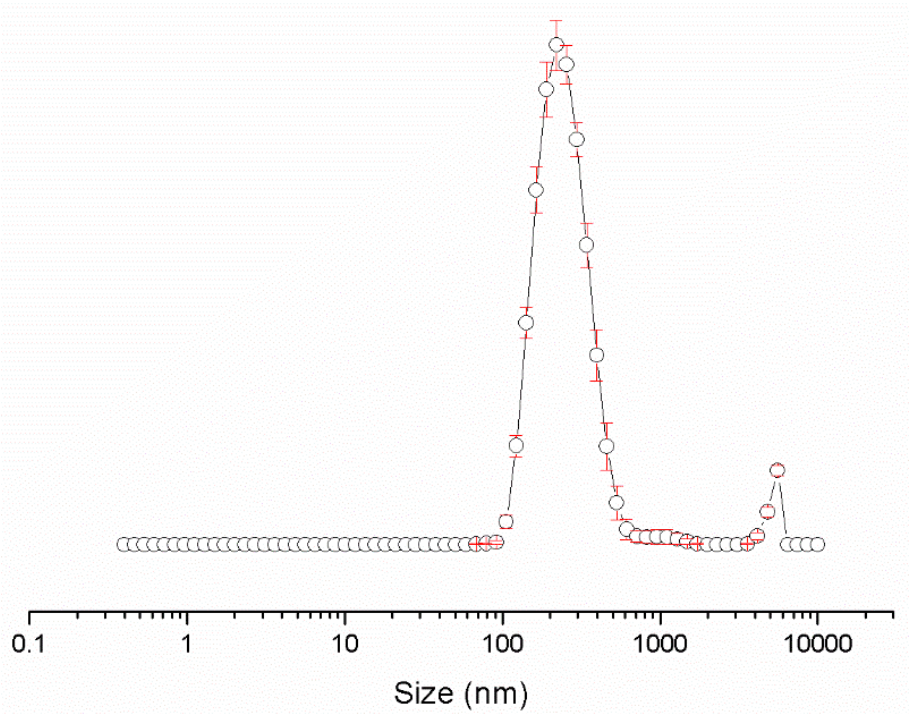

Figure S170 - The average intensity particle size distribution calculated using 9 DLS runs for compound **65** (5.56 mM) in an EtOH:H_2O (1:19) solution at 298.15 K.

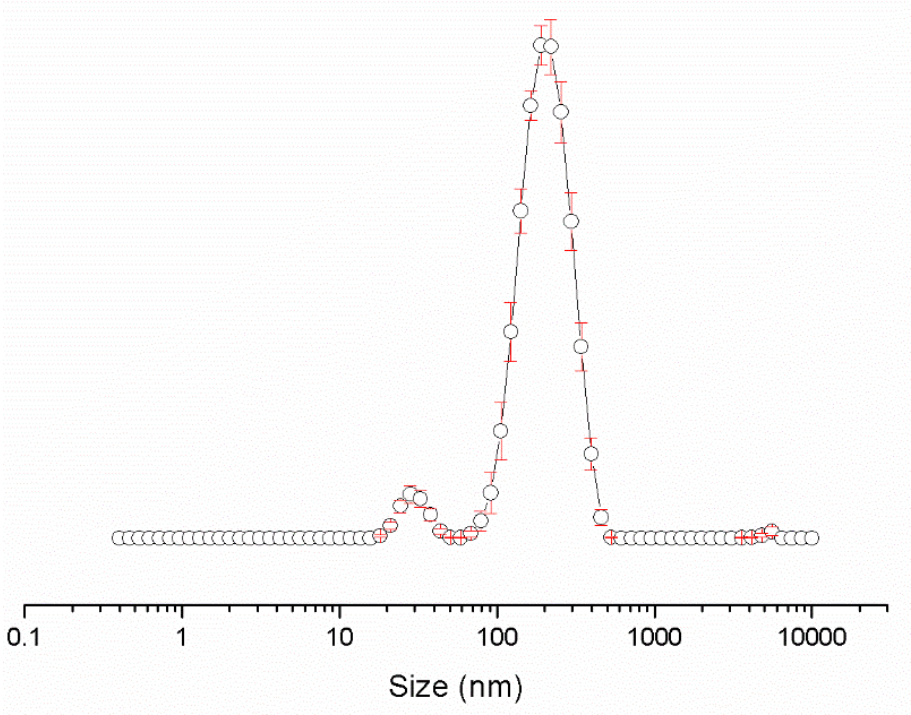

Figure S171 - The average intensity particle size distribution calculated using 9 DLS runs for compound **65** (0.56 mM) in an EtOH:H_2O (1:19) solution at 298.15 K.

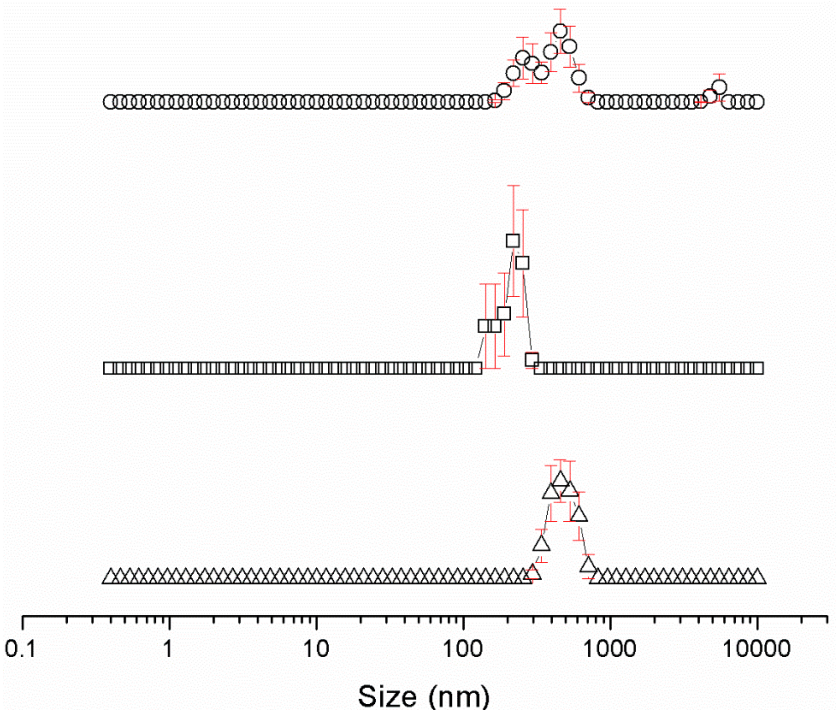

Figure S172 - Average intensity particle size distribution, calculated from 9 DLS runs, of aggregates formed by dissolving compound **66** at a concentration of 5.56 mM in DMSO at Δ) 25 °C, □) heating to 40 °C and ○) cooling to 25 °C. Only 9 of the available 10 DLS runs were used as in some cases, due to the heating and cooling processes there were some obvious temperature equilibration issues for the first run.

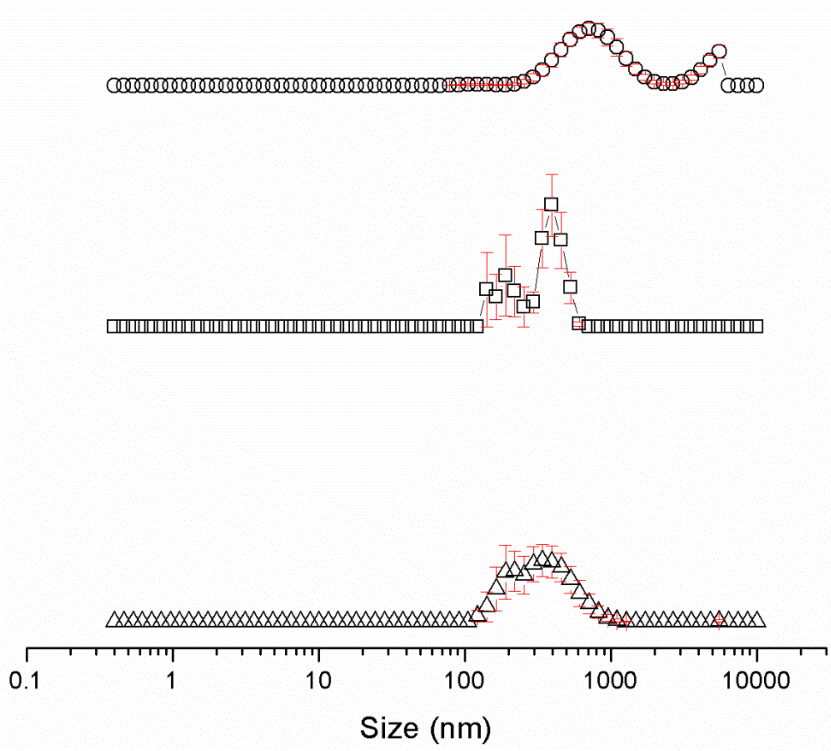

Figure S173 - Average intensity particle size distribution, calculated from 9 DLS runs, of aggregates formed by dissolving compound **66** at a concentration of 0.56 mM in DMSO at Δ) 25 °C, □) heating to 40 °C and ○) cooling to 25 °C. Only 9 of the available 10 DLS runs were used as in some cases, due to the heating and cooling processes there were some obvious temperature equilibration issues for the first run.

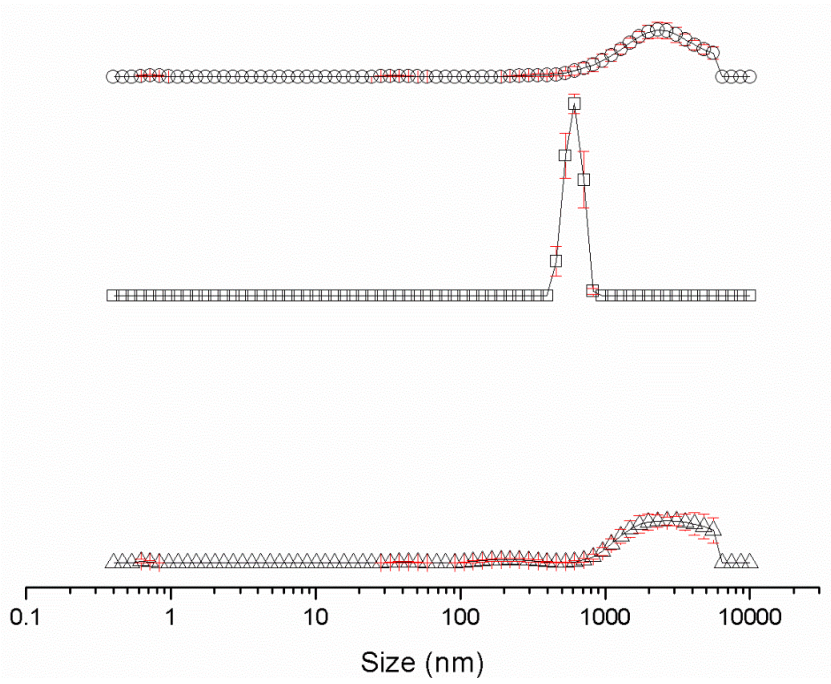

Figure S174 - Average intensity particle size distribution, calculated from 9 DLS runs, of aggregates formed by dissolving compound **67** at a concentration of 5.56 mM in DMSO at Δ) 25 °C, □) heating to 40 °C and ○) cooling to 25 °C. Only 9 of the available 10 DLS runs were used as in some cases, due to the heating and cooling processes there were some obvious temperature equilibration issues for the first run.

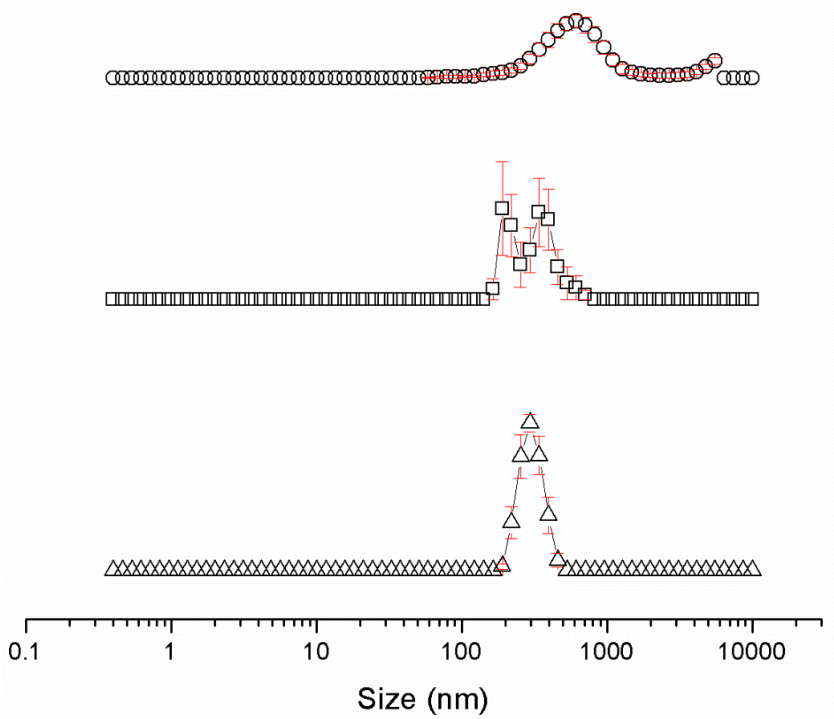

Figure S175 - Average intensity particle size distribution, calculated from 9 DLS runs, of aggregates formed by dissolving compound **67** at a concentration of 0.56 mM in DMSO at Δ) 25 °C, □) heating to 40 °C and ○) cooling to 25 °C. Only 9 of the available 10 DLS runs were used as in some cases, due to the heating and cooling processes there were some obvious temperature equilibration issues for the first run.

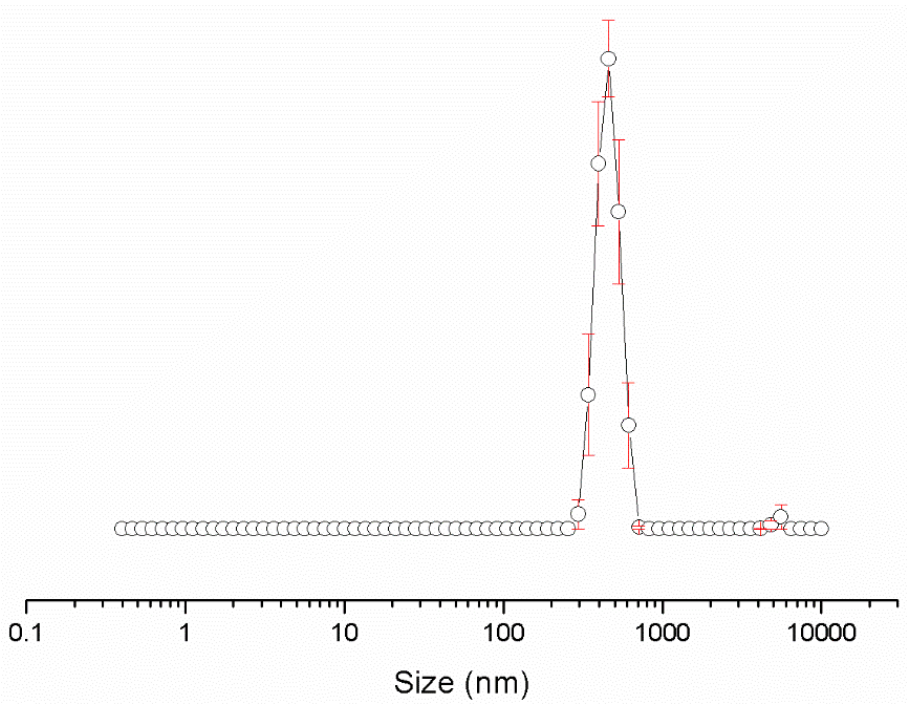

Figure S176 - The average intensity particle size distribution calculated using 9 DLS runs for compound **67** (5.56 mM) in an EtOH:H_2O (1:19) solution at 298.15 K.

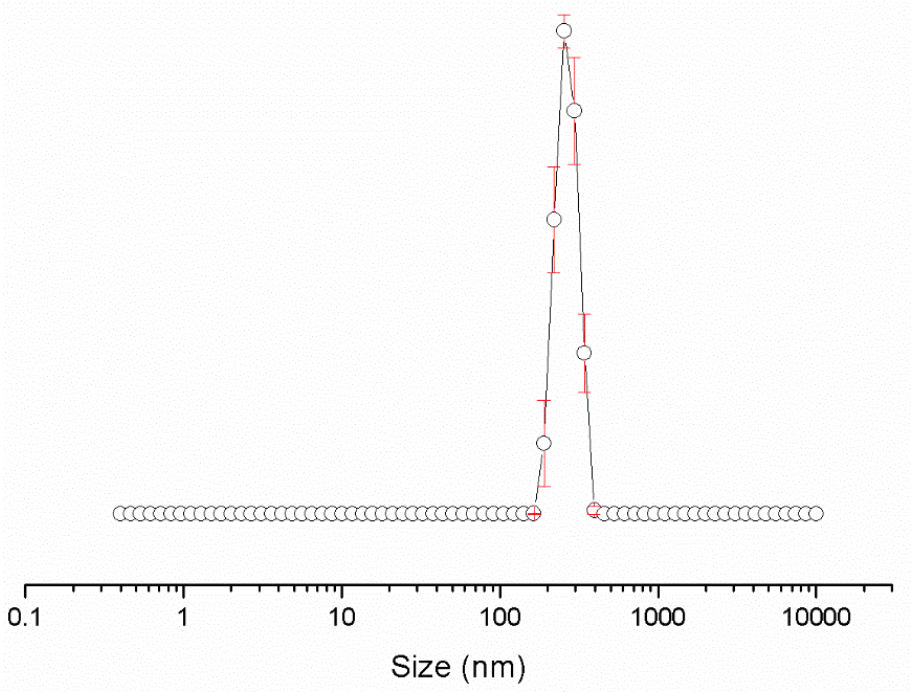

Figure S177 - The average intensity particle size distribution calculated using 9 DLS runs for compound **67** (0.56 mM) in an EtOH:H_2O (1:19) solution at 298.15 K.

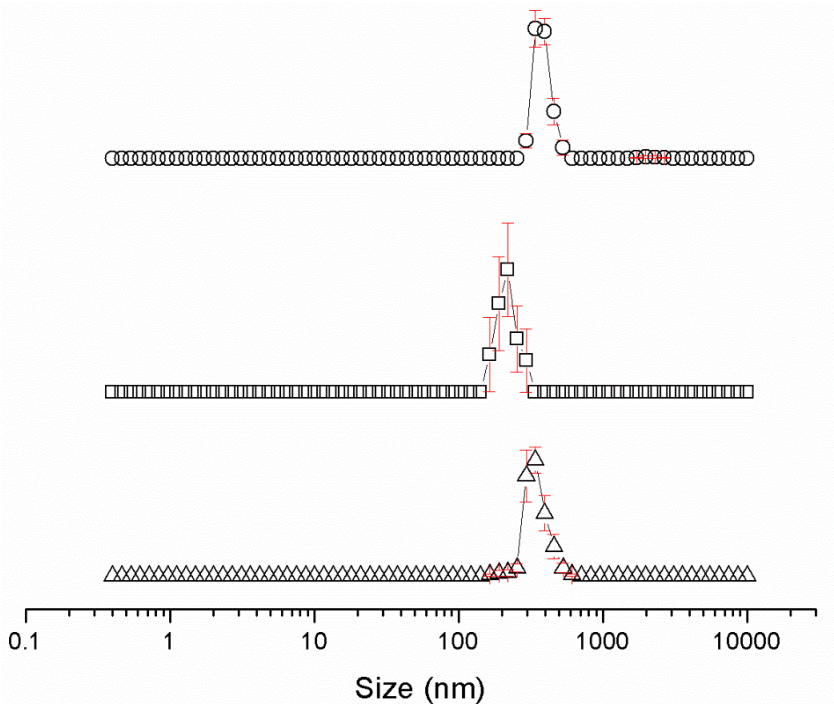

Figure S178 - Average intensity particle size distribution, calculated from 9 DLS runs, of aggregates formed by dissolving compound **68** at a concentration of 5.56 mM in DMSO at Δ) 25 °C, □) heating to 40 °C and ○) cooling to 25 °C. Only 9 of the available 10 DLS runs were used as in some cases, due to the heating and cooling processes there were some obvious temperature equilibration issues for the first run.

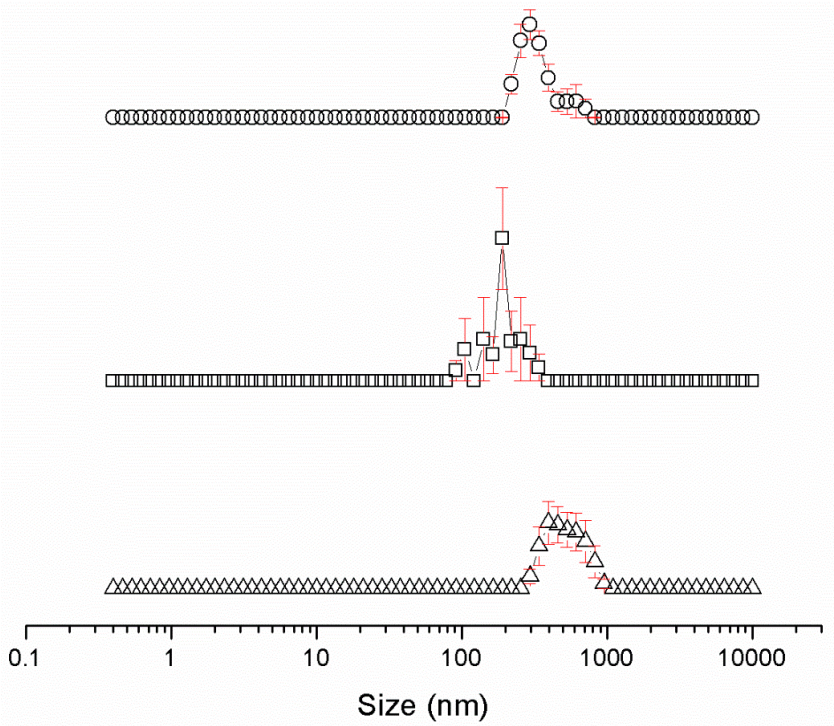

Figure S179 - Average intensity particle size distribution, calculated from 9 DLS runs, of aggregates formed by dissolving compound **68** at a concentration of 0.56 mM in DMSO at Δ) 25 °C, □) heating to 40 °C and ○) cooling to 25 °C. Only 9 of the available 10 DLS runs were used as in some cases, due to the heating and cooling processes there were some obvious temperature equilibration issues for the first run.

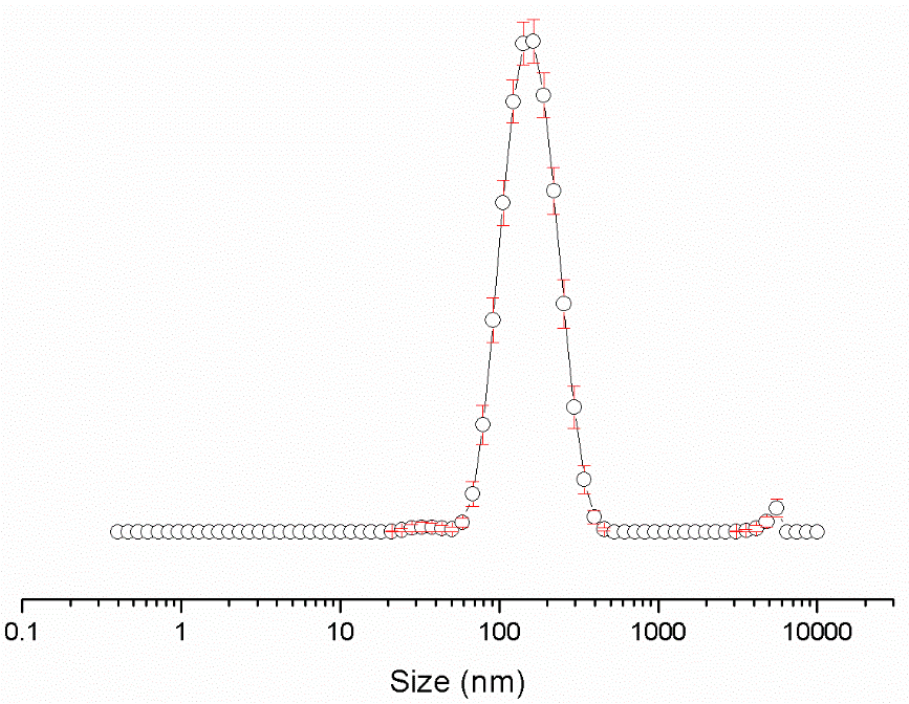

Figure S180 - The average intensity particle size distribution calculated using 9 DLS runs for compound **68** (5.56 mM) in an EtOH:H_2O (1:19) solution at 298.15 K.

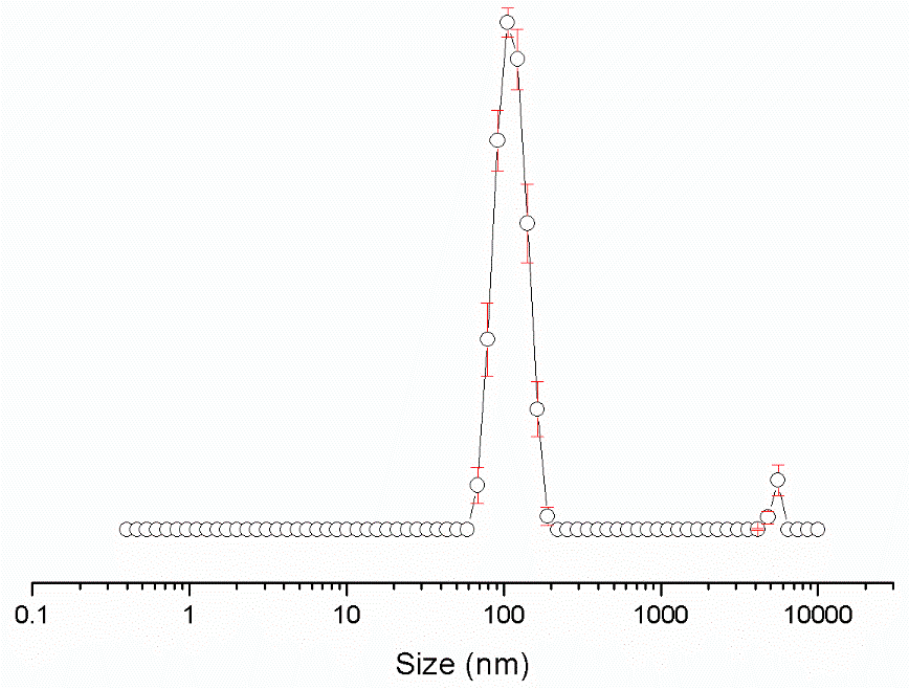

Figure S181 - The average intensity particle size distribution calculated using 9 DLS runs for compound **68** (0.56 mM) in an EtOH:H_2O (1:19) solution at 298.15 K.

1.4.1 Comparative overview

Table S3 - Peak maxima obtained from an average intensity particle size distribution of **42**-**52, 55**-**58, 60**-**62, 64, 65,** and **67-72** obtained at 0.56 mM and 5.56 mM in an EtOH:H_2O (1:19) system by DLS. Hydrodynamic aggregate diameter is given in nm. Polydispersity index (PDI) given in % to 2 dp. An annealing process was applied in which the samples were heated to approximately 40 °C before being allowed to cool to a measurement temperature of 25 °C. (No. = compound number, conc. = concentration). Error = standard error of the mean to 1 dp.

No.	Conc. (mM)	Peak maxima (nm)	PDI (%)	No.	Conc. (mM)	Peak maxima (nm)	PDI (%)
42	5.56	164, 4	37.86 (*± 1.2*)	**57**[a]	5.56	220	24.62 (*± 0.4*)
	0.56	142, 14	29. 11 (*± 0.3*)		0.56	396	23.70 (*± 0.3*)
43	5.56	459, 59	22.10 (*± 0.2*)	**58**	5.56	91	16.90 (*± 0.8*)
	0.56	190, 28	20.56 (*± 0.2*)		0.56	79	19.13 (*± 0.7*)
44	5.56	122	15.54 (*± 0.9*)	**60**	5.56	220	27.81 (*± 1.0*)
	0.56	295	22.03 (*± 0.2*)		0.56	190, 18	20.60 (*± 0.1*)
45	5.56	342, 295	29.89 (*± 1.0*)	**61**	5.56	190	19.32 (*± 0.3*)
	0.56	142, 24	30.09 (*± 0.2*)		0.56	190	19.98 (*± 0.4*)
46	5.56	142	24.10 (*± 0.8*)	**62**	5.56	106	13.02 (*± 0.3*)
	0.56	68-4145	36.89 (*± 1.1*)		0.56	122-5560	29.32 (*± 0.3*)
47	5.56	122	22.40 (*± 0.9*)	**63**	5.56	[*b*]	
	0.56	4145, 44	26.13 (*± 0.7*)		0.56		
48	5.56	531	42.01 (*± 1.3*)	**64**	5.56	396	20.17 (*± 0.1*)
	0.56	295, 21	22.10 (*± 0.2*)		0.56	330, 33	22.39 (*± 0.8*)
49	5.56	220	34.60 (*± 0.9*)	**65**	5.56	220	17.05 (*± 0.2*)
	0.56	91	33.47 (*± 0.2*)		0.56	190,33	22.12 (*± 0.1*)
50	5.56	164	31.20 (*± 0.9*)	**66**	5.56	[*b*]	
	0.56	190	29.18 (*± 0.4*)		0.56		
51	5.56	190	17.90 (*± 0.2*)	**67**	5.56	459	29.32 (*± 0.3*)
	0.56	220	15.87 (*± 0.4*)		0.56	255	22.76 (*± 0.2*)
52	5.56	190	29.80 (*± 0.6*)	**68**	5.56	164	21.20 (*± 0.2*)
	0.56	220	29.66 (*± 0.7*)		0.56	106	16.50 (*± 0.1*)
53	5.56	[*b*]		**69**[a]	5.56	164	38.11 (*± 0.5*)
	0.56				0.56	255	33.21 (*± 0.2*)
54	5.56	[*b*]		**70**[a]	5.56	220	12.80 (*± 0.4*)
	0.56				0.56	164	12.33 (*± 0.4*)
55	5.56	342	14.12 (*± 0.2*)	**71**[a]	5.56	295	20.98 (*± 0.1*)
	0.56	459, 28	17.45 (*± 0.2*)		0.56	220	19.14 (*± 0.1*)
56	5.56	190	39.70 (*± 1.0*)	**72**[a]	5.56	59, 122	27.16 (*± 0.9*)
	0.56	220	24.23 (*± 0.5*)		0.56	2	22.02 (*± 0.2*)

[*a*] Previously published results.[1][*b*] not calculated due to sample solubility.

1.5 Surface tension measurements and CMC determination

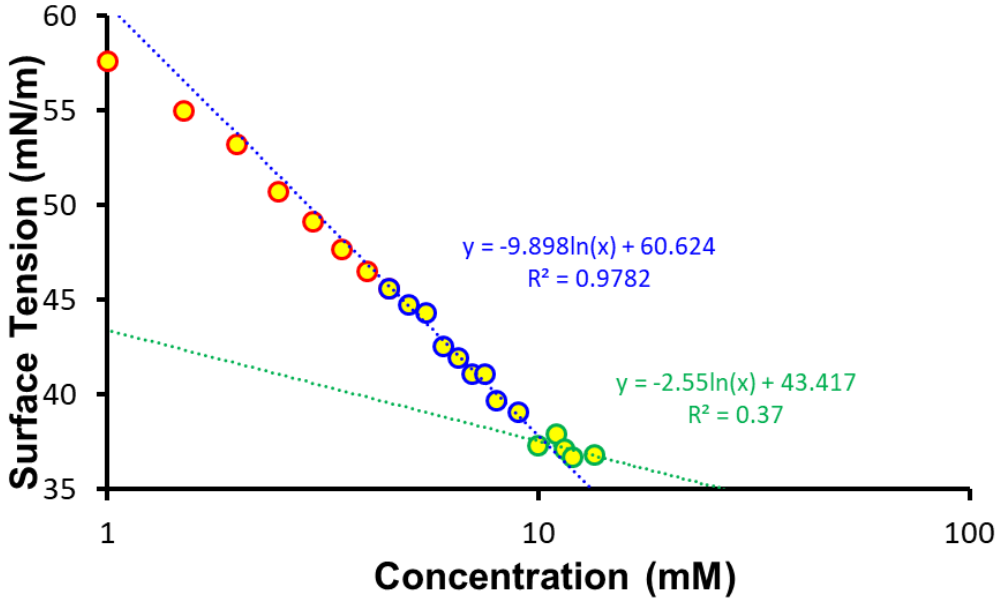

Figure S182 - Calculation of CMC (10.39 mM) for compound **42** in an EtOH:H_2O 1:19 mixture using surface tension measurements.

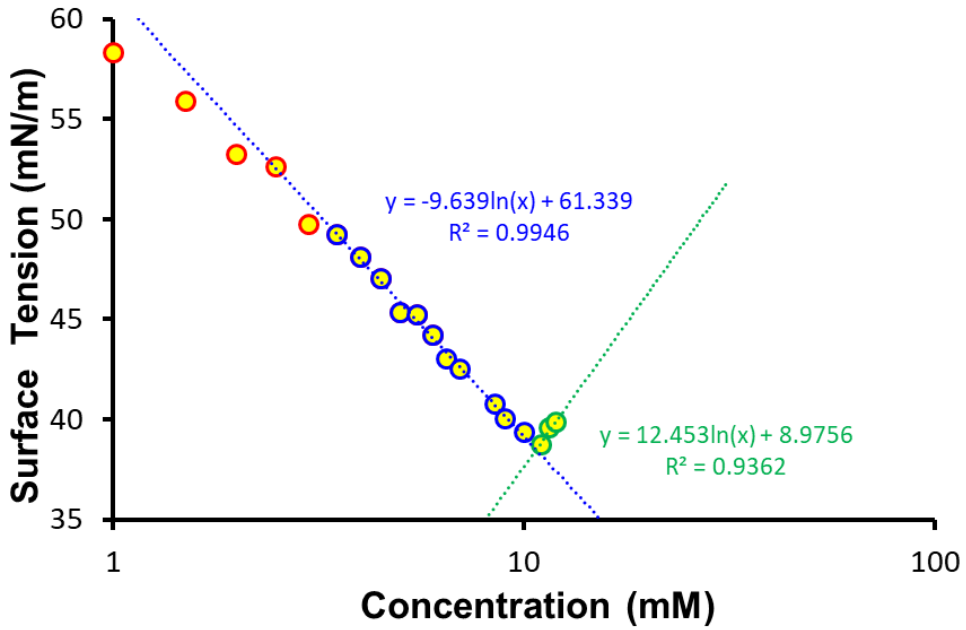

Figure S183 - Calculation of CMC (10.70 mM) for compound **43** in an EtOH:H_2O 1:19 mixture using surface tension measurements.

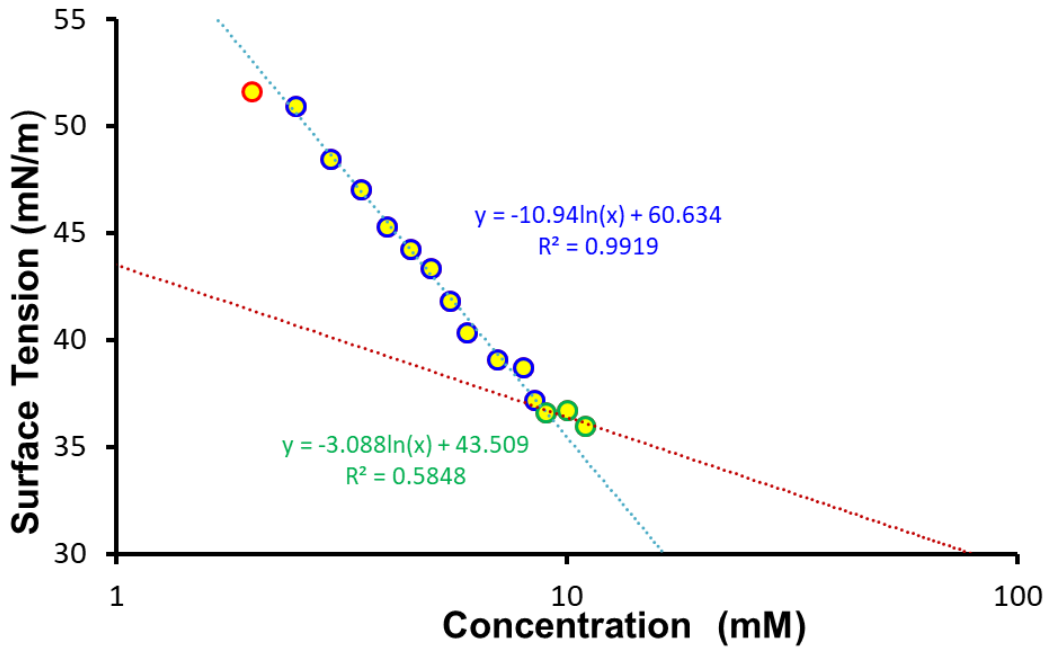

Figure S184 - Calculation of CMC (8.85 mM) for compound **44** in an EtOH:H_2O 1:19 mixture using surface tension measurements.

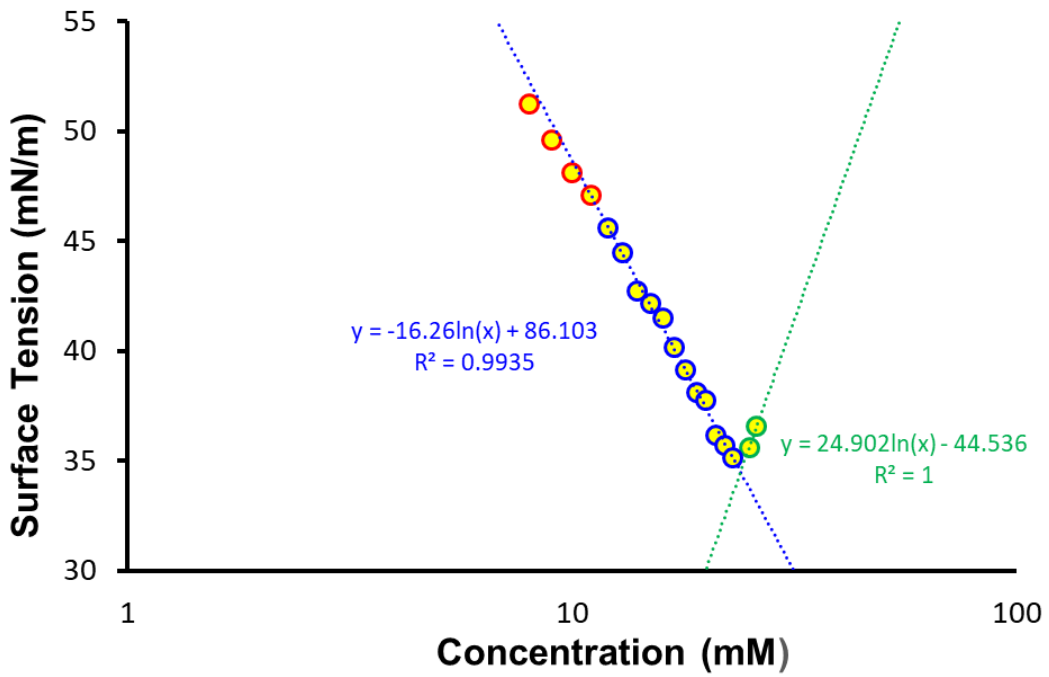

Figure S185 - Calculation of CMC (23.88 mM) for compound **45** in an EtOH:H_2O 1:19 mixture using surface tension measurements.

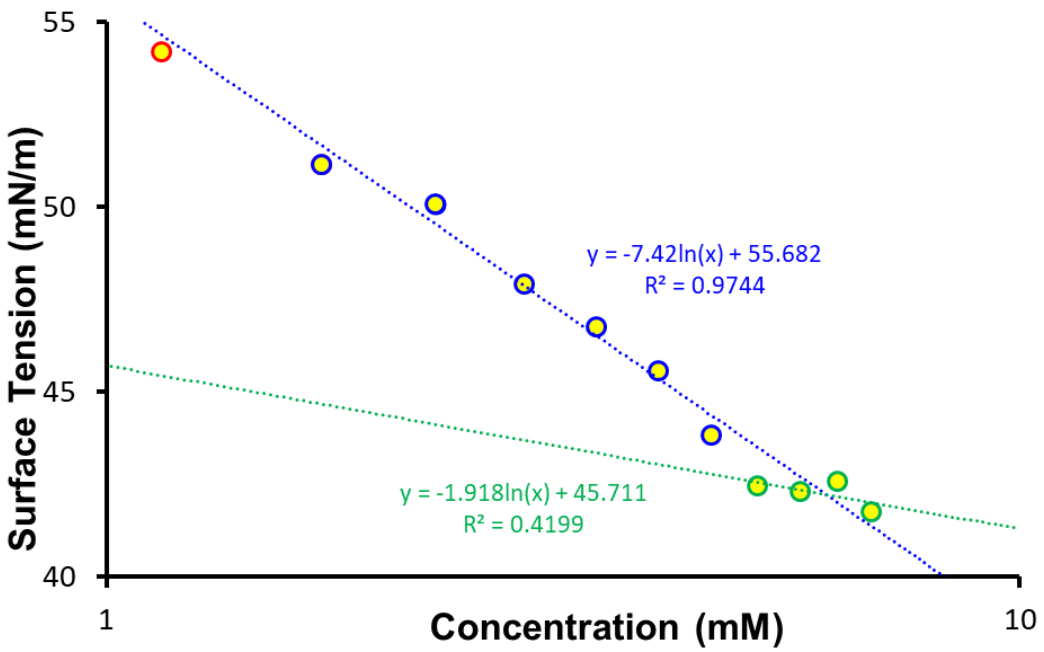

Figure S186 - Calculation of CMC (6.12 mM) for compound **46** in an EtOH:H_2O 1:19 mixture using surface tension measurements.

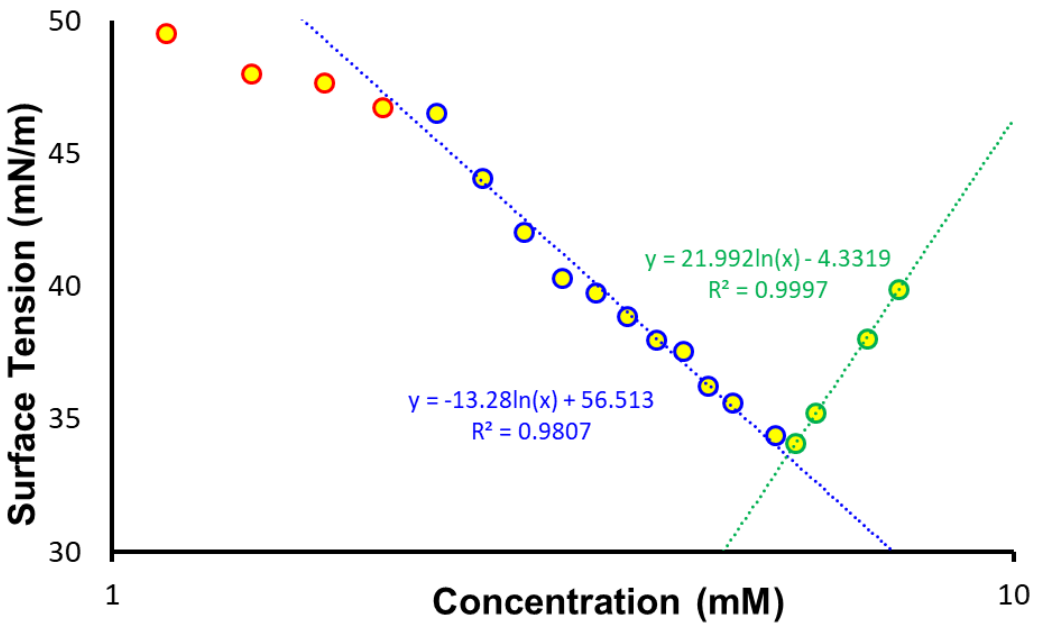

Figure S187 - Calculation of CMC (5.61 mM) for compound **47** in an EtOH:H_2O 1:19 mixture using surface tension measurements.

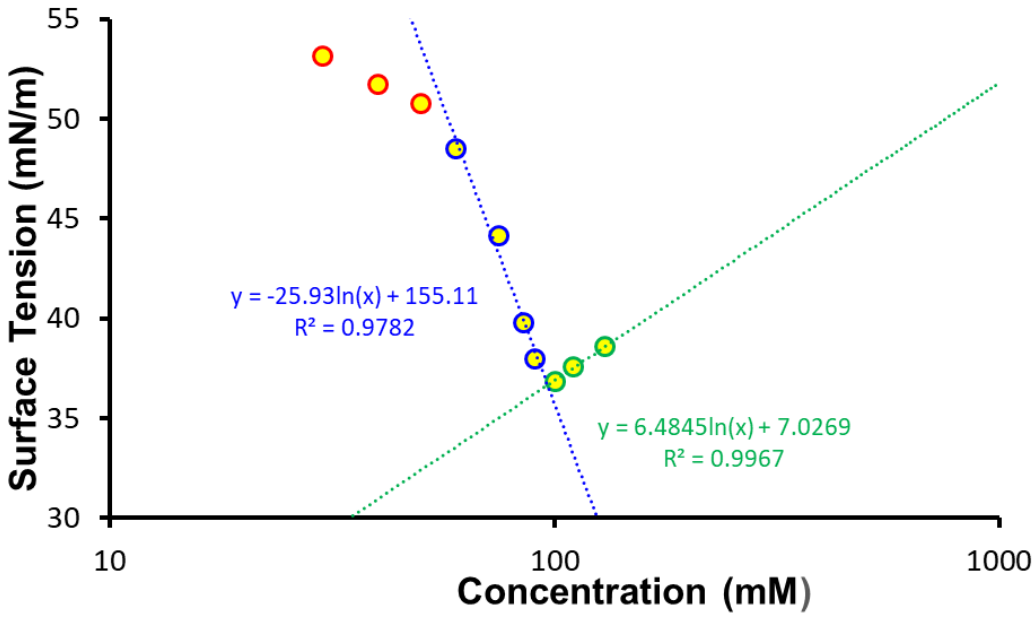

Figure S188 - Calculation of CMC (96.35 mM) for compound **48** in an EtOH:H_2O 1:19 mixture using surface tension measurements.

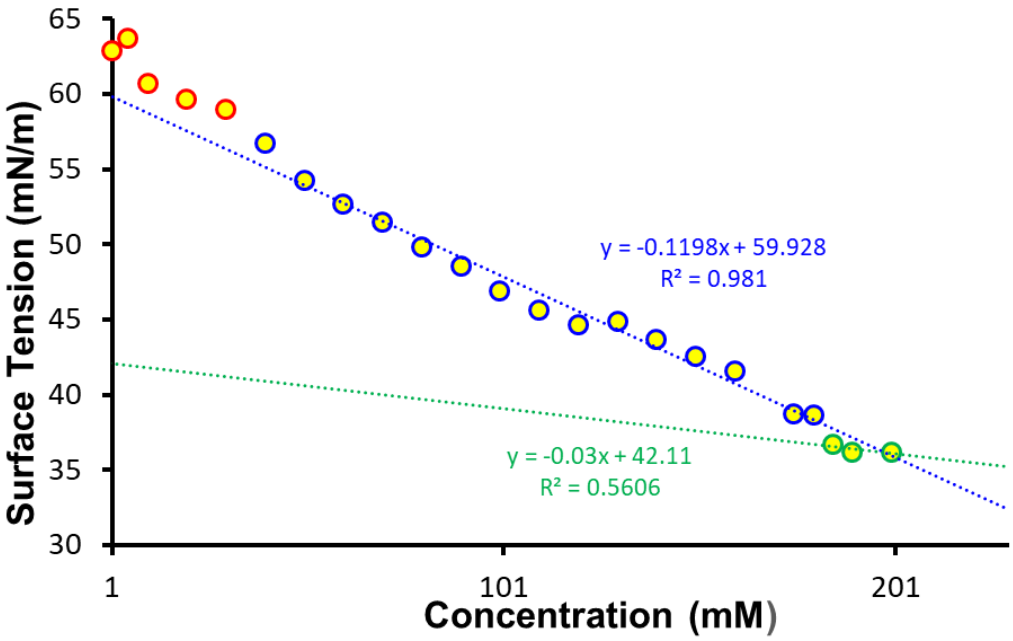

Figure S189 - Calculation of CMC (198.42 mM) for compound **49** in an EtOH:H_2O 1:19 mixture using surface tension measurements.

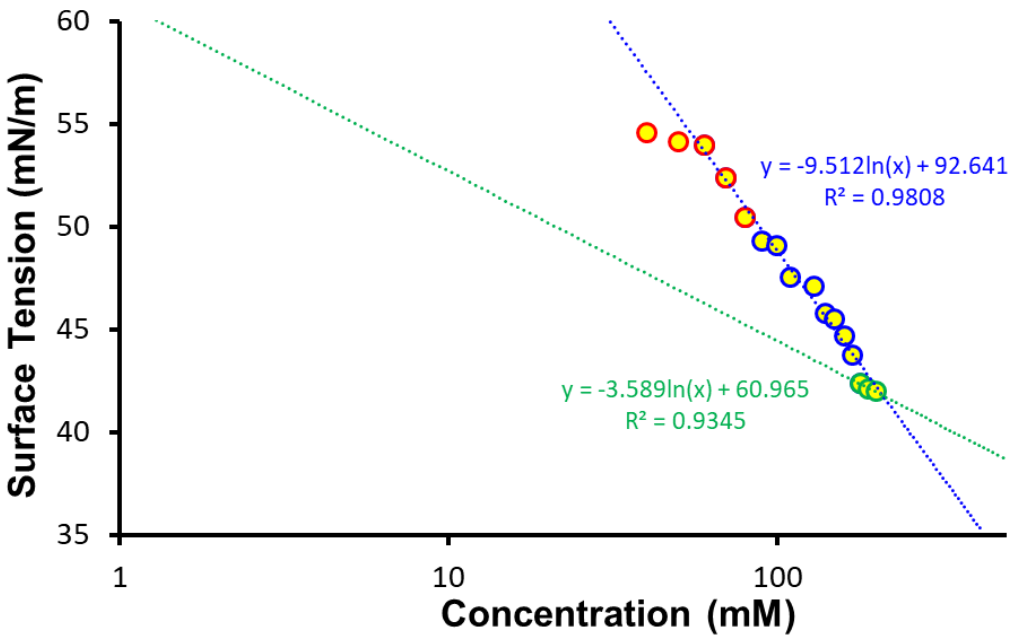

Figure S190 - Calculation of CMC (209.98 mM) for compound **50** in an EtOH:H_2O 1:19 mixture using surface tension measurements.

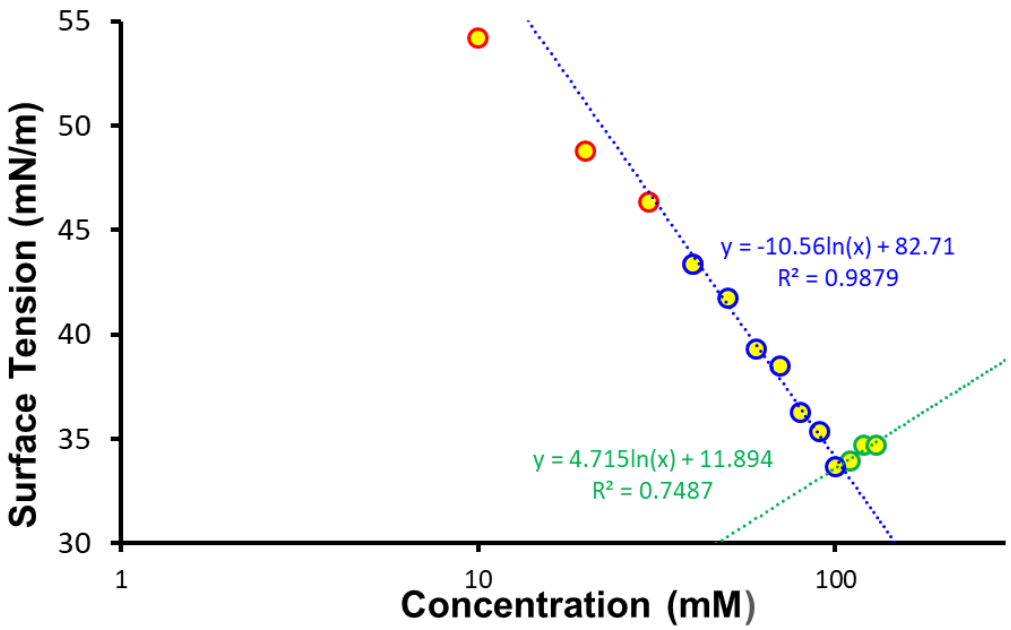

Figure S191 - Calculation of CMC (103.13 mM) for compound **51** in an EtOH:H_2O 1:19 mixture using surface tension measurements.

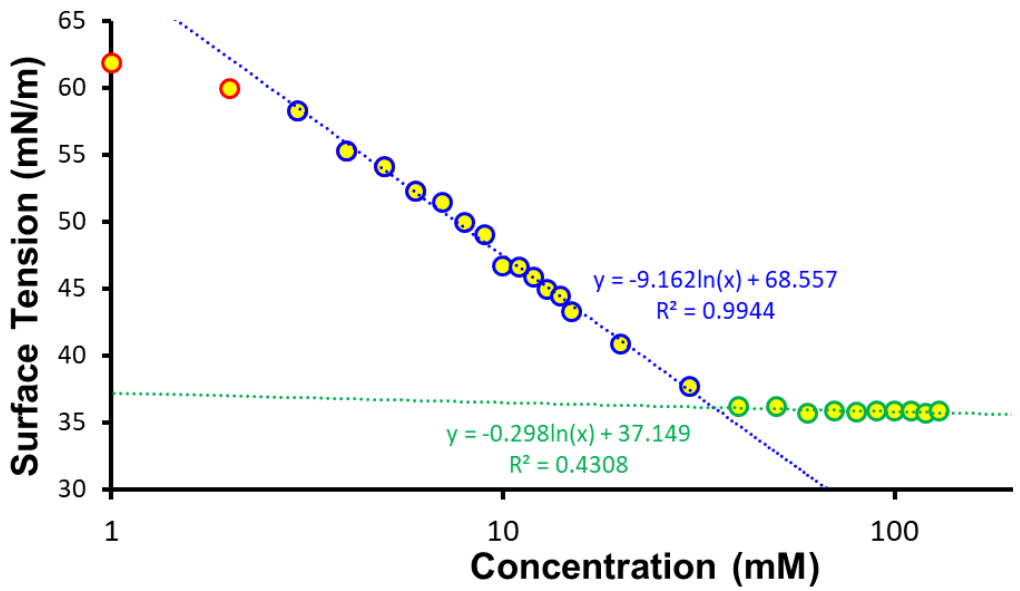

Figure S192 - Calculation of CMC (34.57 mM) for compound **52** in an EtOH:H_2O 1:19 mixture using surface tension measurements.

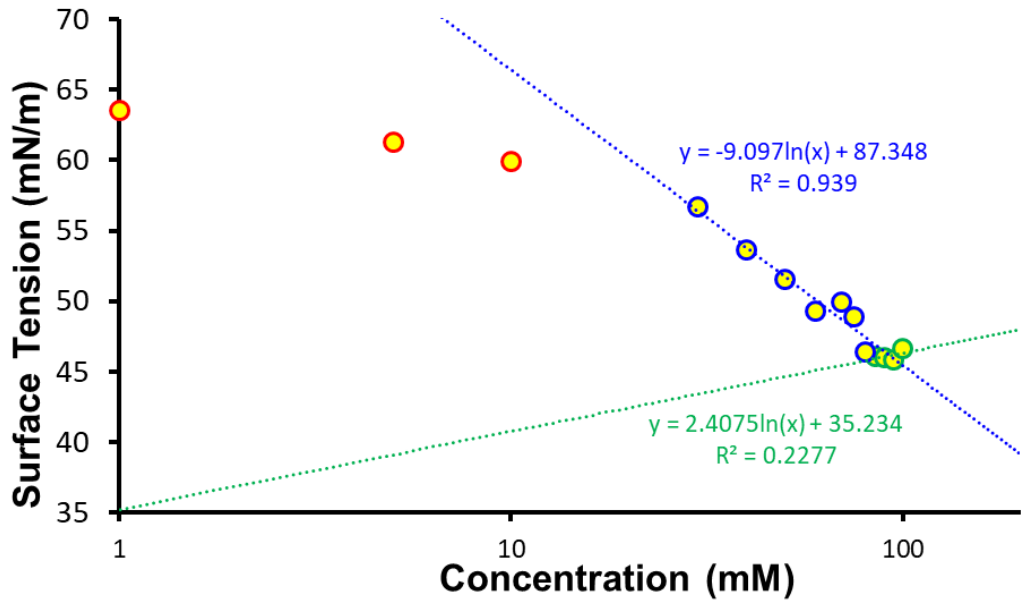

Figure S193 - Calculation of CMC (92.67 mM) for compound **56** in an EtOH:H_2O 1:19 mixture using surface tension measurements.

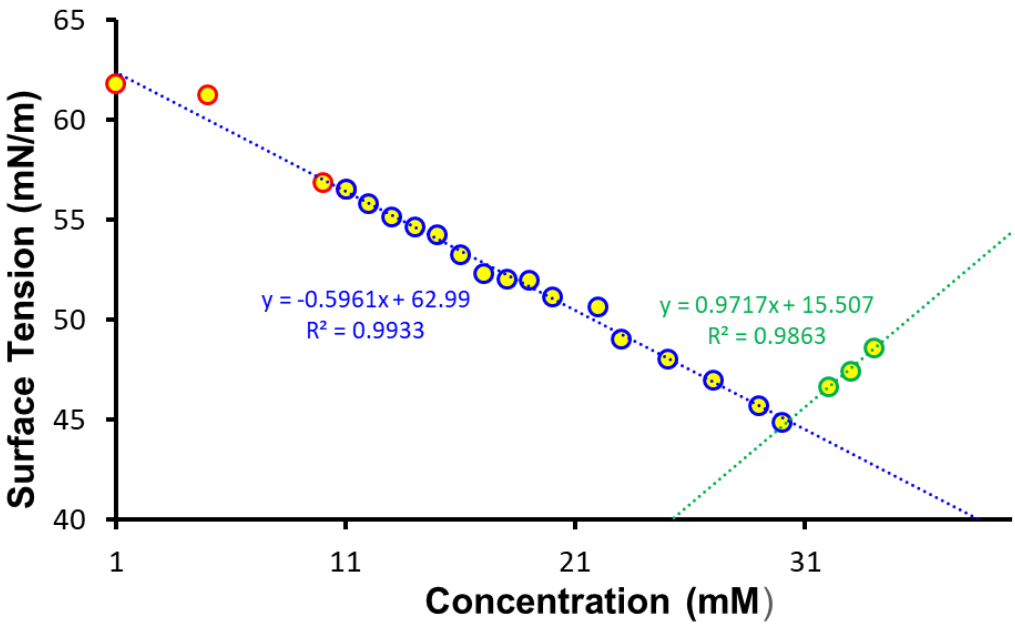

Figure S194 - Calculation of CMC (30.29 mM) for compound **58** in an EtOH:H_2O 1:19 mixture using surface tension measurements.

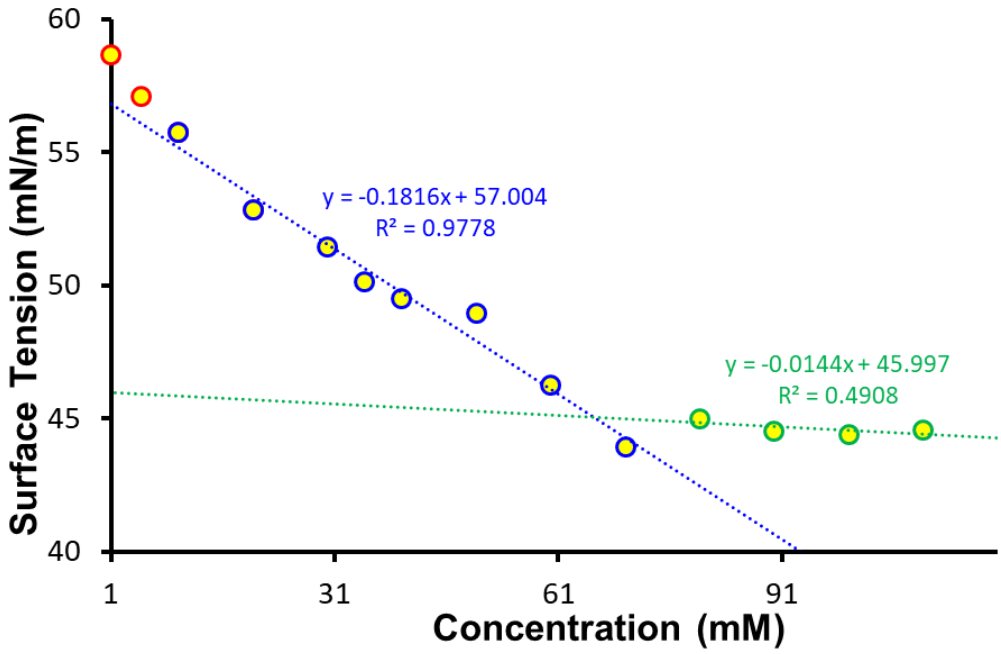

Figure S195 - Calculation of CMC (65.83 mM) for compound **60** in an EtOH:H_2O 1:19 mixture using surface tension measurements.

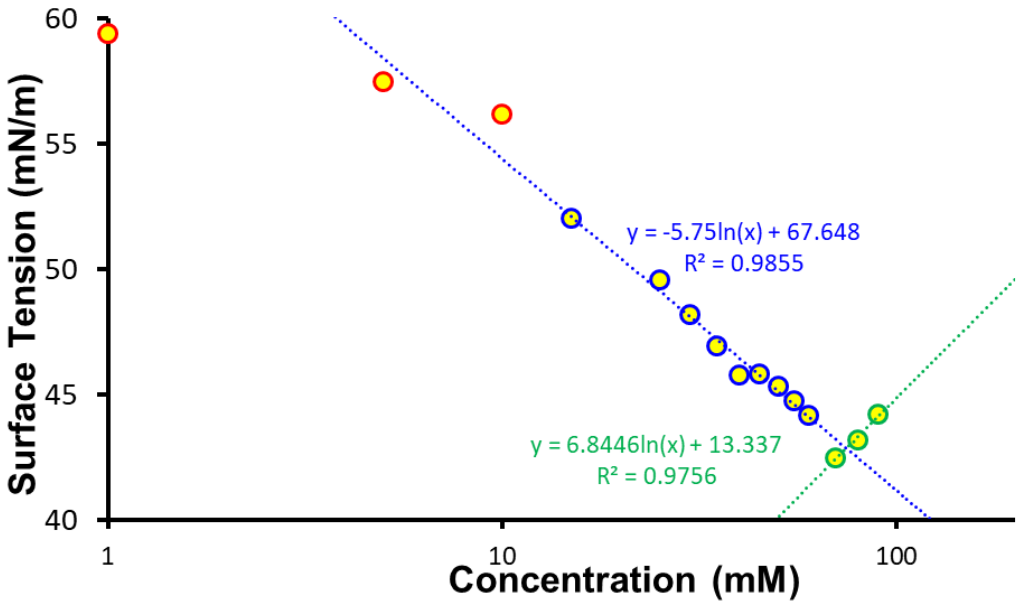

Figure S196 - Calculation of CMC (74.59 mM) for compound **61** in an EtOH:H_2O 1:19 mixture using surface tension measurements.

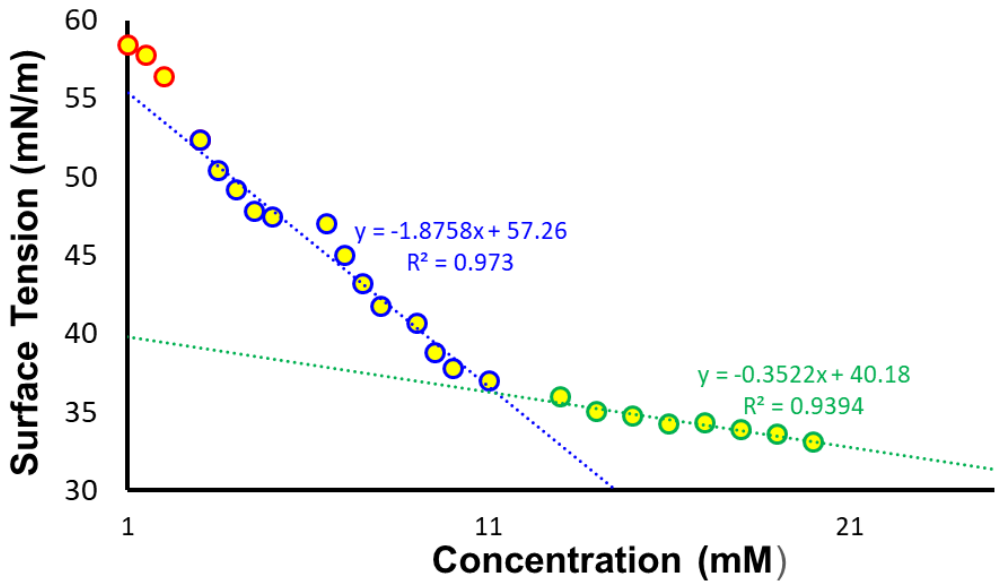

Figure S197 - Calculation of CMC (11.21 mM) for compound **65** in an EtOH:H_2O 1:19 mixture using surface tension measurements.

1.5.1 Comparative overview

Table S4 – CMC and surface tension (obtained at CMC) measurements for compounds **42**-**52, 56**-**61**, **65** and **69**-**72** in a solution of EtOH:H_2O (1:19) at 25 °C.

Compound no.	CMC (mM)	Surface tension (mN/m)	Compound no.	CMC (mM)	Surface tension (mN/m)
42	10.39	37.45	**57**[a]	40.89	47.90
43	10.70	38.49	**58**	30.29	44.94
44	8.85	36.78	**60**	65.83	45.05
45	24.14	34.35	**61**	74.59	42.85
46	6.12	42.24	**62**	[*b*]	
47	5.61	33.59	**63**	[*b*]	
48	96.35	36.65	**64**	[*b*]	
49	198.42	36.16	**65**	11.21	39.33
50	209.98	41.78	**66**	[*b*]	
51	103.13	33.75	**67**	[*b*]	
52	34.57	36.09	**68**	[*b*]	
53	[*b*]		**69**[a]	10.67	46.67
54	[*b*]		**70**[a]	2.52	43.15
55	[*b*]		**71**[a]	9.54	48.71
56	92.67	46.14	**72**[a]	0.50	46.50

[*a*] Previously published results.[1] [*b*] not calculated due to sample insolubility.

1.6 DOSY ^{1}H NMR experiments

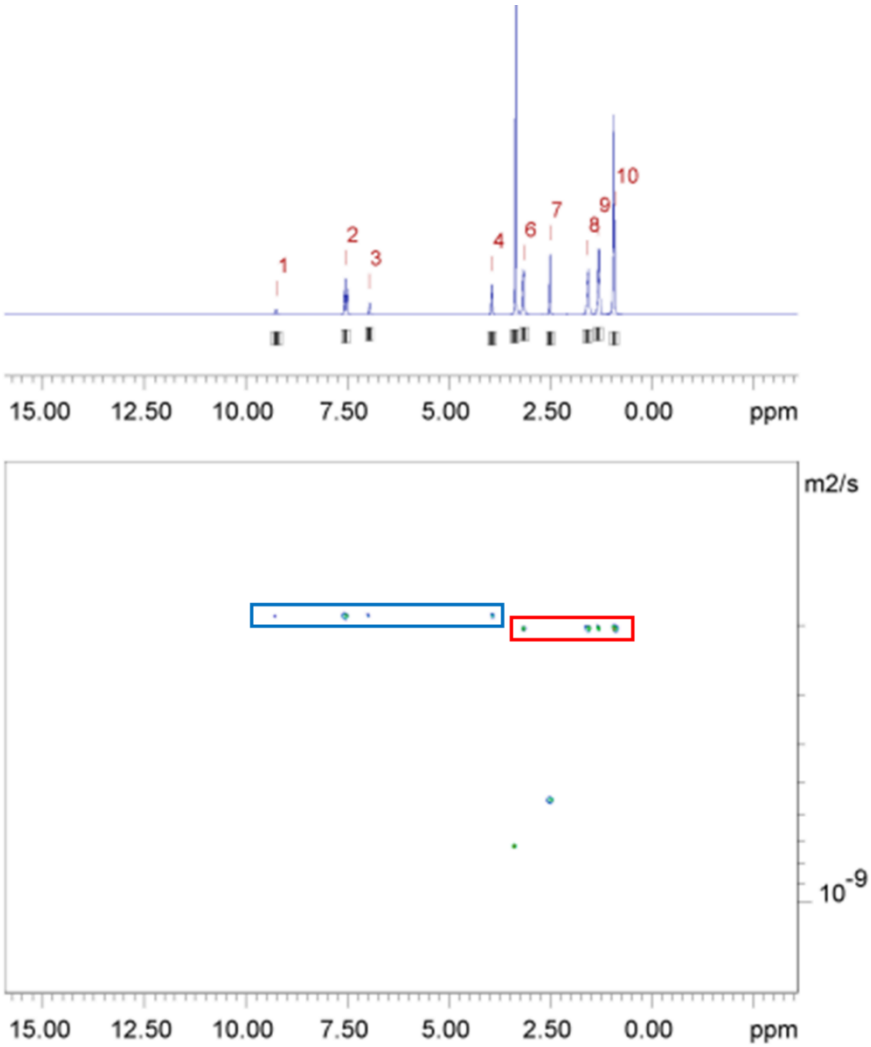

Peak name	F2 [ppm]	Io	error	D [m2/s]	error
1	9.242	9.95e+08	1.860e+06	1.90e-10	8.061e-13
2	7.536	5.89e+09	9.597e+06	1.90e-10	7.015e-13
3	6.957	1.29e+09	2.163e+06	1.91e-10	7.238e-13
4	3.939	2.77e+09	6.086e+06	1.90e-10	9.471e-13
5	3.378	1.71e+10	4.157e+07	7.19e-10	3.645e-12
6	3.148	8.49e+09	1.972e+07	2.05e-10	1.070e-12
7	2.504	4.34e+09	5.952e+06	5.49e-10	1.591e-12
8	1.583	9.23e+09	1.677e+07	2.02e-10	8.250e-13
9	1.329	1.09e+10	1.723e+07	2.02e-10	7.171e-13
10	0.927	1.74e+10	2.516e+07	2.02e-10	6.579e-13

Figure S198 - ^{1}H DOSY NMR spectrum of compounds **42** (55.56 mM) in DMSO-d_6 0.5 % H_2O at 298.15 K and a table reporting the diffusion constants calculated for each peak used to determine the hydrodynamic diameter of the anionic components of **42** (d_H = 1.15 nm). Peaks 1-4 correspond to the anionic component of **42** (blue) while peaks 6 and 8-10 correspond to the cationic component of **42** (red).

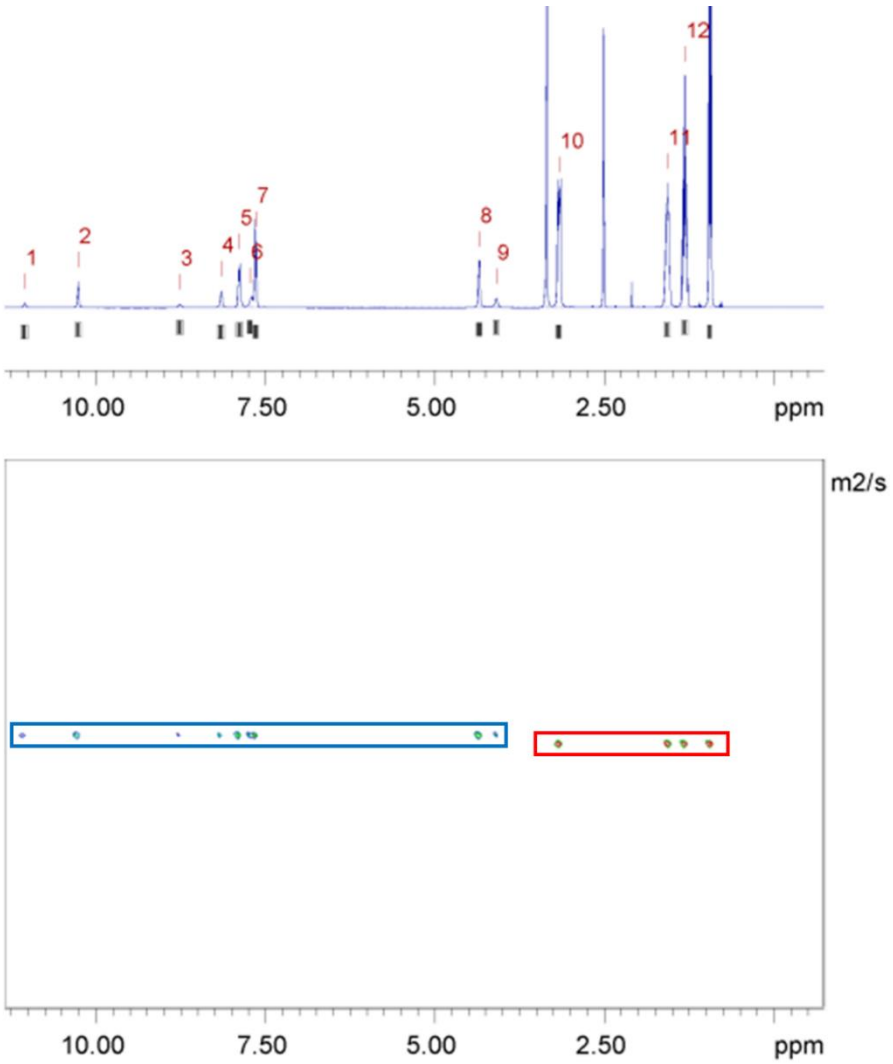

Peak name	F2 [ppm]	Io	error	D [m2/s]	error
1	11.055	1.01e+08	1.993e+04	1.98e-10	8.562e-14
2	10.263	3.33e+08	1.923e+04	1.97e-10	2.484e-14
3	8.764	1.06e+08	2.093e+04	1.97e-10	8.551e-14
4	8.155	3.46e+08	2.027e+04	1.97e-10	2.523e-14
5	7.883	8.96e+08	1.990e+04	1.96e-10	9.546e-15
6	7.726	2.89e+08	1.781e+04	1.97e-10	2.653e-14
7	7.640	1.32e+09	1.783e+04	1.96e-10	5.825e-15
8	4.343	8.28e+08	1.922e+04	1.96e-10	9.963e-15
9	4.095	2.58e+08	1.993e+04	1.96e-10	3.315e-14
10	3.171	3.21e+09	1.684e+04	2.04e-10	2.328e-15
11	1.575	3.49e+09	1.905e+04	2.03e-10	2.418e-15
12	1.317	4.27e+09	1.977e+04	2.03e-10	2.050e-15
13	0.942	6.86e+09	1.555e+04	2.03e-10	1.003e-15

Figure S199 - ^{1}H DOSY NMR spectrum of compounds **45** (55.56 mM) in DMSO-d_6 0.5 % H_2O at 298.15 K and a table reporting the diffusion constants calculated for each peak used to determine the hydrodynamic diameter of the anionic components of **45** (d_H = 1.13 nm). Peaks 1-9 correspond to the anionic component of **45** (blue) while peaks 10-13 correspond to the cationic component of **45** (red).

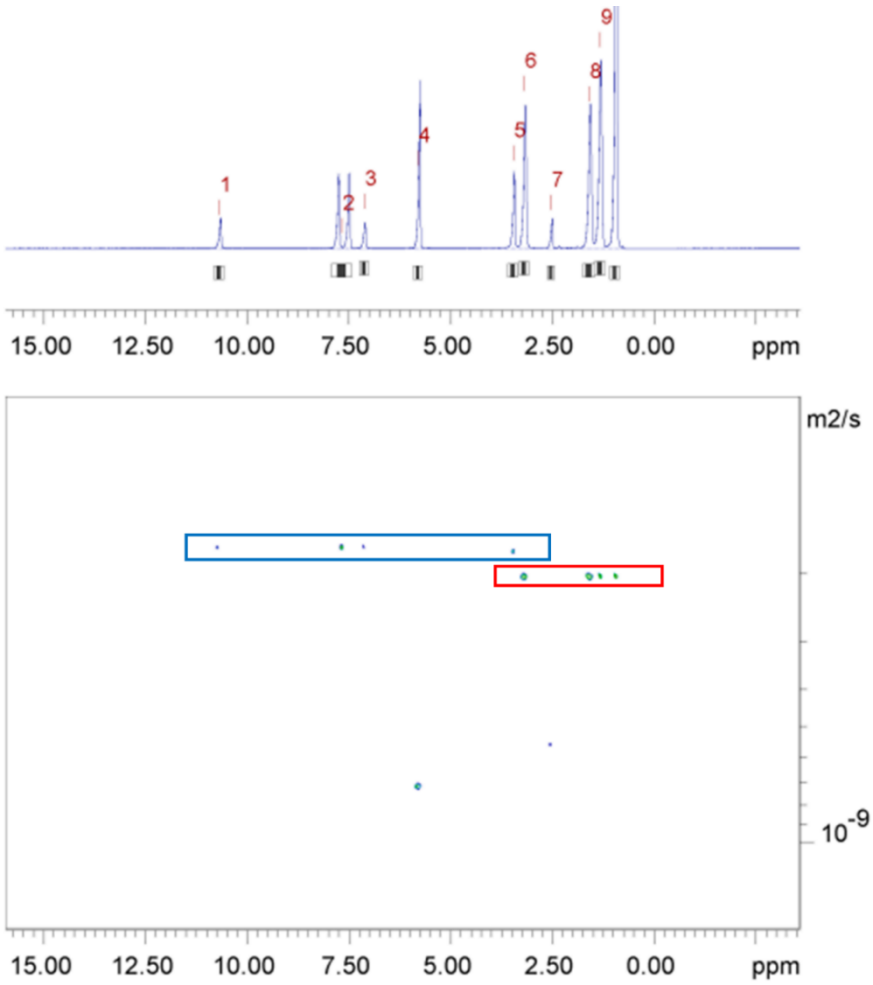

Peak name	F2 [ppm]	Io	error	D [m2/s]	error
1	10.692	4.89e+09	1.071e+06	1.70e-10	8.175e-14
2	7.672	2.56e+10	1.489e+06	1.70e-10	2.173e-14
3	7.129	4.69e+09	1.021e+06	1.71e-10	8.186e-14
4	5.803	2.15e+10	1.613e+06	7.18e-10	1.103e-13
5	3.461	1.19e+10	1.060e+06	1.74e-10	3.393e-14
6	3.192	2.93e+10	1.129e+06	2.05e-10	1.712e-14
7	2.533	4.32e+09	1.253e+06	5.54e-10	3.341e-13
8	1.604	3.37e+10	1.212e+06	2.04e-10	1.592e-14
9	1.331	4.20e+10	1.145e+06	2.05e-10	1.210e-14
10	0.960	6.61e+10	1.092e+06	2.05e-10	7.328e-15

Figure S200 - ^{1}H DOSY NMR spectrum of compounds **65** (55.56 mM) in DMSO-d_6 0.5 % H_2O at 298.15 K and a table reporting the diffusion constants calculated for each peak used to determine the hydrodynamic diameter of the anionic components of **65** (d_H = 1.28 nm). Peaks 1-3 and 5 correspond to the anionic component of **65** (blue) while peaks 6 and 8-10 correspond to the cationic component of **65** (red).

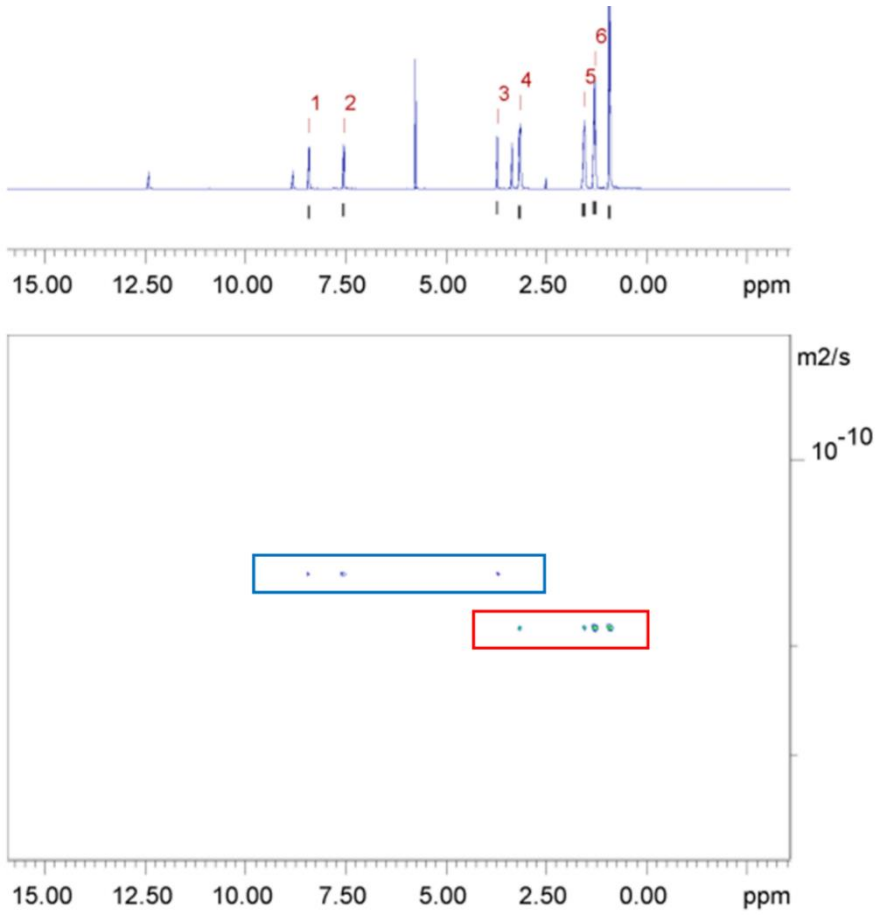

Peak name	F2 [ppm]	Io	error	D [m2/s]	error
1	8.411	4.98e+09	1.239e+05	1.53e-10	8.265e-15
2	7.552	5.02e+09	1.244e+05	1.54e-10	8.276e-15
3	3.719	4.34e+09	1.079e+05	1.53e-10	8.269e-15
4	3.160	1.35e+10	1.538e+05	1.87e-10	4.556e-15
5	1.560	1.55e+10	1.731e+05	1.87e-10	4.473e-15
6	1.288	2.09e+10	1.852e+05	1.87e-10	3.544e-15
7	0.922	3.49e+10	1.604e+05	1.87e-10	1.835e-15

Figure S201 - ^{1}H DOSY NMR spectrum of compounds **68** (55.56 mM) in DMSO-d_6 0.5 % H_2O at 298.15 K and a table reporting the diffusion constants calculated for each peak used to determine the hydrodynamic diameter of the anionic components of **68** (d_H = 1.42 nm). Peaks 1-3 correspond to the anionic component of **68** (blue) while peaks 4-7 correspond to the cationic component of **68** (red).

1.6.1 Comparative overview

Table S5 - Calculated d_H for the anionic species of **42**, **45**, **65**, **68** and **72**.

Compound no.	d_H (nm)
42	1.15
45	1.13
65	1.28
68	1.42
72[a]	1.64

[*a*] Previously published results.[1]

1.7 Quantitative ^{1}H NMR experiments

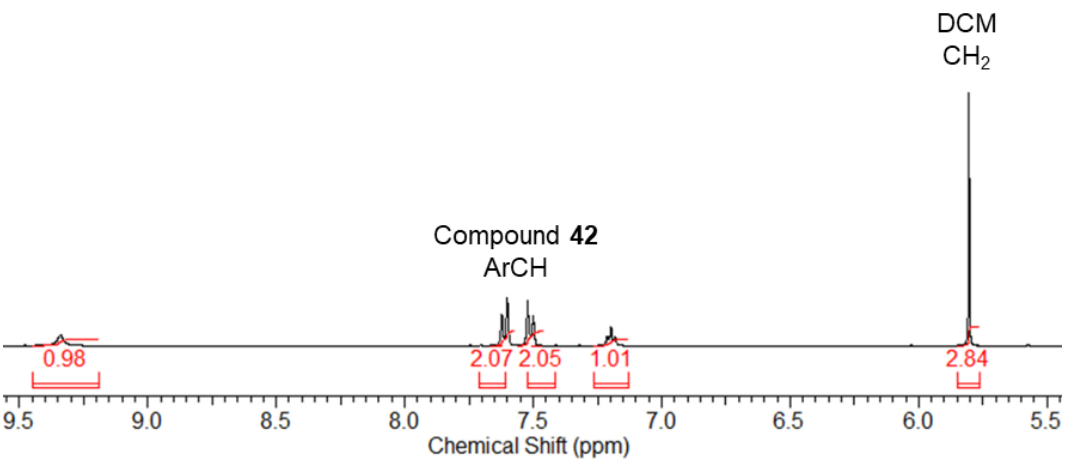

Figure S202 - ^{1}H NMR spectrum with a delay (d_1 = 60 s) of compound **42** (109.8 mM) in DMSO-d_6/ 1.0 % DCM. No apparent loss of compound observed upon comparative signal integration.

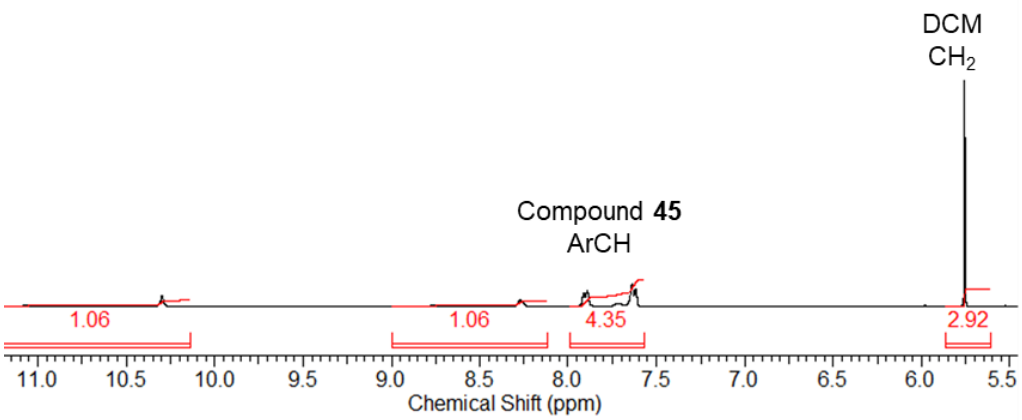

Figure S203 - ^{1}H NMR spectrum with a delay (d_1 = 60 s) of compound **45** (110.6 mM) in DMSO-d_6/ 1.0 % DCM. No apparent loss of compound observed upon comparative signal integration.

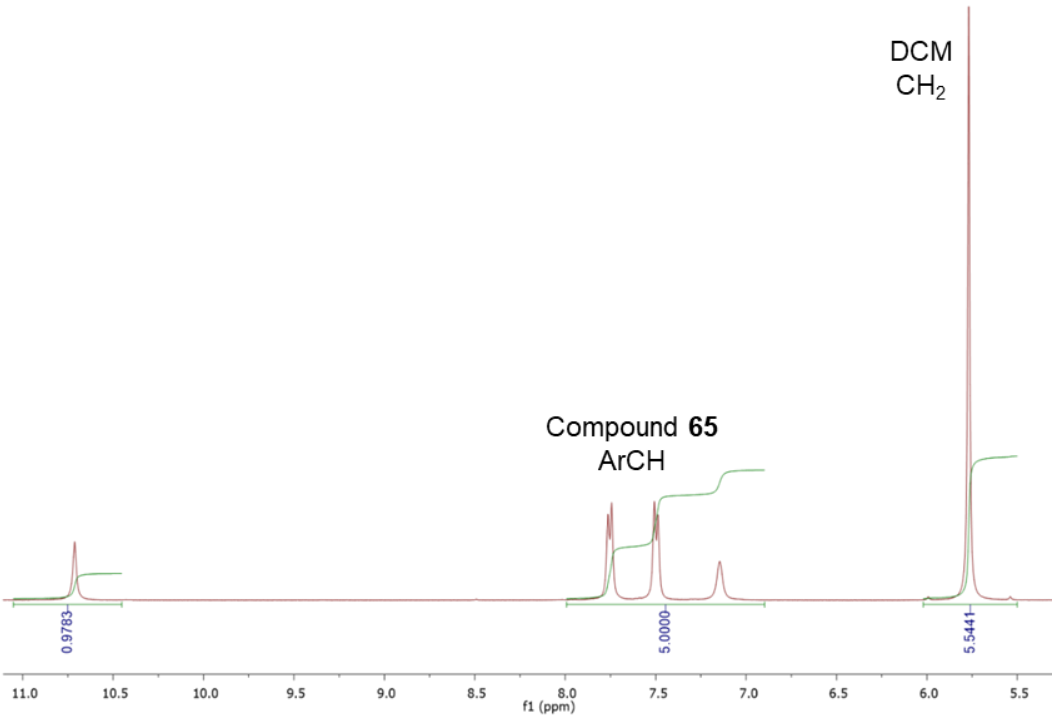

Figure S204 - ^{1}H NMR spectrum with a delay (d_1 = 60 s) of compound **65** (54.6 mM) in DMSO-d_6/ 1.0 % DCM. No apparent loss of compound observed upon comparative signal integration.

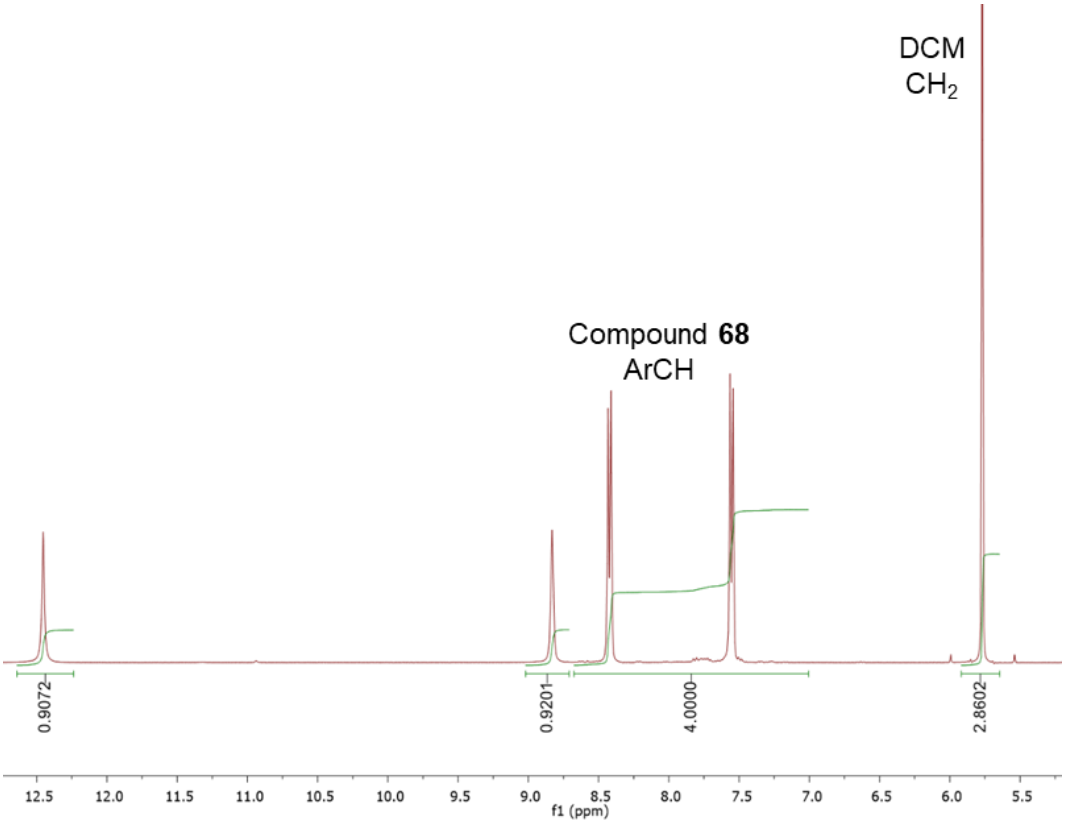

Figure S205 - ^{1}H NMR spectrum with a delay (d_1 = 60 s) of compound **68** (110.6 mM) in DMSO-d_6/ 1.0 % DCM. No apparent loss of compound observed upon comparative signal integration.

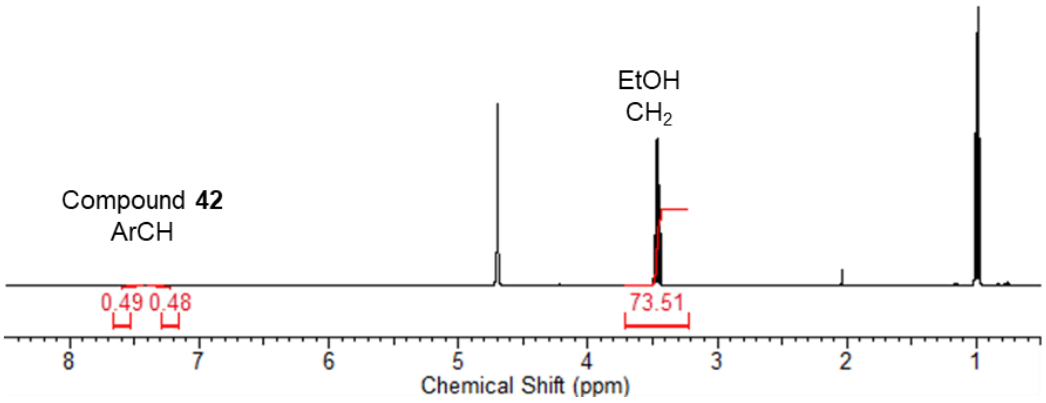

Figure S206 - ^{1}H NMR spectrum with a delay (d_1 = 60 s) of compound **42** (5.80 mM) in D_2O/ 5.0 % EtOH. An apparent 51 % loss of compound was observed upon comparative signal integration.

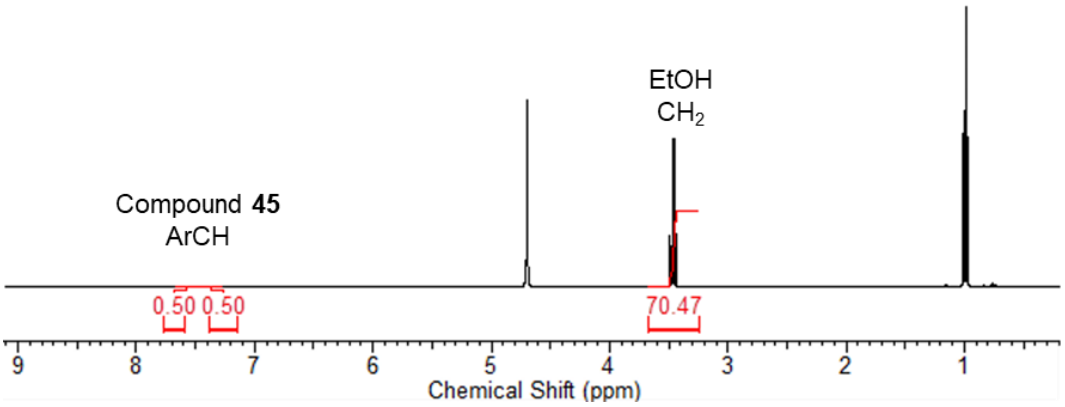

Figure S207 - ^{1}H NMR spectrum with a delay (d_1 = 60 s) of compound **45** (6.10 mM) in D_2O/ 5.0 % EtOH. An apparent 50 % loss of compound was observed upon comparative signal integration.

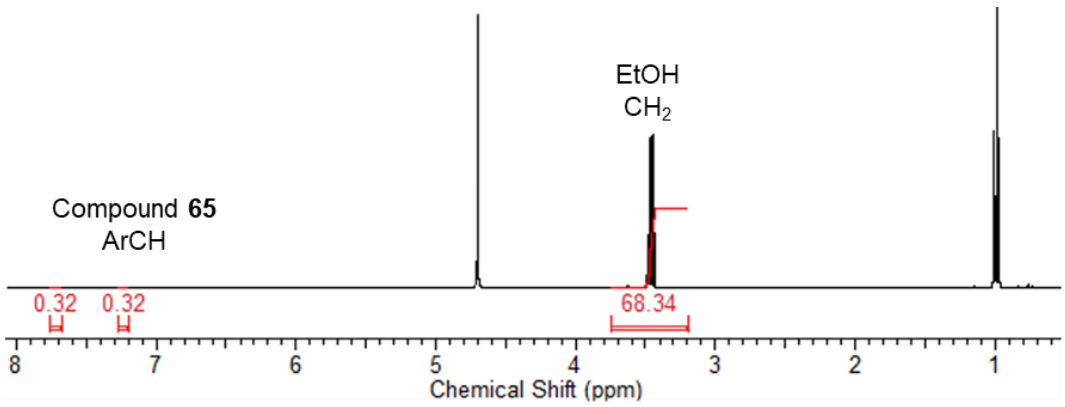

Figure S208 - ^{1}H NMR spectrum with a delay (d_1 = 60 s) of compound **65** (6.30 mM) in D_2O/ 5.0 % EtOH. An apparent 68 % loss of compound was observed upon comparative signal integration.

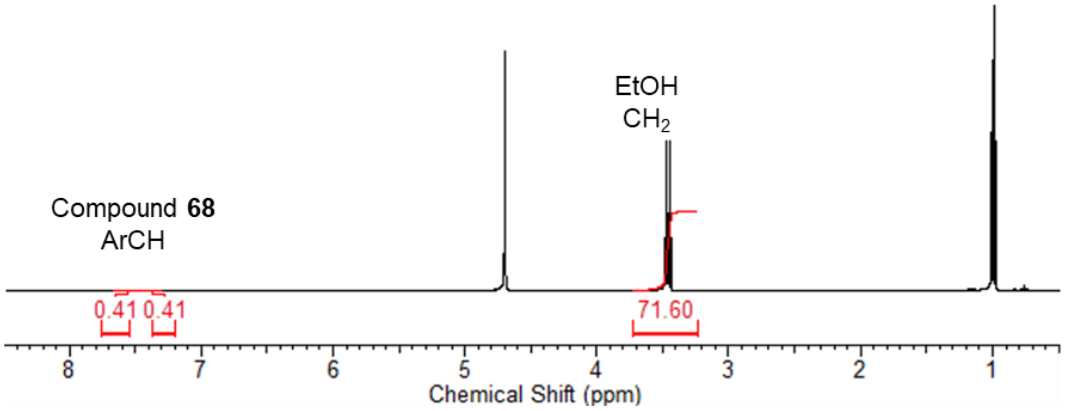

Figure S209 - ^{1}H NMR spectrum with a delay (d_1 = 60 s) of compound **68** (6.01 mM) in D_2O/ 5.0 % EtOH. An apparent 59 % loss of compound was observed upon comparative signal integration.

1.7.1 Comparative overview

Table S6 – Overview of apparent % '*loss*' values for **42**, **45**, **65**, **68** and **72** in an EtOH:D_2O (1:19) solution at ≈ 5.56 mM and DMSO-d_6/ 1.0 % DCM at ≈ 112 mM derived through quantitative ^{1}H NMR experiments.

Compound no.	EtOH:D_2O (1:19) (%)	DMSO-d_6/ 1.0 % DCM (%)
42	51	0
45	50	0
65	68	0[b]
68	59	0
72[a]	10	0

[*a*] Previously published results.[1] [*b*] Conducted at ≈ 55 mM due to insolubility at higher concentrations.

1.8 Zeta potential

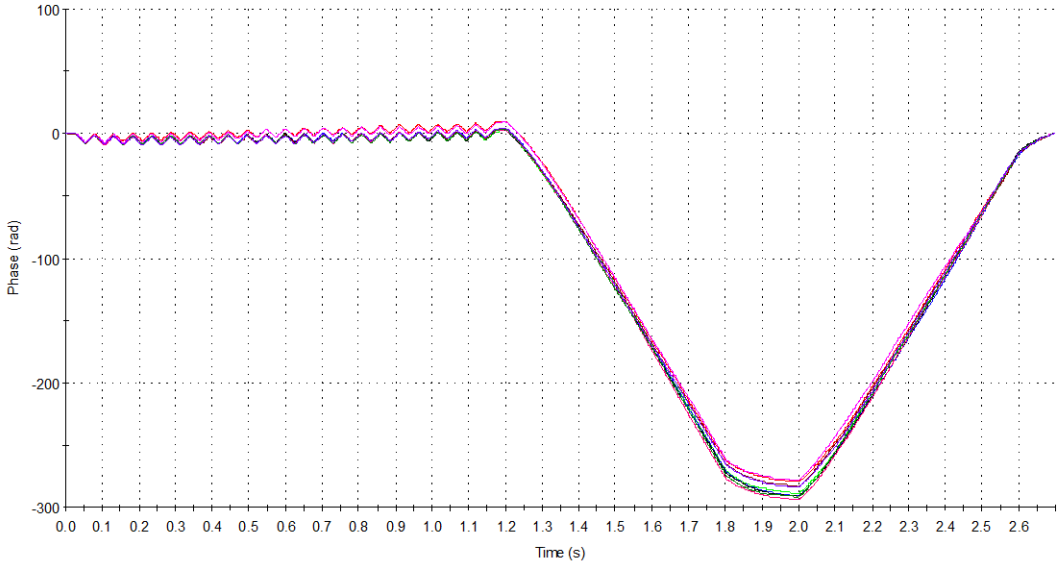

Figure S210 - Phase plot taken during the measurement of 9 Zeta Potential Transfer Standard (PTS) runs of compound **42** at a concentration of 5.56 mM in a solution EtOH:H_2O 1:19. Average measurement value -75.8 mV.

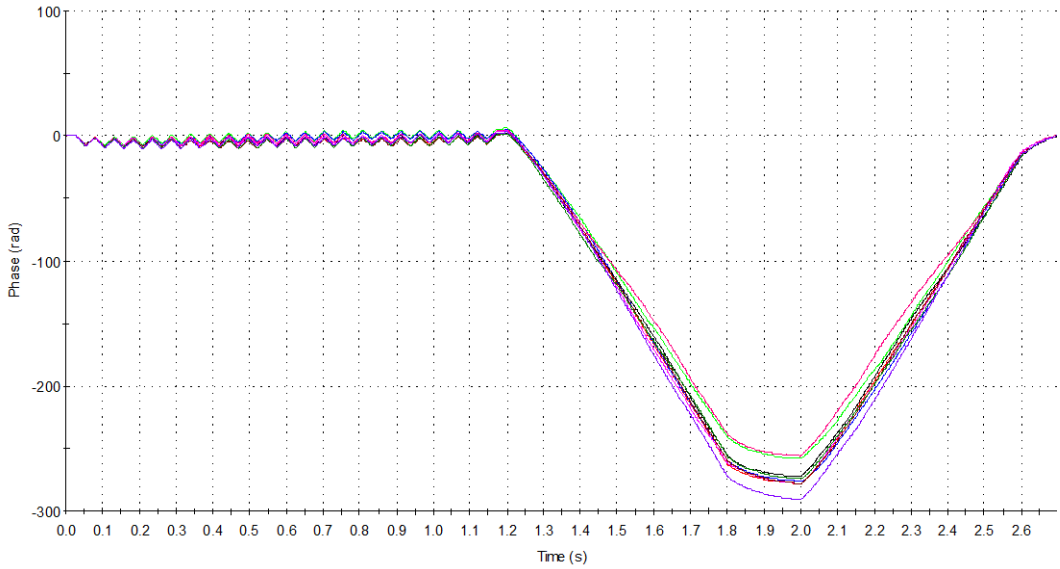

Figure S211 - Phase plot taken during the measurement of 9 Zeta Potential Transfer Standard (PTS) runs of compound **43** at a concentration of 5.56 mM in a solution EtOH:H_2O 1:19. Average measurement value -77.6 mV.

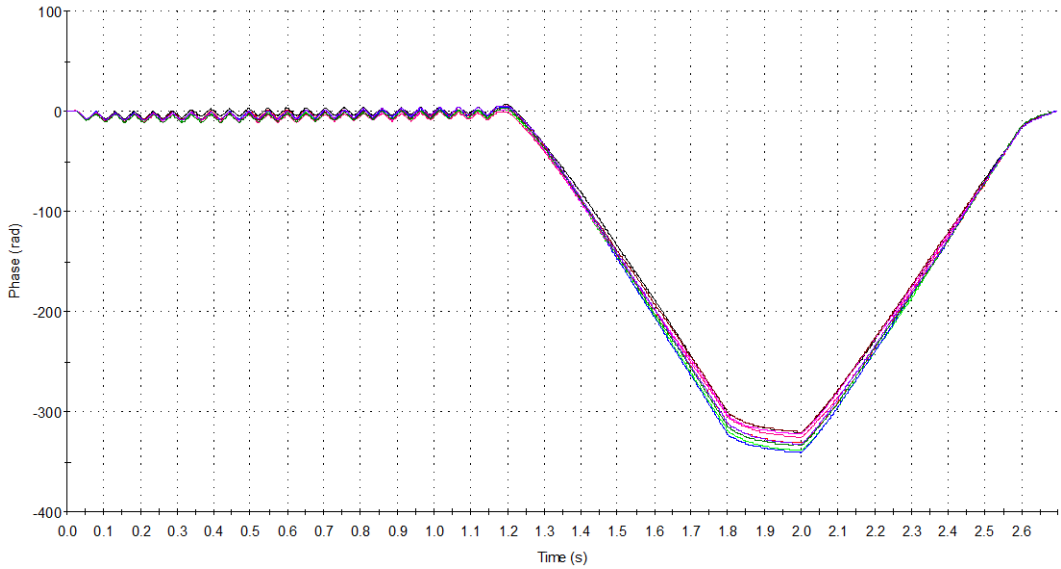

Figure S212 - Phase plot taken during the measurement of 9 Zeta Potential Transfer Standard (PTS) runs of compound **44** at a concentration of 5.56 mM in a solution EtOH:H_2O 1:19. Average measurement value -93.7 mV.

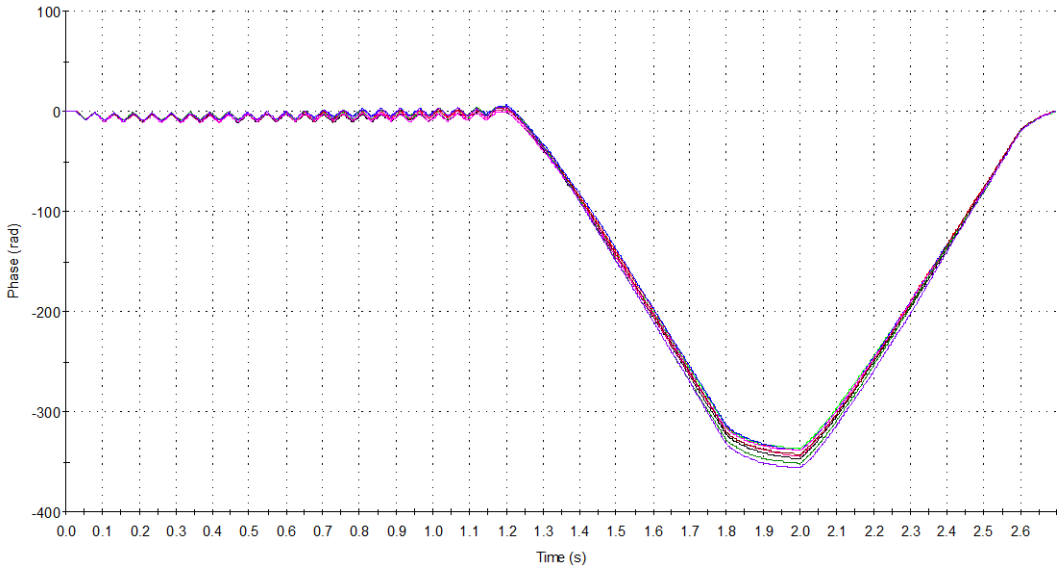

Figure S213 - Phase plot taken during the measurement of 9 Zeta Potential Transfer Standard (PTS) runs of compound **45** at a concentration of 5.56 mM in a solution EtOH:H_2O 1:19. Average measurement value -92.3 mV.

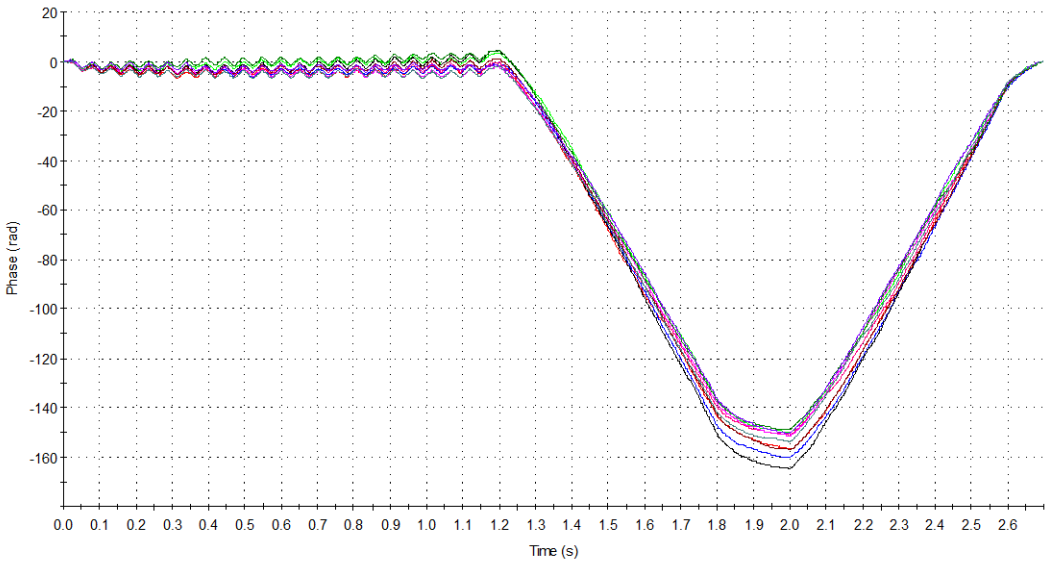

Figure S214 - Phase plot taken during the measurement of 9 Zeta Potential Transfer Standard (PTS) runs of compound **46** at a concentration of 5.56 mM in a solution EtOH:H_2O 1:19. Average measurement value -33.5 mV.

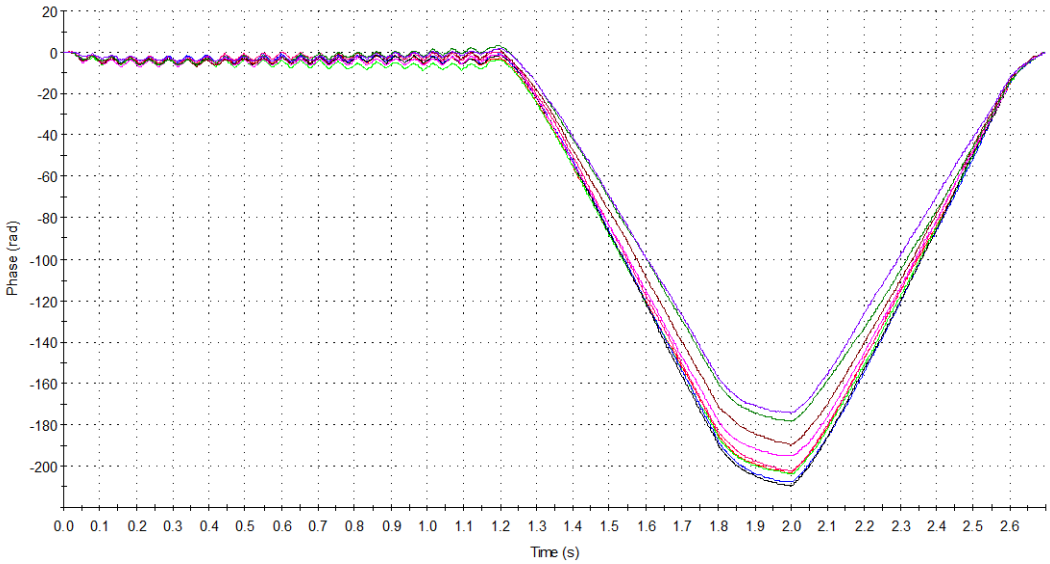

Figure S215 - Phase plot taken during the measurement of 9 Zeta Potential Transfer Standard (PTS) runs of compound **47** at a concentration of 5.56 mM in a solution EtOH:H_2O 1:19. Average measurement value -38.2 mV.

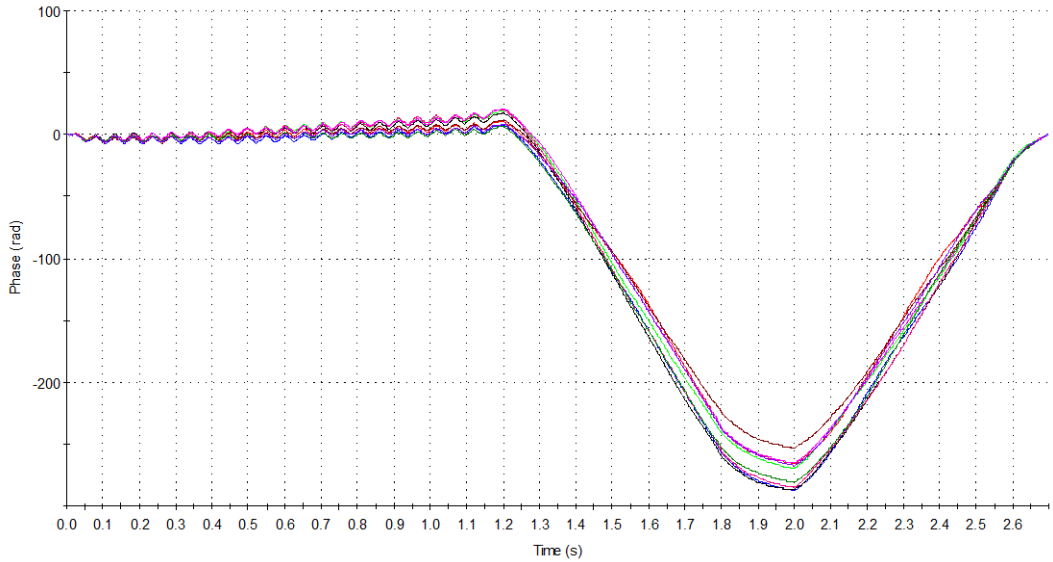

Figure S216 - Phase plot taken during the measurement of 9 Zeta Potential Transfer Standard (PTS) runs of compound **48** at a concentration of 5.56 mM in a solution EtOH:H_2O 1:19. Average measurement value -55.4 mV.

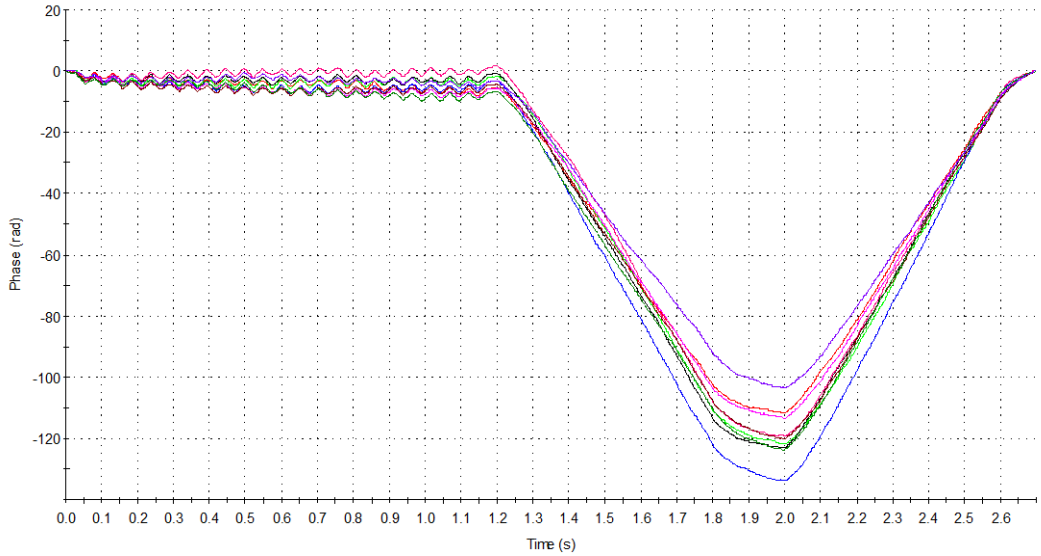

Figure S217 - Phase plot taken during the measurement of 9 Zeta Potential Transfer Standard (PTS) runs of compound **49** at a concentration of 5.56 mM in a solution EtOH:H_2O 1:19. Average measurement value -27.7 mV.

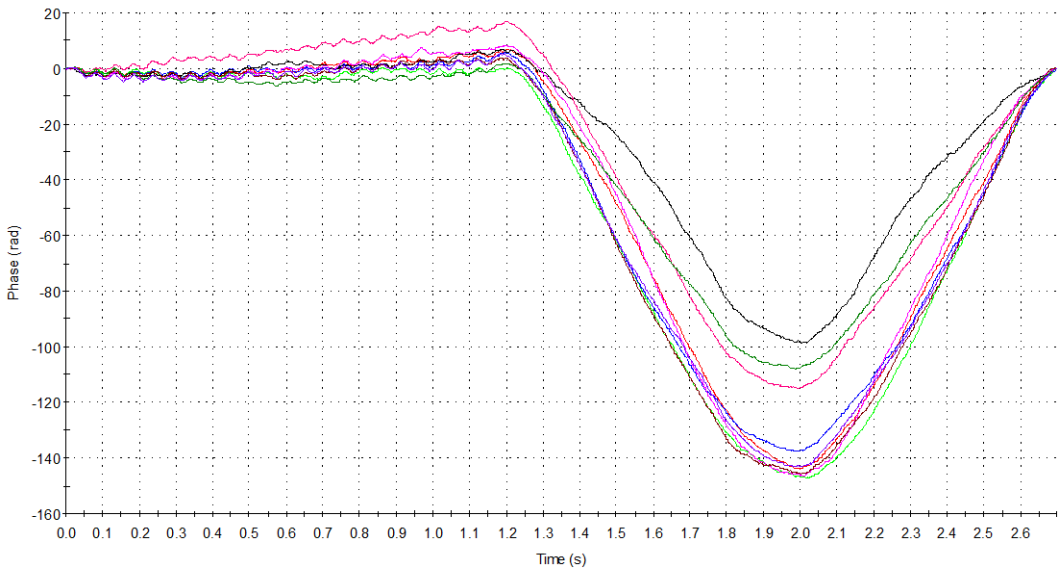

Figure S218 - Phase plot taken during the measurement of 9 Zeta Potential Transfer Standard (PTS) runs of compound **50** at a concentration of 5.56 mM in a solution EtOH:H_2O 1:19. Average measurement value **-**24.4 mV.

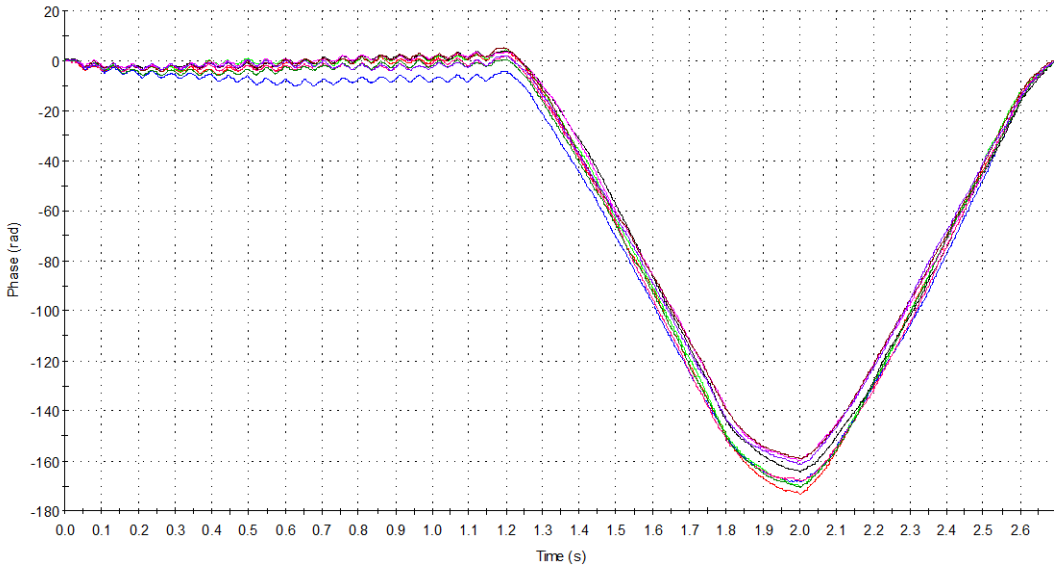

Figure S219 - Phase plot taken during the measurement of 9 Zeta Potential Transfer Standard (PTS) runs of compound **51** at a concentration of 5.56 mM in a solution EtOH:H_2O 1:19. Average measurement value **-**25.7 mV.

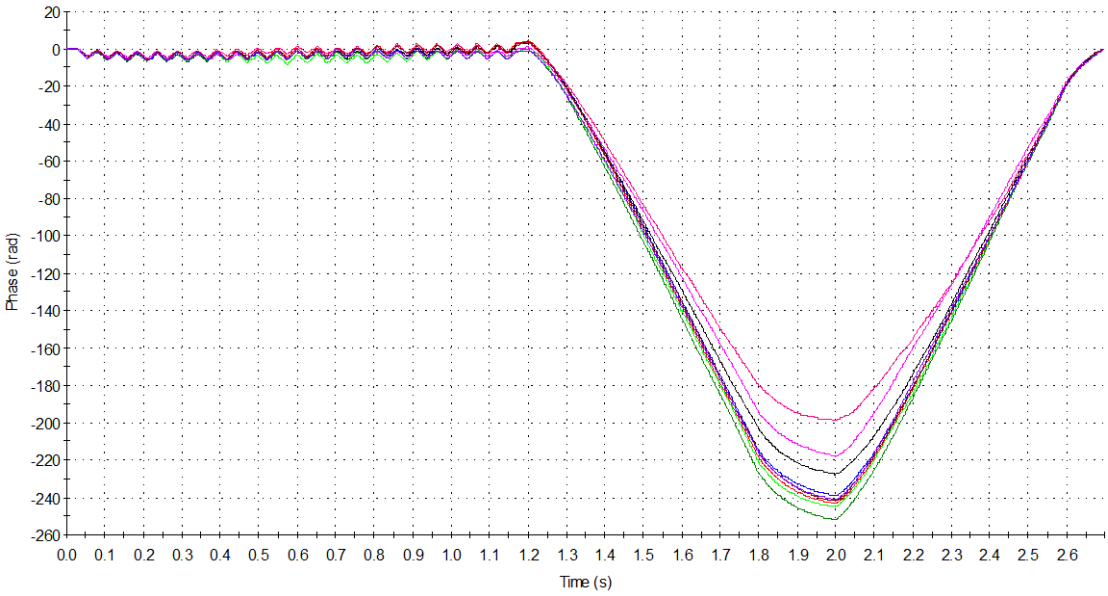

Figure S220 - Phase plot taken during the measurement of 9 Zeta Potential Transfer Standard (PTS) runs of compound **52** at a concentration of 5.56 mM in a solution EtOH:H_2O 1:19. Average measurement value -48.3 mV.

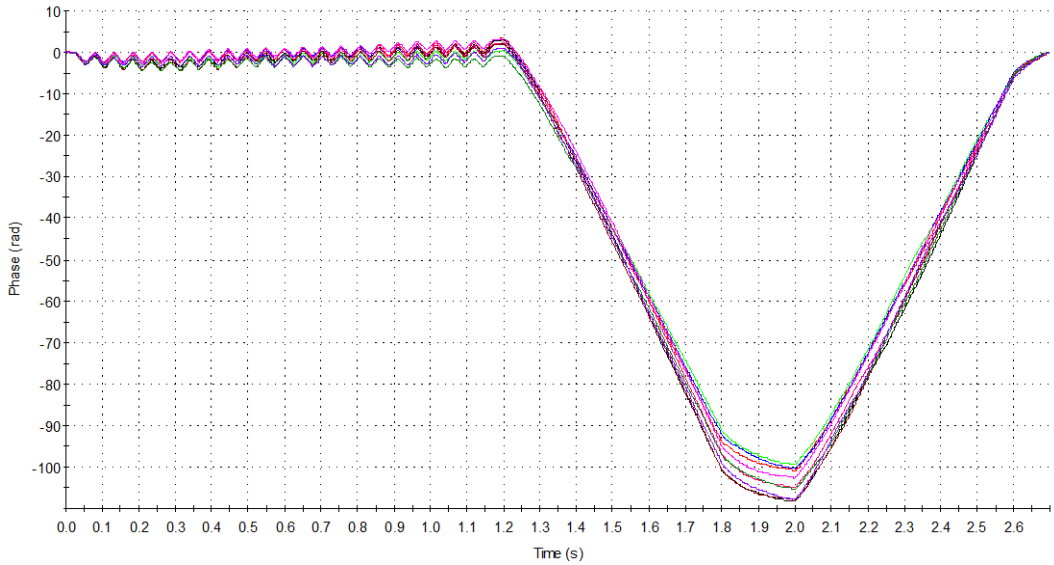

Figure S221 - Phase plot taken during the measurement of 9 Zeta Potential Transfer Standard (PTS) runs of compound **55** at a concentration of 5.56 mM in a solution EtOH:H_2O 1:19. Average measurement value -30.2 mV.

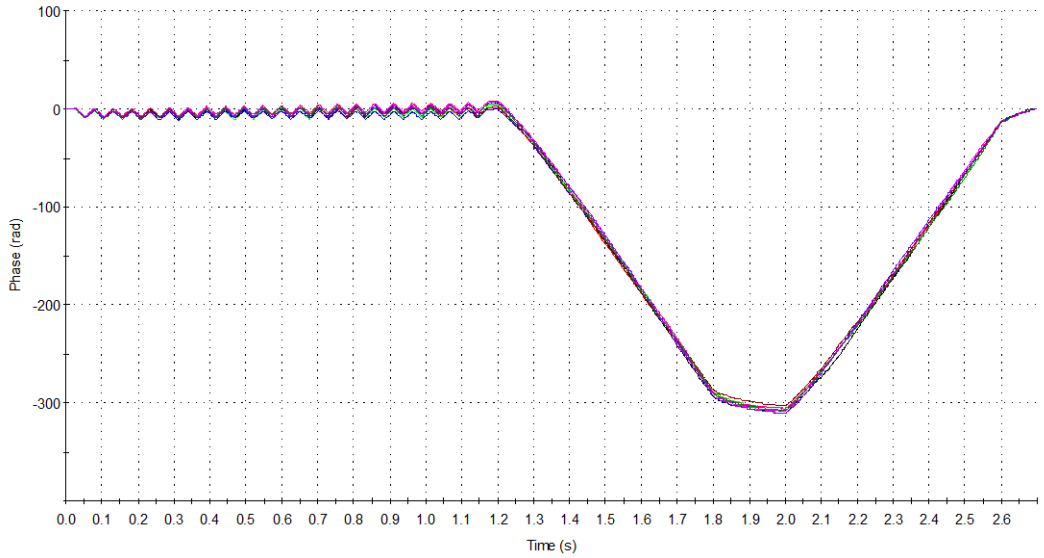

Figure S222 - Phase plot taken during the measurement of 9 Zeta Potential Transfer Standard (PTS) runs of compound **56** at a concentration of 5.56 mM in a solution EtOH:H_2O 1:19. Average measurement value -97.9 mV.

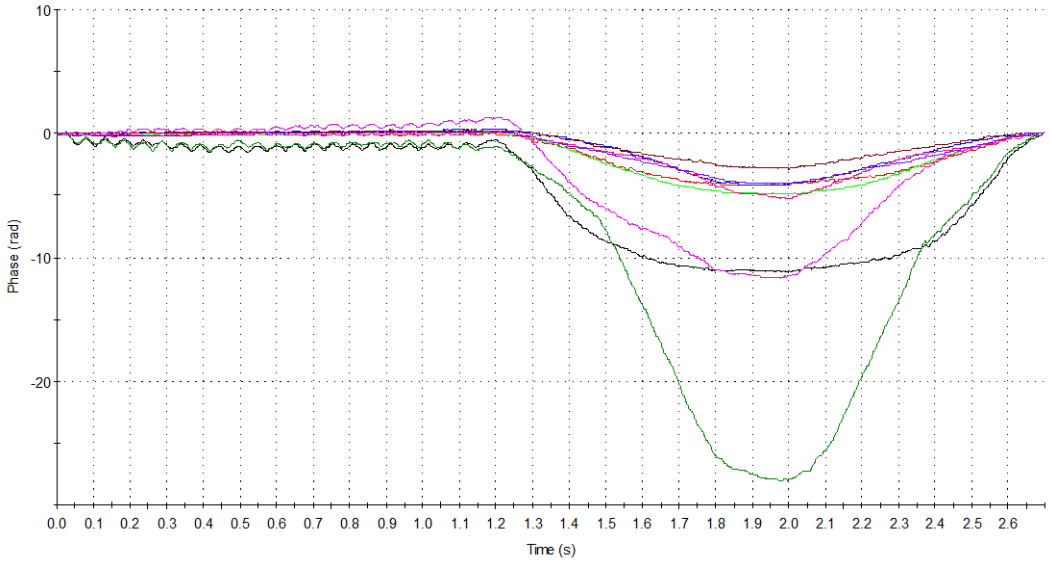

Figure S223 - Phase plot taken during the measurement of 9 Zeta Potential Transfer Standard (PTS) runs of compound **58** at a concentration of 5.56 mM in a solution EtOH:H_2O 1:19. The results from this study are ambiguous and could not be replicated.

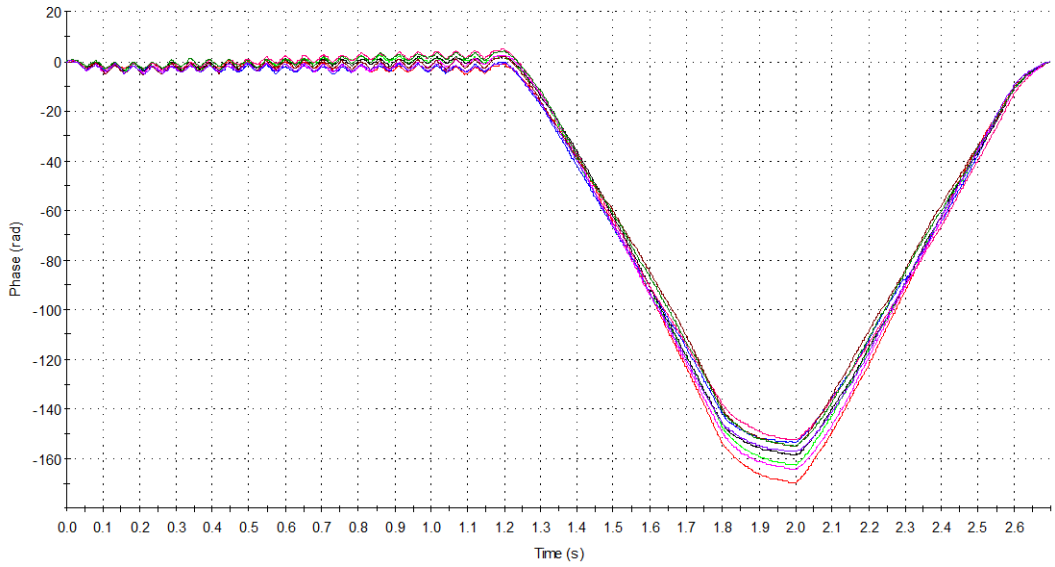

Figure S224 - Phase plot taken during the measurement of 9 Zeta Potential Transfer Standard (PTS) runs of compound **60** at a concentration of 5.56 mM in a solution EtOH:H_2O 1:19. Average measurement value -30.2 mV.

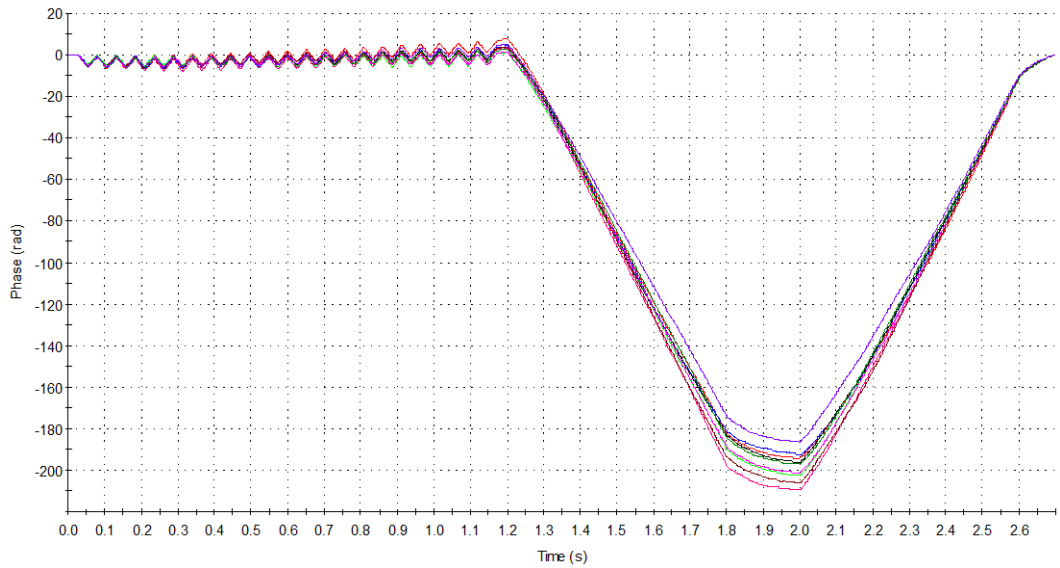

Figure S225 - Phase plot taken during the measurement of 9 Zeta Potential Transfer Standard (PTS) runs of compound **61** at a concentration of 5.56 mM in a solution EtOH:H_2O 1:19. Average measurement value -66.2 mV.

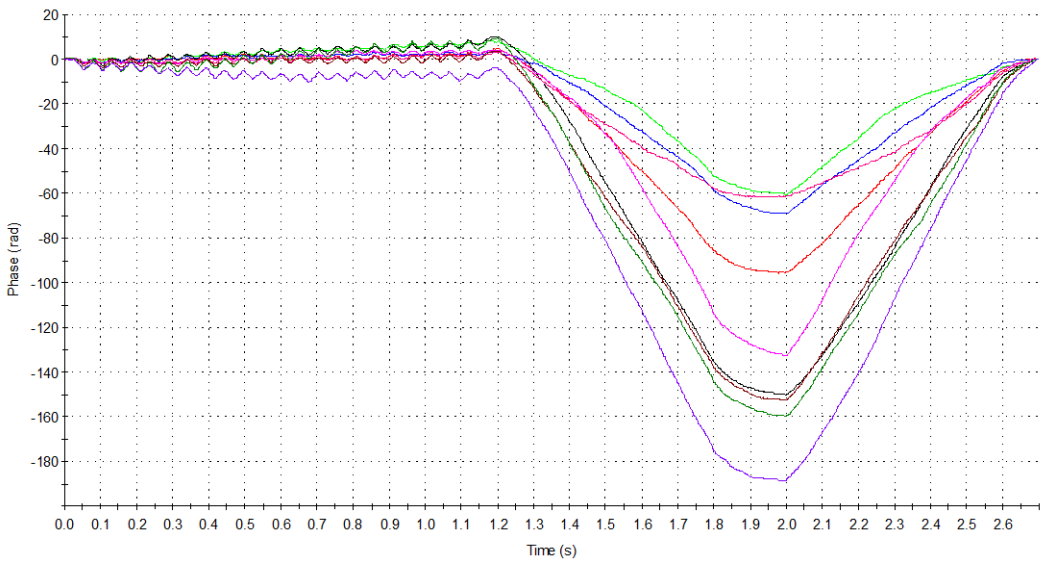

Figure S226 - Phase plot taken during the measurement of 9 Zeta Potential Transfer Standard (PTS) runs of compound **62** at a concentration of 5.56 mM in a solution EtOH:H_2O 1:19. The results from this study are ambiguous and could not be replicated.

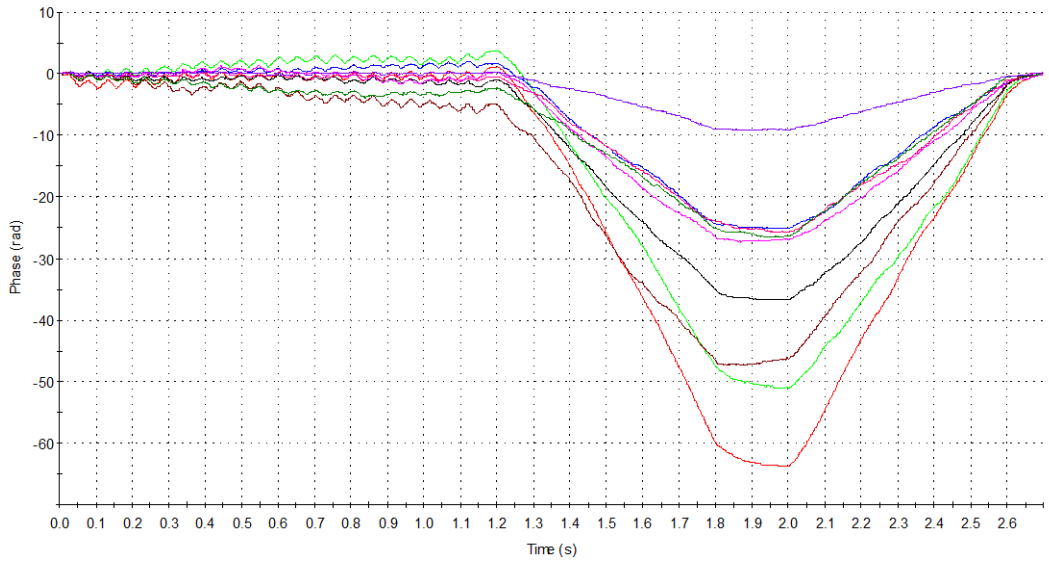

Figure S227 - Phase plot taken during the measurement of 9 Zeta Potential Transfer Standard (PTS) runs of compound **64** at a concentration of 5.56 mM in a solution EtOH:H_2O 1:19. The results from this study are ambiguous and could not be replicated.

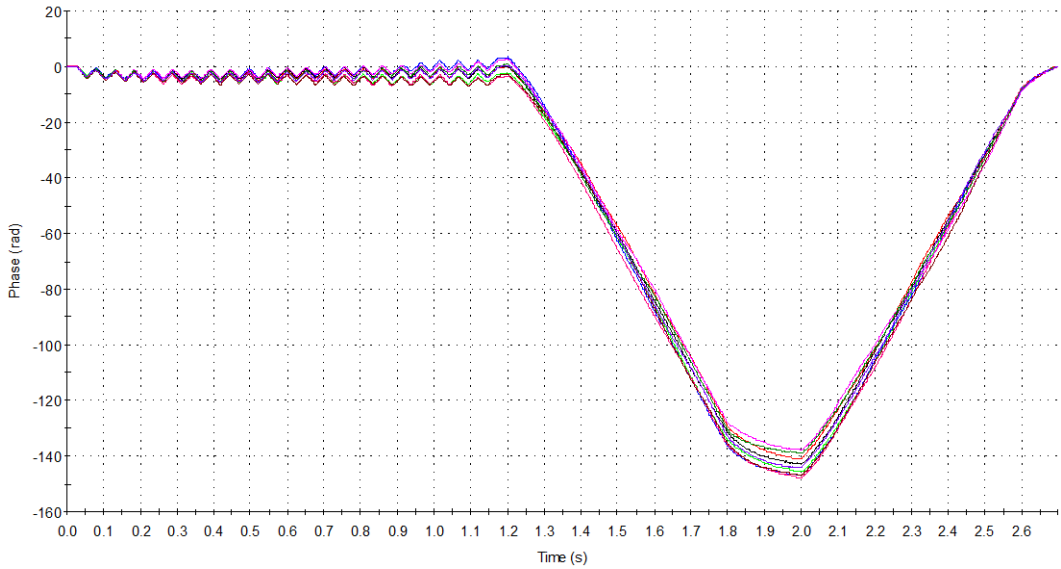

Figure S228 - Phase plot taken during the measurement of 9 Zeta Potential Transfer Standard (PTS) runs of compound **65** at a concentration of 5.56 mM in a solution EtOH:H_2O 1:19. Average measurement value -37.3 mV.

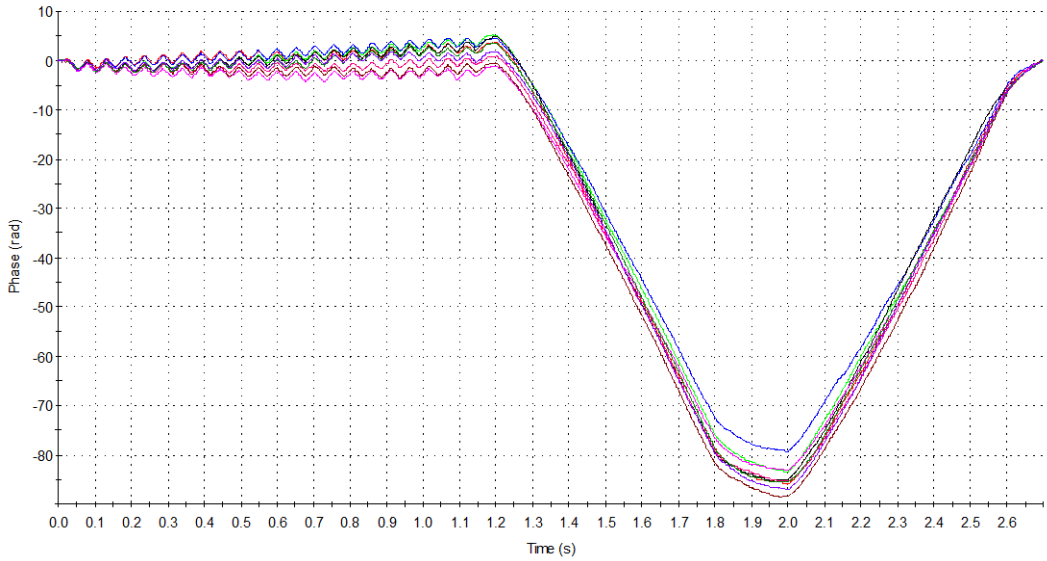

Figure S229 - Phase plot taken during the measurement of 9 Zeta Potential Transfer Standard (PTS) runs of compound **67** at a concentration of 5.56 mM in a solution EtOH:H_2O 1:19. Average measurement value -22.6 mV.

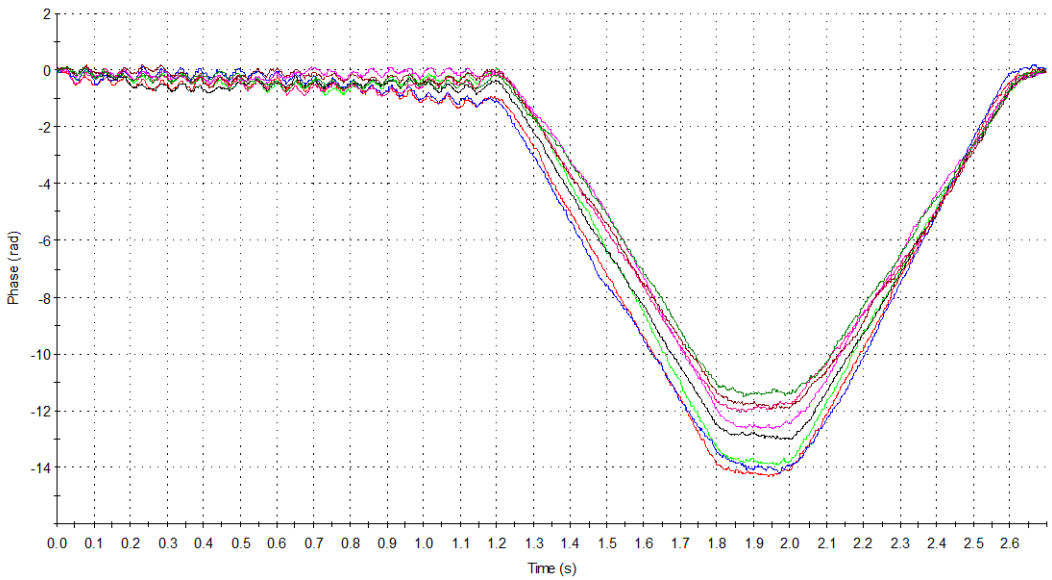

Figure S230 - Phase plot taken during the measurement of 9 Zeta Potential Transfer Standard (PTS) runs of compound **68** at a concentration of 5.56 mM in a solution EtOH:H_2O 1:19. Average measurement value -3.89 mV.

1.8.1 Comparative overview

Table S7 – Zeta potential measurements for compounds **42**-**52, 55**-**57**, **60**, **61**, **65** and **67**-**72** in a solution of EtOH:H_2O (1:19) at 5.56 mM.

Compound no.	Zeta potential (mV)	Compound no.	Zeta potential (mV)
42	-76	**57**[a]	-19
43	-78	**58**	[c]
44	-94	**60**	-30
45	-92	**61**	-66
46	-34	**62**	[c]
47	-38	**63**	[b]
48	-55	**64**	[c]
49	-28	**65**	-37
50	-24	**66**	[b]
51	-26	**67**	-23
52	-48	**68**	-4
53	[b]	**69**[a]	-96
54	[b]	**70**[a]	-82
55	-30	**71**[a]	-79
56	-98	**72**[a]	-101

[*a*] Previously published results.[1] [*b*] not calculated due to sample insolubility. [*c*] Could not be accurately determined due to lack of reproducibility.

1.9 ^{1}H NMR self-association studies

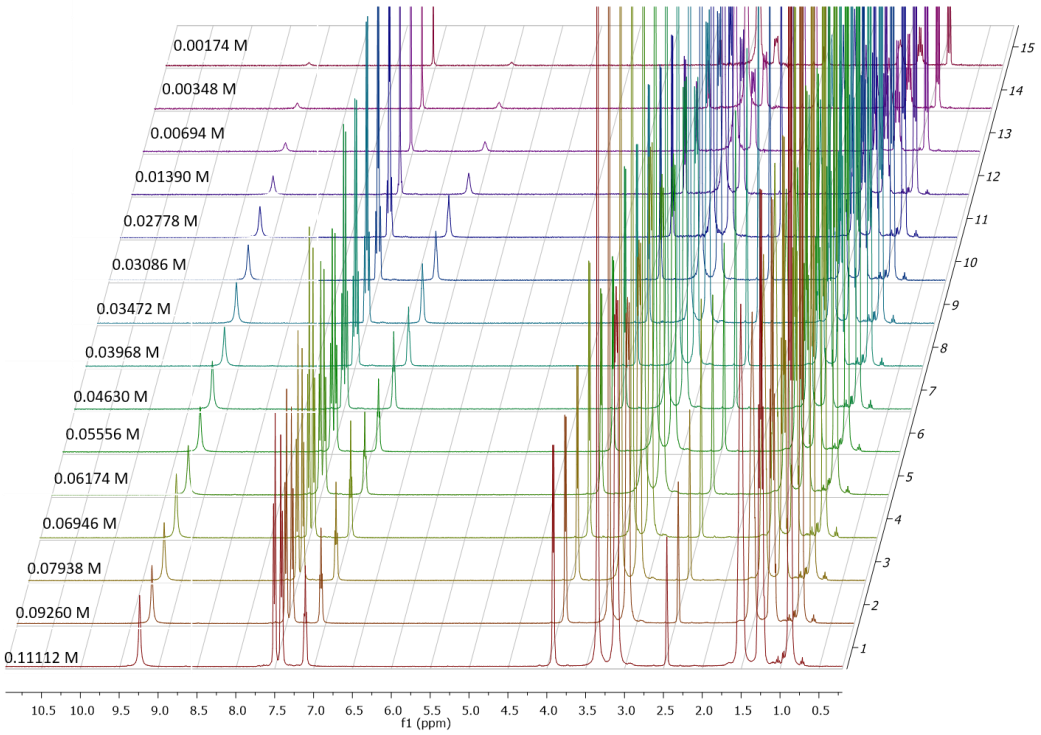

Figure S231 - ^{1}H NMR stack plot of compound **42** in DMSO-d_6 0.5 % H_2O solution. Samples were prepared in series with an aliquot of the most concentrated solution undergoing serial dilution.

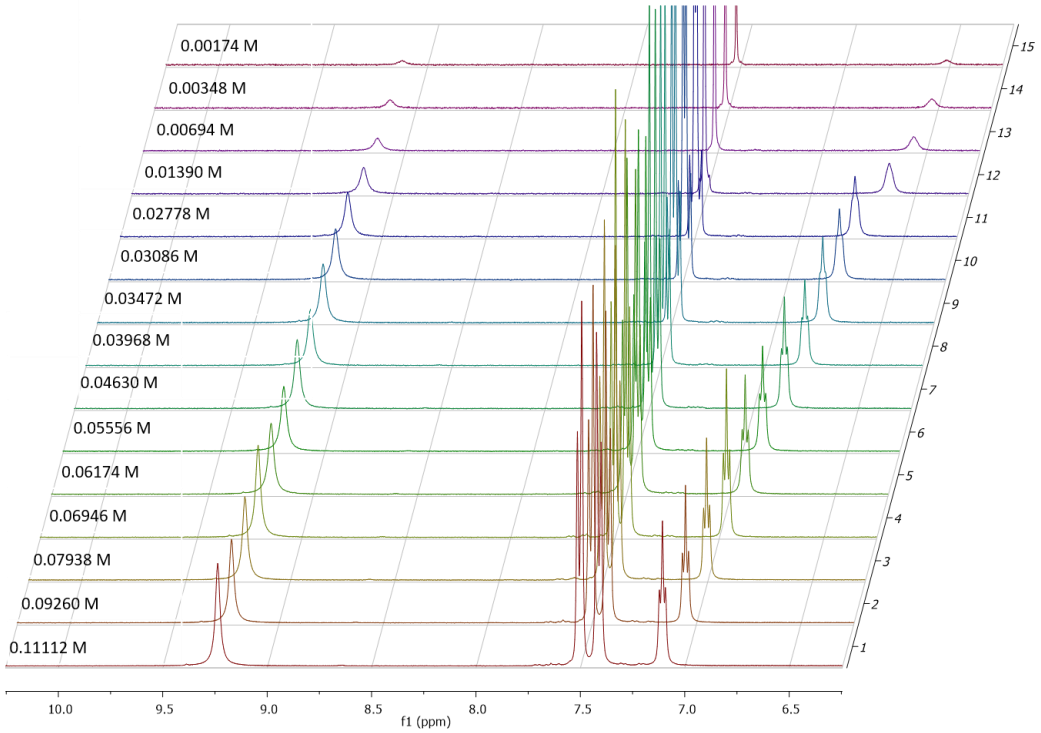

Figure S232 - Enlarged ^{1}H NMR stack plot of compound **42** in DMSO-d_6 0.5 % H_2O solution. Samples were prepared in series with an aliquot of the most concentrated solution undergoing serial dilution.

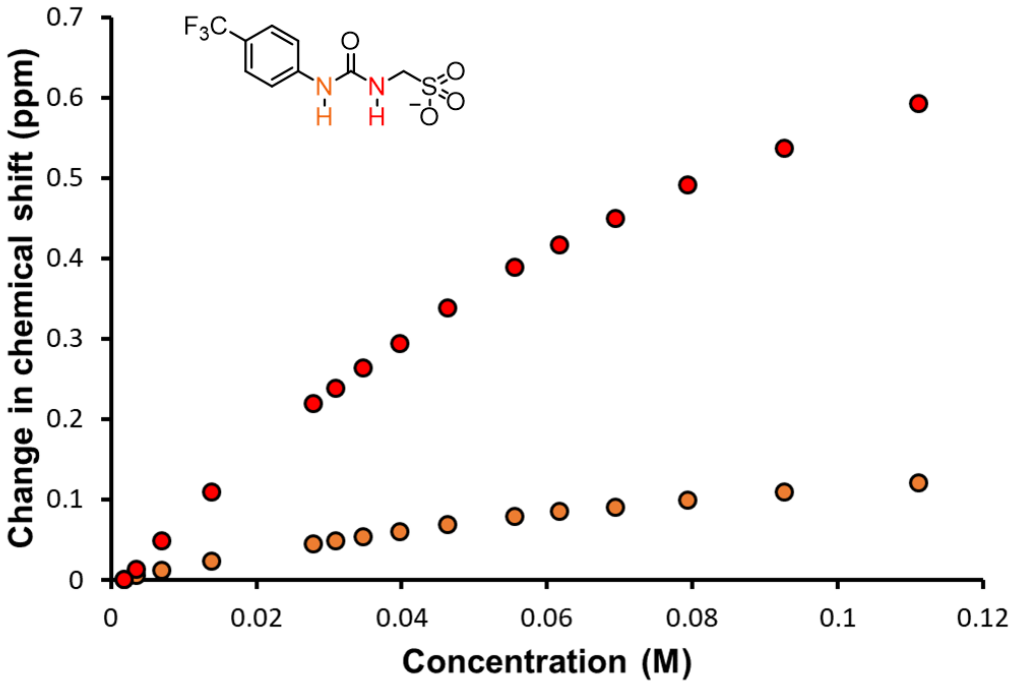

Figure S233 - Graph illustrating the ^{1}H NMR down-field change in chemical shift of urea NH resonances with increasing concentration of compound **42** in DMSO-d_6 0.5 % H_2O (298.15 K).

Self-association constant calculation

Compound **42** - Dilution study in DMSO-d_6 0.5 % H_2O. Values calculated from data gathered from both NH 1 and 2.

Equal K/Dimerisation model

K_e = 5.31 M^{-1} ± 0.6180 % K_{dim} = 2.66 M^{-1} ± 0.3090 %

http://app.supramolecular.org/bindfit/view/d6af9b53-56d3-41af-9eb1-1089d2ebed98

CoEK model

K_e = 12.95 M^{-1} ± 0.7180 % K_{dim} = 6.48 M^{-1} ± 0.3590 % ρ = 0.50 ± 2.1072 %

http://app.supramolecular.org/bindfit/view/01e930a4-468d-42b7-b512-879b89a19e47

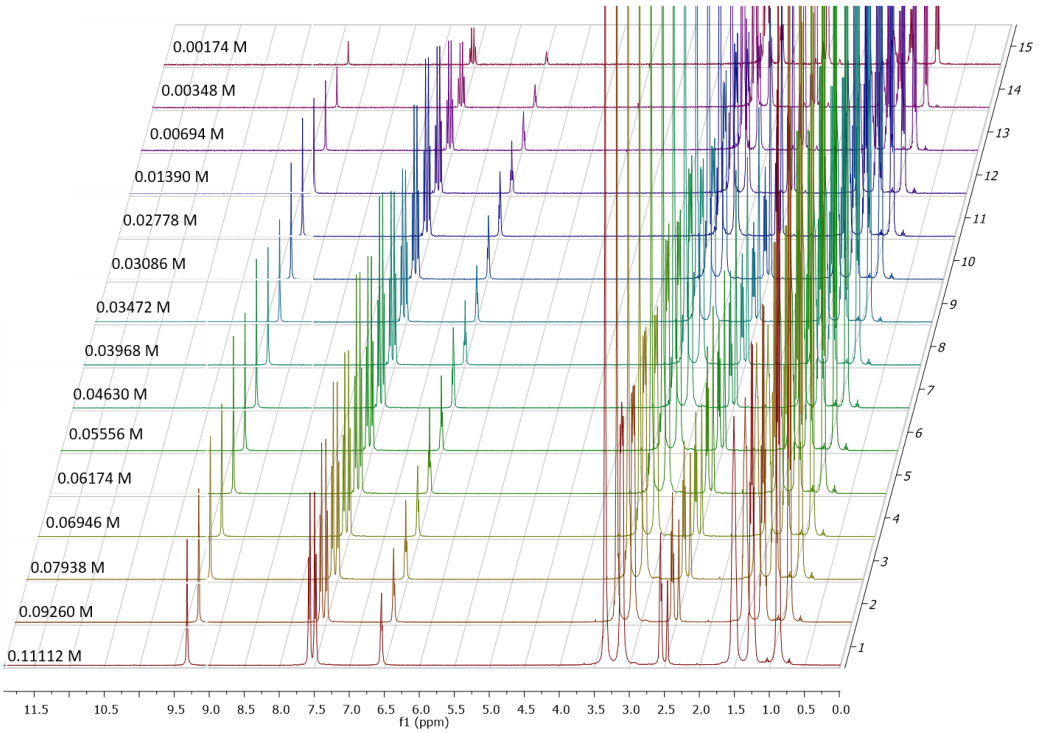

Figure S234 - ^{1}H NMR stack plot of compound **43** in DMSO-d_6 0.5 % H_2O solution. Samples were prepared in series with an aliquot of the most concentrated solution undergoing serial dilution.

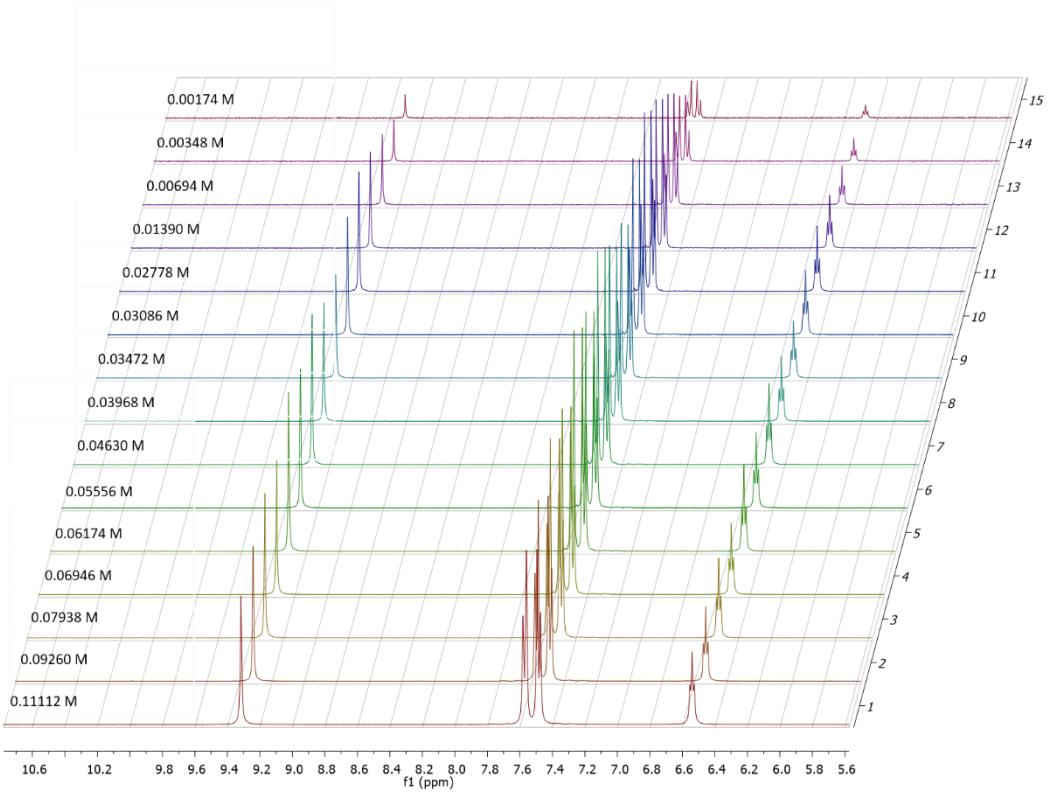

Figure S235 - Enlarged ^{1}H NMR stack plot of compound **43** in DMSO-d_6 0.5 % H_2O solution. Samples were prepared in series with an aliquot of the most concentrated solution undergoing serial dilution.

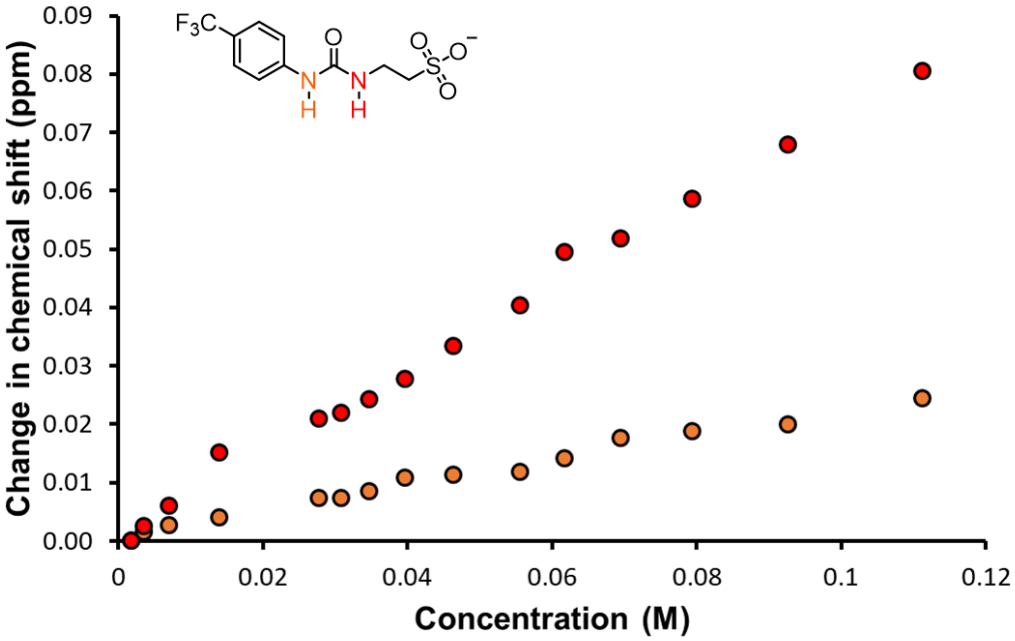

Figure S236 - Graph illustrating the ^{1}H NMR down-field change in chemical shift of urea NH resonances with increasing concentration of compound **43** in DMSO-d_6 0.5 % H_2O (298.15 K).

Self-association constant calculation

<u>Compound **43** - Dilution study in DMSO-d_6 0.5 % H_2O. Values calculated from data gathered from both NH 1 and 2.</u>

Equal K/Dimerisation model

K_e = 0.18 M^{-1} ± 1.9926 % K_{dim} = 0.09 M^{-1} ± 0.9963 %

http://app.supramolecular.org/bindfit/view/611ab18c-91b8-452a-9291-06723b77b27d

CoEK model

K_e = 4.01 M^{-1} ± 12.0440 % K_{dim} = 2.00 M^{-1} ± 6.0220 % ρ = 0.39 ± 20.3336 %

http://app.supramolecular.org/bindfit/view/9ffc706a-1be8-42e0-9add-c45df6b8775f

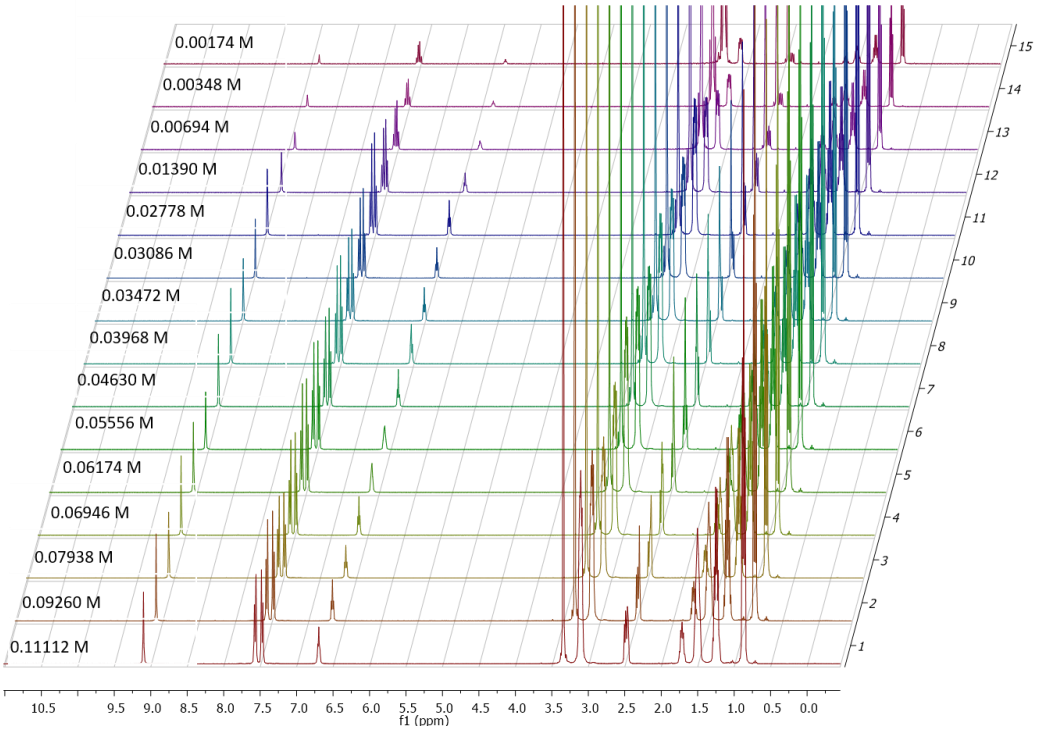

Figure S237 - ^{1}H NMR stack plot of compound **44** in DMSO-d_6 0.5 % H_2O. Samples were prepared in series with an aliquot of the most concentrated solution undergoing serial dilution.

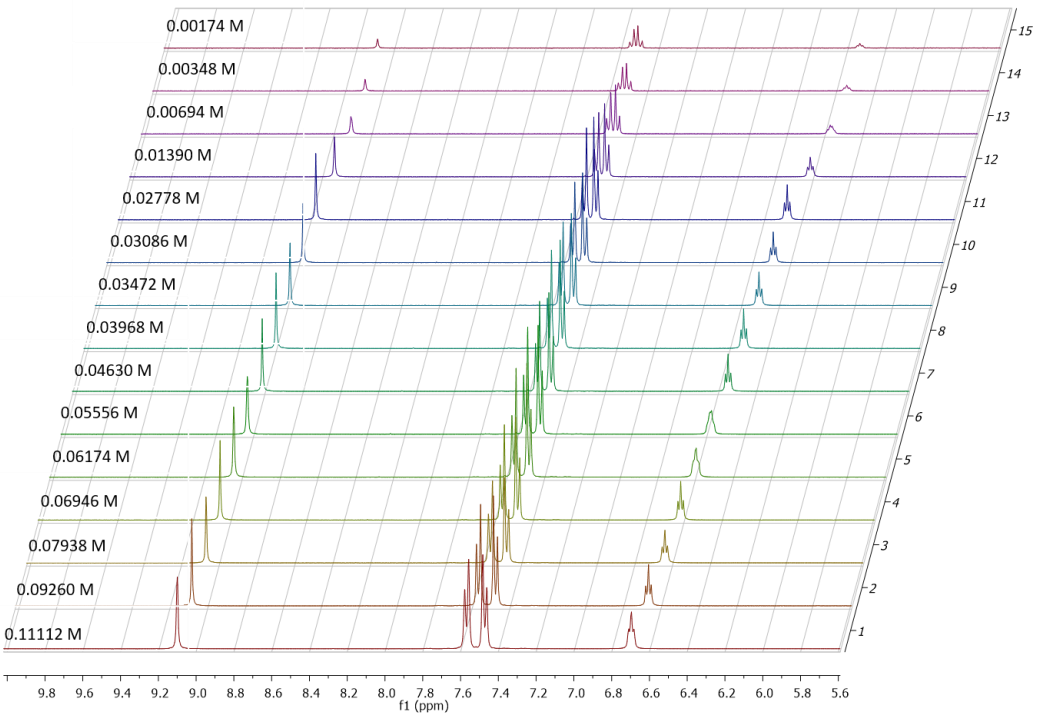

Figure S238 - Enlarged ^{1}H NMR stack plot of compound **44** in DMSO-d_6 0.5 % H_2O solution. Samples were prepared in series with an aliquot of the most concentrated solution undergoing serial dilution.

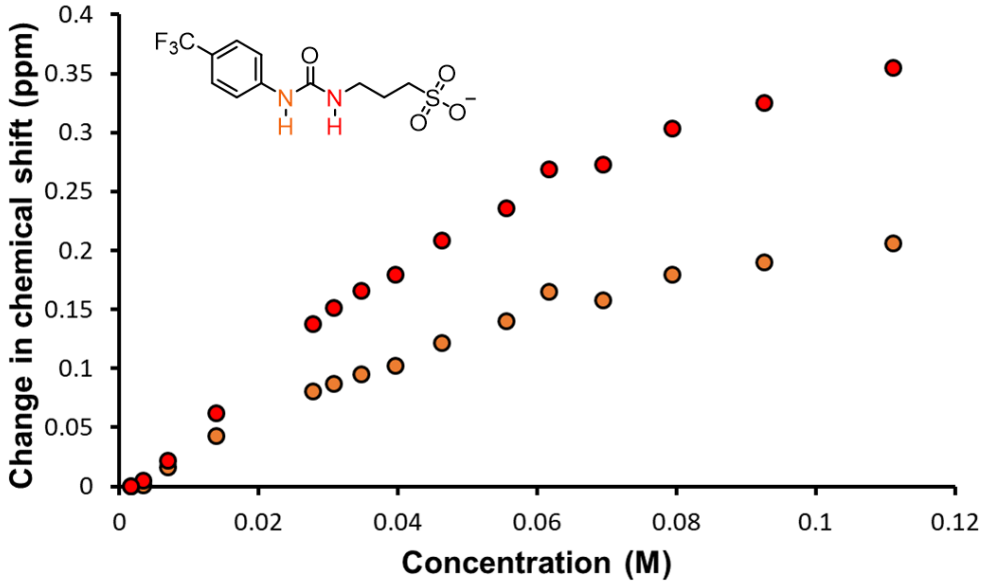

Figure S239 - Graph illustrating the ^{1}H NMR down-field change in chemical shift of urea NH resonances with increasing concentration of compound **44** in DMSO-d_6 0.5 % H_2O (298.15 K).

Self-association constant calculation

Compound **44** - Dilution study in DMSO-d_6 0.5 % H_2O. Values calculated from data gathered from both NH 1 and 2.

Equal K/Dimerisation model

K_e = 6.60 M^{-1} ± 1.9895 % K_{dim} = 3.30 M^{-1} ± 0.9947 %

http://app.supramolecular.org/bindfit/view/80983541-35ea-4fc8-ba61-db06ca69b722

CoEK model

K_e = 19.97 M^{-1} ± 2.7078 % K_{dim} = 9.98 M^{-1} ± 1.3539 % ρ = 0.34 ± 11.5687 %

http://app.supramolecular.org/bindfit/view/f8516087-4785-4676-8b8c-8ac3bc6ec9e6

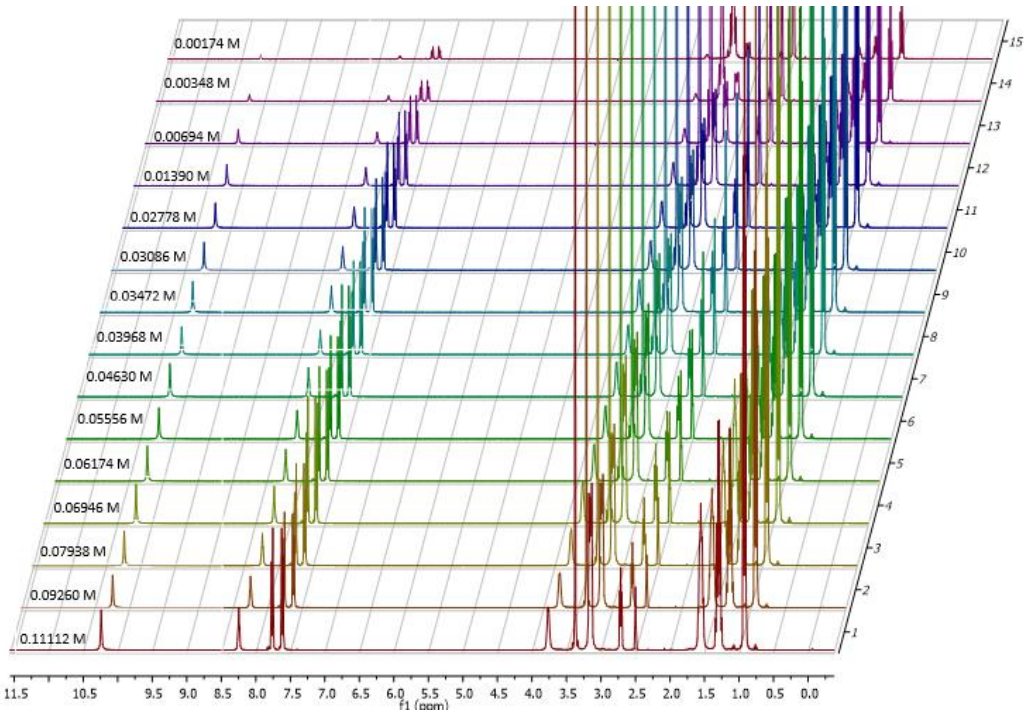

Figure S240 - ^{1}H NMR stack plot of compound **46** in DMSO-d_6 0.5 % H_2O. Samples were prepared in series with an aliquot of the most concentrated solution undergoing serial dilution.

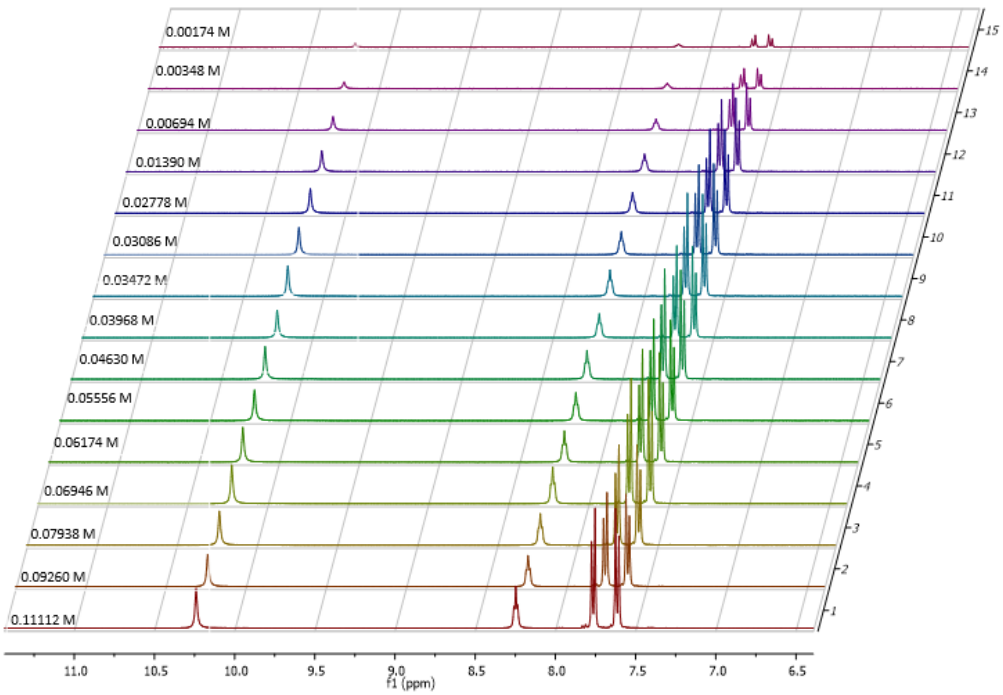

Figure S241 - Enlarged ^{1}H NMR stack plot of compound **46** in DMSO-d_6 0.5 % H_2O solution. Samples were prepared in series with an aliquot of the most concentrated solution undergoing serial dilution.

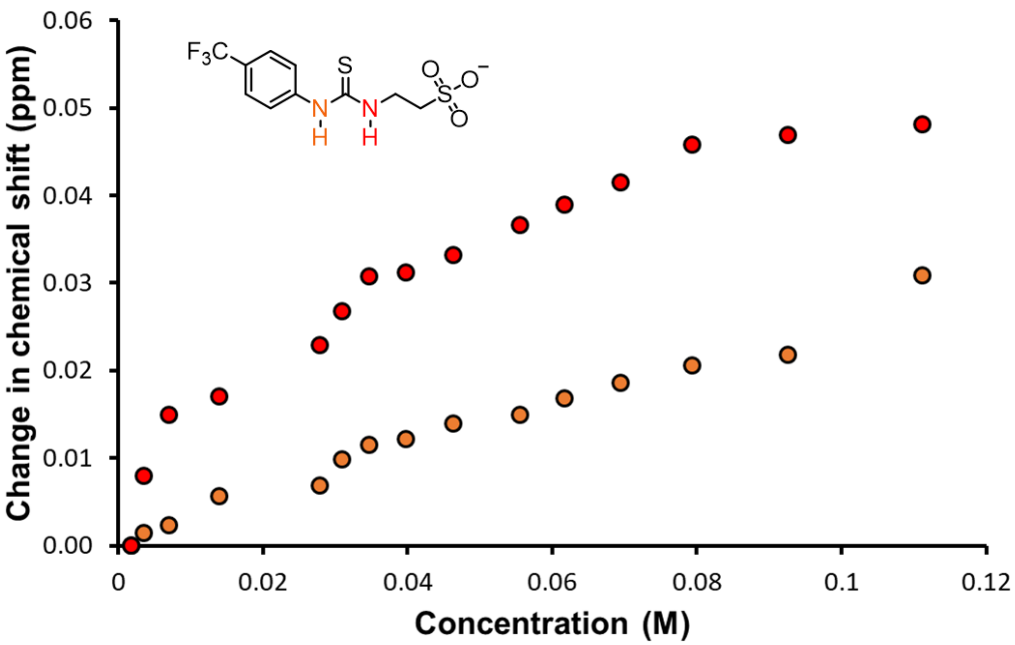

Figure S242 - Graph illustrating the ^{1}H NMR down-field change in chemical shift of thiourea NH resonances with increasing concentration of compound **46** in DMSO-d_6 0.5 % H_2O (298.15 K).

Self-association constant calculation

<u>Compound **46** - Dilution study in DMSO-d_6 0.5 % H_2O. Values calculated from data gathered from both NH 1 and 2.</u>

Equal K/Dimerisation model

K_e = 0.30 M^{-1} ± 4.2417 % K_{dim} = 0.15 M^{-1} ± 2.1208 %

http://app.supramolecular.org/bindfit/view/a78e4b05-98d6-4e0a-a472-36cb6e950e11

CoEK model

K_e = 1.86 M^{-1} ± 50.9685 % K_{dim} = 0.93 M^{-1} ± 25.4842 % ρ = 0.52 ± 66.2743 %

http://app.supramolecular.org/bindfit/view/20409611-869d-4a35-b403-8ce0c8ff9fe2

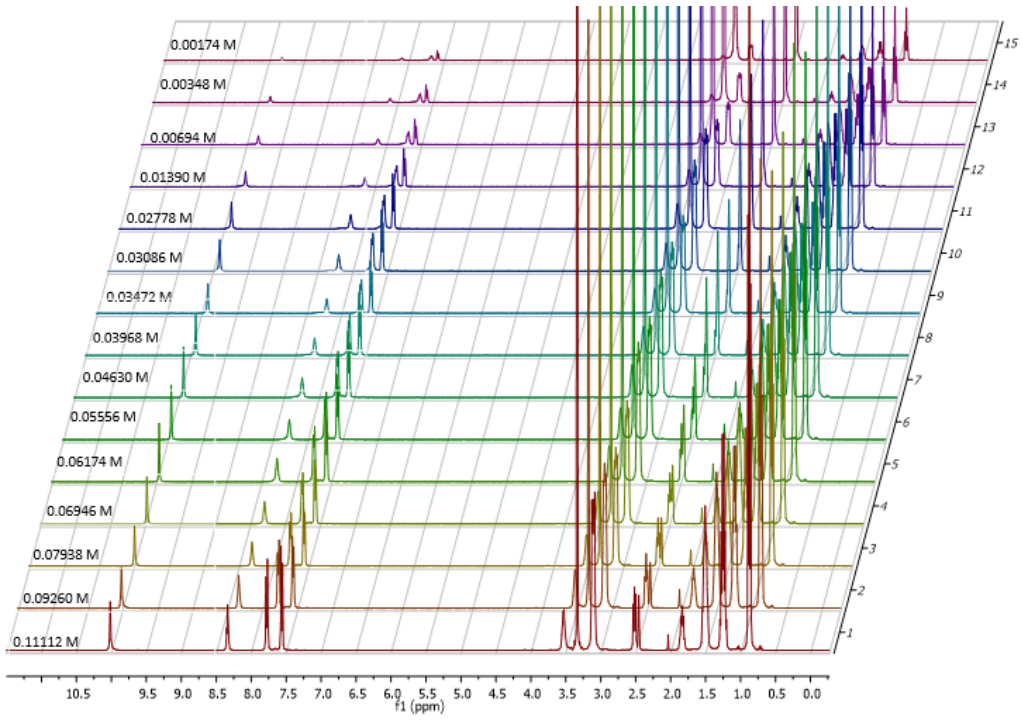

Figure S243 - ^{1}H NMR stack plot of compound **47** in DMSO-d_6 0.5 % H_2O. Samples were prepared in series with an aliquot of the most concentrated solution undergoing serial dilution.

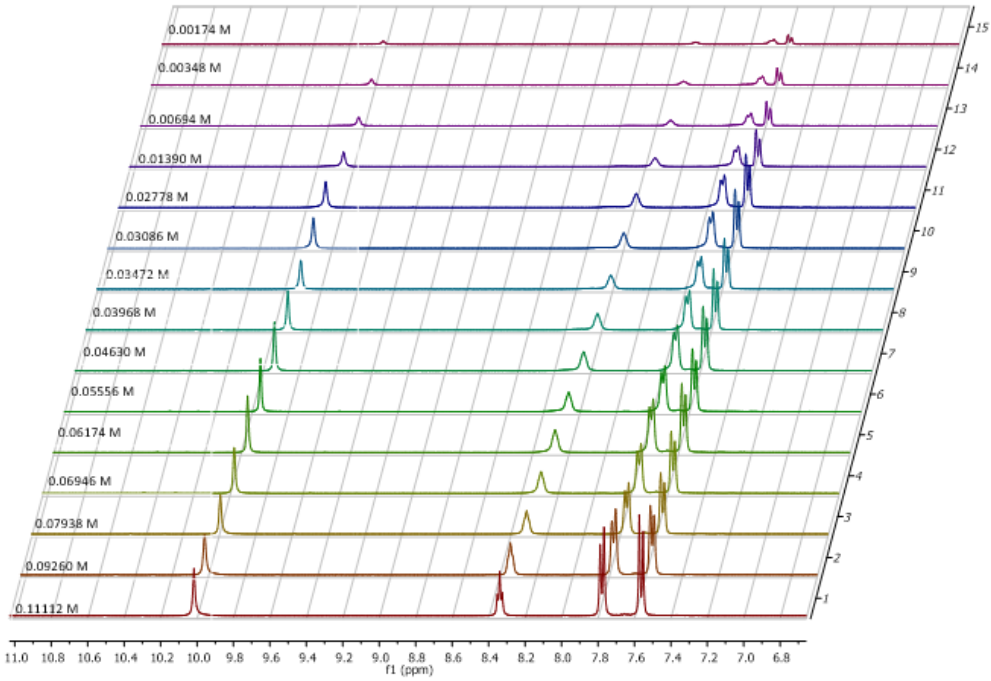

Figure S244 - Enlarged ^{1}H NMR stack plot of compound **47** in DMSO-d_6 0.5 % H_2O solution. Samples were prepared in series with an aliquot of the most concentrated solution undergoing serial dilution.

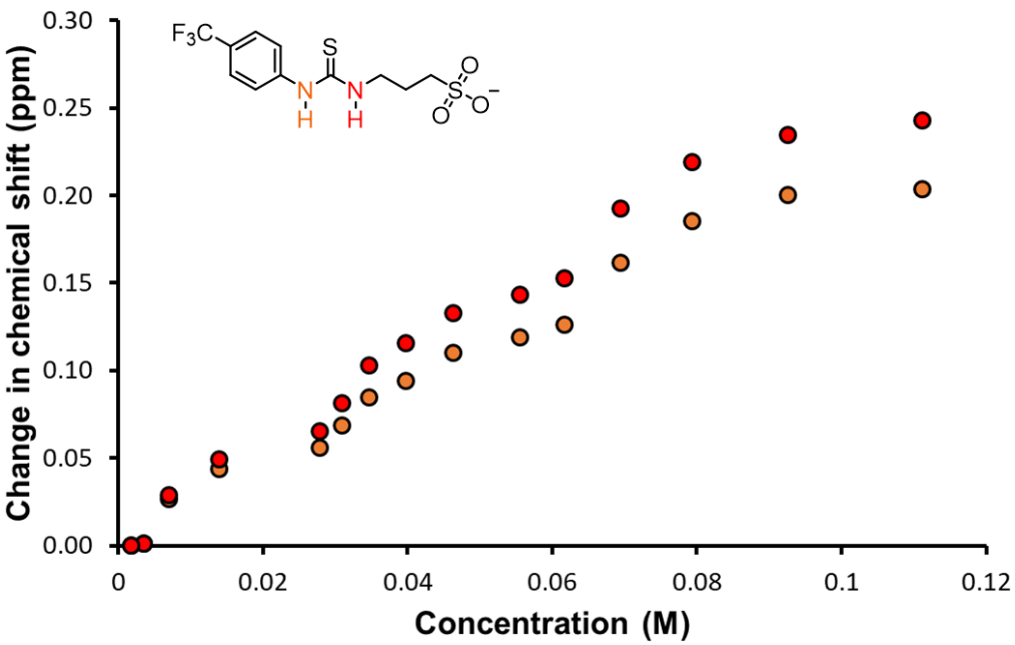

Figure S245 - Graph illustrating the ^{1}H NMR down-field change in chemical shift of thiourea NH resonances with increasing concentration of compound **47** in DMSO-d_6 0.5 % H_2O (298.15 K).

Self-association constant calculation

Compound **47** - Dilution study in DMSO-d_6 0.5 % H_2O. Values calculated from data gathered from both NH 1 and 2.

Equal K/Dimerisation model

K_e = 5.14 M^{-1} ± 2.1382 % K_{dim} = 2.57 M^{-1} ± 1.3691 %

http://app.supramolecular.org/bindfit/view/5ae5efa4-d195-4f17-ad13-dd563321d23b

CoEK model

K_e = 14.13 M^{-1} ± 4.3952 % K_{dim} = 7.07 M^{-1} ± 2.1976 % ρ = 0.44 ± 14.0401 %

http://app.supramolecular.org/bindfit/view/bef26f74-77ff-4256-bd56-7f4492ed5a9f

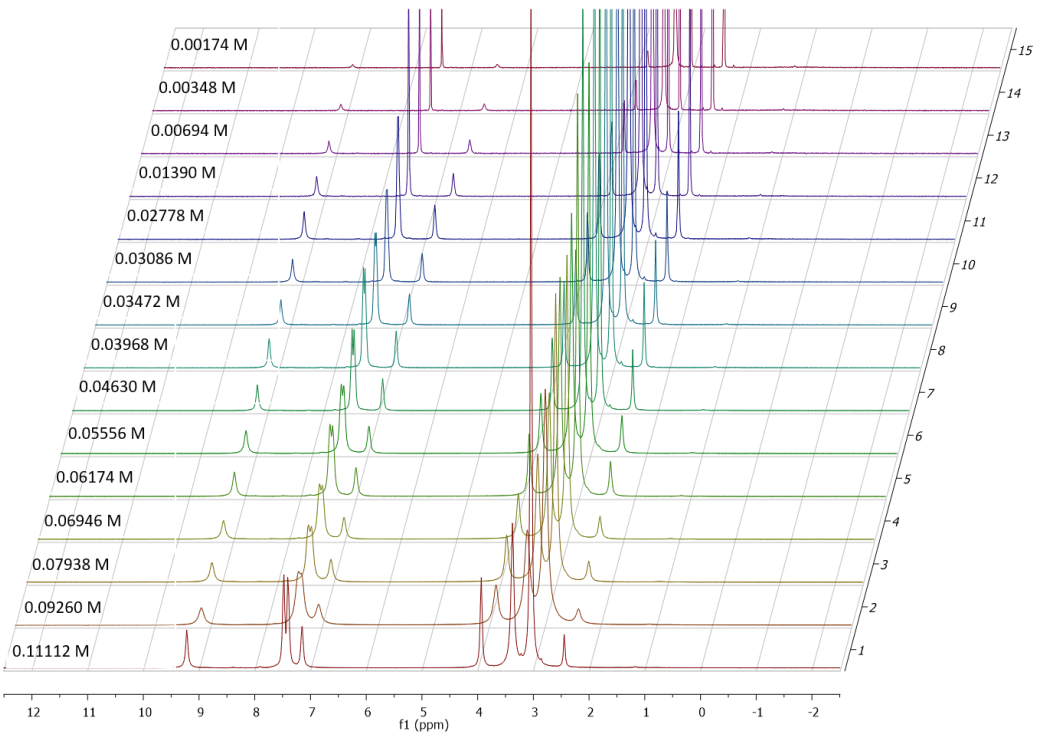

Figure S246 - ^{1}H NMR stack plot of compound **50** in DMSO-d_6 0.5 % H_2O solution. Samples were prepared in series with an aliquot of the most concentrated solution undergoing serial dilution.

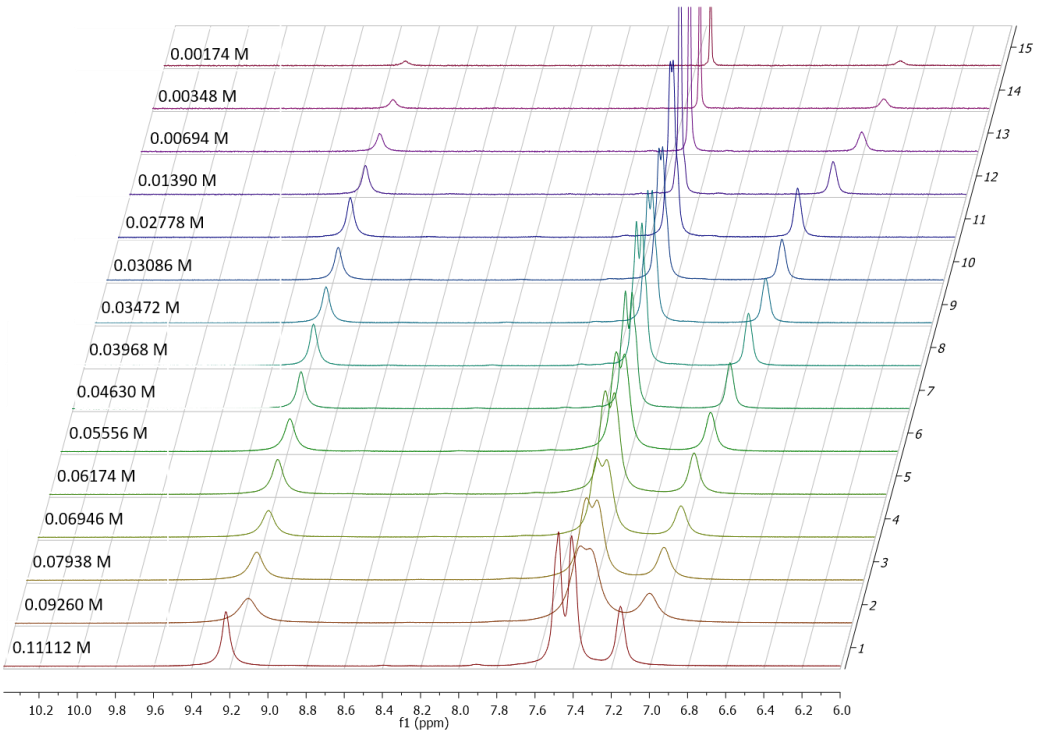

Figure S247 - Enlarged ^{1}H NMR stack plot of compound **50** in DMSO-d_6 0.5 % H_2O solution. Samples were prepared in series with an aliquot of the most concentrated solution undergoing serial dilution.

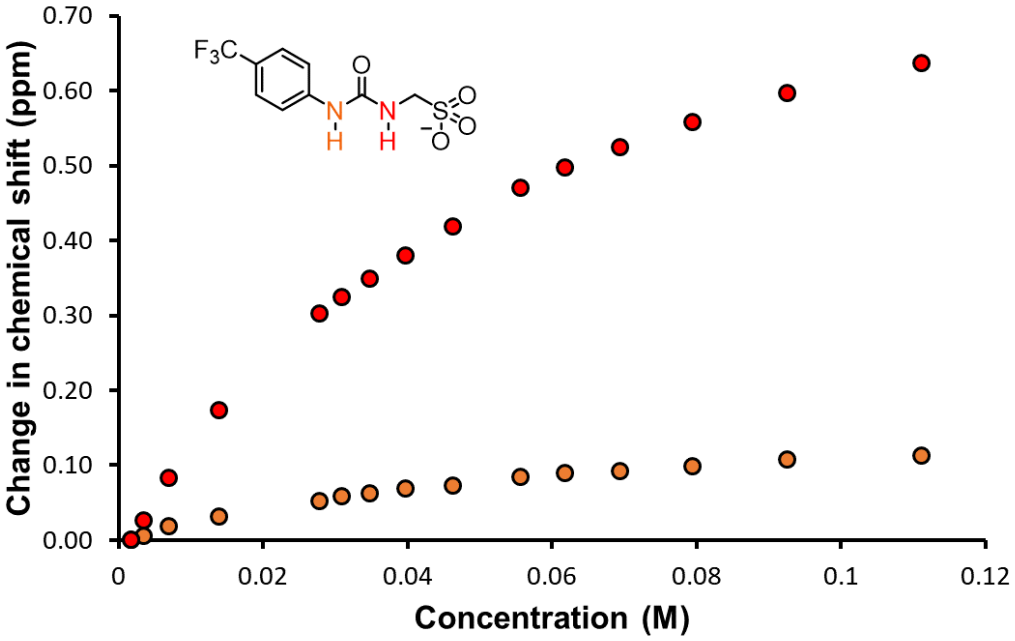

Figure S248 - Graph illustrating the ^{1}H NMR down-field change in chemical shift of urea NH resonances with increasing concentration of compound **50** in DMSO-d_6 0.5 % H_2O (298.15 K).

Self-association constant calculation

Compound **50** - Dilution study in DMSO-d_6 0.5 % H_2O. Values calculated from data gathered from both NH 1 and 2.

Equal K/Dimerisation model

K_e = 13.46 M^{-1} ± 0.6559 % K_{dim} = 6.73 M^{-1} ± 0.3280 %

http://app.supramolecular.org/bindfit/view/663e8a71-6640-464a-90de-6683e7305d91

CoEK model

K_e = 18.24 M^{-1} ± 1.0369 % K_{dim} = 9.12 M^{-1} ± 0.5184 % ρ = 0.75 ± 3.3727 %

http://app.supramolecular.org/bindfit/view/e52669a4-9408-4dd8-9dd3-182c5bec7de6

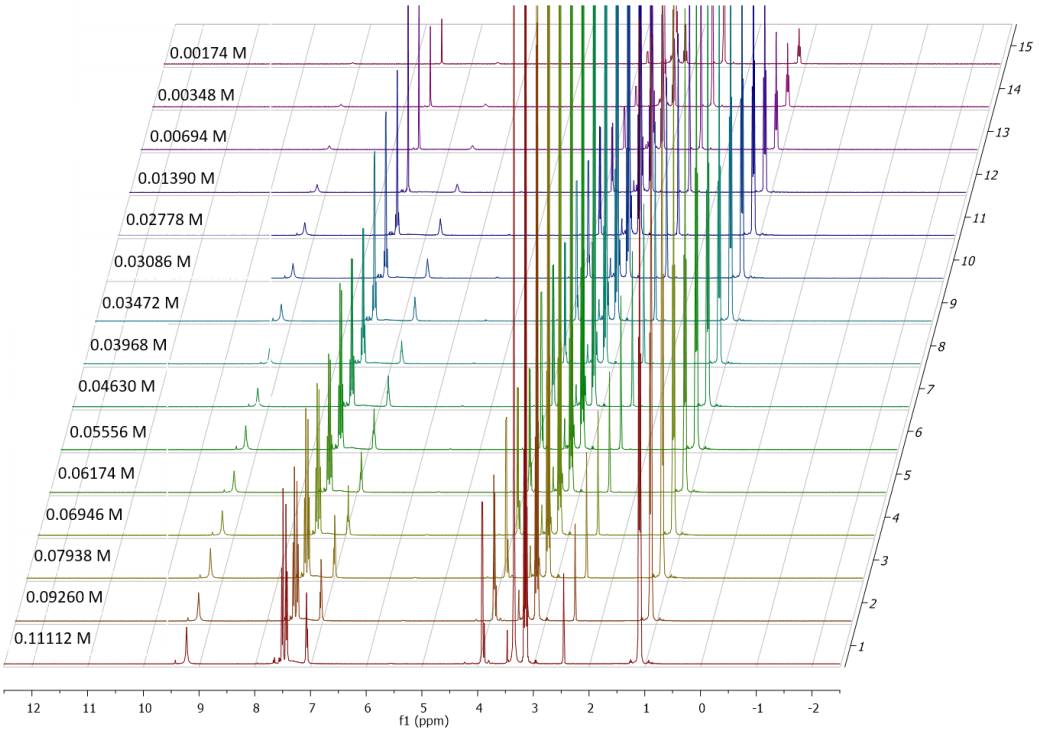

Figure S249 - ^{1}H NMR stack plot of compound **51** in DMSO-d_6 0.5 % H_2O solution. Samples were prepared in series with an aliquot of the most concentrated solution undergoing serial dilution.

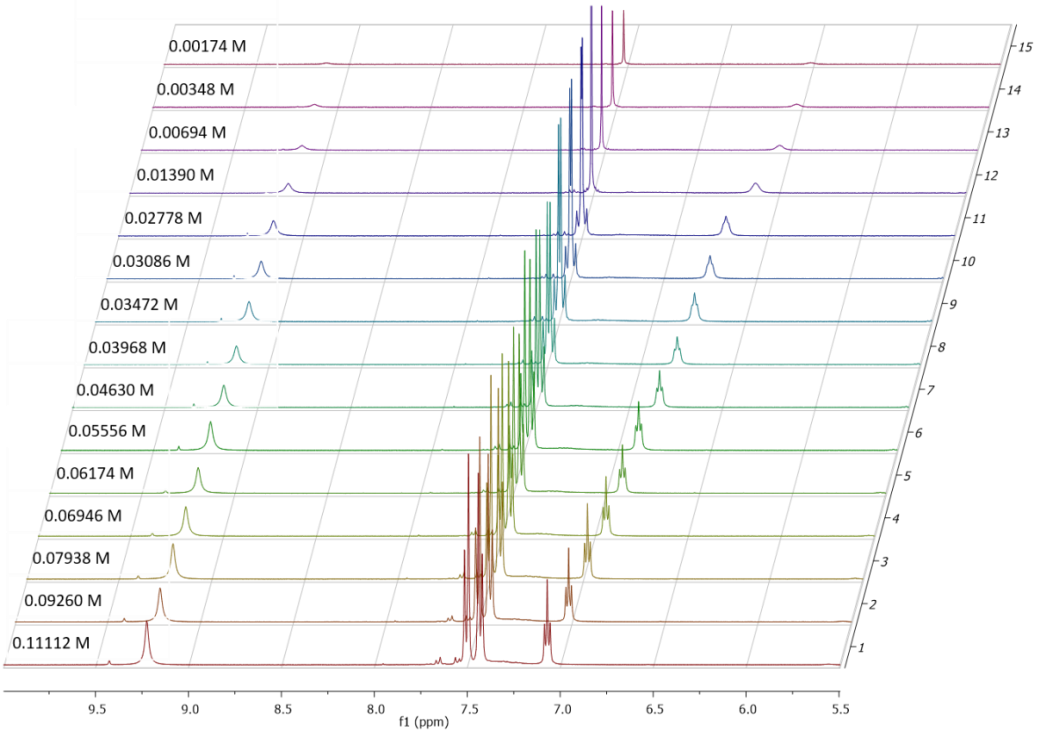

Figure S250 - Enlarged ^{1}H NMR stack plot of compound **51** in DMSO-d_6 0.5 % H_2O solution. Samples were prepared in series with an aliquot of the most concentrated solution undergoing serial dilution.

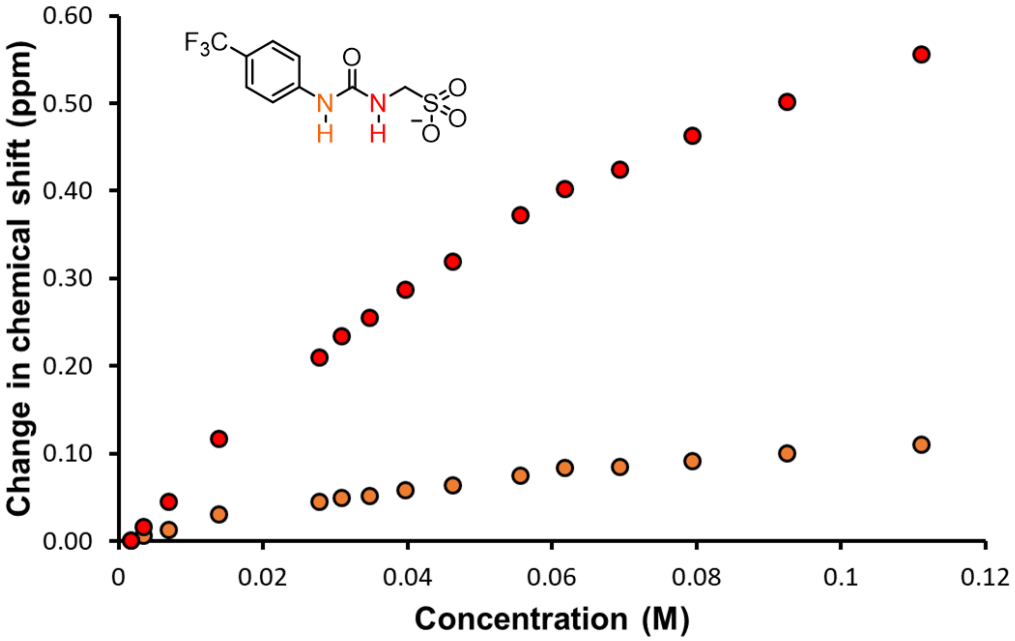

Figure S251 - Graph illustrating the ^{1}H NMR down-field change in chemical shift of urea NH resonances with increasing concentration of compound **51** in DMSO-d_6 0.5 % H_2O (298.15 K).

Self-association constant calculation

Compound **51** - Dilution study in DMSO-d_6 0.5 % H_2O. Values calculated from data gathered from both NH 1 and 2.

Equal K/Dimerisation model

K_e = 6.33 M^{-1} ± 0.8868 % K_{dim} = 3.16 M^{-1} ± 0.4434 %

http://app.supramolecular.org/bindfit/view/803ae004-5fd7-441f-b193-a904f7934214

CoEK model

K_e = 12.02 M^{-1} ± 2.0491 % K_{dim} = 6.01 M^{-1} ± 1.0246 % ρ = 0.61 ± 5.5007 %

http://app.supramolecular.org/bindfit/view/3c74e0d7-8d08-4c52-ab97-3f329b57c46a

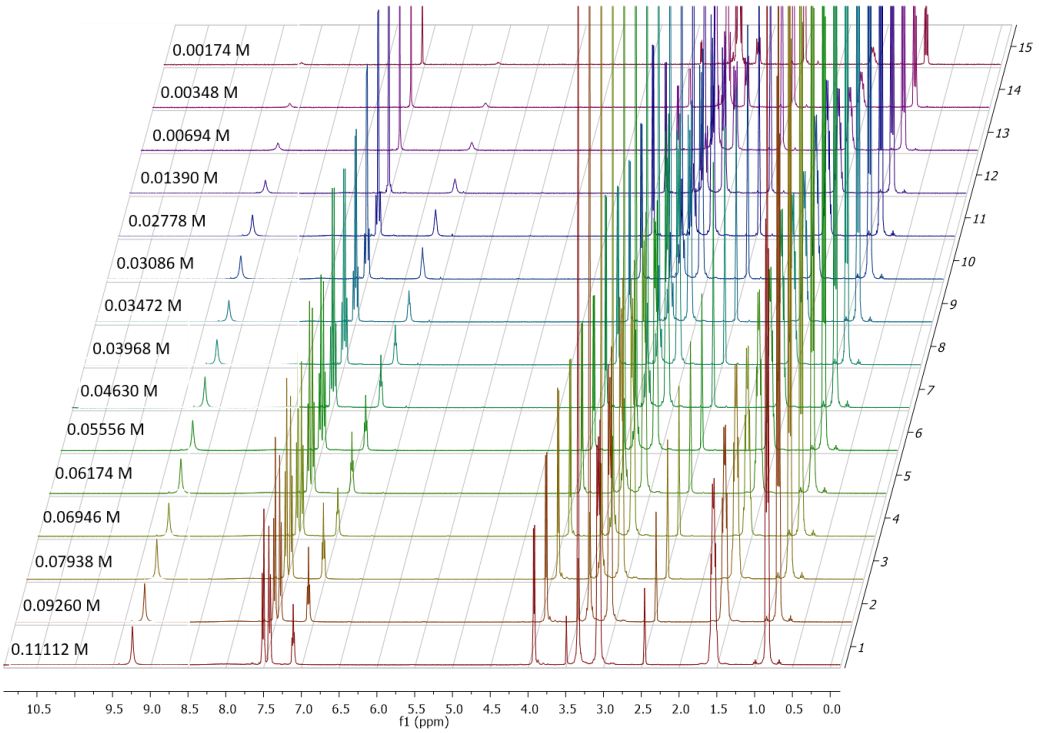

Figure S252 - ^{1}H NMR stack plot of compound **52** in DMSO-d_6 0.5 % H_2O solution. Samples were prepared in series with an aliquot of the most concentrated solution undergoing serial dilution.

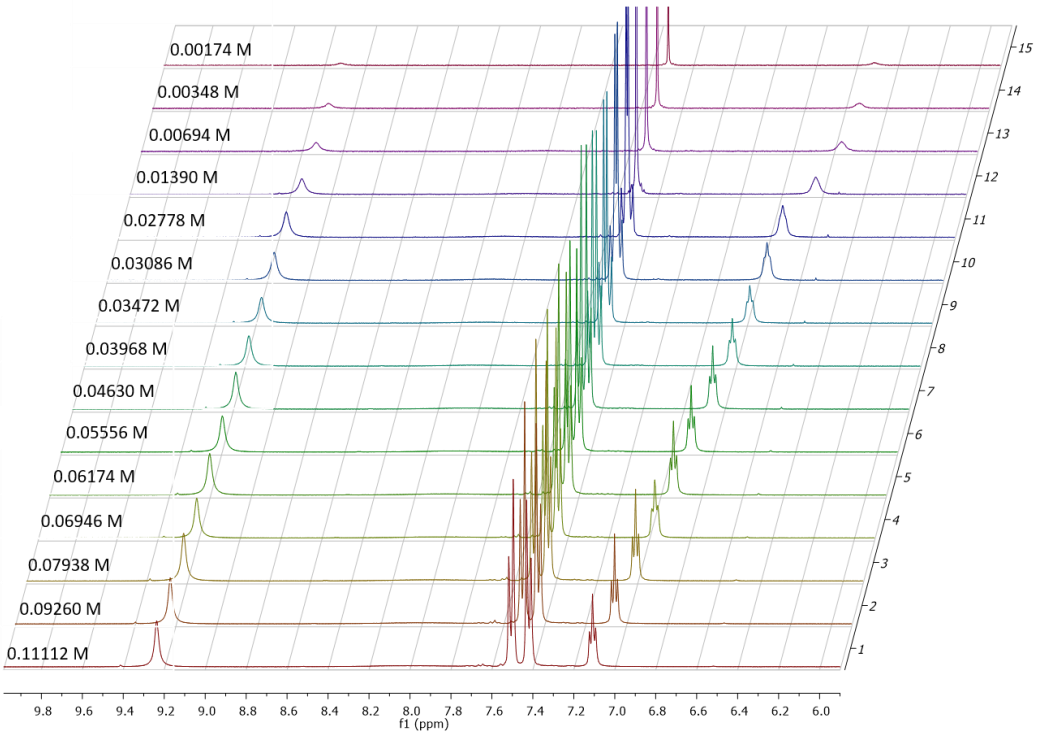

Figure S253 - Enlarged ^{1}H NMR stack plot of compound **52** in DMSO-d_6 0.5 % H_2O solution. Samples were prepared in series with an aliquot of the most concentrated solution undergoing serial dilution.

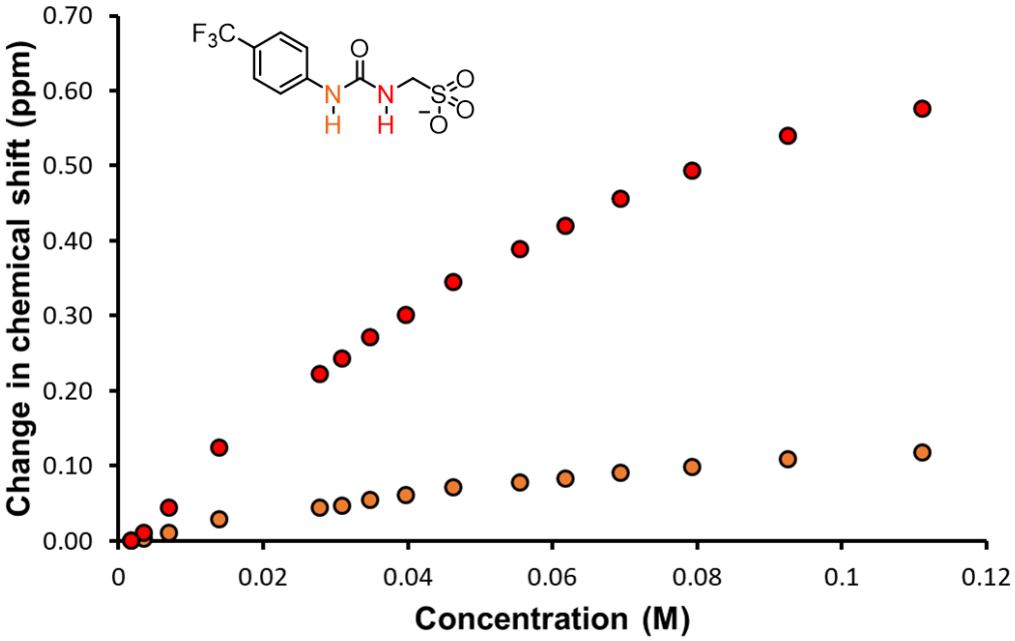

Figure S254 - Graph illustrating the ^{1}H NMR down-field change in chemical shift of urea NH resonances with increasing concentration of compound **52** in DMSO-d_6 0.5 % H_2O (298.15 K).

Self-association constant calculation

Compound **52** - Dilution study in DMSO-d_6 0.5 % H_2O. Values calculated from data gathered from both NH 1 and 2.

Equal K/Dimerisation model

K_e = 6.58 M^{-1} ± 1.1817 % K_{dim} = 3.29 M^{-1} ± 0.5908 %

http://app.supramolecular.org/bindfit/view/39722541-1459-456f-a641-186f57d3eacd

CoEK model

K_e = 14.94 M^{-1} ± 2.1054 % K_{dim} = 7.47 M^{-1} ± 8.1683 % ρ = 0.50 ± 6.7425 %

http://app.supramolecular.org/bindfit/view/c6b1dbf0-cde9-4293-8f15-10c6c2a3cf4e

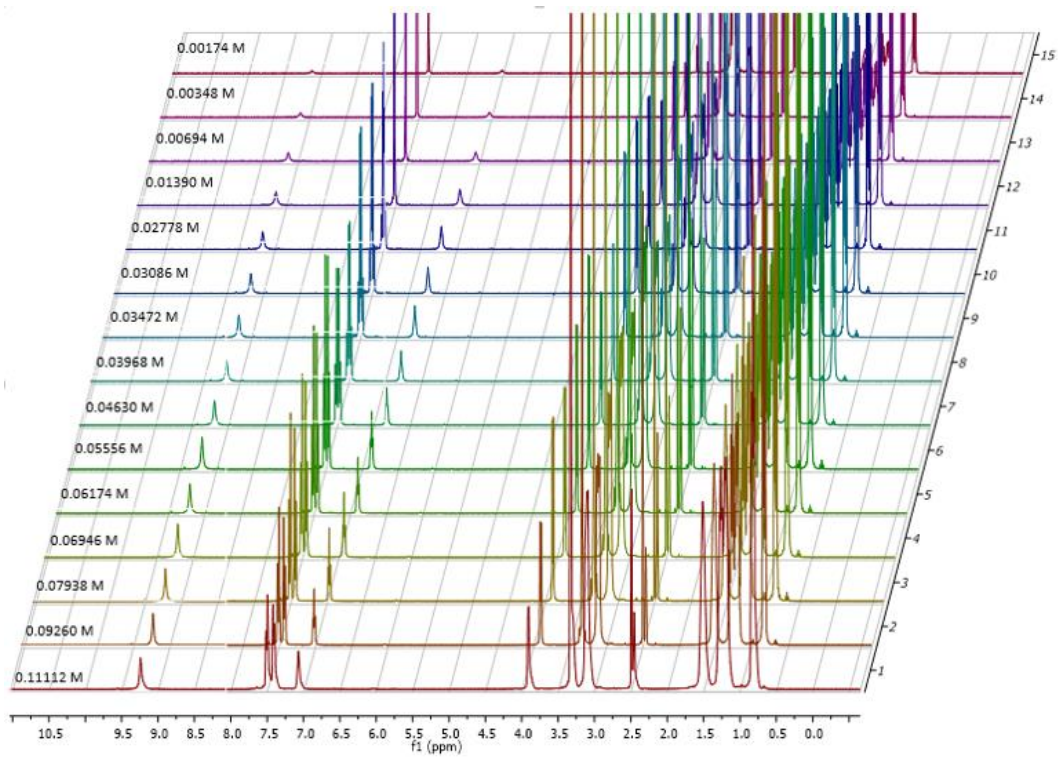

Figure S255 - ^{1}H NMR stack plot of compound **53** in DMSO-d_6 0.5 % H_2O solution. Samples were prepared in series with an aliquot of the most concentrated solution undergoing serial dilution.

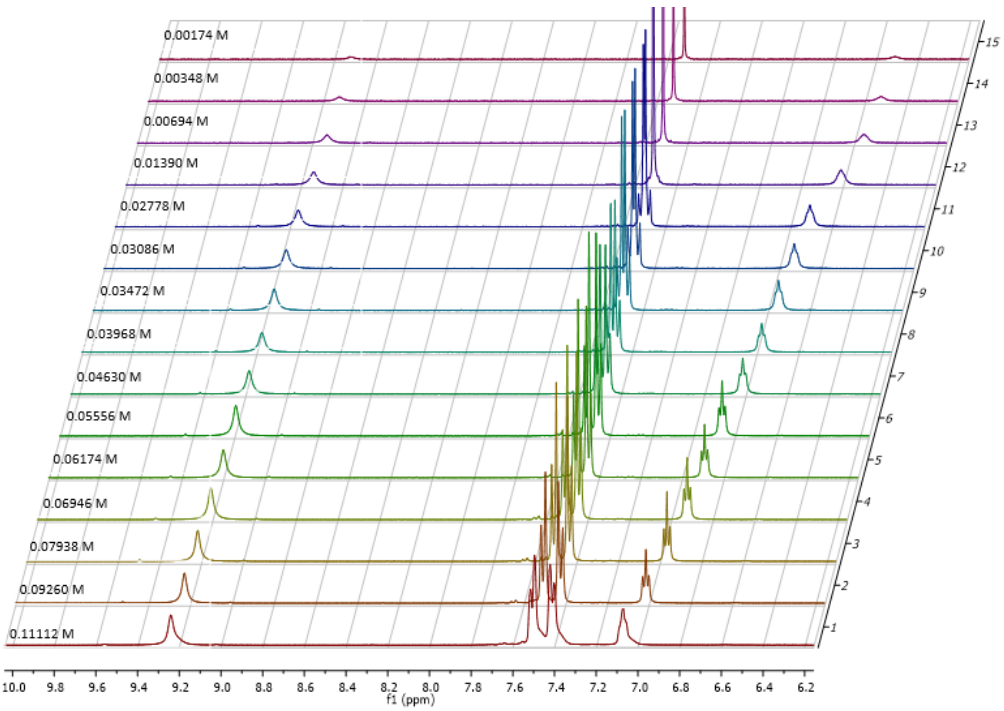

Figure S256 - Enlarged ^{1}H NMR stack plot of compound **53** in DMSO-d_6 0.5 % H_2O solution. Samples were prepared in series with an aliquot of the most concentrated solution undergoing serial dilution.

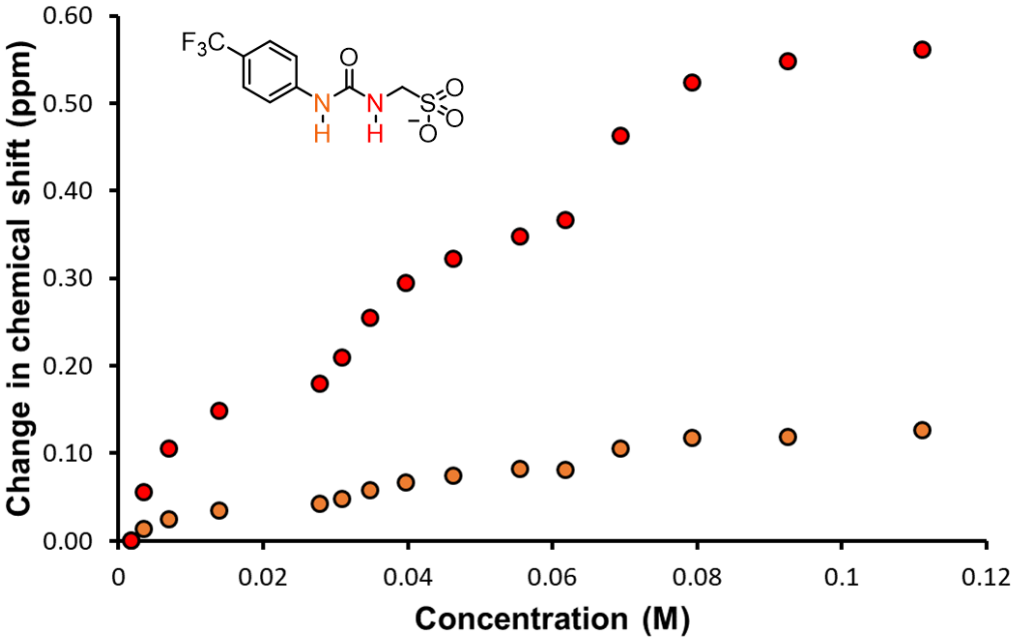

Figure S257 - Graph illustrating the ^{1}H NMR down-field change in chemical shift of urea NH resonances with increasing concentration of compound **53** in DMSO-d_6 0.5 % H_2O (298.15 K).

Self-association constant calculation

Compound **53** - Dilution study in DMSO-d_6 0.5 % H_2O. Values calculated from data gathered from both NH 1 and 2.

Equal K/Dimerisation model

K_e = 4.11 M^{-1} ± 0.5004 % K_{dim} = 2.05 M^{-1} ± 0.2502 %

http://app.supramolecular.org/bindfit/view/30b20e66-3dc5-4558-a3cc-3c701883387e

CoEK model

K_e = 8.84 M^{-1} ± 1.3367 % K_{dim} = 4.42 M^{-1} ± 0.6684 % ρ = 0.60 ± 3.0443 %

http://app.supramolecular.org/bindfit/view/e991d3e2-20cc-4ba4-80ed-afaacef703b5

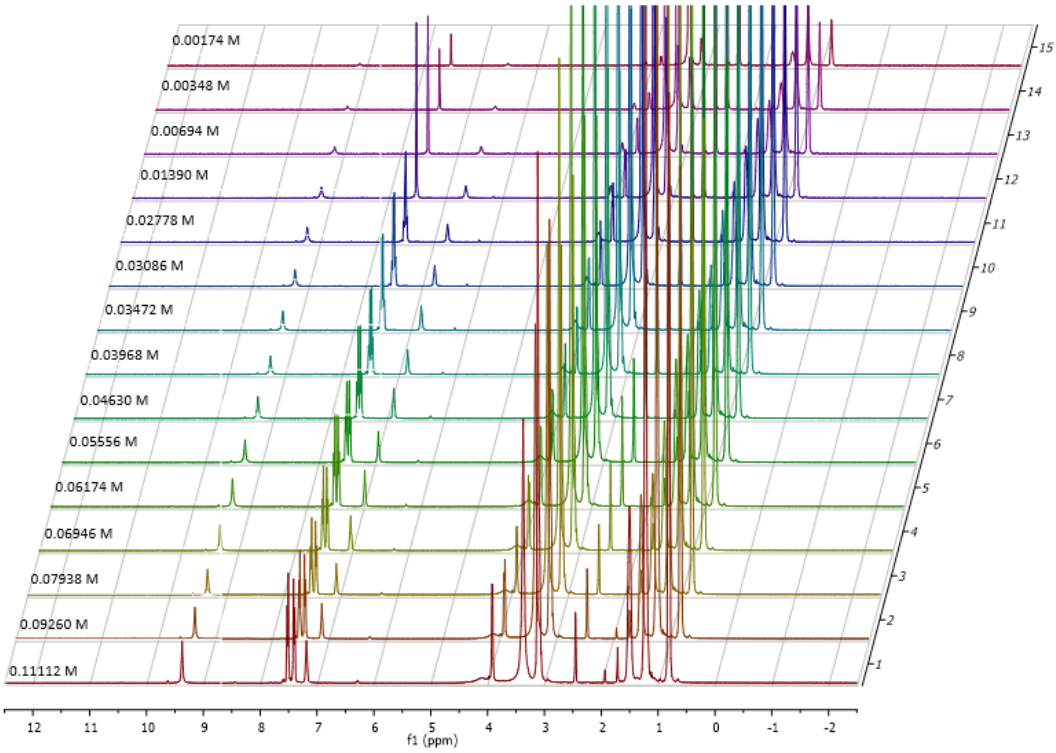

Figure S258 - ^{1}H NMR stack plot of compound **54** in DMSO-d_6 0.5 % H_2O solution. Samples were prepared in series with an aliquot of the most concentrated solution undergoing serial dilution.

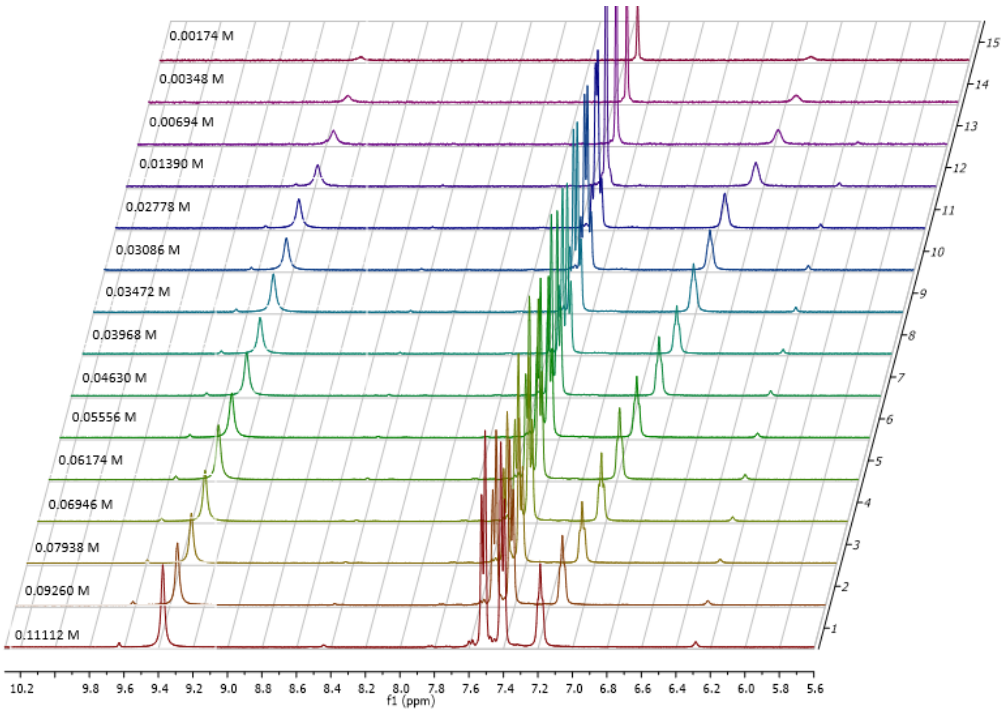

Figure S259 - Enlarged ^{1}H NMR stack plot of compound **54** in DMSO-d_6 0.5 % H_2O solution. Samples were prepared in series with an aliquot of the most concentrated solution undergoing serial dilution.

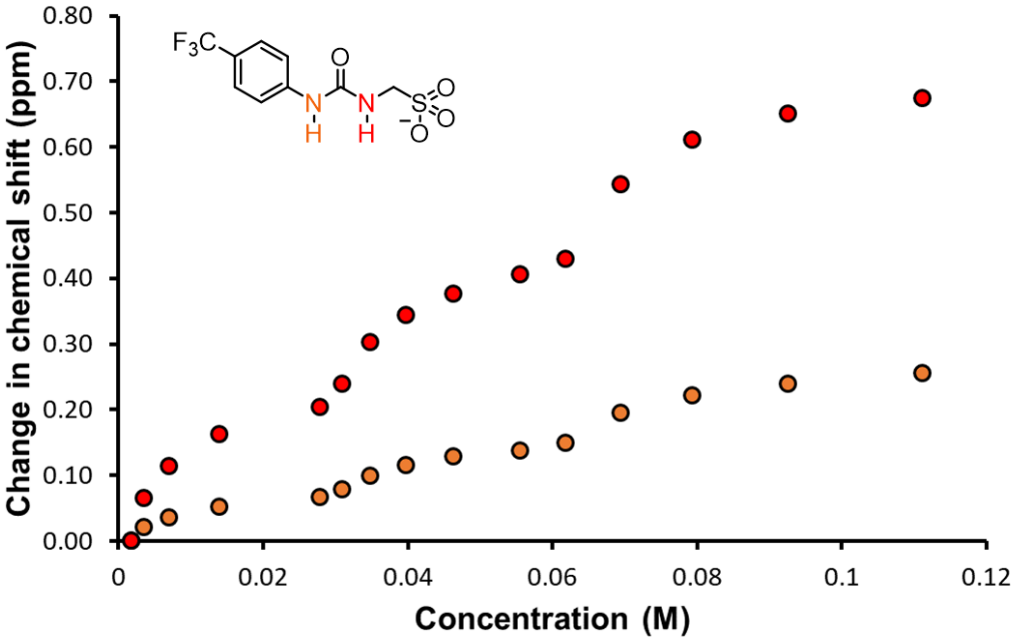

Figure S260 - Graph illustrating the ^{1}H NMR down-field change in chemical shift of urea NH resonances with increasing concentration of compound **54** in DMSO-d_6 0.5 % H_2O (298.15 K).

Self-association constant calculation

Compound **54** - Dilution study in DMSO-d_6 0.5 % H_2O. Values calculated from data gathered from both NH 1 and 2.

Equal K/Dimerisation model

K_e = 5.03 M^{-1} ± 0.9186 % K_{dim} = 2.51 M^{-1} ± 0.4582 %

http://app.supramolecular.org/bindfit/view/4c947200-18e8-44e1-abf1-de45cecd25df

CoEK model

K_e = 9.60 M^{-1} ± 2.6644 % K_{dim} = 4.80 M^{-1} ± 1.3322 % ρ = 0.9 ± 6.2664 %

http://app.supramolecular.org/bindfit/view/4e1c358a-1031-411f-983d-90287bd92e70

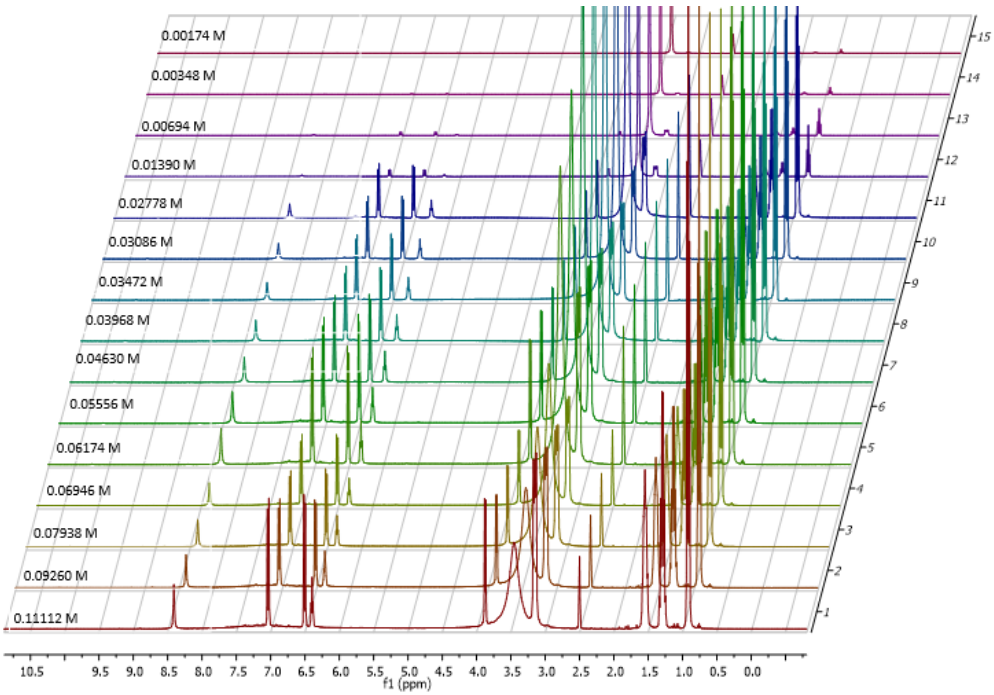

Figure S261 - ^{1}H NMR stack plot of compound **55** in DMSO-d_6 0.5 % H_2O solution. Samples were prepared in series with an aliquot of the most concentrated solution undergoing serial dilution.

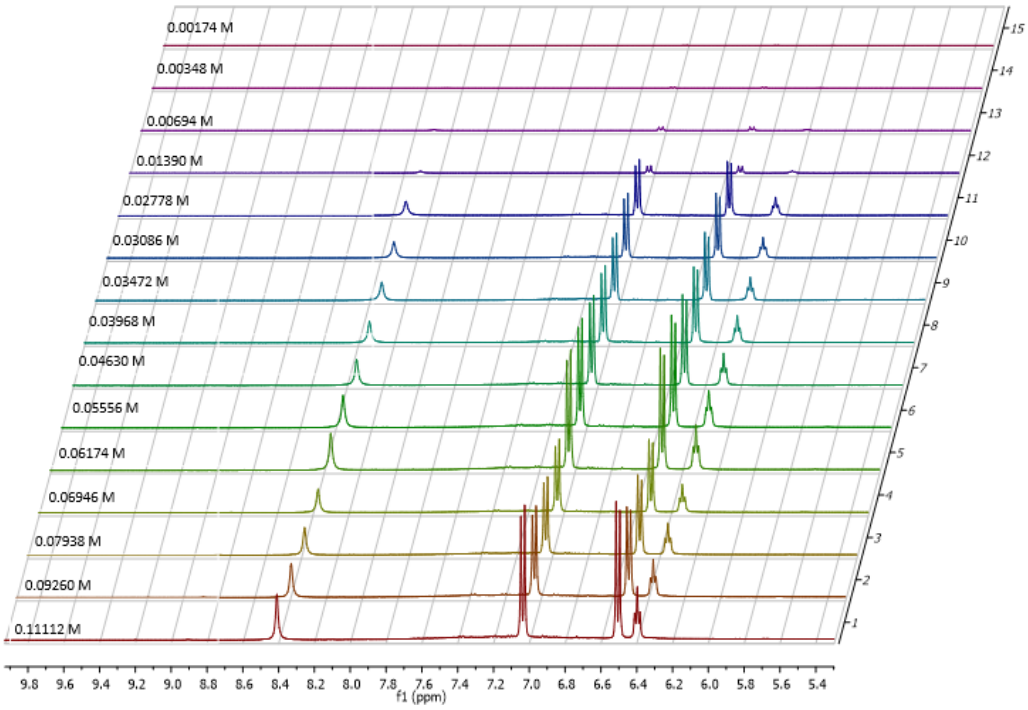

Figure S262 - Enlarged ^{1}H NMR stack plot of compound **55** in DMSO-d_6 0.5 % H_2O solution. Samples were prepared in series with an aliquot of the most concentrated solution undergoing serial dilution.

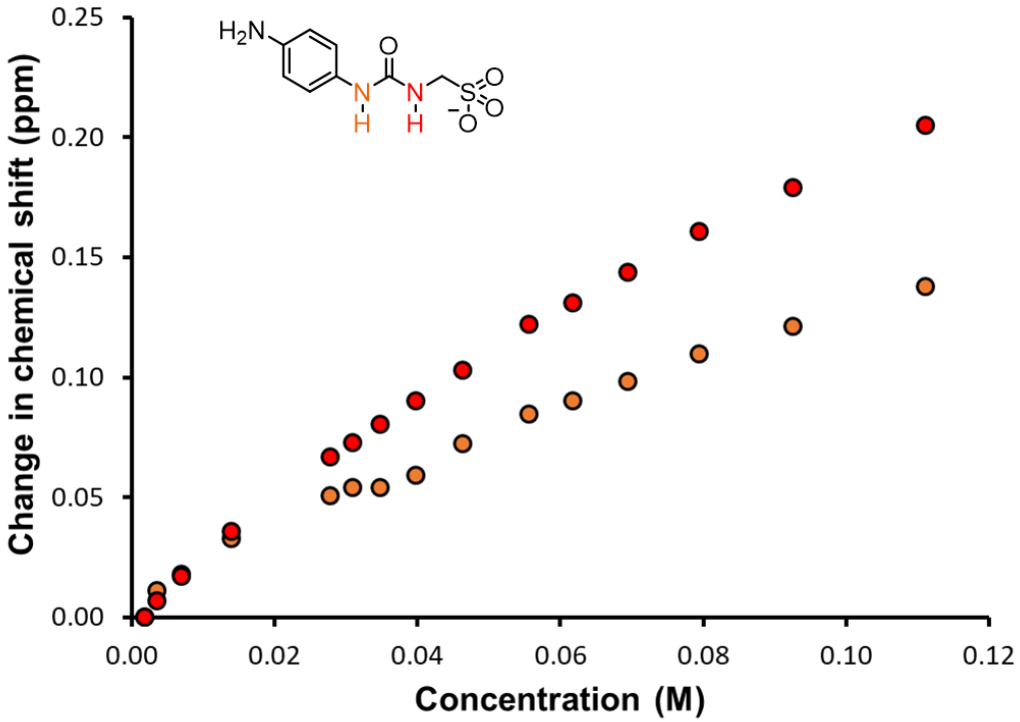

Figure S263 - Graph illustrating the ^{1}H NMR down-field change in chemical shift of urea NH resonances with increasing concentration of compound **55** in DMSO-d_6 0.5 % H_2O (298.15 K).

Self-association constant calculation

Compound **55** - Dilution study in DMSO-d_6 0.5 % H_2O. Values calculated combining the data gathered from both NH 1 and 2.

Equal K/Dimerisation model

K_e = 3.62 M^{-1} ± 1.4514 % K_{dim} = 1.81 M^{-1} ± 0.7257 %

http://app.supramolecular.org/bindfit/view/fbf5eb94-aa6f-4cbc-8ecf-cb89db0283dc

CoEK model

K_e = 4.59 M^{-1} ± 8.2825 % K_{dim} = 2.30 M^{-1} ± 4.1412 % ρ = 0.86 ± 13.4410 %

http://app.supramolecular.org/bindfit/view/6e3dc7a1-4d48-4c5c-9fe3-680fca65e123

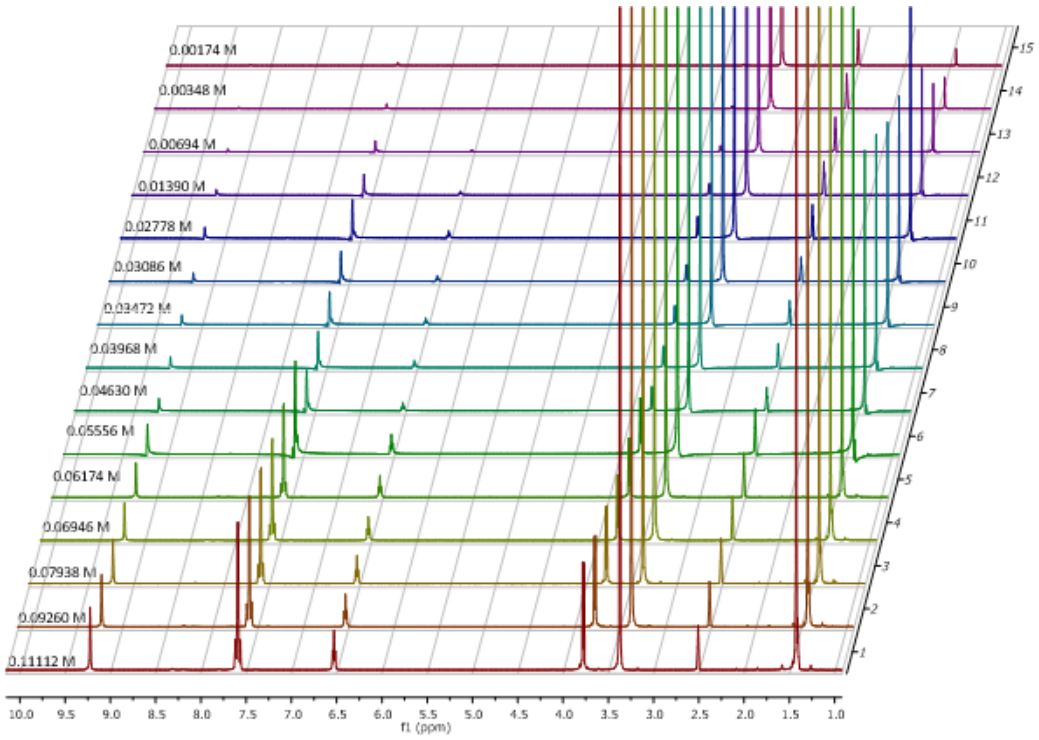

Figure S264 - ^{1}H NMR stack plot of compound **63** in DMSO-d_6 0.5 % H_2O. Samples were prepared in series with an aliquot of the most concentrated solution undergoing serial dilution.

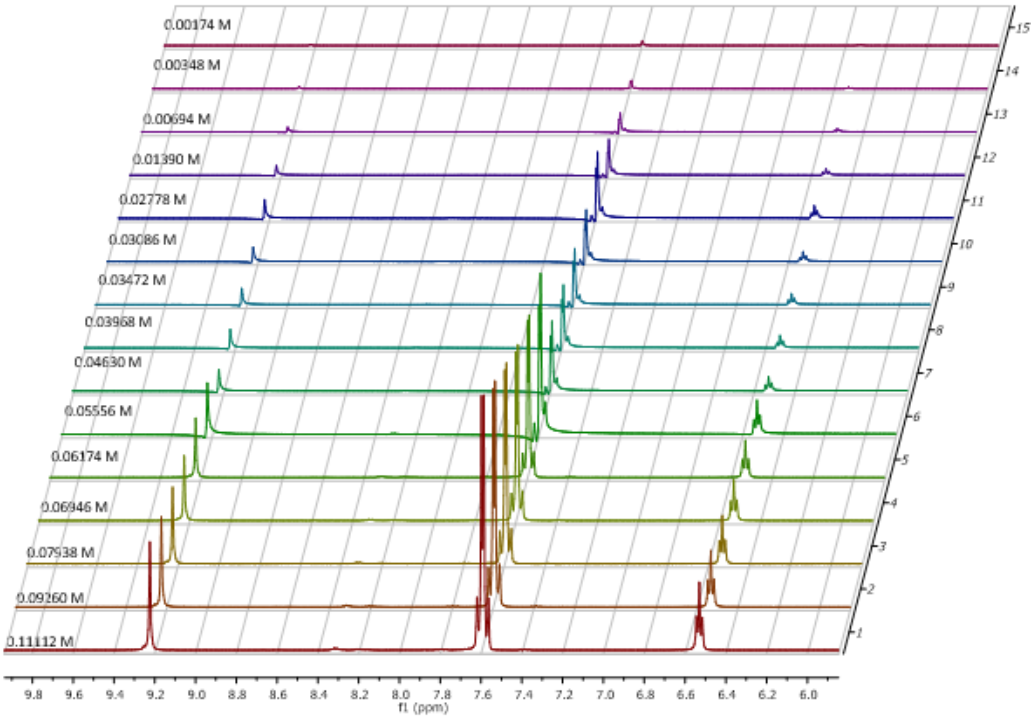

Figure S265 - Enlarged ^{1}H NMR stack plot of compound **63** in DMSO-d_6 0.5 % H_2O solution. Samples were prepared in series with an aliquot of the most concentrated solution undergoing serial dilution.

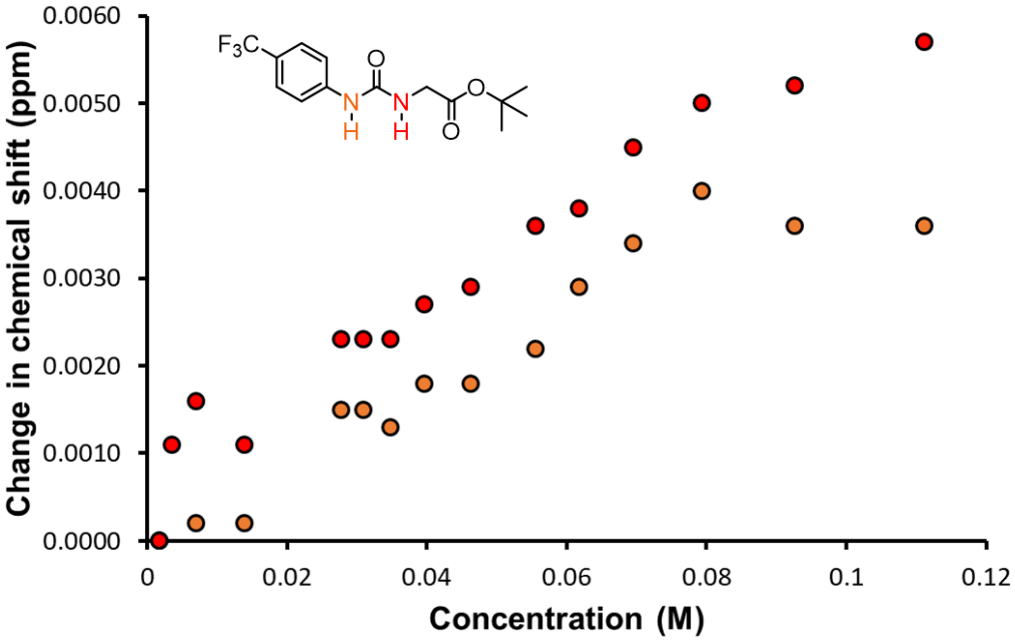

Figure S266 - Graph illustrating no ^{1}H NMR down-field change in chemical shift of urea NH resonances with increasing concentration of compound **63** in DMSO-d_6 0.5 % H_2O (298.15 K).

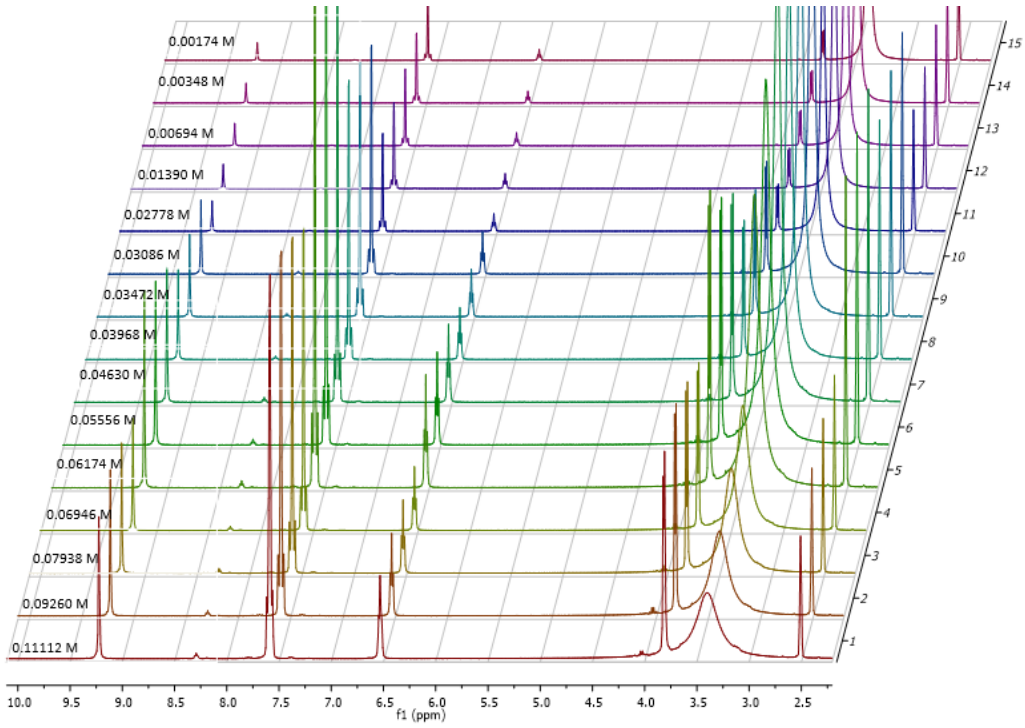

Figure S267 - ^{1}H NMR stack plot of compound **64** in DMSO-d_6 0.5 % H_2O. Samples were prepared in series with an aliquot of the most concentrated solution undergoing serial dilution.

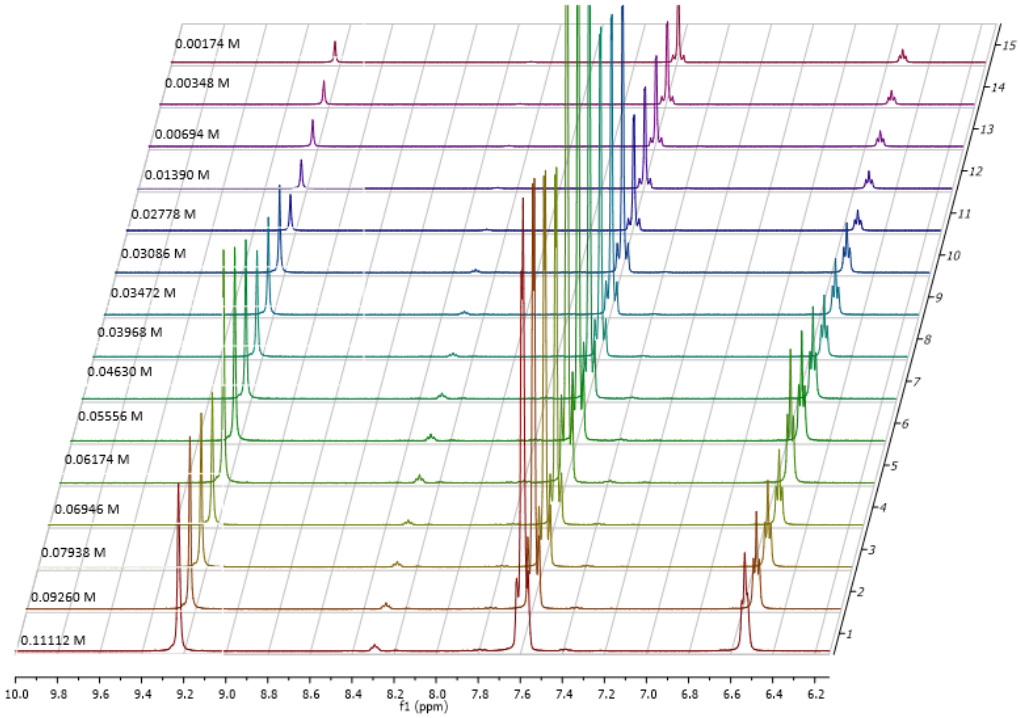

Figure S268 - Enlarged ^{1}H NMR stack plot of compound **64** in DMSO-d_6 0.5 % H_2O solution. Samples were prepared in series with an aliquot of the most concentrated solution undergoing serial dilution.

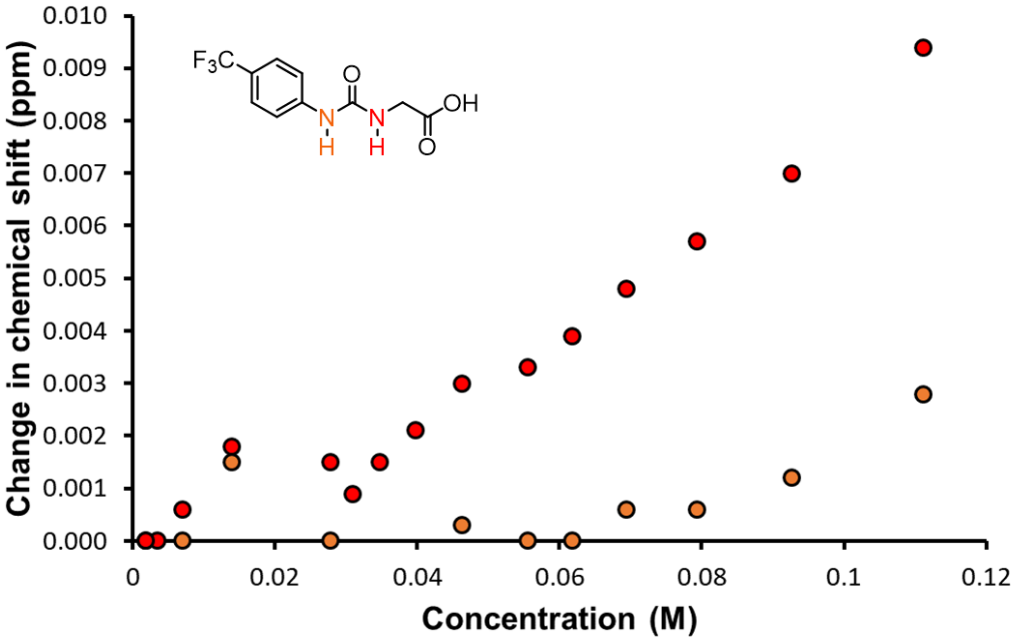

Figure S269 - Graph illustrating the ^{1}H NMR down-field change in chemical shift of urea NH resonances with increasing concentration of compound **64** in DMSO-d_6 0.5 % H_2O (298.15 K).

Self-association constant calculation

Compound **64** - Dilution study in DMSO-d_6 0.5 % H_2O. Values calculated from data gathered from both NH 1 and 2.

Equal K/Dimerisation model

K_e = 5.62e-4 M^{-1} ± 1.2078e-4 % K_{dim} = 2.81e-4 M^{-1} ± 6.0389e-5 %

http://app.supramolecular.org/bindfit/view/8ee9bf55-7b9e-4dec-ae15-609fb8ebf9a3

CoEK model

K_e = 7.12 M^{-1} ± 18.3708 % K_{dim} = 3.56 M^{-1} ± 9.1854 % ρ = 0.07 ± 58.3987 %

http://app.supramolecular.org/bindfit/view/de79dbdc-bb5d-4152-881e-1daead5698c7

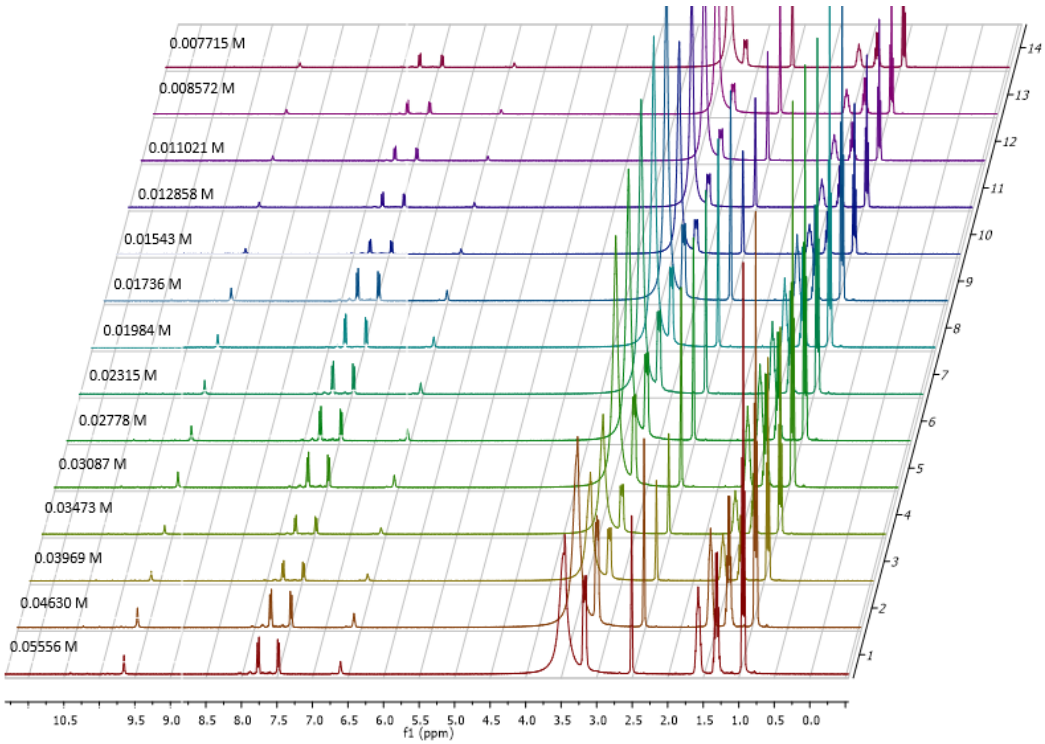

Figure S270 - ^{1}H NMR stack plot of compound **65** in DMSO-d_6 0.5 % H_2O. Samples were prepared in series with an aliquot of the most concentrated solution undergoing serial dilution.

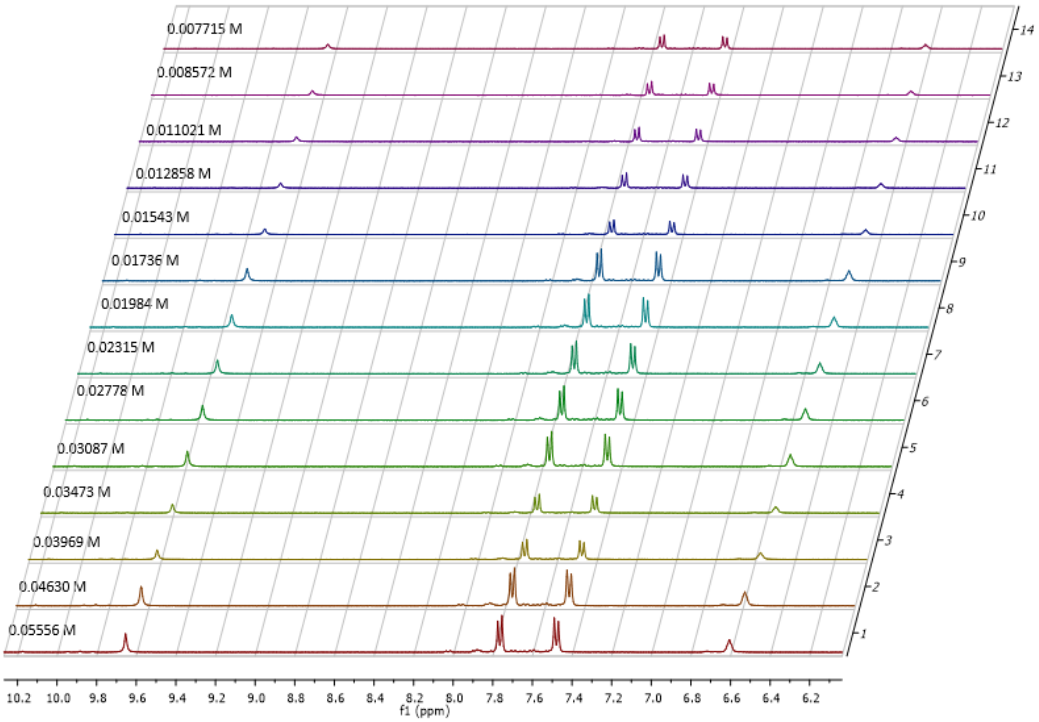

Figure S271 - Enlarged ^{1}H NMR stack plot of compound **65** in DMSO-d_6 0.5 % H_2O solution. Samples were prepared in series with an aliquot of the most concentrated solution undergoing serial dilution.

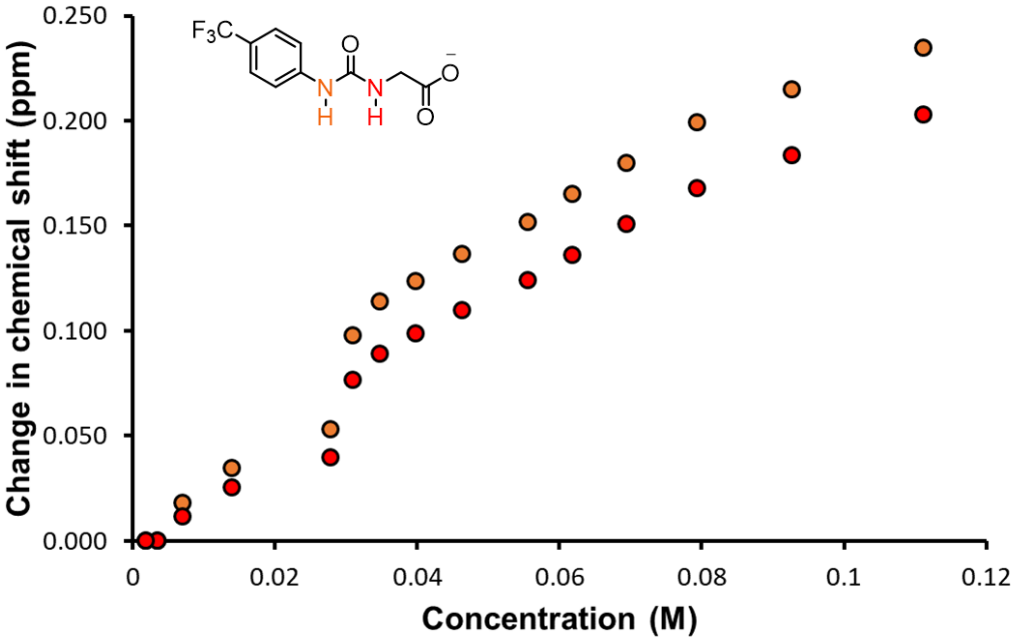

Figure S272 - Graph illustrating the ^{1}H NMR down-field change in chemical shift of urea NH resonances with increasing concentration of compound **65** in DMSO-d_6 0.5 % H_2O (298.15 K).

Self-association constant calculation

Compound **65** - Dilution study in DMSO-d_6 0.5 % H_2O. Values calculated from data gathered from both NH 1 and 2.

Equal K/Dimerisation model

K_e = 82.78 M^{-1} ± 2.5313 % K_{dim} = 41.39 M^{-1} ± 1.2657 %

http://app.supramolecular.org/bindfit/view/2bb99c66-416f-49c8-8a5e-4cbaa0d76147

CoEK model

K_e = 101.81 M^{-1} ± 2.5572 % K_{dim} = 50.90 M^{-1} ± 1.2786 % ρ = 2.57 ± 11.5817 %

http://app.supramolecular.org/bindfit/view/9e0a4b28-c4ff-4c8d-ba68-b0fbac3cde8f

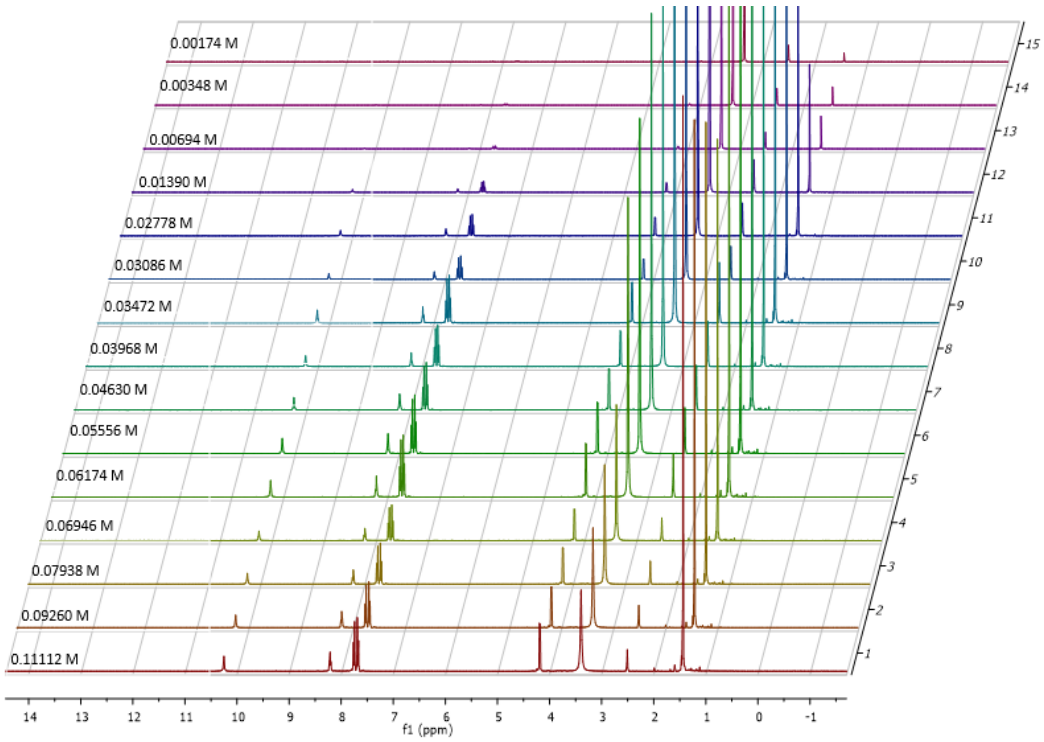

Figure S273 - ^{1}H NMR stack plot of compound **66** in DMSO-d_6 0.5 % H_2O. Samples were prepared in series with an aliquot of the most concentrated solution undergoing serial dilution.

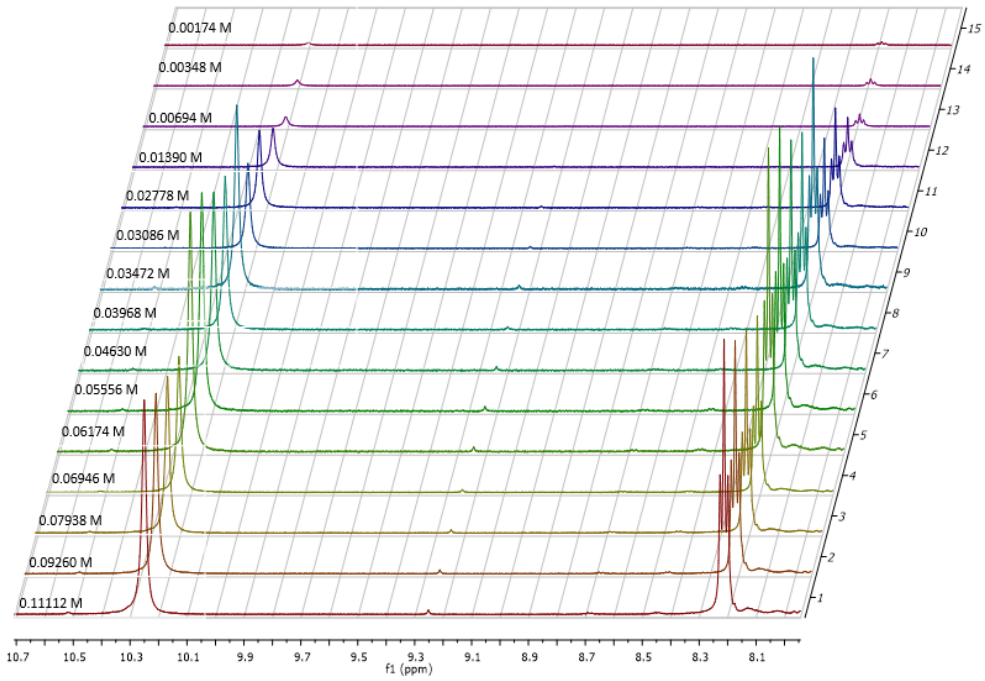

Figure S274 - Enlarged ^{1}H NMR stack plot of compound **66** in DMSO-d_6 0.5 % H_2O solution. Samples were prepared in series with an aliquot of the most concentrated solution undergoing serial dilution.

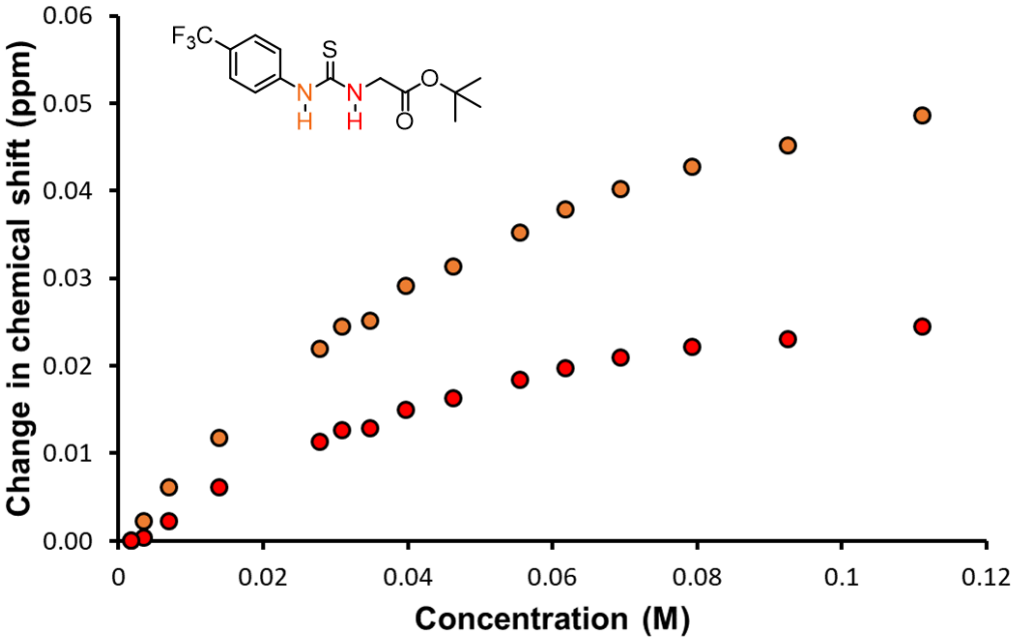

Figure S275 - Graph illustrating the ^{1}H NMR down-field change in chemical shift of thiourea NH resonances with increasing concentration of compound **66** in DMSO-d_6 0.5 % H_2O (298.15 K).

Self-association constant calculation

Compound **66** - Dilution study in DMSO-d_6 0.5 % H_2O. Values calculated from data gathered from both NH 1 and 2.

Equal K/Dimerisation model

K_e = 11.90 M^{-1} ± 1.5194 % K_{dim} = 5.95 M^{-1} ± 0.7597 %

http://app.supramolecular.org/bindfit/view/53cc2518-deff-4532-9e18-67f9bd0c59e8

CoEK model

K_e = 23.75 M^{-1} ± 1.7369 % K_{dim} = 11.87 M^{-1} ± 0.8685 % ρ = 0.46 ± 7.5306 %

http://app.supramolecular.org/bindfit/view/a49ba9f9-8815-4849-93a7-2841a2575f51

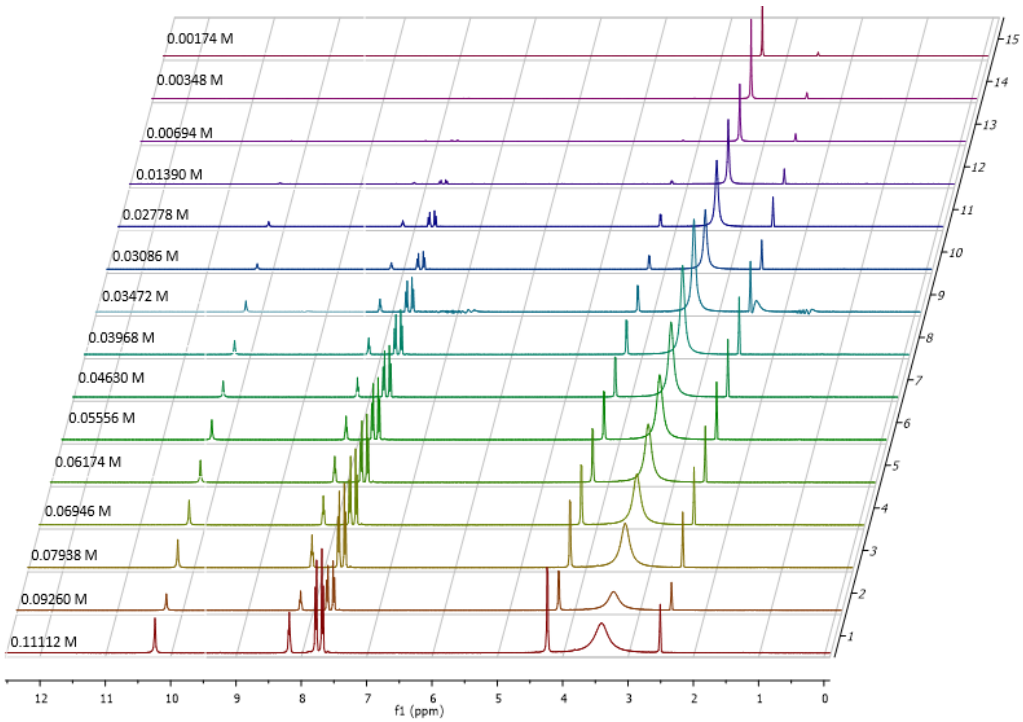

Figure S276 - ^{1}H NMR stack plot of compound **67** in DMSO-d_6 0.5 % H_2O. Samples were prepared in series with an aliquot of the most concentrated solution undergoing serial dilution.

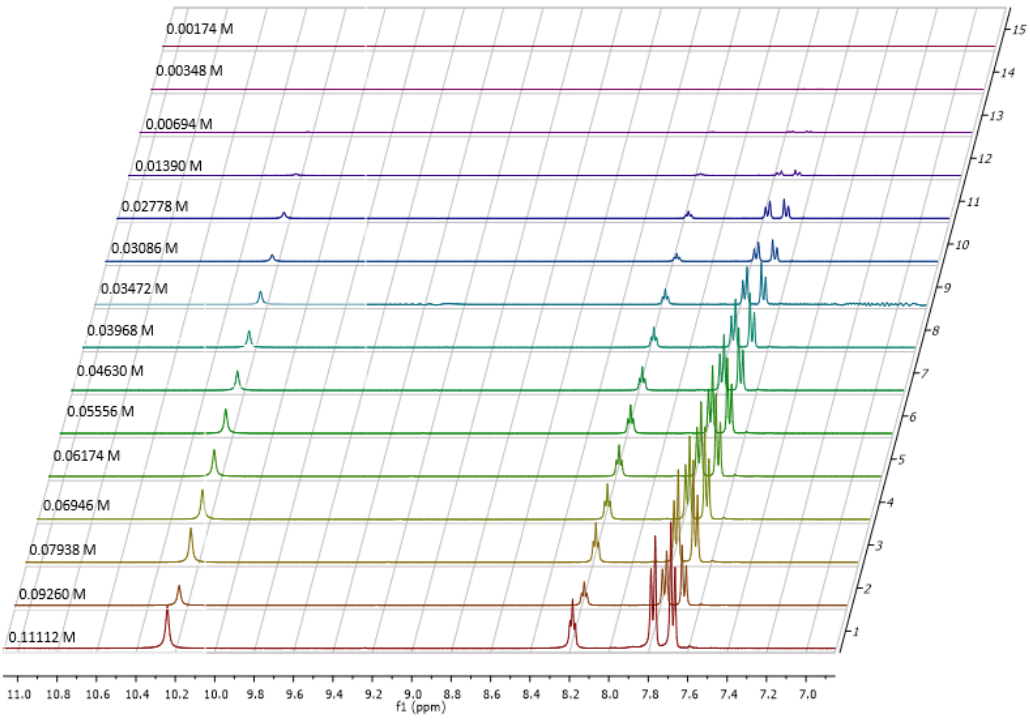

Figure S277 - Enlarged ^{1}H NMR stack plot of compound **67** in DMSO-d_6 0.5 % H_2O solution. Samples were prepared in series with an aliquot of the most concentrated solution undergoing serial dilution.

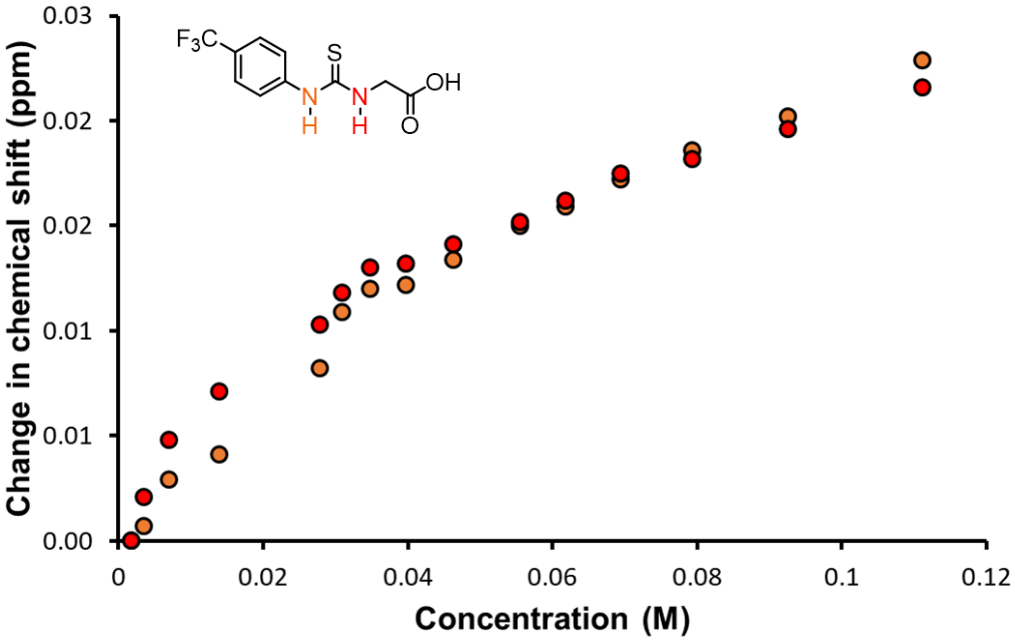

Figure S278 - Graph illustrating the ^{1}H NMR down-field change in chemical shift of thiourea NH resonances with increasing concentration of compound **67** in DMSO-d_6 0.5 % H_2O (298.15 K).

Self-association constant calculation

Compound **67** - Dilution study in DMSO-d_6 0.5 % H_2O. Values calculated from data gathered from both NH 1 and 2.

Equal K/Dimerisation model

K_e = 10.81 M^{-1} ± 3.5045 % K_{dim} = 5.40 M^{-1} ± 1.7522 %

http://app.supramolecular.org/bindfit/view/aa5fa670-4533-4b7b-b741-e3176349d4f3

CoEK model

K_e = 4.59 M^{-1} ± 20.8121 % K_{dim} = 2.30 M^{-1} ± 10.4061 % ρ = 1.88 ± 31.0686 %

http://app.supramolecular.org/bindfit/view/22a940f7-8289-4c34-a9f8-b9a646651bb3

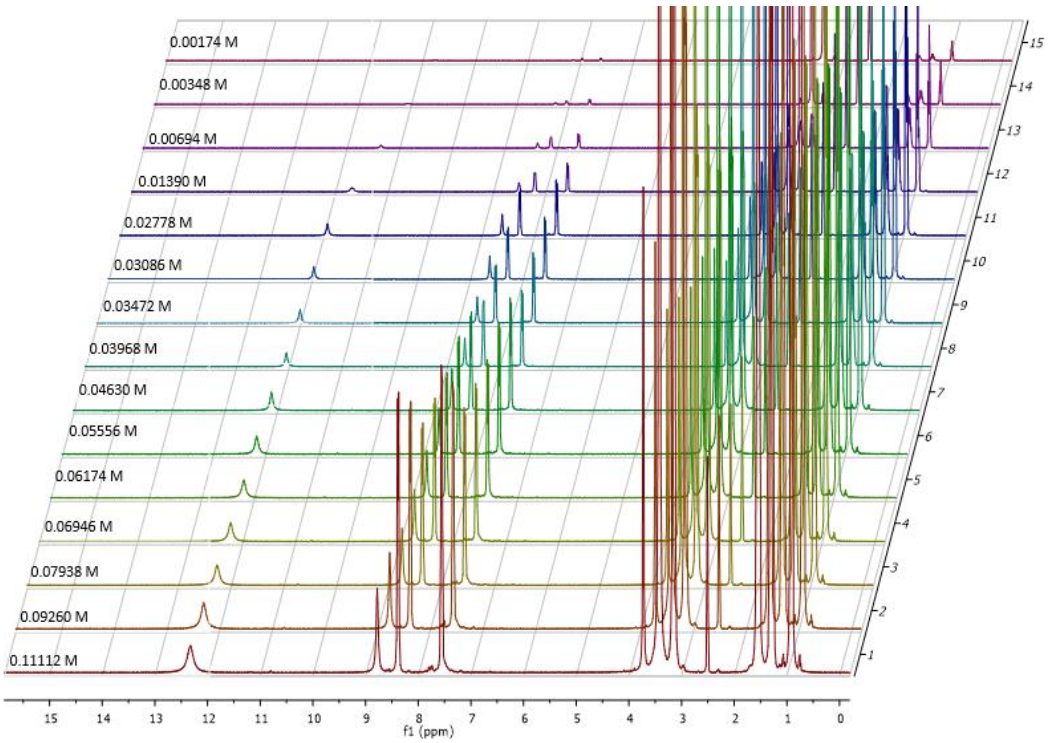

Figure S279 - ^{1}H NMR stack plot of compound **68** in DMSO-d_6 0.5 % H_2O. Samples were prepared in series with an aliquot of the most concentrated solution undergoing serial dilution.

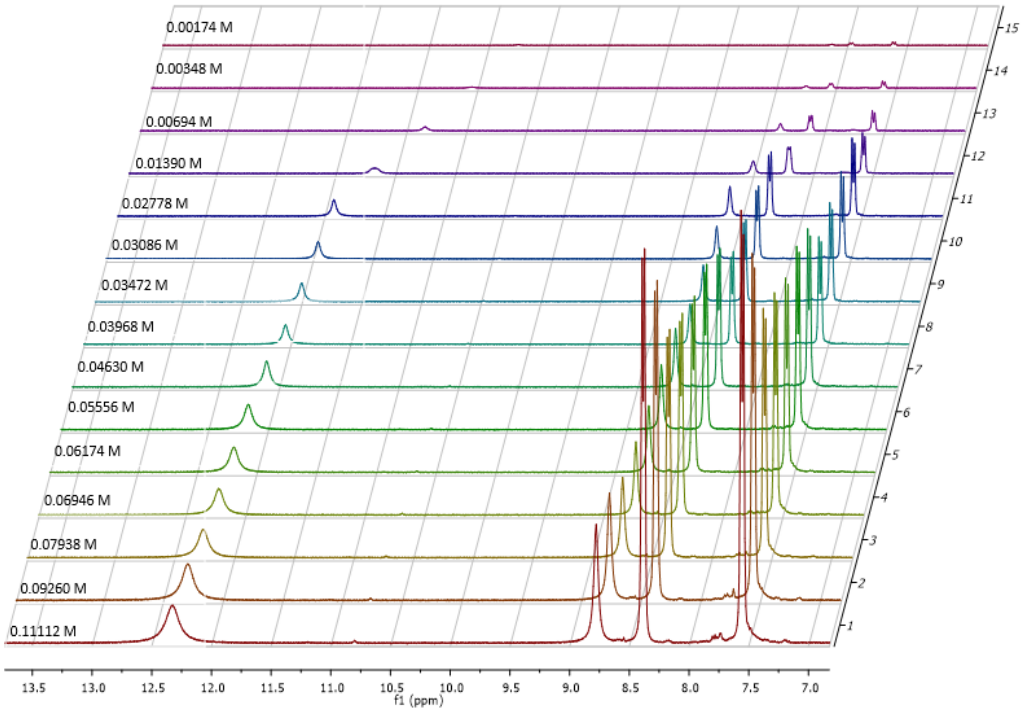

Figure S280 - Enlarged ^{1}H NMR stack plot of compound **68** in DMSO-d_6 0.5 % H_2O solution. Samples were prepared in series with an aliquot of the most concentrated solution undergoing serial dilution.

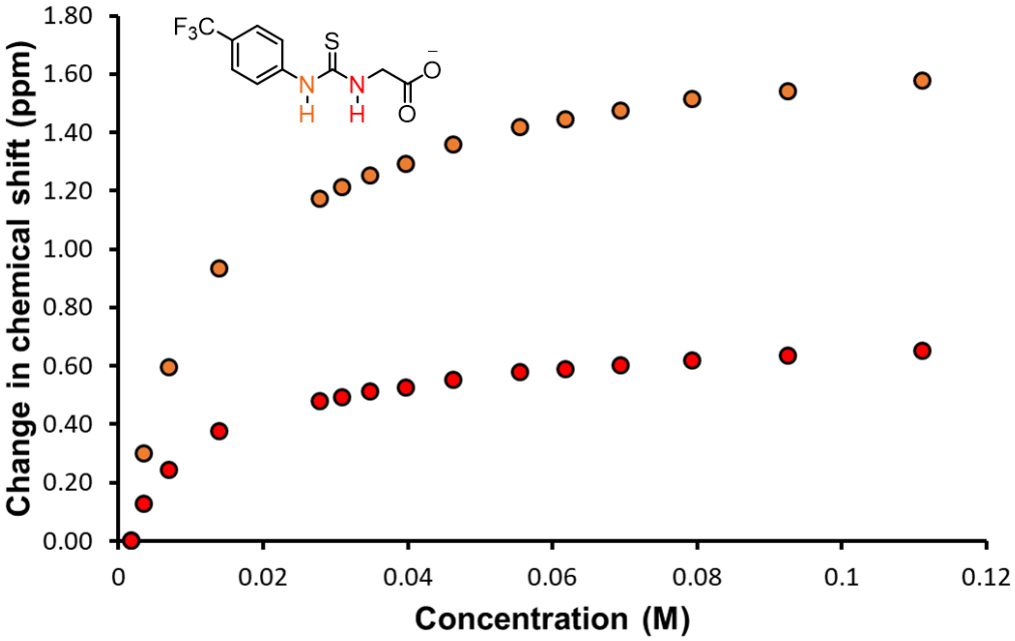

Figure S281 - Graph illustrating the ^{1}H NMR down-field change in chemical shift of thiourea NH resonances with increasing concentration of compound **68** in DMSO-d_6 0.5 % H_2O (298.15 K).

Self-association constant calculation

Compound **68** - Dilution study in DMSO-d_6 0.5 % H_2O. Values calculated from data gathered from both NH 1 and 2.

Equal K/Dimerisation model

K_e = 209.34 M^{-1} ± 1.2548 % K_{dim} = 104.67 M^{-1} ± 0.6274 %

http://app.supramolecular.org/bindfit/view/7fa20ef7-0dc5-4dff-b81d-5457f6b2140c

CoEK model

K_e = 226.07 M^{-1} ± 1.3871 % K_{dim} = 113.04 M^{-1} ± 0.6935 % ρ = 1.18 ± 3.2623 %

http://app.supramolecular.org/bindfit/view/0be23f65-5265-4cc4-a392-eb0bf3952332

Table S8 – ^{1}H NMR resonances of the ethane sulfonate portion of compounds **73**-**80**.

Compound	Ethane sulfonate cation	Concentration (mM)					
		55.56		5.56		0.56	
		CH_2 (ppm)	CH_3 (ppm)	CH_2 (ppm)	CH_3 (ppm)	CH_2 (ppm)	CH_3 (ppm)
73	Na^+	2.4807	1.0890	2.3754	1.0520	2.3410	1.0416
74	$PyrH^+$	2.4385	1.0687	2.3818	2.0486	2.3593	1.0410
75	TMA	2.3684	1.0468	2.3566	1.0416	2.3535	1.0404
76	TEA	2.3636	1.0440	2.3675	1.0449	2.3596	1.0422
77	TPA	2.3630	1.0446	2.3547	1.0407	2.3529	1.0398
78	TBA	2.3599	1.0471	2.3566	1.0446	2.3560	1.0440
79	TPeA	2.3648	1.0453	2.3581	1.0419	2.3590	1.0416
80	THA	2.3666	1.0459	2.3569	1.0413	2.3550	1.0404

1.9.1 Comparative overview

Table S9 - Self-association constants (M^{-1}) calculated for **42**–**44**, **46**, **47**, **50**–**58** and **63**–**72** in a DMSO-d_6 0.5 % H_2O solution at 298.15 K. These constants were obtained from the fitting of ^{1}H NMR dilution data and refined to EK and CoEK models using Bindfit v0.5.[2]

No.			**42**		**43**		**44**		**46**		**47**	
Model	EK (M^{-1})	K_e	5.3	± 0.6 %	0.2	± 2.0 %	6.6	± 2.0 %	0.3	± 4.2 %	5.1	± 2.1 %
		K_{dim}	2.7	± 0.3 %	0.1	± 1.0 %	3.3	± 1.0 %	0.2	± 2.1 %	2.6	± 1.4 %
	CoEK (M^{-1})	K_e	13.0	± 0.7 %	4.0	± 12.0 %	20.0	± 2.7 %	1.9	± 51.0 %	14.1	± 4.4 %
		K_{dim}	6.5	± 0.4 %	2.0	± 6.0 %	10.0	± 1.4 %	0.9	± 25.5 %	7.1	± 2.2 %
		p	0.5	± 2.1 %	0.4	± 20.3 %	0.3	± 11.6 %	0.5	± 66.3 %	0.4	± 14.0 %
No.			**50**[b]		**51**		**52**		**53**		**54**	
Model	EK (M^{-1})	K_e	13.5	± 0.7 %	6.3	± 0.9 %	6.6	± 1.2 %	4.1	± 0.5 %	5.0	± 0.9 %
		K_{dim}	6.7	± 0.3 %	3.2	± 0.4 %	3.3	± 0.6 %	2.1	± 0.3 %	2.5	± 0.5 %
	CoEK (M^{-1})	K_e	18.2	± 1.0 %	12.0	± 2.0 %	14.9	± 2.1 %	8.8	± 1.3 %	9.6	± 2.7 %
		K_{dim}	9.1	± 0.5 %	6.0	± 1.0 %	7.5	± 1.1 %	4.4	± 0.7 %	4.8	± 1.3 %
		p	0.8	± 3.4 %	0.6	± 5.5 %	0.5	± 6.7 %	0.6	± 3.0 %	0.9	± 6.3 %
No.			**55**[b]		**56**		**57**[a]		**58**[b]		**63**	
Model	EK (M^{-1})	K_e	3.6	± 1.5 %	1.2	± 3.0 %	0.6	± 3.0 %	8.9	± 5.1 %	[d]	
		K_{dim}	1.8	± 0.7 %	0.6	± 1.5 %	0.3	± 1.5 %	4.5	± 2.6 %		
	CoEK (M^{-1})	K_e	4.6	± 8.3 %	18.0	± 4.1 %	13.0	± 5.7 %	32.2	± 5.1 %		
		K_{dim}	2.3	± 4.1 %	9.0	± 2.1 %	6.5	± 2.9 %	16.1	± 2.6 %		
		p	0.9	± 13.4 %	0.1	± 21.5 %	0.2	± 23.8 %	0.2	± 37.5 %		
No.			**64**		**65**		**66**		**67**		**68**	
Model	EK (M^{-1})	K_e	< 0.1		82.8	± 2.5 %	11.9	± 1.5 %	10.8	± 3.5 %	209.3	± 1.3 %
		K_{dim}	< 0.1		41.4	± 1.3 %	6.0	± 0.8 %	5.4	± 1.8 %	104.7	± 0.7 %
	CoEK (M^{-1})	K_e	7.1	± 18.3 %	101.8	± 5.1 %	23.8	± 1.7 %	4.6	± 20.8 %	226.1	± 1.4 %
		K_{dim}	3.6	± 9.2 %	5.9	± 2.6 %	11.9	± 0.9 %	2.3	± 10.4 %	113.0	± 0.7 %
		p	0.1	± 58.4 %	2.6	± 37.5 %	0.5	± 7.5 %	1.9	± 31.1 %	1.2	± 3.3 %
No.			**69** [a, c]		**70**[a]		**71**[a]		**72**[a]			
Model	EK (M^{-1})	K_e	< 0.1		2.9	± 0.5 %	1.2	± 2.1 %	5.3	± 0.6 %		
		K_{dim}	< 0.1		1.5	± 0.2 %	0.6	± 1.1 %	2.7	± 0.3 %		
	CoEK (M^{-1})	K_e	0.5	± 43.1 %	8.6	± 1.1 %	6.2	± 8.8 %	13.0	± 0.7 %		
		K_{dim}	0.3	± 21.5 %	4.3	± 0.5 %	3.1	± 4.4 %	6.5	± 0.3 %		
		p	0.0	± 47.0 %	0.5	± 2.5 %	0.4	± 17.8 %	0.5	± 2.0 %		

[*a*] Previously published results.[1] [*b*] Possibility of more complex binding events than are being modelled. [*c*] Data fitted using L-BFGS-B (quasi-Newtown) rather than Nelder–Mead (Simplex) methods. [*d*] Could not be fitted.

1.10 Low-level computational modelling

Computational calculations to identify primary hydrogen bond donating and accepting sites were conducted in line with studies reported by Hunter using Spartan '16.[3] Calculations were performed using semi-empirical PM6 methods, after energy minimisation calculations, to identify E_{max}, E_{min} and polarizability values. PM6 was used over AM1 in line with research conducted by Stewart.[4]

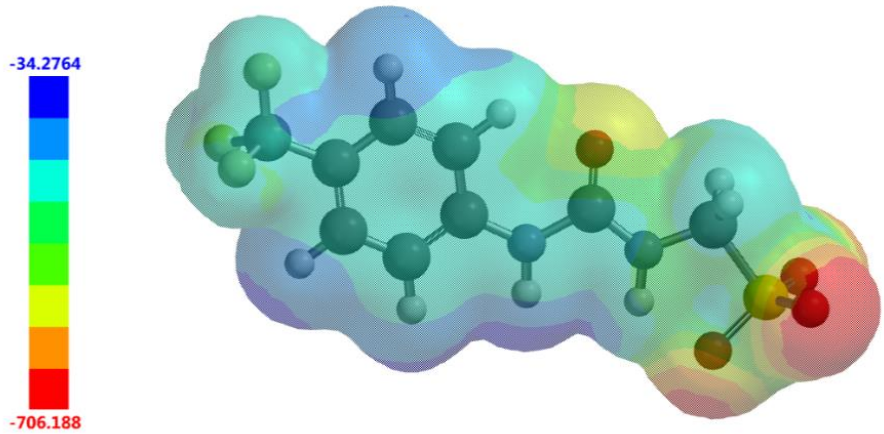

Figure S282 - Electrostatic potential map calculated for the anionic component of **42**. E_{max} and E_{min} values depicted in the Figure legends are given in kJ/mol.

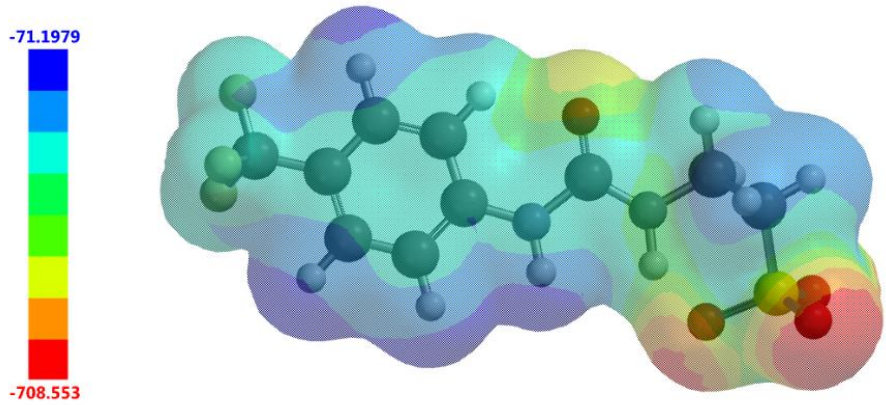

Figure S283 - Electrostatic potential map calculated for the anionic component of **43**. E_{max} and E_{min} values depicted in the Figure legends are given in kJ/mol.

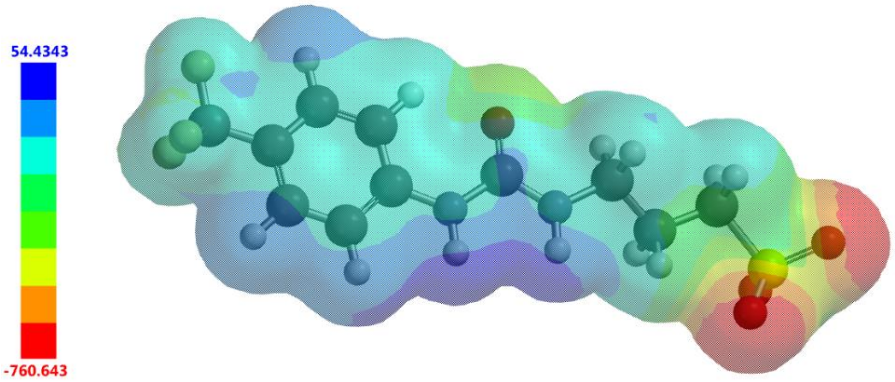

Figure S284 - Electrostatic potential map calculated for the anionic component of **44**. E_{max} and E_{min} values depicted in the Figure legends are given in kJ/mol.

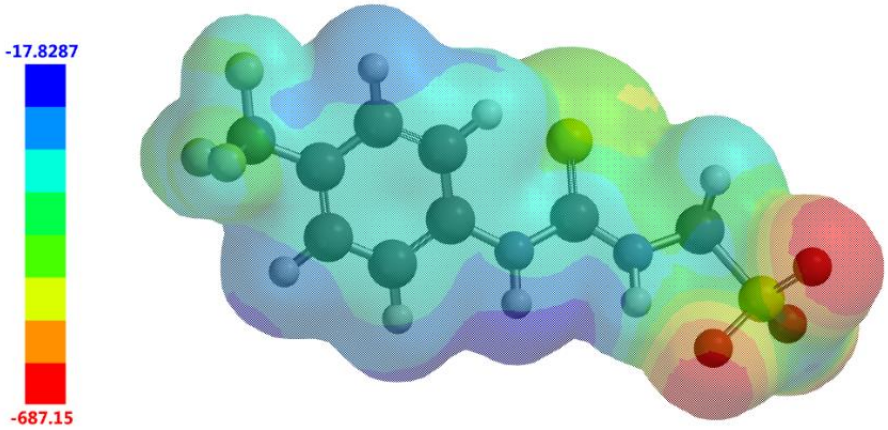

Figure S285 - Electrostatic potential map calculated for the anionic component of **45**. E_{max} and E_{min} values depicted in the Figure legends are given in kJ/mol.

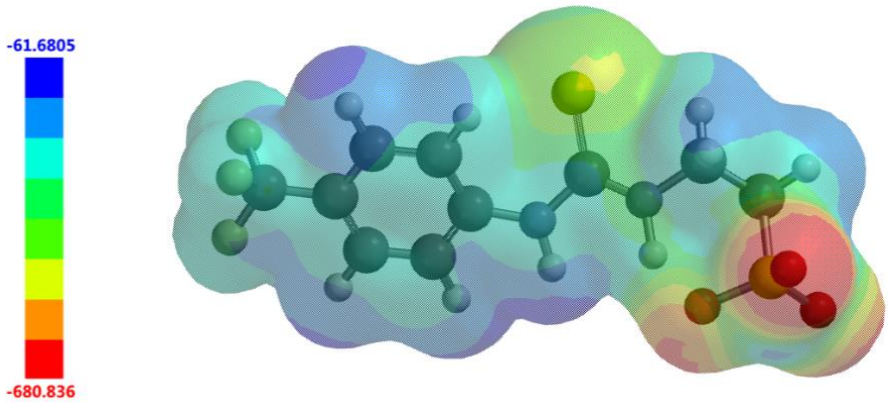

Figure S286 - Electrostatic potential map calculated for the anionic component of **46**. E_{max} and E_{min} values depicted in the Figure legends are given in kJ/mol.

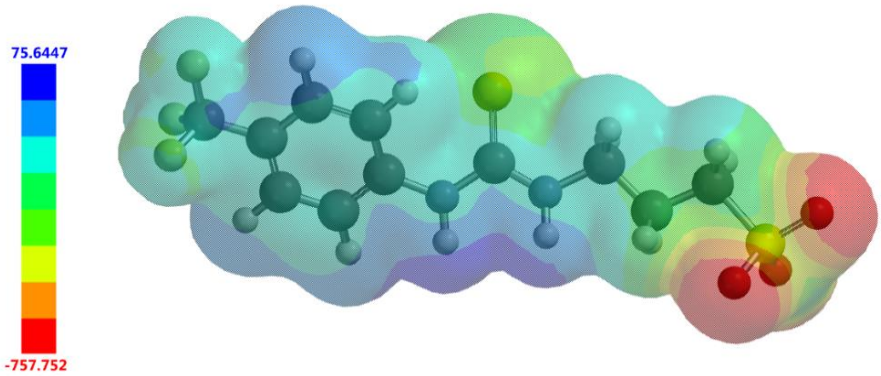

Figure S287 - Electrostatic potential map calculated for the anionic component of **47**. E_{max} and E_{min} values depicted in the Figure legends are given in kJ/mol.

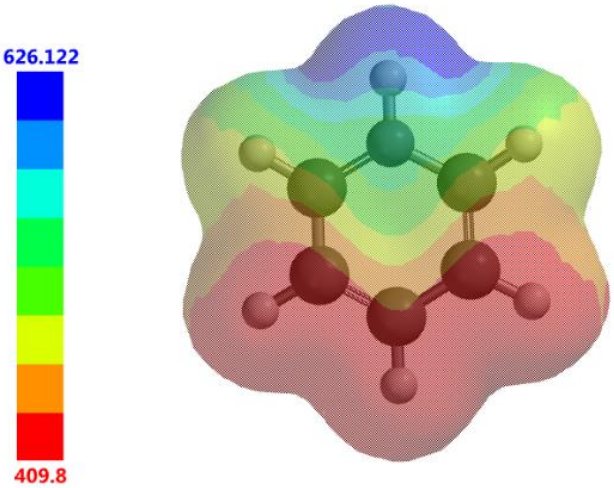

Figure S288 - Electrostatic potential map calculated for the cationic component of **49**. E_{max} and E_{min} values depicted in the Figure legends are given in kJ/mol.

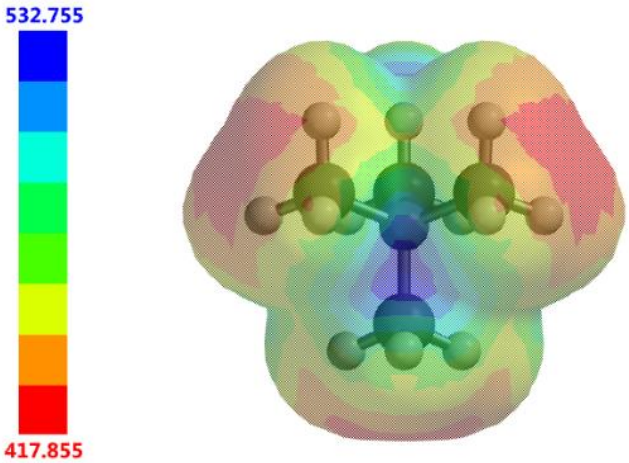

Figure S289 - Electrostatic potential map calculated for the cationic component of **50**. E_{max} and E_{min} values depicted in the Figure legends are given in kJ/mol.

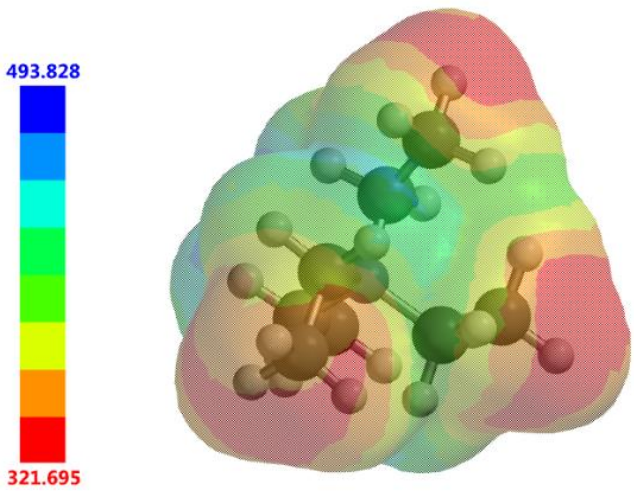

Figure S290 - Electrostatic potential map calculated for the cationic component of **51**. E_{max} and E_{min} values depicted in the Figure legends are given in kJ/mol.

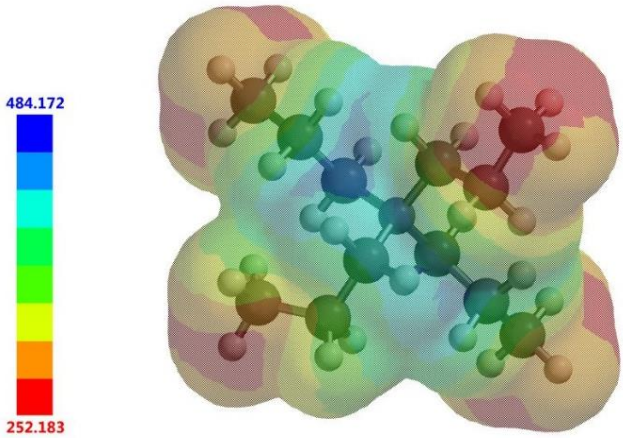

Figure S291 - Electrostatic potential map calculated for the cationic component of **52**. E_{max} and E_{min} values depicted in the Figure legends are given in kJ/mol.

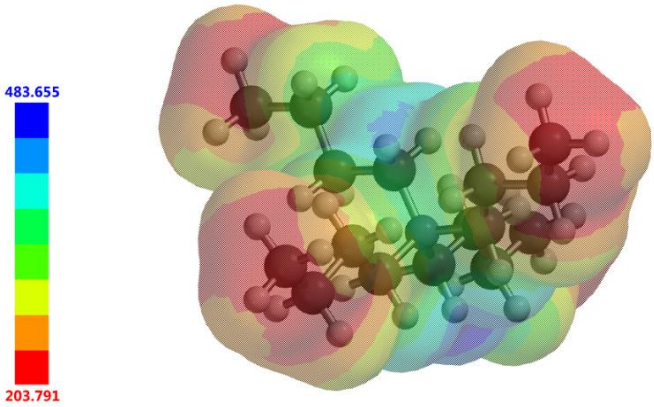

Figure S292 - Electrostatic potential map calculated for the cationic component of **42**. E_{max} and E_{min} values depicted in the Figure legends are given in kJ/mol.

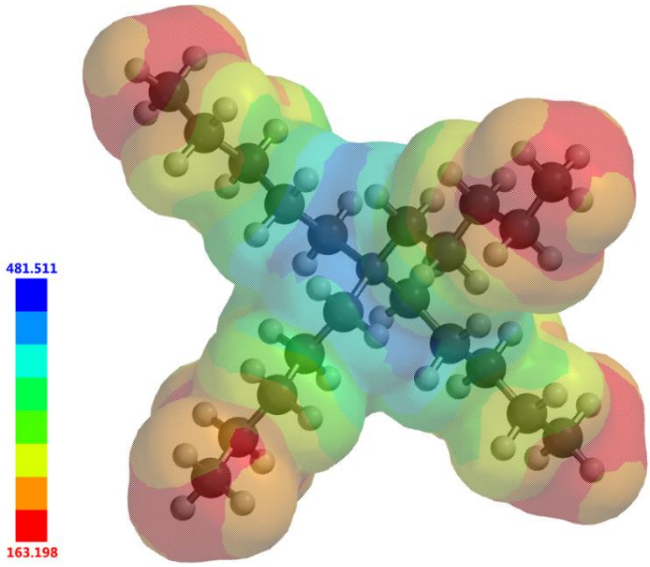

Figure S293 - Electrostatic potential map calculated for the cationic component of **53**. E_{max} and E_{min} values depicted in the Figure legends are given in kJ/mol.

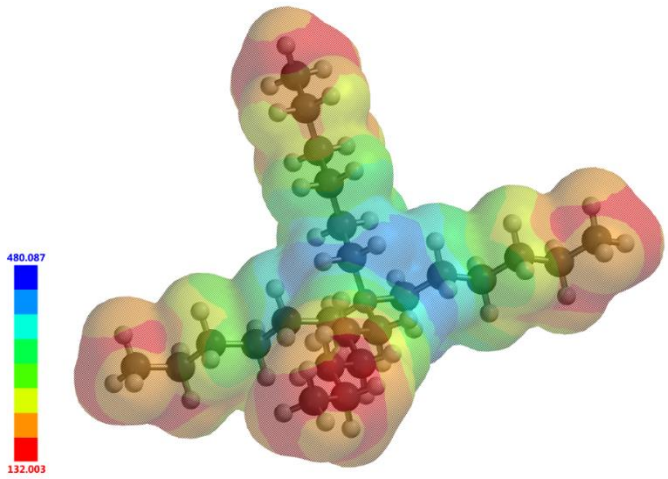

Figure S294 - Electrostatic potential map calculated for the cationic component of **54**. E_{max} and E_{min} values depicted in the Figure legends are given in kJ/mol.

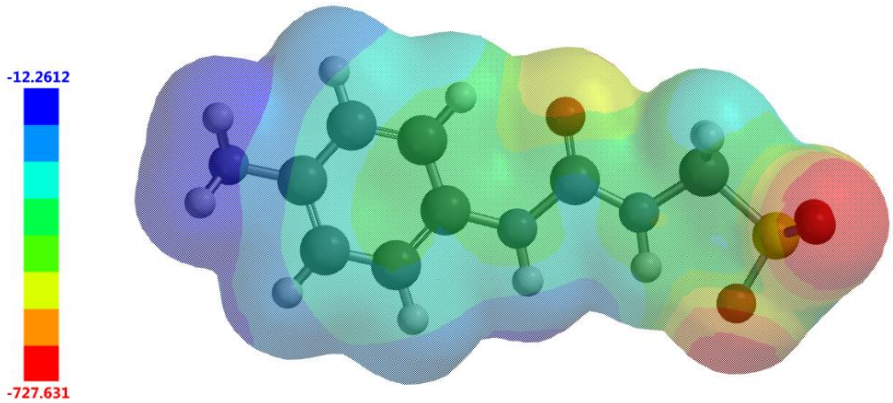

Figure S295 - Electrostatic potential map calculated for the anionic component of **55**. E_{max} and E_{min} values depicted in the Figure legends are given in kJ/mol.

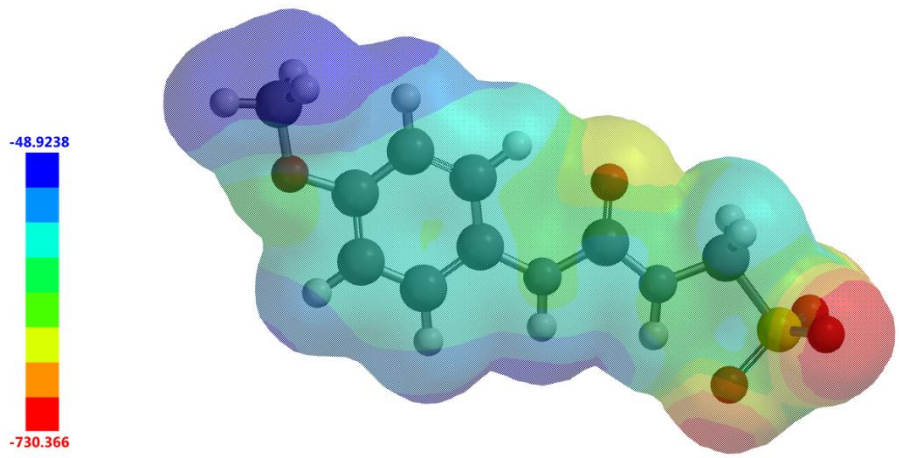

Figure S296 - Electrostatic potential map calculated for the anionic component of **56**. E_{max} and E_{min} values depicted in the Figure legends are given in kJ/mol.

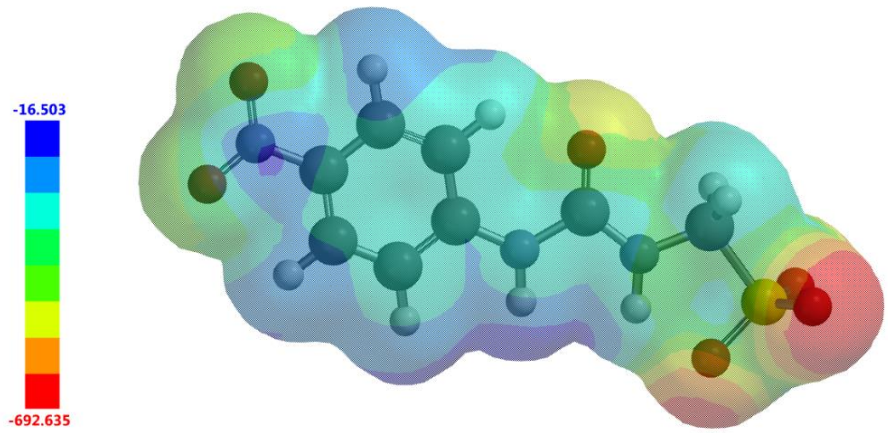

Figure S297 - Electrostatic potential map calculated for the anionic component of **58**. E_{max} and E_{min} values depicted in the Figure legends are given in kJ/mol.

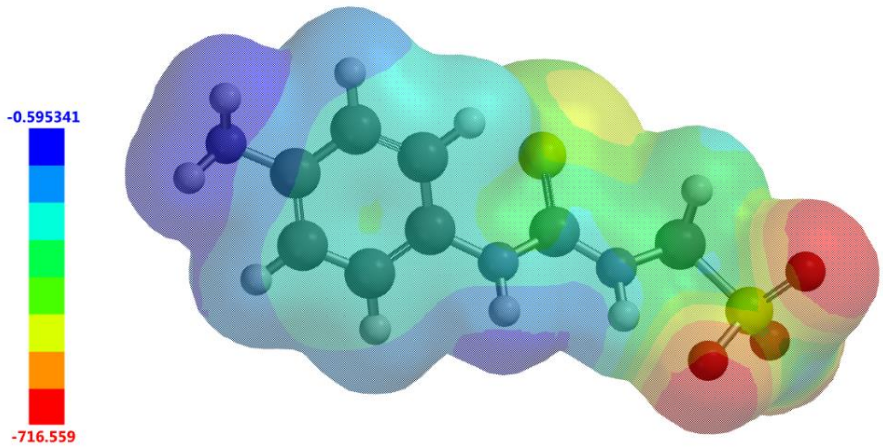

Figure S298 - Electrostatic potential map calculated for the anionic component of **59**. E_{max} and E_{min} values depicted in the Figure legends are given in kJ/mol.

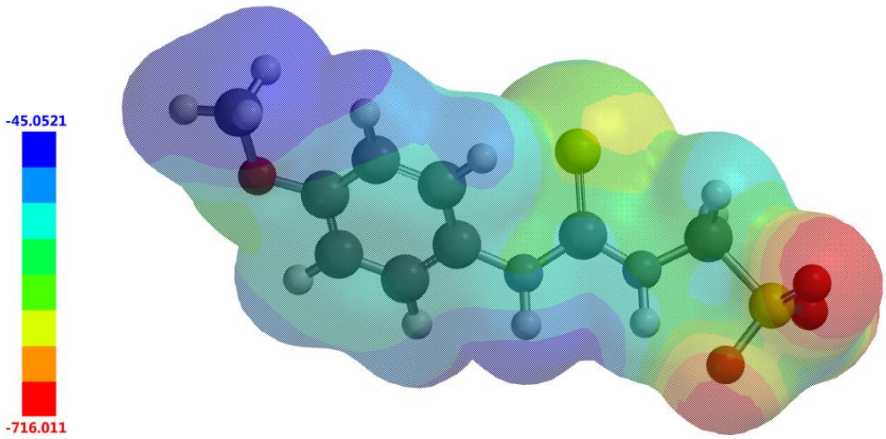

Figure S299 - Electrostatic potential map calculated for the anionic component of **60**. E_{max} and E_{min} values depicted in the Figure legends are given in kJ/mol.

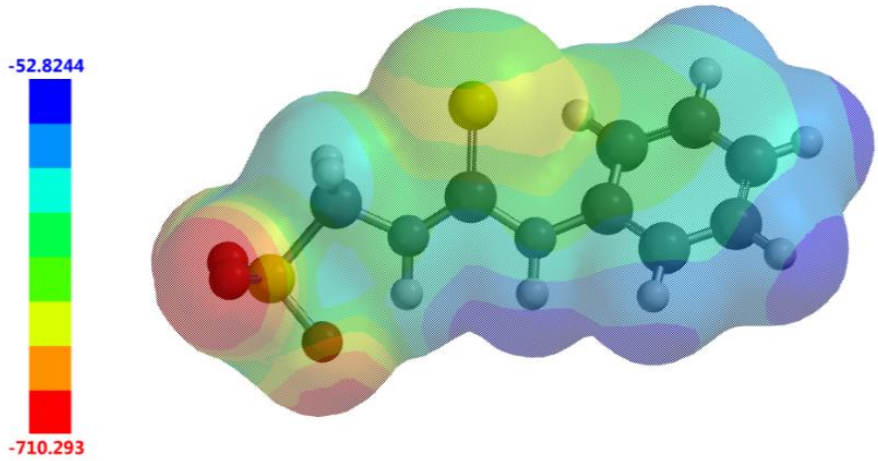

Figure S300 - Electrostatic potential map calculated for the anionic component of **61**. E_{max} and E_{min} values depicted in the Figure legends are given in kJ/mol.

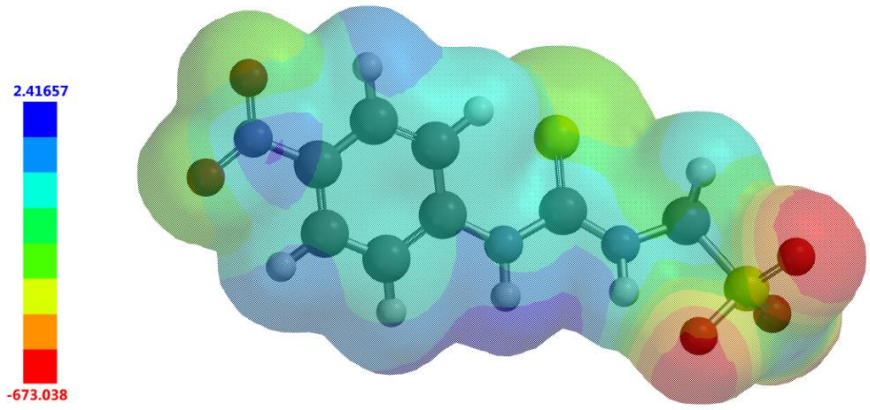

Figure S301 - Electrostatic potential map calculated for the anionic component of **62**. E_{max} and E_{min} values depicted in the Figure legends are given in kJ/mol.

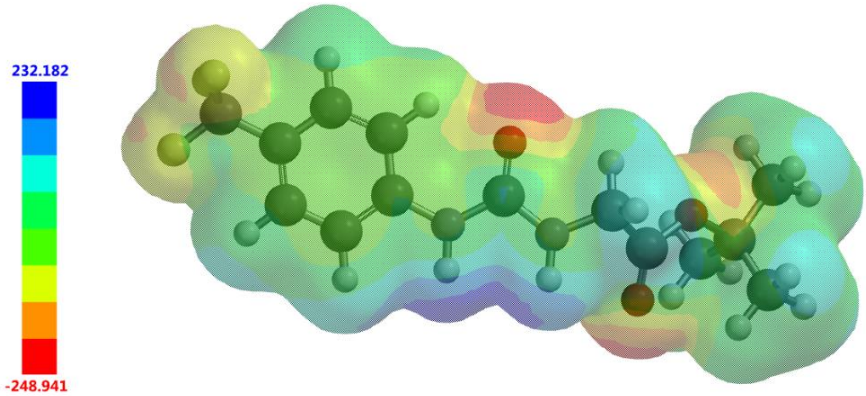

Figure S302 - Electrostatic potential map calculated for **63**. E_{max} and E_{min} values depicted in the Figure legends are given in kJ/mol.

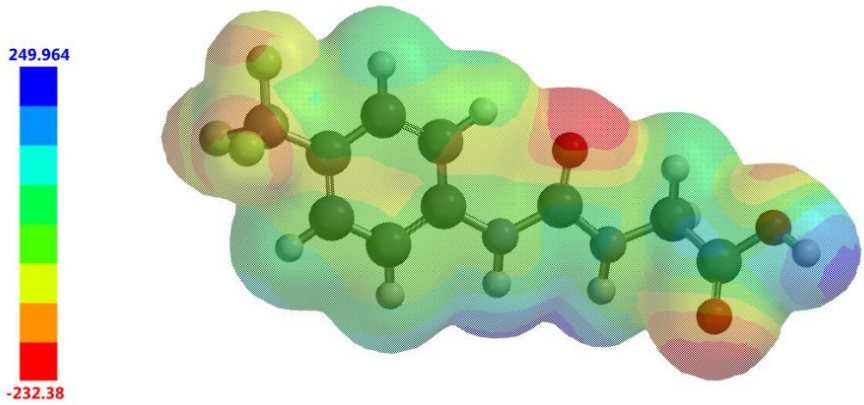

Figure S303 - Electrostatic potential map calculated for **64**. E_{max} and E_{min} values depicted in the Figure legends are given in kJ/mol.

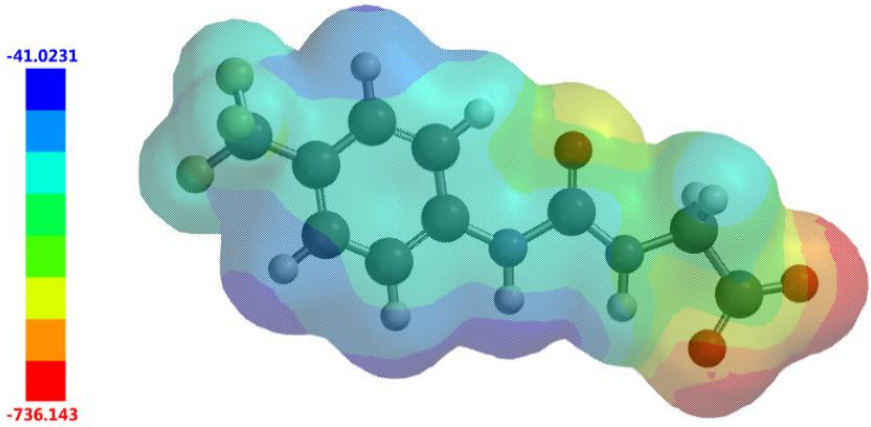

Figure S304 - Electrostatic potential map calculated for the anionic component of **65**. E_{max} and E_{min} values depicted in the Figure legends are given in kJ/mol.

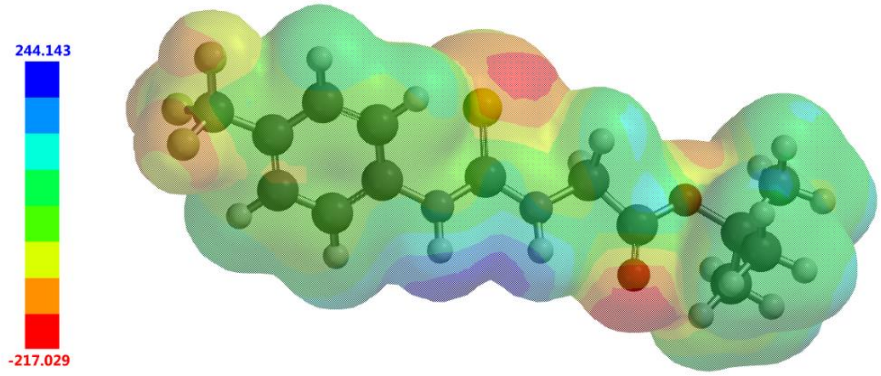

Figure S305 - Electrostatic potential map calculated for **66**. E_{max} and E_{min} values depicted in the Figure legends are given in kJ/mol.

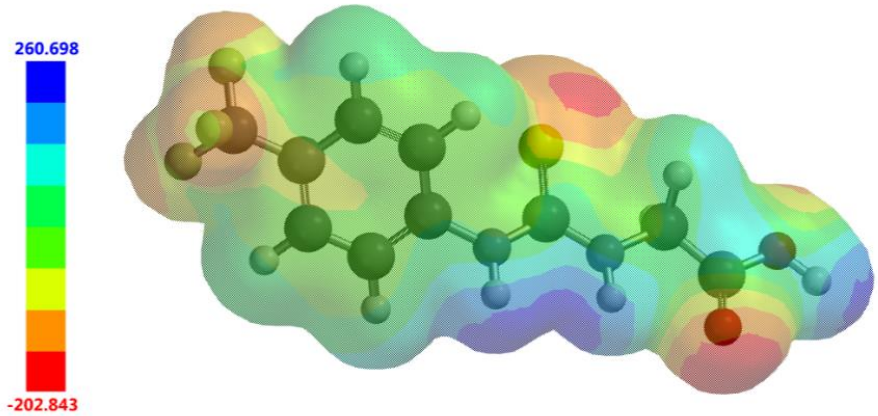

Figure S306 - Electrostatic potential map calculated for **67**. E_{max} and E_{min} values depicted in the Figure legends are given in kJ/mol.

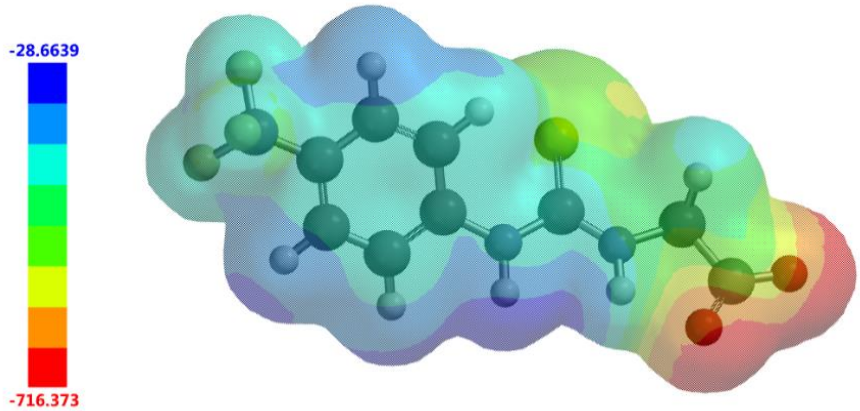

Figure S307 - Electrostatic potential map calculated for the anionic component of **68**. E_{max} and E_{min} values depicted in the Figure legends are given in kJ/mol.

1.10.1 Comparative overview

Table S10 - E_{max} and E_{min} surface values (kJ mol^{-1}) calculated for **42** -**72** using semi-empirical PM6 modelling methods with Spartan '16 software. No. = compound number.

No.	E_{max} (kJ/mol)	E_{min} (kJ/mol)	No.	E_{max} (kJ/mol)	E_{min} (kJ/mol)	No.	E_{max} (kJ/mol)	E_{min} (kJ/mol)
42, 48-54	-34.28	-706.12	**57**[a]	-69.10	-728.74	**65**	-41.02	-736.14
43	-71.20	-708.55	**58**	-16.50	-692.64	**66**	244.14	-217.03
44	-54.43	-760.64	**59**	-0.595	-716.56	**67**	260.70	-202.84
45	-17.83	-687.15	**60**	-45.05	-716.01	**68**	-28.66	-716.37
46	-61.68	-680.84	**61**	-52.82	-710.29	**69**[a]	-65.85	-720.79
47	-75.64	-757.75	**62**	2.417	-673.04	**70**[a]	-60.12	-714.30
55	-12.26	-727.63	**63**	232.18	-248.94	**71**[a]	-66.07	-723.07
56	-48.92	-730.37	**64**	249.96	-232.38	**72**[a]	-31.97	-703.73

[*a*] Previously published results.[1]

1.11 References

1 L. J. White, N. J. Wells, L. R. Blackholly, H. J. Shepherd, B. Wilson, G. P. Bustone, T. J. Runacres and J. R. Hiscock, *Chem. Sci.*, 2017, **8**, 7620–7630.

2 Supramolecular.org - Binding Constant Calculators | Supramolecular, http://app.supramolecular.org/bindfit/, (accessed 1 July 2020).

3 C. A. Hunter, *Angew. Chemie Int. Ed.*, 2004, **43**, 5310–5324.

4 J. J. P. Stewart, *J. Mol. Model.*, 2007, **13**, 1173–1213.

Appendix 2: Chapter 3

2.1 Characterisation NMR

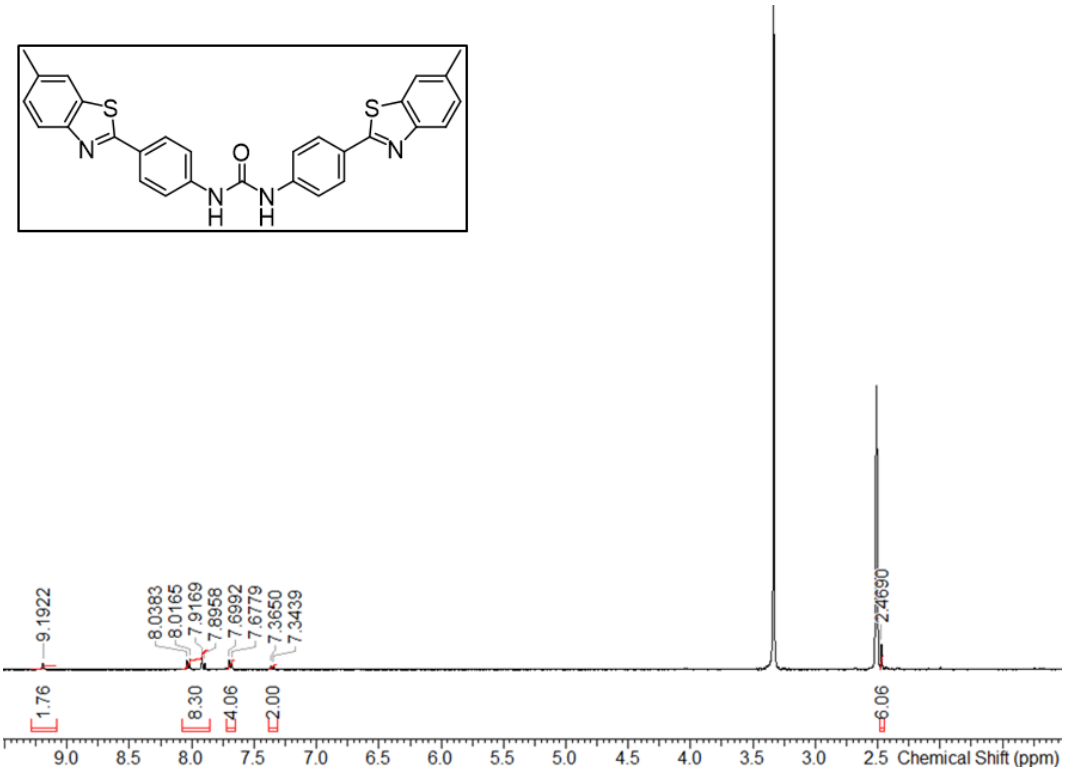

Figure S308 - ^{1}H NMR spectrum of compound **104** in DMSO-d_6 conducted at 298.15 K.

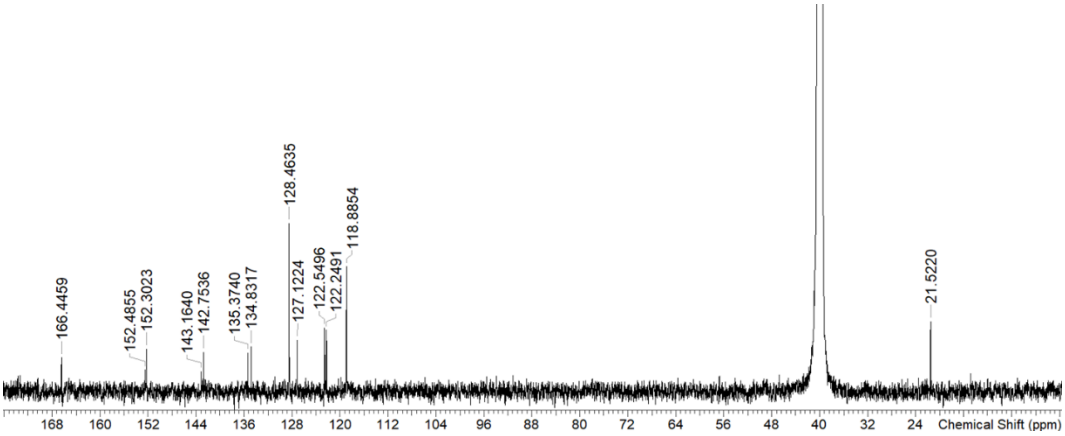

Figure S309 - ^{13}C NMR spectrum of compound **104** in DMSO-d_6 conducted at 298.15 K.

2.2 Dynamic light scattering data

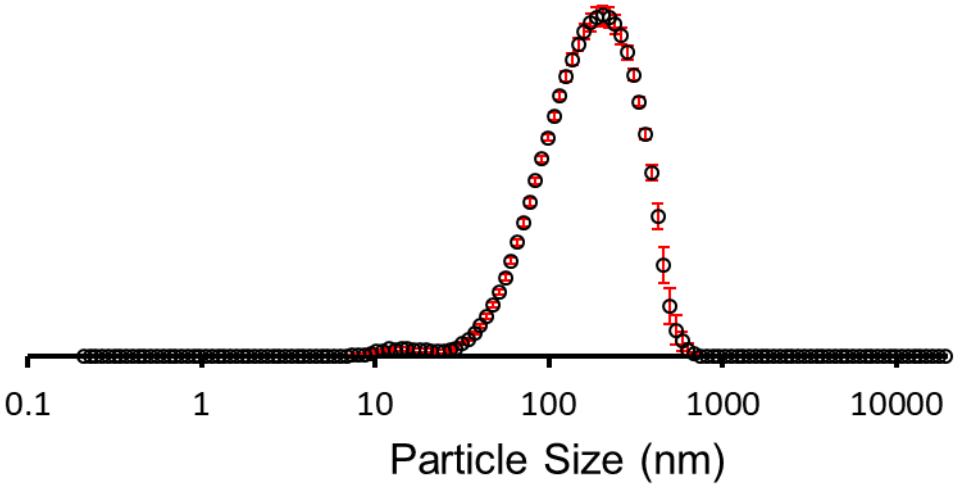

Figure S310 - The average intensity particle size distribution calculated using 9 DLS runs for compound **72** (5 mg/mL) in an EtOH:H_2O (1:19) solution at 298.15 K.

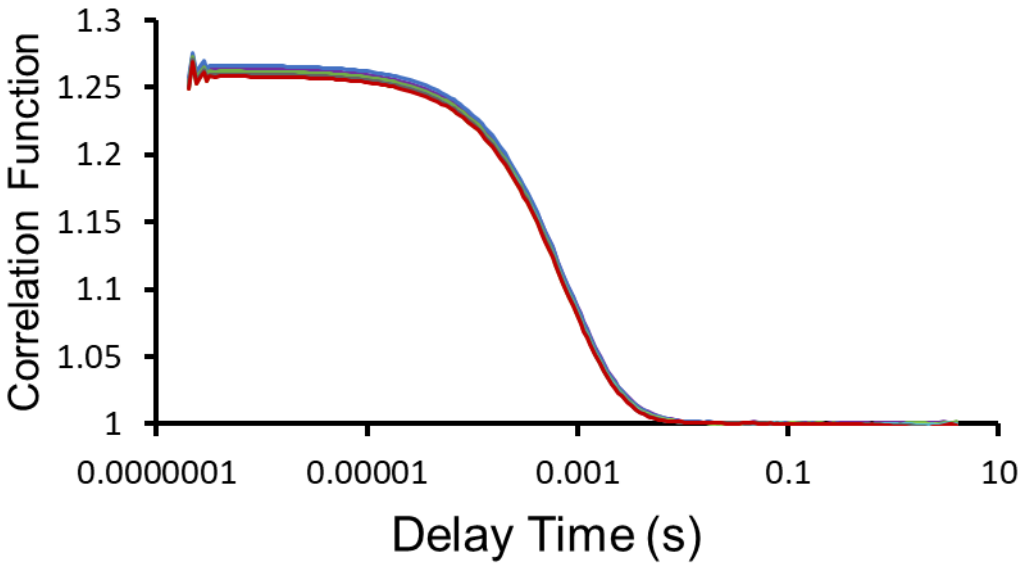

Figure S311 - Correlation function data for 9 DLS runs of compound **72** (5 mg/mL) in an EtOH:H_2O (1:19) solution at 298.15 K.

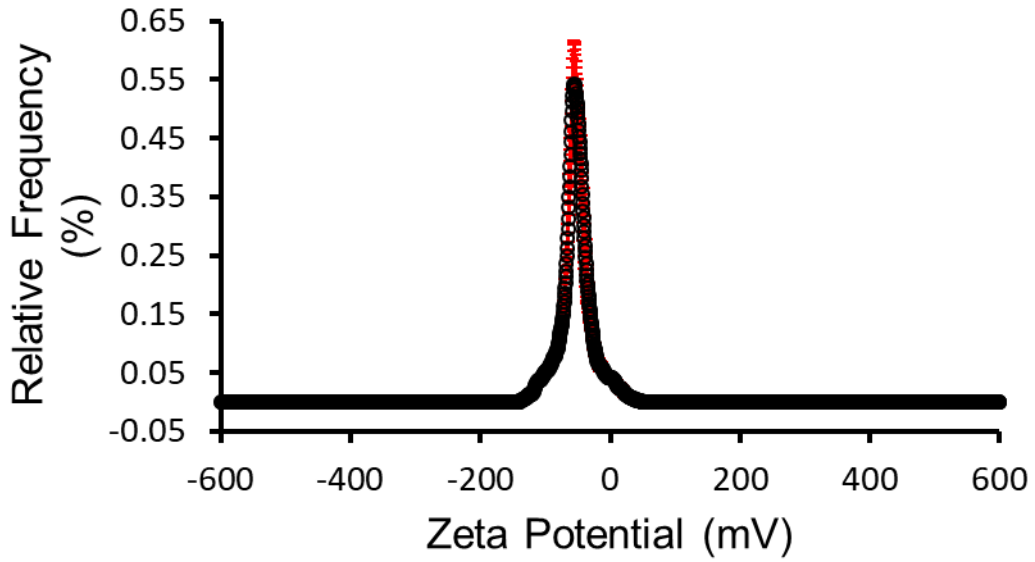

Figure S312 - The average zeta potential distribution calculated using 10 runs for compound **72** (5 mg/mL) in an EtOH:H_2O (1:19) solution at 298.15 K. Average measurement value -59.0 mV.

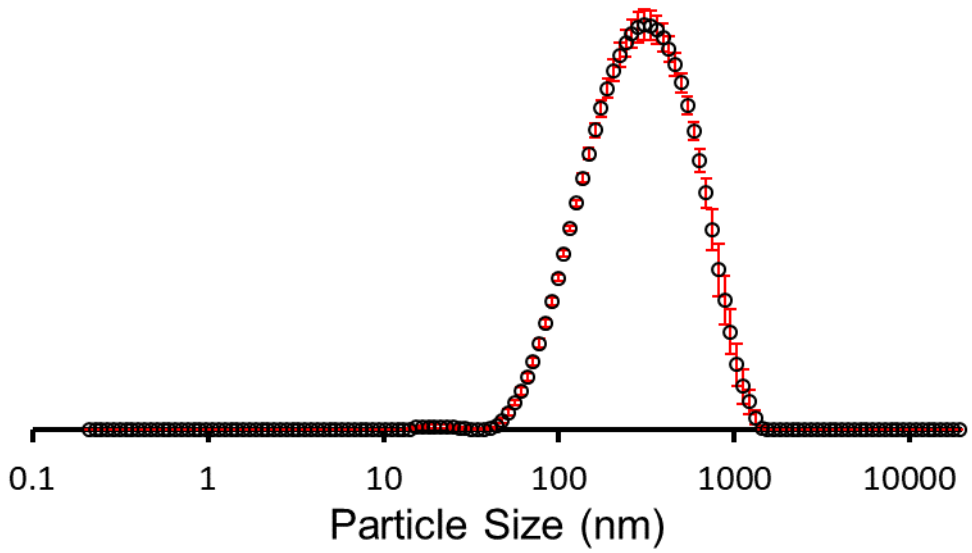

Figure S313 - The average intensity particle size distribution calculated using 10 DLS runs for compound **72** (5 mg/mL) in a H_2O solution at 298.15 K.

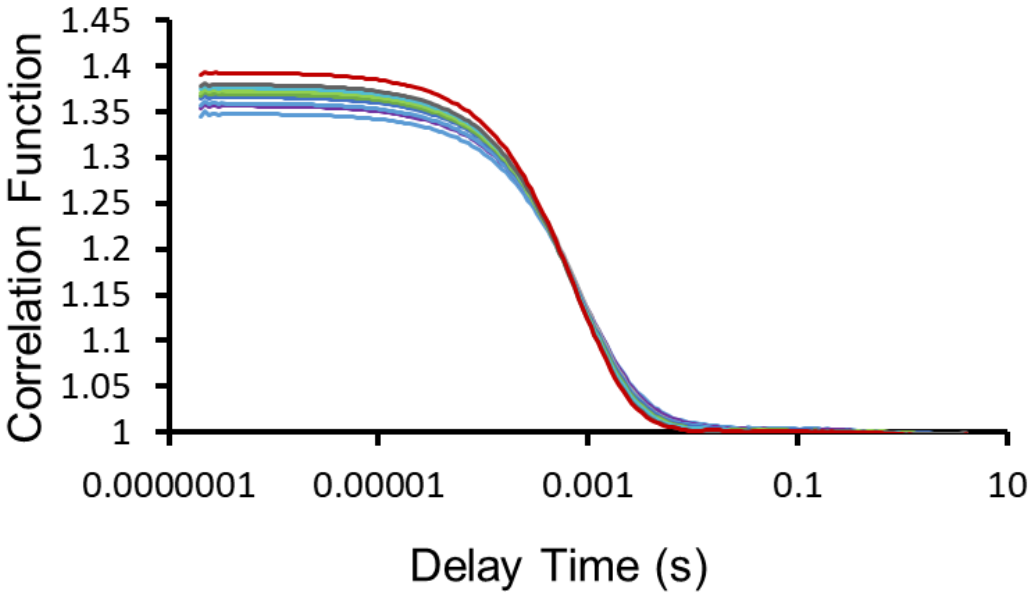

Figure S314 - Correlation function data for 10 DLS runs of compound **72** (5 mg/mL) in a H_2O solution at 298.15 K.

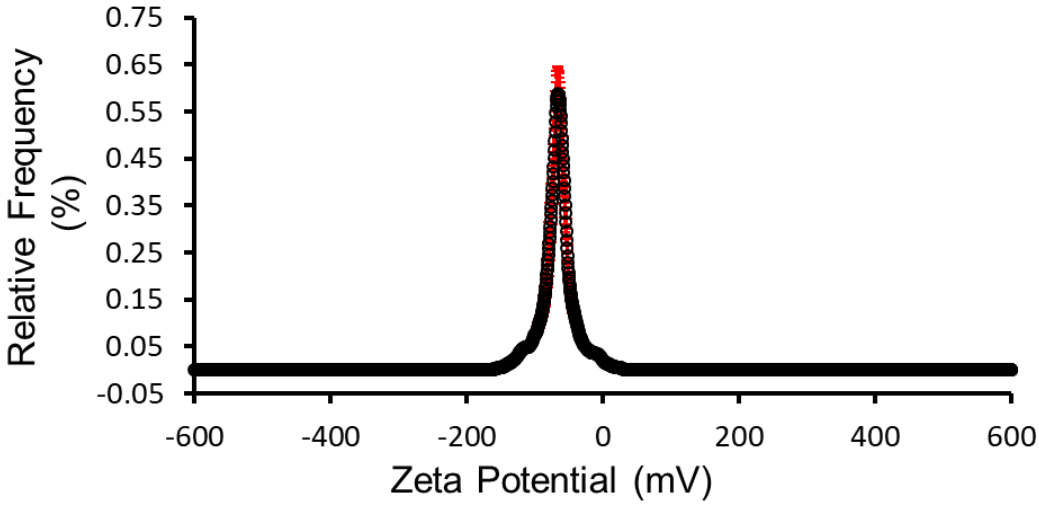

Figure S315 - The average zeta potential distribution calculated using 10 runs for compound **72** (5 mg/mL) in a H_2O solution at 298.15 K. Average measurement value -71.4 mV.

2.2.1 Comparative overview

Table S11 - Summary of average intensity particle size distribution, polydispersity and zeta potential data for compound **72** at 5 mg/ mL. Error = standard error of the mean to 1 dp.

Solution	Peak maxima (nm)	Polydispersity (%)	Zeta potential (mV)
H_2O:EtOH 19:1	197	26 (± 0.4)	-59.0
H_2O	349	22 (± 1.2)	-71.4

2.3 Inversion test

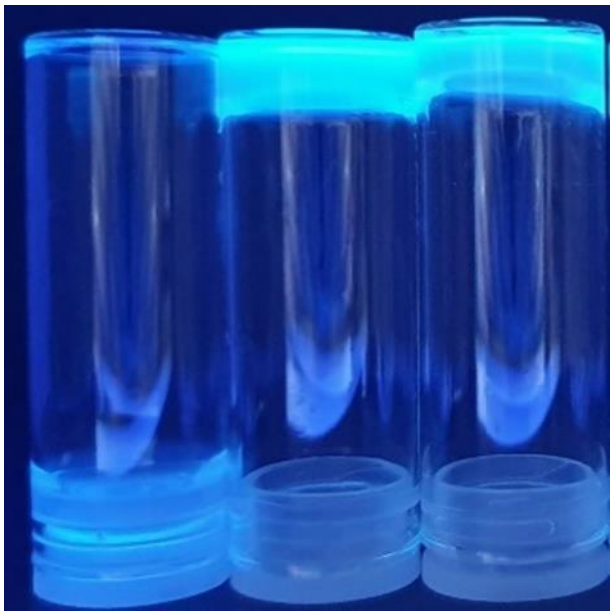

Figure S316 – Compound **72** (5 mg) in 1 mL of H_2O (left) hydrogel of compound **72** (5 mg) in 1 mL aqueous NaCl (0.505 M) (centre), hydrogel of compound **72** (5 mg) in 1 mL of aqueous NaH_2PO_4 (0.505 M) (right).

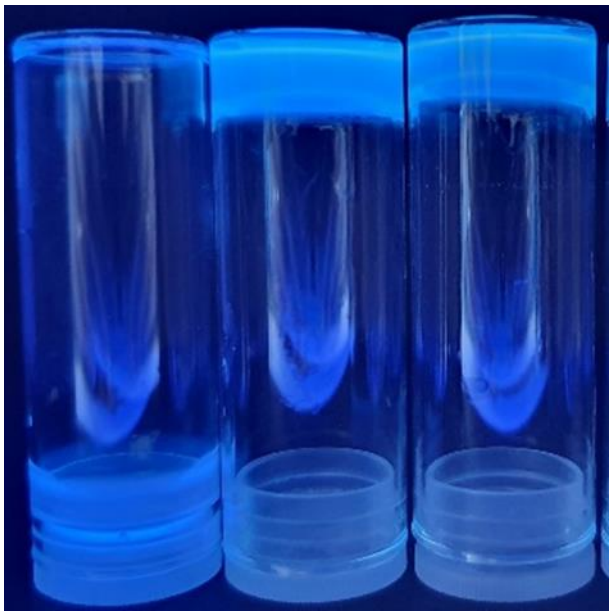

Figure S317 – Compound **72** (1.5 mg) in 1 mL of H_2O (left), hydrogel of compound **72** at MGC (1.5 mg) in 1 mL aqueous NaCl (0.505 M) (centre), hydrogel of compound **72** at MGC (1.5 mg) in 1 mL of aqueous NaH_2PO_4 (0.505 M) (right).

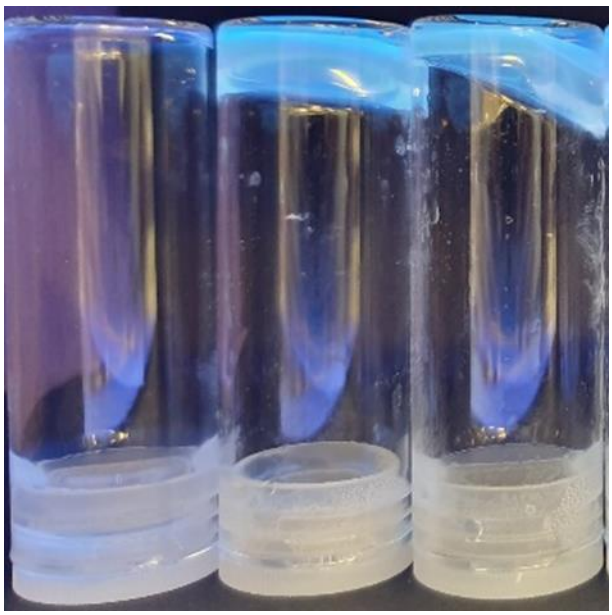

Figure S318 – Compound **72** (1.5 mg) in 1 mL of H_2O (left), partial hydrogel of compound **72** (1 mg) in 1 mL aqueous NaCl (0.505 M) (centre), partial hydrogel of compound **72** (1 mg) in 1 mL of aqueous NaH_2PO_4 (0.505 M) (right).

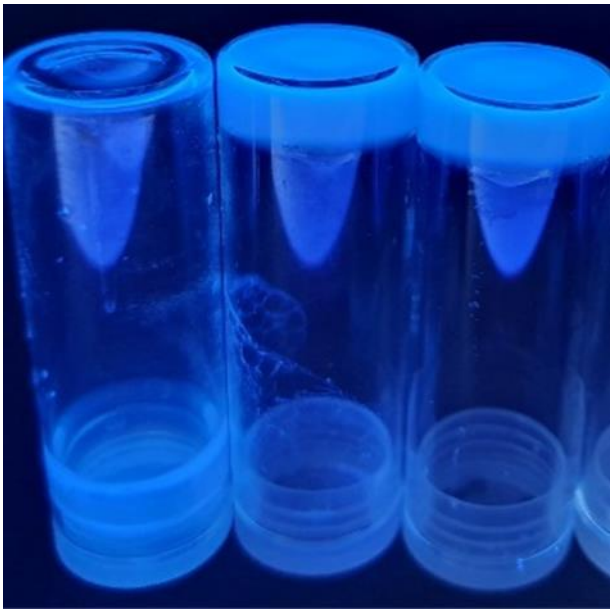

Figure S319 - Compound **72** (5 mg) in 1 mL of H_2O (left) hydrogel of compound **72** (5 mg) in 1 mL aqueous NaCl (0.505 M) (centre), hydrogel of compound **72** (5 mg) in 1 mL of aqueous Na_2CO_3 (0.505 M) (right).

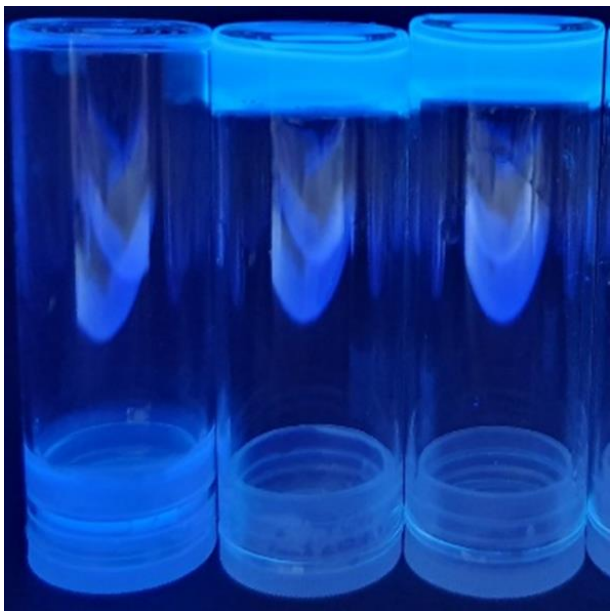

Figure S320 - Compound **72** (3 mg) in 1 mL of H_2O (left), hydrogel of compound **72** (3 mg) in 1 mL aqueous NaCl (0.505 M) (centre), hydrogel of compound **72** at MGC (3 mg) in 1 mL of aqueous Na_2CO_3 (0.505 M) (right).

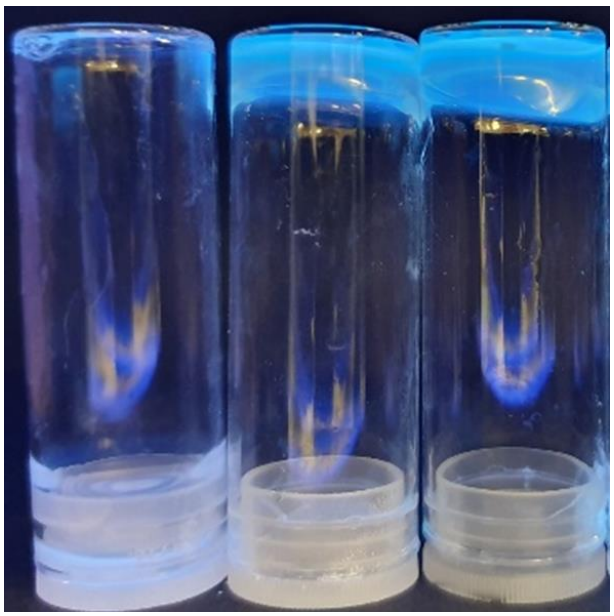

Figure S321 - Compound **72** (2.5 mg) in 1 mL of H_2O (left), hydrogel of compound **72** (2.5 mg) in 1 mL aqueous NaCl (0.505 M) (centre), partial hydrogel of compound **72** (2.5 mg) in 1 mL of aqueous Na_2CO_3 (0.505 M) (right).

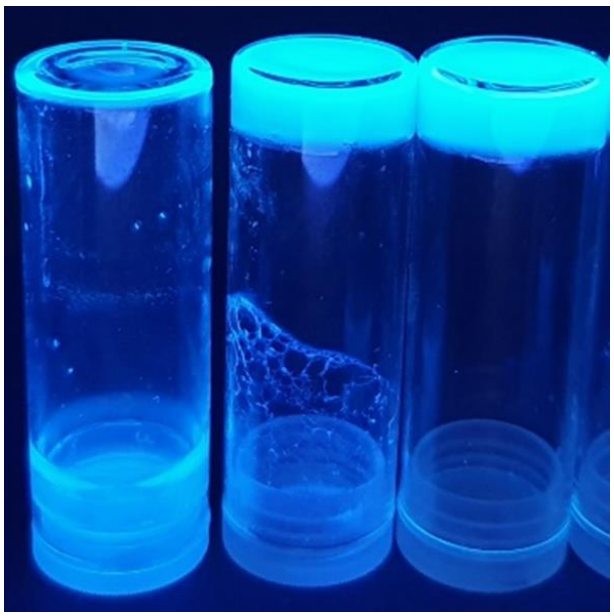

Figure S322 - Compound **72** (5 mg) in 1 mL of H_2O (left) hydrogel of compound **72** (5 mg) in 1 mL aqueous NaCl (0.505 M) (centre), hydrogel of compound **72** (5 mg) in 1 mL of aqueous $NaNO_3$ (0.505 M) (right).

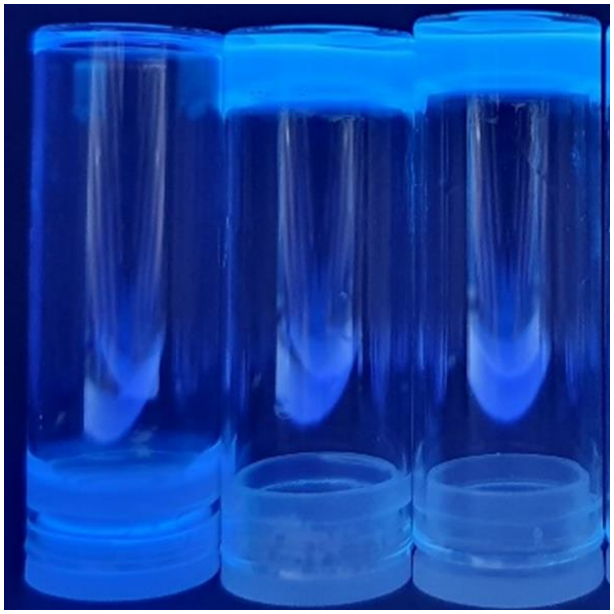

Figure S323 - Compound **72** (1.5 mg) in 1 mL of H_2O (left), hydrogel of compound **72** at MGC (1.5 mg) in 1 mL aqueous NaCl (0.505 M) (centre), hydrogel of compound **72** at MGC (1.5 mg) in 1 mL of aqueous $NaNO_3$ (0.505 M) (right).

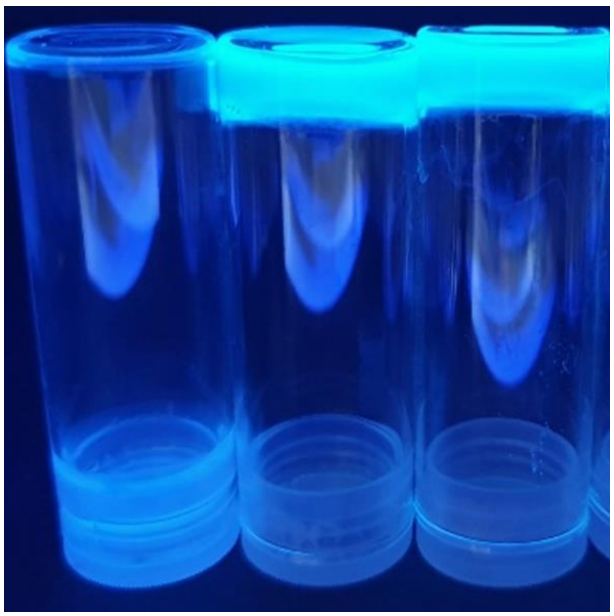

Figure S324 - Compound **72** (1 mg) in 1 mL of H_2O (left), partial hydrogel of compound **72** (1 mg) in 1 mL aqueous NaCl (0.505 M) (centre), partial hydrogel of compound **72** (1 mg) in 1 mL of aqueous $NaNO_3$ (0.505 M) (right).

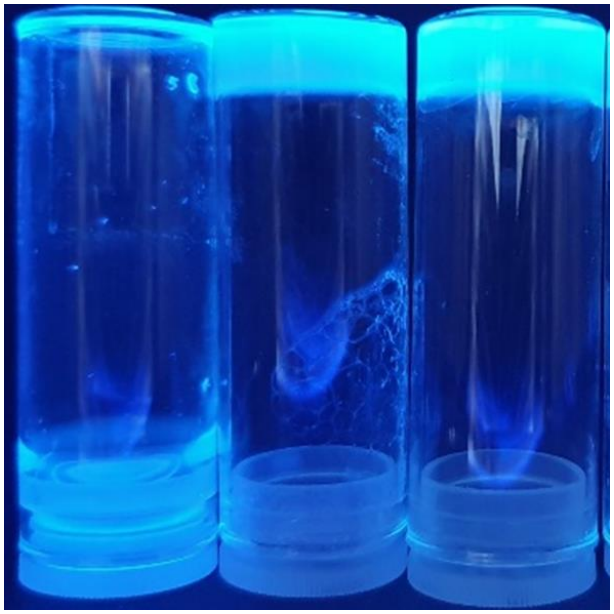

Figure S325 - Compound **72** (5 mg) in 1 mL of H_2O (left) hydrogel of compound **72** (5 mg) in 1 mL aqueous NaCl (0.505 M) (centre), hydrogel of compound **72** (5 mg) in 1 mL of aqueous NaOBz (0.505 M) (right).

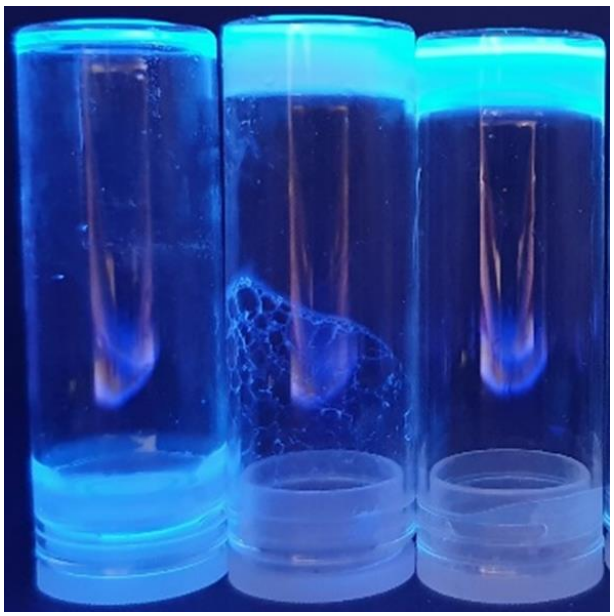

Figure S326 - Compound **72** (1.5 mg) in 1 mL of H_2O (left), hydrogel of compound **72** at MGC (1.5 mg) in 1 mL aqueous NaCl (0.505 M) (centre), hydrogel of compound **72** at MGC (1.5 mg) in 1 mL of aqueous NaOBz (0.505 M) (right).

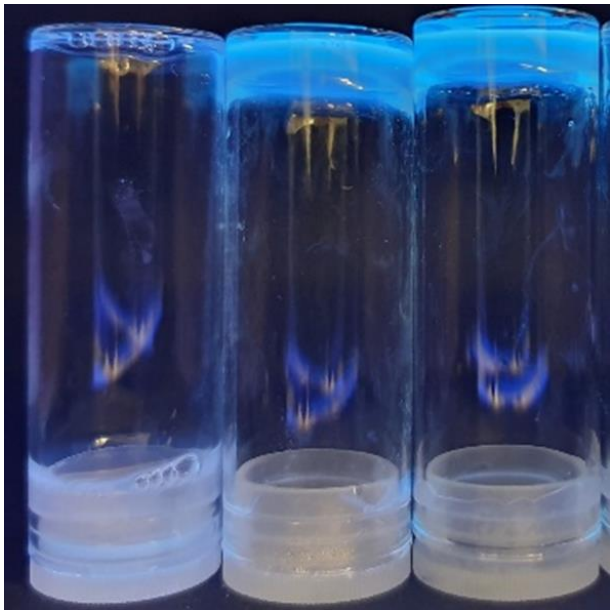

Figure S327 - Compound **72** (1 mg) in 1 mL of H_2O (left), partial hydrogel of compound **72** (1 mg) in 1 mL aqueous NaCl (0.505 M) (centre), partial hydrogel of compound **72** (1 mg) in 1 mL of aqueous NaOBz (0.505 M) (right).

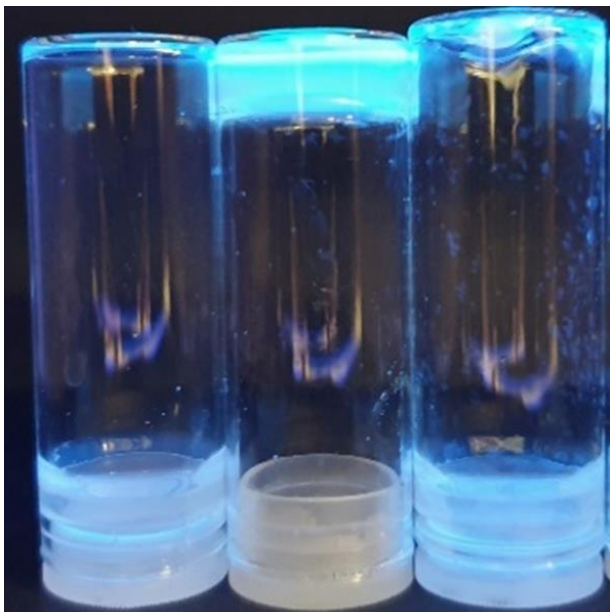

Figure S328 - Compound **72** (5 mg) in 1 mL of H_2O (left) hydrogel of compound **72** (5 mg) in 1 mL aqueous NaCl (0.505 M) (centre), partial hydrogel of compound **72** (5 mg) in 1 mL of aqueous Na_2HPO_4 (0.505 M) (right).

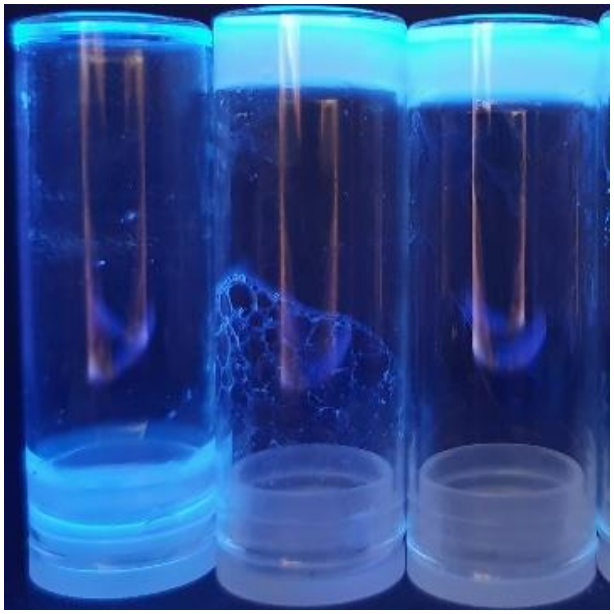

Figure S329 - Compound **72** (5 mg) in 1 mL of H_2O (left) hydrogel of compound **72** (5 mg) in 1 mL aqueous NaCl (0.505 M) (centre), hydrogel of compound **72** (5 mg) in 1 mL of aqueous Na_2SO_4 (0.505 M) (right).

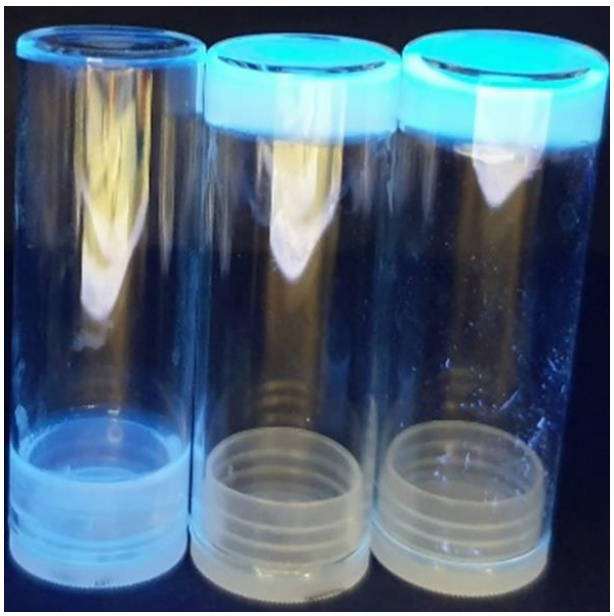

Figure S330 - Compound **72** (3.5 mg) in 1 mL of H_2O (left), hydrogel of compound **72** (3.5 mg) in 1 mL aqueous NaCl (0.505 M) (centre), hydrogel of compound **72** at MGC (3.5 mg) in 1 mL of aqueous Na_2SO_4 (0.505 M) (right).

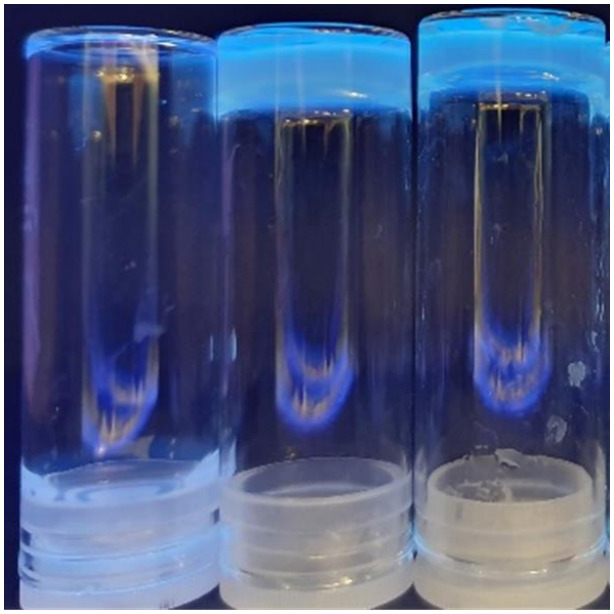

Figure S331 - Compound **72** (3 mg) in 1 mL of H_2O (left), hydrogel of compound **72** (3 mg) in 1 mL aqueous NaCl (0.505 M) (centre), partial hydrogel of compound **72** (3 mg) in 1 mL of aqueous Na_2SO_4 (0.505 M) (right).

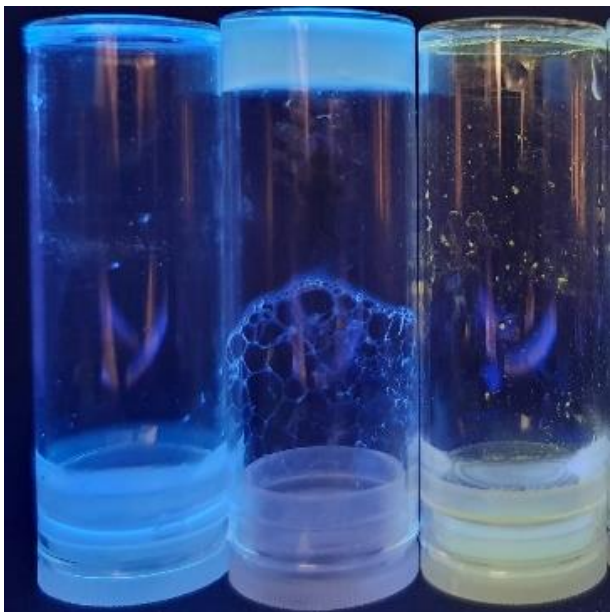

Figure S332 - Compound **72** (5 mg) in 1 mL of H_2O (left) hydrogel of compound **72** (5 mg) in 1 mL aqueous NaCl (0.505 M) (centre), compound **72** (5 mg) in 1 mL of aqueous $NaHSO_4$ (0.505 M) (right).

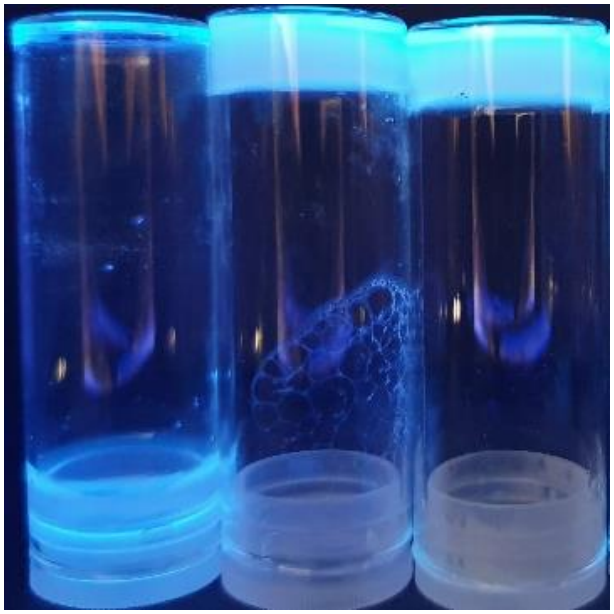

Figure S333 - Compound **72** (5 mg) in 1 mL of H_2O (left) hydrogel of compound **72** (5 mg) in 1 mL aqueous NaCl (0.505 M) (centre), hydrogel of compound **72** (5 mg) in 1 mL of aqueous $NaHCO_3$ (0.505 M) (right).

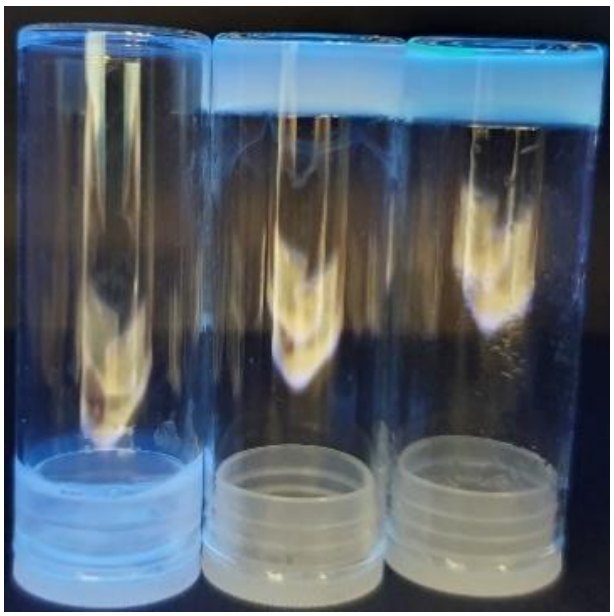

Figure S334 - Compound **72** (4 mg) in 1 mL of H_2O (left), hydrogel of compound **72** (4 mg) in 1 mL aqueous NaCl (0.505 M) (centre), hydrogel of compound **72** at MGC (4 mg) in 1 mL of aqueous $NaHCO_3$ (0.505 M) (right).

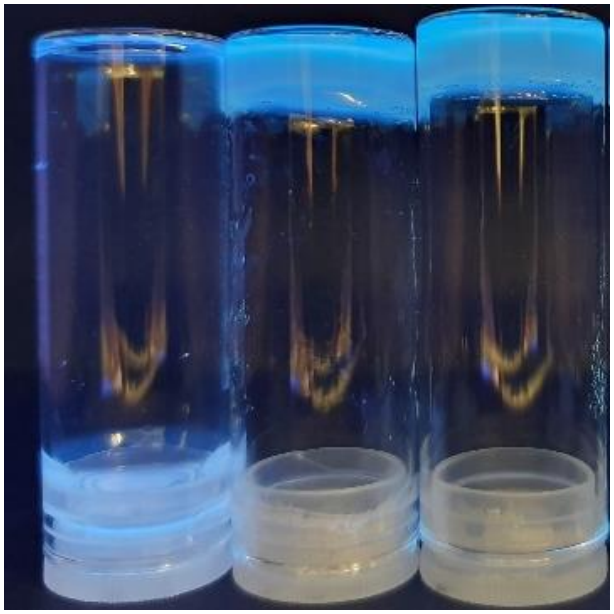

Figure S335 - Compound **72** (3.5 mg) in 1 mL of H_2O (left), hydrogel of compound **72** (3.5 mg) in 1 mL aqueous NaCl (0.505 M) (centre), partial hydrogel of compound **72** (3.5 mg) in 1 mL of aqueous $NaHCO_3$ (0.505 M) (right).

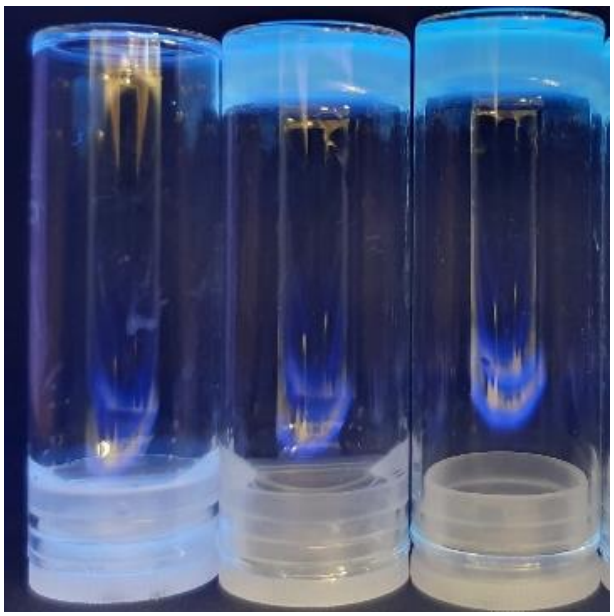

Figure S336 - Compound **72** (5 mg) in 1 mL of H_2O (left) hydrogel of compound **72** (5 mg) in 1 mL aqueous NaCl (0.505 M) (centre), hydrogel of compound **72** (5 mg) in 1 mL of aqueous NaOAc (0.505 M) (right).

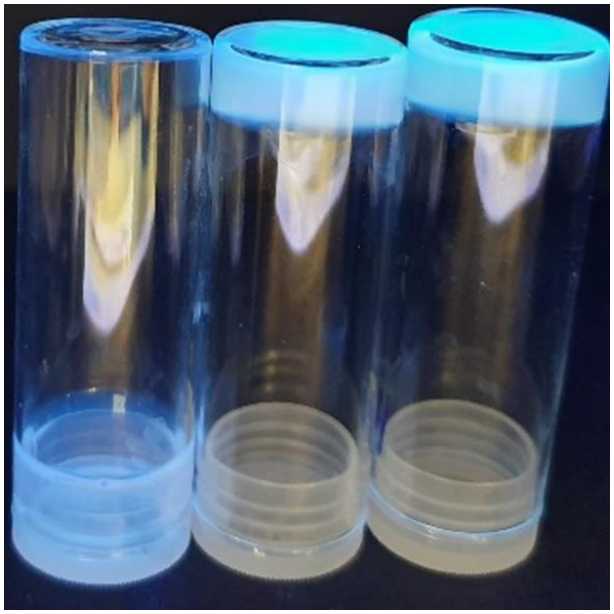

Figure S337 - Compound **72** (3.5 mg) in 1 mL of H_2O (left), hydrogel of compound **72** (3.5 mg) in 1 mL aqueous NaCl (0.505 M) (centre), hydrogel of compound **72** at MGC (3.5 mg) in 1 mL of aqueous NaOAc (0.505 M) (right).

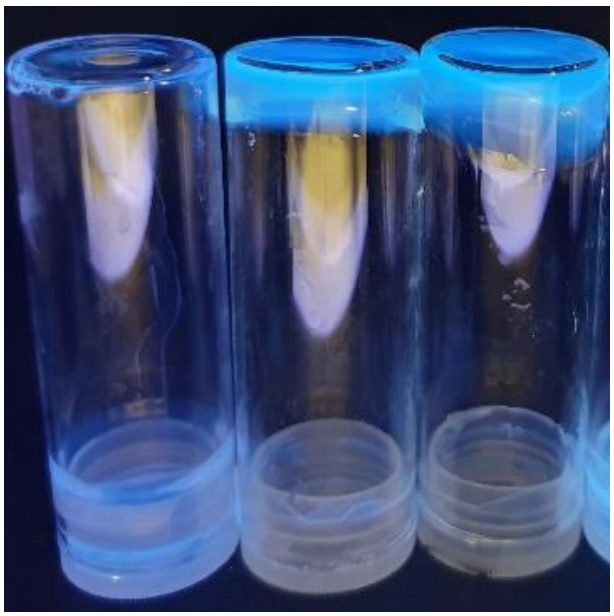

Figure S338 - Compound **72** (3 mg) in 1 mL of H_2O (left), hydrogel of compound **72** (3 mg) in 1 mL aqueous NaCl (0.505 M) (centre), partial hydrogel of compound **72** (3 mg) in 1 mL of aqueous NaOAc (0.505 M) (right).

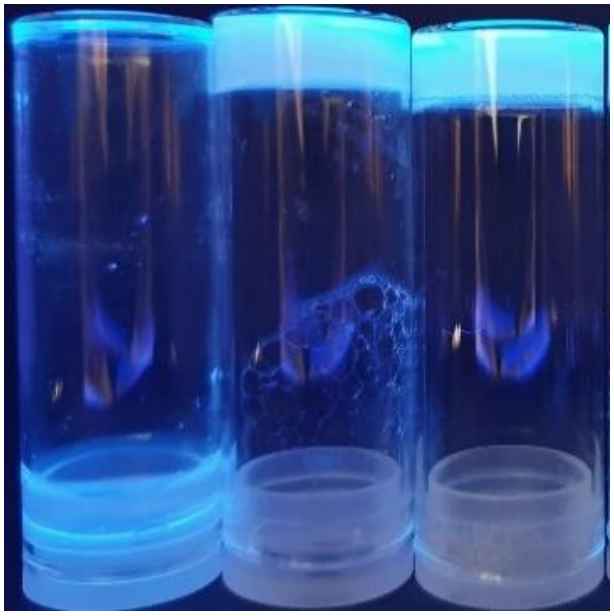

Figure S339 - Compound **72** (5 mg) in 1 mL of H_2O (left) hydrogel of compound **72** (5 mg) in 1 mL aqueous NaCl (0.505 M) (centre), hydrogel of compound **72** (5 mg) in 1 mL of aqueous NaF (0.505 M) (right).

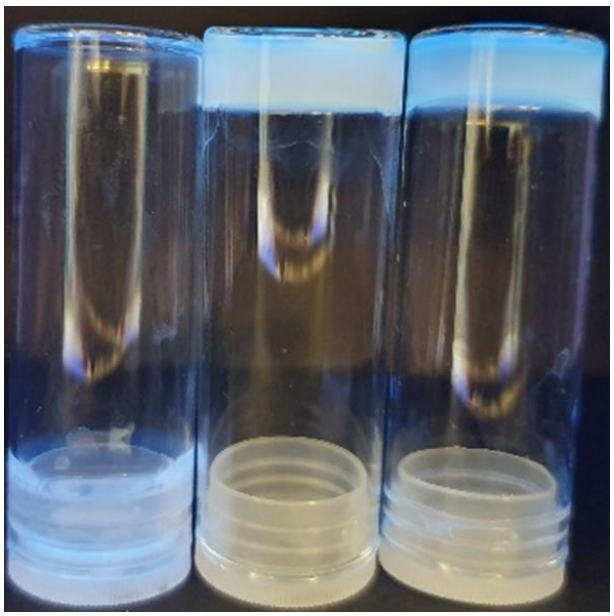

Figure S340 - Compound **72** (2 mg) in 1 mL of H_2O (left), hydrogel of compound **72** (2 mg) in 1 mL aqueous NaCl (0.505 M) (centre), hydrogel of compound **72** at MGC (2 mg) in 1 mL of aqueous NaF (0.505 M) (right).

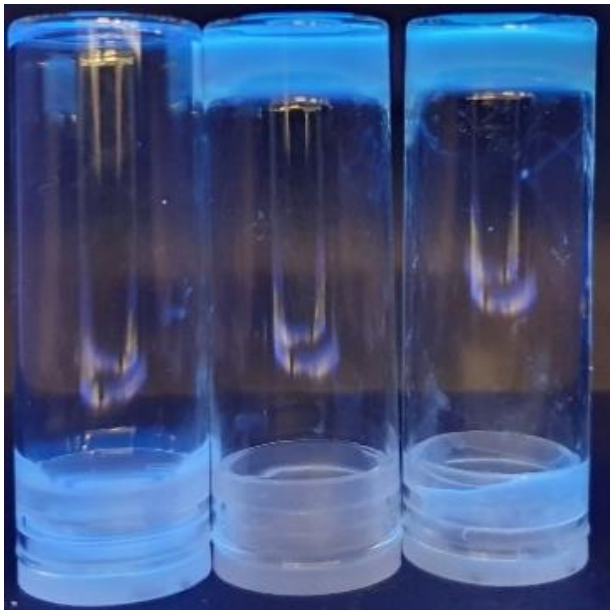

Figure S341 - Compound **72** (1.5 mg) in 1 mL of H_2O (left), hydrogel of compound **72** (1.5 mg) in 1 mL aqueous NaCl (0.505 M) (centre), partial hydrogel of compound **72** (1.5 mg) in 1 mL of aqueous NaF (0.505 M) (right).

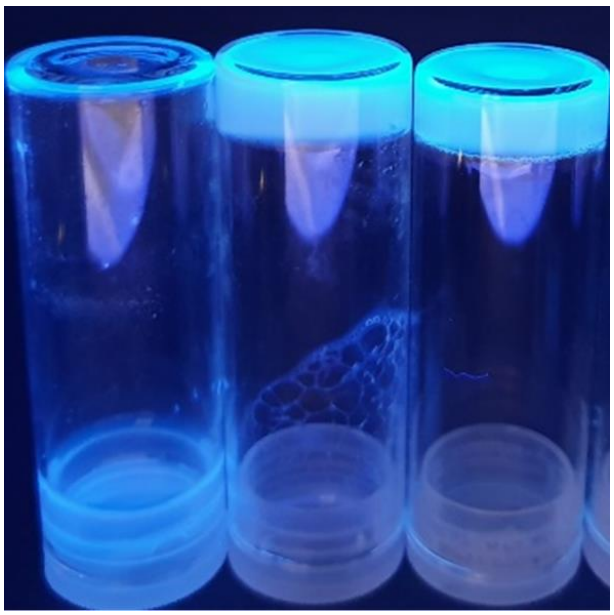

Figure S342 - Compound **72** (5 mg) in 1 mL of H_2O (left) hydrogel of compound **72** (5 mg) in 1 mL aqueous NaCl (0.505 M) (centre), hydrogel of compound **72** (5 mg) in 1 mL of aqueous KCl (0.505 M) (right).

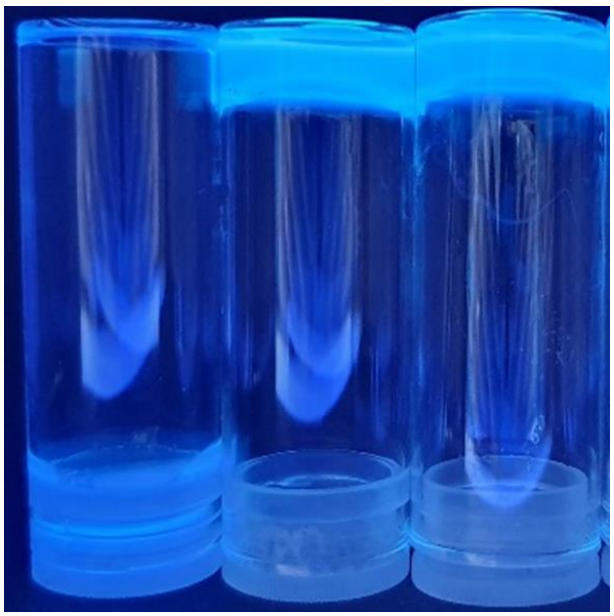

Figure S343 - Compound **72** (2.5 mg) in 1 mL of H_2O (left), hydrogel of compound **72** (2.5 mg) in 1 mL aqueous NaCl (0.505 M) (centre), hydrogel of compound **72** at MGC (2.5 mg) in 1 mL of aqueous KCl (0.505 M) (right).

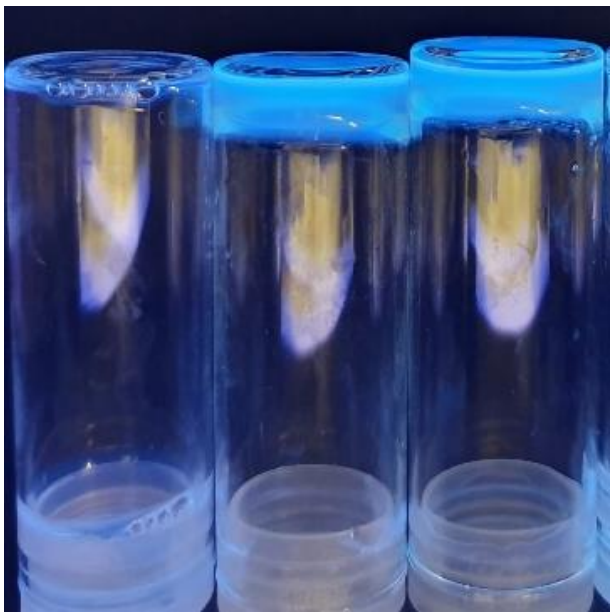

Figure S344 - Compound **72** (2 mg) in 1 mL of H_2O (left), hydrogel of compound **72** (2 mg) in 1 mL aqueous NaCl (0.505 M) (centre), partial hydrogel of compound **72** (2 mg) in 1 mL of aqueous KCl (0.505 M) (right).

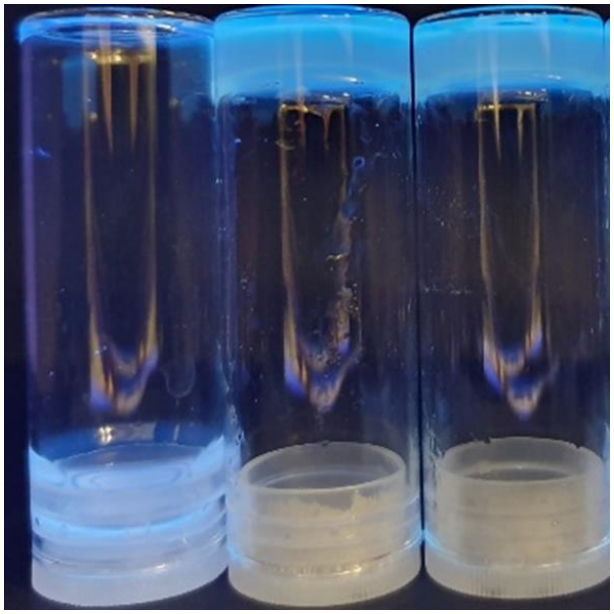

Figure S345 - Compound **72** (5 mg) in 1 mL of H_2O (left) hydrogel of compound **72** (5 mg) in 1 mL aqueous NaCl (0.505 M) (centre), hydrogel of compound **72** (5 mg) in 1 mL of aqueous RbCl (0.505 M) (right).

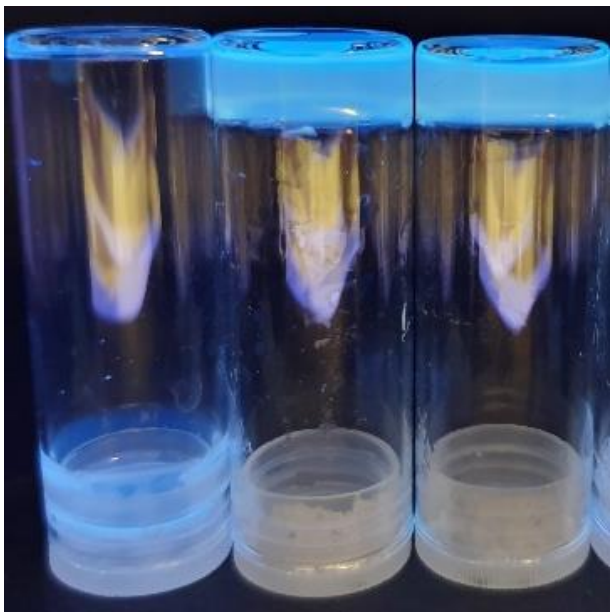

Figure S346 - Compound **72** (3.5 mg) in 1 mL of H_2O (left), hydrogel of compound **72** (3.5 mg) in 1 mL aqueous NaCl (0.505 M) (centre), hydrogel of compound **72** at MGC (3.5 mg) in 1 mL of aqueous RbCl (0.505 M) (right).

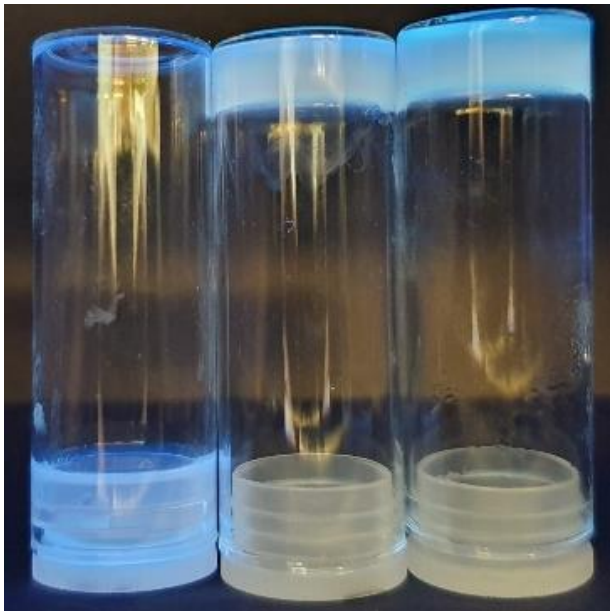

Figure S347 - Compound **72** (3 mg) in 1 mL of H_2O (left), hydrogel of compound **72** (3 mg) in 1 mL aqueous NaCl (0.505 M) (centre), partial hydrogel of compound **72** (3 mg) in 1 mL of aqueous RbCl (0.505 M) (right).

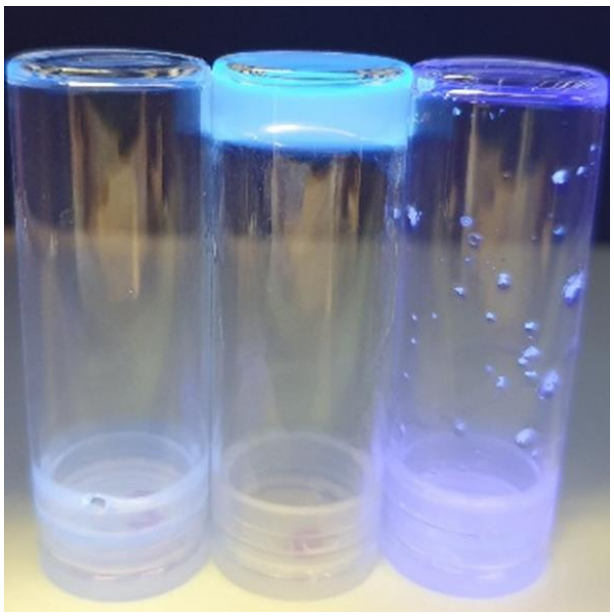

Figure S348 - Compound **72** (5 mg) in 1 mL of H_2O (left) hydrogel of compound **72** (5 mg) in 1 mL aqueous NaCl (0.505 M) (centre), compound **72** (5 mg) in 1 mL of aqueous TBACl (0.505 M) (right).

Figure S349 - Compound **72** (5 mg) in 1 mL of aqueous NaCl on a 1:1 molar ratio with ampicillin (**105**)

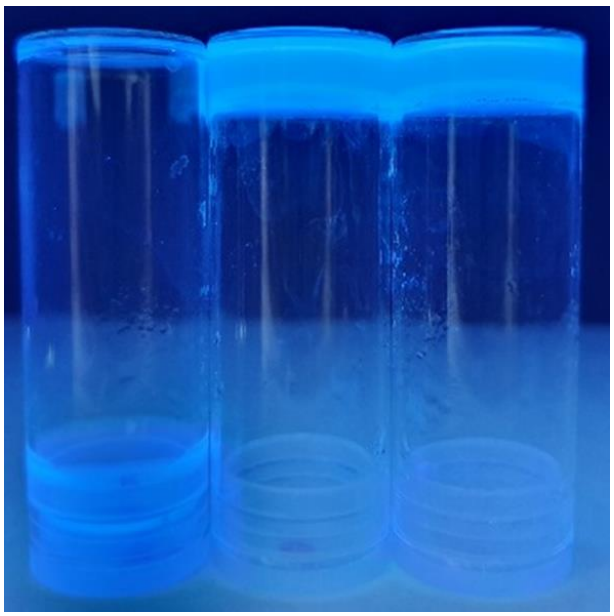

Figure S350 - Compound **72** (1.5 mg) in 1 mL of H_2O (left), hydrogel of compound **72** at MGC (1.5 mg) in 1 mL aqueous NaCl (0.505 M) (centre), hydrogel of compound **72** (1.5 mg) on a 1:1 molar ratio with ampicillin (**105**) in 1 mL of aqueous NaCl (0.505 M) (right).

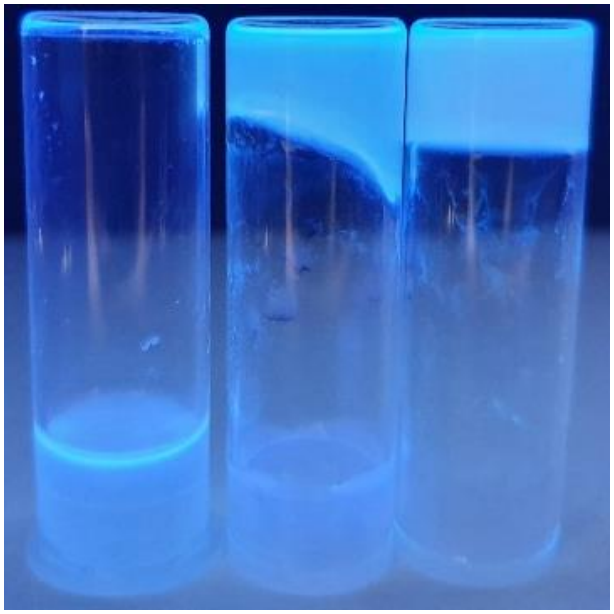

Figure S351 - Compound **72** (1 mg) in 1 mL of H_2O (left), partial hydrogel of compound **72** (1 mg) in 1 mL aqueous NaCl (0.505 M) (centre), hydrogel of compound **72** (1 mg) on a 1:1 molar ratio with ampicillin (**105**) in 1 mL of aqueous NaCl (0.505 M) (right).

2.3.1 Comparative overview

Table S12 - Summary of: average (*n*=3) salt solution (0.505 M) pH values obtained at 25 °C; average (*n*=3) aqueous solution formed by dissolving 2 g of the appropriate hydrogel in 20 mL of H_2O at 25 °C; average (*n*=3) melting point obtained for 1 mL of a hydrogel containing **72** (5 mg) and the appropriate aqueous salt solution (0.505 M); MGC determined though inversion testing for samples containing **72** and various aqueous salt solutions (0.505 M) at 25 °C.

Salt	pH (salt soln.)	pH (gel soln.)	T_m (° C)	MGC (mg/mL)
NaCl	7.00 ± 0.02	6.23 ± 0.02	51.23 ± 0.10	1.5
KCl	6.28 ± 0.02	6.16 ± 0.02	54.75 ± 0.09	2.5
RbCl	7.81 ± 0.02	6.63 ± 0.02	50.91 ± 0.18	3.5
TBACl	4.22 ± 0.02	[*b*]	[*b*]	[*d*]
NaF	8.82 ± 0.04	7.40 ± 0.03	46.91 ± 0.07	2.0
$NaHCO_3$	8.54 ± 0.04	10.03 ± 0.01	45.39 ± 0.12	4.0
NaOAc	7.76 ± 0.02	7.07 ± 0.02	46.03 ± 0.13	3.5
NaOBz	7.00 ± 0.04	5.76 ± 0.03	52.35 ± 0.09	1.5
$NaNO_3$	6.32 ± 0.01	6.74 ± 0.02	54.48 ± 0.15	1.5
NaH_2PO_4	4.01 ± 0.01	4.75 ± 0.03	43.94 ± 0.10	1.5
$NaHSO_4$	1.26 ± 0.03	[*b*]	[*b*]	[*d*]
Na_2CO_3	11.63 ± 0.03	11.40 ± 0.00	42.94 ± 0.13	3.0
Na_2HPO_4	8.49 ± 0.00	8.34 ± 0.00	[*c*]	[*c*]
Na_2SO_4	7.00 ± 0.02	6.92 ± 0.05	43.22 ± 0.12	3.5
NaCl/Amp[*a*]	7.00 ± 0.02	7.12 ± 0.02	52.26 ± 0.07	< 1.0[*e*]

[*a*] NaCl supplied as an aqueous solution 0.505 M, ampicillin (**105**) supplied in a 1:1 molar ratio with **72**; [*b*] precipitate formation prevented measurement; [*c*] partial gel formed at 5 mg/mL; [*d*] precipitation at 5 mg/mL, no gel formation; and [*e*] refers to **72** only.

2.4 Rheological data

2.4.1 Amplitude sweep

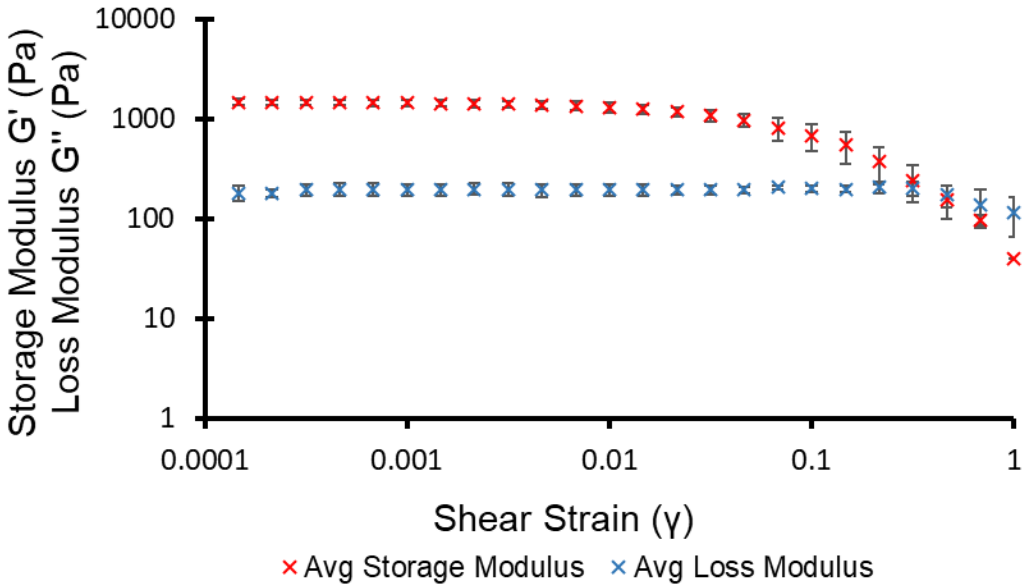

Figure S352 – Graph showing average results (*n*=3) from amplitude sweep experiments used to define the linear viscoelastic region of the sample at 298.15 K. Compound **72** (5 mg) in 1 mL aqueous NaCl (0.505 M) (1 = 100 %).

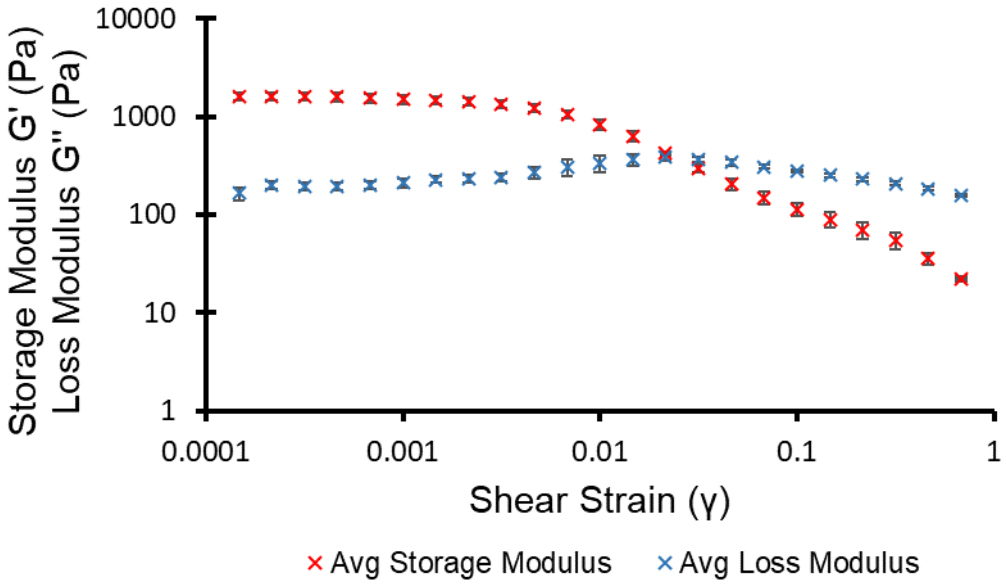

Figure S353 – Graph showing average results (*n*=3) from amplitude sweep experiments used to define the linear viscoelastic region of the sample at 298.15 K. Compound **72** (5 mg) in 1 mL aqueous NaH_2PO_4 (0.505 M) (1 = 100 %).

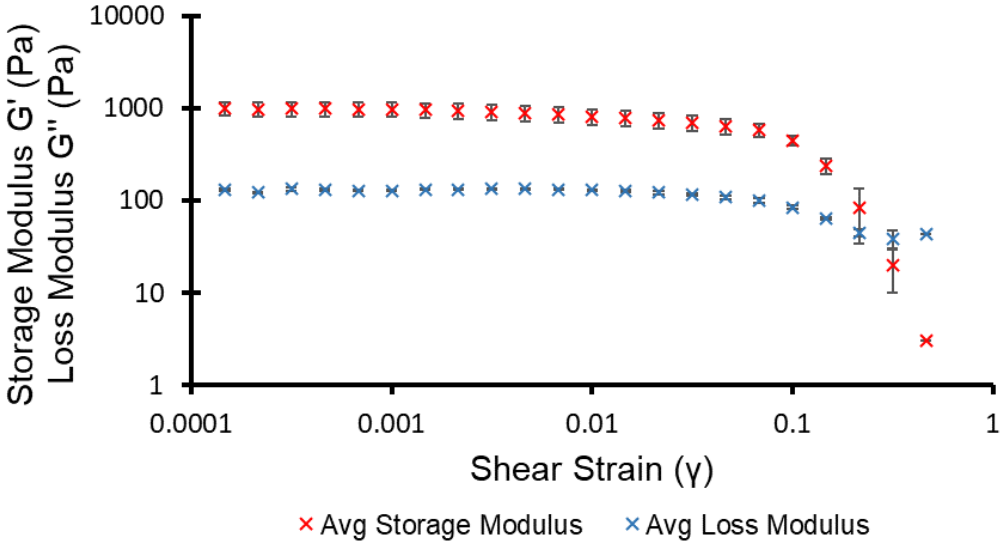

Figure S354 – Graph showing average results (*n*=3) from amplitude sweep experiments used to define the linear viscoelastic region of the sample at 298.15 K. Compound **72** (5 mg) in 1 mL aqueous Na_2CO_3 (0.505 M) (1 = 100 %).

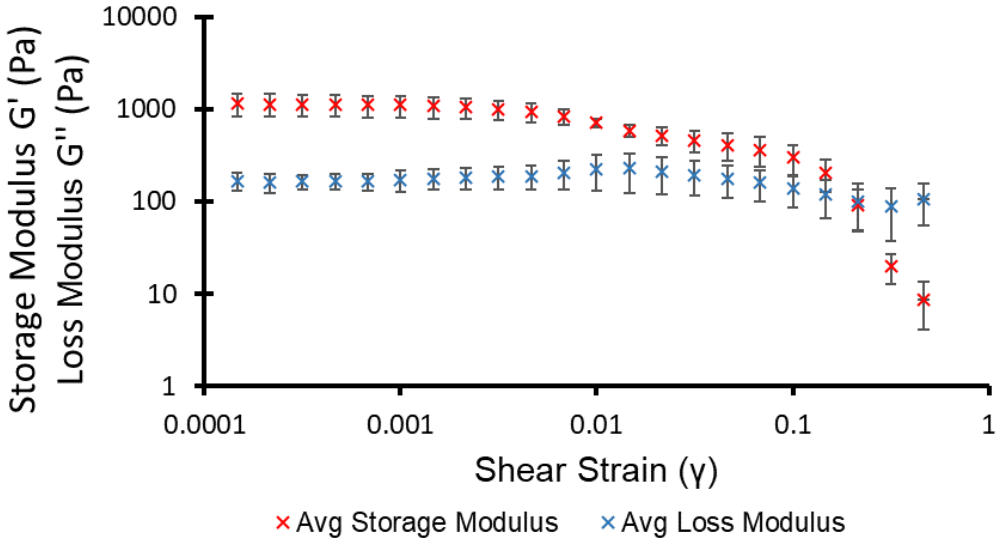

Figure S355 – Graph showing average results (*n*=3) from amplitude sweep experiments used to define the linear viscoelastic region of the sample at 298.15 K. Compound **72** (5 mg) in 1 mL aqueous $NaNO_3$ (0.505 M) (1 = 100 %).

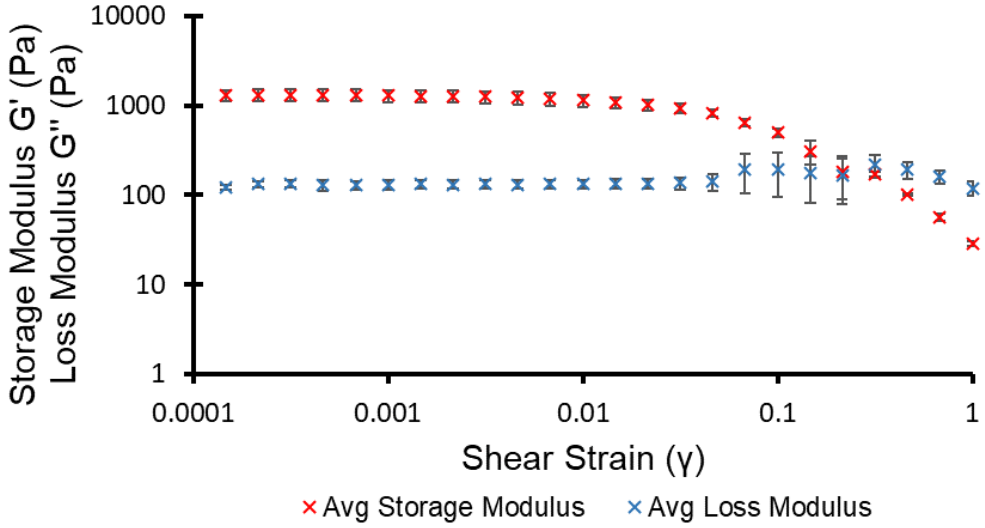

Figure S356 – Graph showing average results (*n*=3) from amplitude sweep experiments used to define the linear viscoelastic region of the sample at 298.15 K. Compound **72** (5 mg) in 1 mL aqueous NaOBz (0.505 M) (1 = 100 %).

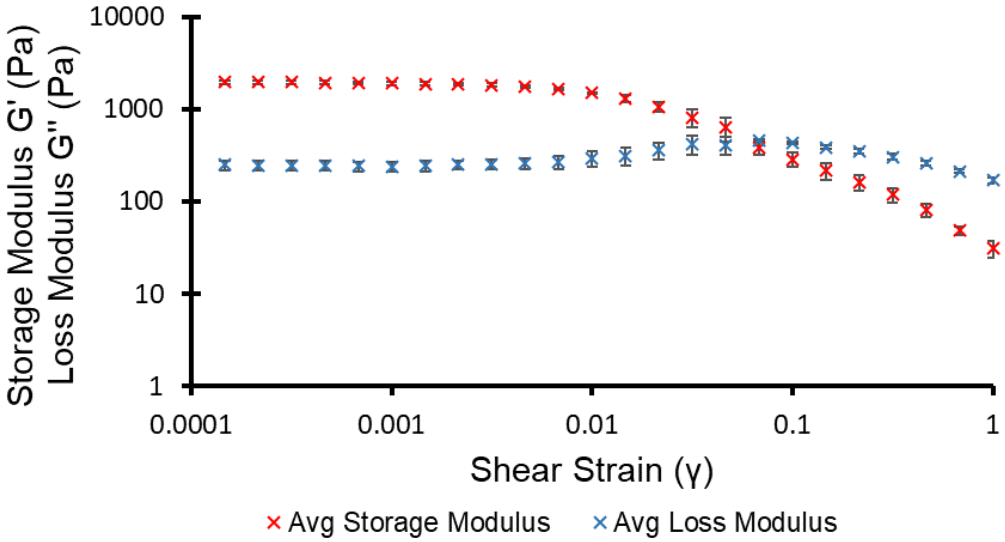

Figure S357 – Graph showing average results (*n*=3) from amplitude sweep experiments used to define the linear viscoelastic region of the sample at 298.15 K. Compound **72** (5 mg) in 1 mL aqueous Na_2SO_4 (0.505 M) (1 = 100 %).

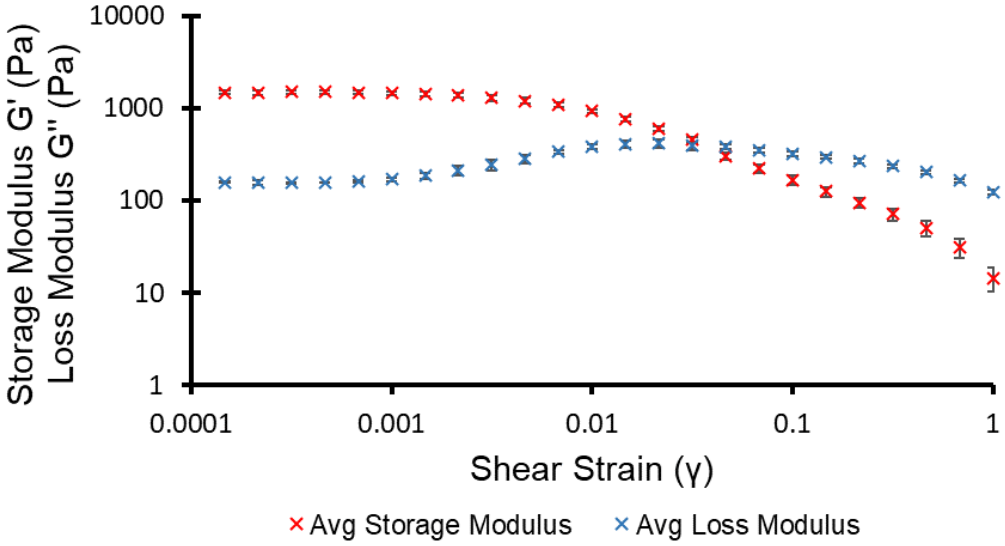

Figure S358 – Graph showing average results (*n*=3) from amplitude sweep experiments used to define the linear viscoelastic region of the sample at 298.15 K. Compound **72** (5 mg) in 1 mL aqueous $NaHCO_3$ (0.505 M) (1 = 100 %).

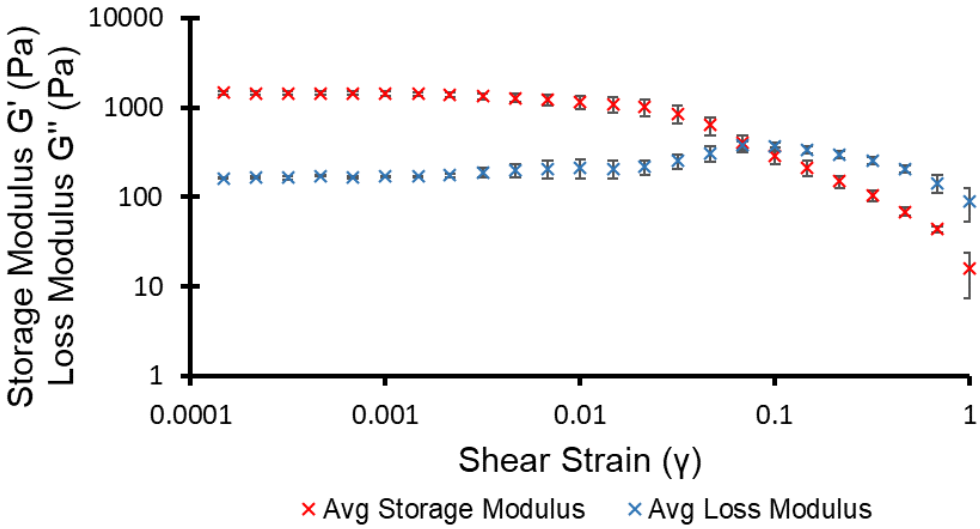

Figure S359 – Graph showing average results (*n*=3) from amplitude sweep experiments used to define the linear viscoelastic region of the sample at 298.15 K. Compound **72** (5 mg) in 1 mL aqueous NaOAc (0.505 M) (1 = 100 %).

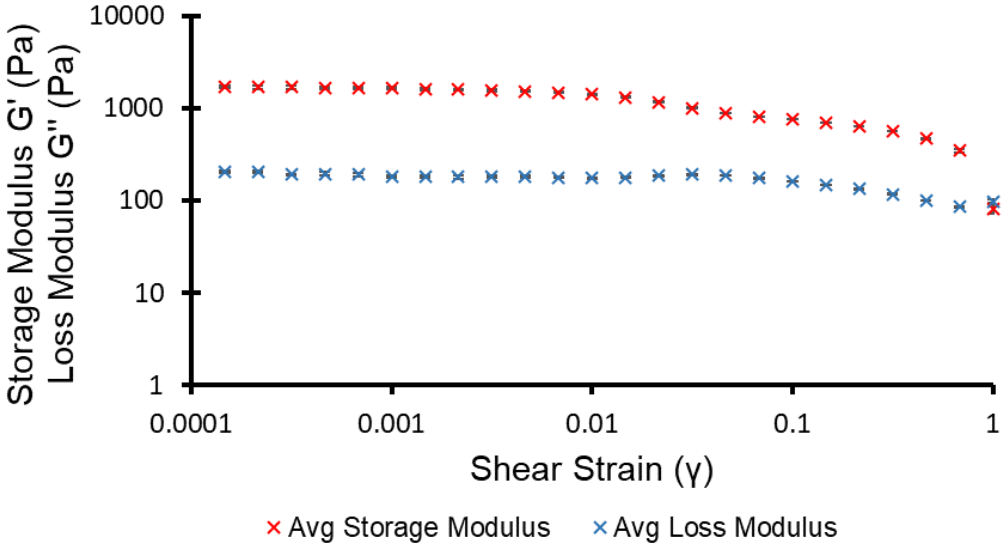

Figure S360 – Graph showing average results (*n*=3) from amplitude sweep experiments used to define the linear viscoelastic region of the sample at 298.15 K. Compound **72** (5 mg) in 1 mL aqueous NaF (0.505 M) (1 = 100 %).

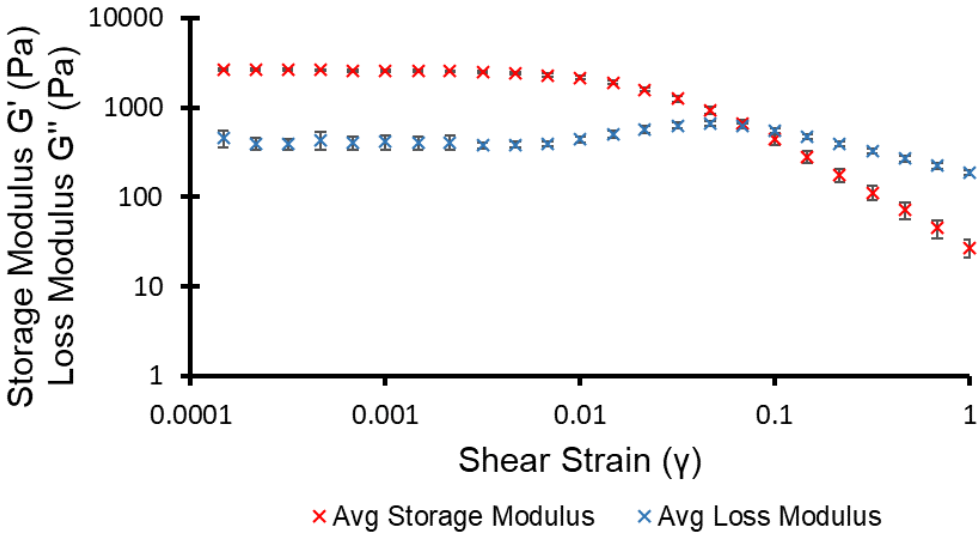

Figure S361 – Graph showing average results (*n*=3) from amplitude sweep experiments used to define the linear viscoelastic region of the sample at 298.15 K. Compound **72** (5 mg) in 1 mL aqueous KCl (0.505 M) (1 = 100 %).

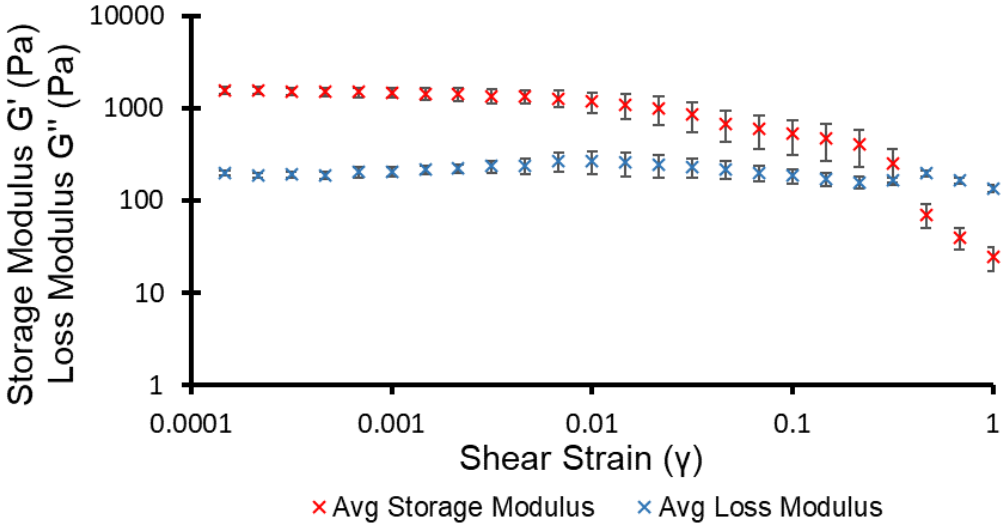

Figure S362 – Graph showing average results (*n*=3) from amplitude sweep experiments used to define the linear viscoelastic region of the sample at 298.15 K. Compound **72** (5 mg) in 1 mL aqueous RbCl (0.505 M) (1 = 100 %).

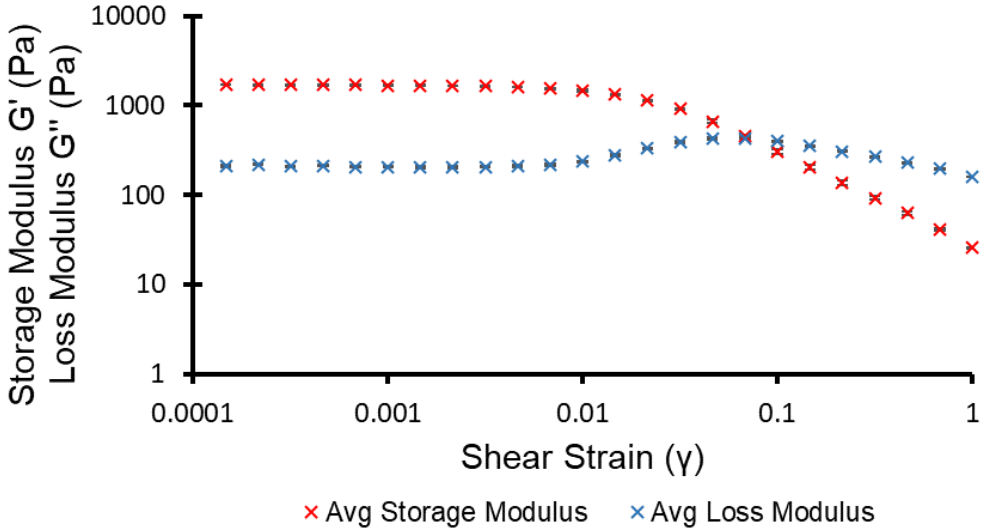

Figure S363 – Graph showing average results (*n*=3) from amplitude sweep experiments used to define the linear viscoelastic region of the sample at 298.15 K. Compound **72** (5 mg) and ampicillin (3 mg) in 1 mL aqueous NaCl (0.505 M) (1 = 100 %).

2.4.2 Frequency sweep

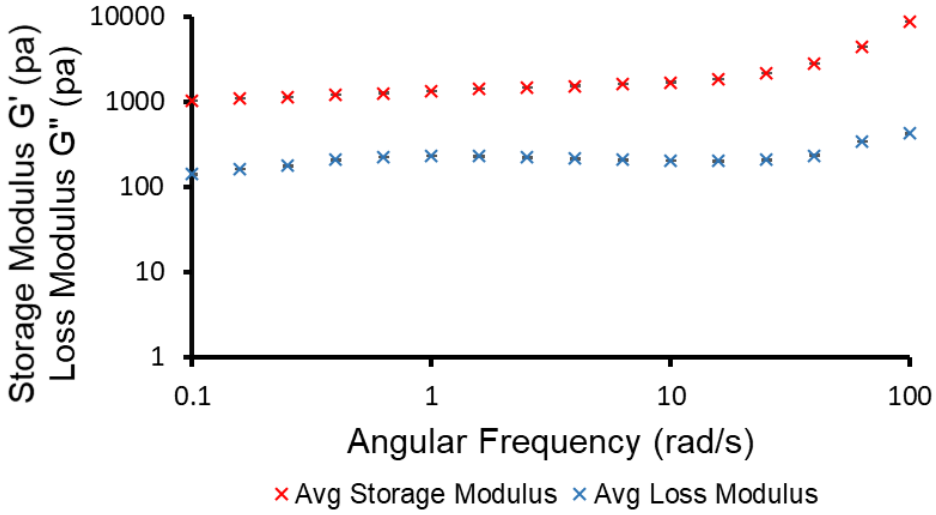

Figure S364 – Graph showing average results (*n*=3) from frequency sweep experiments obtained from the linear viscoelastic region under a constant shear strain (γ) of 0.925 % (298.15 K). Compound **72** (5 mg) in 1 mL aqueous NaCl (0.505 M).

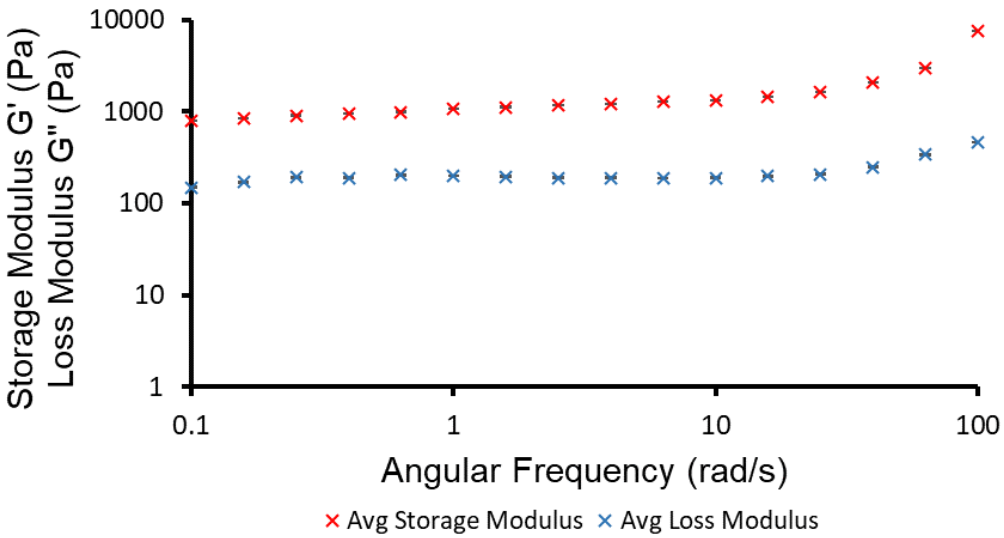

Figure S365 – Graph showing average results (*n*=3) from frequency sweep experiments obtained from the linear viscoelastic region under a constant shear strain (γ) of 0.925 % (298.15 K). Compound **72** (5 mg) in 1 mL aqueous NaH_2PO_4 (0.505 M).

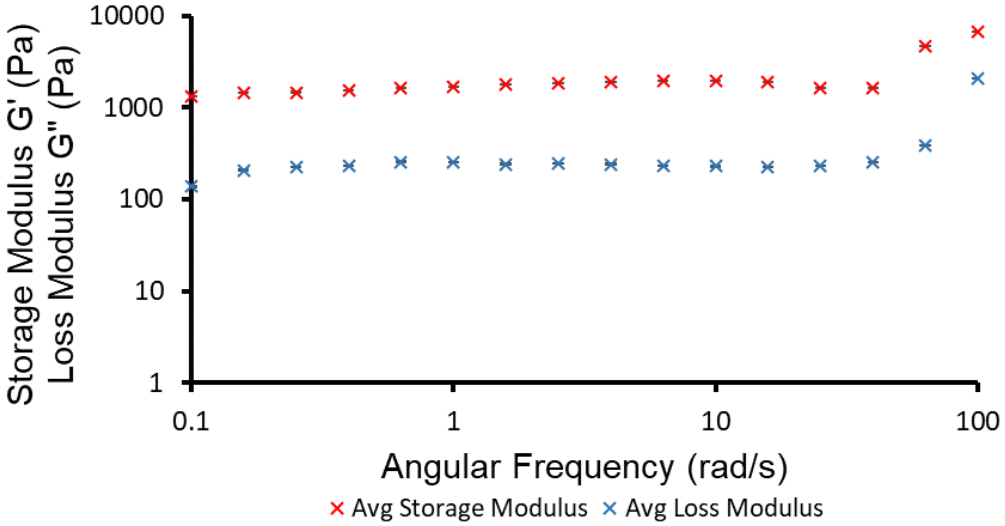

Figure S366 – Graph showing average results (*n*=3) from frequency sweep experiments obtained from the linear viscoelastic region under a constant shear strain (γ) of 0.925 % (298.15 K). Compound **72** (5 mg) in 1 mL aqueous Na_2CO_3 (0.505 M).

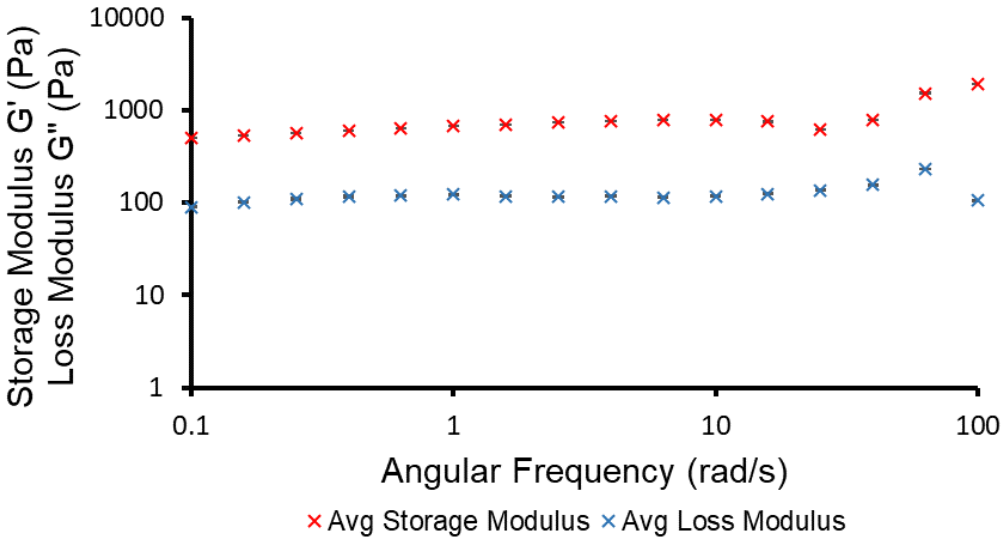

Figure S367 – Graph showing average results (*n*=3) from frequency sweep experiments obtained from the linear viscoelastic region under a constant shear strain (γ) of 0.925 % (298.15 K). Compound **72** (5 mg) in 1 mL aqueous $NaNO_3$ (0.505 M).

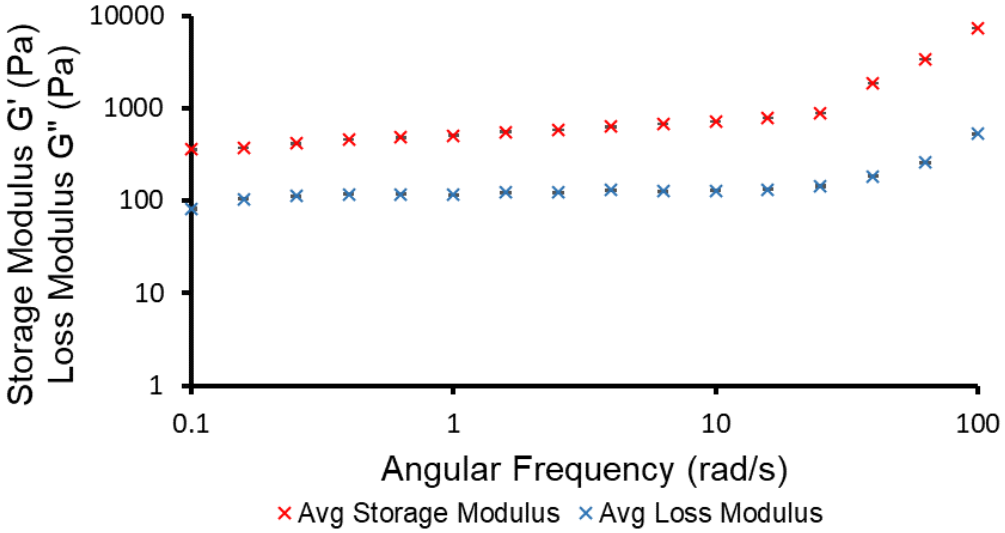

Figure S368 – Graph showing average results (*n*=3) from frequency sweep experiments obtained from the linear viscoelastic region under a constant shear strain (γ) of 0.925 % (298.15 K). Compound **72** (5 mg) in 1 mL aqueous NaOBz (0.505 M).

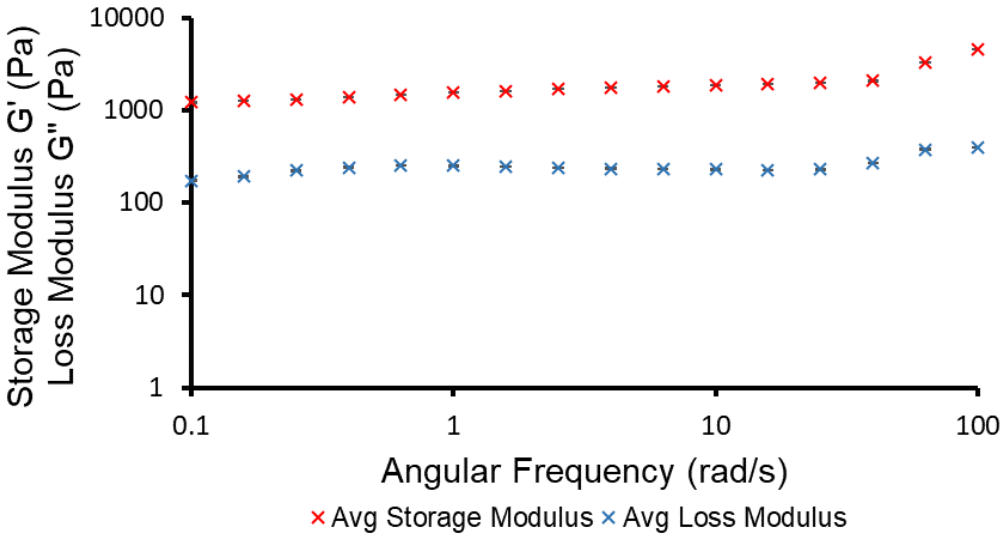

Figure S369 – Graph showing average results (*n*=3) from frequency sweep experiments obtained from the linear viscoelastic region under a constant shear strain (γ) of 0.925 % (298.15 K). Compound **72** (5 mg) in 1 mL aqueous Na_2SO_4 (0.505 M).

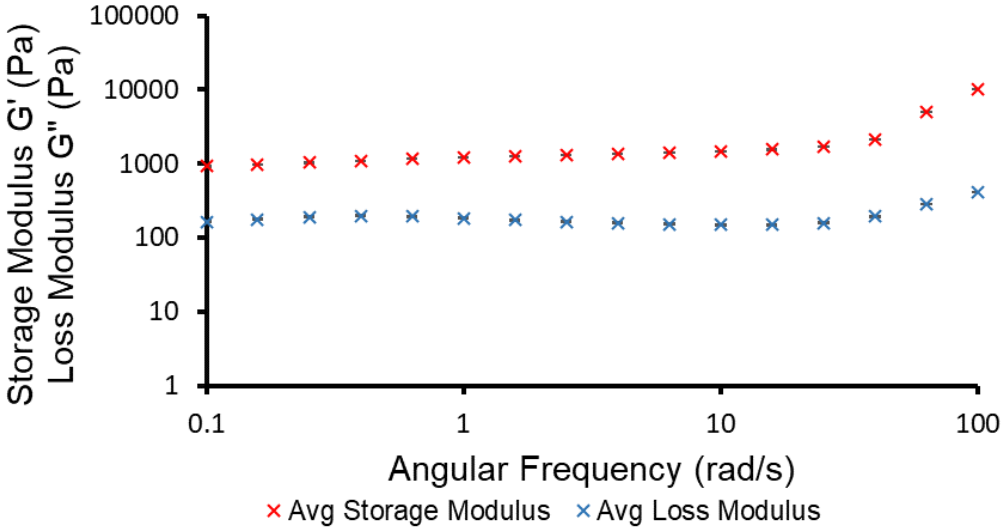

Figure S370 – Graph showing average results (*n*=3) from frequency sweep experiments obtained from the linear viscoelastic region under a constant shear strain (γ) of 0.925 % (298.15 K). Compound **72** (5 mg) in 1 mL aqueous $NaHCO_3$ (0.505 M).

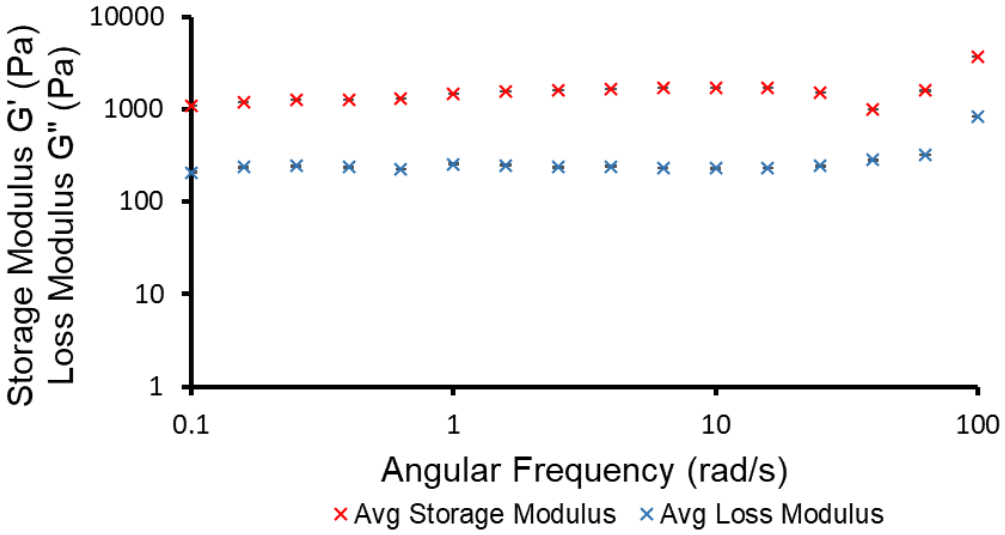

Figure S371 – Graph showing average results (*n*=3) from frequency sweep experiments obtained from the linear viscoelastic region under a constant shear strain (γ) of 0.925 % (298.15 K). Compound **72** (5 mg) in 1 mL aqueous NaOAc (0.505 M).

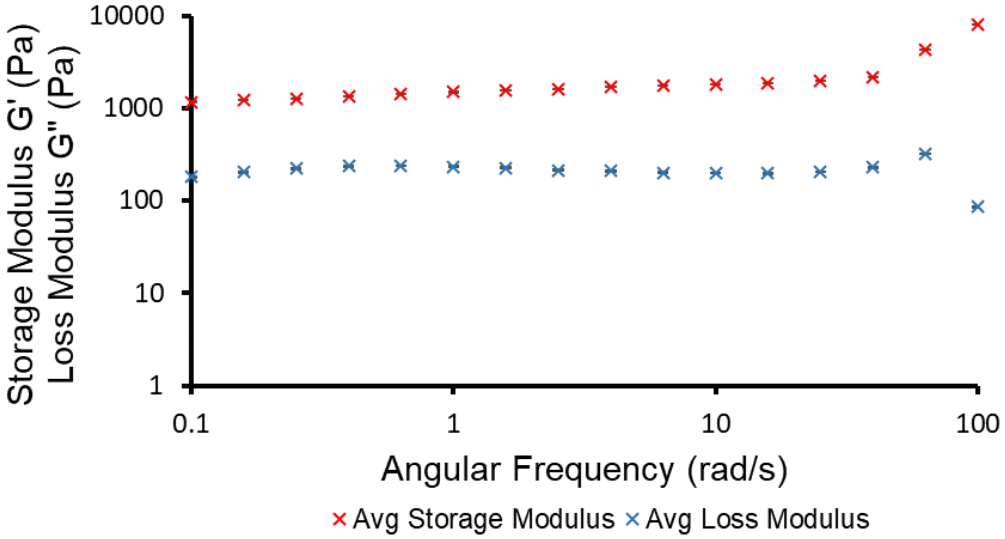

Figure S372 – Graph showing average results (*n*=3) from frequency sweep experiments obtained from the linear viscoelastic region under a constant shear strain (γ) of 0.925 % (298.15 K). Compound **72** (5 mg) in 1 mL aqueous NaF (0.505 M).

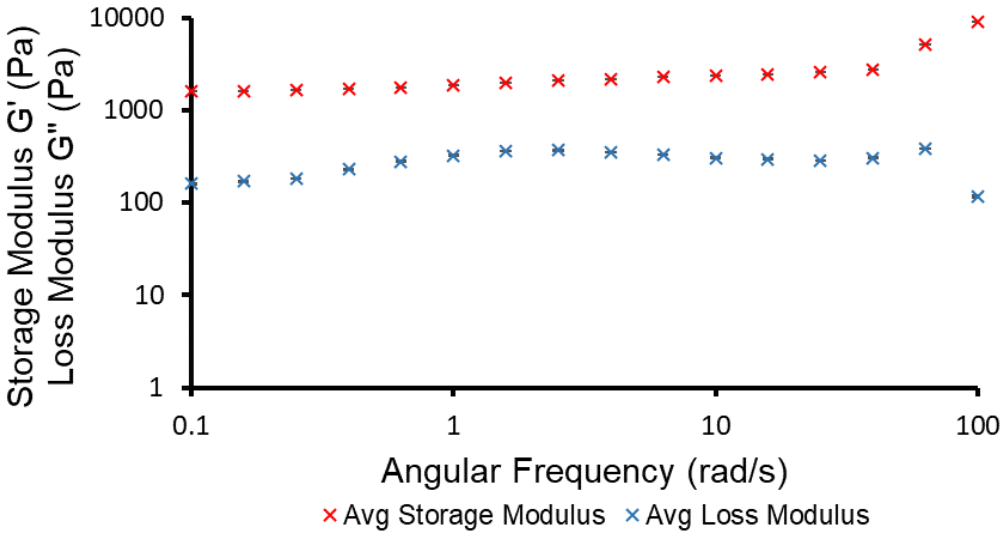

Figure S373 – Graph showing average results (*n*=3) from frequency sweep experiments obtained from the linear viscoelastic region under a constant shear strain (γ) of 0.925 % (298.15 K). Compound **72** (5 mg) in 1 mL aqueous KCl (0.505 M).

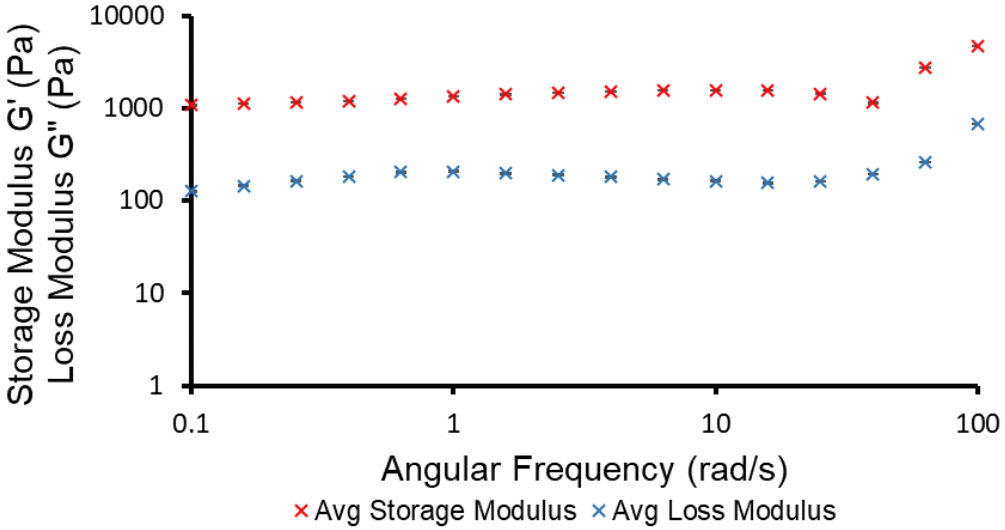

Figure S374 – Graph showing average results (*n*=3) from frequency sweep experiments obtained from the linear viscoelastic region under a constant shear strain (γ) of 0.925 % (298.15 K). Compound **72** (5 mg) in 1 mL aqueous RbCl (0.505 M).

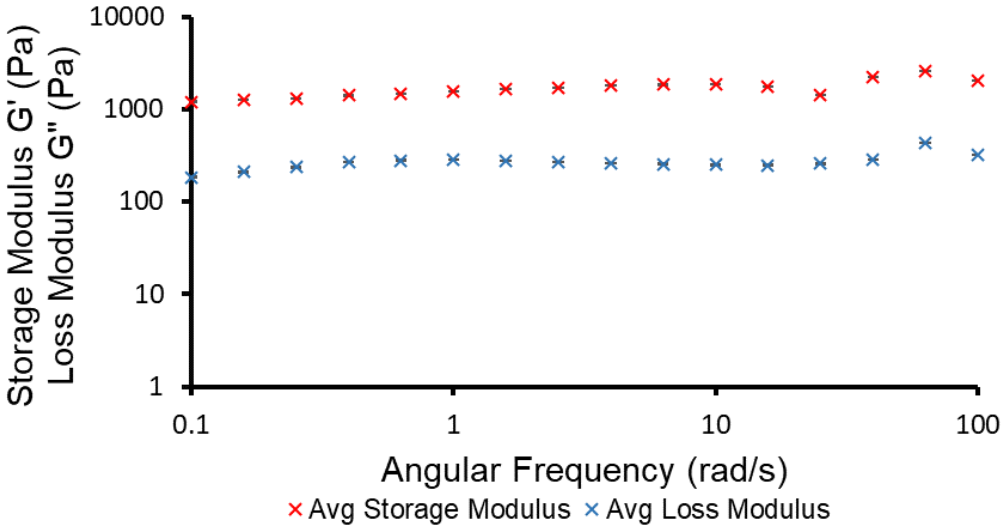

Figure S375 – Graph showing average results (*n*=3) from frequency sweep experiments obtained from the linear viscoelastic region under a constant shear strain (γ) of 0.925 % (298.15 K). Compound **72** (5 mg) and ampicillin (**105**) (3 mg) in 1 mL aqueous NaCl (0.505 M).

2.4.3 Comparative overview

Table S13 - Summary of rheological data for each hydrogel (hydrogel contains **72** (5 mg/mL) in the appropriate aqueous salt solution (0.505 M)). Characterisation experiments were performed at 25 °C: average gel/sol transition points obtained from *n*=3 shear strain (γ) amplitude sweeps; average storage (G') and loss (G'') moduli obtained from *n*=3 angular frequency sweeps (γ = 0.1 %).

Salt	Gel-Sol transition γ (%)	Storage modulus G' (Pa)	Error (Pa)	Loss modulus G'' (Pa)	Error (Pa)
NaCl	46.4	1307	± 11	202	± 12
KCl	6.8	1867	± 74	274	± 12
RbCl	46.4	1308	± 85	176	± 9
NaF	100.0	1448	± 70	216	± 11
$NaHCO_3$	4.6	1166	± 54	175	± 14
NaOAc	100.0	1409	± 65	235	± 39
NaOBz	21.5	503	± 23	115	± 7
$NaNO_3$	21.5	650	± 21	112	± 8
NaH_2PO_4	3.2	1117	± 37	192	± 10
Na_2CO_3	31.6	1653	± 28	226	± 20
Na_2SO_4	6.8	1503	± 130	228	± 18
NaCl/Amp[a]	6.8	1521	± 3	252	± 2

[*a*] NaCl supplied as an aqueous solution 0.505 M, ampicillin (**105**) supplied in a 1:1 molar ratio with **72**.

2.5 Microscopy and energy dispersive X-ray analysis

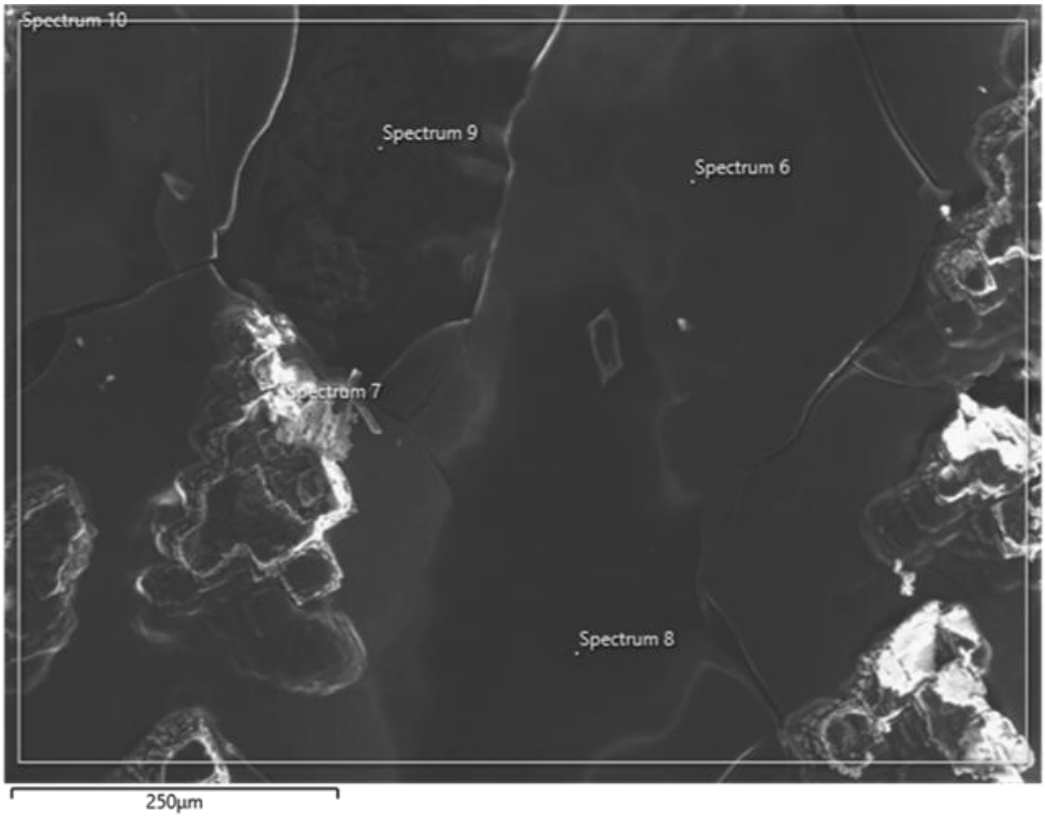

Figure S376 – Scanning electron microscopy image of a xerogel prepared from a dehydrated hydrogel containing compound **72** (5 mg/mL) in aqueous NaCl (0.505 M).

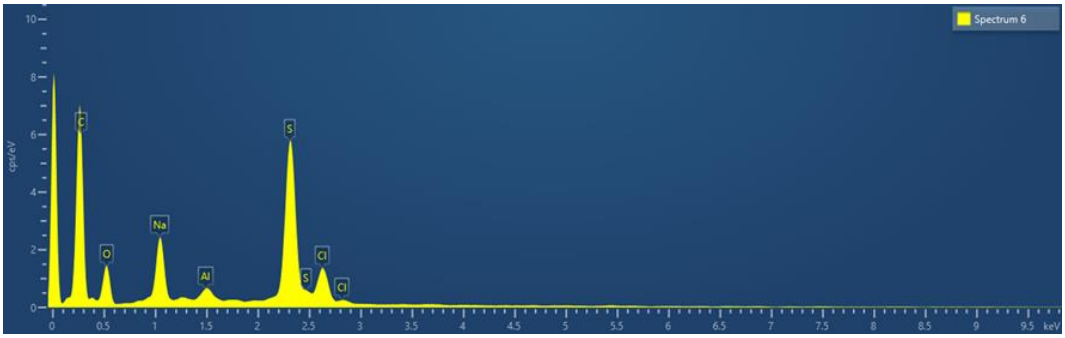

Figure S377 – Energy-dispersive X-ray spectrum showing elemental analysis of the xerogel imaged in Figure S376.

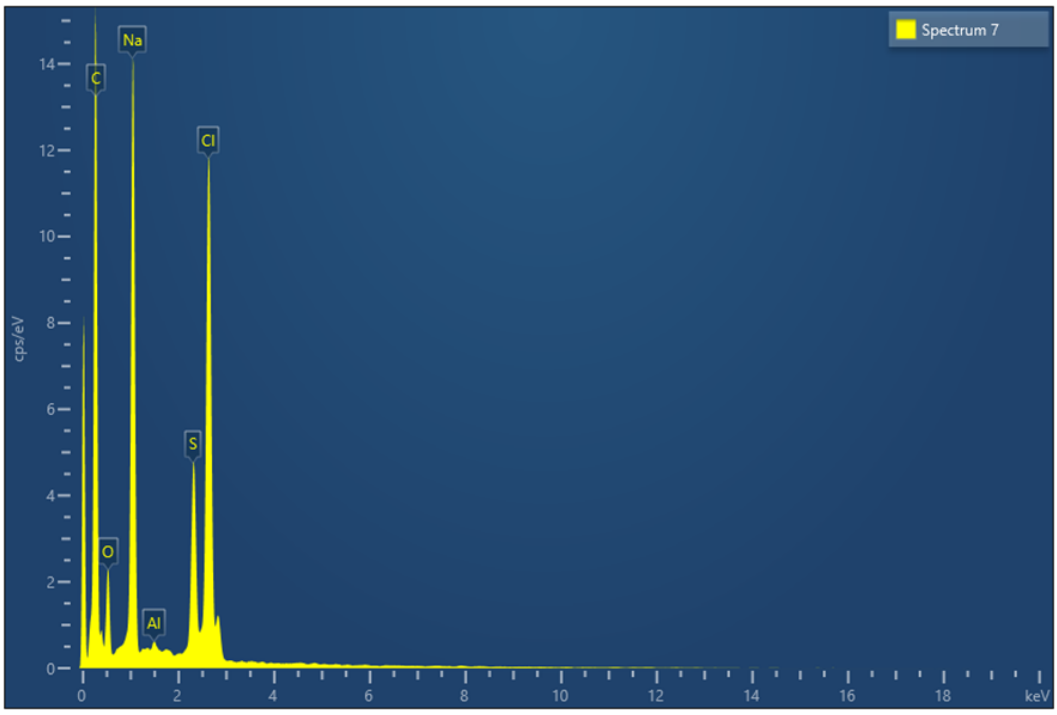

Figure S378 – Energy-dispersive X-ray spectrum showing elemental analysis of the xerogel imaged in Figure S376.

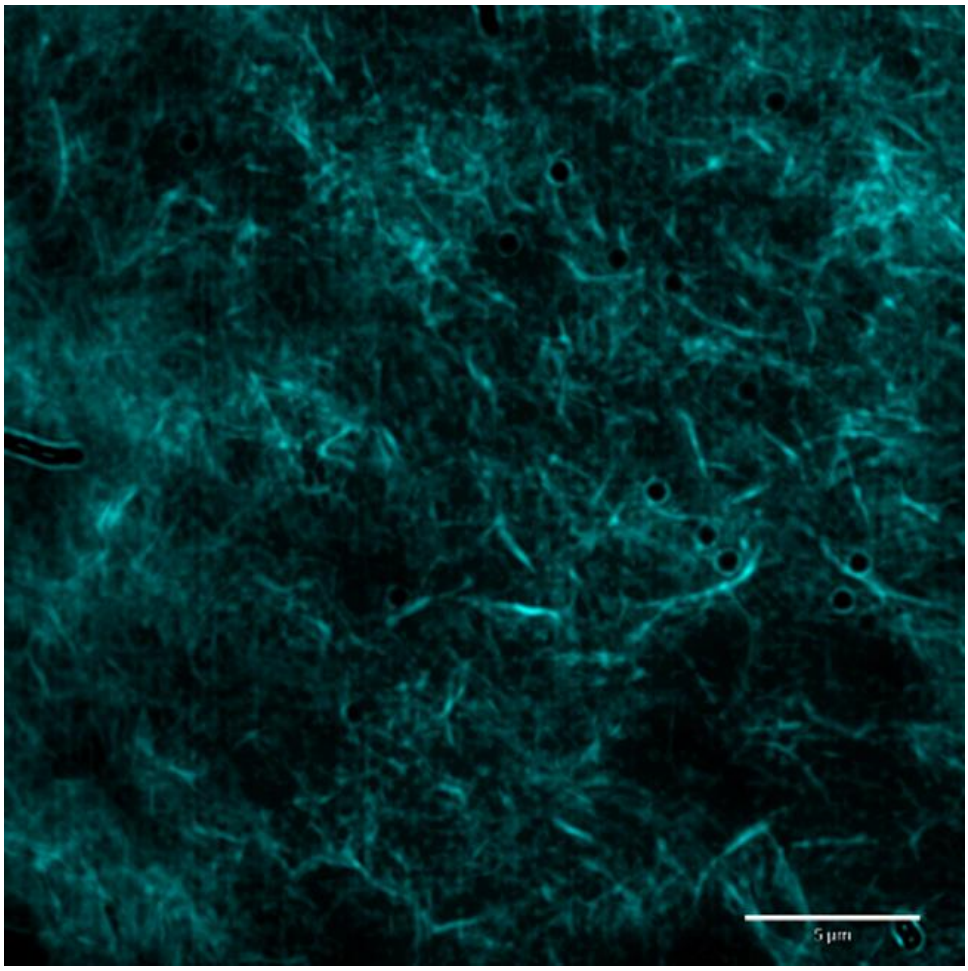

Figure S379 – Fluorescence microscopy image of a hydrogel containing compound **72** (5 mg/ mL) in aqueous NaCl (0.505 M).

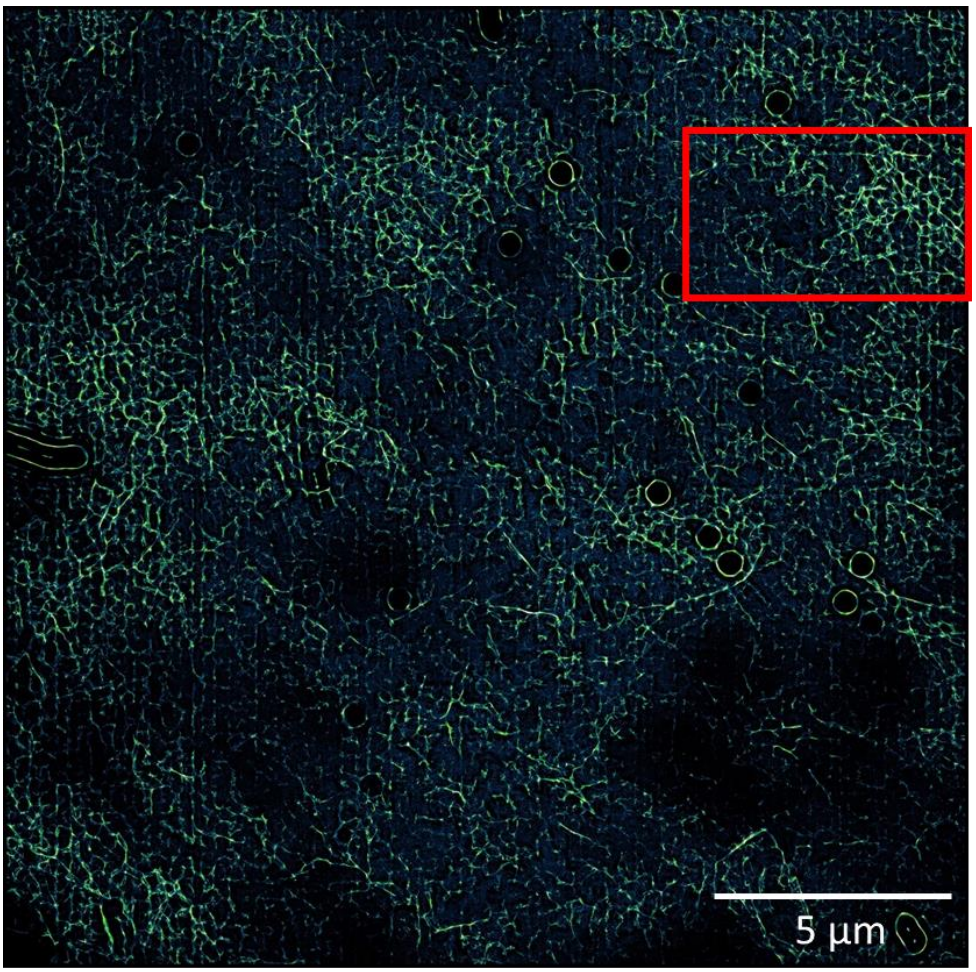

Figure S380 – Refined fluorescence microscopy image of the hydrogel observed in Figure S379.

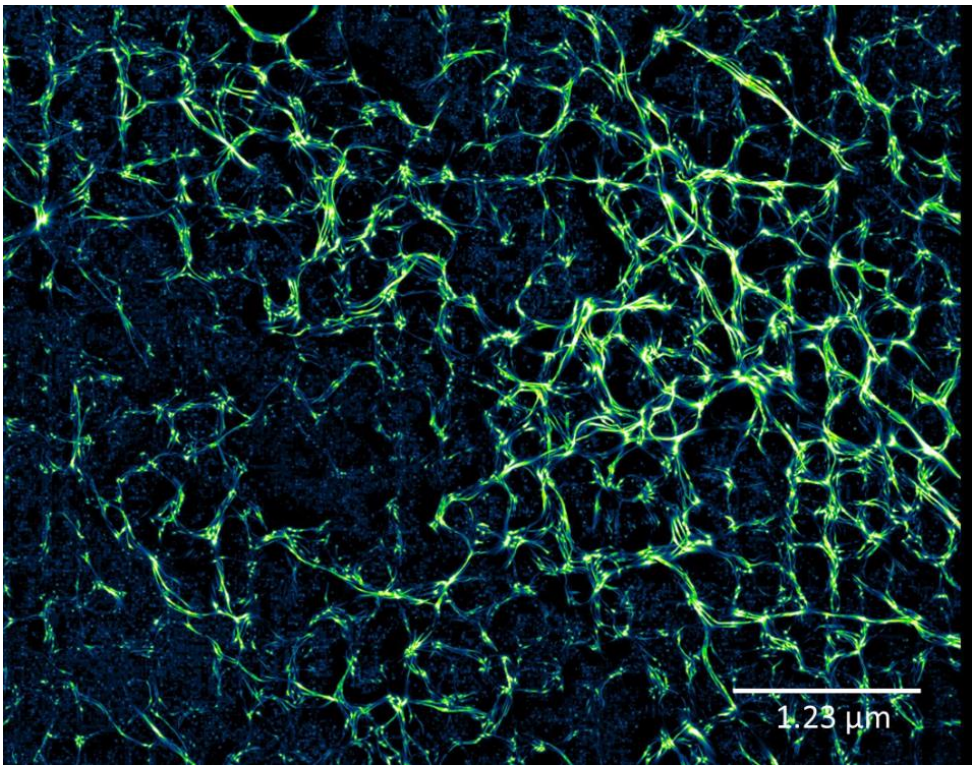

Figure S381 – Enlarged image of outlined red box observed for the hydrogel shown in Figure S380.

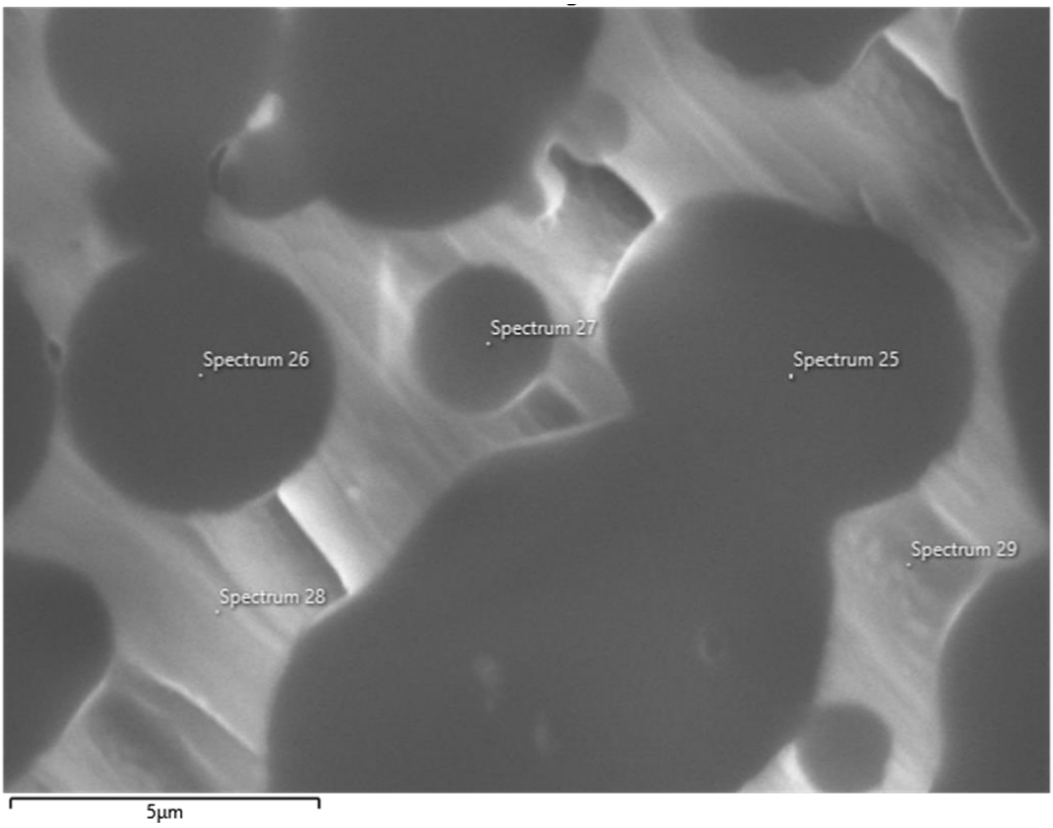

Figure S382 – Scanning electron microscopy image of a xerogel prepared from a dehydrated hydrogel containing compound **72** (5 mg/mL) in aqueous NaH_2PO_4 (0.505 M).

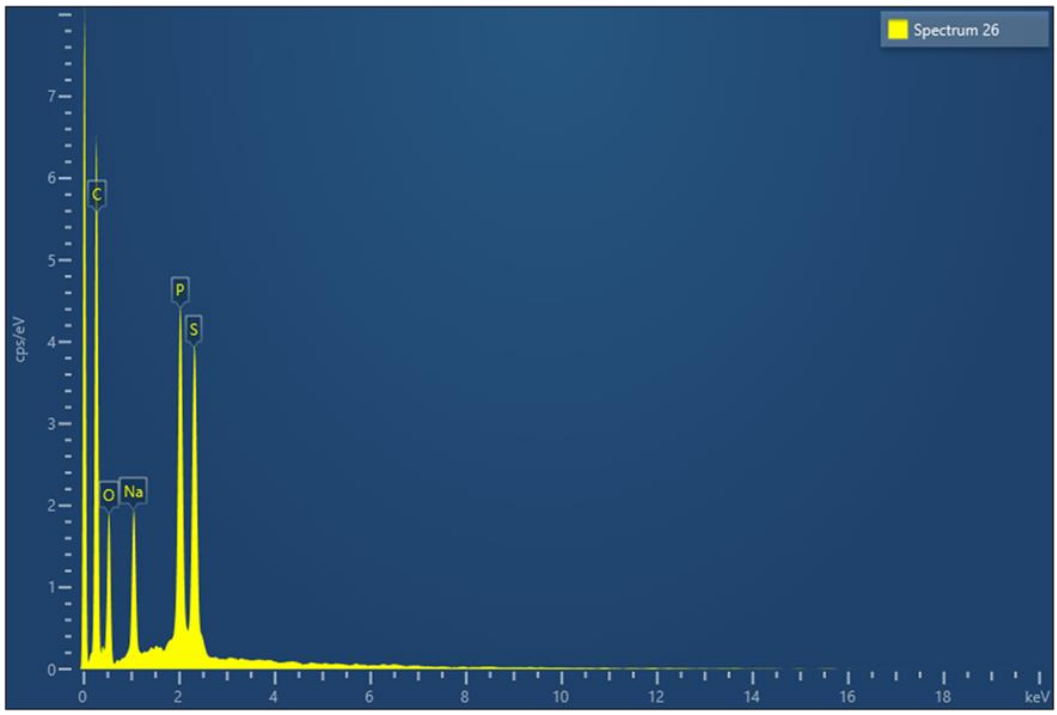

Figure S383 – Energy-dispersive X-ray spectrum showing elemental analysis of the xerogel imaged in Figure S382.

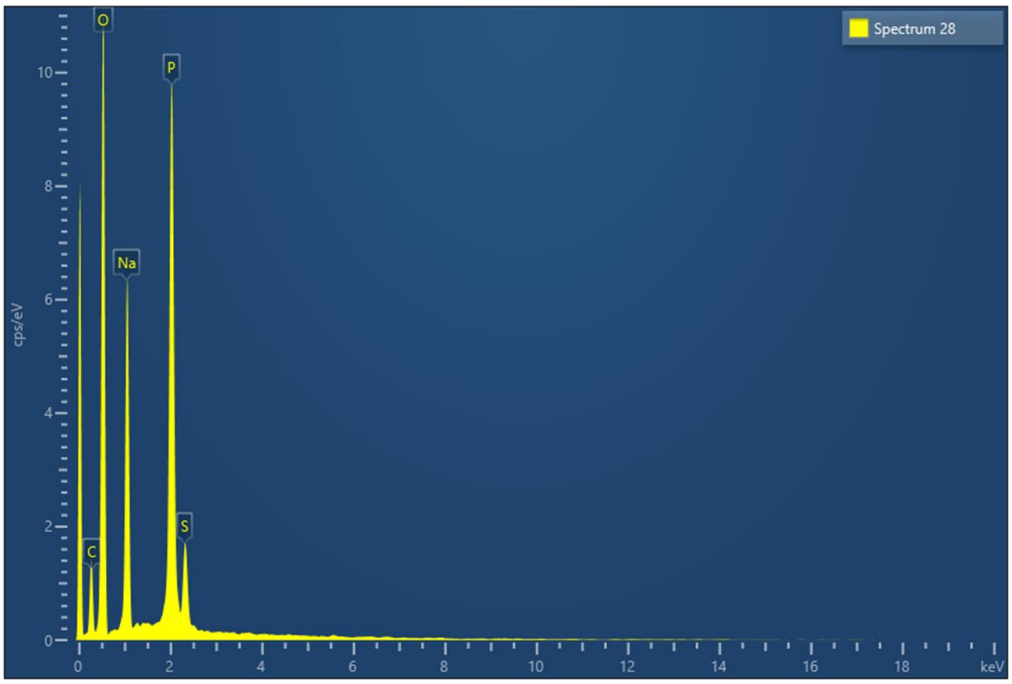

Figure S384 – Energy-dispersive X-ray spectrum showing elemental analysis of the xerogel imaged in Figure S382.

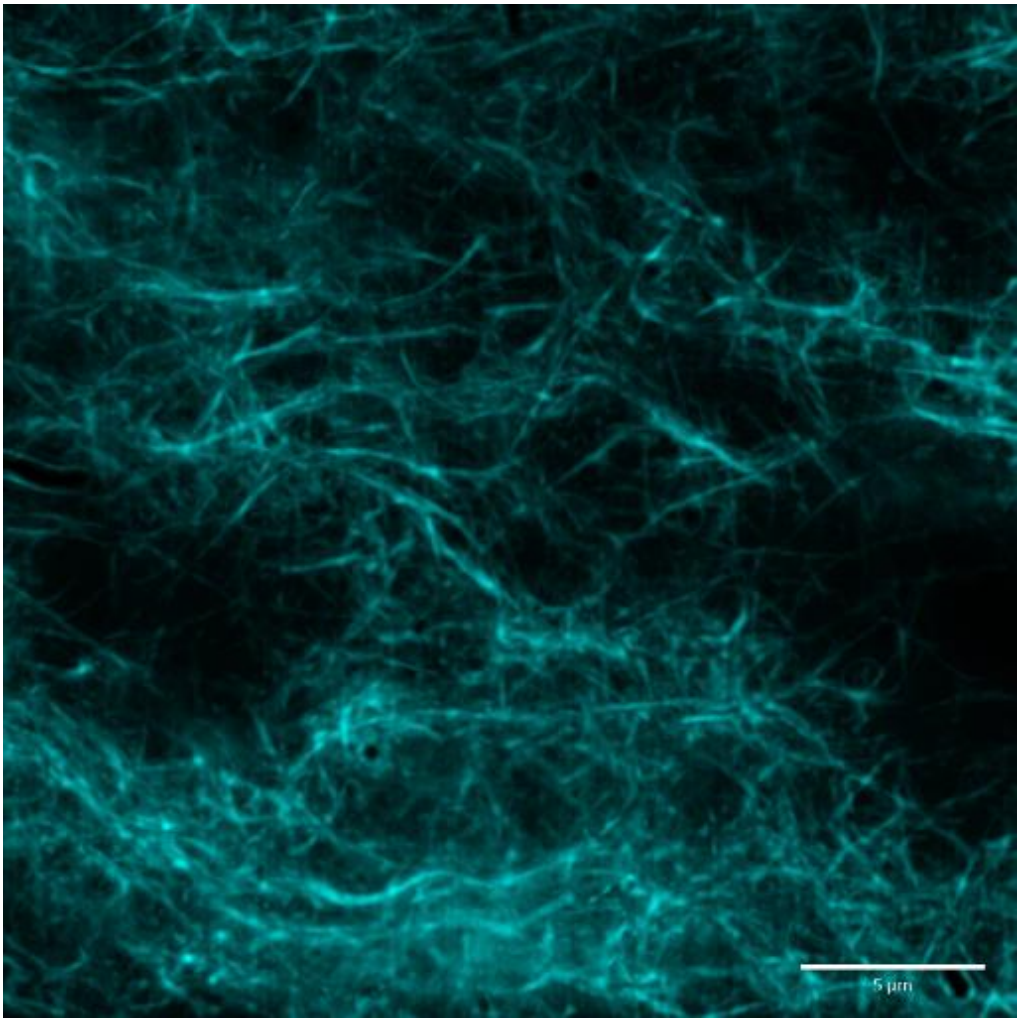

Figure S385 - Fluorescence microscopy image of a hydrogel containing compound **72** (5 mg/mL) in aqueous NaH_2PO_4 (0.505 M).

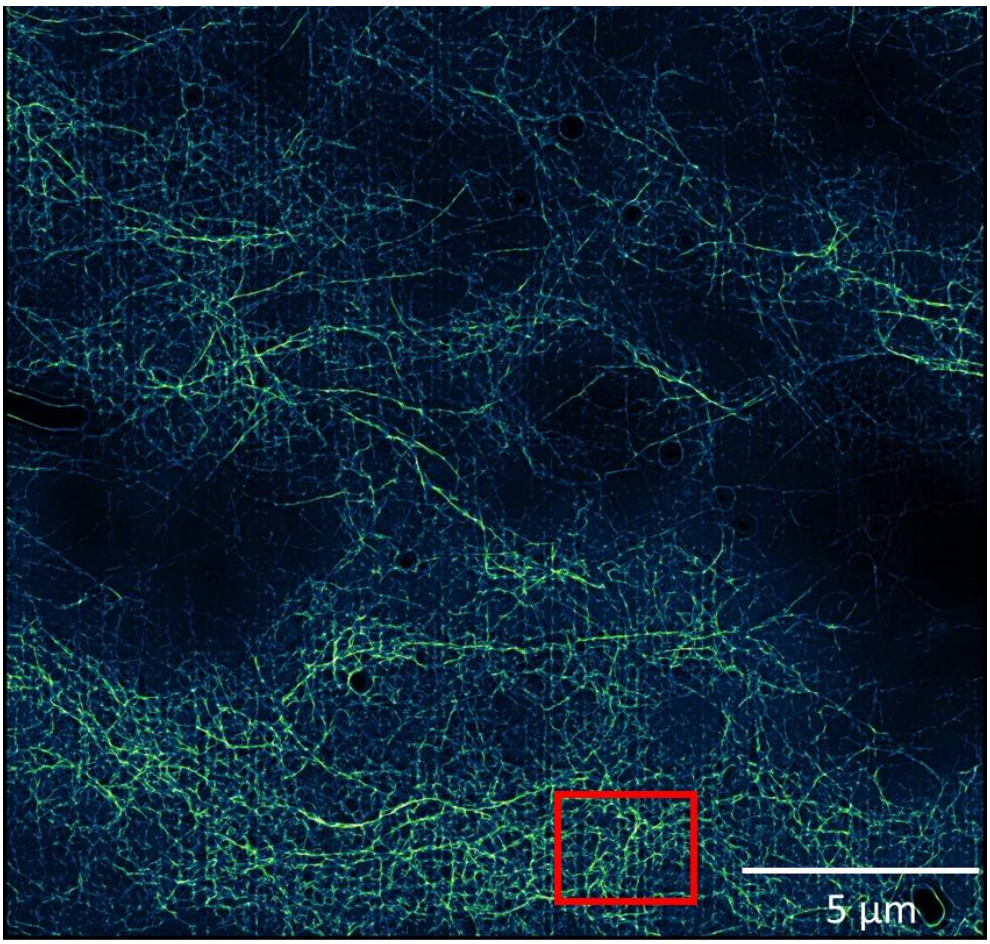

Figure S386 - Refined fluorescence microscopy image of the hydrogel observed in Figure S385.

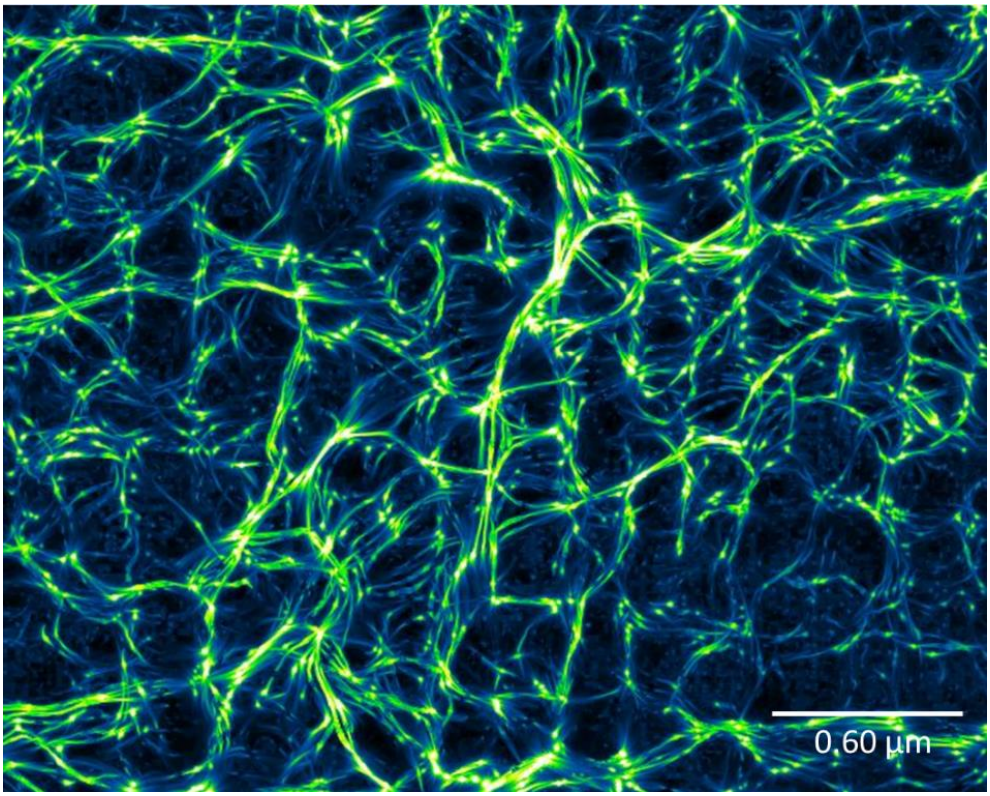

Figure S387 - Enlarged image of outlined red box observed for the hydrogel shown in Figure S386.

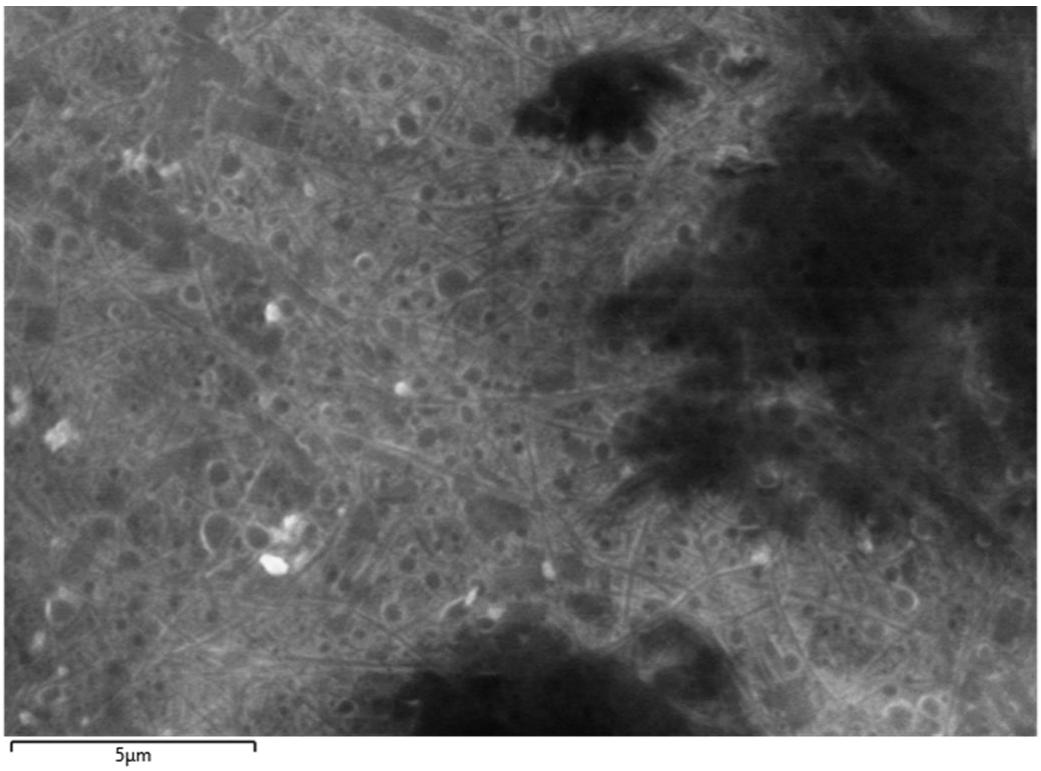

Figure S388 - Scanning electron microscopy image of a xerogel prepared from a dehydrated hydrogel containing compound **72** (5 mg/mL) in aqueous $NaHCO_3$ (0.505 M).

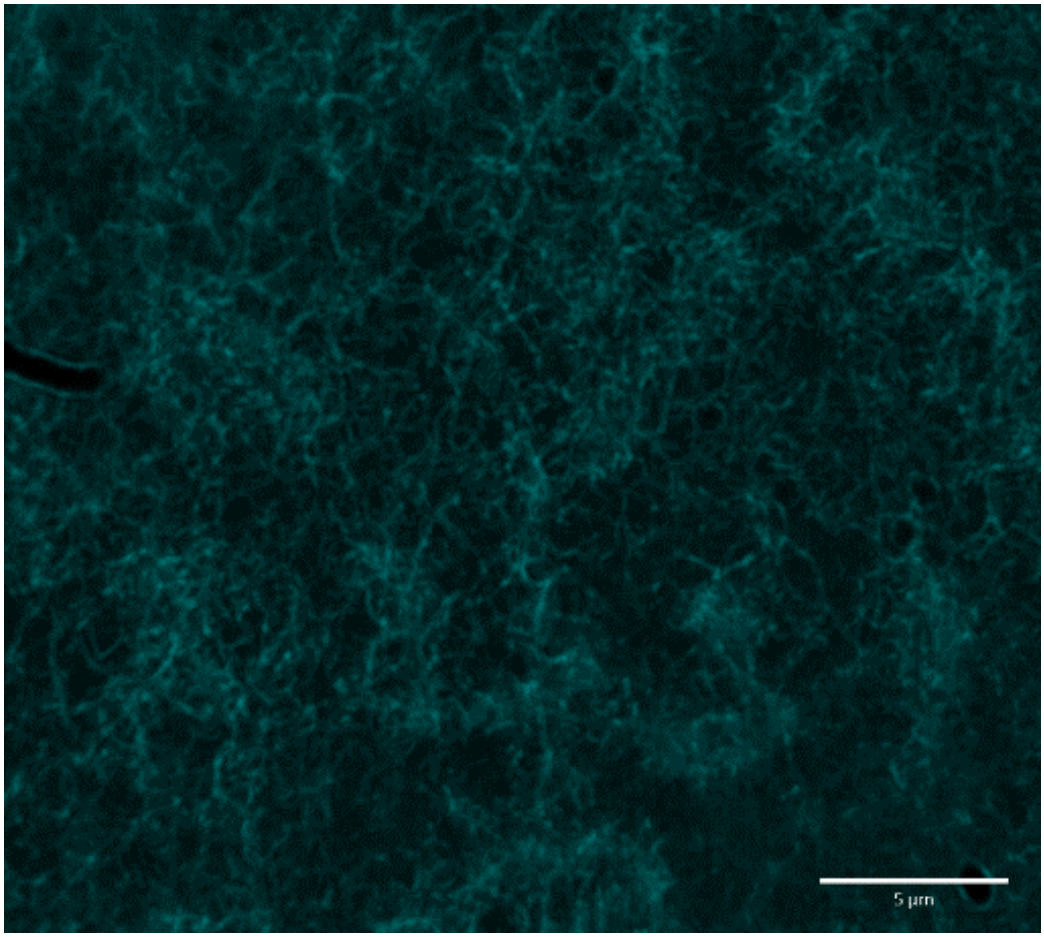

Figure S389 - Fluorescence microscopy image of a hydrogel containing compound **72** (5 mg/mL) in aqueous $NaHCO_3$ (0.505 M).

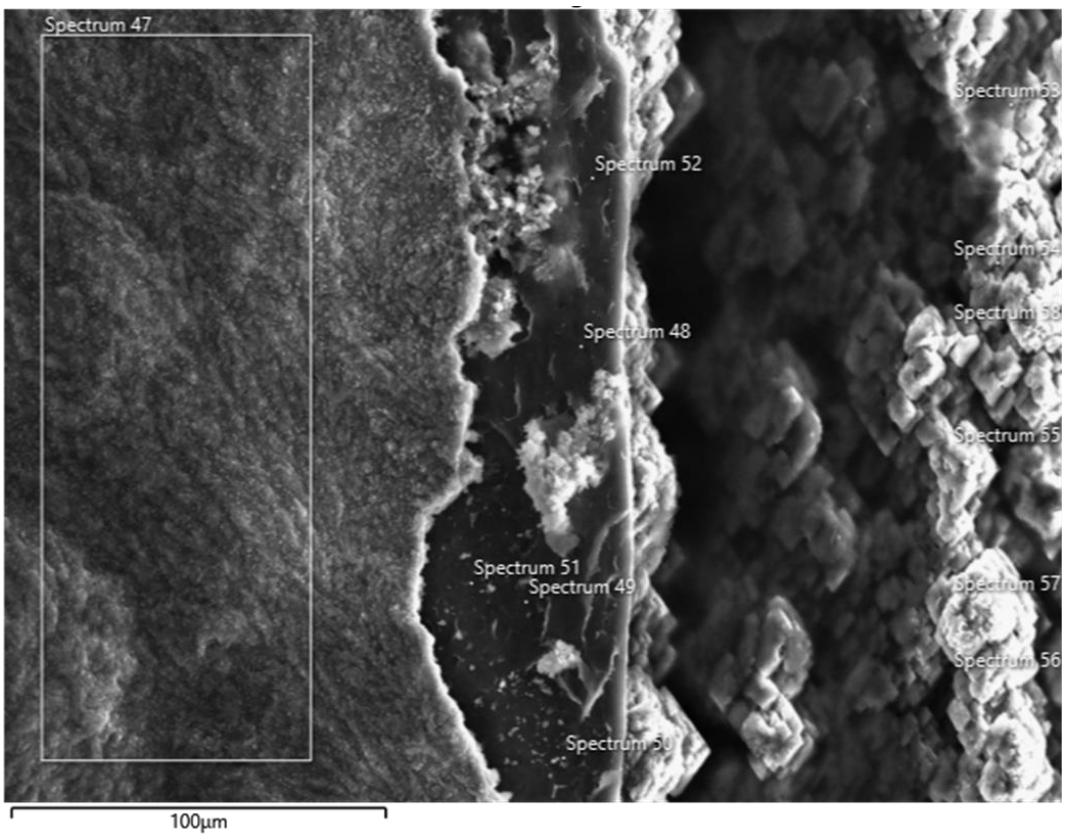

Figure S390 – Scanning electron microscopy image of a xerogel prepared from a dehydrated hydrogel containing compound **72** (5 mg/mL) in aqueous $NaNO_3$ (0.505 M).

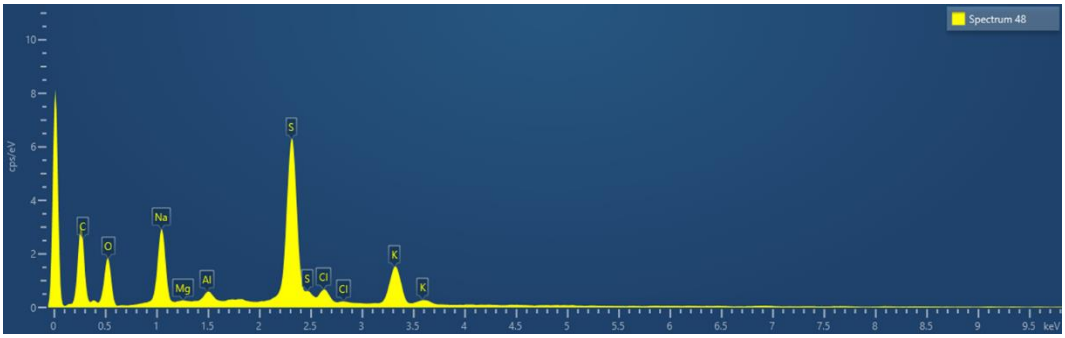

Figure S391 – Energy-dispersive X-ray spectrum showing elemental analysis of the xerogel imaged in Figure S390.

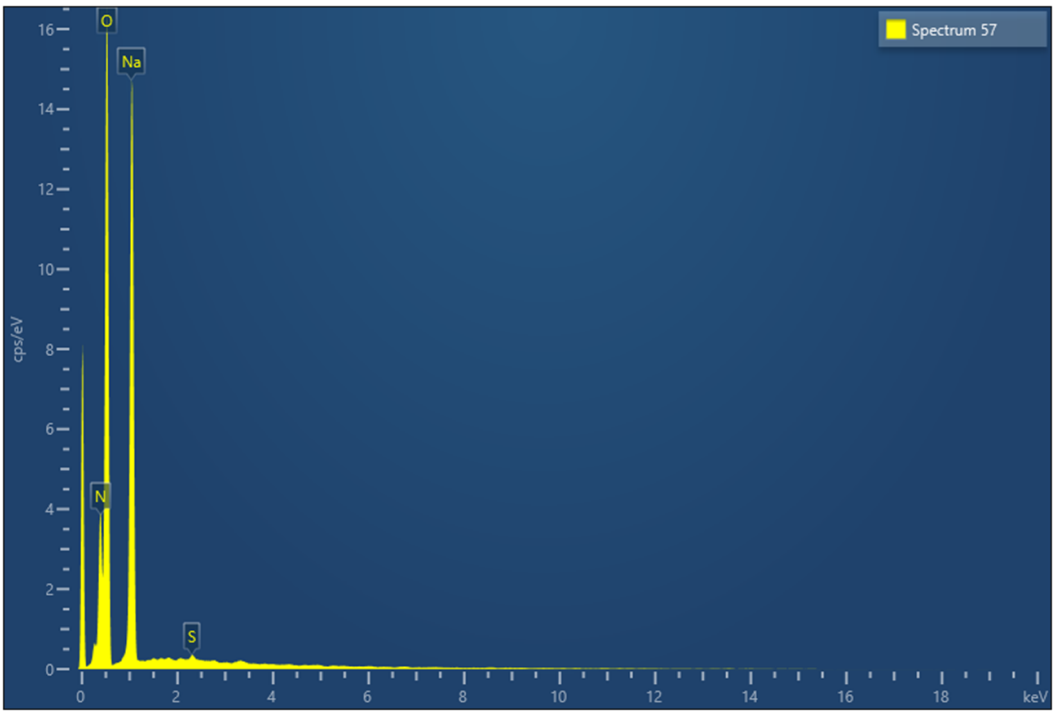

Figure S392 – Energy-dispersive X-ray spectrum showing elemental analysis of the xerogel imaged in Figure S390.

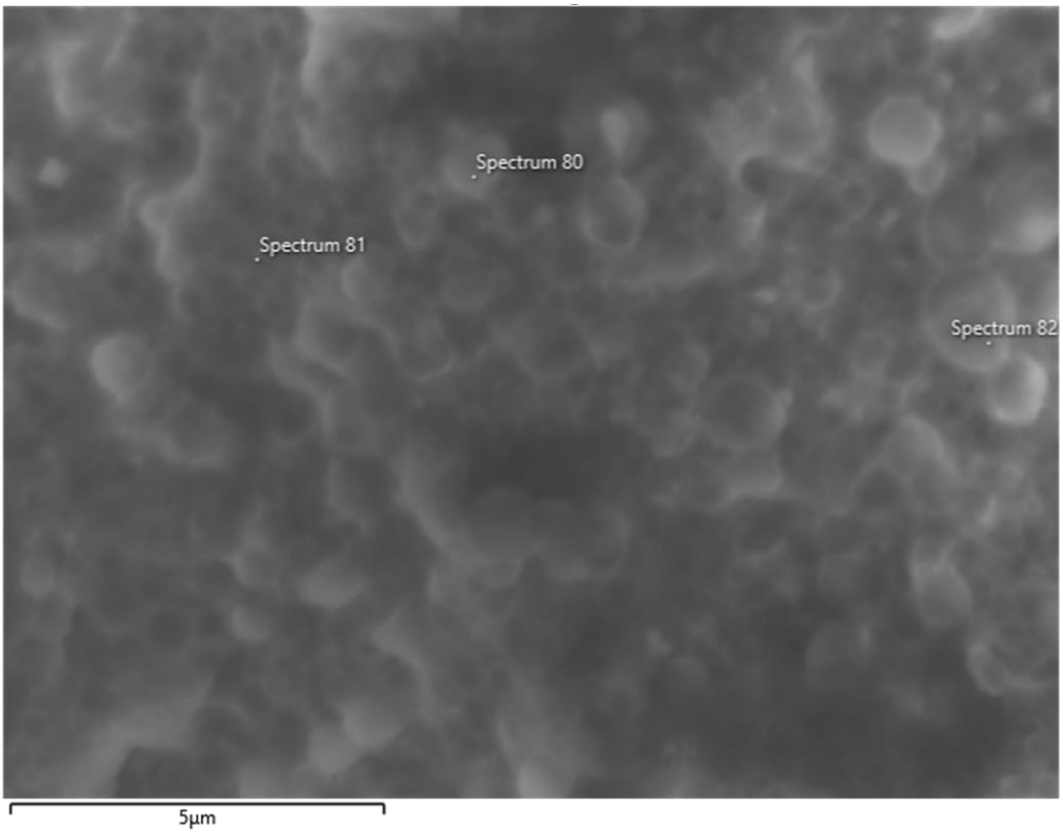

Figure S393 – Scanning electron microscopy image of a xerogel prepared from a dehydrated hydrogel containing compound **72** (5 mg/mL) in aqueous Na_2HPO_4 (0.505 M).

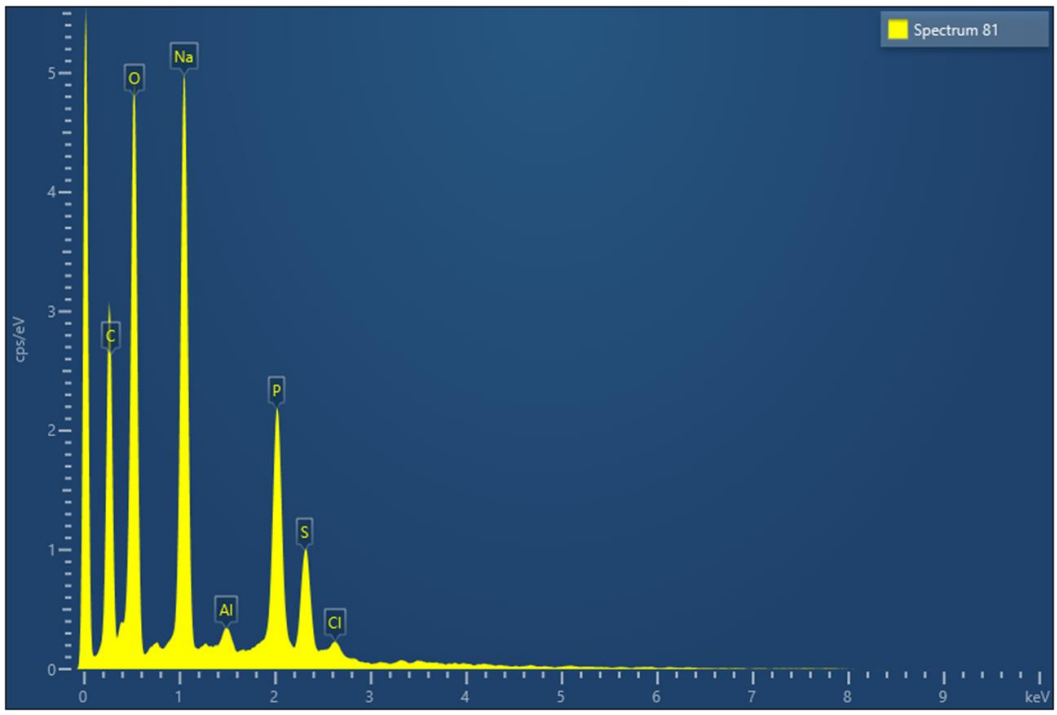

Figure S394 – Energy-dispersive X-ray spectrum showing elemental analysis of the xerogel imaged in Figure S393.

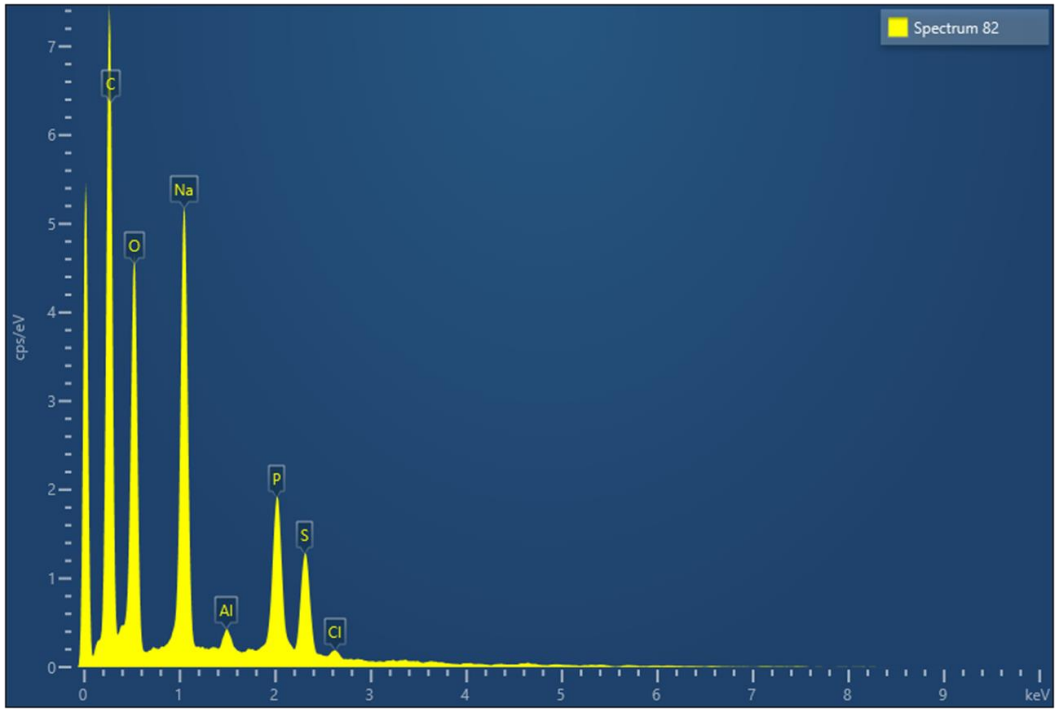

Figure S395 – Energy-dispersive X-ray spectrum showing elemental analysis of the xerogel imaged in Figure S393.

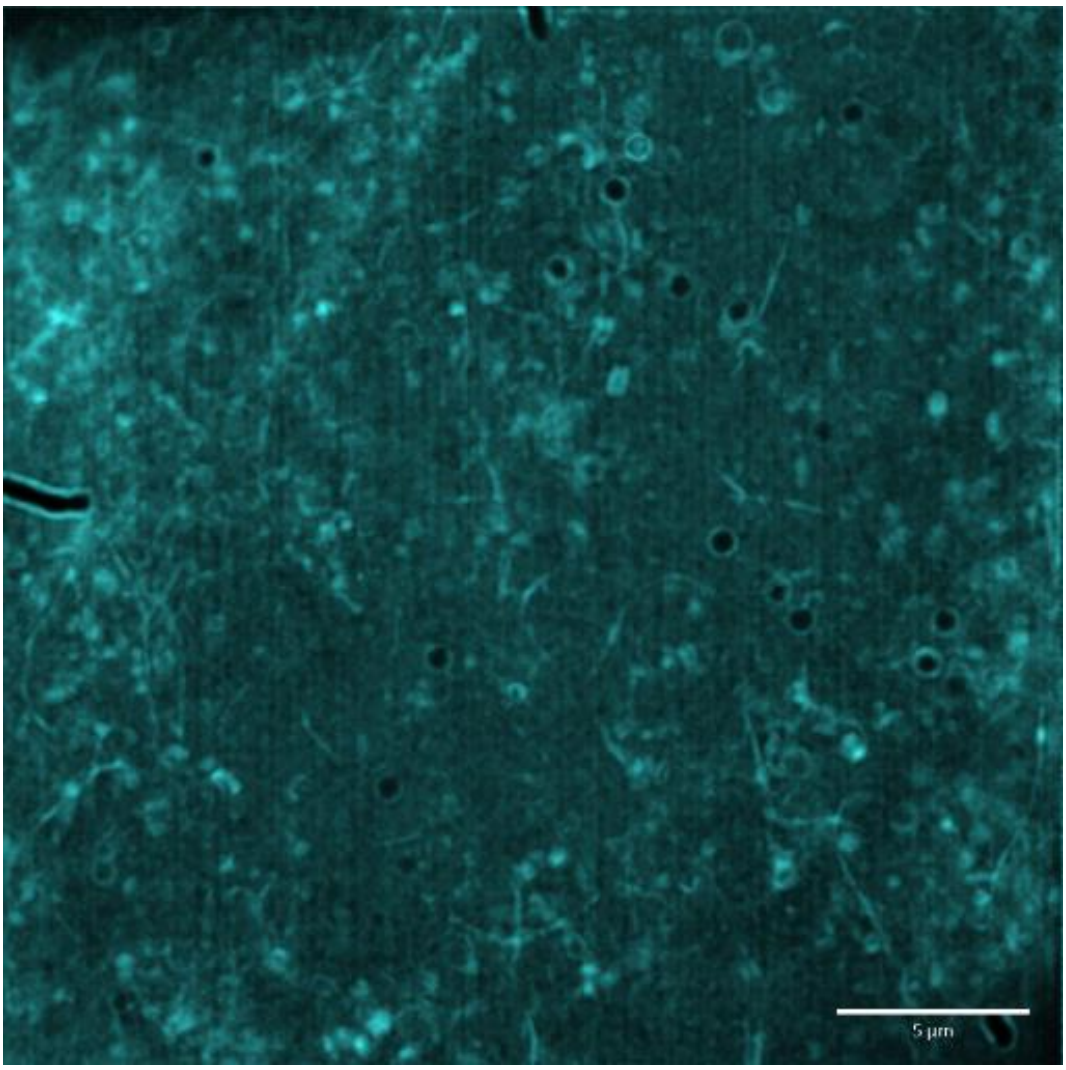

Figure S396 - Fluorescence microscopy image of a hydrogel containing compound **72** (5 mg/ mL) in aqueous Na_2HPO_4 (0.505 M).

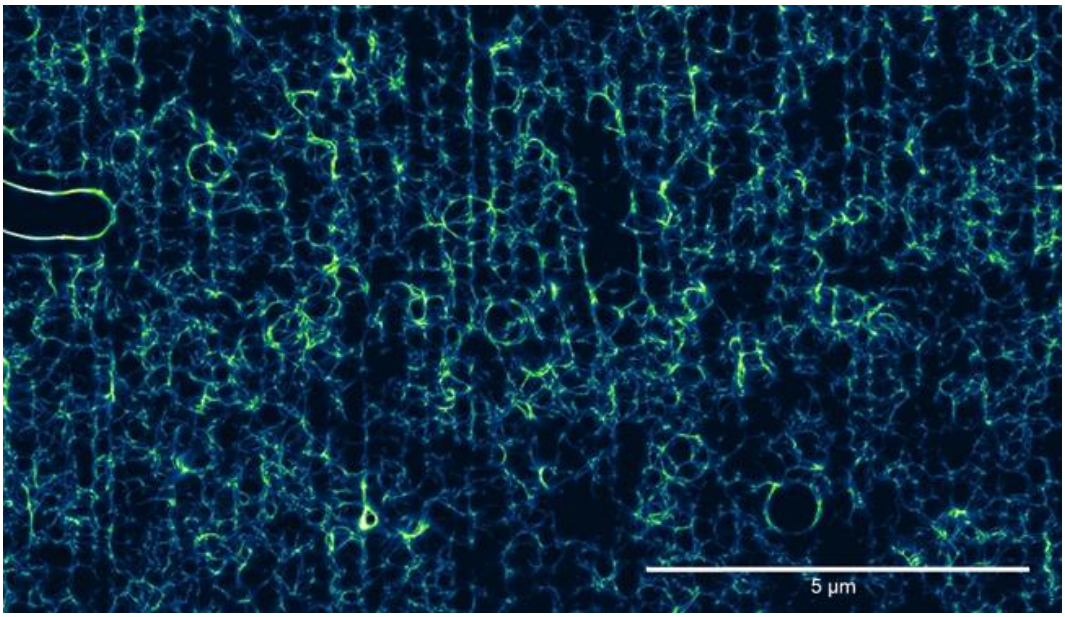

Figure S397 - Refined fluorescence microscopy image of the hydrogel observed in Figure S396.

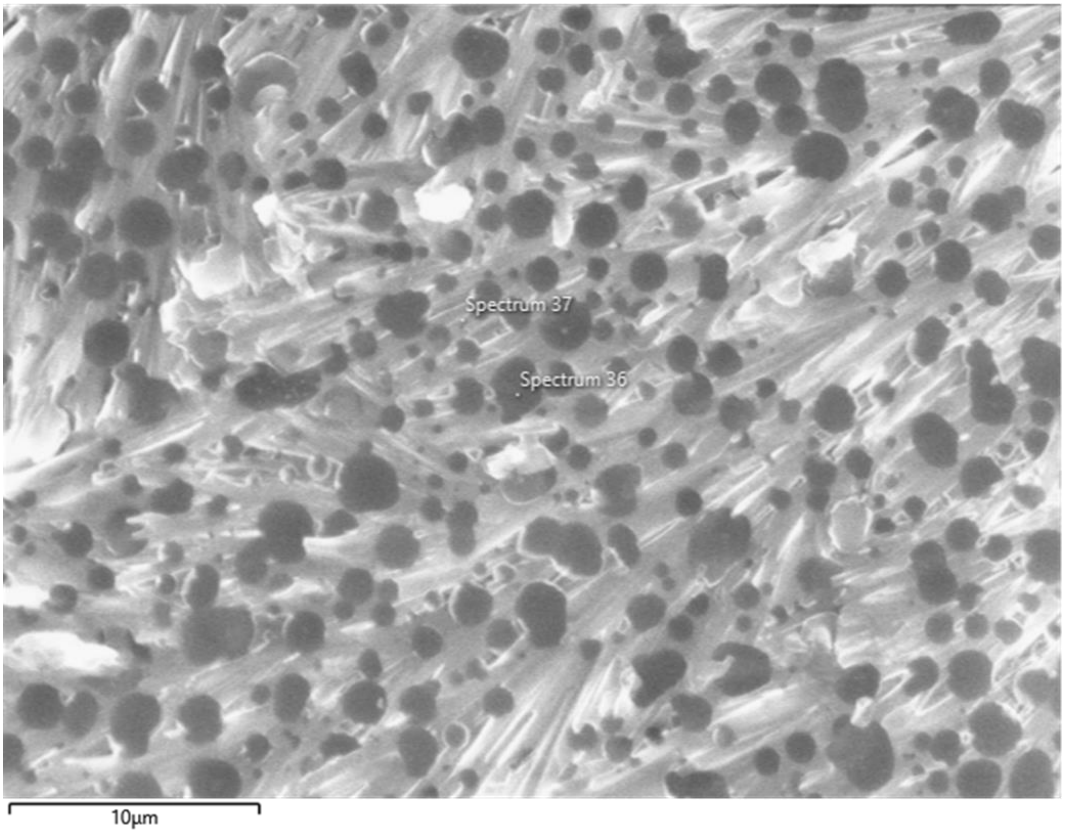

Figure S398 – Scanning electron microscopy image of a xerogel prepared from a dehydrated hydrogel containing compound **72** (5 mg/mL) in aqueous Na_2CO_3 (0.505 M).

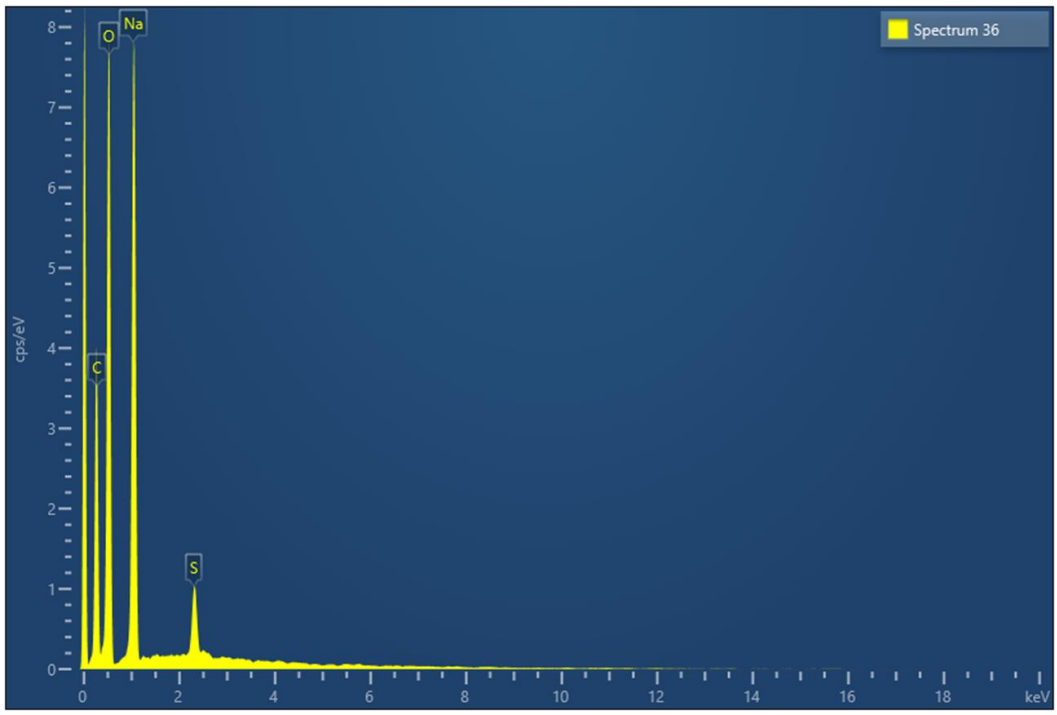

Figure S399 – Energy-dispersive X-ray spectrum showing elemental analysis of the xerogel imaged in Figure S398.

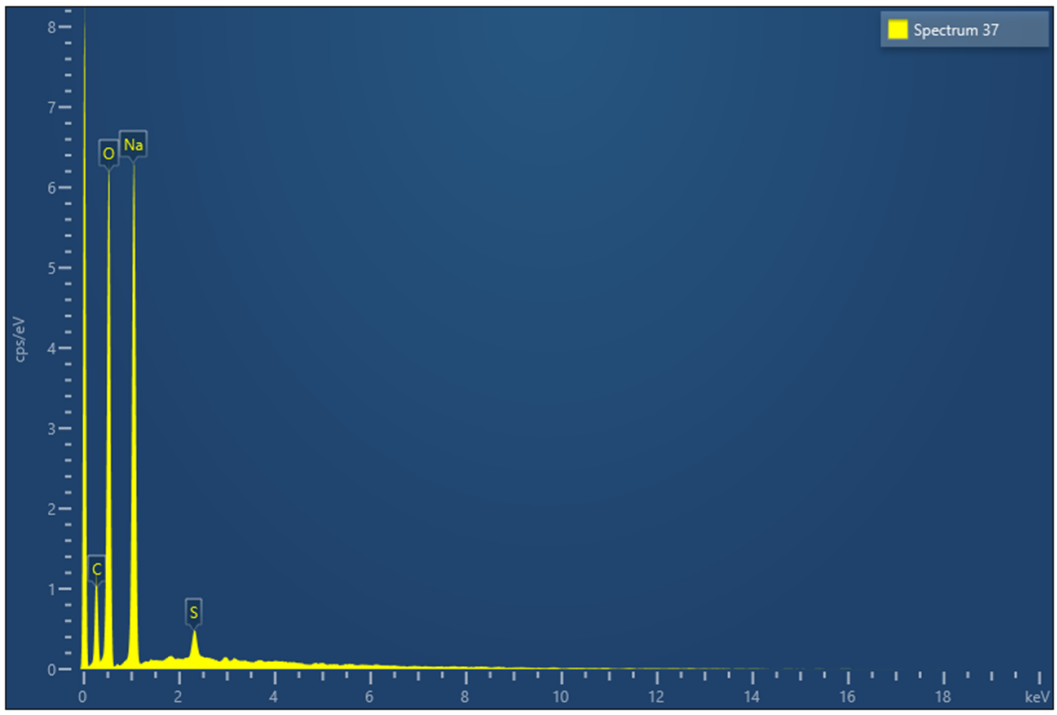

Figure S400 – Energy-dispersive X-ray spectrum showing elemental analysis of the xerogel imaged in Figure S398.

2.6 MIC_{50} Growth Curves

2.6.1 USA 300 Methicillin-resistant *Staphylococcus aureus* (MRSA)

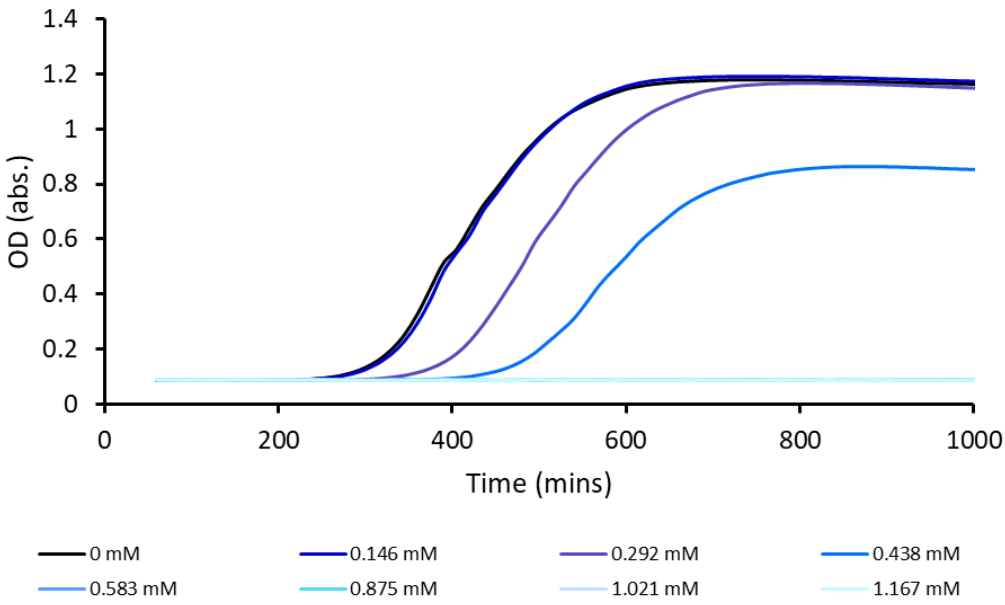

Figure S401 - Averaged growth curves created from absorbance readings of *S. aureus* in the presence of compound **42** at varying concentrations.

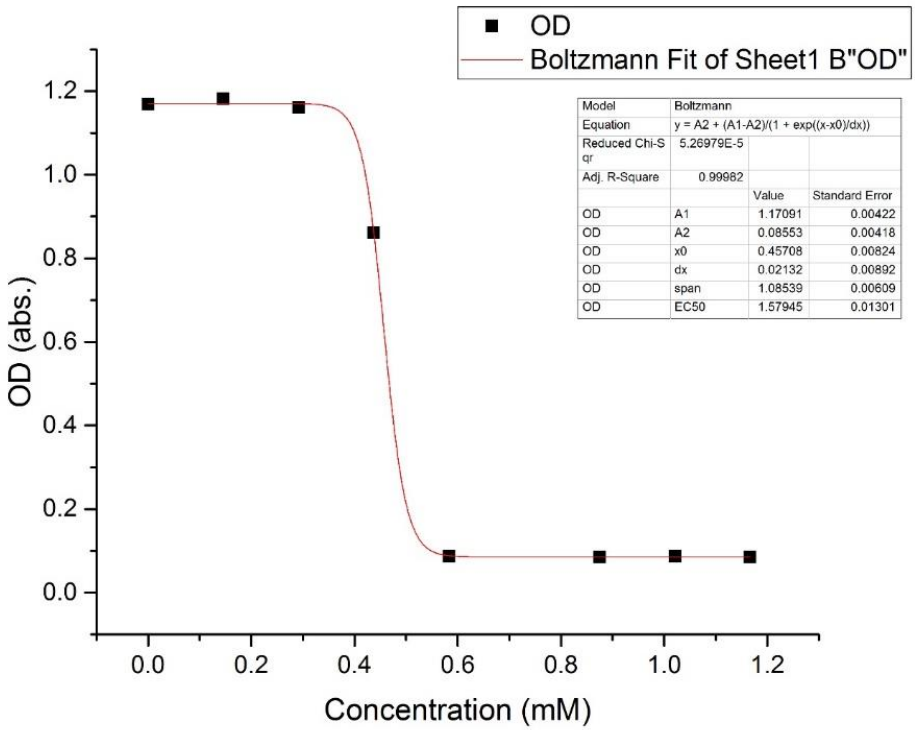

Figure S402 - Origin graph created using absorbance values at 900 minutes for compound **42** at varying concentrations.

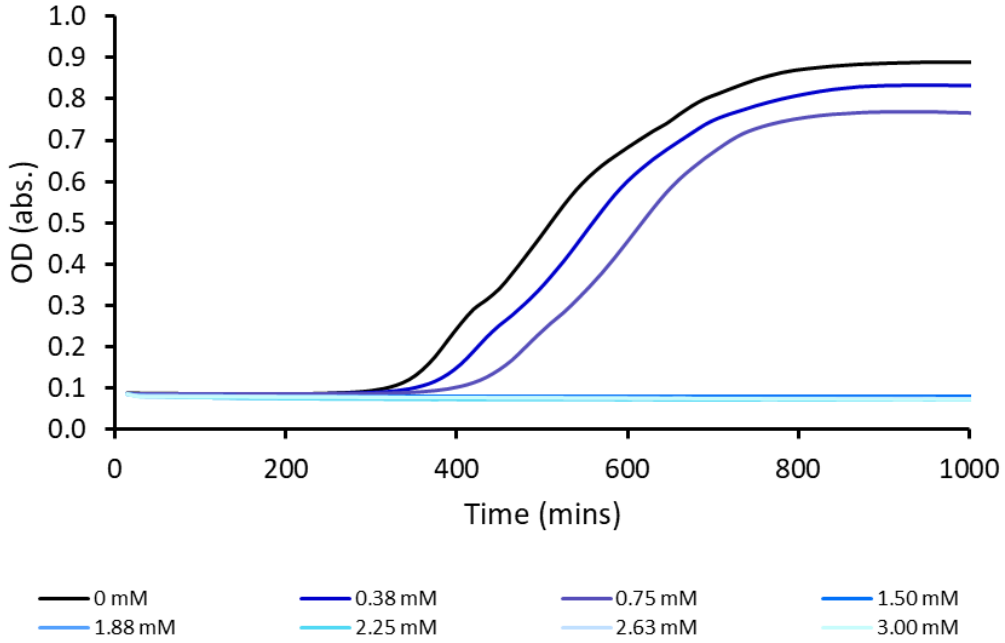

Figure S403 - Averaged growth curves created from absorbance readings of *S. aureus* in the presence of compound **71** at varying concentrations.

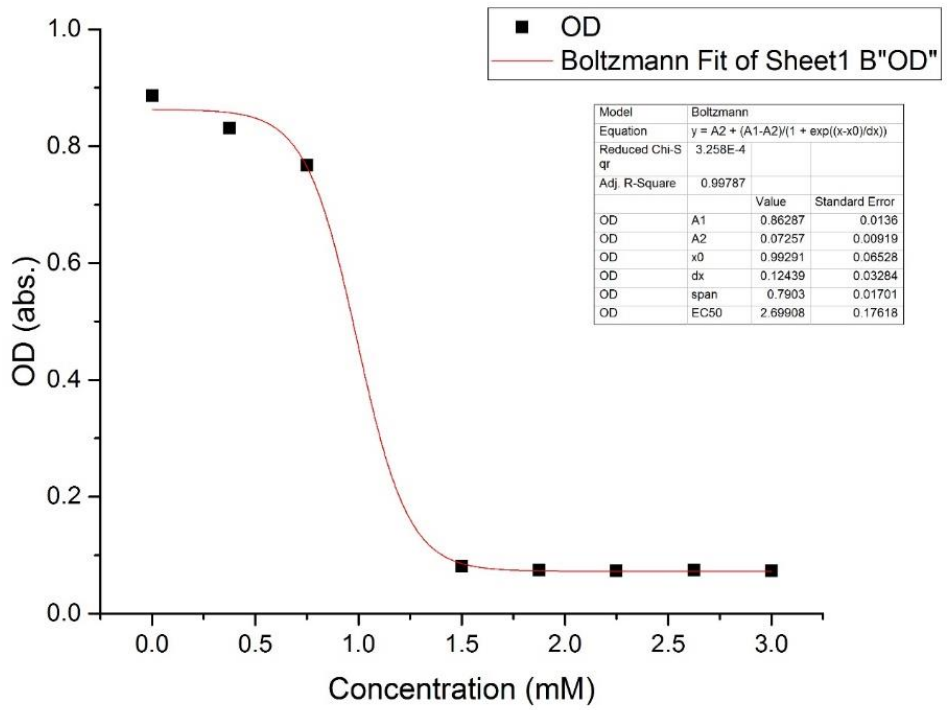

Model	Boltzmann		
Equation	y = A2 + (A1-A2)/(1 + exp((x-x0)/dx))		
Reduced Chi-Sqr	3.258E-4		
Adj. R-Square	0.99787		
		Value	Standard Error
OD	A1	0.86287	0.0136
OD	A2	0.07257	0.00919
OD	x0	0.99291	0.06528
OD	dx	0.12439	0.03284
OD	span	0.7903	0.01701
OD	EC50	2.69908	0.17618

Figure S404 - Origin graph created using absorbance values at 900 minutes for compound **71** at varying concentrations.

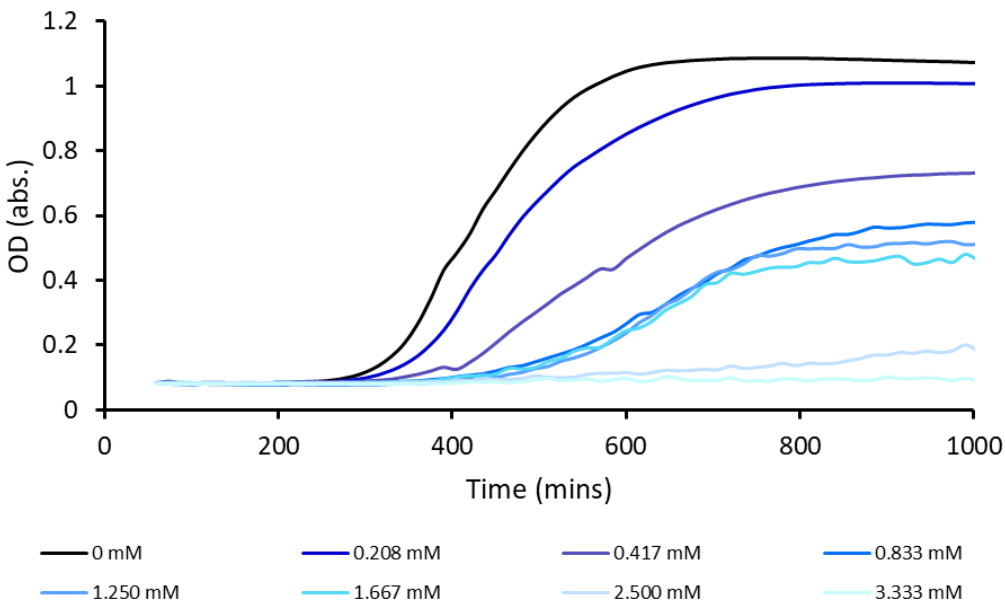

Figure S405 - Averaged growth curves created from absorbance readings of *S. aureus* in the presence of compound **72** at varying concentrations.

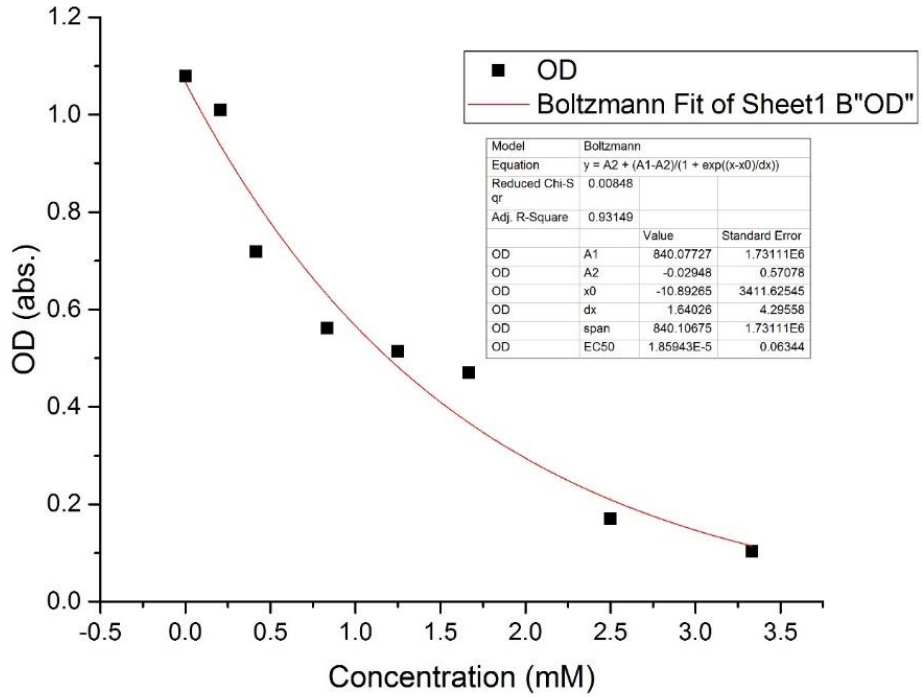

Figure S406 - Origin graph created using absorbance values at 900 minutes for compound **72** at varying concentrations.

2.6.2 *Escherichia coli* DH10β (*E. coli*)

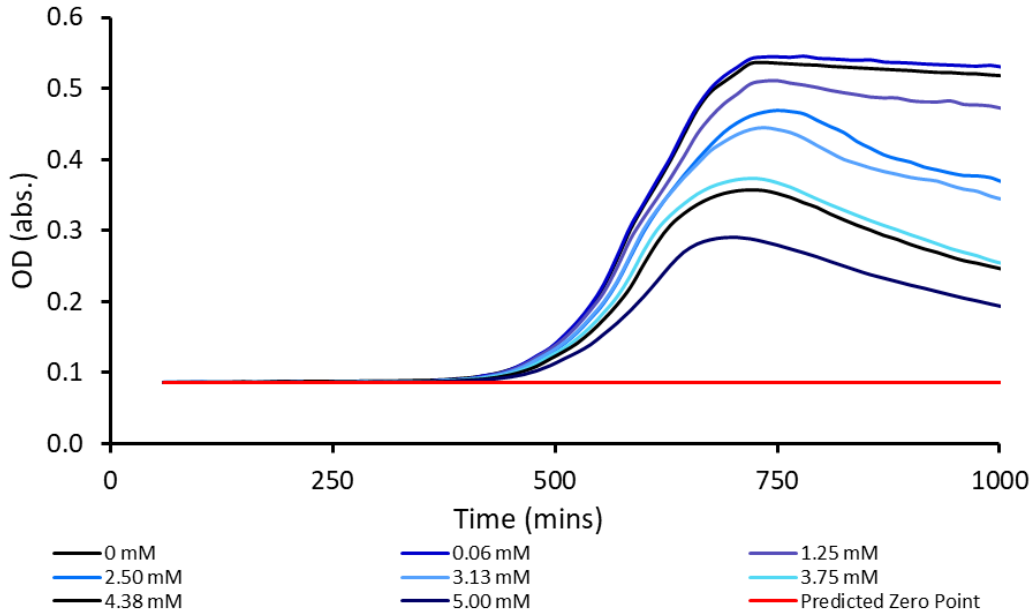

Figure S407 - Averaged growth curves created from absorbance readings of *E. coli* DH10β in the presence of compound **42** at varying concentrations. MIC_{50} was calculated using predicted endpoint due to solubility.

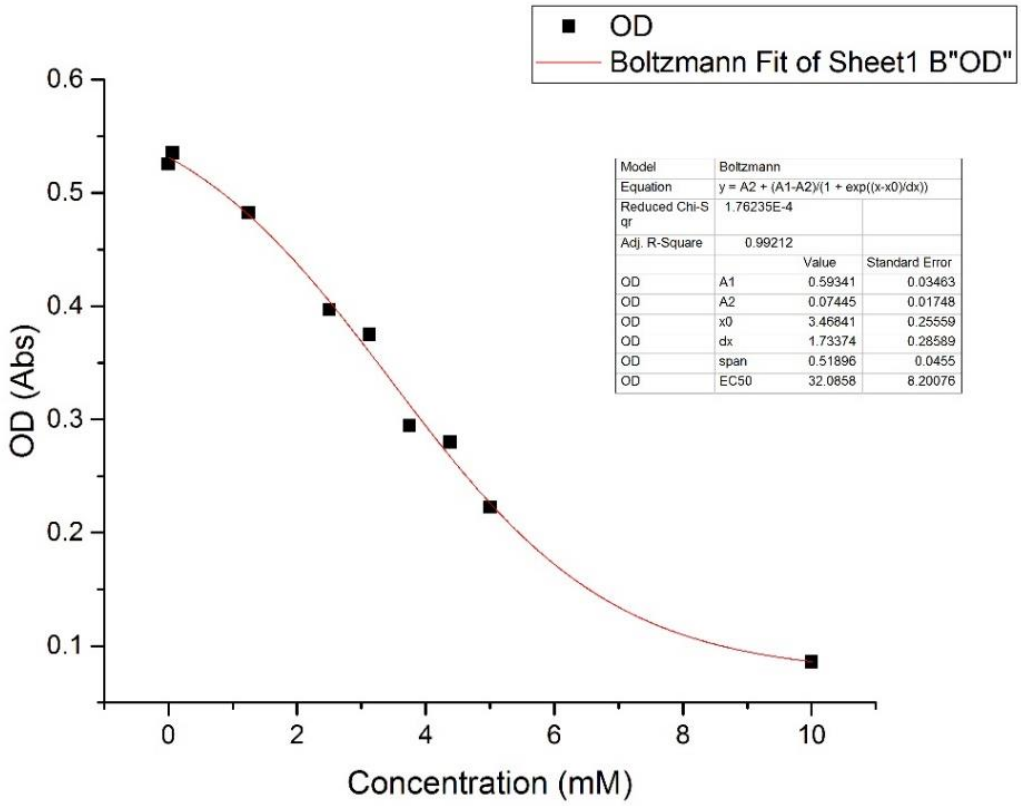

Model	Boltzmann		
Equation	y = A2 + (A1-A2)/(1 + exp((x-x0)/dx))		
Reduced Chi-Sqr	1.76235E-4		
Adj. R-Square	0.99212		
		Value	Standard Error
OD	A1	0.59341	0.03463
OD	A2	0.07445	0.01748
OD	x0	3.46841	0.25559
OD	dx	1.73374	0.28589
OD	span	0.51896	0.0455
OD	EC50	32.0858	8.20076

Figure S408 - Origin graph created using absorbance values at 900 minutes for compound **42** at varying concentrations.

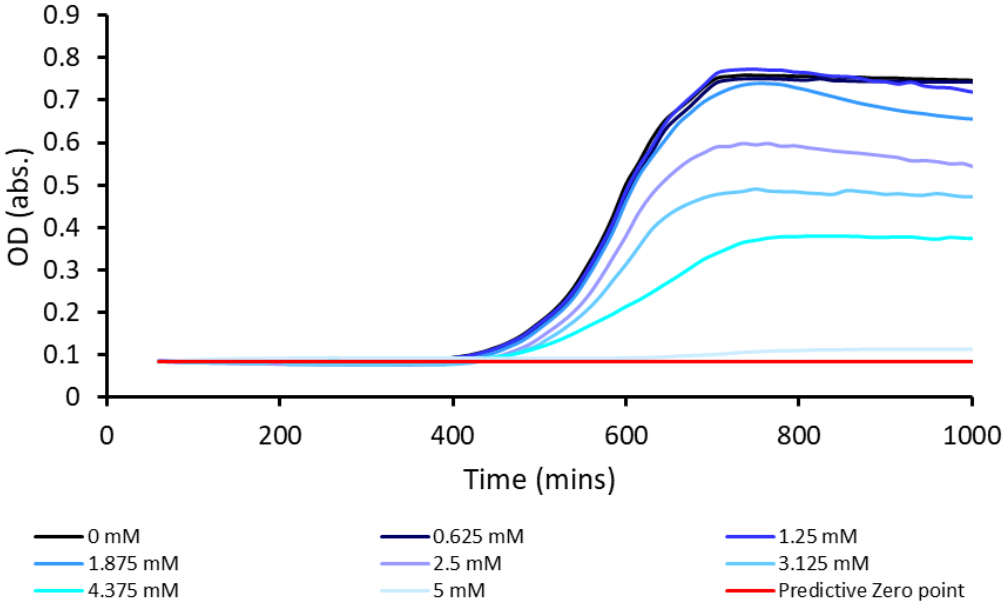

Figure S409 - Averaged growth curves created from absorbance readings of *E. coli* DH10β in the presence of compound **71** at varying concentrations. MIC_{50} was calculated using predicted endpoint due to solubility.

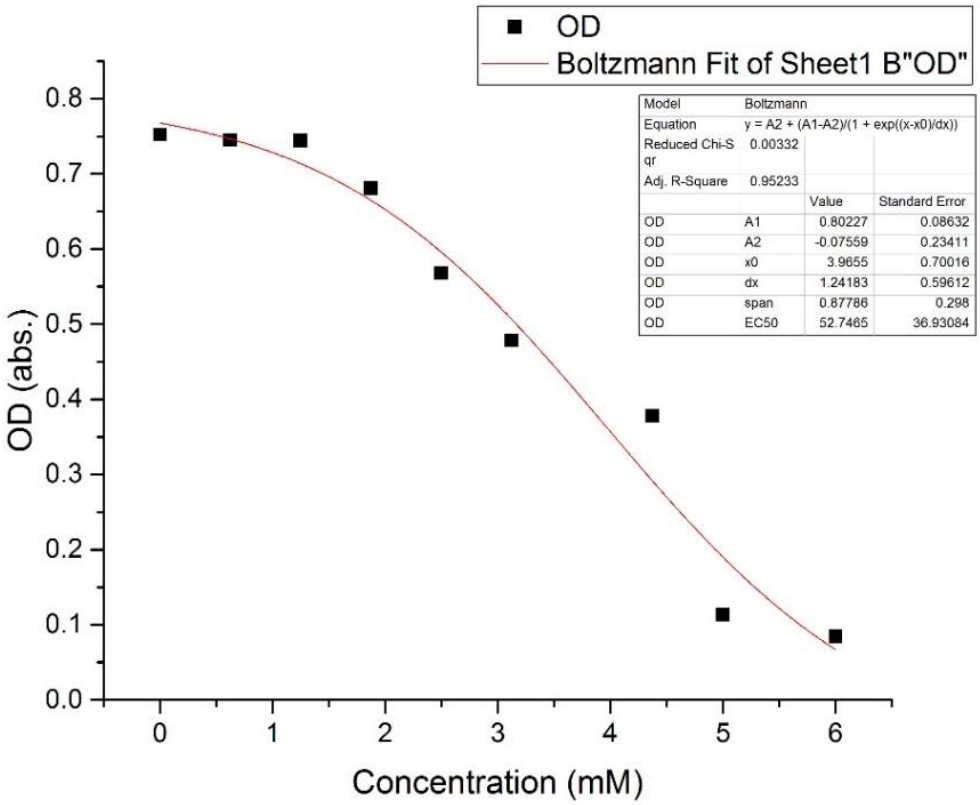

Figure S410 - Origin graph created using absorbance values at 900 minutes for compound **71** at varying concentrations.

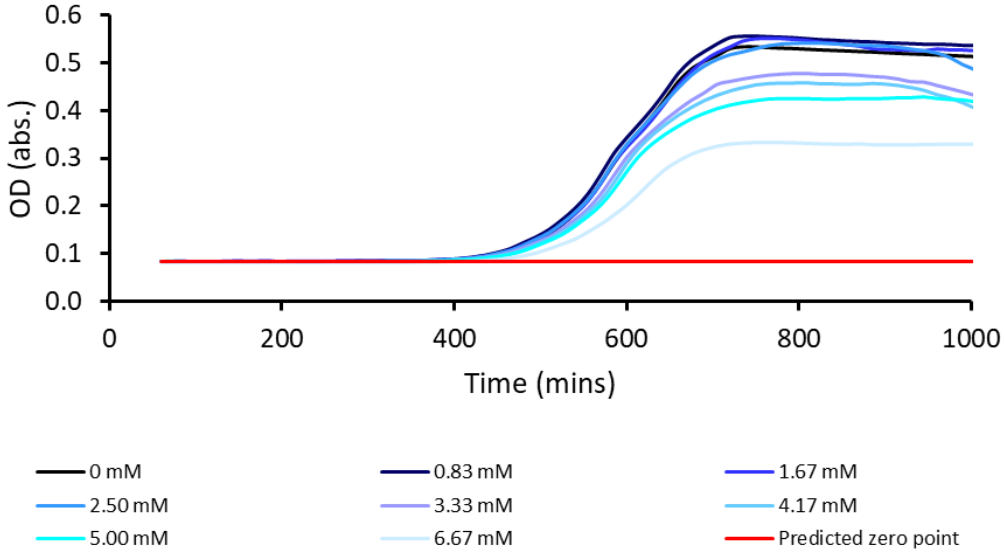

Figure S411 - Averaged growth curves created from absorbance readings of *E. coli* DH10β in the presence of compound **72** at varying concentrations. MIC_{50} was calculated using predicted endpoint due to solubility.

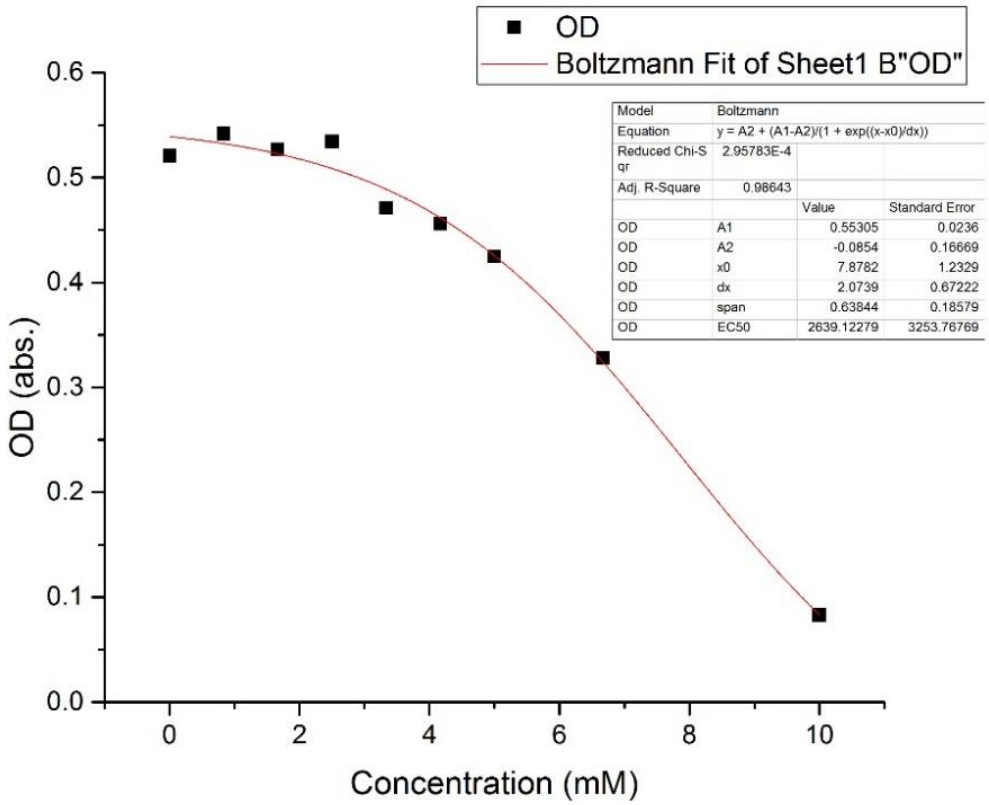

Figure S412 - Origin graph created using absorbance values at 900 minutes for compound **72** at varying concentrations.

2.6.3 Comparative overview

Table S14 -The MIC_{50} values (mM) as determined for **42**, **71, 72** and TBACl against clinically relevant Gram-positive MRSA USA300 and Gram-negative *E. coli* DH10B at an initial calibrated cell concentration equal to the 0.5 McFarland standard after 900 minutes (optical density measured at 600 nm).

SSA	MRSA	*E. coli*	Ratio
42	0.46	3.85	1:3.6
71	0.99	3.57	1:5.4
72	0.93	5.02	1:8.4
TBACl	3.18	6.36	1:2.0

2.7 Hydrogel antimicrobial efficacy experiments

2.7.1 Disk diffusion assays *E. coli* DH5B

Biological repeat 1 **Biological repeat 2** **Biological repeat 3**

Figure S413 - Disk diffusion assays showing the zone of inhibition of growth of *Escherichia coli* DH10β due to the presence of ≈ 50 mg SSA hydrogel gel of **72** formed in an aqueous NaCl solution (0.505 M) on the surface of the plate.

Biological repeat 1 **Biological repeat 2** **Biological repeat 3**

Figure S414 - Disk diffusion assays showing the zone of inhibition of growth of *Escherichia coli* DH10β due to the presence of ≈ 50 mg SSA hydrogel gel of **72** formed in an aqueous NaCl solution (0.505 M) co-formulated in a 1:1 molar ratio with ampicillin (**105**), on the surface of the plate.

Biological repeat 1 **Biological repeat 2** **Biological repeat 3**

Figure S415 - Disk diffusion assays showing the zone of inhibition of growth of *Escherichia coli* DH10β due to the presence of ≈ 50 mg SSA hydrogel gel of **72** formed in an aqueous NaCl solution (0.505 M) in a well in the plate.

Biological repeat 1 **Biological repeat 2** **Biological repeat 3**

Figure S416 - Disk diffusion assays showing the zone of inhibition of growth of *Escherichia coli* DH10β due to the presence of ≈ 50 mg SSA hydrogel gel of **72** formed in an aqueous NaCl solution (0.505 M) co-formulated in a 1:1 molar ratio with ampicillin, in a well in the plate.

Biological repeat 1 **Biological repeat 2** **Biological repeat 3**

Figure S417 - Disk diffusion assays showing the zone of inhibition of growth of *Escherichia coli* DH10β due to the presence of ampicillin (**105**) solution (8.1 mM in an aqueous NaCl solution (0.505 M) in a well in the plate.

Biological repeat 1 **Biological repeat 2** **Biological repeat 3**

Figure S418 - Disk diffusion assays showing the zone of inhibition of growth of *Escherichia coli* DH10β due to the presence of an aqueous NaCl solution (0.505 M) in a well in the plate.

2.7.2 Disk diffusion assays MRSA USA300

Biological repeat 1 **Biological repeat 2** **Biological repeat 3**

Figure S419 - Disk diffusion assays showing the zone of inhibition of growth of Methicillin resistant *Staphylococcus aureus* USA300 due to the presence of ≈ 50 mg SSA hydrogel gel of **72** formed in an aqueous NaCl solution (0.505 M) on the surface of the plate.

Biological repeat 1 **Biological repeat 2** **Biological repeat 3**

Figure S420 - Disk diffusion assays showing the zone of inhibition of growth of Methicillin resistant *Staphylococcus aureus* USA300 due to the presence of ≈ 50 mg SSA hydrogel gel of **72** formed in an aqueous NaCl solution (0.505 M) co-formulated in a 1:1 molar ratio with ampicillin (**105**), on the surface of the plate.

Biological repeat 1 **Biological repeat 2** **Biological repeat 3**

Figure S421 - Disk diffusion assays showing the zone of inhibition of growth of Methicillin resistant *Staphylococcus aureus* USA300 due to the presence of ≈ 50 mg SSA hydrogel gel of **72** formed in an aqueous NaCl solution (0.505 M) in a well in the plate.

Biological repeat 1 **Biological repeat 2** **Biological repeat 3**

Figure S422 - Disk diffusion assays showing the zone of inhibition of growth of Methicillin resistant *Staphylococcus aureus* USA300 due to the presence of ≈ 50 mg SSA hydrogel gel of **72** formed in an aqueous NaCl solution (0.505 M) co-formulated in a 1:1 molar ratio with ampicillin (**105**), in a well in the plate.

Biological repeat 1 **Biological repeat 2** **Biological repeat 3**

Figure S423 - Disk diffusion assays showing the zone of inhibition of growth of Methicillin resistant *Staphylococcus aureus* USA300 due to the presence of ampicillin (**105**) solution (8.1 mM in an aqueous NaCl solution, 0.505 M) in a well in the plate.

Biological repeat 1 **Biological repeat 2** **Biological repeat 3**

Figure S424 - Disk diffusion assays showing the zone of inhibition of growth of Methicillin resistant *Staphylococcus aureus* USA300 due to the presence of an aqueous NaCl solution (0.505 M) in a well in the plate.

2.7.3 Comparative overview

Table S15 - The measured zone of inhibition (diameter) in mm of the inhibition of growth in each experimental condition described in Figures S413-S424.

Figure	Biological repeat 1 (mm)	Biological repeat 2 (mm)	Biological repeat 3 (mm)	Mean average (mm)	Standard deviation
S413	13	18	14	14.8	1.92
S414	59	59	60	59.2	0.56
S415	13	21	19	17.4	3.52
S416	53	55	52	53.6	1.15
S417	51	51	56	52.3	2.34
S418	0	0	12	3.9	5.47
S419	17	16	14	15.9	1.19
S420	22	25	23	23.3	1.46
S421	15	13	13	13.8	0.63
S422	18	16	17	17.1	0.77
S423	16	16	14	15.3	0.613
S424	0	0	0	0	0

Appendix 3: Chapter 4

3.1 UV-Vis spectroscopy

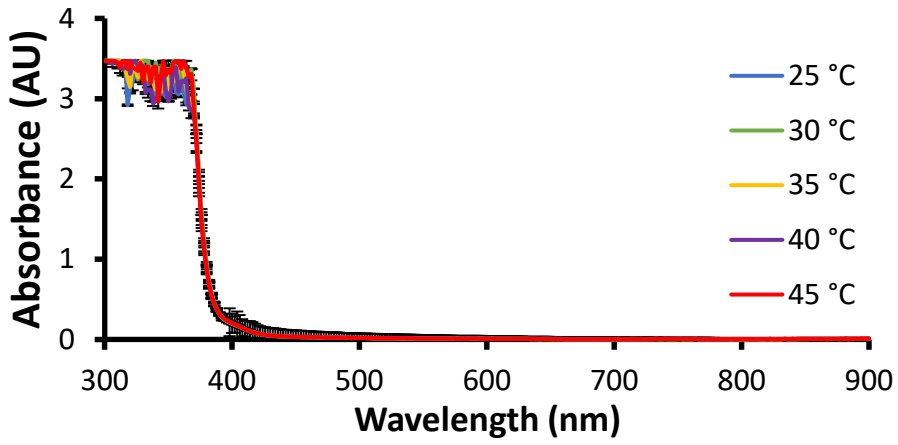

Figure S425 – Average (*n*=3) absorbance graph of **72** (1.5 mg/mL) in H_2O recorded for each 200 µL sample at 5-degree increments from 25-45 °C.

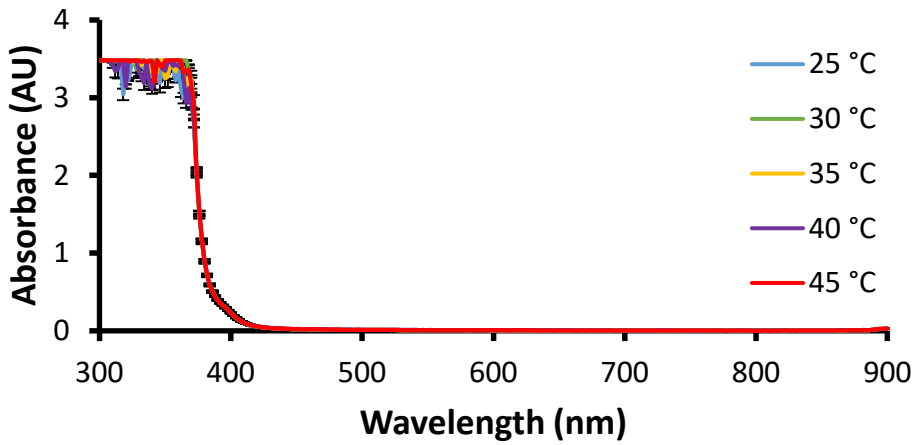

Figure S426 – Average (*n*=3) absorbance graph of **72** (1.5 mg/mL) in DMSO recorded for each 200 µL sample at 5-degree increments from 25-45 °C.

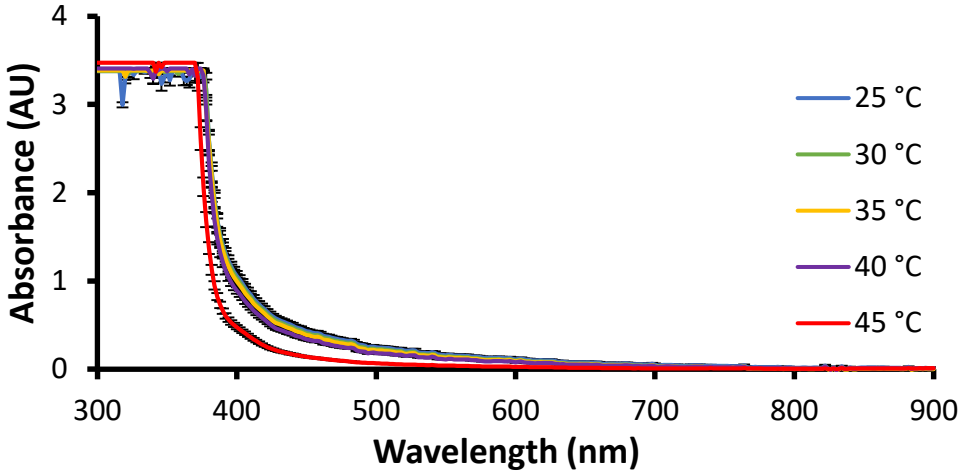

Figure S427 – Average (*n*=3) absorbance graph of **72** (1.5 mg/mL) in aqueous Na_2HPO_4 (0.505 M) recorded for each 200 µL sample at 5-degree increments from 25-45 °C.

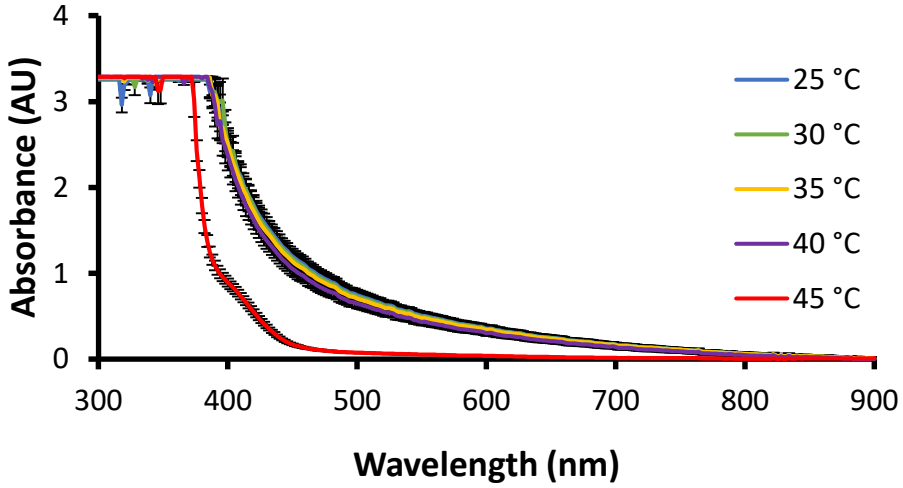

Figure S428 – Average (*n*=3) absorbance graph of **72** (1.5 mg/mL) in aqueous NaH_2PO_4 (0.505 M) recorded for each 200 µL sample at 5-degree increments from 25-45 °C.

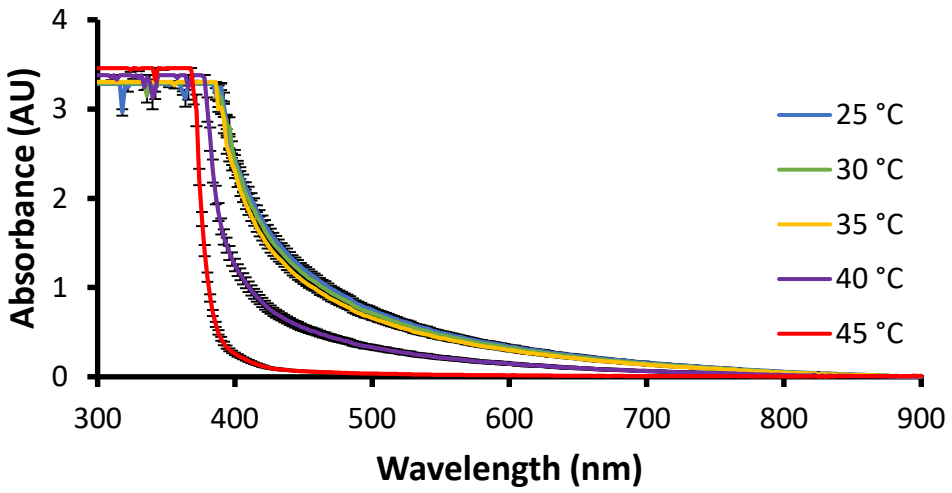

Figure S429 – Average (*n*=3) absorbance graph of **72** (1.5 mg/mL) in aqueous Na_2CO_3 (0.505 M) recorded for each 200 µL sample at 5-degree increments from 25-45 °C.

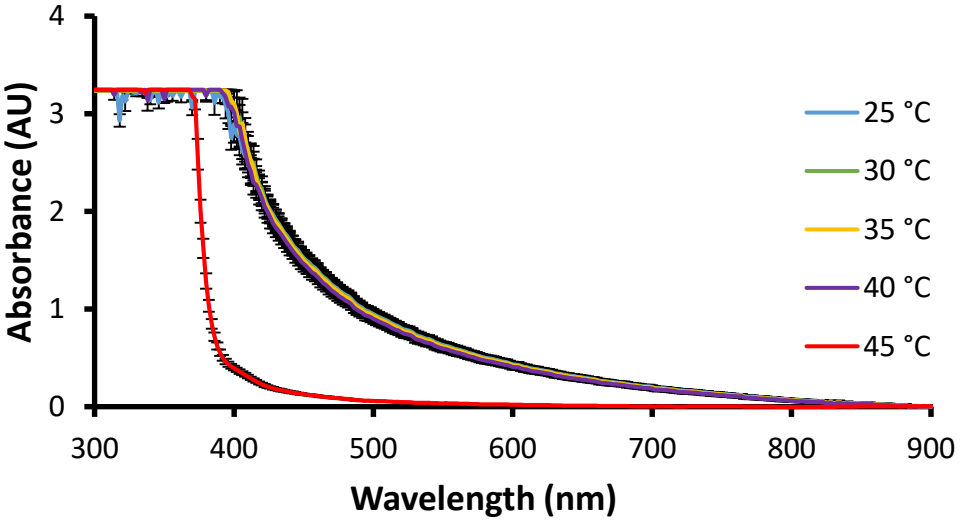

Figure S430 – Average (*n*=3) absorbance graph of **72** (1.5 mg/mL) in aqueous Na_2SO_4 (0.505 M) recorded for each 200 µL sample at 5-degree increments from 25-45 °C.

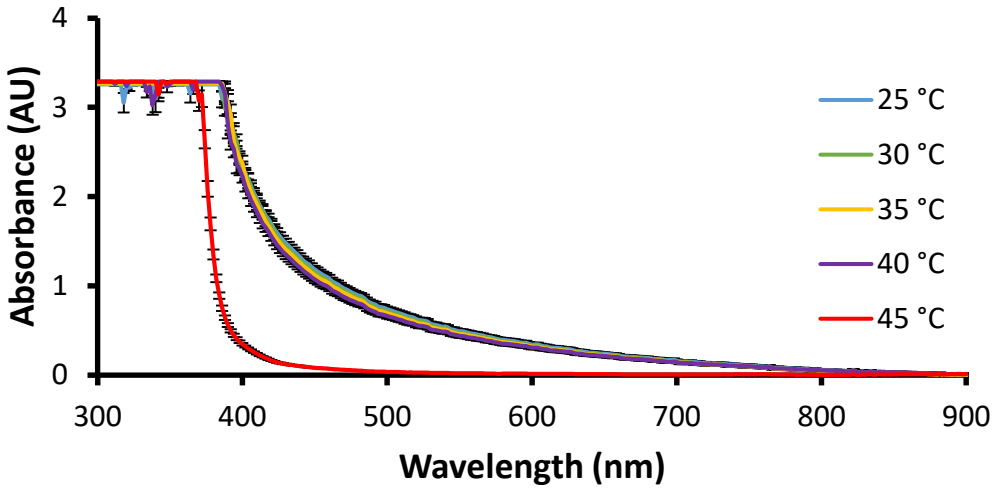

Figure S431 – Average (*n*=3) absorbance graph of **72** (1.5 mg/mL) in aqueous $NaHCO_3$ (0.505 M) recorded for each 200 µL sample at 5-degree increments from 25-45 °C.

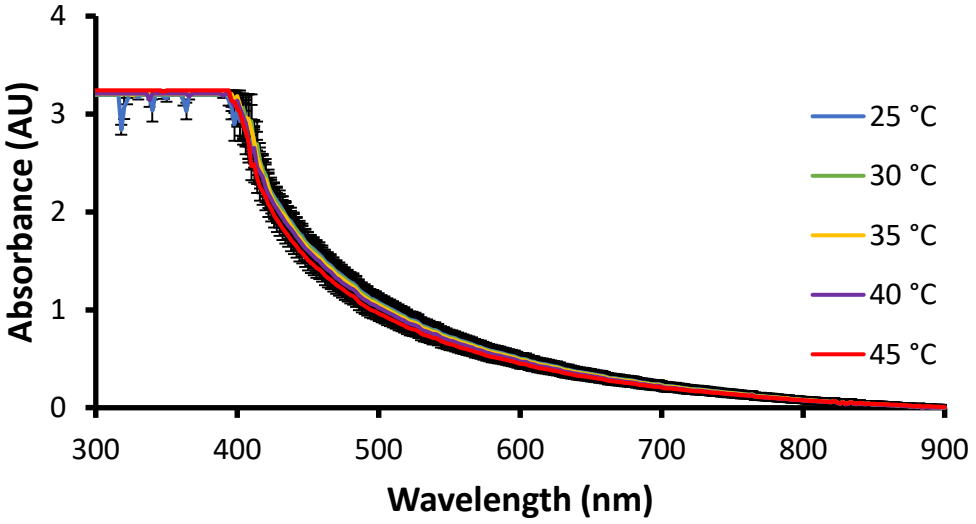

Figure S432 – Average (*n*=3) absorbance graph of **72** (1.5 mg/mL) in aqueous NaOAc (0.505 M) recorded for each 200 µL sample at 5-degree increments from 25-45 °C.

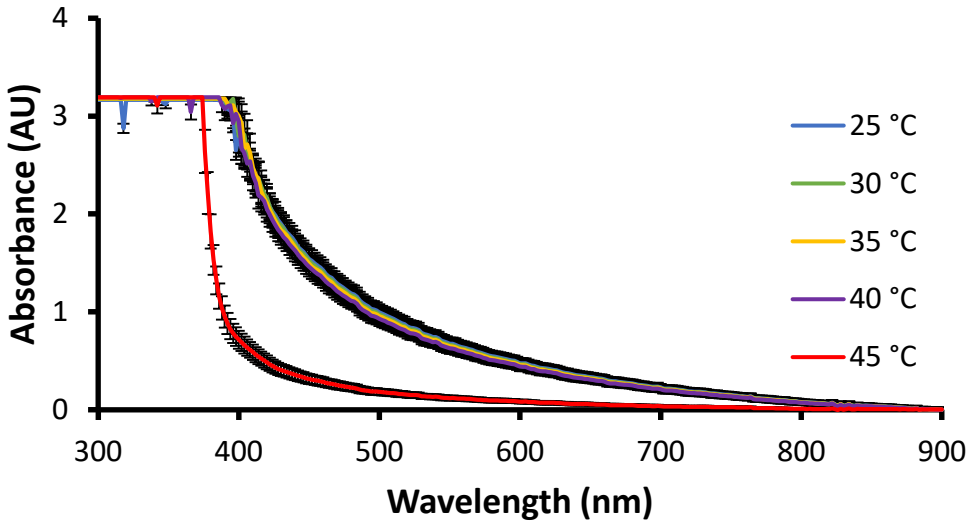

Figure S433 – Average (*n*=3) absorbance graph of **72** (1.5 mg/mL) in aqueous NaF (0.505 M) recorded for each 200 µL sample at 5-degree increments from 25-45 °C.

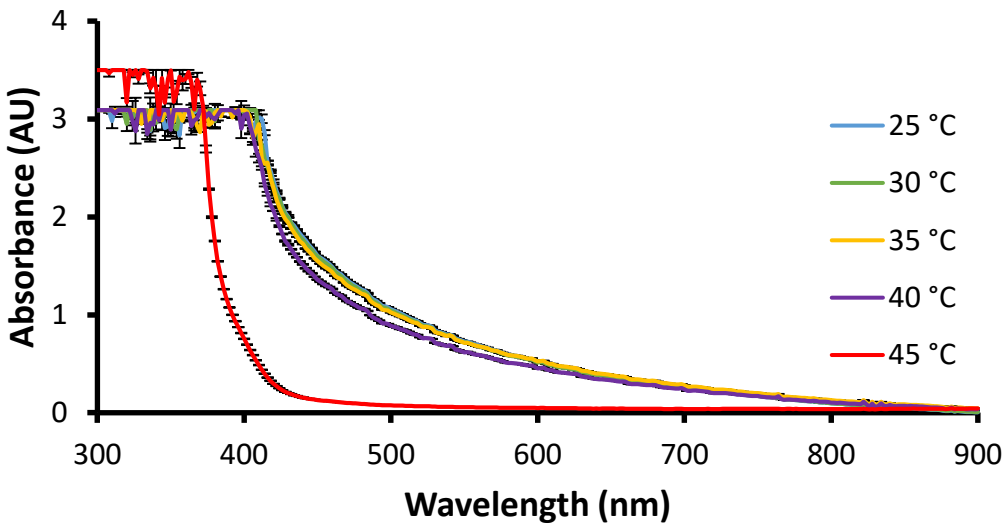

Figure S434 – Average (*n*=3) absorbance graph of **72** (1.5 mg/mL) in aqueous RbCl (0.505 M) recorded for each 200 µL sample at 5-degree increments from 25-45 °C.

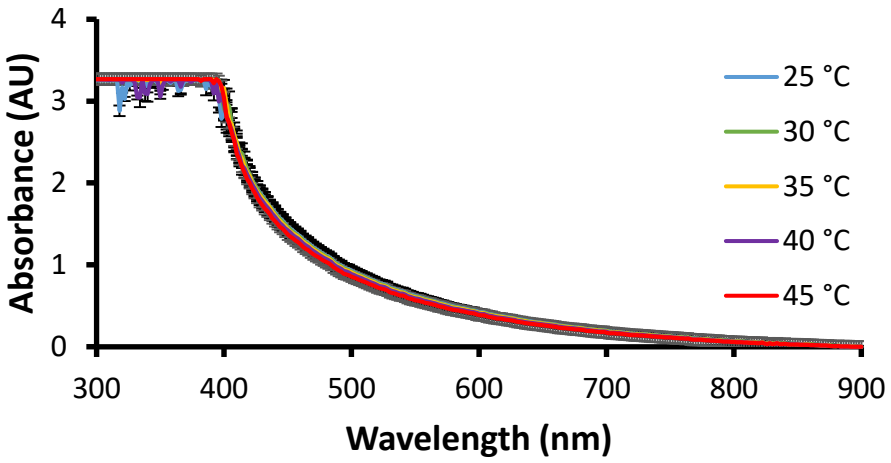

Figure S435 – Average (*n*=3) absorbance graph of **72** (1.5 mg/mL) in aqueous NaCl (0.505 M) recorded for each 200 µL sample at 5-degree increments from 25-45 °C.

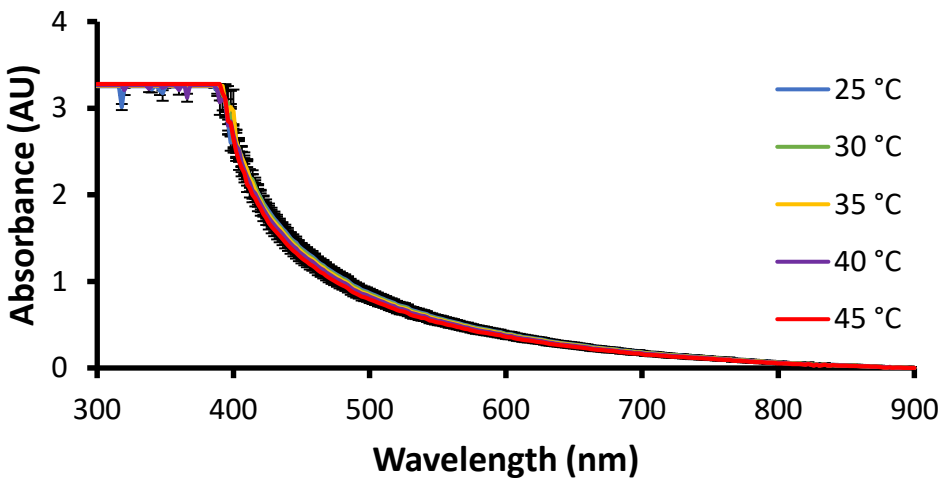

Figure S436 – Average (*n*=3) absorbance graph of **72** (1.5 mg/mL) in aqueous $NaNO_3$ (0.505 M) recorded for each 200 µL sample at 5-degree increments from 25-45 °C.

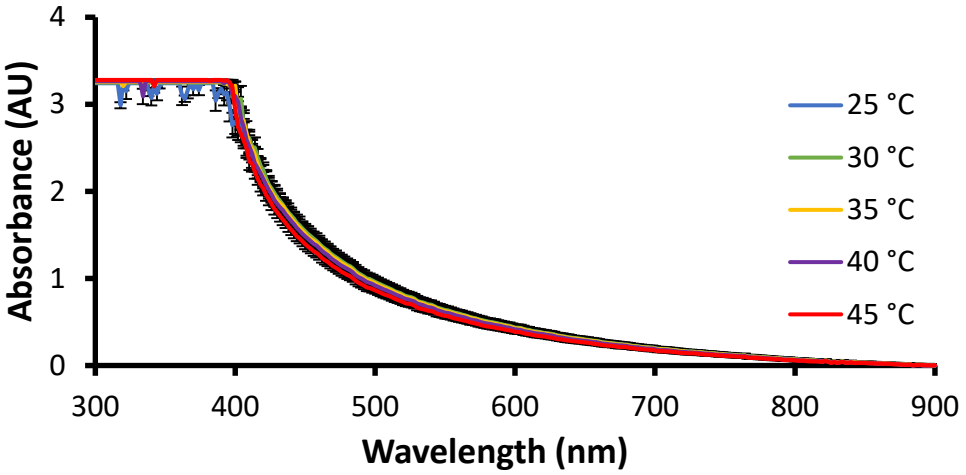

Figure S437 – Average (*n*=3) absorbance graph of **72** (1.5 mg/mL) in aqueous NaOBz (0.505 M) recorded for each 200 µL sample at 5-degree increments from 25-45 °C.

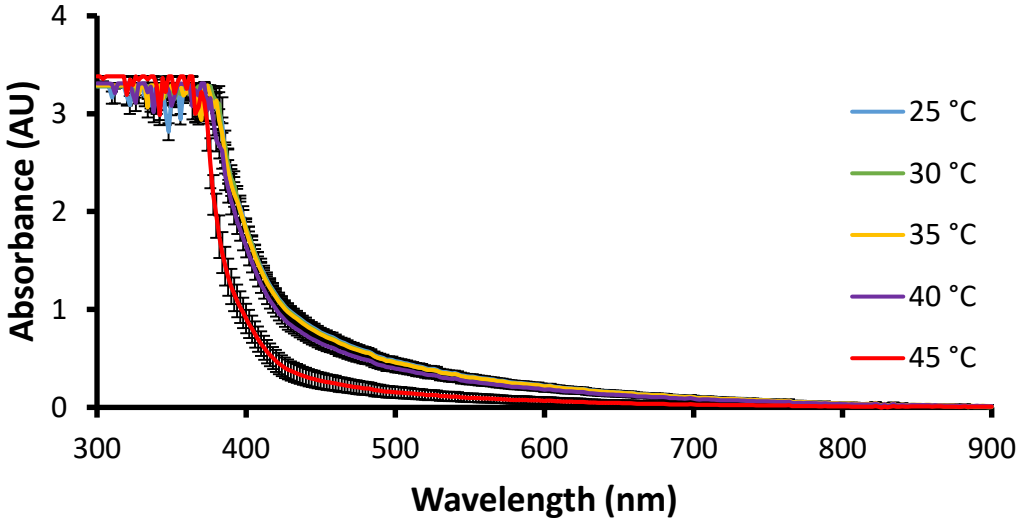

Figure S438 – Average (*n*=3) absorbance graph of **72** (1.5 mg/mL) in aqueous KCl (0.505 M) recorded for each 200 µL sample at 5-degree increments from 25-45 °C.

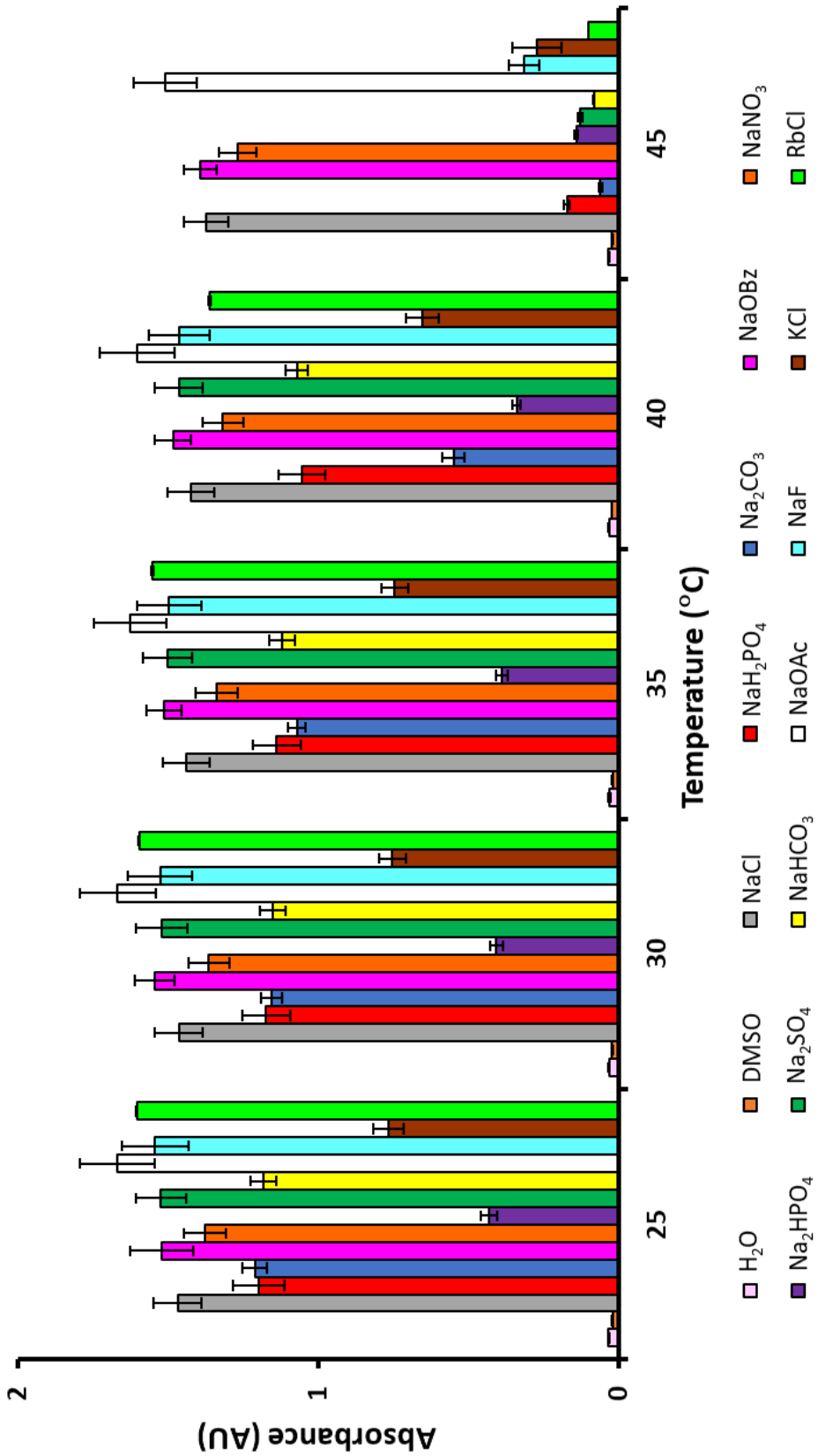

Figure S439 - Average (*n*=3) Abs.$_{450}$ values for solutions/partial/hydrogels of **72** (1.5 mg/mL) in H_2O, DMSO and various aqueous salt solutions (0.505 M) at 25-45 °C. Error bars represent the full range of Abs.$_{450}$ for three repetitions.

3.1.1 Comparative overview

Table S16 - Average (*n*=3) absorbance values obtained at 450 nm ($Abs._{450}$) for **72** (1.5 mg/mL) in H_2O. DMSO and aqueous salt solutions (0.505 M), at 5-degree increments from 25-45 °C. Error = standard error of the mean (±).

Solution	**Temp (°C)**					**Solution**	**Temp (°C)**				
	25	30	35	40	45		25	30	35	40	45
H_2O	0.03 *± 0.00*	0.03 *± 0.00*	0.03 *± 0.00*	0.03 *± 0.00*	0.03 *± 0.00*	NaOAc	1.67 *± 0.12*	1.67 *± 0.13*	1.63 *± 0.12*	1.60 *± 0.12*	1.51 *± 0.10*
DMSO	0.02 *± 0.00*	0.02 *± 0.00*	0.02 *± 0.00*	0.02 *± 0.00*	0.02 *± 0.00*	NaF	1.54 *± 0.11*	1.53 *± 0.11*	1.50 *± 0.11*	1.46 *± 0.10*	0.31 *± 0.05*
Na_2HPO_4	0.43 *± 0.03*	0.41 *± 0.02*	0.39 *± 0.02*	0.34 *± 0.01*	0.14 *± 0.01*	RbCl	1.60 *± 0.00*	1.60 *± 0.00*	1.55 *± 0.00*	1.36 *± 0.00*	0.10 *± 0.00*
NaH_2PO_4	1.20 *± 0.09*	1.17 *± 0.08*	1.14 *± 0.08*	1.05 *± 0.08*	0.17 *± 0.01*	NaCl	1.47 *± 0.08*	1.46 *± 0.08*	1.44 *± 0.08*	1.42 *± 0.08*	1.37 *± 0.07*
Na_2CO_3	1.21 *± 0.04*	1.15 *± 0.04*	1.07 *± 0.03*	0.55 *± 0.04*	0.06 *± 0.01*	$NaNO_3$	1.38 *± 0.07*	1.36 *± 0.07*	1.34 *± 0.07*	1.32 *± 0.07*	1.27 *± 0.06*
Na_2SO_4	1.52 *± 0.08*	1.52 *± 0.09*	1.50 *± 0.08*	1.46 *± 0.08*	0.13 *± 0.01*	NaOBz	1.52 *± 0.10*	1.54 *± 0.07*	1.51 *± 0.06*	1.48 *± 0.06*	1.39 *± 0.05*
$NaHCO_3$	1.18 *± 0.04*	1.15 *± 0.04*	1.12 *± 0.04*	1.07 *± 0.04*	0.08 *± 0.00*	KCl	0.77 *± 0.05*	0.75 *± 0.05*	0.75 *± 0.05*	0.65 *± 0.06*	0.27 *± 0.08*

3.2 Spectral well-scans

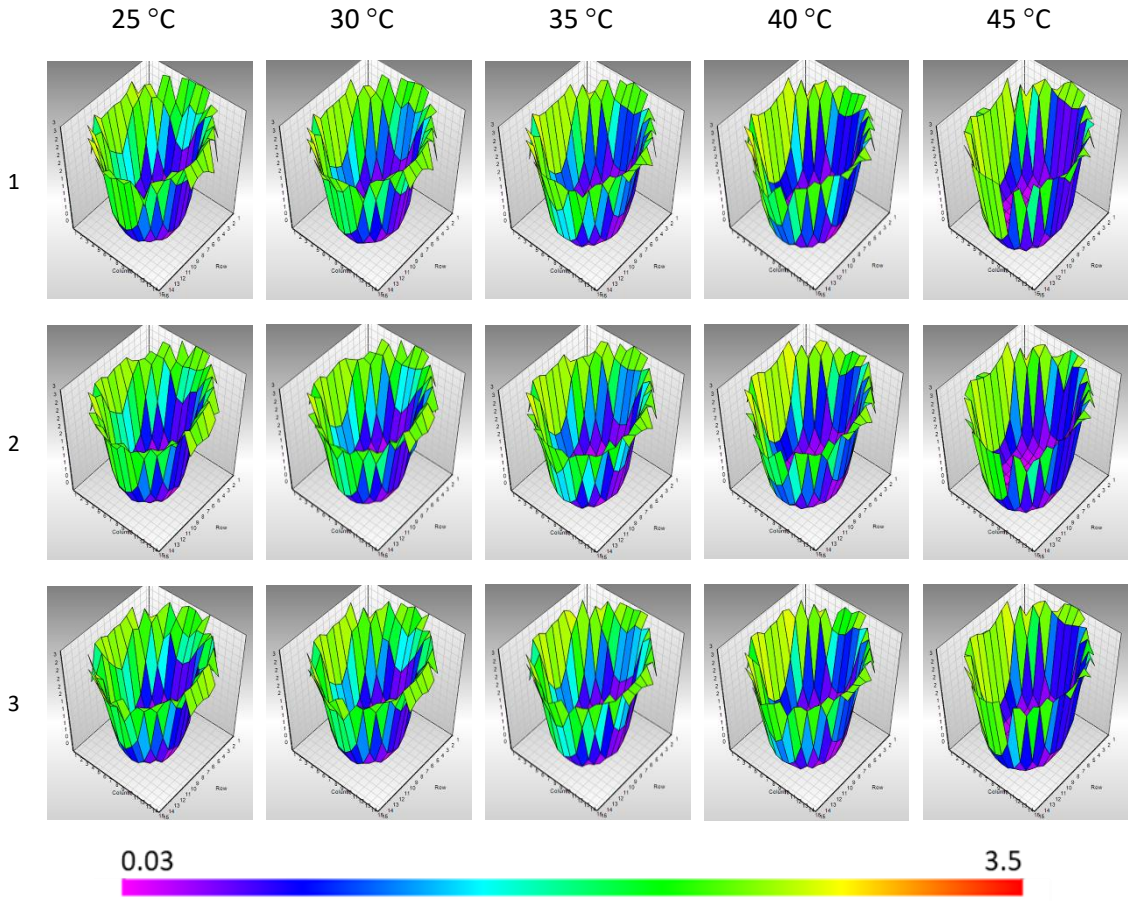

Figure S440 - Spectral analysis microplate well scans (*n*=3) conducted at OD_{450} with **72** (1.5 mg/mL) in H_2O, recorded for each 200 µL sample at 5-degree increments from 25-45 °C.

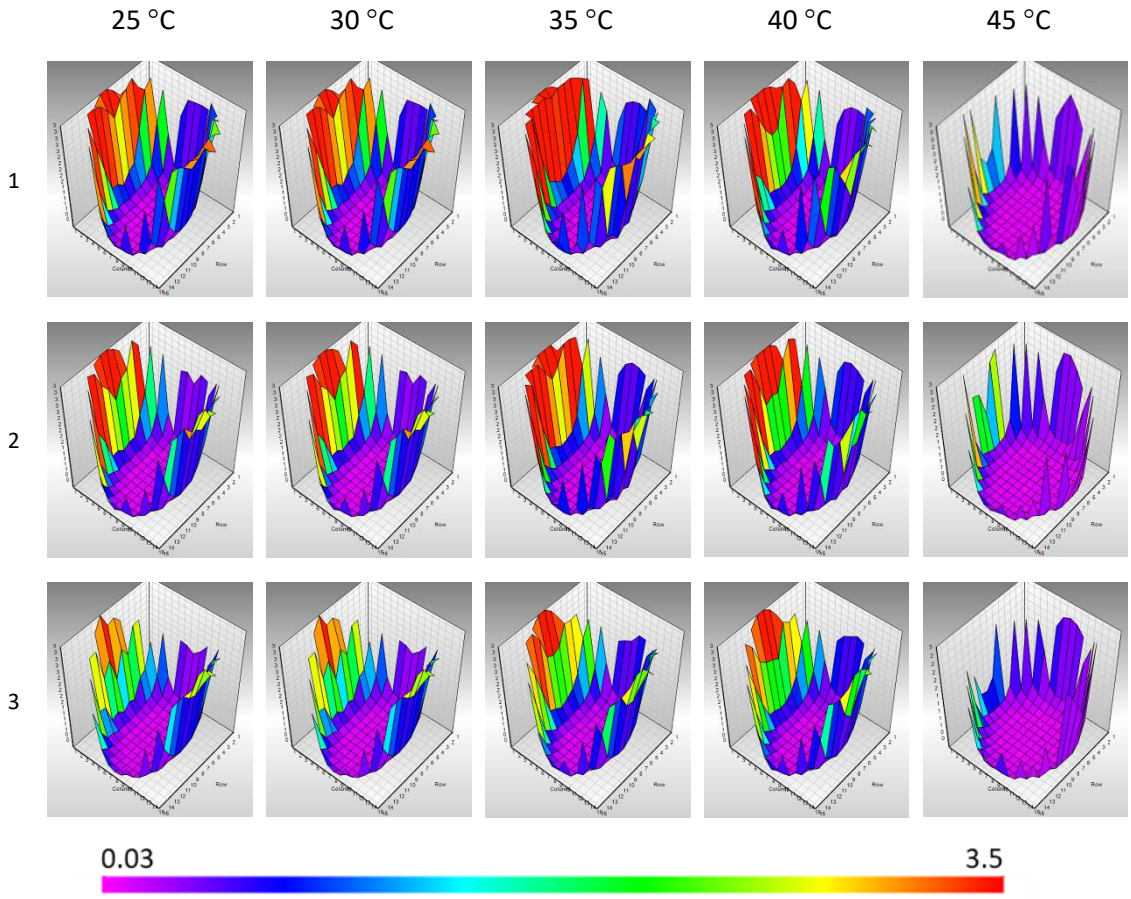

Figure S441 - Spectral analysis microplate well scans (*n*=3) conducted at OD_{450} with **72** (1.5 mg/mL) in DMSO, recorded for each 200 µL sample at 5-degree increments from 25-45 °C.

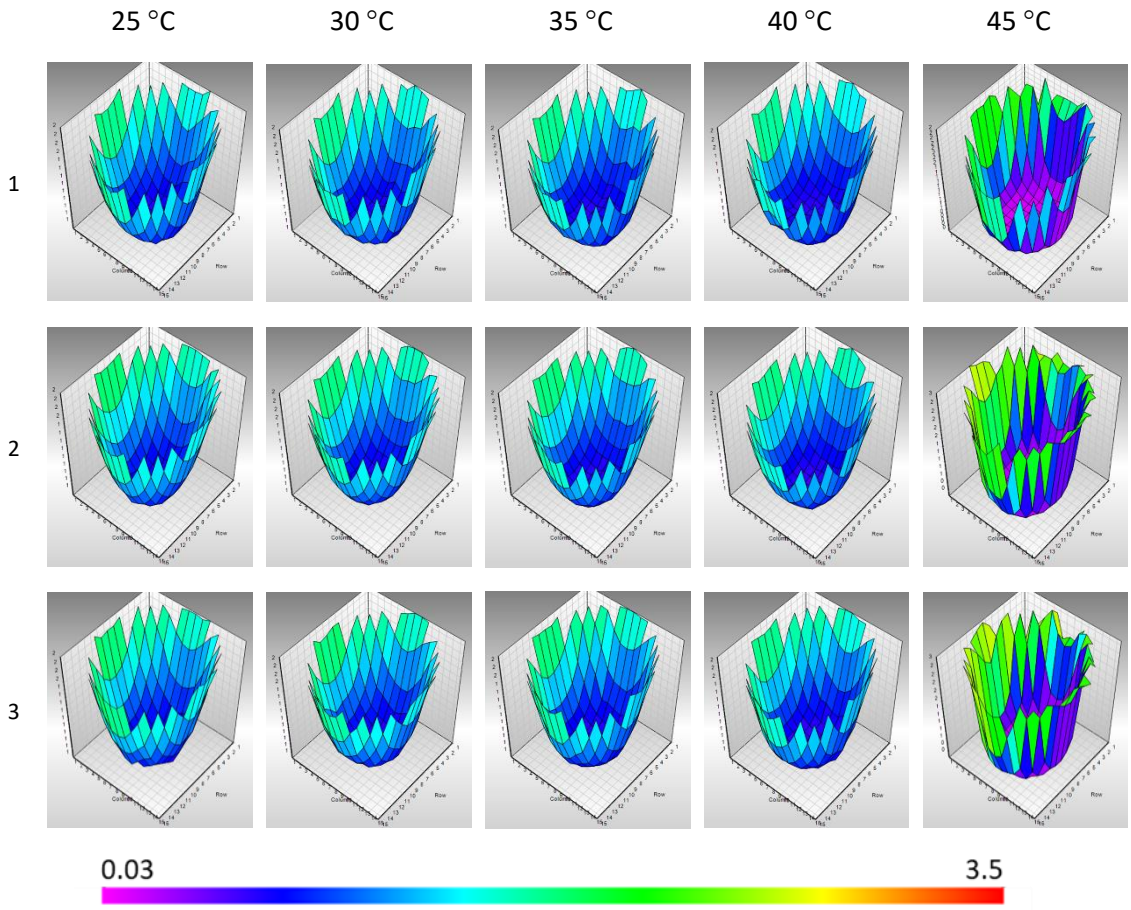

Figure S442 - Spectral analysis microplate well scans (*n*=3) conducted at OD_{450} with **72** (1.5 mg/mL) in aqueous Na_2HPO_4 (0.505 M), recorded for each 200 µL sample at 5-degree increments from 25-45 °C.

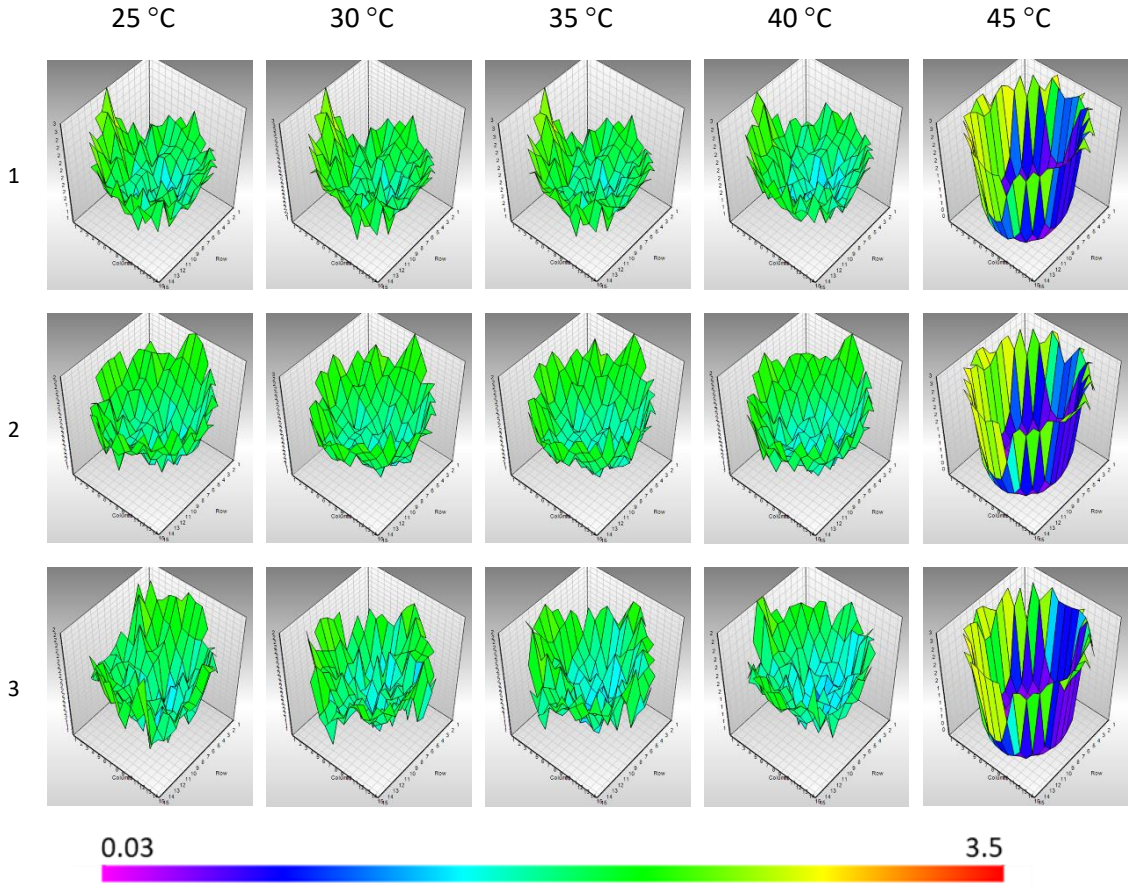

Figure S443 - Spectral analysis microplate well scans (*n*=3) conducted at OD_{450} with **72** (1.5 mg/mL) in aqueous NaH_2PO_4 (0.505 M), recorded for each 200 µL sample at 5-degree increments from 25-45 °C.

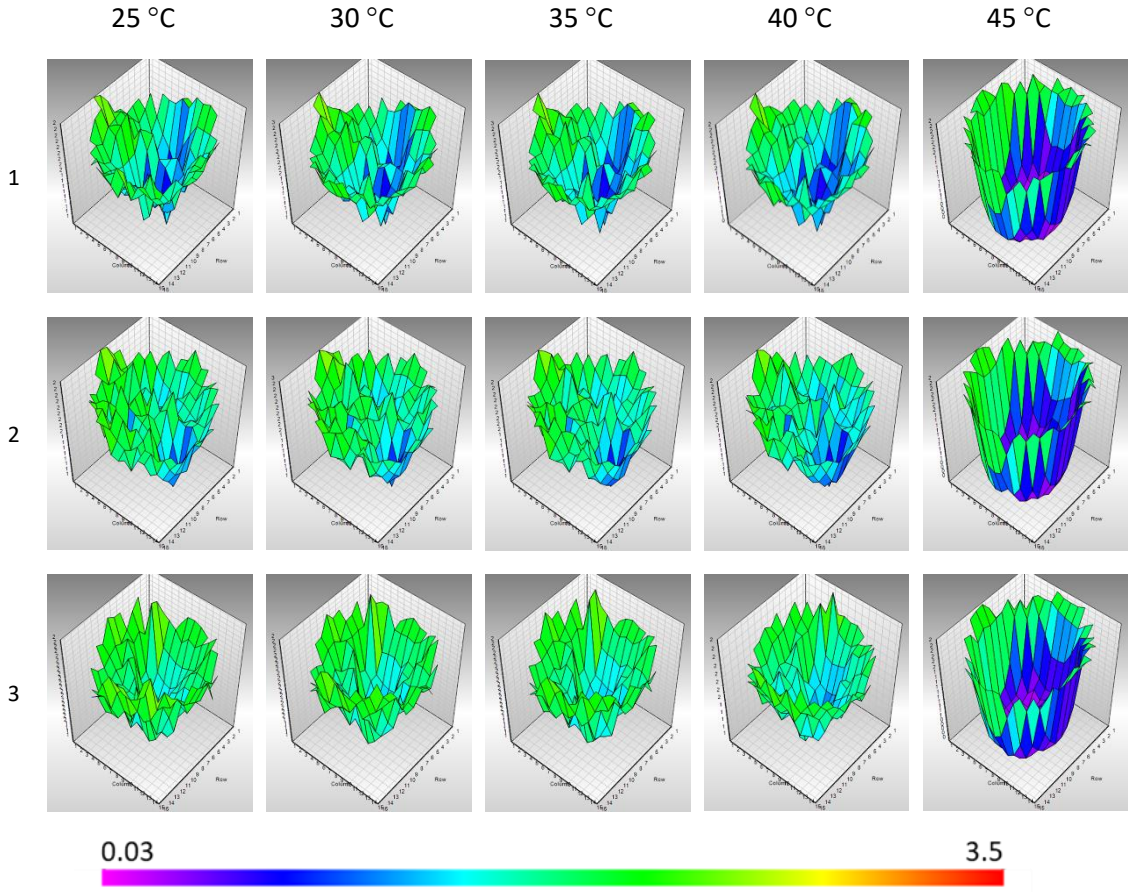

Figure S444 - Spectral analysis microplate well scans (*n*=3) conducted at OD_{450} with **72** (1.5 mg/mL) in aqueous Na_2CO_3 (0.505 M), recorded for each 200 µL sample at 5-degree increments from 25-45 °C.

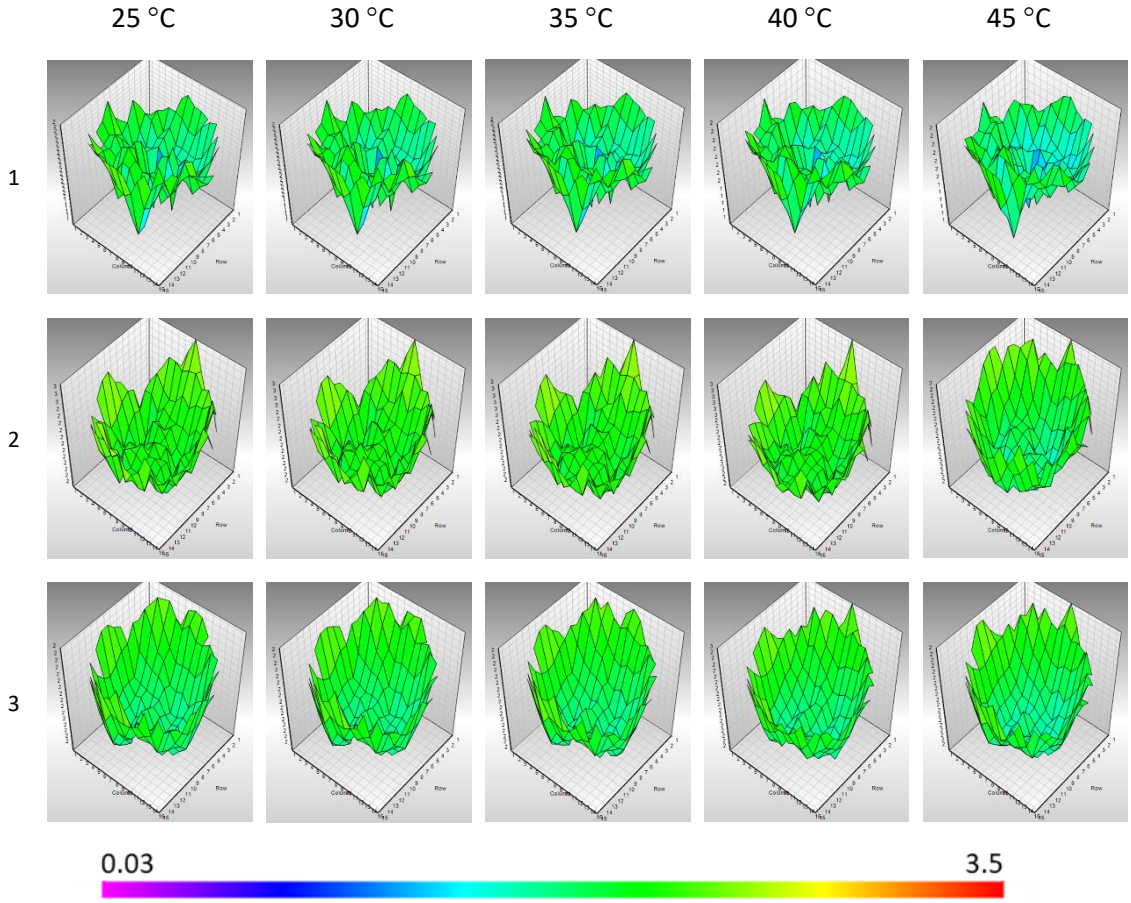

Figure S445 - Spectral analysis microplate well scans (*n*=3) conducted at OD_{450} with **72** (1.5 mg/mL) in aqueous Na_2SO_4 (0.505 M), recorded for each 200 µL sample at 5-degree increments from 25-45 °C.

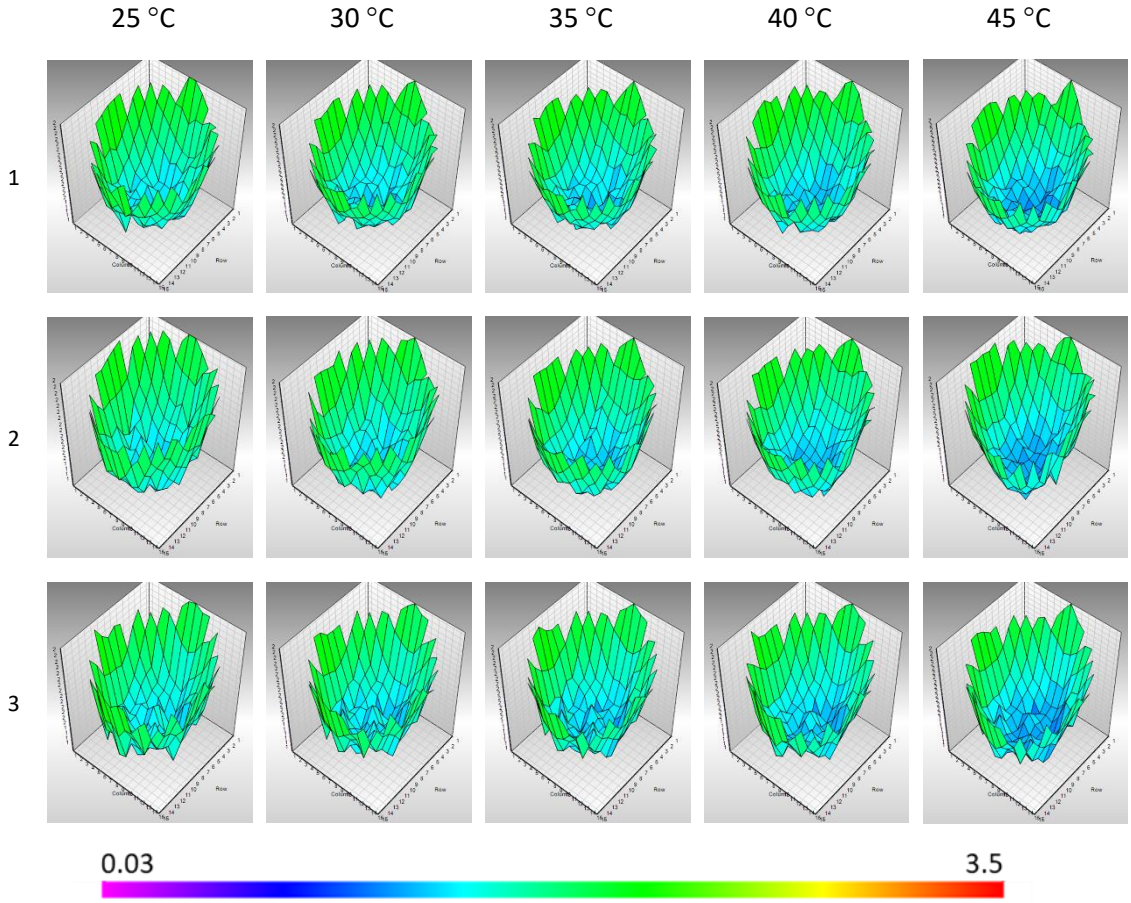

Figure S446 - Spectral analysis microplate well scans (*n*=3) conducted at OD_{450} with **72** (1.5 mg/mL) in aqueous $NaHCO_3$ (0.505 M), recorded for each 200 µL sample at 5-degree increments from 25-45 °C.

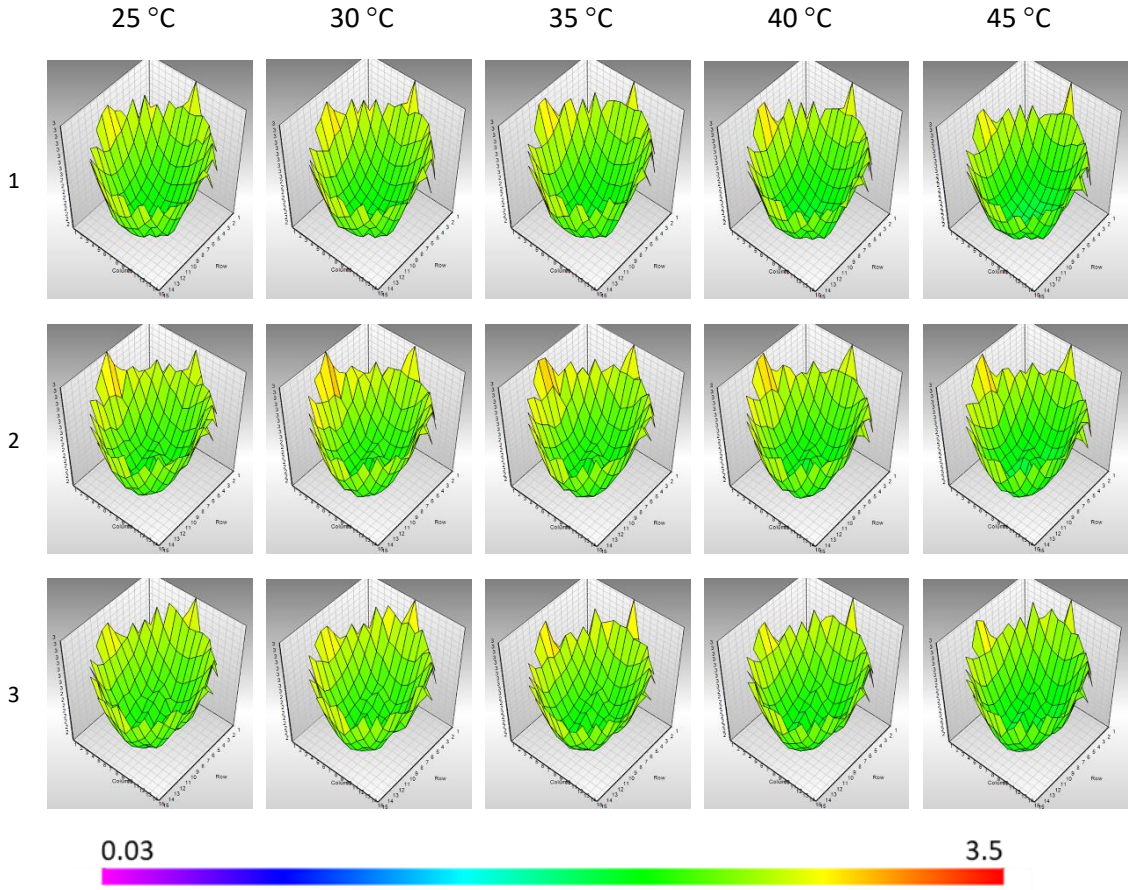

Figure S447 - Spectral analysis microplate well scans (*n*=3) conducted at OD_{450} with **72** (1.5 mg/mL) in aqueous NaOAc (0.505 M), recorded for each 200 µL sample at 5-degree increments from 25-45 °C.

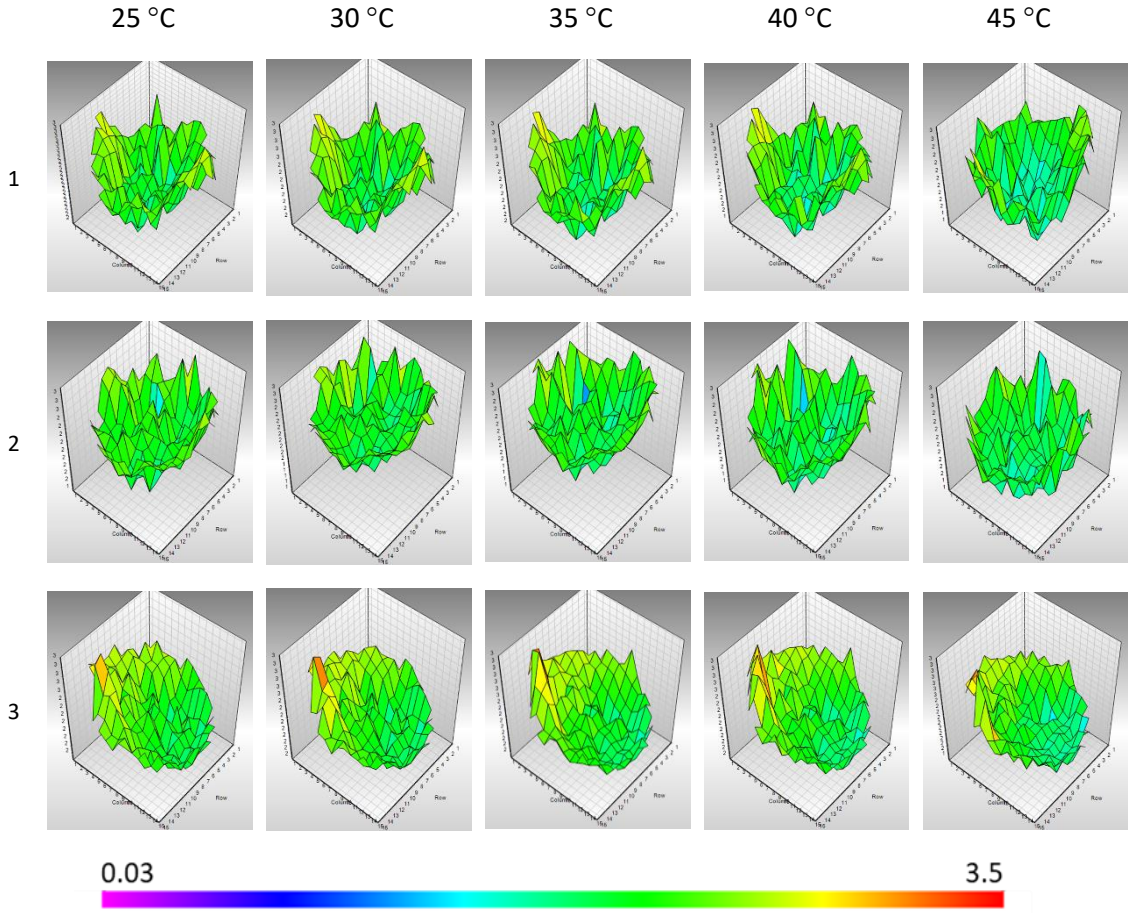

Figure S448 - Spectral analysis microplate well scans (*n*=3) conducted at OD_{450} with **72** (1.5 mg/mL) in aqueous NaF (0.505 M), recorded for each 200 µL sample at 5-degree increments from 25-45 °C.

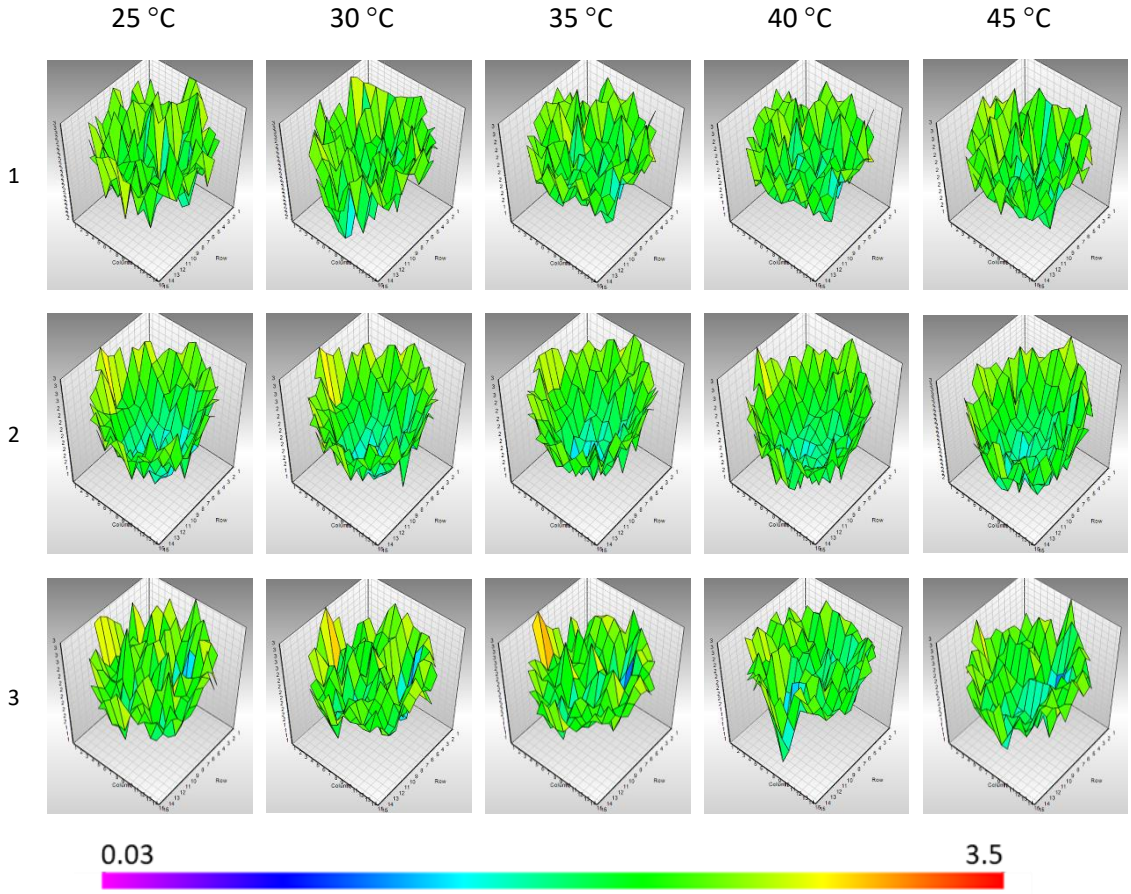

Figure S449 - Spectral analysis microplate well scans (*n*=3) conducted at OD_{450} with **72** (1.5 mg/mL) in aqueous RbCl (0.505 M), recorded for each 200 µL sample at 5-degree increments from 25-45 °C.

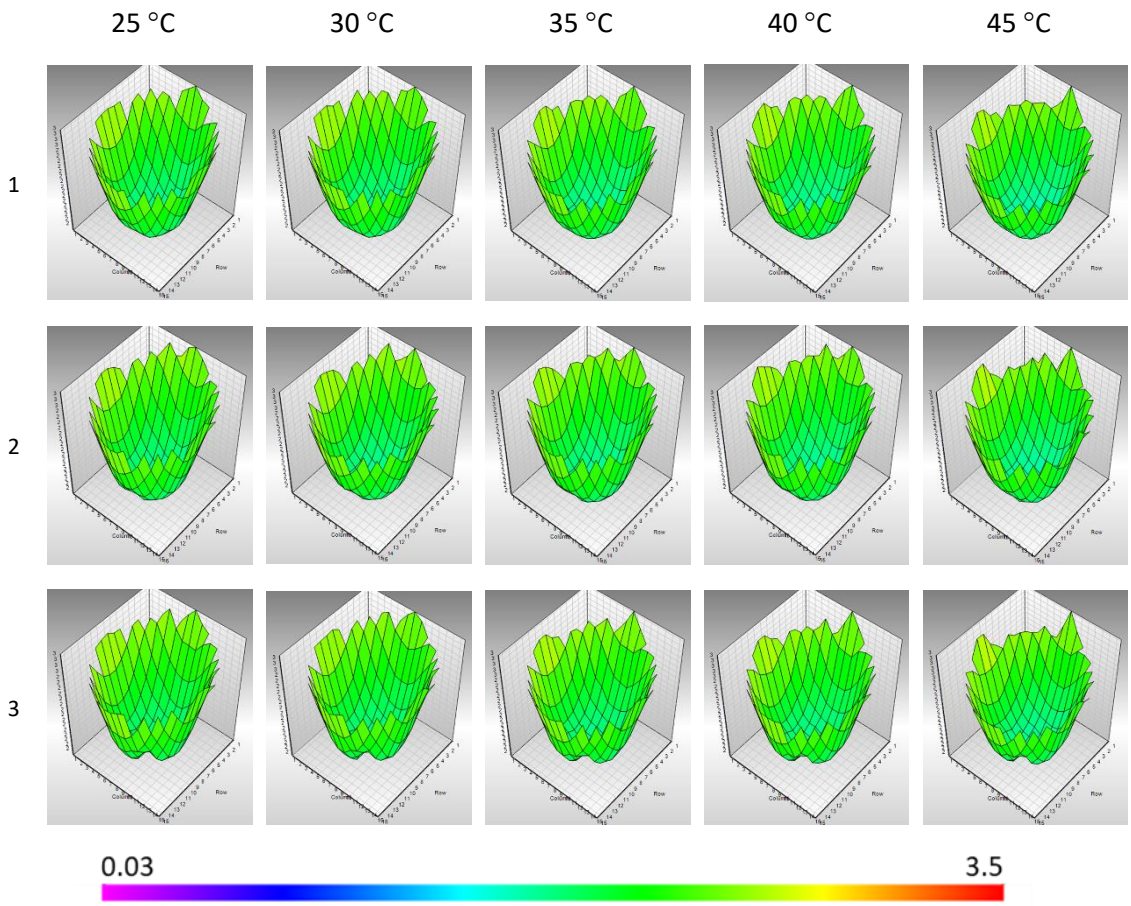

Figure S450 - Spectral analysis microplate well scans (*n*=3) conducted at OD_{450} with **72** (1.5 mg/mL) in aqueous NaCl (0.505 M), recorded for each 200 µL sample at 5-degree increments from 25-45 °C.

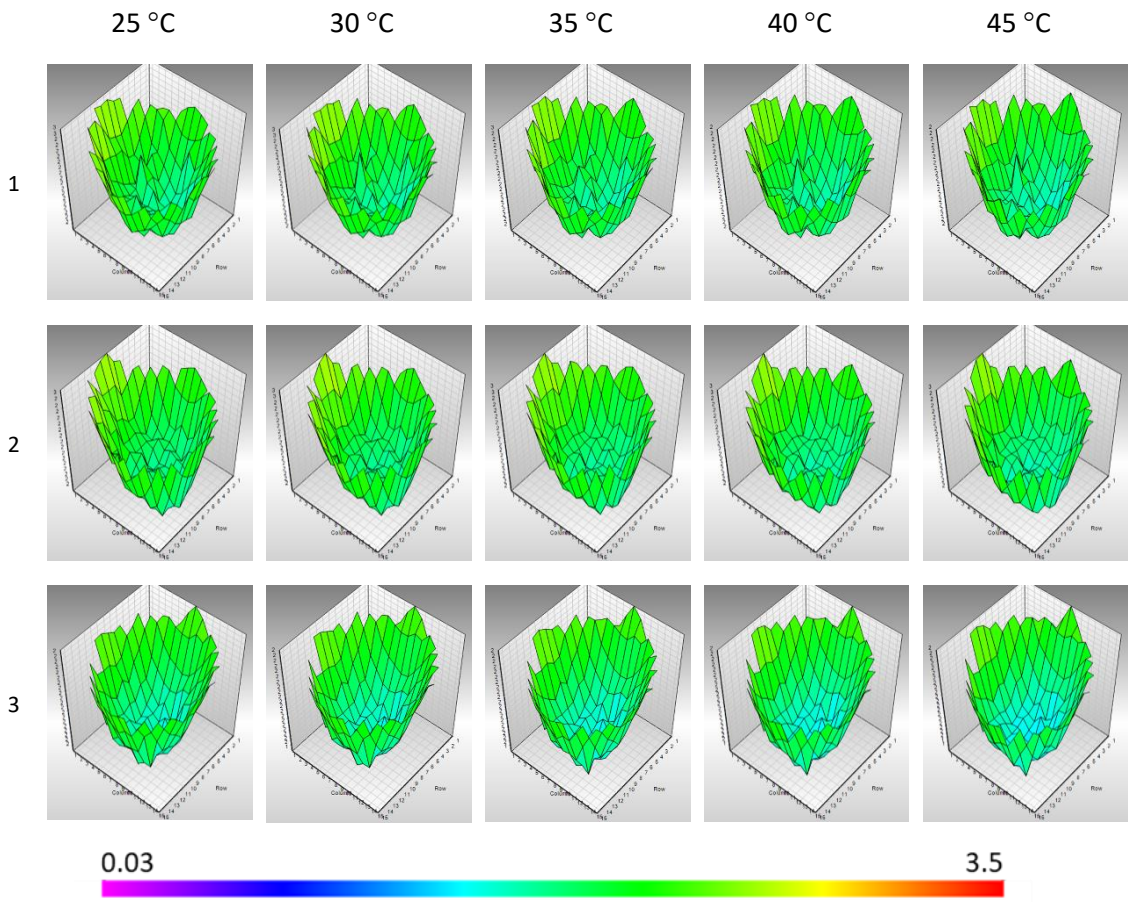

Figure S451 - Spectral analysis microplate well scans (*n*=3) conducted at OD_{450} with **72** (1.5 mg/mL) in aqueous $NaNO_3$ (0.505 M), recorded for each 200 µL sample at 5-degree increments from 25-45 °C.

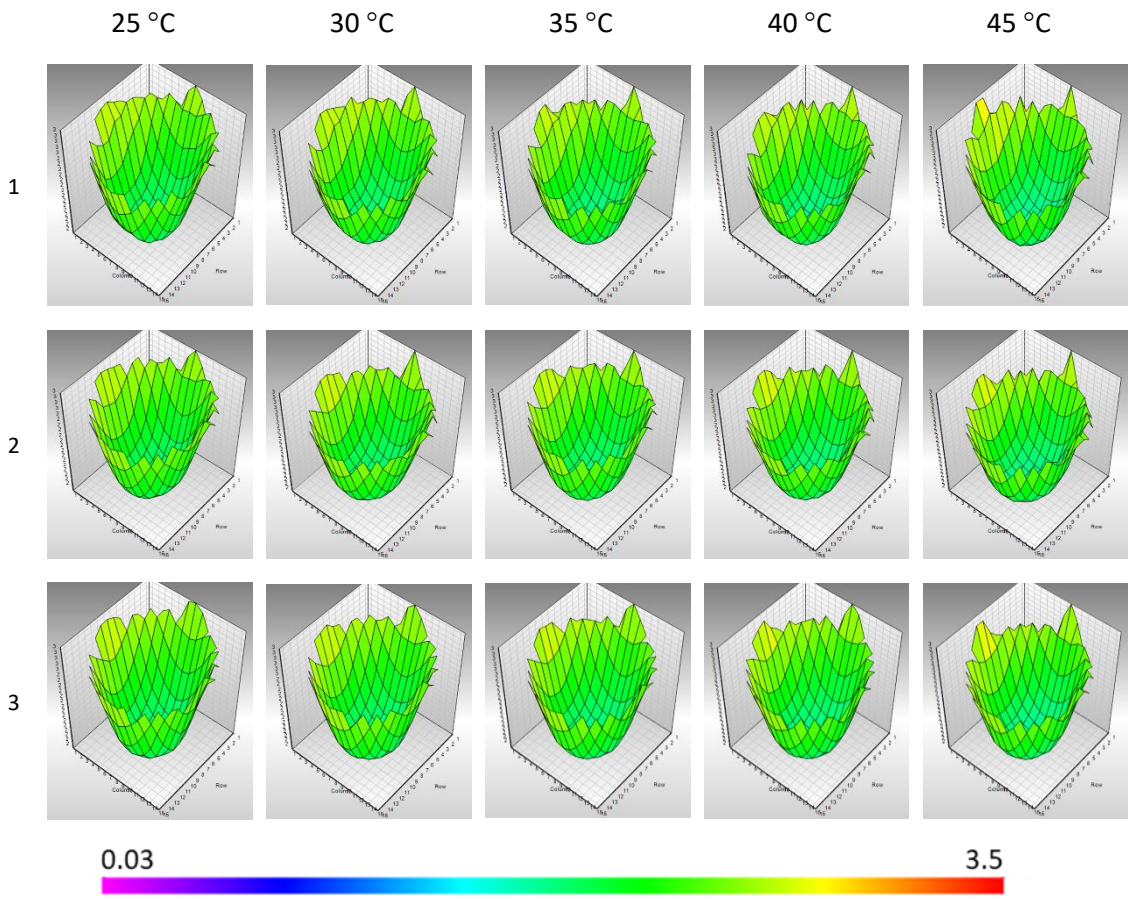

Figure S452 - Spectral analysis microplate well scans (*n*=3) conducted at OD_{450} with **72** (1.5 mg/mL) in aqueous NaOBz (0.505 M), recorded for each 200 µL sample at 5-degree increments from 25-45 °C.

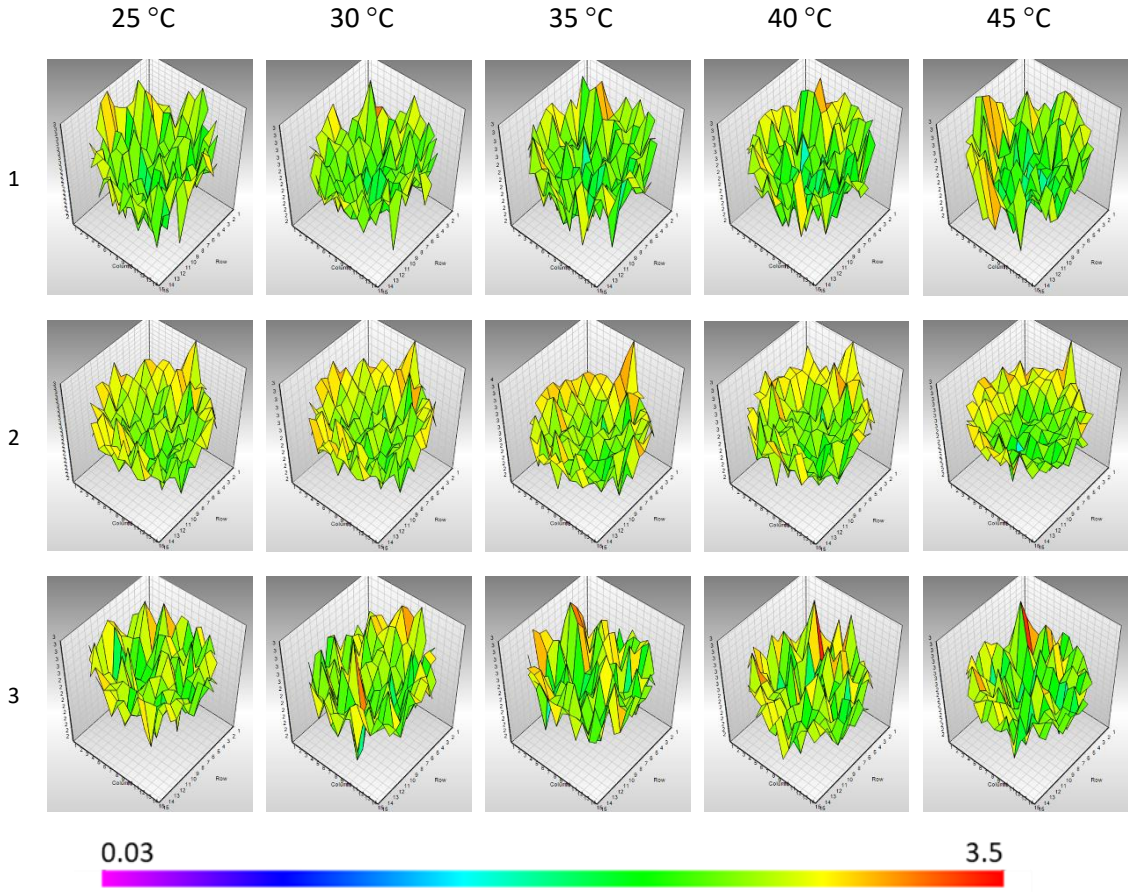

Figure S453 - Spectral analysis microplate well scans (*n*=3) conducted at OD_{450} with **72** (1.5 mg/mL) in aqueous KCl (0.505 M), recorded for each 200 µL sample at 5-degree increments from 25-45 °C.

3.3 Optical density intensity maps

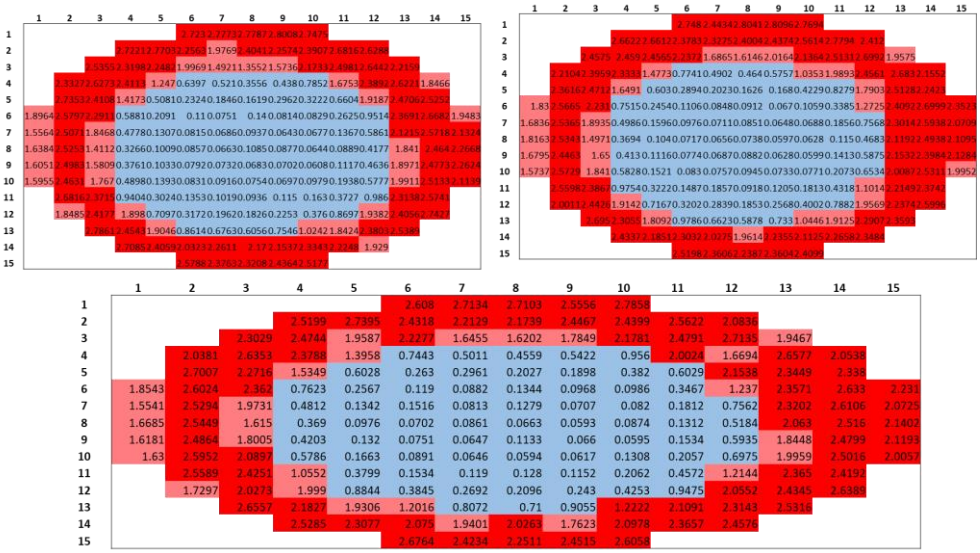

Figure S454 - OD_{450} *n*=3 intensity maps produced for **72** (1.5 mg/mL) in H_2O at 25 °C. Blue: OD_{450} = 0.00-0.99 AU. Pink: OD_{450} = 1.00-1.99 AU. Red: OD_{450} = 2.00-3.00 AU.

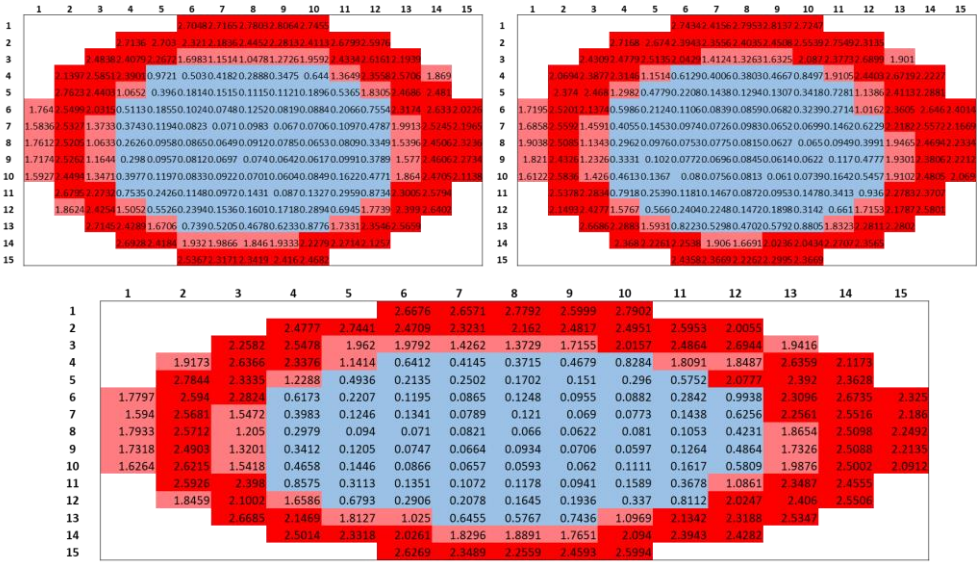

Figure S455 - OD_{450} *n*=3 intensity maps produced for **72** (1.5 mg/mL) in H_2O at 30 °C. Blue: OD_{450} = 0.00-0.99 AU. Pink: OD_{450} = 1.00-1.99 AU. Red: OD_{450} = 2.00-3.00 AU.

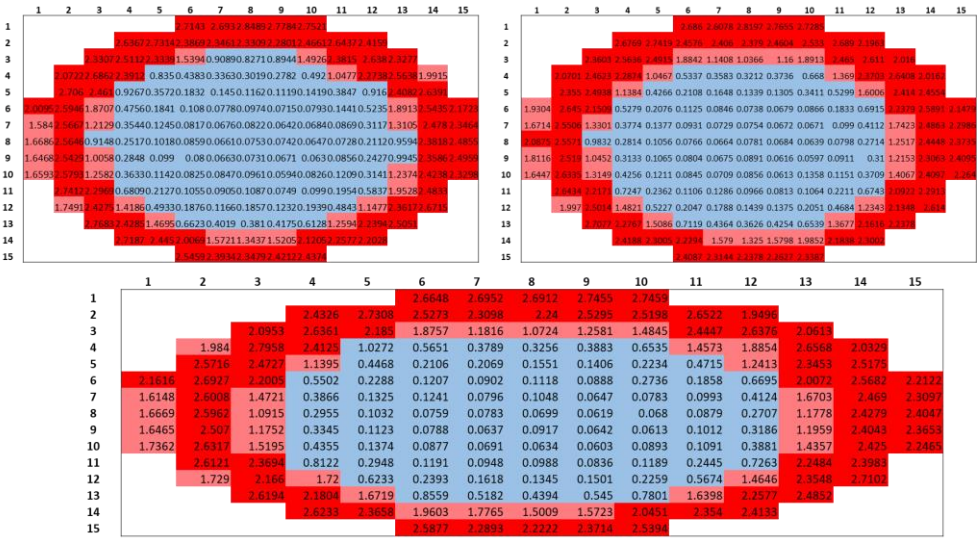

Figure S456 - OD_{450} *n*=3 intensity maps produced for **72** (1.5 mg/mL) in H_2O at 35 °C. Blue: OD_{450} = 0.00-0.99 AU. Pink: OD_{450} = 1.00-1.99 AU. Red: OD_{450} = 2.00-3.00 AU.

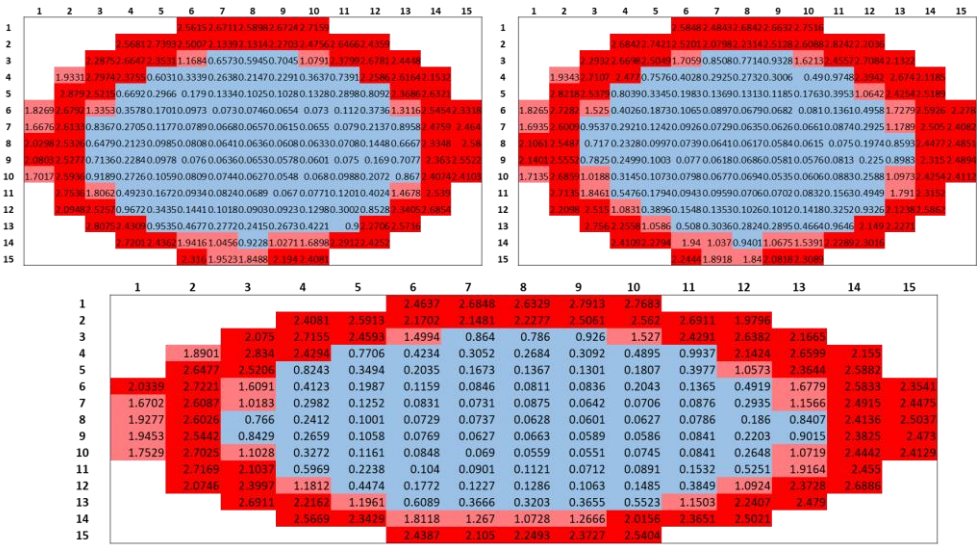

Figure S457 - OD_{450} *n*=3 intensity maps produced for **72** (1.5 mg/mL) in H_2O at 40 °C. Blue: OD_{450} = 0.00-0.99 AU. Pink: OD_{450} = 1.00-1.99 AU. Red: OD_{450} = 2.00-3.00 AU.

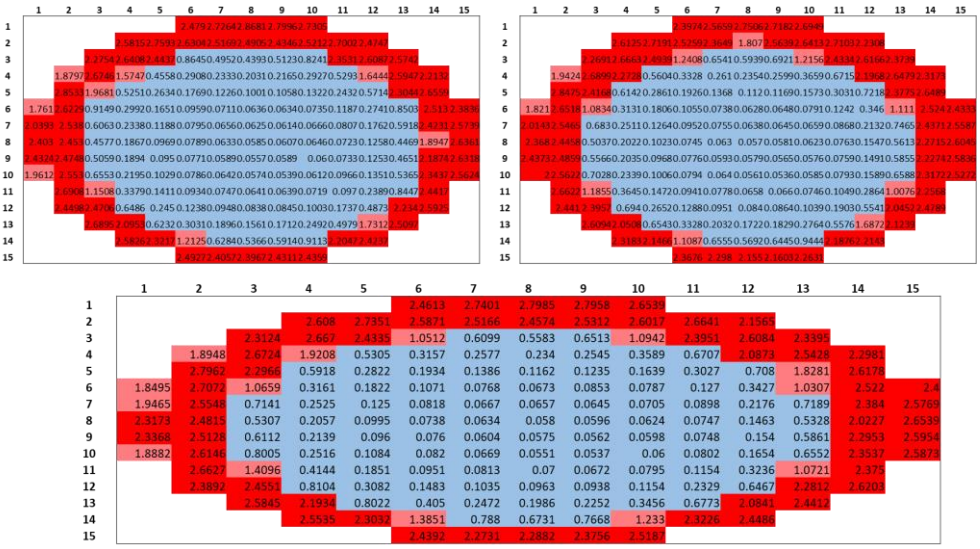

Figure S458 - OD_{450} *n*=3 intensity maps produced for **72** (1.5 mg/mL) in H_2O at 45 °C. Blue: OD_{450} = 0.00-0.99 AU. Pink: OD_{450} = 1.00-1.99 AU. Red: OD_{450} = 2.00-3.00 AU.

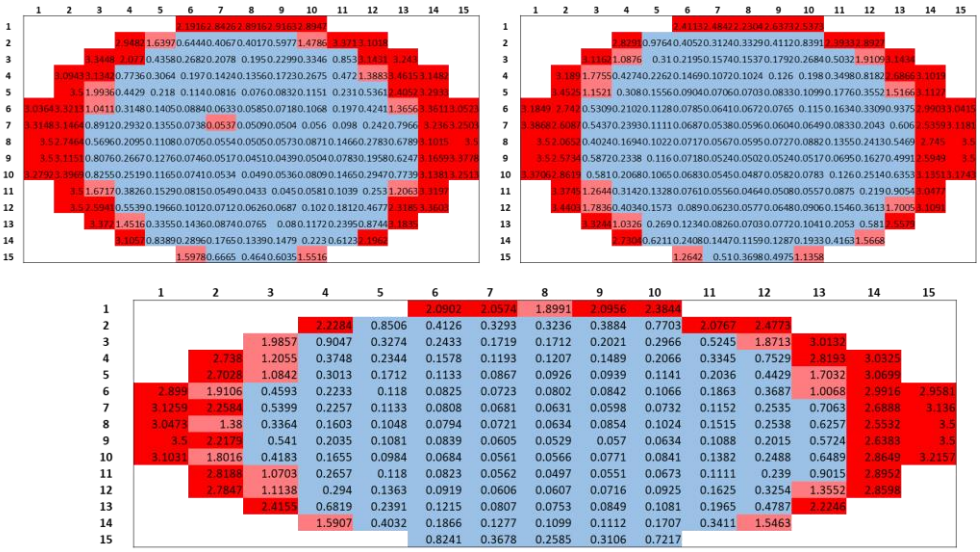

Figure S459 - OD_{450} *n*=3 intensity maps produced for **72** (1.5 mg/mL) in DMSO at 25 °C. Blue: OD_{450} = 0.00-0.99 AU. Pink: OD_{450} = 1.00-1.99 AU. Red: OD_{450} = 2.00-3.00 AU.

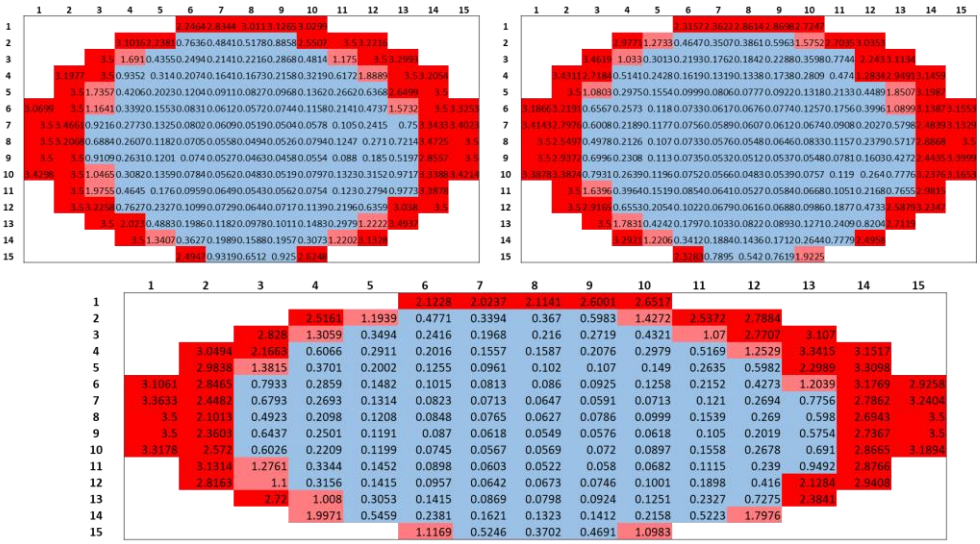

Figure S460 - OD_{450} *n*=3 intensity maps produced for **72** (1.5 mg/mL) in DMSO at 30 °C. Blue: OD_{450} = 0.00-0.99 AU. Pink: OD_{450} = 1.00-1.99 AU. Red: OD_{450} = 2.00-3.00 AU.

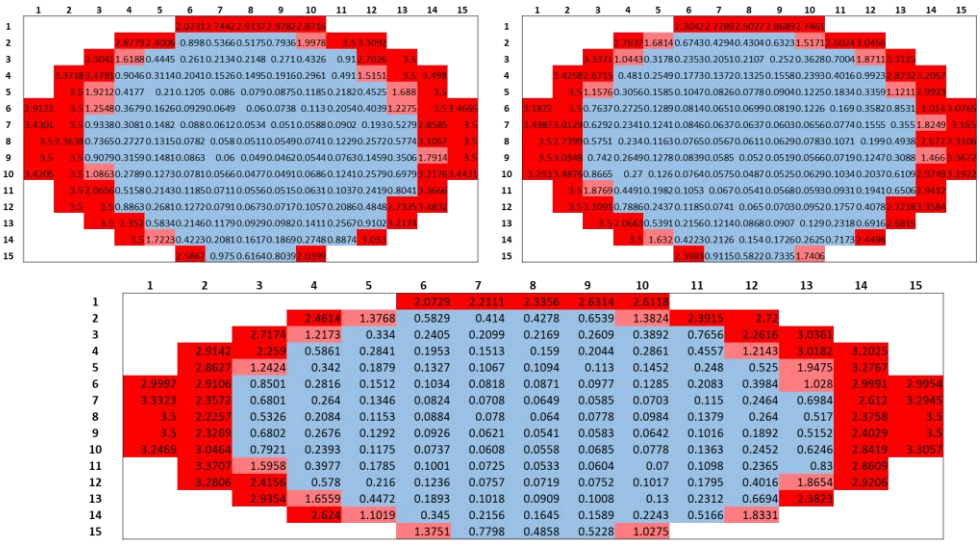

Figure S461 - OD_{450} *n*=3 intensity maps produced for **72** (1.5 mg/mL) in DMSO at 35 °C. Blue: OD_{450} = 0.00-0.99 AU. Pink: OD_{450} = 1.00-1.99 AU. Red: OD_{450} = 2.00-3.00 AU.

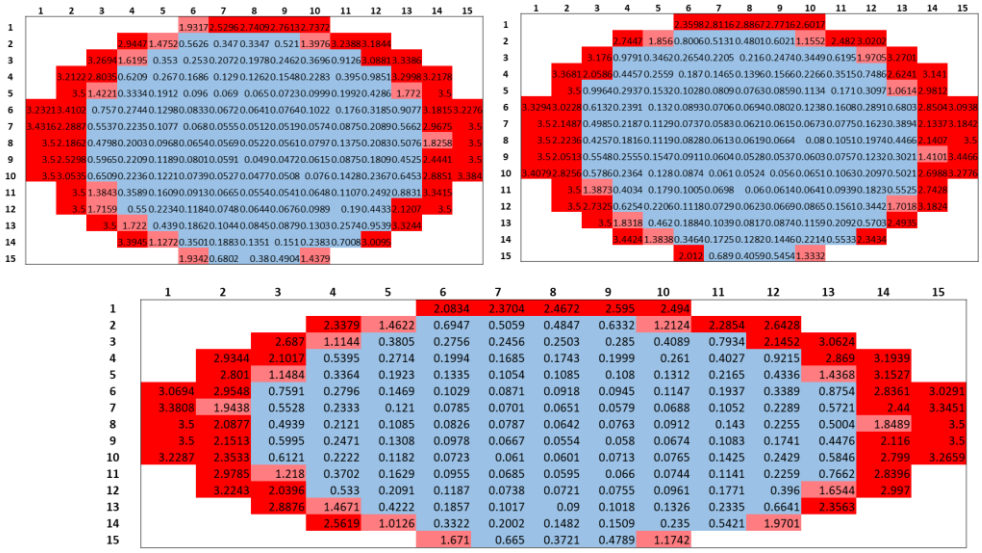

Figure S462 - OD_{450} *n*=3 intensity maps produced for **72** (1.5 mg/mL) in DMSO at 40 °C. Blue: OD_{450} = 0.00-0.99 AU. Pink: OD_{450} = 1.00-1.99 AU. Red: OD_{450} = 2.00-3.00 AU.

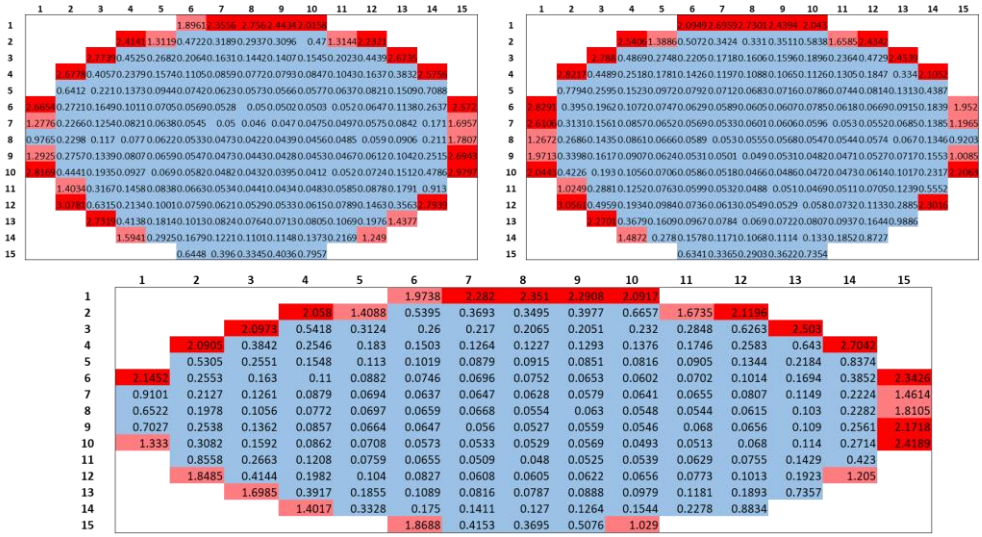

Figure S463 - OD_{450} *n*=3 intensity maps produced for **72** (1.5 mg/mL) in DMSO at 45 °C. Blue: OD_{450} = 0.00-0.99 AU. Pink: OD_{450} = 1.00-1.99 AU. Red: OD_{450} = 2.00-3.00 AU.

	1	2	3	4	5	6	7	8	9	10	11	12	13	14	15
1						1.8414	1.8255	1.8257	1.8349	1.9224					
2				1.8152	1.6987	1.5721	1.4432	1.4117	1.5395	1.6584	1.7956	1.8532			
3			1.7901	1.5558	1.2881	1.0939	1.0301	1.029	1.1445	1.2121	1.3771	1.6093	1.8271		
4		1.8096	1.5211	1.1595	0.9642	0.8512	0.8273	0.8216	0.9332	0.9859	1.0222	1.2464	1.5875	1.8641	
5		1.6391	1.2057	0.9319	0.8078	0.7023	0.6988	0.7169	0.8103	0.755	0.8322	0.998	1.316	1.7186	
6	1.8262	1.416	0.997	0.815	0.6888	0.6466	0.6584	0.6604	0.7114	0.7067	0.7178	0.8275	1.0881	1.5157	1.8702
7	1.7547	1.2641	0.8963	0.7519	0.6391	0.6149	0.6205	0.6819	0.6773	0.6838	0.6829	0.7813	0.9659	1.3736	1.8118
8	1.7122	1.1779	0.8696	0.708	0.6408	0.6181	0.6228	0.646	0.6736	0.6633	0.6439	0.7128	0.8906	1.288	1.7945
9	1.7166	1.2094	0.8794	0.7104	0.6254	0.6323	0.6506	0.6724	0.6501	0.6289	0.6624	0.7106	0.9235	1.2839	1.8007
10	1.7677	1.3044	0.9368	0.7552	0.6977	0.6831	0.6739	0.6491	0.6824	0.6337	0.6726	0.7594	0.9859	1.3861	1.8271
11		1.4776	1.0663	0.8338	0.7683	0.7094	0.6955	0.6977	0.6998	0.681	0.7036	0.8261	1.1107	1.5466	
12		1.6935	1.2878	1.0375	0.8639	0.7906	0.7627	0.7347	0.7345	0.7589	0.8131		1.1.3447	1.7802	
13			1.5879	1.2581	1.0596	0.9621	0.8802	0.8539	0.8607	0.9271	1.0414	1.3103	1.6732		
14				1.6305	1.4024	1.2434	1.1346	1.0866	1.1037	1.2256	1.4368	1.6802			
15						1.7427	1.5797	1.5301	1.5843	1.694					

	1	2	3	4	5	6	7	8	9	10	11	12	13	14	15
1						1.8685	1.8825	1.8894	1.876	1.8589					
2				1.8462	1.794	1.6647	1.576	1.5359	1.5637	1.6586	1.8375	1.9072			
3			1.8327	1.669	1.4238	1.2488	1.159	1.126	1.1781	1.2779	1.5699	1.7713	1.908		
4		1.8379	1.6462	1.2999	1.0919	0.9516	0.9047	0.895	0.9368	1.04	1.2258	1.4528	1.7363	1.8779	
5		1.7308	1.3678	1.0599	0.8817	0.7667	0.7291	0.7538	0.8071	0.8445	0.997	1.1634	1.4355	1.7936	
6	1.8264	1.5442	1.157	0.8874	0.7275	0.6754	0.6587	0.6586	0.7027	0.762	0.8364	1.0093	1.2351	1.6103	1.8682
7	1.8033	1.4059	1.037	0.8128	0.689	0.6306	0.6377	0.6262	0.6839	0.6798	0.7483	0.8833	1.1155	1.4578	1.8318
8	1.7802	1.3381	0.9913	0.7671	0.6626	0.6196	0.6064	0.632	0.6287	0.6478	0.7064	0.8399	1.0526	1.3984	1.8131
9	1.7796	1.357	1.0039	0.7888	0.6968	0.655	0.624	0.6448	0.6335	0.6464	0.7001	0.8342	1.066	1.3951	1.8178
10	1.8185	1.4303	1.0839	0.8674	0.7237	0.667	0.6734	0.6384	0.6279	0.6674	0.7181	0.8737	1.1111	1.4661	1.8363
11		1.5686	1.2098	0.9514	0.7955	0.7146	0.6927	0.6543	0.6678	0.6912	0.7834	0.9748	1.2025	1.6079	
12		1.772	1.398	1.1555	0.9513	0.8349	0.7633	0.71	0.747	0.8089	0.9329	1.1099	1.4252	1.7749	
13			1.7051	1.4679	1.1894	1.0121	0.9382	0.9039	0.923	0.9982	1.1421	1.3697	1.7014		
14				1.7206	1.4781	1.2781	1.1783	1.1479	1.1684	1.2879	1.4826	1.7067			
15						1.6815	1.5848	1.5589	1.5973	1.689					

	1	2	3	4	5	6	7	8	9	10	11	12	13	14	15
1						1.8697	1.889	1.8931	1.8801	1.9059					
2				1.8804	1.8075	1.6492	1.5564	1.5244	1.5802	1.6962	1.8186	1.8961			
3			1.8726	1.6716	1.4812	1.2218	1.1416	1.1073	1.1468	1.2199	1.4384	1.6674	1.8832		
4		1.8889	1.6543	1.2972	1.087	0.9698	0.8775	0.8274	0.8591	0.9362	1.1036	1.3352	1.6731	1.8996	
5		1.7086	1.3272	1.0889	0.8907	0.7531	0.7194	0.6832	0.6806	0.7315	0.8847	1.0606	1.3699	1.8123	
6	1.8288	1.4748	1.117	0.8692	0.7409	0.6533	0.6552	0.6325	0.6828	0.6345	0.7277	0.8987	1.2033	1.6012	1.8942
7	1.784	1.3471	0.9654	0.7693	0.6557	0.5781	0.6314	0.589	0.6253	0.6098	0.6356	0.8471	1.0649	1.4642	1.8916
8	1.7809	1.2725	0.9444	0.7422	0.6278	0.599	0.5955	0.6192	0.6188	0.6902	0.5819	0.784	1.0574	1.3948	1.8539
9	1.7637	1.2887	0.934	0.7171	0.6523	0.5907	0.572	0.5858	0.5985	0.5985	0.6511	0.812	1.0309	1.4144	1.8956
10	1.8314	1.3707	1.0029	0.7554	0.6785	0.6243	0.574	0.6009	0.5999	0.6356	0.7121	0.8816	1.1147	1.5337	1.8535
11		1.5675	1.1304	0.8884	0.7495	0.6376	0.6546	0.66	0.6263	0.6897	0.7786	0.9753	1.239	1.656	
12		1.7623	1.3734	1.0686	0.8616	0.782	0.7026	0.6745	0.7794	0.8766	0.9506	1.1779	1.4952	1.8224	
13			1.6895	1.3674	1.1495	0.9959	0.9479	0.9256	0.9725	1.0927	1.2096	1.4615	1.7566		
14				1.7394	1.5131	1.3895	1.2451	1.2275	1.2669	1.401	1.5674	1.7846			
15						1.8247	1.7216	1.7048	1.7143	1.8156					

Figure S464 - OD_{450} *n*=3 intensity maps produced for **72** (1.5 mg/mL) in aqueous Na_2HPO_4 (0.505 M) at 25 °C. Blue: OD_{450} = 0.00-0.99 AU. Pink: OD_{450} = 1.00-1.99 AU. Red: OD_{450} = 2.00-3.00 AU.

	1	2	3	4	5	6	7	8	9	10	11	12	13	14	15
1						1.8433	1.8263	1.9231	1.8973	1.8555					
2				1.817	1.687	1.5236	1.4852	1.466	1.5421	1.5654	1.7315	1.8423			
3			1.7528	1.55	1.2607	1.0857	1.0516	1.0797	1.1147	1.1161	1.3152	1.5971	1.8225		
4		1.7965	1.5047	1.1408	0.9392	0.8402	0.8245	0.9072	0.8221	0.8587	0.9863	1.2321	1.5812	1.8607	
5		1.6116	1.1707	0.9056	0.7858	0.7199	0.7017	0.7713	0.729	0.7165	0.7875	0.9544	1.2655	1.7014	
6	1.809	1.3918	0.9671	0.7947	0.694	0.6497	0.6423	0.6941	0.6845	0.6583	0.6917	0.8032	1.0424	1.4718	1.8442
7	1.7262	1.2261	0.8791	0.7115	0.654	0.6318	0.6126	0.6638	0.6585	0.6272	0.6491	0.7238	0.9229	1.3249	1.8084
8	1.6924	1.1442	0.8266	0.6969	0.6118	0.5967	0.6005	0.6412	0.6612	0.5954	0.6428	0.6814	0.8842	1.2463	1.7867
9	1.6801	1.1527	0.8517	0.6873	0.6228	0.598	0.6224	0.6641	0.6491	0.6173	0.6061	0.7111	0.8922	1.2727	1.7826
10	1.7511	1.2405	0.8713	0.7163	0.6416	0.6212	0.6318	0.6579	0.6515	0.6681	0.6763	0.7166	0.9258	1.3562	1.8177
11		1.4334	1.0048	0.7938	0.7041	0.6589	0.6637	0.6734	0.688	0.6806	0.7119	0.8044	1.0582	1.5258	
12		1.6707	1.2367	0.96	0.7925	0.7595	0.7304	0.722	0.7237	0.7446	0.8264	0.9754	1.3222	1.7278	
13			1.5547	1.2178	1.0051	0.8954	0.8668	0.8341	0.8795	0.9125	1.022	1.2866	1.6295		
14				1.5877	1.3366	1.1643	1.0809	1.1046	1.0912	1.207	1.4004	1.6773			
15						1.6077	1.5249	1.5564	1.553	1.656					

	1	2	3	4	5	6	7	8	9	10	11	12	13	14	15
1						1.8552	1.9197	1.9373	1.9296	1.8652					
2				1.8318	1.7626	1.6106	1.5735	1.6091	1.6226	1.7171	1.8278	1.8608			
3			1.8139	1.631	1.3963	1.205	1.1463	1.1811	1.1915	1.272	1.4622	1.6948	1.8427		
4		1.8185	1.6228	1.2798	1.0474	0.9482	0.9128	0.9086	0.9313	1.0079	1.1354	1.359	1.6626	1.8394	
5		1.7138	1.3206	1.0415	0.8636	0.7769	0.7747	0.7735	0.768	0.7947	0.9178	1.0864	1.4003	1.7517	
6	1.8168	1.5119	1.1168	0.866	0.7236	0.6766	0.6349	0.6824	0.6645	0.7101	0.7852	0.9563	1.1806	1.5739	1.8535
7	1.7775	1.3625	0.9927	0.7869	0.6741	0.6181	0.6324	0.6256	0.6526	0.6465	0.6979	0.8331	1.0782	1.4309	1.8224
8	1.7458	1.299	0.9474	0.7263	0.6415	0.6108	0.5826	0.6179	0.6158	0.6251	0.6496	0.7957	1.0166	1.3538	1.7937
9	1.7374	1.2869	0.9553	0.7478	0.6645	0.6064	0.5765	0.6174	0.635	0.6179	0.6676	0.7925	1.0043	1.3624	1.8009
10	1.7758	1.3655	1.015	0.7812	0.6692	0.6309	0.6188	0.6418	0.6244	0.6434	0.7104	0.8408	1.0546	1.4159	1.8141
11		1.5216	1.1361	0.896	0.7476	0.6905	0.681	0.6515	0.6503	0.6827	0.7808	0.9377	1.1806	1.5745	
12		1.7224	1.3618	1.0737	0.9079	0.7985	0.758	0.7399	0.7482	0.8059	0.9104	1.0874	1.3857	1.7329	
13			1.6444	1.3273	1.1133	0.9754	0.9229	0.8918	0.9114	0.9768	1.1123	1.3471	1.6544		
14				1.6673	1.4271	1.285	1.2284	1.1563	1.1612	1.2617	1.4544	1.6931			
15						1.7151	1.6148	1.5619	1.5873	1.6597					

	1	2	3	4	5	6	7	8	9	10	11	12	13	14	15
1						1.8676	1.9039	1.9576	1.9605	1.9407					
2				1.8544	1.7884	1.6524	1.5374	1.529	1.6071	1.7381	1.8086	1.8744			
3			1.8329	1.6448	1.3934	1.2281	1.1291	1.0961	1.1003	1.232	1.4163	1.6724	1.8462		
4		1.8296	1.601	1.2592	1.0173	0.9528	0.8662	0.8082	0.8518	0.9203	1.0685	1.3033	1.6583	1.8506	
5		1.6973	1.2642	1.0004	0.8077	0.7287	0.6967	0.6772	0.6752	0.7377	0.8354	1.0377	1.3578	1.7497	
6	1.8085	1.4979	1.066	0.8715	0.7433	0.6464	0.6233	0.6232	0.6488	0.6419	0.7271	0.8799	1.1328	1.5963	1.8622
7	1.817	1.3162	0.9906	0.7636	0.674	0.6218	0.6088	0.5969	0.5768	0.612	0.6732	0.7687	1.0214	1.4362	1.8307
8	1.775	1.2548	0.9668	0.7458	0.6419	0.5893	0.5863	0.5546	0.5666	0.5785	0.6651	0.7263	0.9732	1.3655	1.8155
9	1.7522	1.2535	0.8907	0.658	0.5859	0.5975	0.604	0.5636	0.5375	0.6265	0.6431	0.7416	0.9786	1.3764	1.8053
10	1.8285	1.3343	1.0079	0.716	0.6524	0.6319	0.5735	0.5783	0.606	0.6146	0.6772	0.7971	1.0594	1.4697	1.7853
11		1.4907	1.104	0.855	0.6961	0.6223	0.631	0.6427	0.645	0.6556	0.7426	0.9079	1.1694	1.6055	
12		1.745	1.3477	1.0632	0.8255	0.7188	0.7293	0.7302	0.7403	0.8129	0.958	1.1459	1.4352	1.7725	
13			1.6395	1.3344	1.0809	0.9886	0.8999	0.876	0.9355	1.0187	1.1997	1.4366	1.7638		
14				1.6981	1.4693	1.2831	1.1889	1.1778	1.2306	1.4141	1.5529	1.7849			
15						1.7575	1.6493	1.6088	1.6563	1.7903					

Figure S465 - OD_{450} *n*=3 intensity maps produced for **72** (1.5 mg/mL) in aqueous Na_2HPO_4 (0.505 M) at 30 °C. Blue: OD_{450} = 0.00-0.99 AU. Pink: OD_{450} = 1.00-1.99 AU. Red: OD_{450} = 2.00-3.00 AU.

	1	2	3	4	5	6	7	8	9	10	11	12	13	14	15
1						1.8265	1.8246	1.8783	1.9372	1.8451					
2				1.8015	1.6935	1.5207	1.4254	1.4632	1.5515	1.5341	1.6814	1.8124			
3			1.7497	1.5463	1.2811	1.0758	1.0133	1.0799	1.1626	1.0956	1.2696	1.5405	1.781		
4		1.789	1.5123	1.1504	0.9341	0.8345	0.7972	0.8473	0.8298	0.8146	0.9286	1.1641	1.5048	1.8165	
5		1.6238	1.1966	0.9067	0.7515	0.6932	0.6633	0.7308	0.7061	0.7038	0.7553	0.9032	1.1949	1.6209	
6	1.8034	1.4097	0.9756	0.7756	0.6763	0.6388	0.6175	0.6693	0.6515	0.6411	0.672	0.7677	0.9764	1.4047	1.8063
7	1.732	1.2468	0.8734	0.7067	0.6363	0.6063	0.5895	0.6519	0.6297	0.6036	0.6277	0.677	0.8519	1.236	1.7419
8	1.7033	1.1586	0.8188	0.6888	0.5934	0.5855	0.5862	0.6124	0.6423	0.5878	0.6217	0.6541	0.8324	1.1529	1.6981
9	1.702	1.172	0.8427	0.6748	0.6106	0.5829	0.6017	0.6492	0.6222	0.5986	0.5823	0.6665	0.8201	1.1632	1.6827
10	1.7558	1.2605	0.8682	0.7005	0.6309	0.5993	0.6124	0.6379	0.6146	0.6365	0.6527	0.6745	0.8592	1.2613	1.7537
11		1.4298	1.0088	0.7855	0.6926	0.6437	0.6438	0.6505	0.6682	0.6494	0.6753	0.746	0.9708	1.4211	
12		1.672	1.2335	0.9393	0.7699	0.738	0.707	0.7034	0.7016	0.7209	0.7764	0.9044	1.2199	1.6466	
13			1.5412	1.192	0.9842	0.859	0.8342	0.7956	0.8279	0.8609	0.9552	1.2053	1.5421		
14				1.5616	1.3022	1.1317	1.05	1.0459	1.03	1.1389	1.3235	1.6			
15						1.5738	1.4865	1.5192	1.4987	1.5977					

	1	2	3	4	5	6	7	8	9	10	11	12	13	14	15
1						1.8526	1.9102	1.9489	1.9211	1.8555					
2				1.8302	1.7577	1.608	1.577	1.5854	1.6042	1.6705	1.7969	1.8369			
3			1.8098	1.644	1.3964	1.1941	1.1301	1.1631	1.1514	1.2184	1.4061	1.6418	1.8135		
4		1.8131	1.6373	1.2857	1.0353	0.9346	0.8933	0.8862	0.8929	0.9594	1.0719	1.2931	1.5993	1.8162	
5		1.7269	1.3428	1.0396	0.8479	0.7677	0.7485	0.7528	0.7399	0.7573	0.8607	1.017	1.3234	1.6873	
6	1.8068	1.5253	1.1293	0.8556	0.7202	0.6649	0.6136	0.666	0.647	0.6818	0.7392	0.89	1.1105	1.4877	1.8235
7	1.7916	1.3794	0.9873	0.784	0.6692	0.6116	0.6183	0.6084	0.6297	0.624	0.663	0.7735	1.0042	1.336	1.7601
8	1.7512	1.3174	0.9468	0.7258	0.6217	0.6058	0.5715	0.6029	0.5996	0.5897	0.6352	0.7388	0.9451	1.26	1.7104
9	1.7566	1.3224	0.9542	0.7345	0.635	0.5863	0.5696	0.5926	0.6146	0.5903	0.6349	0.7408	0.9227	1.2499	1.7067
10	1.778	1.3734	1.0043	0.766	0.6489	0.6176	0.6007	0.6177	0.6109	0.6164	0.6684	0.7842	0.9702	1.3208	1.7537
11		1.5241	1.1217	0.8756	0.7307	0.6726	0.6601	0.6273	0.6317	0.6456	0.7224	0.8692	1.0929	1.4815	
12		1.7172	1.3598	1.0509	0.8654	0.7745	0.7136	0.7064	0.7079	0.7577	0.8319	1.0067	1.3016	1.6472	
13			1.6248	1.3103	1.074	0.937	0.8893	0.8667	0.862	0.9315	1.0371	1.2601	1.5718		
14				1.6448	1.3963	1.2115	1.1721	1.1252	1.1142	1.1901	1.3776	1.6134			
15						1.6539	1.6224	1.5286	1.5321	1.6154					

	1	2	3	4	5	6	7	8	9	10	11	12	13	14	15
1						1.8584	1.8733	1.883	1.8646	1.8651					
2				1.8389	1.8265	1.6382	1.5224	1.5006	1.5369	1.6465	1.7646	1.8552			
3			1.84	1.6816	1.4344	1.2029	1.0857	1.0653	1.056	1.1712	1.3524	1.6142	1.8509		
4		1.8045	1.668	1.3019	1.1445	0.8451	0.8587	0.8214	0.796	0.8619	0.9879	1.2363	1.5957	1.8554	
5		1.6906	1.2749	1.0514	0.826	0.7223	0.6735	0.6773	0.6427	0.6834	0.7686	0.9762	1.279	1.711	
6	1.7895	1.4718	1.0571	0.8041	0.6949	0.6171	0.6342	0.6058	0.6486	0.5891	0.6914	0.8035	1.0687	1.4754	1.8392
7	1.7545	1.3467	0.9575	0.7222	0.609	0.6018	0.6094	0.5692	0.5929	0.6076	0.603	0.7084	0.9915	1.325	1.8148
8	1.7661	1.2854	0.9089	0.7108	0.6052	0.6025	0.5498	0.5735	0.5739	0.5979	0.5533	0.6794	0.9035	1.2694	1.7423
9	1.7661	1.274	0.9104	0.701	0.6337	0.5432	0.5331	0.5502	0.5634	0.5462	0.5992	0.7242	0.9198	1.2627	1.773
10	1.7879	1.3556	0.9445	0.7305	0.6525	0.594	0.5408	0.5635	0.5655	0.5889	0.6483	0.745	0.9904	1.378	1.8251
11		1.5463	1.086	0.8594	0.6989	0.6043	0.6162	0.6055	0.577	0.6411	0.7178	0.8379	1.0973	1.5434	
12		1.7181	1.3415	1.0158	0.8048	0.7221	0.6726	0.6441	0.6969	0.769	0.843	1.0425	1.3572	1.7164	
13			1.6548	1.3216	1.0763	0.9291	0.8546	0.8226	0.8612	0.9792	1.0823	1.3366	1.6354		
14				1.6748	1.4564	1.3182	1.1556	1.1199	1.1482	1.2909	1.4638	1.6881			
15						1.7377	1.6496	1.5828	1.6226	1.7142					

Figure S466 - OD_{450} *n*=3 intensity maps produced for **72** (1.5 mg/mL) in aqueous Na_2HPO_4 (0.505 M) at 35 °C. Blue: OD_{450} = 0.00-0.99 AU. Pink: OD_{450} = 1.00-1.99 AU. Red: OD_{450} = 2.00-3.00 AU.

	1	2	3	4	5	6	7	8	9	10	11	12	13	14	15
1						1.8369	1.8517	1.8867	1.7967	1.7896					
2				1.7911	1.6674	1.5075	1.4368	1.3978	1.3874	1.4633	1.611	1.765			
3			1.773	1.518	1.2408	1.0816	1.0191	1.0139	1.007	1.0531	1.2285	1.4952	1.7384		
4		1.7831	1.4692	1.1262	0.9344	0.8291	0.7985	0.7576	0.7746	0.8196	0.881	1.122	1.4678	1.7466	
5		1.5825	1.1486	0.8845	0.7632	0.7128	0.664	0.6619	0.668	0.6881	0.7277	0.8649	1.1587	1.5797	
6	1.8142	1.3464	0.9289	0.7307	0.6719	0.641	0.6497	0.6139	0.6172	0.5968	0.6233	0.7065	0.9283	1.382	1.7512
7	1.721	1.2056	0.8321	0.6782	0.6287	0.6141	0.5832	0.6216	0.5816	0.5761	0.5786	0.6383	0.8229	1.1989	1.6799
8	1.6756	1.1176	0.7955	0.6551	0.5733	0.5721	0.5717	0.617	0.5658	0.5502	0.5609	0.6362	0.7683	1.1212	1.645
9	1.6754	1.118	0.8051	0.6614	0.5972	0.5972	0.6047	0.6123	0.5678	0.541	0.5645	0.6262	0.757	1.1109	1.6423
10	1.7322	1.1923	0.8188	0.6639	0.5987	0.6102	0.6097	0.628	0.5656	0.5637	0.5942	0.6438	0.8141	1.2112	1.6897
11		1.3842	0.9347	0.7238	0.6423	0.6275	0.6476	0.6693	0.6009	0.5944	0.62	0.7089	0.9135	1.3635	
12		1.6065	1.1681	0.8698	0.7207	0.6639	0.6623	0.7098	0.6432	0.6614	0.7017	0.8363	1.1558	1.5832	
13			1.4785	1.1162	0.8768	0.7714	0.8108	0.8578	0.7527	0.7747	0.8697	1.1181	1.4684		
14				1.5052	1.2198	1.038	1.0976	1.0581	0.9635	1.0368	1.2677	1.5211			
15						1.527	1.5645	1.4324	1.4092	1.5221					

	1	2	3	4	5	6	7	8	9	10	11	12	13	14	15
1						1.8698	1.9002	1.9549	1.8859	1.824					
2				1.8039	1.727	1.6381	1.6104	1.5461	1.5657	1.632	1.7582	1.8051			
3			1.7941	1.6052	1.3556	1.1835	1.1485	1.1274	1.1125	1.19	1.3748	1.599	1.7824		
4		1.7937	1.5904	1.2462	1.0217	0.9022	0.8532	0.8711	0.8512	0.9054	1.0187	1.2481	1.575	1.7924	
5		1.685	1.3058	0.9895	0.8282	0.7489	0.6994	0.7173	0.7019	0.7249	0.8193	0.9811	1.2779	1.6643	
6	1.7877	1.4902	1.0927	0.8353	0.708	0.6432	0.6083	0.6436	0.6329	0.6498	0.6967	0.8437	1.0532	1.4525	1.782
7	1.7599	1.3446	0.9639	0.7404	0.6408	0.5881	0.5806	0.5802	0.5983	0.5997	0.6376	0.7468	0.9354	1.289	1.7118
8	1.7197	1.2715	0.9055	0.6976	0.5984	0.5791	0.5415	0.5771	0.576	0.5608	0.624	0.7111	0.8821	1.2071	1.6681
9	1.7073	1.273	0.8957	0.6941	0.6085	0.5519	0.5446	0.567	0.5831	0.5666	0.6026	0.7085	0.8745	1.1853	1.6617
10	1.7466	1.3282	0.952	0.7262	0.617	0.5956	0.5749	0.586	0.584	0.5896	0.632	0.7389	0.9116	1.2712	1.6926
11		1.4707	1.0737	0.8289	0.6851	0.6376	0.6305	0.6017	0.6093	0.6134	0.668	0.8174	1.0158	1.4168	
12		1.6654	1.2846	0.981	0.7929	0.7393	0.6818	0.678	0.6884	0.7286	0.7828	0.9357	1.2315	1.6146	
13			1.5644	1.2437	1.0129	0.8803	0.8206	0.8174	0.8147	0.8763	0.9801	1.1984	1.5193		
14				1.5872	1.3292	1.144	1.0965	1.0933	1.0676	1.132	1.3149	1.5644			
15						1.5776	1.5219	1.4915	1.4876	1.5655					

	1	2	3	4	5	6	7	8	9	10	11	12	13	14	15
1						1.848	1.8707	1.8773	1.8398	1.8418					
2				1.8405	1.7741	1.6372	1.5132	1.4614	1.4968	1.6074	1.7412	1.8293			
3			1.8298	1.677	1.3835	1.1866	1.09	1.0214	1.0427	1.1316	1.3218	1.5792	1.8187		
4		1.7801	1.5849	1.2475	1.0711	0.8499	0.8558	0.7758	0.764	0.8583	0.9538	1.2072	1.542	1.8202	
5		1.6609	1.2424	0.9569	0.7644	0.6949	0.6437	0.6515	0.6351	0.649	0.7174	0.9391	1.2508	1.6924	
6	1.7771	1.4468	1.0166	0.752	0.6803	0.6038	0.6056	0.585	0.6181	0.5813	0.6272	0.7392	1.0043	1.4362	1.8334
7	1.733	1.3006	0.9222	0.7033	0.5741	0.5897	0.5695	0.5391	0.5528	0.5732	0.5935	0.6463	0.9393	1.2815	1.7781
8	1.7138	1.2356	0.8623	0.6757	0.5997	0.5809	0.5253	0.5394	0.5453	0.5365	0.5396	0.6176	0.8255	1.2085	1.7389
9	1.7298	1.2205	0.8775	0.6829	0.5905	0.5177	0.5127	0.5188	0.5355	0.543	0.563	0.6811	0.8916	1.2102	1.7075
10	1.7435	1.2985	0.9155	0.705	0.6143	0.5539	0.5085	0.5201	0.5492	0.5693	0.592	0.712	0.9173	1.3065	1.7861
11		1.4824	1.043	0.8001	0.6681	0.5699	0.5661	0.5485	0.5537	0.599	0.6868	0.7762	1.0252	1.4706	
12		1.6619	1.2774	0.956	0.7732	0.6377	0.6275	0.6554	0.6624	0.6905	0.8084	0.9684	1.2797	1.6871	
13			1.5888	1.2497	0.9727	0.8461	0.8015	0.7816	0.7909	0.8643	0.1058	1.2661	1.5717		
14				1.6256	1.4592	1.2173	1.0851	1.0511	1.098	1.2025	1.3968	1.6371			
15						1.6674	1.5982	1.5056	1.566	1.653					

Figure S467 - OD_{450} *n*=3 intensity maps produced for **72** (1.5 mg/mL) in aqueous Na_2HPO_4 (0.505 M) at 40 °C. Blue: OD_{450} = 0.00-0.99 AU. Pink: OD_{450} = 1.00-1.99 AU. Red: OD_{450} = 2.00-3.00 AU.

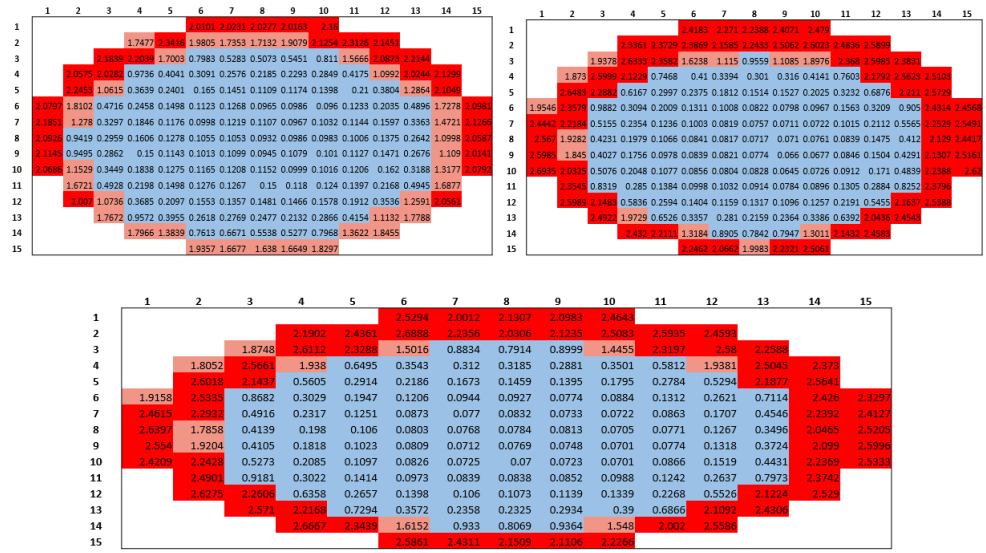

Figure S468 - OD_{450} *n*=3 intensity maps produced for **72** (1.5 mg/mL) in aqueous Na_2HPO_4 (0.505 M) at 45 °C. Blue: OD_{450} = 0.00-0.99 AU. Pink: OD_{450} = 1.00-1.99 AU. Red: OD_{450} = 2.00-3.00 AU.

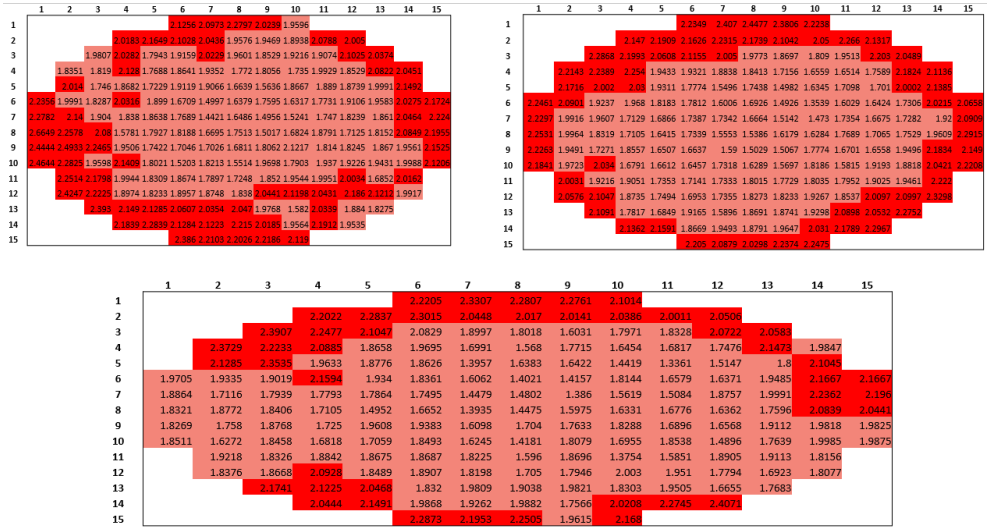

Figure S469 - OD_{450} *n*=3 intensity maps produced for **72** (1.5 mg/mL) in aqueous NaH_2PO_4 (0.505 M) at 25 °C. Blue: OD_{450} = 0.00-0.99 AU. Pink: OD_{450} = 1.00-1.99 AU. Red: OD_{450} = 2.00-3.00 AU.

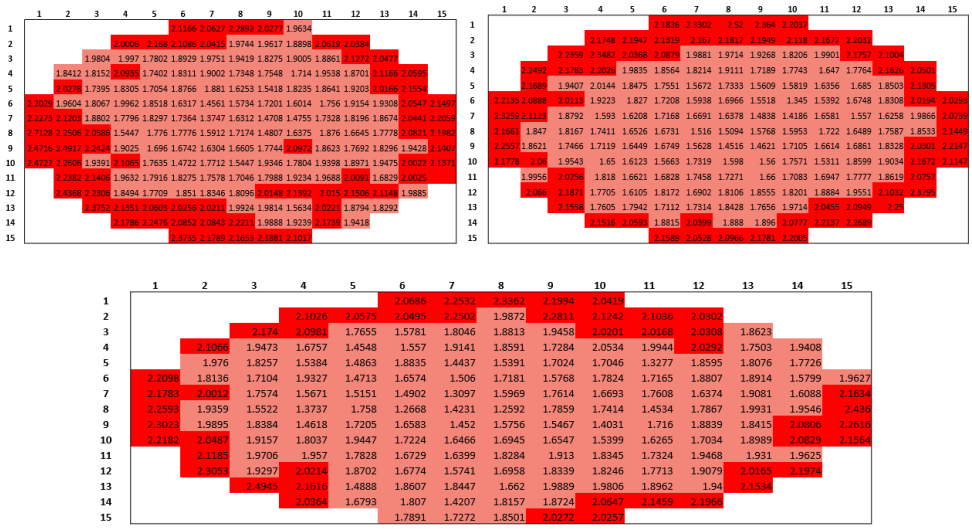

Figure S470 - OD_{450} *n*=3 intensity maps produced for **72** (1.5 mg/mL) in aqueous NaH_2PO_4 (0.505 M) at 30 °C. Blue: OD_{450} = 0.00-0.99 AU. Pink: OD_{450} = 1.00-1.99 AU. Red: OD_{450} = 2.00-3.00 AU.

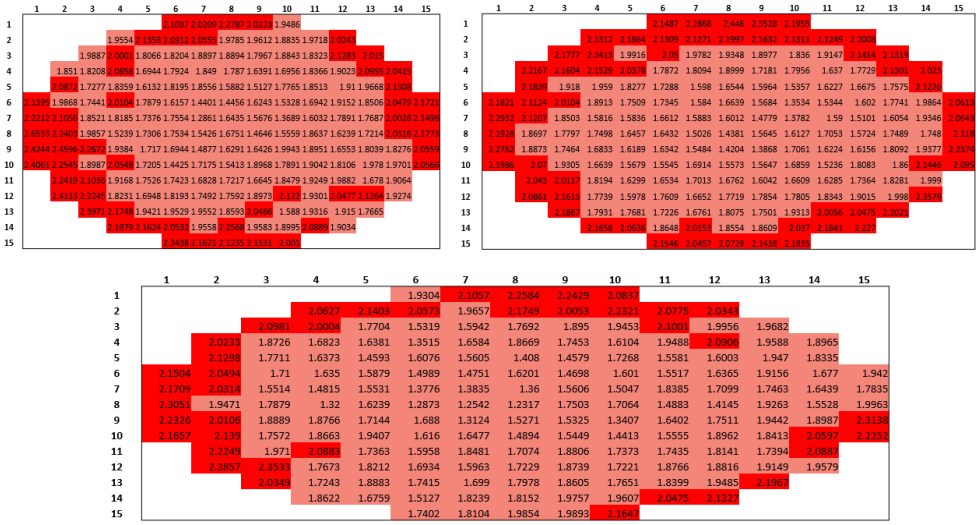

Figure S471 - OD_{450} *n*=3 intensity maps produced for **72** (1.5 mg/mL) in aqueous NaH_2PO_4 (0.505 M) at 35 °C. Blue: OD_{450} = 0.00-0.99 AU. Pink: OD_{450} = 1.00-1.99 AU. Red: OD_{450} = 2.00-3.00 AU.

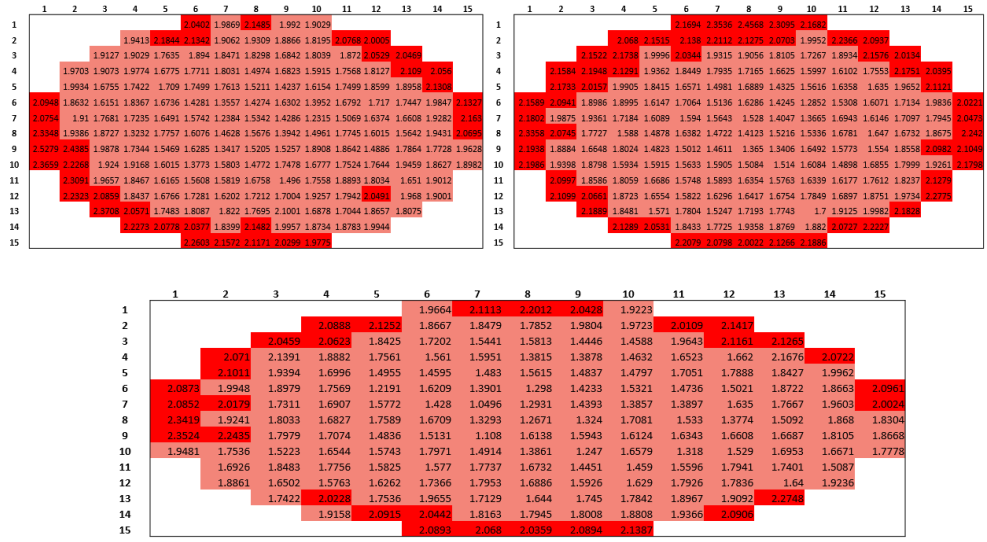

Figure S472 - OD_{450} *n*=3 intensity maps produced for **72** (1.5 mg/mL) in aqueous NaH_2PO_4 (0.505 M) at 40 °C. Blue: OD_{450} = 0.00-0.99 AU. Pink: OD_{450} = 1.00-1.99 AU. Red: OD_{450} = 2.00-3.00 AU.

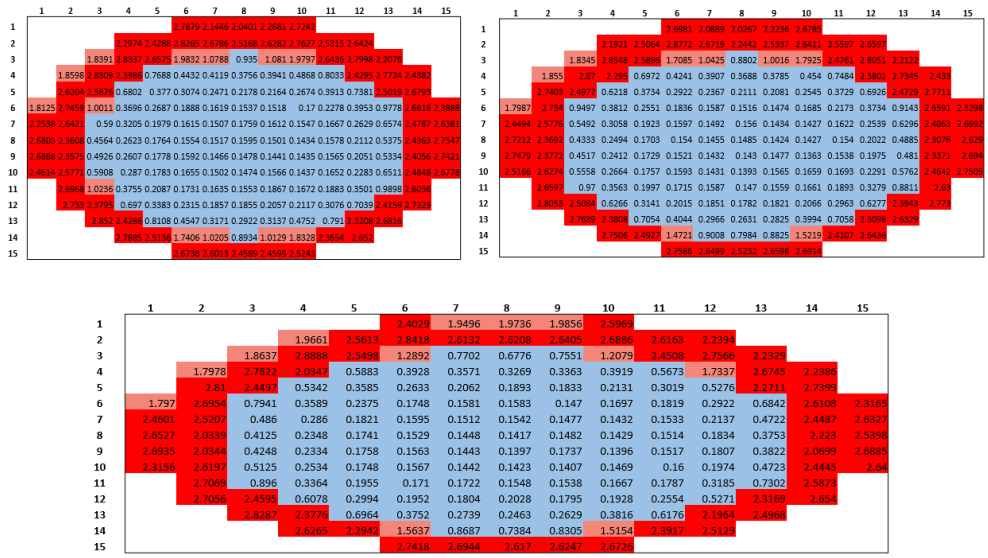

Figure S473 - OD_{450} *n*=3 intensity maps produced for **72** (1.5 mg/mL) in aqueous NaH_2PO_4 (0.505 M) at 45 °C. Blue: OD_{450} = 0.00-0.99 AU. Pink: OD_{450} = 1.00-1.99 AU. Red: OD_{450} = 2.00-3.00 AU.

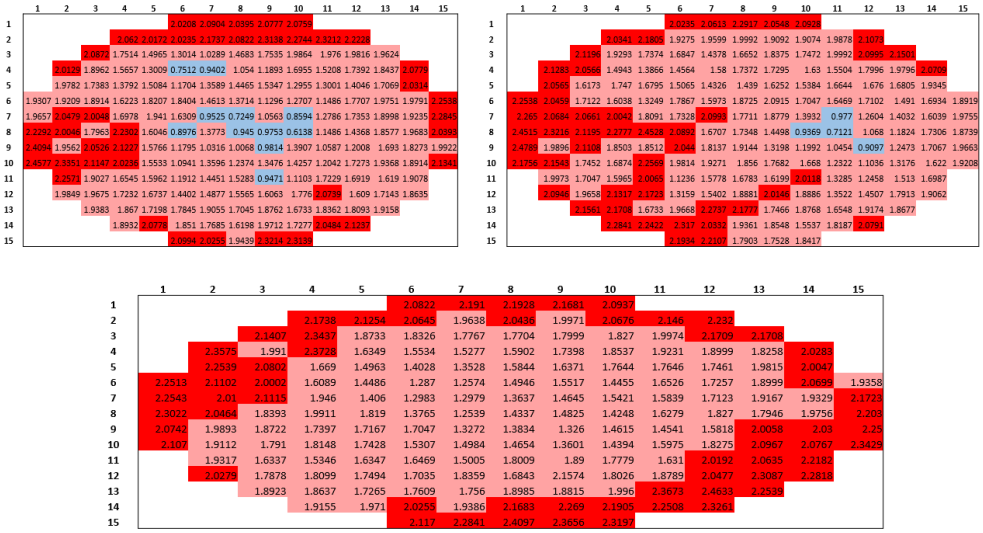

Figure S474 - OD_{450} *n*=3 intensity maps produced for **72** (1.5 mg/mL) in aqueous Na_2CO_3 (0.505 M) at 25 °C. Blue: OD_{450} = 0.00-0.99 AU. Pink: OD_{450} = 1.00-1.99 AU. Red: OD_{450} = 2.00-3.00 AU.

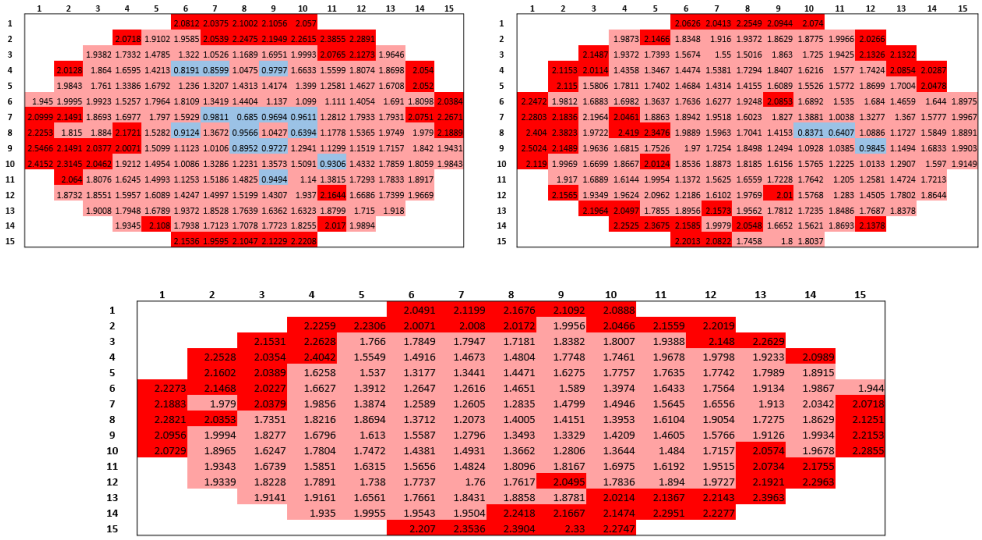

Figure S475 - OD_{450} *n*=3 intensity maps produced for **72** (1.5 mg/mL) in aqueous Na_2CO_3 (0.505 M) at 30 °C. Blue: OD_{450} = 0.00-0.99 AU. Pink: OD_{450} = 1.00-1.99 AU. Red: OD_{450} = 2.00-3.00 AU.

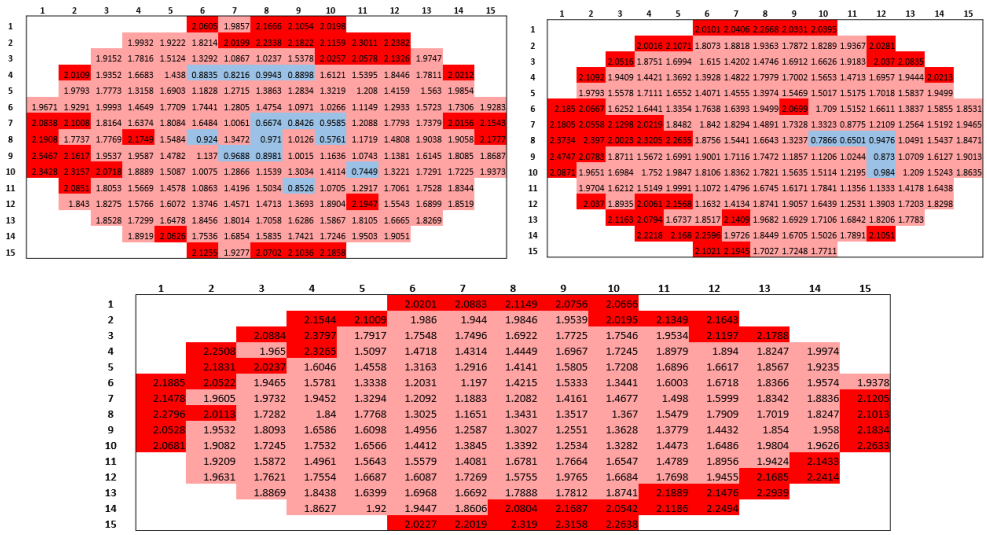

Figure S476 - OD_{450} *n*=3 intensity maps produced for **72** (1.5 mg/mL) in aqueous Na_2CO_3 (0.505 M) at 35 °C. Blue: OD_{450} = 0.00-0.99 AU. Pink: OD_{450} = 1.00-1.99 AU. Red: OD_{450} = 2.00-3.00 AU.

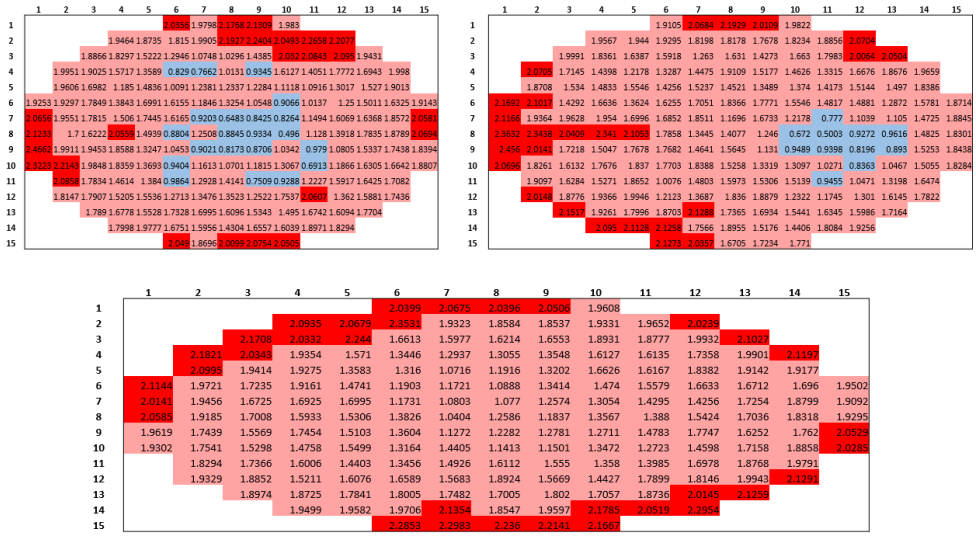

Figure S477 - OD_{450} *n*=3 intensity maps produced for **72** (1.5 mg/mL) in aqueous Na_2CO_3 (0.505 M) at 40 °C. Blue: OD_{450} = 0.00-0.99 AU. Pink: OD_{450} = 1.00-1.99 AU. Red: OD_{450} = 2.00-3.00 AU.

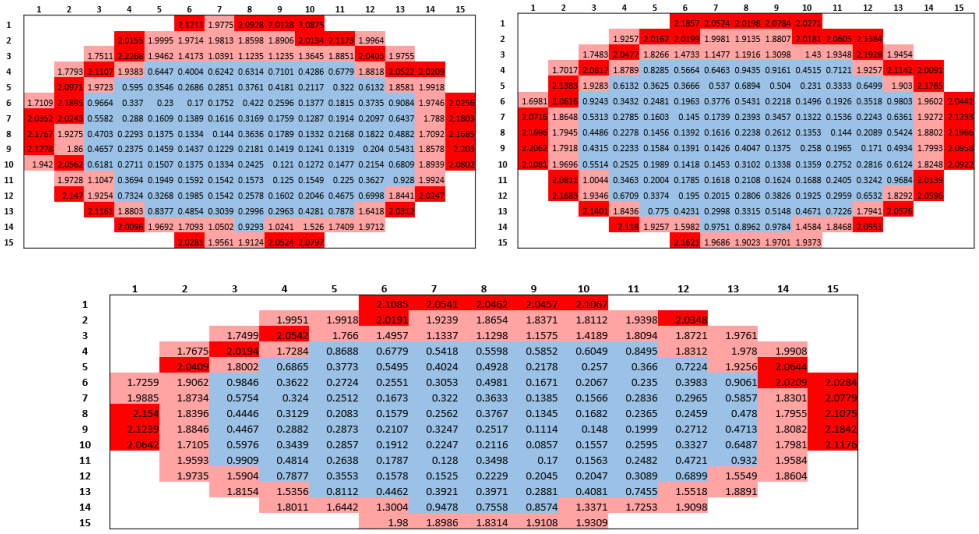

Figure S478 - OD_{450} *n*=3 intensity maps produced for **72** (1.5 mg/mL) in aqueous Na_2CO_3 (0.505 M) at 45 °C. Blue: OD_{450} = 0.00-0.99 AU. Pink: OD_{450} = 1.00-1.99 AU. Red: OD_{450} = 2.00-3.00 AU.

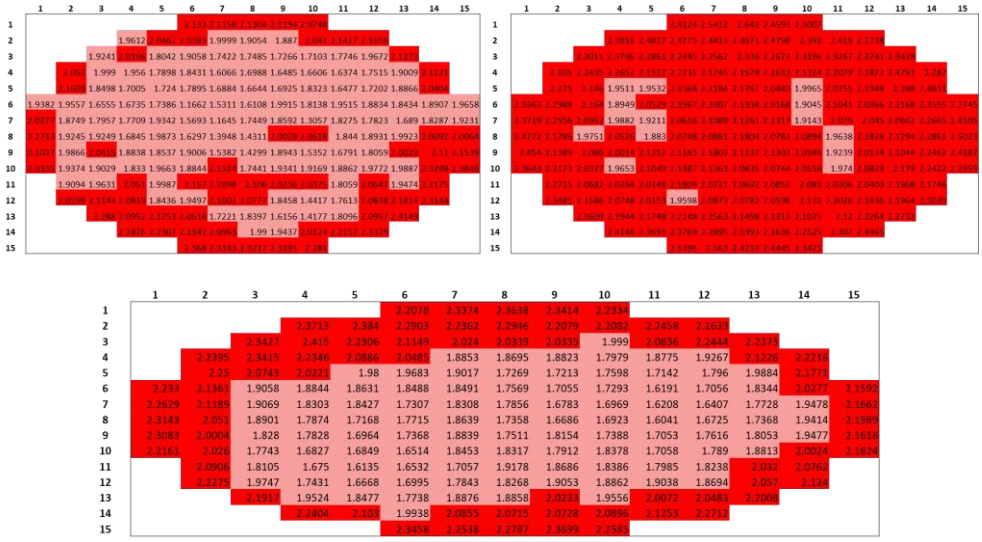

Figure S479 - OD_{450} *n*=3 intensity maps produced for **72** (1.5 mg/mL) in aqueous Na_2SO_4 (0.505 M) at 25 °C. Blue: OD_{450} = 0.00-0.99 AU. Pink: OD_{450} = 1.00-1.99 AU. Red: OD_{450} = 2.00-3.00 AU.

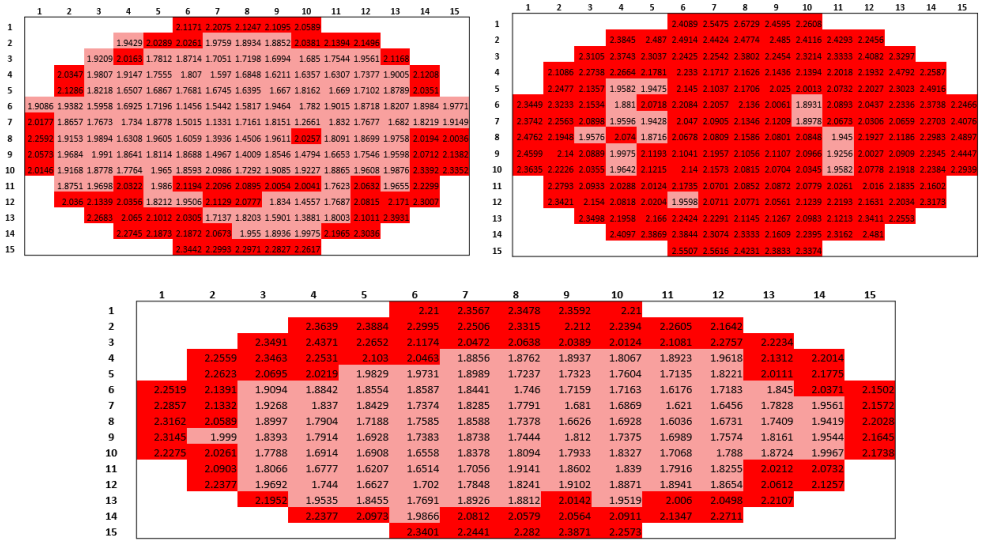

Figure S480 - OD_{450} *n*=3 intensity maps produced for **72** (1.5 mg/mL) in aqueous Na_2SO_4 (0.505 M) at 30 °C. Blue: OD_{450} = 0.00-0.99 AU. Pink: OD_{450} = 1.00-1.99 AU. Red: OD_{450} = 2.00-3.00 AU.

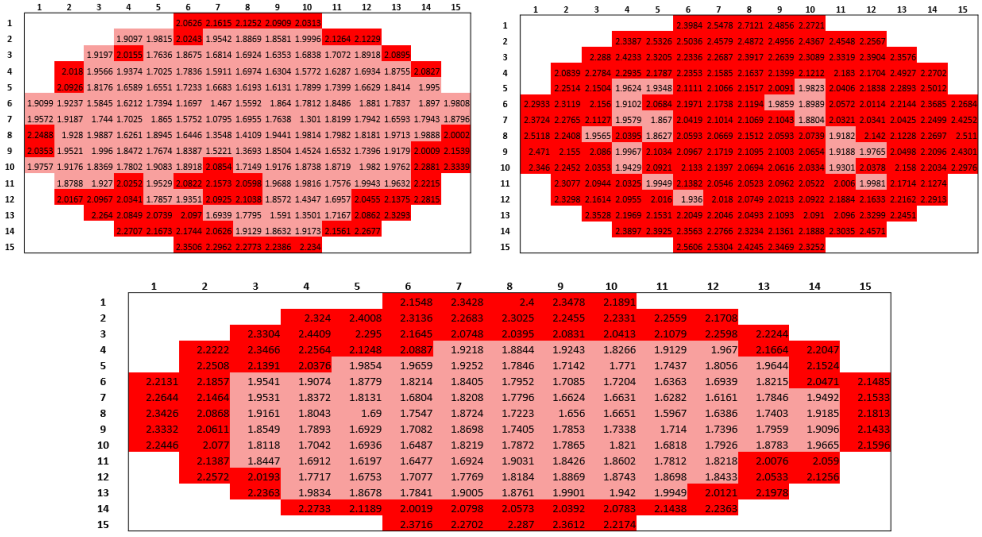

Figure S481 - OD_{450} *n*=3 intensity maps produced for **72** (1.5 mg/mL) in aqueous Na_2SO_4 (0.505 M) at 35 °C. Blue: OD_{450} = 0.00-0.99 AU. Pink: OD_{450} = 1.00-1.99 AU. Red: OD_{450} = 2.00-3.00 AU.

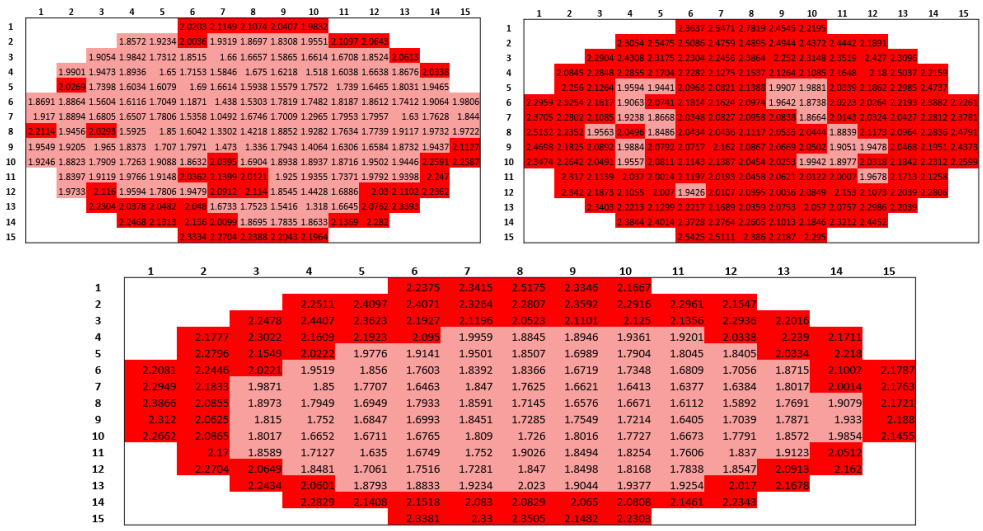

Figure S482 - OD_{450} *n*=3 intensity maps produced for **72** (1.5 mg/mL) in aqueous Na_2SO_4 (0.505 M) at 40 °C. Blue: OD_{450} = 0.00-0.99 AU. Pink: OD_{450} = 1.00-1.99 AU. Red: OD_{450} = 2.00-3.00 AU.

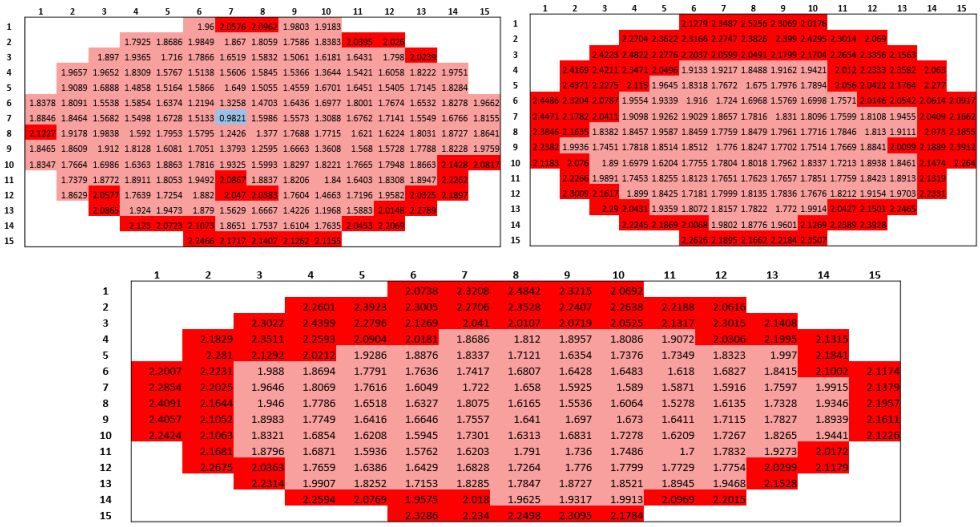

Figure S483 - OD_{450} *n*=3 intensity maps produced for **72** (1.5 mg/mL) in aqueous Na_2SO_4 (0.505 M) at 45 °C. Blue: OD_{450} = 0.00-0.99 AU. Pink: OD_{450} = 1.00-1.99 AU. Red: OD_{450} = 2.00-3.00 AU.

	1	2	3	4	5	6	7	8	9	10	11	12	13	14	15
1						2.1083	2.2741	2.2721	2.1931	2.0805					
2				2.1444	2.1154	2.0372	2.0329	1.9119	1.995	1.9877	2.0414	2.0351			
3			2.1762	2.0306	1.9531	1.8624	1.7735	1.6851	1.6651	1.6992	1.8224	2.0534	2.0586		
4		2.1561	2.029	1.8281	1.7212	1.6568	1.5703	1.6085	1.5401	1.6668	1.6848	1.7766	1.9149	2.0442	
5		2.0885	1.8743	1.6978	1.5689	1.387	1.3884	1.379	1.4867	1.5606	1.4883	1.5534	1.7479	2.0062	
6	2.1325	1.9389	1.758	1.5704	1.4557	1.3625	1.3551	1.245	1.3936	1.4135	1.2881	1.4542	1.6575	1.9073	2.0719
7	2.1296	1.8174	1.627	1.4988	1.4644	1.4564	1.3208	1.3225	1.2446	1.2742	1.2894	1.3723	1.5544	1.7893	2.0296
8	2.1103	1.7183	1.5645	1.333	1.4176	1.3251	1.2516	1.3305	1.3458	1.398	1.348	1.4372	1.5805	1.7957	2.1004
9	2.0748	1.7782	1.4675	1.4176	1.3799	1.4027	1.4507	1.4202	1.3886	1.4486	1.429	1.4706	1.5826	1.7599	2.0359
10	2.039	1.728	1.492	1.5035	1.3538	1.329	1.444	1.4558	1.3826	1.3636	1.3667	1.5097	1.6353	1.7883	2.017
11		1.9339	1.5923	1.4491	1.5043	1.4732	1.4804	1.3445	1.3413	1.4095	1.4951	1.5944	1.7005	1.9531	
12		2.01	1.7799	1.5685	1.4398	1.3483	1.2498	1.5046	1.5507	1.473	1.6345	1.7049	1.8527	2.0702	
13			1.8866	1.6906	1.5206	1.5117	1.5455	1.5673	1.6146	1.6328	1.6774	1.8387	2.0575		
14				1.9505	1.7851	1.7223	1.6542	1.733	1.6503	1.737	1.8691	2.0369			
15						2.0213	1.941	1.9093	2.0127	2.0763					

	1	2	3	4	5	6	7	8	9	10	11	12	13	14	15
1						2.0786	2.1598	2.1573	2.0803	1.9861					
2				2.1378	2.0987	1.9748	1.9147	1.8934	1.8582	1.9904	2.0295	2.0937			
3			2.1358	2.0439	1.8543	1.7071	1.6552	1.7199	1.5437	1.7026	1.8295	1.984	2.0447		
4		2.1165	1.996	1.8124	1.6739	1.5704	1.5551	1.5731	1.5353	1.6399	1.6414	1.707	1.8537	2.0231	
5		2.0678	1.8017	1.702	1.574	1.4878	1.4438	1.4563	1.4393	1.423	1.4904	1.5609	1.7048	1.9787	
6	2.1244	1.8638	1.6993	1.5772	1.3887	1.3411	1.3067	1.3616	1.2683	1.3682	1.4032	1.4909	1.562	1.8612	2.0019
7	2.0963	1.8173	1.4435	1.5593	1.5071	1.2951	1.3111	1.3121	1.3261	1.4202	1.3624	1.5004	1.6416	1.7657	2.059
8	2.0639	1.7969	1.4847	1.3824	1.4248	1.336	1.329	1.3866	1.3351	1.3956	1.4046	1.3705	1.5724	1.7891	2.0883
9	2.017	1.7968	1.6099	1.4713	1.3383	1.3116	1.4475	1.3582	1.375	1.2987	1.3468	1.4545	1.6329	1.8073	2.0713
10	2.0207	1.7636	1.553	1.3987	1.3205	1.4137	1.2734	1.3638	1.367	1.328	1.3867	1.5352	1.6825	1.8826	2.0817
11		1.8478	1.6332	1.4568	1.3904	1.3792	1.3079	1.3713	1.3401	1.4532	1.4366	1.6551	1.8058	2.0002	
12		1.9792	1.685	1.5642	1.422	1.4293	1.4026	1.3905	1.3868	1.4274	1.6166	1.7316	1.8537	2.0472	
13			1.9325	1.7157	1.5836	1.4795	1.4845	1.5234	1.4906	1.5234	1.6735	1.8259	2.0424		
14				1.996	1.7335	1.5649	1.6073	1.5715	1.6453	1.7743	1.8586	2.029			
15						1.9147	1.8858	1.8855	1.8984	2.0014					

	1	2	3	4	5	6	7	8	9	10	11	12	13	14	15
1						2.1095	2.1756	2.1946	2.1479	2.156					
2				2.0755	2.0598	1.9742	1.8708	1.8266	1.8713	1.9822	2.0266	2.1326			
3			2.0476	1.9464	1.7455	1.6014	1.5458	1.5025	1.6589	1.7232	1.8151	1.9656	2.0226		
4		2.074	1.9264	1.6448	1.5352	1.4948	1.4733	1.3552	1.4844	1.5992	1.6686	1.6424	1.8487	2.0105	
5		1.9876	1.7548	1.6226	1.5062	1.4723	1.3596	1.2553	1.3811	1.5543	1.6331	1.4473	1.6412	1.9424	
6	2.0038	1.8177	1.6212	1.5531	1.4332	1.2509	1.4879	1.2521	1.2845	1.3187	1.4277	1.5157	1.6101	1.861	1.982
7	2.0303	1.7267	1.5205	1.4281	1.4706	1.4551	1.5282	1.3864	1.3501	1.4224	1.3855	1.4435	1.6204	1.8209	1.9964
8	1.9756	1.7443	1.447	1.3865	1.4075	1.3019	1.4134	1.3621	1.387	1.4123	1.3827	1.4021	1.629	1.7799	2.1069
9	2.0335	1.7452	1.4701	1.5179	1.3955	1.3375	1.3112	1.4345	1.5622	1.4633	1.3579	1.306	1.5252	1.769	2.0488
10	2.1304	1.7698	1.4749	1.3893	1.5364	1.3985	1.3585	1.3904	1.4447	1.4913	1.5683	1.5095	1.6558	1.7428	2.0006
11		1.9088	1.5232	1.4644	1.3932	1.37	1.4645	1.2957	1.3459	1.4618	1.4927	1.5433	1.7277	1.8937	
12		1.9981	1.7457	1.3338	1.5941	1.4764	1.3944	1.4691	1.4772	1.4886	1.6259	1.5991	1.7522	2.0019	
13			1.8929	1.6459	1.5321	1.5434	1.3719	1.3895	1.6341	1.6185	1.5496	1.7358	1.8714		
14				2.0047	1.9352	1.7218	1.7262	1.6464	1.7482	1.7577	1.8636	1.9384			
15						2.1072	2.0063	1.9656	2.0216	2.0246					

Figure S484 - OD_{450} *n*=3 intensity maps produced for **72** (1.5 mg/mL) in aqueous $NaHCO_3$ (0.505 M) at 25 °C. Blue: OD_{450} = 0.00-0.99 AU. Pink: OD_{450} = 1.00-1.99 AU. Red: OD_{450} = 2.00-3.00 AU.

	1	2	3	4	5	6	7	8	9	10	11	12	13	14	15
1						2.1073	2.2319	2.2999	2.1608	2.0595					
2				2.1572	2.1224	2.0338	1.9813	1.9926	1.9323	2.0485	2.0543	1.9602			
3			2.1745	2.0725	1.8518	1.9067	1.7453	1.7021	1.7046	1.6692	1.8294	2.0194	2.0676		
4		2.1406	2.0146	1.8405	1.658	1.6967	1.5263	1.5403	1.6419	1.5345	1.6916	1.8147	2.0071	2.0245	
5		2.0743	1.8289	1.6904	1.5227	1.4592	1.4439	1.3468	1.4252	1.4755	1.5655	1.6308	1.7658	2.0236	
6	2.1107	1.9242	1.6991	1.5329	1.4149	1.3884	1.4007	1.1938	1.406	1.4459	1.3968	1.389	1.5924	1.8978	2.0835
7	2.1247	1.7809	1.6204	1.4352	1.4106	1.4345	1.3465	1.2869	1.2084	1.2796	1.253	1.3754	1.483	1.8009	2.0774
8	2.0837	1.7593	1.5144	1.333	1.4232	1.2981	1.2151	1.3086	1.2958	1.3329	1.2494	1.3879	1.5184	1.753	2.031
9	2.0523	1.7361	1.4867	1.3667	1.3259	1.4006	1.4262	1.3978	1.3683	1.3851	1.3973	1.3633	1.4887	1.7355	2.0998
10	2.0878	1.7778	1.5094	1.5101	1.3446	1.2844	1.4416	1.4333	1.3233	1.3045	1.3987	1.4831	1.5664	1.7811	2.0198
11		1.9109	1.5665	1.4294	1.4129	1.4166	1.4921	1.2343	1.3144	1.392	1.4406	1.5588	1.6904	1.8701	
12		1.9952	1.7564	1.5933	1.4102	1.2653	1.3601	1.5399	1.4488	1.4541	1.5722	1.6612	1.7848	2.0328	
13			1.9208	1.6831	1.605	1.5071	1.5017	1.5292	1.5603	1.6073	1.6675	1.7641	2.0257		
14				1.9193	1.7855	1.7082	1.7023	1.6536	1.6874	1.7762	1.8489	2.0377			
15						1.9671	1.9333	1.9633	1.9787	2.0319					

	1	2	3	4	5	6	7	8	9	10	11	12	13	14	15
1						2.1413	2.1662	2.2287	2.1212	1.9845					
2				2.1393	2.105	2.0507	1.9625	1.8572	1.9416	1.9781	2.0423	1.9656			
3			2.1264	2.0014	1.8462	1.7726	1.7083	1.6294	1.6682	1.7423	1.7908	2.0094	2.0753		
4		2.1149	1.9589	1.7397	1.6975	1.7027	1.5755	1.5511	1.5365	1.611	1.532	1.8136	1.9704	2.0929	
5		2.0654	1.8041	1.5173	1.5414	1.4077	1.3285	1.3985	1.4828	1.5613	1.5829	1.6548	1.8083	2.0015	
6	2.0941	1.9176	1.6536	1.4609	1.4957	1.4409	1.3053	1.2977	1.3763	1.3402	1.3955	1.5342	1.6268	1.8681	2.0278
7	2.0086	1.8187	1.6298	1.4809	1.3697	1.3483	1.3004	1.2926	1.3283	1.2573	1.3295	1.4246	1.5427	1.7499	2.0083
8	2.0216	1.7214	1.4916	1.4111	1.3121	1.2927	1.3455	1.3422	1.3189	1.3784	1.2316	1.3362	1.4866	1.6791	2.0114
9	2.0444	1.7317	1.5266	1.419	1.2711	1.3579	1.2876	1.3284	1.3041	1.3736	1.3916	1.4348	1.6069	1.7226	2.0074
10	2.0449	1.7133	1.5455	1.3851	1.3816	1.2647	1.3012	1.3674	1.294	1.295	1.2716	1.4364	1.5923	1.7928	2.0515
11		1.818	1.5921	1.5053	1.3918	1.3472	1.334	1.2979	1.322	1.3672	1.4242	1.5882	1.7051	1.9116	
12		2.0453	1.7097	1.451	1.4771	1.3167	1.3361	1.4492	1.4126	1.3904	1.623	1.6848	1.8351	2.0467	
13			1.8917	1.6109	1.6093	1.5425	1.465	1.4322	1.5153	1.677	1.7774	1.8605	2.0467		
14				1.9138	1.7921	1.6277	1.6212	1.6603	1.6993	1.775	1.8707	2.0059			
15						1.9712	1.9223	1.8737	1.9249	2.0331					

	1	2	3	4	5	6	7	8	9	10	11	12	13	14	15
1						2.0979	2.1657	2.2213	2.1566	2.1437					
2				2.0589	2.0676	1.952	1.8859	1.8407	1.8531	1.9688	2.0371	2.1035			
3			2.0586	1.9179	1.7416	1.6262	1.5651	1.5743	1.5672	1.7319	1.8368	1.9756	2.0184		
4		2.0831	1.9213	1.6438	1.5196	1.5278	1.4416	1.3506	1.4463	1.537	1.6894	1.6712	1.8807	1.9912	
5		1.963	1.7295	1.5914	1.4953	1.4574	1.2842	1.2711	1.3477	1.5052	1.6189	1.4714	1.652	1.9322	
6	2.0067	1.827	1.5571	1.5405	1.4276	1.1893	1.4245	1.2716	1.2269	1.2902	1.4192	1.4785	1.5468	1.8705	1.9549
7	2.0012	1.7419	1.5465	1.3485	1.4036	1.4171	1.5086	1.3645	1.354	1.3819	1.3372	1.4114	1.5858	1.8054	1.9705
8	2.0082	1.7082	1.4445	1.3593	1.3814	1.255	1.3834	1.3337	1.3605	1.3871	1.4051	1.3967	1.6108	1.7904	2.0719
9	2.0787	1.7357	1.4723	1.5647	1.367	1.3286	1.2857	1.4053	1.5518	1.3695	1.3303	1.3095	1.5355	1.7894	2.0531
10	2.0797	1.7574	1.4416	1.3083	1.5511	1.3779	1.3129	1.3487	1.4359	1.5554	1.4907	1.3987	1.6385	1.7599	2.014
11		1.8776	1.5036	1.4265	1.3387	1.3558	1.4234	1.262	1.3225	1.4408	1.4323	1.5071	1.7116	1.8836	
12		2.0142	1.7221	1.2922	1.4805	1.4467	1.3991	1.4184	1.4781	1.459	1.5935	1.5409	1.744	2.0102	
13			1.9021	1.6808	1.5588	1.5323	1.3632	1.4039	1.5855	1.6331	1.491	1.6909	1.8625		
14				1.9684	1.8919	1.7085	1.6649	1.6244	1.6848	1.7477	1.8022	1.8951			
15						2.1154	1.9939	1.9453	1.9851	1.9589					

Figure S485 - OD_{450} *n*=3 intensity maps produced for **72** (1.5 mg/mL) in aqueous $NaHCO_3$ (0.505 M) at 30 °C. Blue: OD_{450} = 0.00-0.99 AU. Pink: OD_{450} = 1.00-1.99 AU. Red: OD_{450} = 2.00-3.00 AU.

	1	2	3	4	5	6	7	8	9	10	11	12	13	14	15
1						2.0661	2.1882	2.304	2.1822	2.035					
2				2.1132	2.1282	2.0216	1.9827	2.0018	1.9206	2.0394	2.0951	1.9788			
3			2.1477	2.0705	1.8755	1.8556	1.769	1.7334	1.6892	1.7067	1.8148	1.9812	2.0696		
4		2.0895	2.0419	1.8534	1.6673	1.6717	1.5131	1.5162	1.6231	1.5111	1.6697	1.7925	2.0175	2.0097	
5		2.0665	1.8732	1.6939	1.5278	1.4741	1.3888	1.2798	1.3776	1.4352	1.5945	1.6262	1.7463	1.9566	
6	2.1095	1.9493	1.7126	1.5075	1.3983	1.3809	1.3943	1.1972	1.3879	1.3726	1.4389	1.3726	1.5571	1.8636	2.0418
7	2.1238	1.8206	1.5997	1.4395	1.3694	1.3964	1.3541	1.2295	1.2071	1.2866	1.2739	1.3394	1.4703	1.7445	2.0663
8	2.1169	1.7925	1.525	1.3017	1.3889	1.3006	1.1714	1.27	1.2366	1.3129	1.1742	1.3095	1.4937	1.7034	1.9552
9	2.0485	1.7302	1.5021	1.3791	1.3097	1.3819	1.4003	1.3555	1.3404	1.331	1.3368	1.3493	1.4962	1.7161	2.0353
10	2.1059	1.8333	1.5291	1.494	1.3457	1.258	1.4091	1.4069	1.3156	1.277	1.375	1.4386	1.5449	1.7438	1.9976
11		1.9434	1.5679	1.4277	1.3782	1.4008	1.4597	1.2054	1.2803	1.3398	1.3736	1.5044	1.6503	1.8137	
12		1.9834	1.755	1.5569	1.4234	1.2588	1.3453	1.4791	1.3994	1.4121	1.5141	1.6032	1.7433	1.9975	
13			1.941	1.7173	1.599	1.4964	1.4823	1.5033	1.4757	1.574	1.6239	1.7258	1.929		
14				1.8977	1.797	1.6903	1.6925	1.6082	1.6535	1.7453	1.8182	2.0263			
15						1.9714	1.9012	1.9475	1.9432	1.9811					

	1	2	3	4	5	6	7	8	9	10	11	12	13	14	15
1						2.1037	2.1821	2.2611	2.1215	2.0019					
2				2.1115	2.0953	1.9829	1.9889	1.9598	1.9626	1.9986	2.0774	2.0161			
3			2.0905	2.0215	1.8067	1.7487	1.7089	1.6932	1.6479	1.7509	1.827	1.97	2.0367		
4		2.0777	2.0414	1.8012	1.5737	1.6791	1.5914	1.5304	1.5264	1.5711	1.6952	1.7451	1.9271	2.0264	
5		2.0208	1.8388	1.5914	1.4482	1.5025	1.3721	1.2993	1.4322	1.4479	1.5452	1.4782	1.7973	2.0219	
6	2.0622	1.896	1.7029	1.5523	1.366	1.4714	1.2904	1.2228	1.2941	1.3903	1.4849	1.5843	1.6293	1.9027	2.0943
7	2.0585	1.781	1.5695	1.4343	1.3491	1.3071	1.2999	1.2625	1.2784	1.2459	1.3761	1.4652	1.5231	1.6906	1.9726
8	2.0537	1.7046	1.5324	1.4166	1.253	1.2756	1.3121	1.2591	1.2064	1.2573	1.2998	1.3643	1.4643	1.6048	1.9012
9	2.0726	1.6904	1.5297	1.3708	1.3485	1.3196	1.2267	1.2842	1.2553	1.3387	1.2938	1.3279	1.4554	1.6108	1.96
10	2.0749	1.7976	1.5308	1.4194	1.3182	1.2822	1.3051	1.3574	1.2431	1.3814	1.347	1.4566	1.5292	1.6941	1.9707
11		1.8659	1.5157	1.4636	1.3925	1.3175	1.2931	1.3713	1.2577	1.333	1.3381	1.4207	1.6104	1.7992	
12		2.0138	1.6737	1.5923	1.4711	1.3827	1.3942	1.4022	1.3292	1.383	1.5134	1.5947	1.7634	1.9758	
13			1.9082	1.695	1.524	1.4976	1.4245	1.4657	1.5057	1.5991	1.6546	1.777	1.9149		
14				1.9896	1.7638	1.7082	1.6479	1.6312	1.692	1.7945	1.906	2.0047			
15						1.9615	1.899	1.9087	1.9325	2.0044					

	1	2	3	4	5	6	7	8	9	10	11	12	13	14	15
1						2.09	2.1452	2.2251	2.1606	2.129					
2				2.0433	2.0501	1.9592	1.9005	1.8294	1.8365	1.912	2.0445	2.0694			
3			2.0714	1.9341	1.7871	1.6289	1.5489	1.5588	1.5109	1.7349	1.8065	1.9448	2.0478		
4		2.0753	1.9614	1.6827	1.523	1.4829	1.3885	1.363	1.3784	1.4937	1.6779	1.6822	1.8833	1.9923	
5		1.9723	1.7362	1.5336	1.4801	1.3982	1.2936	1.3711	1.2968	1.3848	1.6148	1.5631	1.6142	1.8931	
6	2.0108	1.8585	1.5482	1.5023	1.4415	1.1611	1.346	1.3173	1.1492	1.2485	1.3511	1.4709	1.5308	1.8239	1.9559
7	2.0023	1.8013	1.5642	1.3437	1.3486	1.3508	1.4885	1.3891	1.3379	1.3367	1.3011	1.3789	1.5654	1.7767	1.9334
8	2.0431	1.7319	1.4239	1.3277	1.3517	1.1816	1.3546	1.326	1.3327	1.3363	1.3946	1.3686	1.5294	1.7566	1.9891
9	2.1306	1.7475	1.4993	1.5556	1.3104	1.31	1.2649	1.3737	1.5092	1.3099	1.3616	1.2732	1.5175	1.7334	2.0447
10	2.0697	1.7901	1.458	1.2823	1.5232	1.3546	1.3013	1.3338	1.4087	1.5482	1.4421	1.3227	1.5817	1.7435	1.991
11		1.8805	1.5437	1.3984	1.35	1.3175	1.3986	1.2554	1.2784	1.3835	1.375	1.4578	1.6585	1.8239	
12		2.0174	1.7302	1.3047	1.4378	1.4235	1.3798	1.3762	1.4328	1.4112	1.5186	1.515	1.7128	1.9613	
13			1.9359	1.7407	1.5699	1.5091	1.3401	1.385	1.5386	1.6121	1.4547	1.6402	1.8168		
14				1.9704	1.8891	1.6971	1.6238	1.5939	1.6288	1.7164	1.7331	1.8536			
15						2.0901	1.9713	1.9099	1.9526	1.9163					

Figure S486 - OD_{450} *n*=3 intensity maps produced for **72** (1.5 mg/mL) in aqueous $NaHCO_3$ (0.505 M) at 35 °C. Blue: OD_{450} = 0.00-0.99 AU. Pink: OD_{450} = 1.00-1.99 AU. Red: OD_{450} = 2.00-3.00 AU.

	1	2	3	4	5	6	7	8	9	10	11	12	13	14	15
1						2.0531	2.2067	2.2664	2.1821	1.9641					
2				2.0711	2.0906	2.0252	1.9903	1.8955	1.9653	1.9608	2.0478	1.9691			
3			2.136	2.0295	1.9583	1.8103	1.712	1.6765	1.5863	1.7466	1.89	2.0159	1.9825		
4		2.1348	2.0477	1.8045	1.7283	1.5917	1.514	1.5582	1.4783	1.6361	1.6474	1.7301	1.8972	1.9811	
5		2.0917	1.8722	1.6497	1.6007	1.3524	1.2825	1.3103	1.4017	1.4923	1.4422	1.4774	1.6912	1.9828	
6	2.0952	1.9606	1.6988	1.511	1.4069	1.2615	1.246	1.2016	1.3023	1.3188	1.2034	1.3951	1.5294	1.8738	1.9958
7	2.0739	1.8491	1.6046	1.4285	1.3766	1.3509	1.2278	1.2471	1.1899	1.2137	1.2044	1.3271	1.5052	1.7465	1.9616
8	2.1475	1.7481	1.5642	1.3493	1.2892	1.2785	1.2039	1.2547	1.2342	1.3204	1.2727	1.3489	1.4568	1.649	2.0221
9	2.1028	1.7599	1.5069	1.2971	1.3586	1.3202	1.2939	1.2923	1.2913	1.3527	1.3308	1.4088	1.4897	1.6672	1.9443
10	2.03	1.8142	1.5226	1.4321	1.3009	1.2645	1.3327	1.4103	1.3548	1.2655	1.2727	1.3855	1.5575	1.7616	1.9623
11		1.8568	1.586	1.4294	1.3994	1.4111	1.3632	1.3017	1.2295	1.2931	1.3607	1.4683	1.5922	1.8188	
12		2.0348	1.7575	1.4706	1.4463	1.3031	1.177	1.3275	1.4472	1.3496	1.4718	1.5857	1.7265	1.9828	
13			1.9102	1.6947	1.5027	1.4917	1.3915	1.4438	1.438	1.5363	1.5881	1.7387	1.9721		
14				1.9219	1.7298	1.6276	1.5849	1.6211	1.6015	1.6491	1.7881	1.9544			
15						1.9058	1.8535	1.8544	1.904	1.9806					

	1	2	3	4	5	6	7	8	9	10	11	12	13	14	15
1						2.0718	2.1642	2.241	2.178	1.9613					
2				2.0892	2.0645	1.9982	1.9321	1.9777	1.9656	2.0589	2.0919	1.9961			
3			2.0521	2.0578	1.8313	1.7113	1.6992	1.6931	1.6693	1.6753	1.832	1.9835	2.0123		
4		2.0635	1.9971	1.7935	1.5644	1.5983	1.5433	1.5182	1.5161	1.5547	1.6176	1.7772	1.8986	1.9688	
5		1.98	1.8295	1.5915	1.418	1.4756	1.4344	1.3051	1.4003	1.4789	1.538	1.5896	1.7622	2.0034	
6	2.0427	1.849	1.6923	1.528	1.391	1.3486	1.3067	1.2329	1.2198	1.3752	1.4853	1.4633	1.5991	1.877	2.0037
7	2.0495	1.8016	1.5652	1.3833	1.3214	1.2848	1.2586	1.231	1.2375	1.2366	1.3648	1.416	1.6197	1.7628	2.0501
8	2.0561	1.693	1.4951	1.3533	1.2063	1.2671	1.2667	1.1986	1.1786	1.233	1.2785	1.31	1.4581	1.6087	1.9589
9	2.0404	1.6999	1.4742	1.3426	1.3322	1.2525	1.1934	1.2192	1.2265	1.3109	1.1428	1.2798	1.4639	1.5922	1.9312
10	2.0621	1.7896	1.5603	1.4147	1.3019	1.2681	1.281	1.3108	1.2639	1.3382	1.3601	1.3249	1.4407	1.6611	1.9402
11		1.8199	1.4702	1.4718	1.329	1.273	1.2455	1.2701	1.256	1.247	1.2691	1.4098	1.563	1.778	
12		1.9679	1.7253	1.5441	1.4864	1.3603	1.3875	1.369	1.2744	1.362	1.4409	1.518	1.6815	1.9262	
13			1.9438	1.6634	1.5581	1.4491	1.4098	1.4417	1.4477	1.5923	1.5977	1.7224	1.8941		
14				1.9725	1.7895	1.682	1.6132	1.6313	1.6646	1.7485	1.8573	1.956			
15						1.9635	1.8995	1.8789	1.8951	1.9359					

	1	2	3	4	5	6	7	8	9	10	11	12	13	14	15
1						2.0732	2.163	2.2199	2.1493	2.1179					
2				2.0363	2.0574	1.9806	1.8703	1.8195	1.8429	1.9613	2.0032	2.0786			
3			2.0453	1.9352	1.7598	1.6095	1.5157	1.5099	1.5792	1.6927	1.81	1.9398	1.9802		
4		2.0551	1.9347	1.6617	1.5008	1.4758	1.3846	1.3003	1.4086	1.4991	1.648	1.6342	1.8216	1.9453	
5		1.9958	1.7664	1.5946	1.4576	1.3818	1.239	1.2072	1.2795	1.4552	1.5602	1.434	1.6122	1.8955	
6	2.0015	1.8205	1.5984	1.4686	1.3801	1.1444	1.3402	1.219	1.1846	1.2303	1.3407	1.4509	1.56	1.8397	1.9293
7	2.0091	1.7485	1.5004	1.3683	1.3606	1.341	1.4152	1.326	1.2724	1.3253	1.3014	1.3493	1.5604	1.7624	1.9346
8	1.9995	1.7552	1.4477	1.3108	1.3472	1.2233	1.3662	1.2591	1.29	1.2876	1.3326	1.3067	1.5137	1.7016	2.0265
9	2.0256	1.7577	1.4567	1.3986	1.2996	1.2244	1.2344	1.3158	1.4233	1.3206	1.3191	1.2252	1.443	1.6845	1.9649
10	2.1311	1.8183	1.4387	1.3684	1.3817	1.269	1.278	1.3399	1.3608	1.386	1.4515	1.3426	1.5421	1.6722	1.9175
11		1.8984	1.5341	1.409	1.3514	1.2909	1.3338	1.2922	1.2385	1.3549	1.3697	1.3784	1.5915	1.7736	
12		1.966	1.7537	1.3485	1.4926	1.3445	1.3386	1.3714	1.3728	1.4157	1.5256	1.4999	1.62	1.9222	
13			1.9089	1.608	1.4582	1.4423	1.2717	1.318	1.5134	1.5088	1.4674	1.6158	1.7862		
14				2.0344	1.8907	1.666	1.5781	1.4965	1.6025	1.6404	1.744	1.8597			
15						2.0471	1.9328	1.8882	1.907	1.9506					

Figure S487 - OD_{450} *n*=3 intensity maps produced for **72** (1.5 mg/mL) in aqueous $NaHCO_3$ (0.505 M) at 40 °C. Blue: OD_{450} = 0.00-0.99 AU. Pink: OD_{450} = 1.00-1.99 AU. Red: OD_{450} = 2.00-3.00 AU.

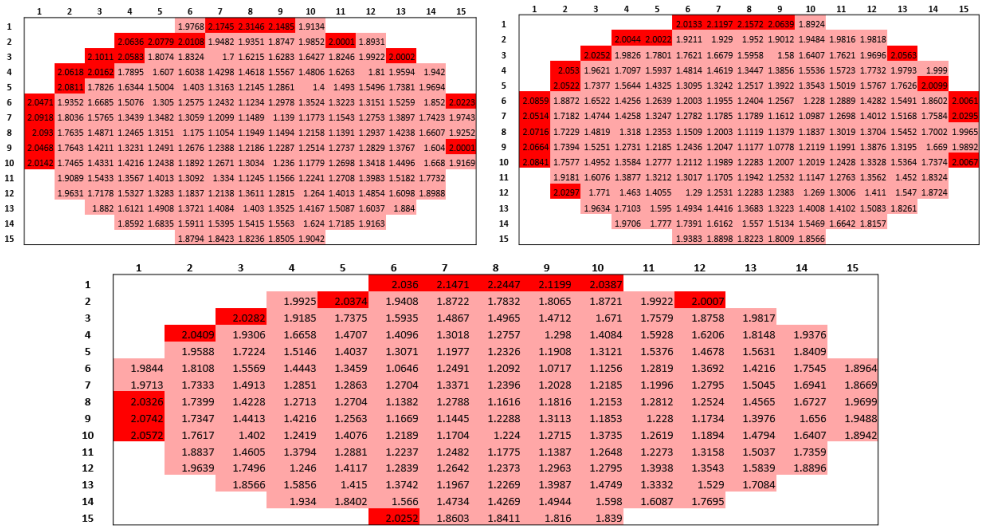

Figure S488 - OD_{450} *n*=3 intensity maps produced for **72** (1.5 mg/mL) in aqueous $NaHCO_3$ (0.505 M) at 45 °C. Blue: OD_{450} = 0.00-0.99 AU. Pink: OD_{450} = 1.00-1.99 AU. Red: OD_{450} = 2.00-3.00 AU.

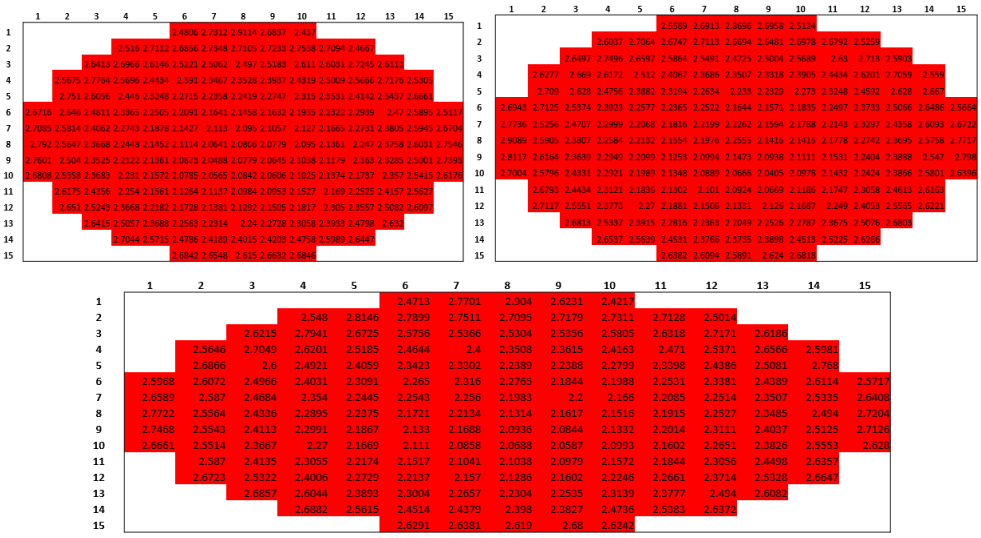

Figure S489 - OD_{450} *n*=3 intensity maps produced for **72** (1.5 mg/mL) in aqueous NaOAc (0.505 M) at 25 °C. Blue: OD_{450} = 0.00-0.99 AU. Pink: OD_{450} = 1.00-1.99 AU. Red: OD_{450} = 2.00-3.00 AU.

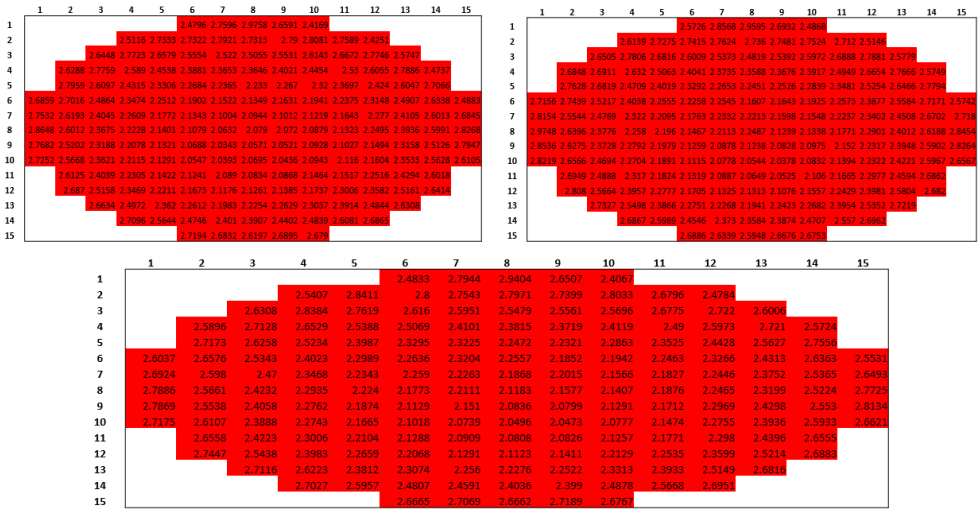

Figure S490 - OD_{450} *n*=3 intensity maps produced for **72** (1.5 mg/mL) in aqueous NaOAc (0.505 M) at 30 °C. Blue: OD_{450} = 0.00-0.99 AU. Pink: OD_{450} = 1.00-1.99 AU. Red: OD_{450} = 2.00-3.00 AU.

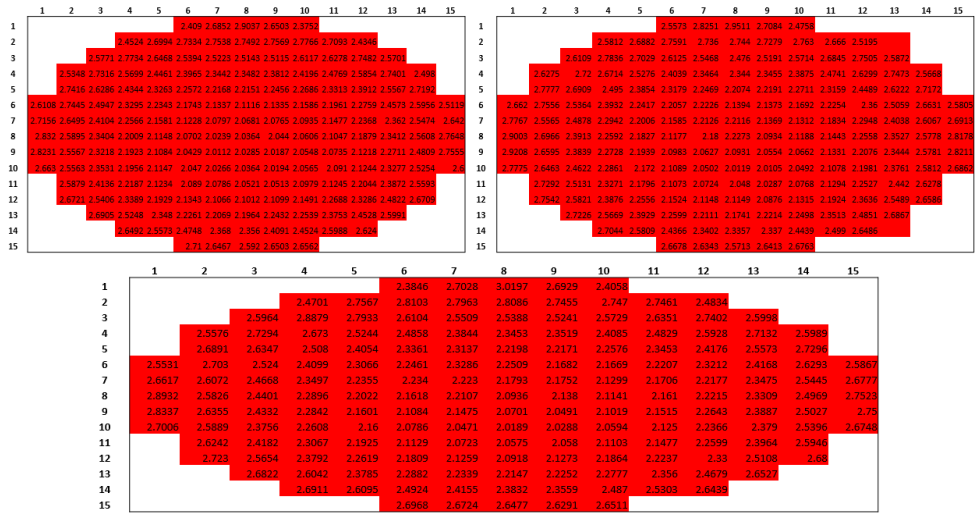

Figure S491 - OD_{450} *n*=3 intensity maps produced for **72** (1.5 mg/mL) in aqueous NaOAc (0.505 M) at 35 °C. Blue: OD_{450} = 0.00-0.99 AU. Pink: OD_{450} = 1.00-1.99 AU. Red: OD_{450} = 2.00-3.00 AU.

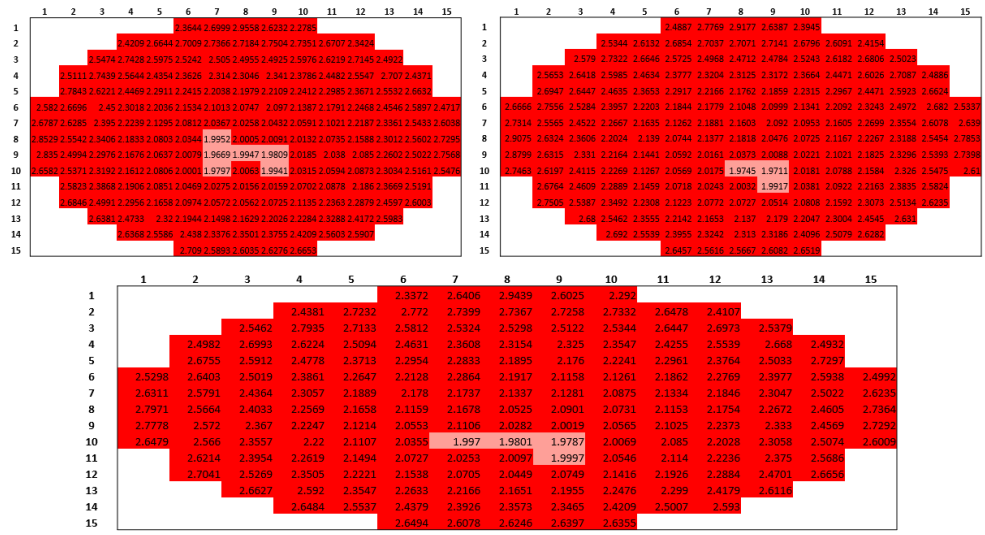

Figure S492 - OD_{450} *n*=3 intensity maps produced for **72** (1.5 mg/mL) in aqueous NaOAc (0.505 M) at 40 °C. Blue: OD_{450} = 0.00-0.99 AU. Pink: OD_{450} = 1.00-1.99 AU. Red: OD_{450} = 2.00-3.00 AU.

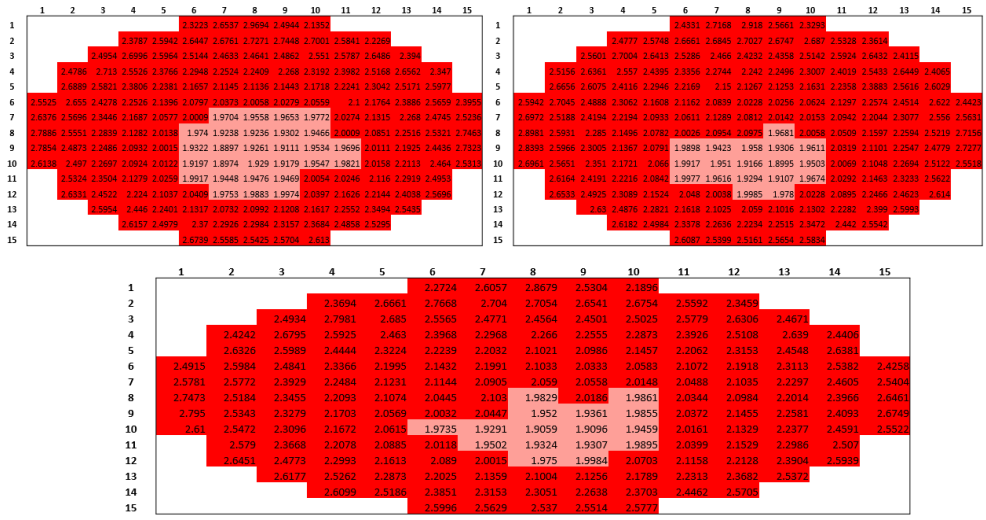

Figure S493 - OD_{450} *n*=3 intensity maps produced for **72** (1.5 mg/mL) in aqueous NaOAc (0.505 M) at 45 °C. Blue: OD_{450} = 0.00-0.99 AU. Pink: OD_{450} = 1.00-1.99 AU. Red: OD_{450} = 2.00-3.00 AU.

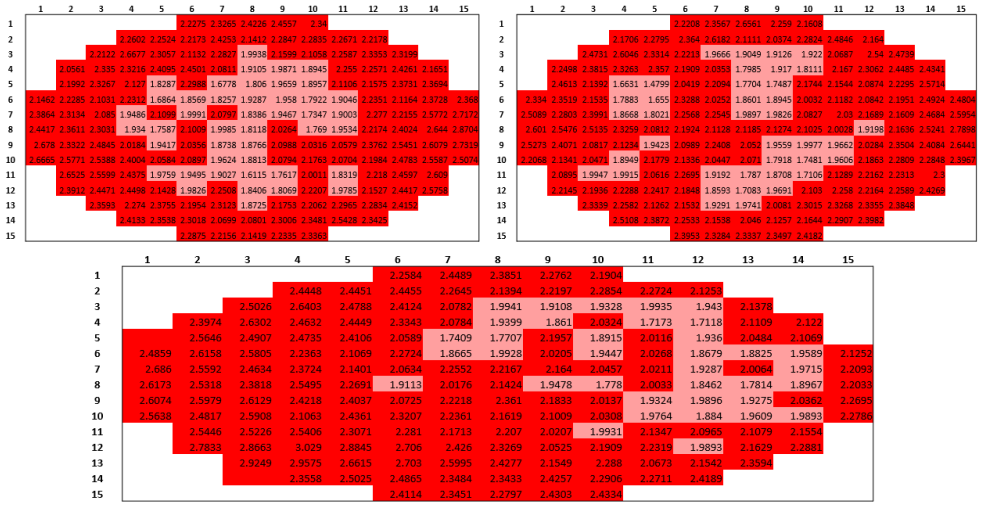

Figure S494 - OD_{450} *n*=3 intensity maps produced for **72** (1.5 mg/mL) in aqueous NaF (0.505 M) at 25 °C. Blue: OD_{450} = 0.00-0.99 AU. Pink: OD_{450} = 1.00-1.99 AU. Red: OD_{450} = 2.00-3.00 AU.

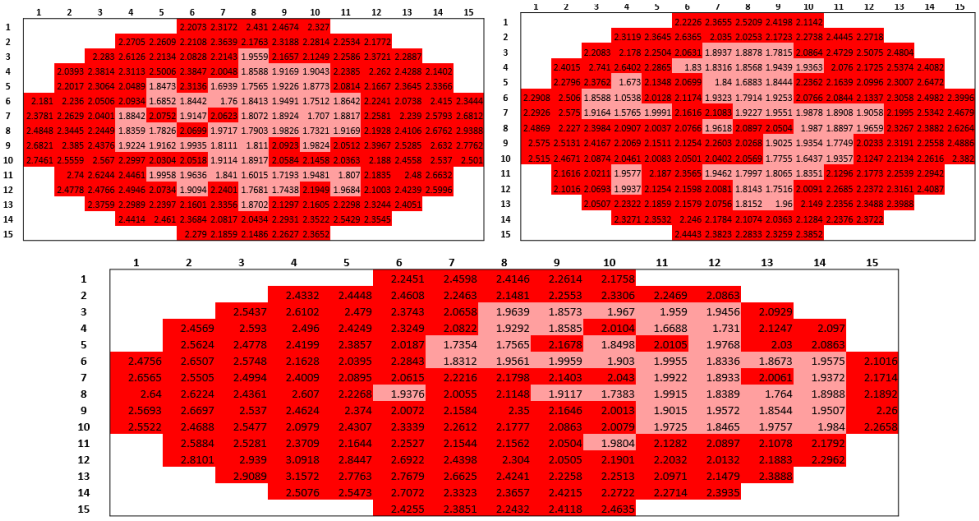

Figure S495 - OD_{450} *n*=3 intensity maps produced for **72** (1.5 mg/mL) in aqueous NaF (0.505 M) at 30 °C. Blue: OD_{450} = 0.00-0.99 AU. Pink: OD_{450} = 1.00-1.99 AU. Red: OD_{450} = 2.00-3.00 AU.

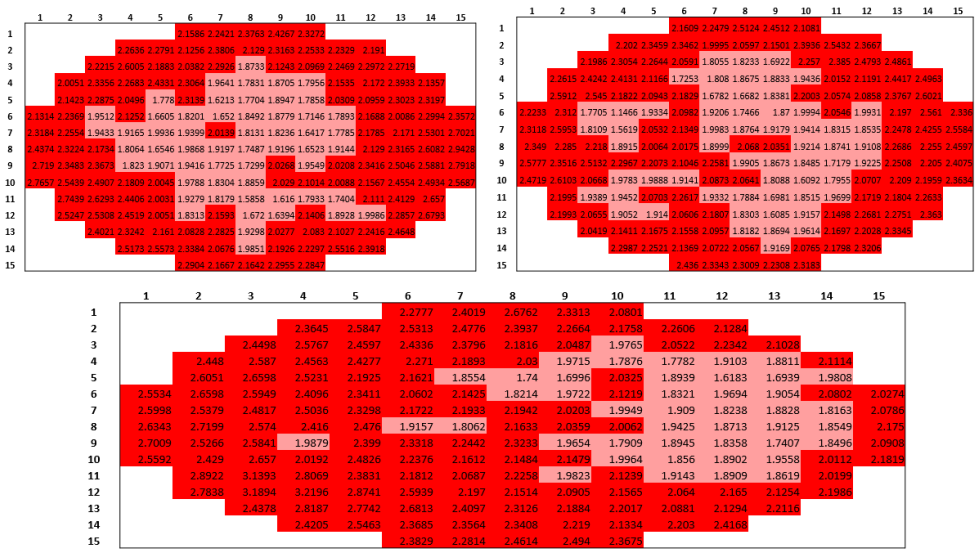

Figure S496 - OD_{450} *n*=3 intensity maps produced for **72** (1.5 mg/mL) in aqueous NaF (0.505 M) at 35 °C. Blue: OD_{450} = 0.00-0.99 AU. Pink: OD_{450} = 1.00-1.99 AU. Red: OD_{450} = 2.00-3.00 AU.

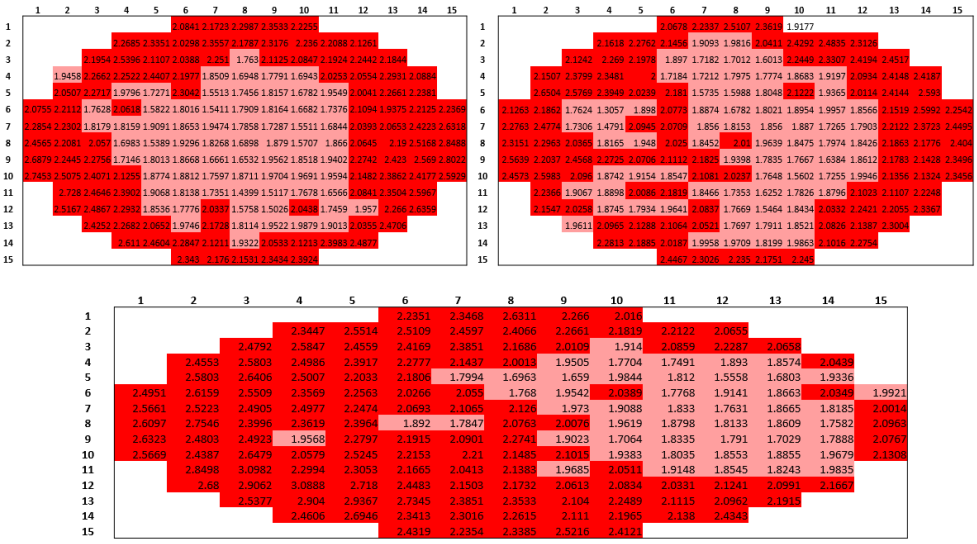

Figure S497 - OD_{450} *n*=3 intensity maps produced for **72** (1.5 mg/mL) in aqueous NaF (0.505 M) at 40 °C. Blue: OD_{450} = 0.00-0.99 AU. Pink: OD_{450} = 1.00-1.99 AU. Red: OD_{450} = 2.00-3.00 AU.

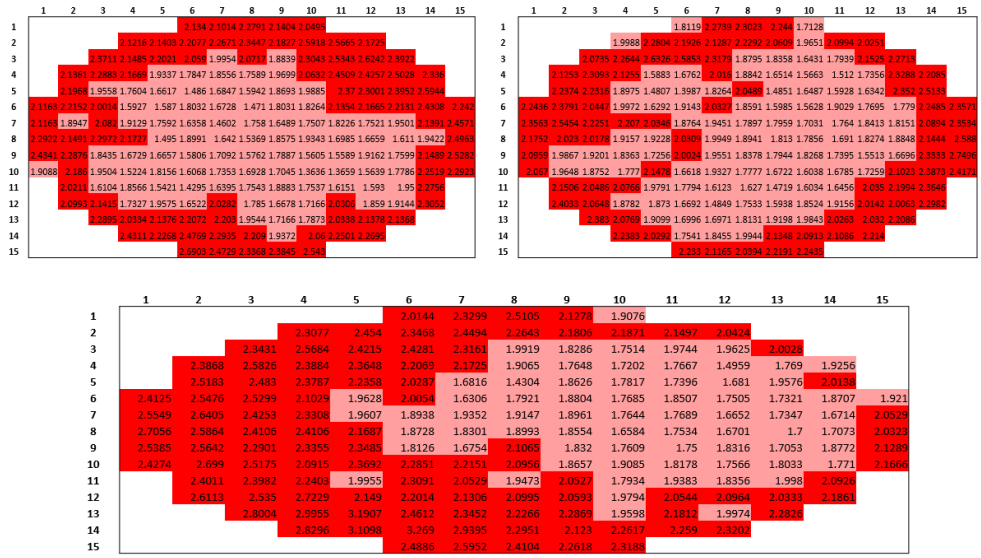

Figure S498 - OD_{450} *n*=3 intensity maps produced for **72** (1.5 mg/mL) in aqueous NaF (0.505 M) at 45 °C. Blue: OD_{450} = 0.00-0.99 AU. Pink: OD_{450} = 1.00-1.99 AU. Red: OD_{450} = 2.00-3.00 AU.

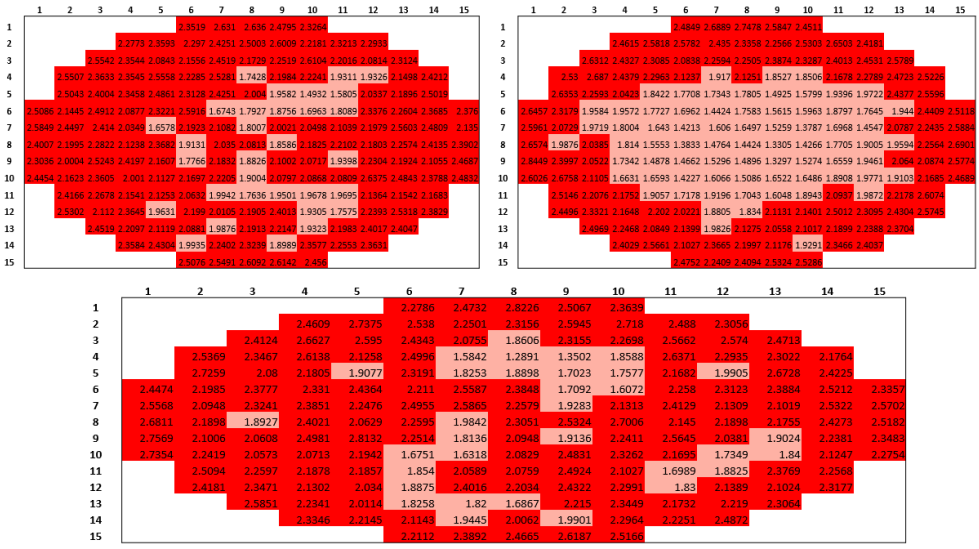

Figure S499 - OD_{450} *n*=3 intensity maps produced for **72** (1.5 mg/mL) in aqueous RbCl (0.505 M) at 25 °C. Blue: OD_{450} = 0.00-0.99 AU. Pink: OD_{450} = 1.00-1.99 AU. Red: OD_{450} = 2.00-3.00 AU.

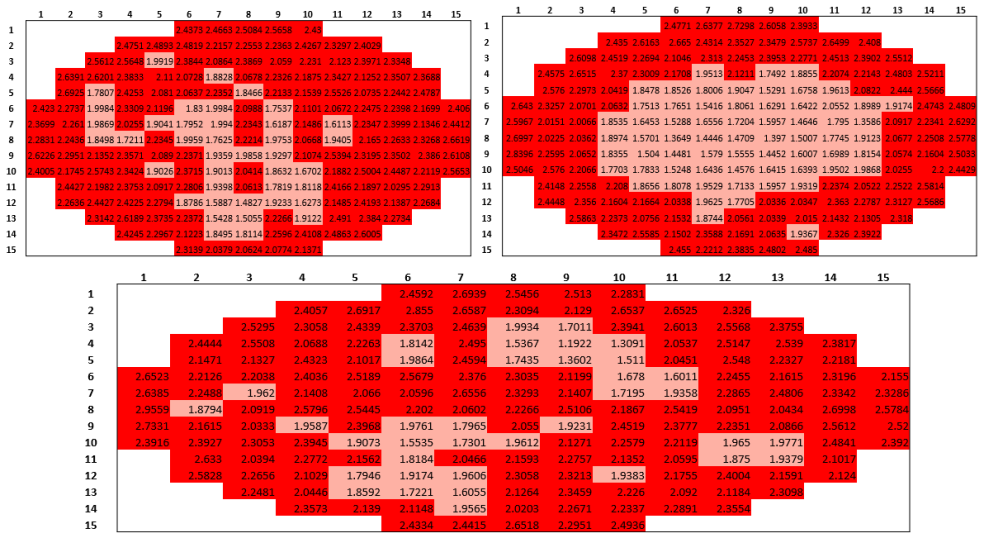

Figure S500 - OD_{450} *n*=3 intensity maps produced for **72** (1.5 mg/mL) in aqueous RbCl (0.505 M) at 30 °C. Blue: OD_{450} = 0.00-0.99 AU. Pink: OD_{450} = 1.00-1.99 AU. Red: OD_{450} = 2.00-3.00 AU.

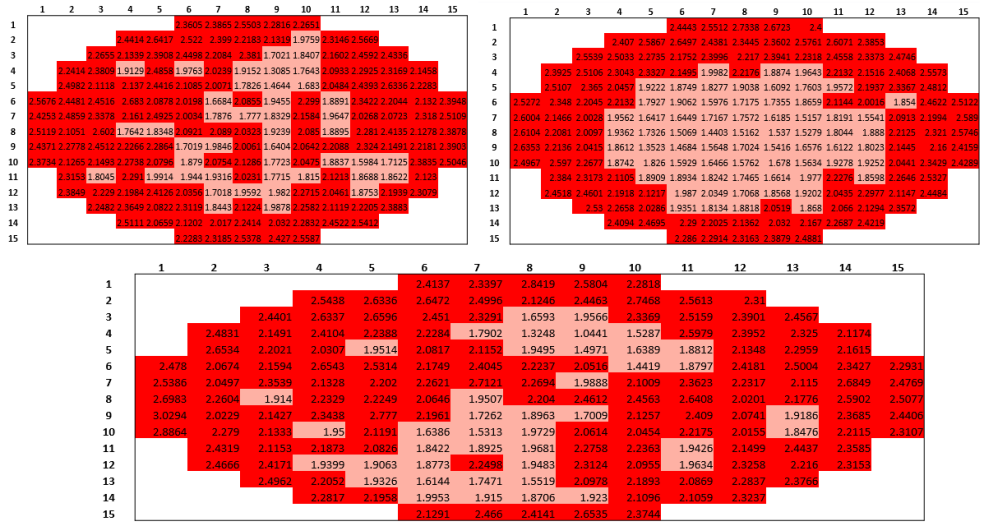

Figure S501 - OD_{450} *n*=3 intensity maps produced for **72** (1.5 mg/mL) in aqueous RbCl (0.505 M) at 35 °C. Blue: OD_{450} = 0.00-0.99 AU. Pink: OD_{450} = 1.00-1.99 AU. Red: OD_{450} = 2.00-3.00 AU.

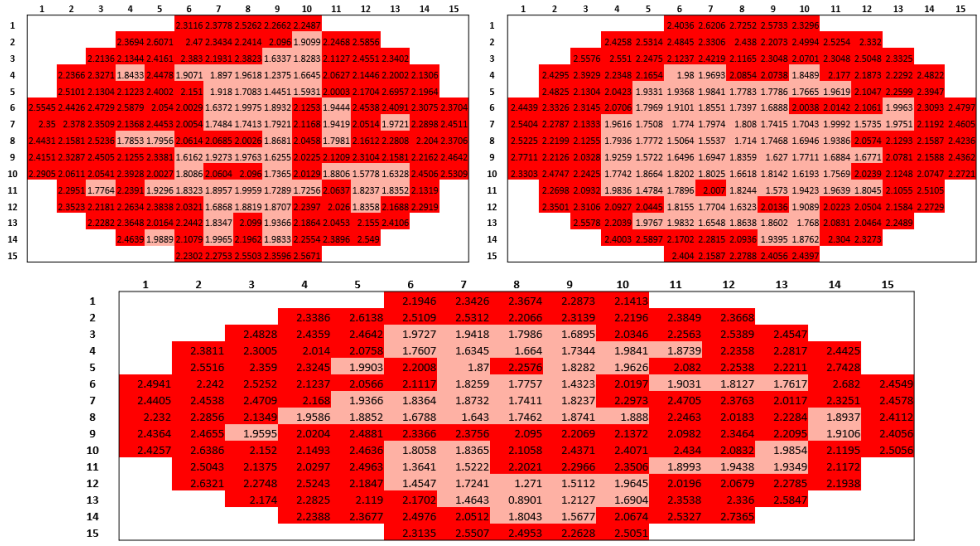

Figure S502 - OD_{450} *n*=3 intensity maps produced for **72** (1.5 mg/mL) in aqueous RbCl (0.505 M) at 40 °C. Blue: OD_{450} = 0.00-0.99 AU. Pink: OD_{450} = 1.00-1.99 AU. Red: OD_{450} = 2.00-3.00 AU.

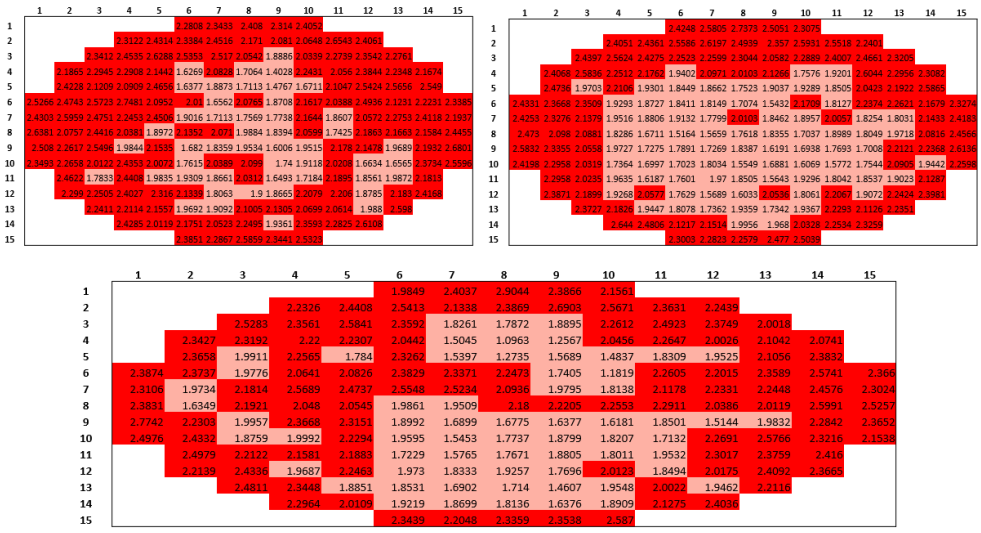

Figure S503 - OD_{450} *n*=3 intensity maps produced for **72** (1.5 mg/mL) in aqueous RbCl (0.505 M) at 45 °C. Blue: OD_{450} = 0.00-0.99 AU. Pink: OD_{450} = 1.00-1.99 AU. Red: OD_{450} = 2.00-3.00 AU.

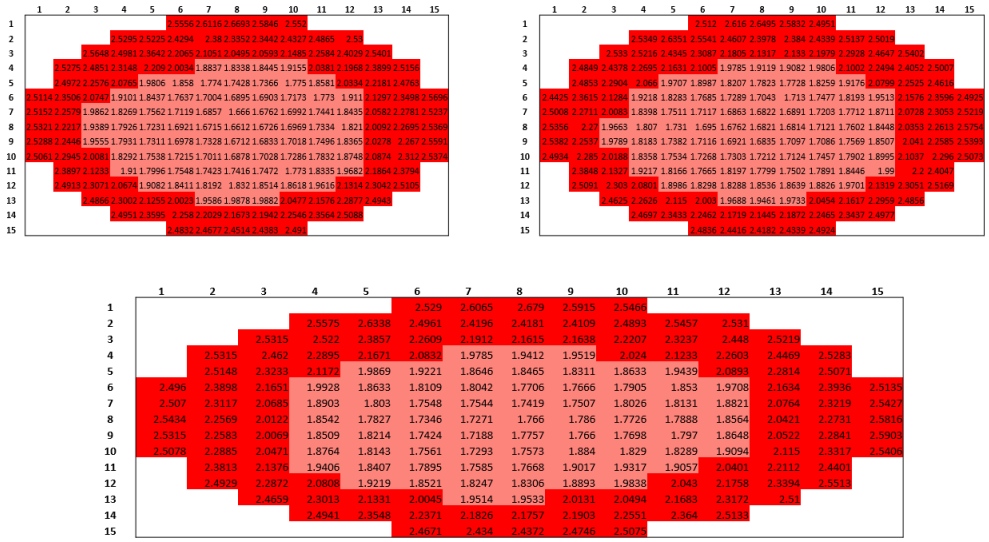

Figure S504 - OD_{450} *n*=3 intensity maps produced for **72** (1.5 mg/mL) in aqueous NaCl (0.505 M) at 25 °C. Blue: OD_{450} = 0.00-0.99 AU. Pink: OD_{450} = 1.00-1.99 AU. Red: OD_{450} = 2.00-3.00 AU.

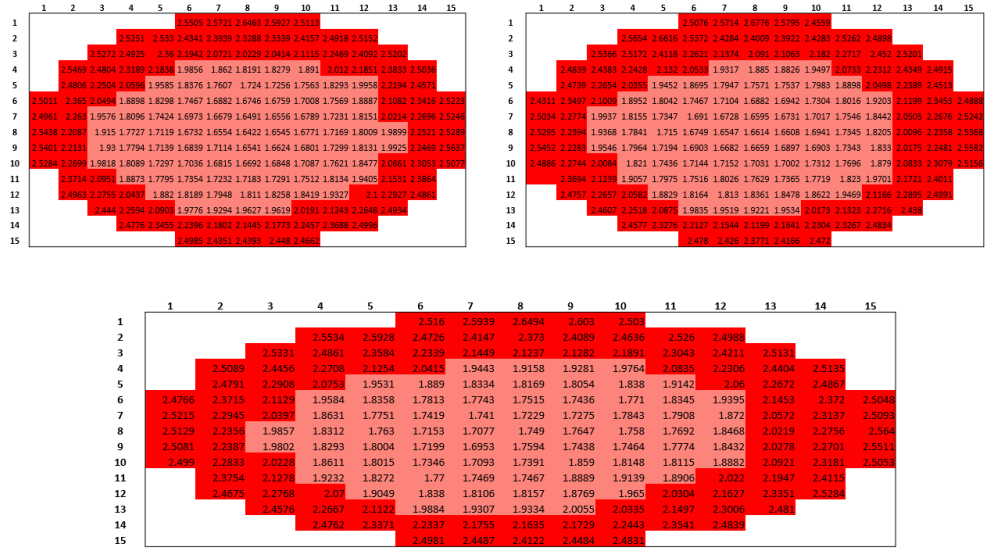

Figure S505 - OD_{450} *n*=3 intensity maps produced for **72** (1.5 mg/mL) in aqueous NaCl (0.505 M) at 30 °C. Blue: OD_{450} = 0.00-0.99 AU. Pink: OD_{450} = 1.00-1.99 AU. Red: OD_{450} = 2.00-3.00 AU.

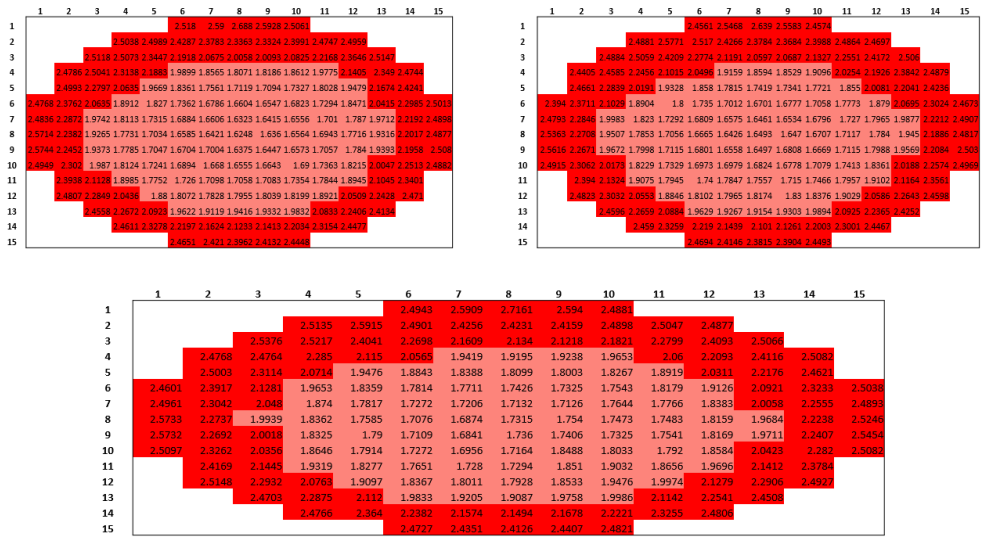

Figure S506 - OD_{450} *n*=3 intensity maps produced for **72** (1.5 mg/mL) in aqueous NaCl (0.505 M) at 35 °C. Blue: OD_{450} = 0.00-0.99 AU. Pink: OD_{450} = 1.00-1.99 AU. Red: OD_{450} = 2.00-3.00 AU.

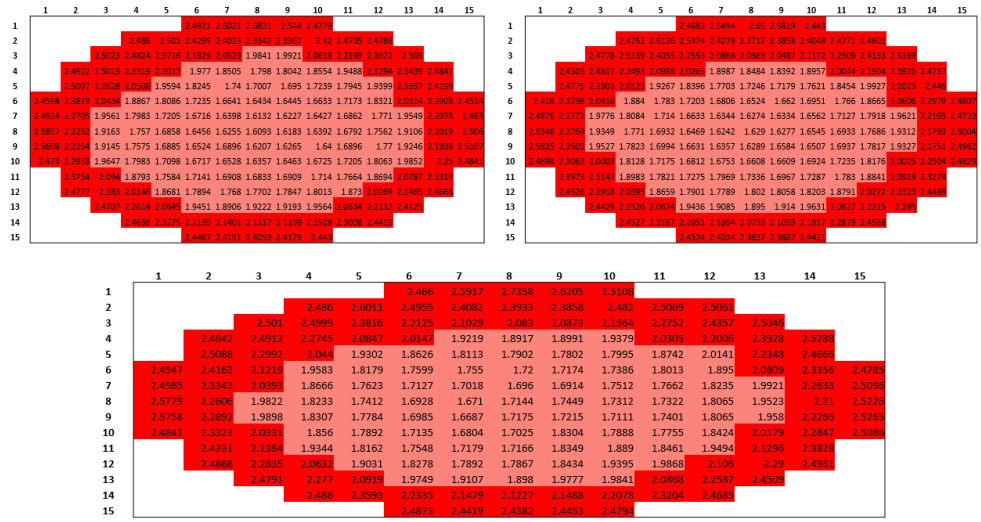

Figure S507 - OD_{450} *n*=3 intensity maps produced for **72** (1.5 mg/mL) in aqueous NaCl (0.505 M) at 40 °C. Blue: OD_{450} = 0.00-0.99 AU. Pink: OD_{450} = 1.00-1.99 AU. Red: OD_{450} = 2.00-3.00 AU.

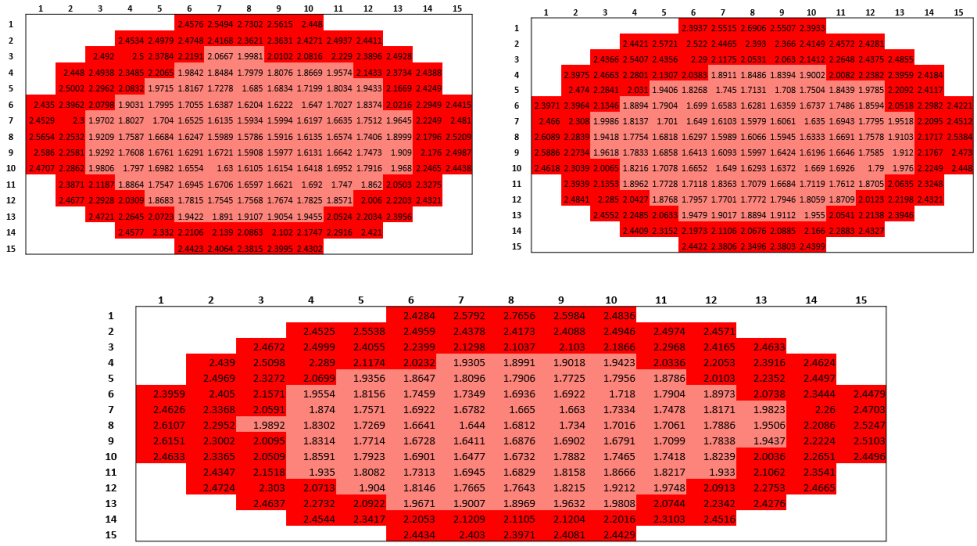

Figure S508 - OD_{450} *n*=3 intensity maps produced for **72** (1.5 mg/mL) in aqueous NaCl (0.505 M) at 45 °C. Blue: OD_{450} = 0.00-0.99 AU. Pink: OD_{450} = 1.00-1.99 AU. Red: OD_{450} = 2.00-3.00 AU.

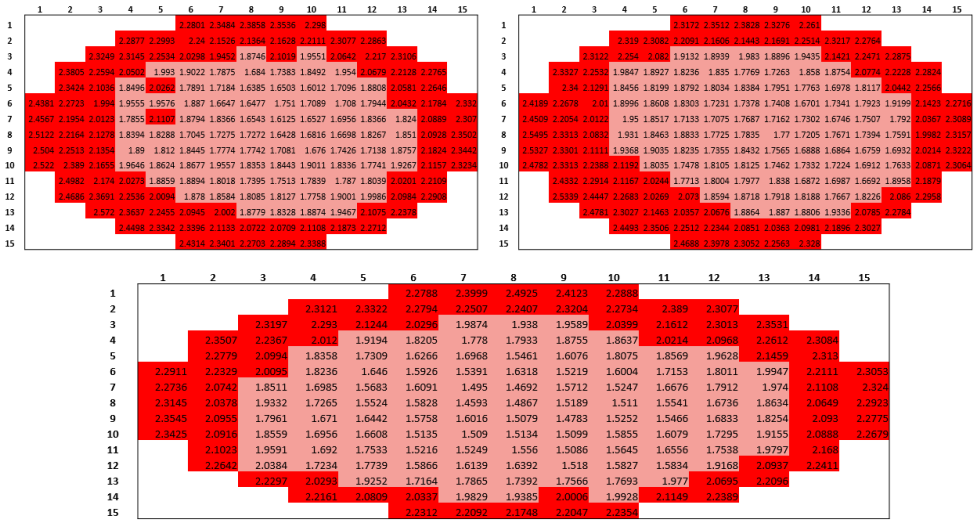

Figure S509 - OD_{450} *n*=3 intensity maps produced for **72** (1.5 mg/mL) in aqueous $NaNO_3$ (0.505 M) at 25 °C. Blue: OD_{450} = 0.00-0.99 AU. Pink: OD_{450} = 1.00-1.99 AU. Red: OD_{450} = 2.00-3.00 AU.

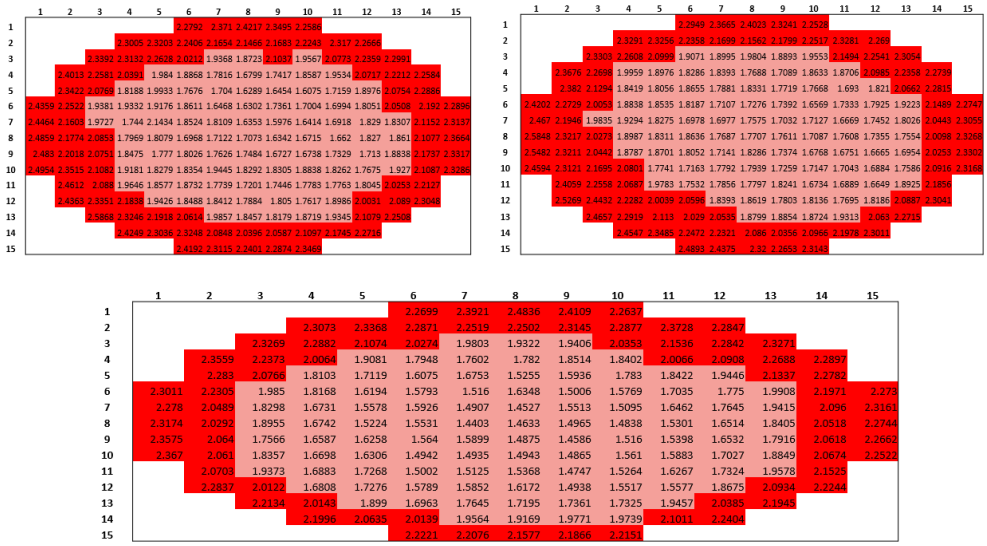

Figure S510 - OD_{450} *n*=3 intensity maps produced for **72** (1.5 mg/mL) in aqueous $NaNO_3$ (0.505 M) at 30 °C. Blue: OD_{450} = 0.00-0.99 AU. Pink: OD_{450} = 1.00-1.99 AU. Red: OD_{450} = 2.00-3.00 AU.

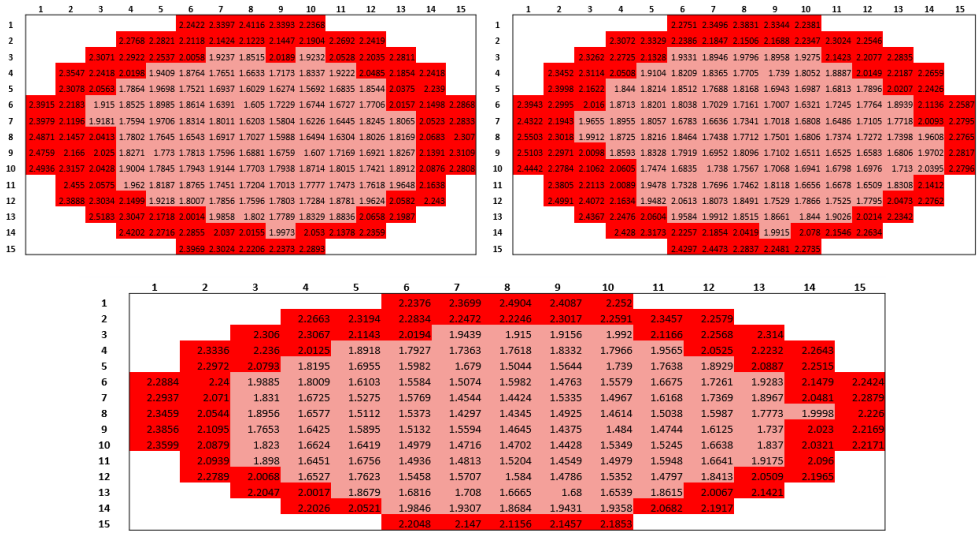

Figure S511 - OD_{450} *n*=3 intensity maps produced for **72** (1.5 mg/mL) in aqueous $NaNO_3$ (0.505 M) at 35 °C. Blue: OD_{450} = 0.00-0.99 AU. Pink: OD_{450} = 1.00-1.99 AU. Red: OD_{450} = 2.00-3.00 AU.

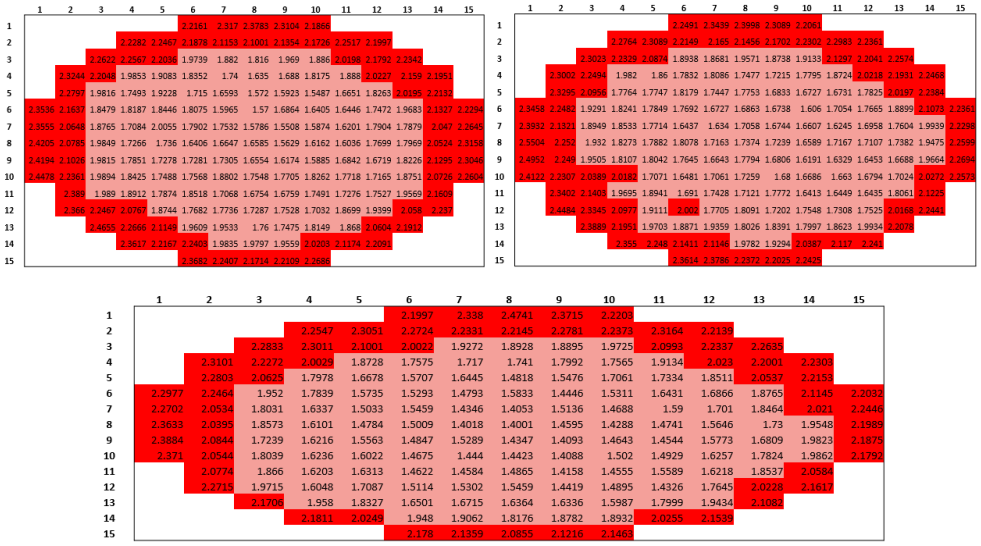

Figure S512 - OD_{450} *n*=3 intensity maps produced for **72** (1.5 mg/mL) in aqueous $NaNO_3$ (0.505 M) at 40 °C. Blue: OD_{450} = 0.00-0.99 AU. Pink: OD_{450} = 1.00-1.99 AU. Red: OD_{450} = 2.00-3.00 AU.

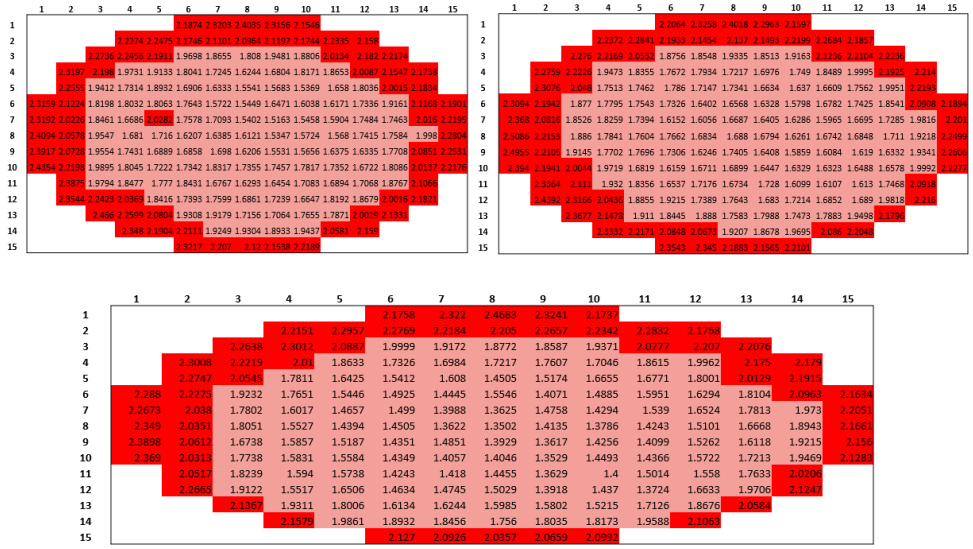

Figure S513 - OD_{450} *n*=3 intensity maps produced for **72** (1.5 mg/mL) in aqueous $NaNO_3$ (0.505 M) at 45 °C. Blue: OD_{450} = 0.00-0.99 AU. Pink: OD_{450} = 1.00-1.99 AU. Red: OD_{450} = 2.00-3.00 AU.

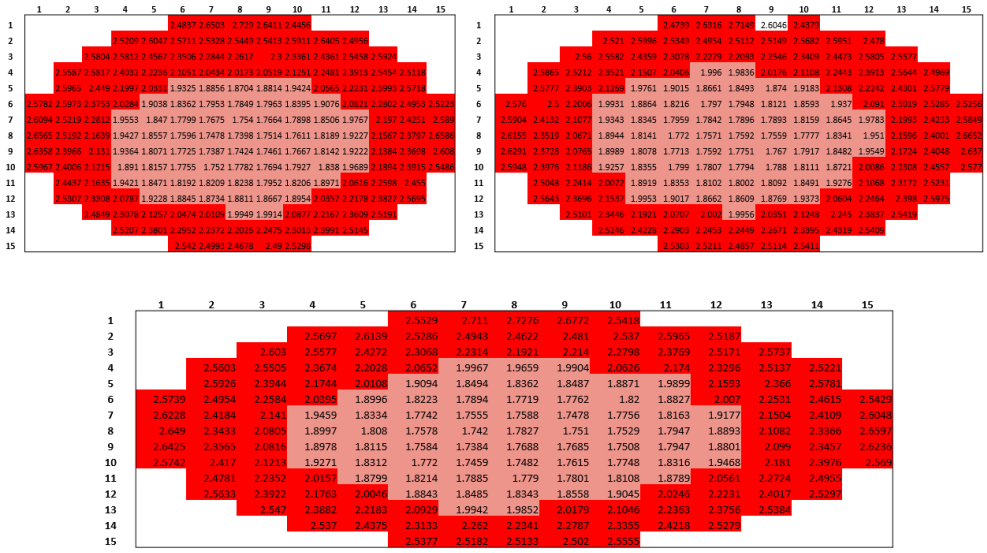

Figure S514 - OD_{450} *n*=3 intensity maps produced for **72** (1.5 mg/mL) in aqueous NaOBz (0.505 M) at 25 °C. Blue: OD_{450} = 0.00-0.99 AU. Pink: OD_{450} = 1.00-1.99 AU. Red: OD_{450} = 2.00-3.00 AU.

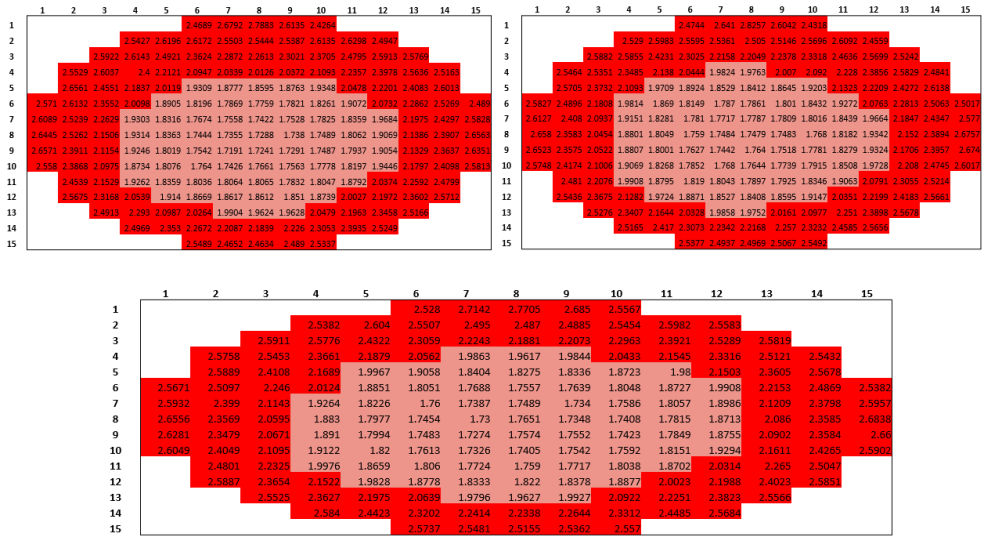

Figure S515 - OD_{450} *n*=3 intensity maps produced for **72** (1.5 mg/mL) in aqueous NaOBz (0.505 M) at 30 °C. Blue: OD_{450} = 0.00-0.99 AU. Pink: OD_{450} = 1.00-1.99 AU. Red: OD_{450} = 2.00-3.00 AU.

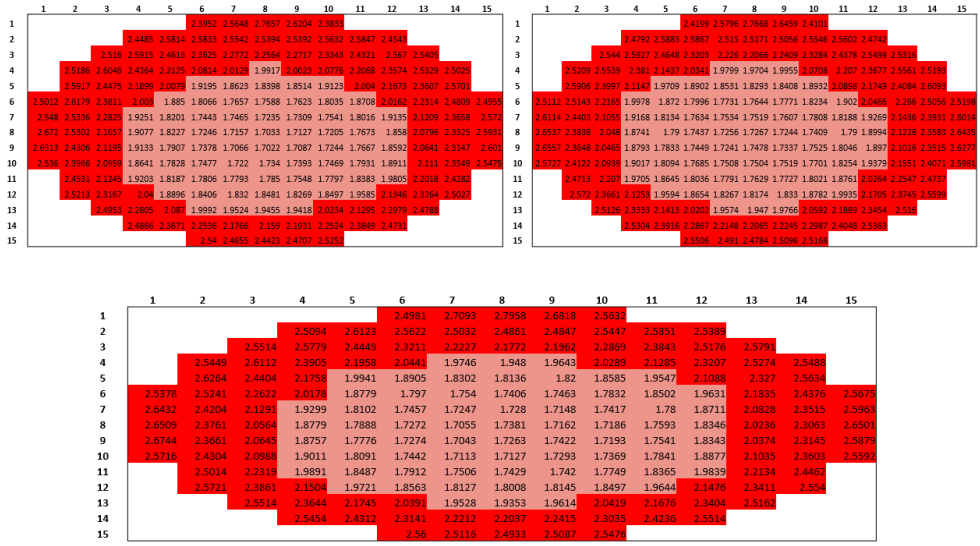

Figure S516 - OD_{450} *n*=3 intensity maps produced for **72** (1.5 mg/mL) in aqueous NaOBz (0.505 M) at 35 °C. Blue: OD_{450} = 0.00-0.99 AU. Pink: OD_{450} = 1.00-1.99 AU. Red: OD_{450} = 2.00-3.00 AU.

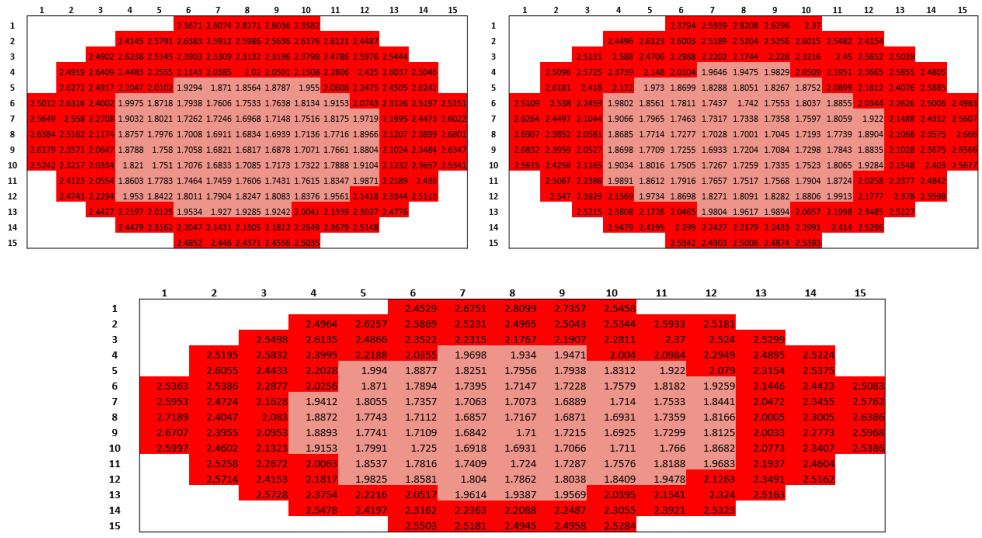

Figure S517 - OD_{450} *n*=3 intensity maps produced for **72** (1.5 mg/mL) in aqueous NaOBz (0.505 M) at 40 °C. Blue: OD_{450} = 0.00-0.99 AU. Pink: OD_{450} = 1.00-1.99 AU. Red: OD_{450} = 2.00-3.00 AU.

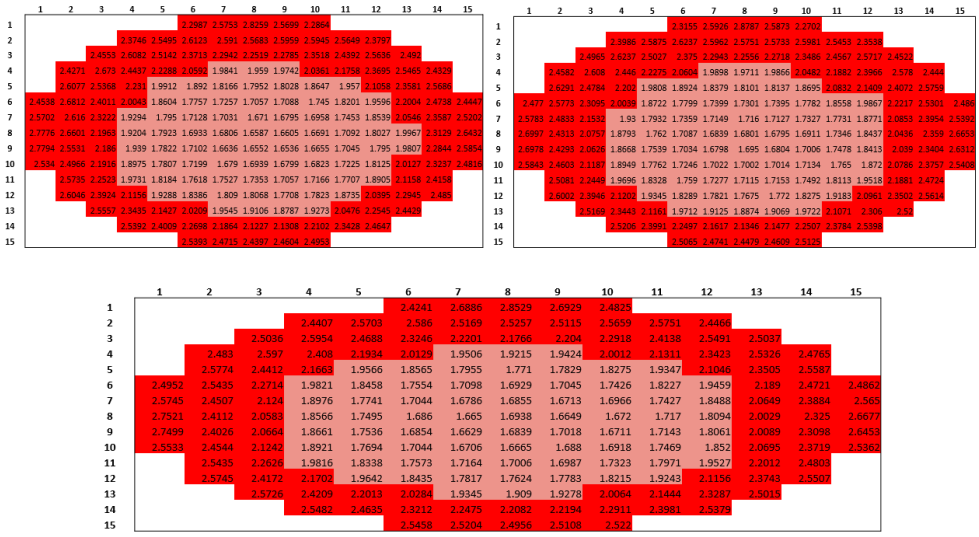

Figure S518 - OD_{450} *n*=3 intensity maps produced for **72** (1.5 mg/mL) in aqueous NaOBz (0.505 M) at 45 °C. Blue: OD_{450} = 0.00-0.99 AU. Pink: OD_{450} = 1.00-1.99 AU. Red: OD_{450} = 2.00-3.00 AU.

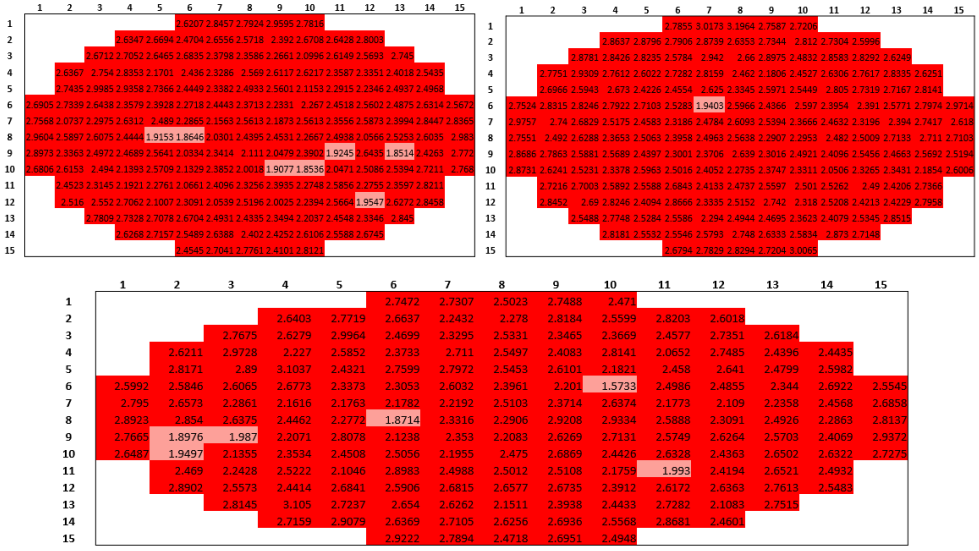

Figure S519 - OD_{450} *n*=3 intensity maps produced for **72** (1.5 mg/mL) in aqueous KCl (0.505 M) at 25 °C. Blue: OD_{450} = 0.00-0.99 AU. Pink: OD_{450} = 1.00-1.99 AU. Red: OD_{450} = 2.00-3.00 AU.

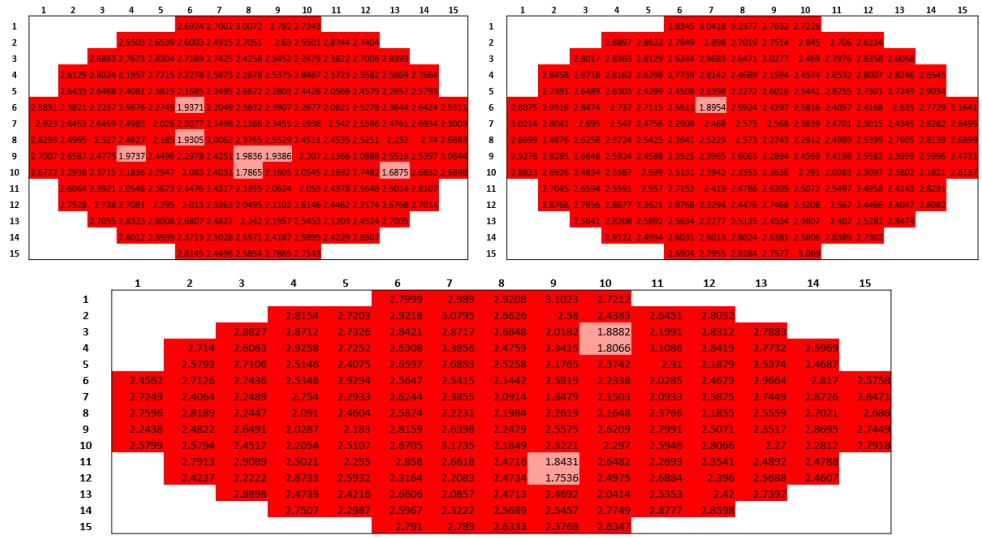

Figure S520 - OD_{450} *n*=3 intensity maps produced for **72** (1.5 mg/mL) in aqueous KCl (0.505 M) at 30 °C. Blue: OD_{450} = 0.00-0.99 AU. Pink: OD_{450} = 1.00-1.99 AU. Red: OD_{450} = 2.00-3.00 AU.

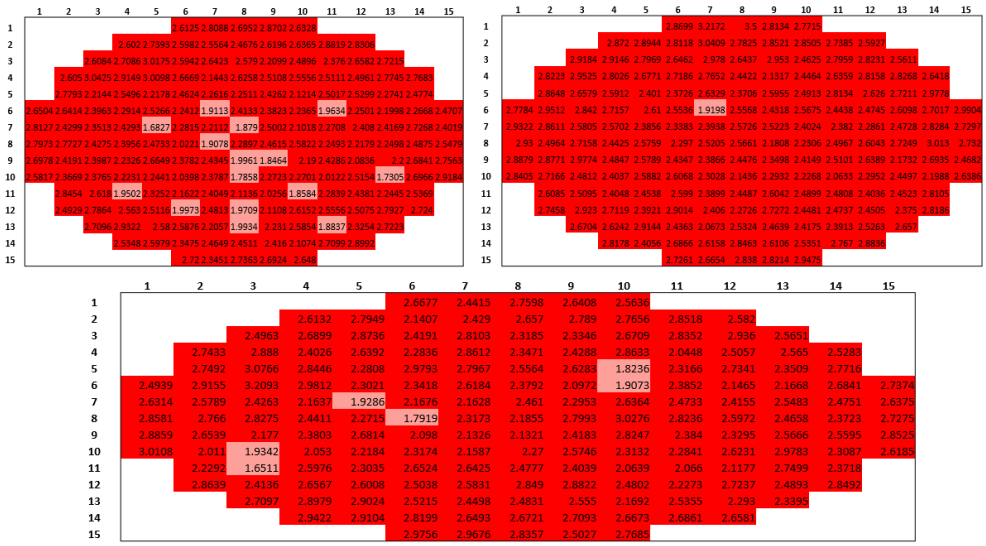

Figure S521 - OD_{450} *n*=3 intensity maps produced for **72** (1.5 mg/mL) in aqueous KCl (0.505 M) at 35 °C. Blue: OD_{450} = 0.00-0.99 AU. Pink: OD_{450} = 1.00-1.99 AU. Red: OD_{450} = 2.00-3.00 AU.

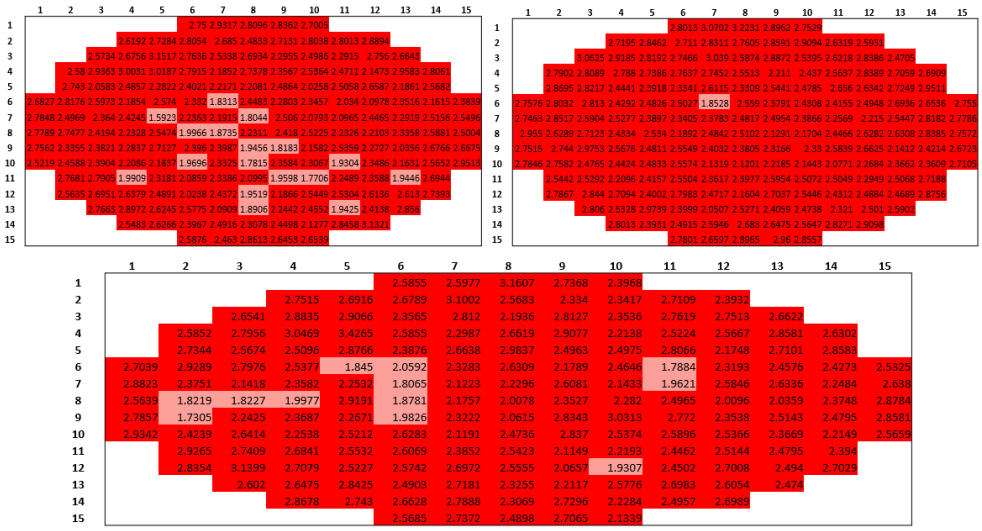

Figure S522 - OD_{450} *n*=3 intensity maps produced for **72** (1.5 mg/mL) in aqueous KCl (0.505 M) at 40 °C. Blue: OD_{450} = 0.00-0.99 AU. Pink: OD_{450} = 1.00-1.99 AU. Red: OD_{450} = 2.00-3.00 AU.

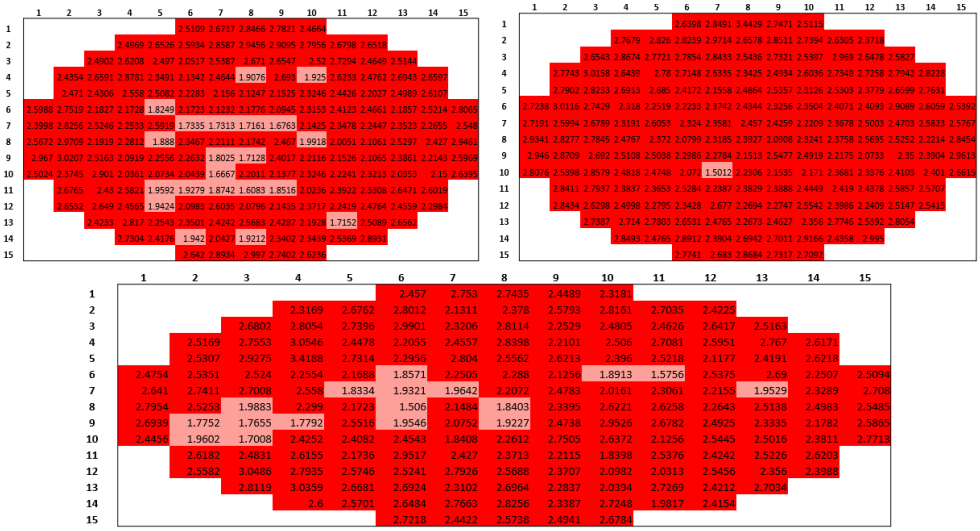

Figure S523 - OD_{450} *n*=3 intensity maps produced for **72** (1.5 mg/mL) in aqueous KCl (0.505 M) at 45 °C. Blue: OD_{450} = 0.00-0.99 AU. Pink: OD_{450} = 1.00-1.99 AU. Red: OD_{450} = 2.00-3.00 AU.

3.3.1 Comparative overview

Table S17 - Average (*n*=3) OD_{450} minimum, maximum and ratio values (maximum/minimum) taken from the spectral microplate well scan data of **72** (1.5 mg/mL) in H_2O, DMSO and various aqueous salt solutions (0.505 M) at 25 °C - 45 °C. Error = standard error of the mean (±).

Soln.	OD_{450}	Temp (°C)					Soln.	OD_{450}	Temp (°C)				
		25	30	35	40	45			25	30	35	40	45
H_2O	Min	0.06	0.06	0.06	0.05	0.05	NaOAc	Min	2.05	2.04	2.01	1.97	1.90
	Error (±)	*0.00*	*0.00*	*0.00*	*0.00*	*0.00*		*Error (±)*	*0.01*	*0.01*	*0.00*	*0.01*	*0.01*
	Max	2.80	2.80	2.82	2.85	2.84		Max	2.91	2.96	2.96	2.94	2.92
	Error (±)	*0.01*	*0.01*	*0.03*	*0.03*	*0.04*		*Error (±)*	*0.00*	*0.02*	*0.06*	*0.02*	*0.05*
	Min/Max	0.02	0.02	0.02	0.02	0.02		Min/Max	0.7	0.69	0.68	0.67	0.65
	Error (±)	*0.00*	*0.00*	*0.00*	*0.00*	*0.00*		*Error (±)*	*0.00*	*0.00*	*0.01*	*0.01*	*0.01*
DMSO	Min	0.05	0.05	0.05	0.05	0.05	NaF	Min	1.60	1.44	1.45	1.43	1.40
	Error (±)	*0.00*	*0.00*	*0.00*	*0.00*	*0.00*		*Error (±)*	*0.12*	*0.34*	*0.26*	*0.13*	*0.03*
	Max	3.50	3.50	3.50	3.50	2.95		Max	2.90	2.95	2.92	2.87	2.90
	Error (±)	*0.00*	*0.00*	*0.00*	*0.00*	*0.21*		*Error (±)*	*0.12*	*0.21*	*0.31*	*0.22*	*0.32*
	Min/Max	0.01	0.01	0.01	0.01	0.02		Min/Max	0.55	0.49	0.5	0.5	0.48
	Error (±)	*0.00*	*0.00*	*0.00*	*0.00*	*0.00*		*Error (±)*	*0.01*	*0.04*	*0.01*	*0.00*	*0.03*
Na_2HPO_4	Min	0.60	0.57	0.56	0.53	0.08	RbCl	Min	1.37	1.34	1.24	1.20	1.34
	Error (±)	*0.02*	*0.03*	*0.03*	*0.02*	*0.01*		*Error (±)*	*0.11*	*0.15*	*0.17*	*0.30*	*0.22*
	Max	1.91	1.94	1.92	1.91	2.57		Max	2.77	2.83	2.82	2.74	2.80
	Error (±)	*0.01*	*0.02*	*0.04*	*0.04*	*0.20*		*Error (±)*	*0.11*	*0.13*	*0.19*	*0.04*	*0.09*
	Min/Max	0.31	0.29	0.29	0.28	0.03		Min/Max	0.50	0.48	0.44	0.44	0.48
	Error (±)	*0.01*	*0.02*	*0.01*	*0.01*	*0.00*		*Error (±)*	*0.07*	*0.08*	*0.05*	*0.02*	*0.10*
NaH_2PO_4	Min	1.38	1.33	1.29	1.19	0.14	NaCl	Min	1.69	1.66	1.65	1.63	1.61
	Error (±)	*0.06*	*0.06*	*0.06*	*0.12*	*0.00*		*Error (±)*	*0.03*	*0.03*	*0.03*	*0.03*	*0.03*
	Max	2.51	2.58	2.50	2.45	2.87		Max	2.67	2.66	2.70	2.69	2.73
	Error (±)	*0.14*	*0.12*	*0.14*	*0.09*	*0.02*		*Error (±)*	*0.01*	*0.02*	*0.01*	*0.04*	*0.04*
	Min/Max	0.55	0.51	0.52	0.49	0.05		Min/Max	0.63	0.63	0.61	0.61	0.59
	Error (±)	*0.01*	*0.01*	*0.03*	*0.00*	*0.00*		*Error (±)*	*0.01*	*0.01*	*0.01*	*0.01*	*0.01*
Na_2CO_3	Min	0.86	0.83	0.80	0.68	0.11	$NaNO_3$	Min	1.58	1.57	1.54	1.52	1.48
	Error (±)	*0.34*	*0.33*	*0.32*	*0.31*	*0.02*		*Error (±)*	*0.11*	*0.11*	*0.10*	*0.11*	*0.12*
	Max	2.47	2.48	2.47	2.43	2.21		Max	2.54	2.55	2.52	2.50	2.48
	Error (±)	*0.01*	*0.07*	*0.08*	*0.06*	*0.02*		*Error (±)*	*0.04*	*0.06*	*0.03*	*0.05*	*0.02*
	Min/Max	0.35	0.33	0.32	0.28	0.05		Min/Max	0.62	0.61	0.61	0.61	0.60
	Error (±)	0.10	0.08	0.10	0.08	0.01		*Error (±)*	*0.00*	*0.00*	*0.01*	*0.02*	*0.05*
Na_2SO_4	Min	1.55	1.54	1.51	1.50	1.36	NaOBz	Min	1.74	1.73	1.71	1.69	1.67
	Error (±)	*0.36*	*0.37*	*0.40*	*0.41*	*0.33*		*Error (±)*	*0.01*	*0.01*	*0.01*	*0.01*	*0.01*
	Max	2.49	2.50	2.50	2.55	2.43		Max	2.72	2.80	2.78	2.82	2.85
	Error (±)	*0.13*	*0.15*	*0.19*	*0.22*	*0.13*		*Error (±)*	*0.01*	*0.03*	*0.02*	*0.01*	*0.03*
	Min/Max	0.62	0.61	0.6	0.59	0.56		Min/Max	0.64	0.62	0.62	0.6	0.58
	Error (±)	0.14	0.14	0.15	0.14	0.05		*Error (±)*	*0.00*	*0.00*	*0.00*	*0.00*	*0.00*
$NaHCO_3$	Min	1.25	1.21	1.18	1.15	1.08	KCl	Min	1.79	1.78	1.75	1.73	1.54
	Error (±)	*0.01*	*0.02*	*0.03*	*0.02*	*0.02*		*Error (±)*	*0.19*	*0.11*	*0.15*	*0.13*	*0.06*
	Max	2.21	2.25	2.26	2.24	2.24		Max	3.10	3.20	3.25	3.27	3.29
	Error (±)	*0.06*	*0.04*	*0.04*	*0.02*	*0.08*		*Error (±)*	*0.10*	*0.03*	*0.23*	*0.14*	*0.24*
	Min/Max	0.57	0.54	0.52	0.51	0.48		Min/Max	0.58	0.56	0.54	0.53	0.47
	Error (±)	*0.02*	*0.02*	*0.01*	*0.00*	*0.01*		*Error (±)*	*0.04*	*0.03*	*0.01*	*0.02*	*0.03*

3.4 Fluorescence spectroscopy

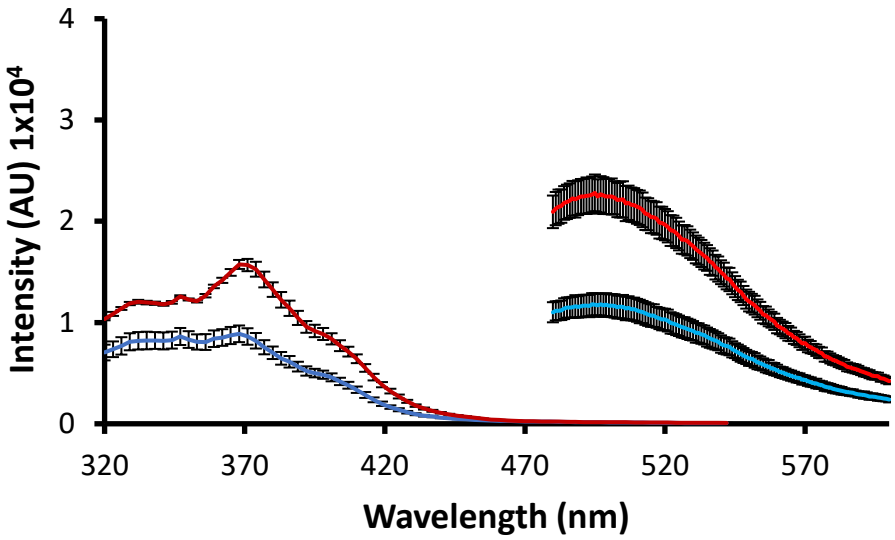

Figure S524 - Average (*n*=3) fluorescence excitation (left) and emission (right) spectra of **72** (1.5 mg/mL) at 25 °C (blue) and 45 °C (red) in H_2O.

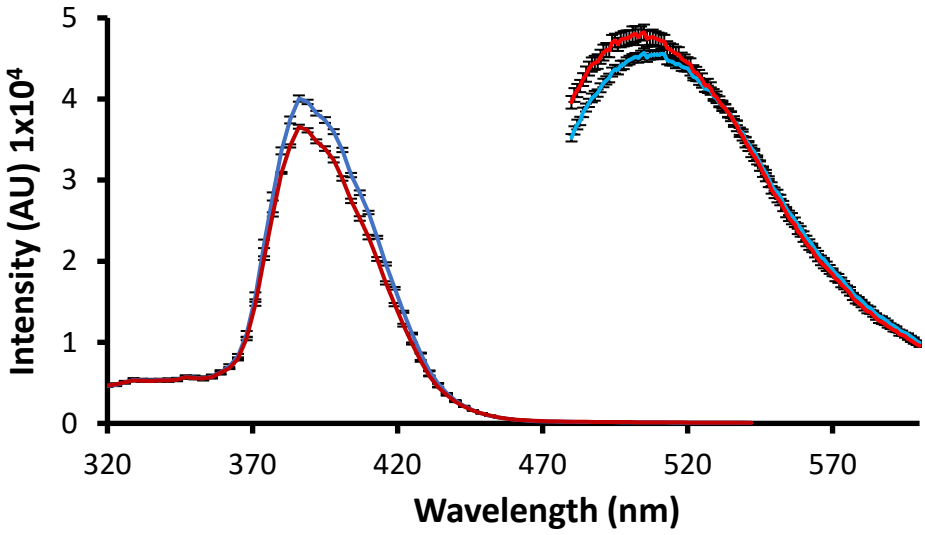

Figure S525 - Average (*n*=3) fluorescence excitation (left) and emission (right) spectra of **72** (1.5 mg/mL) at 25 °C (blue) and 45 °C (red) in DMSO.

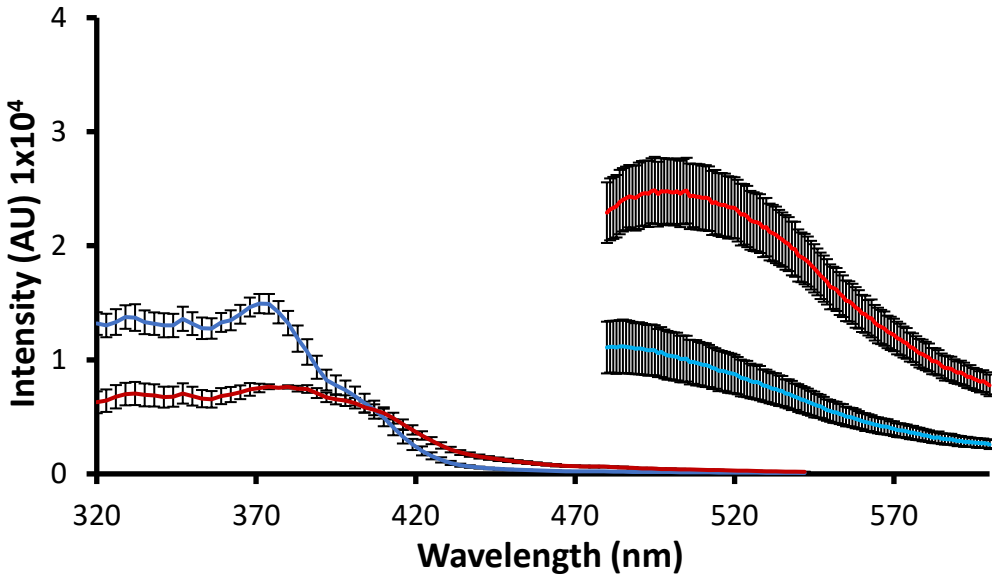

Figure S526 - Average (*n*=3) fluorescence excitation (left) and emission (right) spectra of **72** (1.5 mg/mL) at 25 °C (blue) and 45 °C (red) in aqueous Na_2HPO_4 (0.505 M).

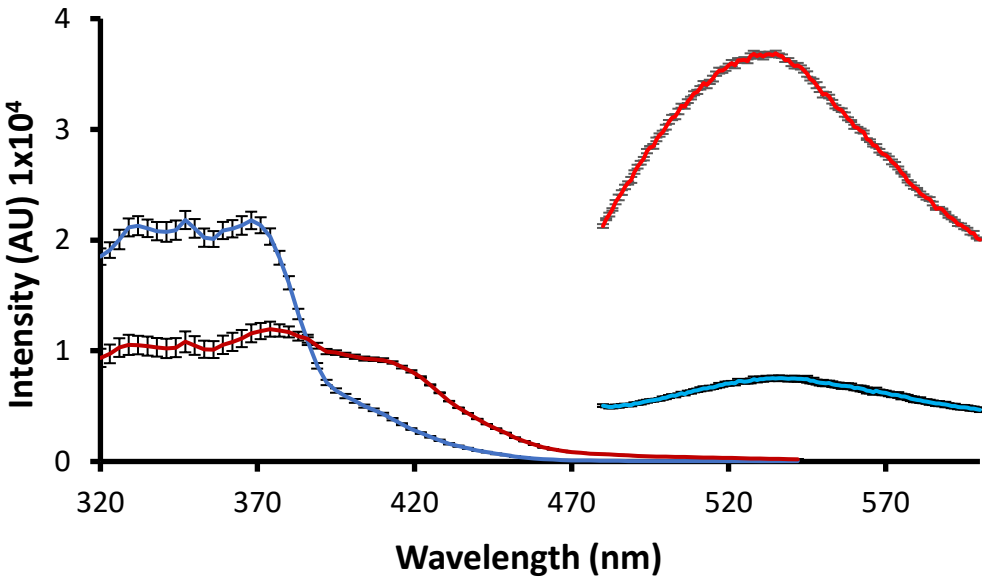

Figure S527 - Average (*n*=3) fluorescence excitation (left) and emission (right) spectra of **72** (1.5 mg/mL) at 25 °C (blue) and 45 °C (red) in aqueous NaH_2PO_4 (0.505 M).

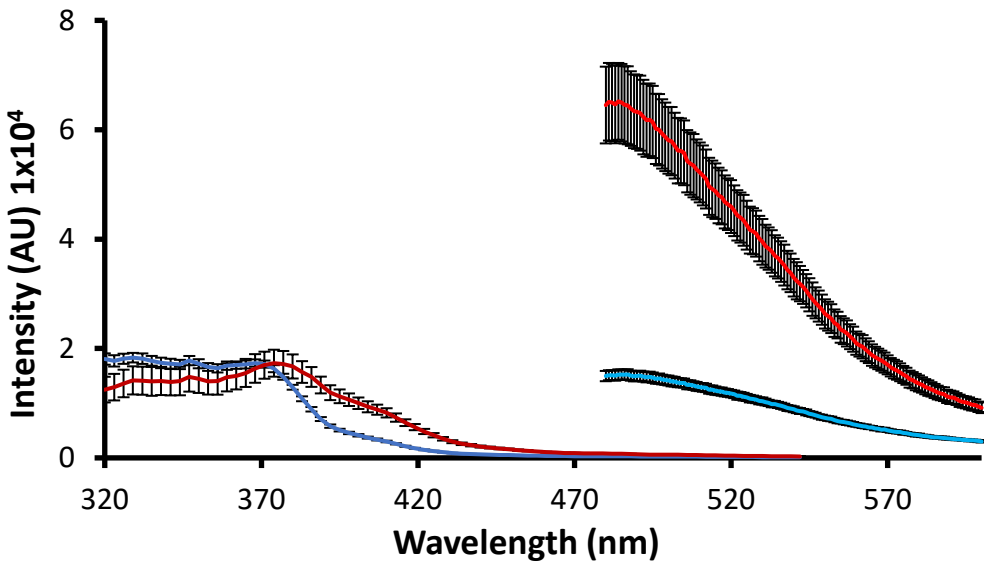

Figure S528 - Average (*n*=3) fluorescence excitation (left) and emission (right) spectra of **72** (1.5 mg/mL) at 25 °C (blue) and 45 °C (red) in aqueous Na_2CO_3 (0.505 M).

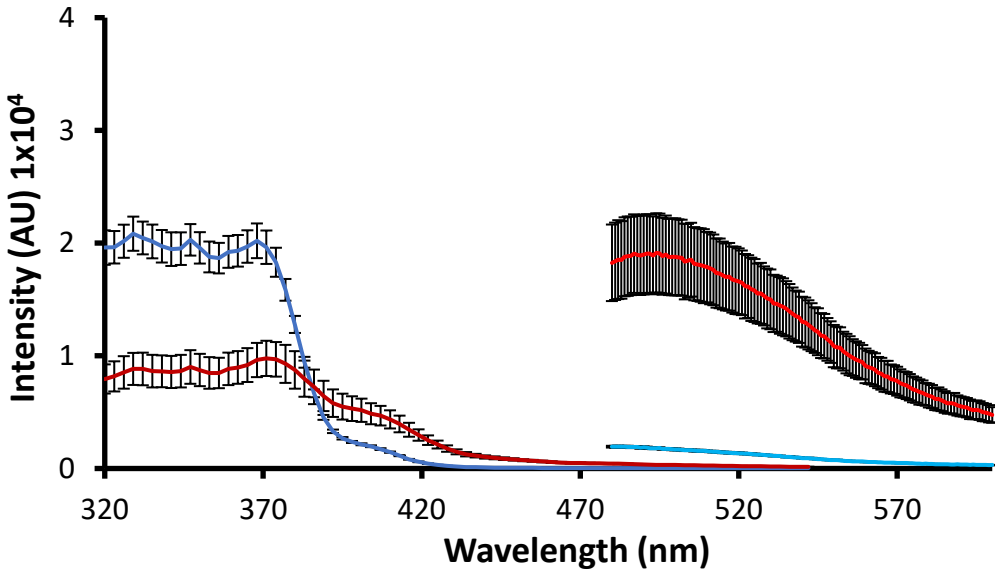

Figure S529 - Average (*n*=3) fluorescence excitation (left) and emission (right) spectra of **72** (1.5 mg/mL) at 25 °C (blue) and 45 °C (red) in aqueous Na_2SO_4 (0.505 M).

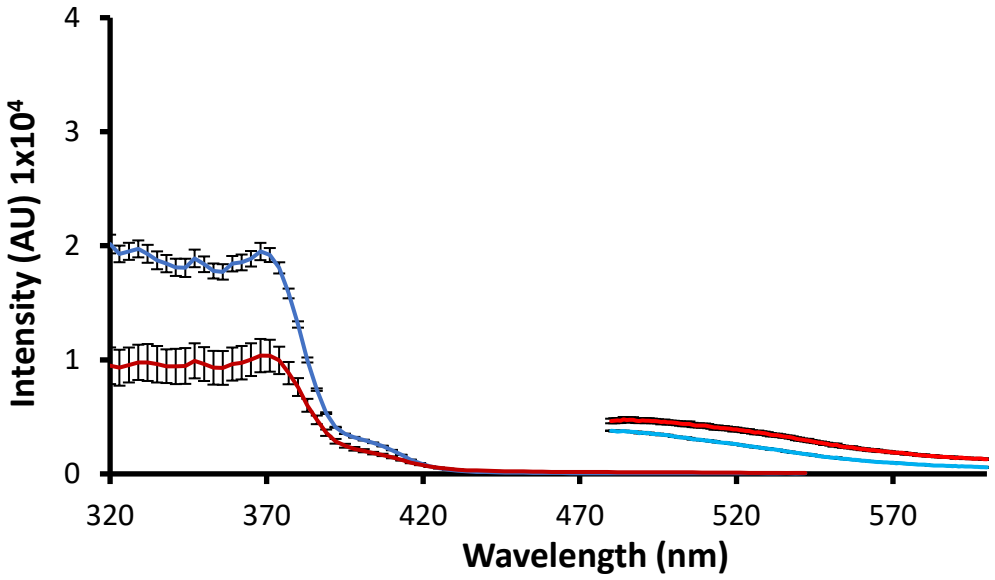

Figure S530 - Average (*n*=3) fluorescence excitation (left) and emission (right) spectra of **72** (1.5 mg/mL) at 25 °C (blue) and 45 °C (red) in aqueous $NaHCO_3$ (0.505 M).

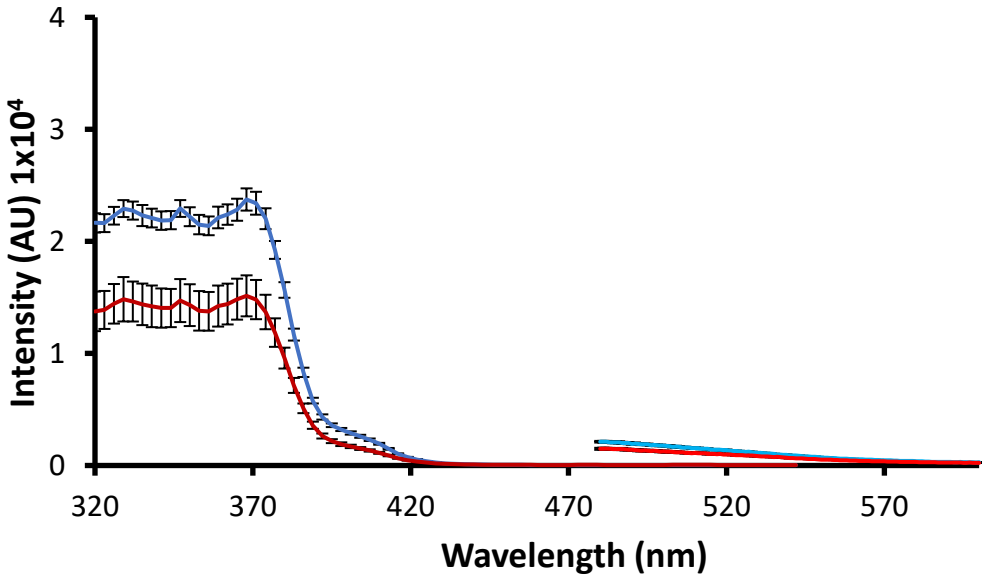

Figure S531 - Average (*n*=3) fluorescence excitation (left) and emission (right) spectra of **72** (1.5 mg/mL) at 25 °C (blue) and 45 °C (red) in aqueous NaOAc (0.505 M).

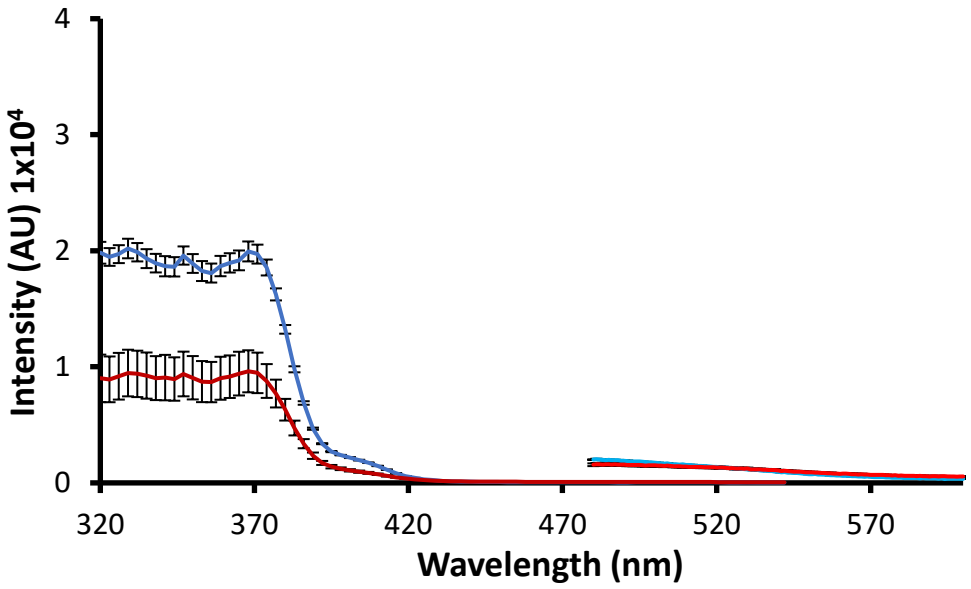

Figure S532 - Average (*n*=3) fluorescence excitation (left) and emission (right) spectra of **72** (1.5 mg/mL) at 25 °C (blue) and 45 °C (red) in aqueous NaF (0.505 M).

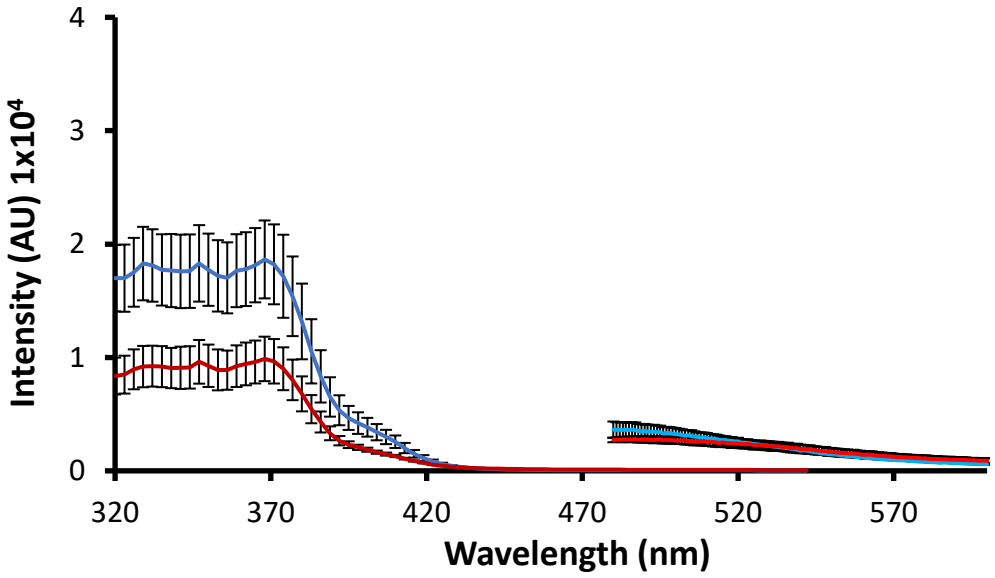

Figure S533 - Average (*n*=3) fluorescence excitation (left) and emission (right) spectra of **72** (1.5 mg/mL) at 25 °C (blue) and 45 °C (red) in aqueous RbCl (0.505 M).

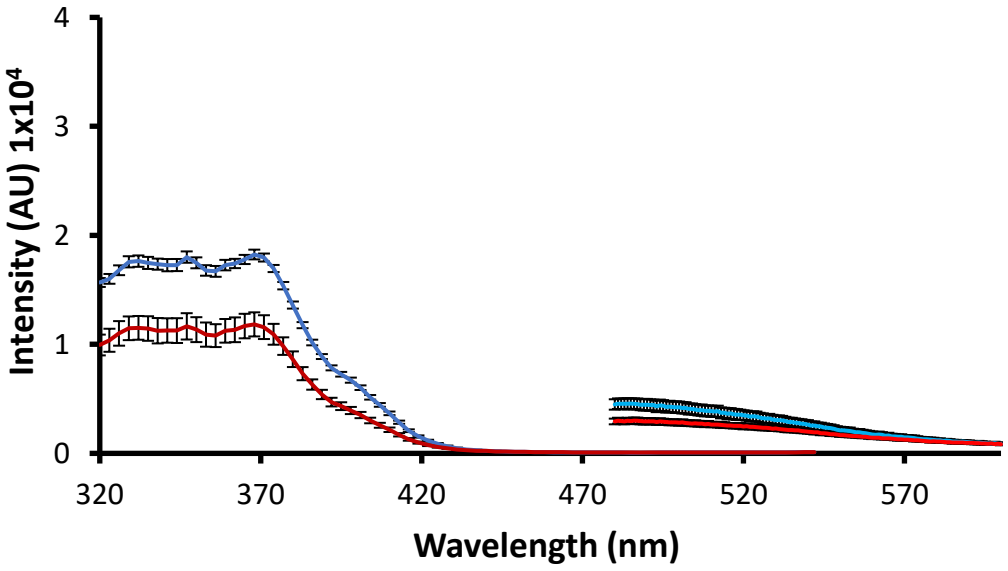

Figure S534 - Average (*n*=3) fluorescence excitation (left) and emission (right) spectra of **72** (1.5 mg/mL) at 25 °C (blue) and 45 °C (red) in aqueous NaCl (0.505 M).

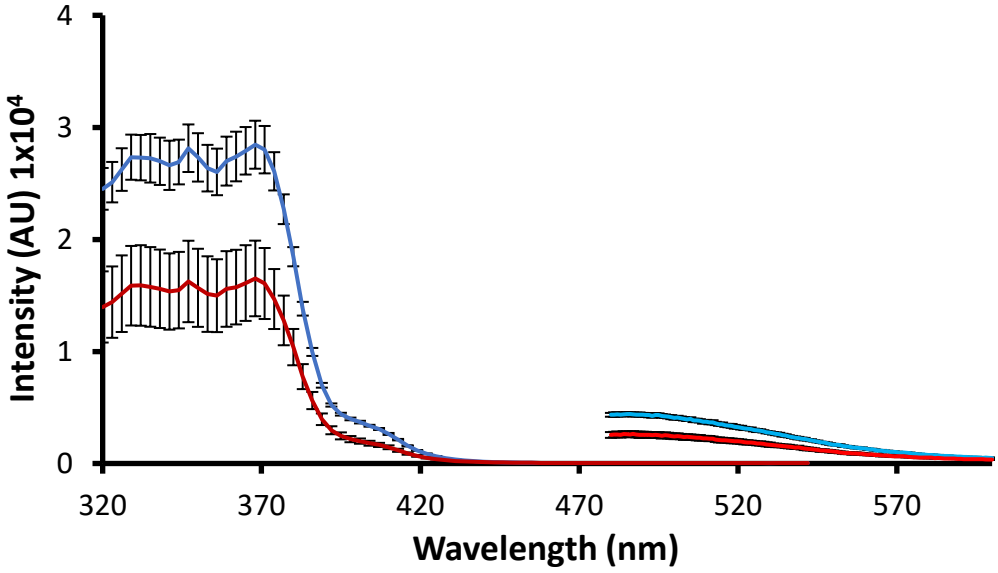

Figure S535 - Average (*n*=3) fluorescence excitation (left) and emission (right) spectra of **72** (1.5 mg/mL) at 25 °C (blue) and 45 °C (red) in aqueous $NaNO_3$ (0.505 M).

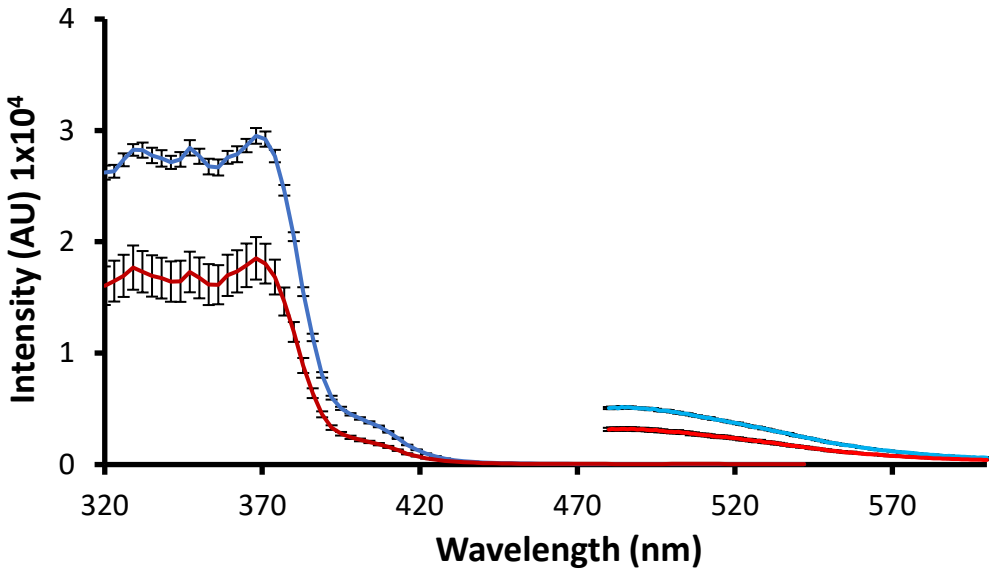

Figure S536 - Average (*n*=3) fluorescence excitation (left) and emission (right) spectra of **72** (1.5 mg/mL) at 25 °C (blue) and 45 °C (red) in aqueous NaOBz (0.505 M).

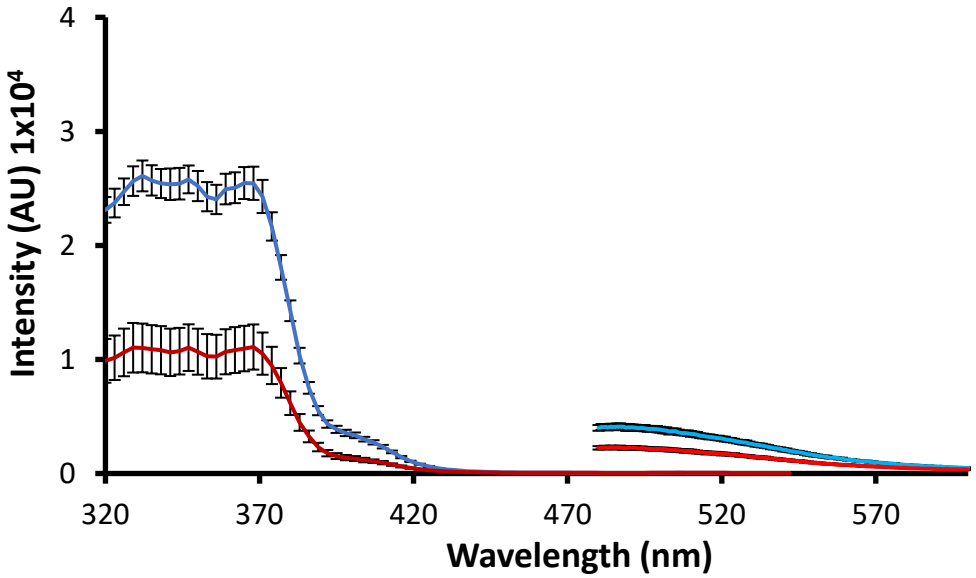

Figure S537 - Average (*n*=3) fluorescence excitation (left) and emission (right) spectra of **72** (1.5 mg/mL) at 25 °C (blue) and 45 °C (red) in aqueous KCl (0.505 M).

3.5 Uniformity experiments

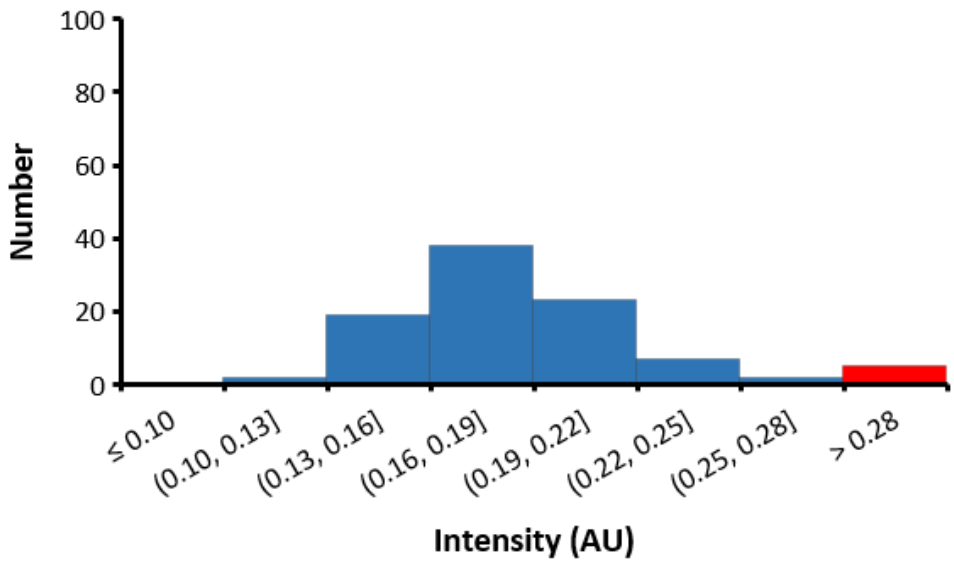

Figure S538 – Standard deviation (σ) data of the mean (μ) taken from Abs.$_{450}$ measurements of **72** (1.5 mg/mL), in H_2O at 25 °C across the entirety of the 96-well microplate - 95 % of the data is within 2 σμ (blue).

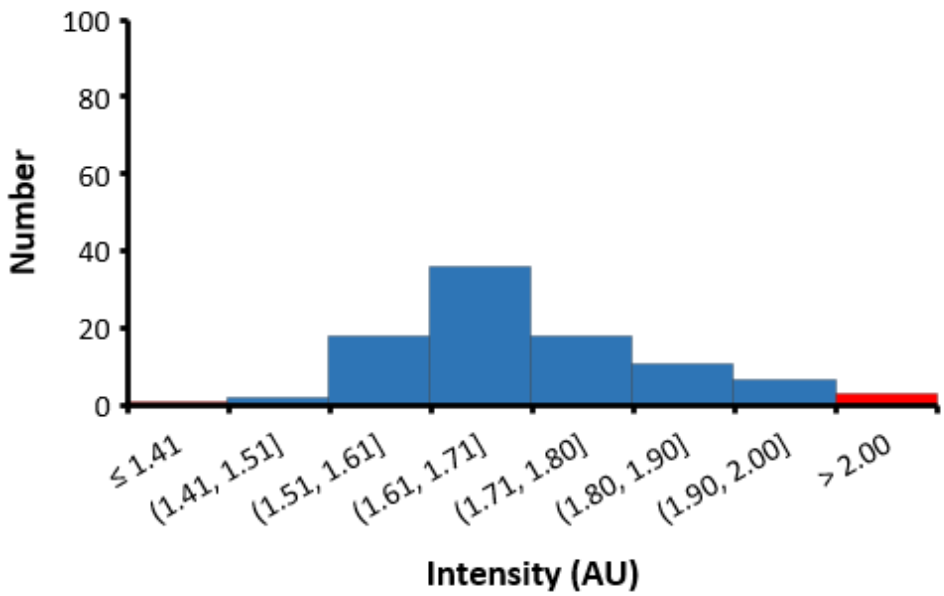

Figure S539 – Standard deviation (σ) data of the mean (μ) taken from Abs.$_{450}$ measurements of **72** (1.5 mg/mL), in aqueous NaCl (0.505 M) at 25 °C across the entirety of the 96-well microplate - > 95 % of the data is within 2 σμ (blue).

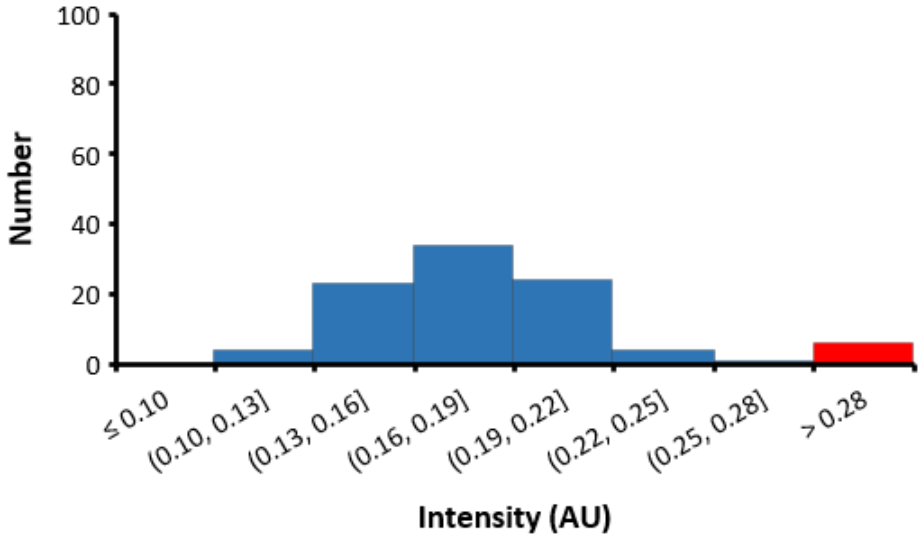

Figure S540 – Standard deviation (σ) data of the mean (μ) taken from Abs.$_{450}$ measurements of **72** (1.5 mg/mL), in H_2O at 30 °C across the entirety of the 96-well microplate - 90 % of the data is within 2 σμ (blue).

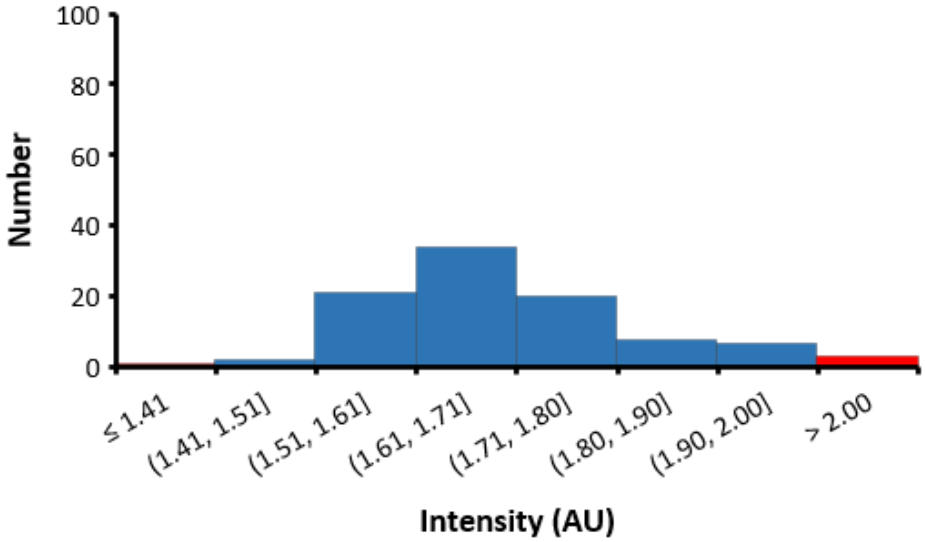

Figure S541 – Standard deviation (σ) data of the mean (μ) taken from Abs.$_{450}$ measurements of **72** (1.5 mg/mL), in aqueous NaCl (0.505 M) at 30 °C across the entirety of the 96-well microplate - 94 % of the data is within 2 σμ (blue).

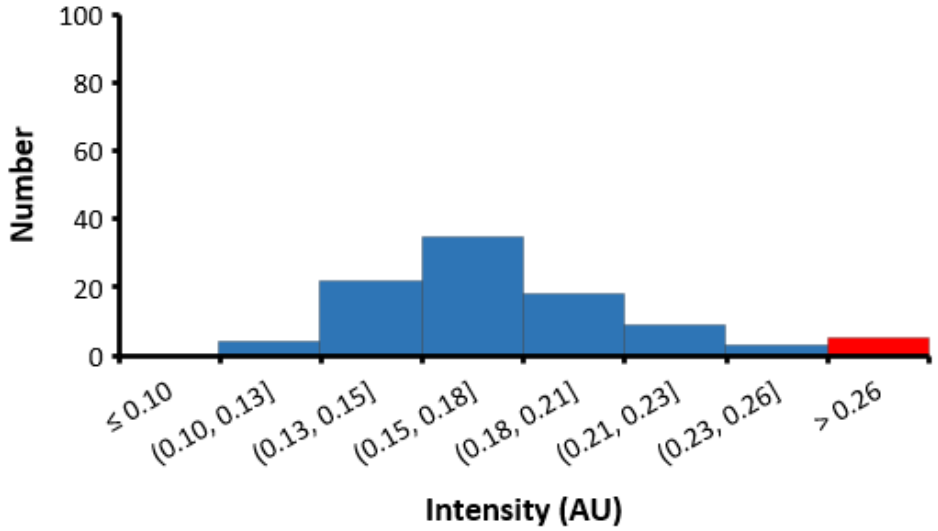

Figure S542 – Standard deviation (σ) data of the mean (μ) taken from Abs.$_{450}$ measurements of **72** (1.5 mg/mL), in H_2O at 35 °C across the entirety of the 96-well microplate - > 95 % of the data is within 2 σμ (blue).

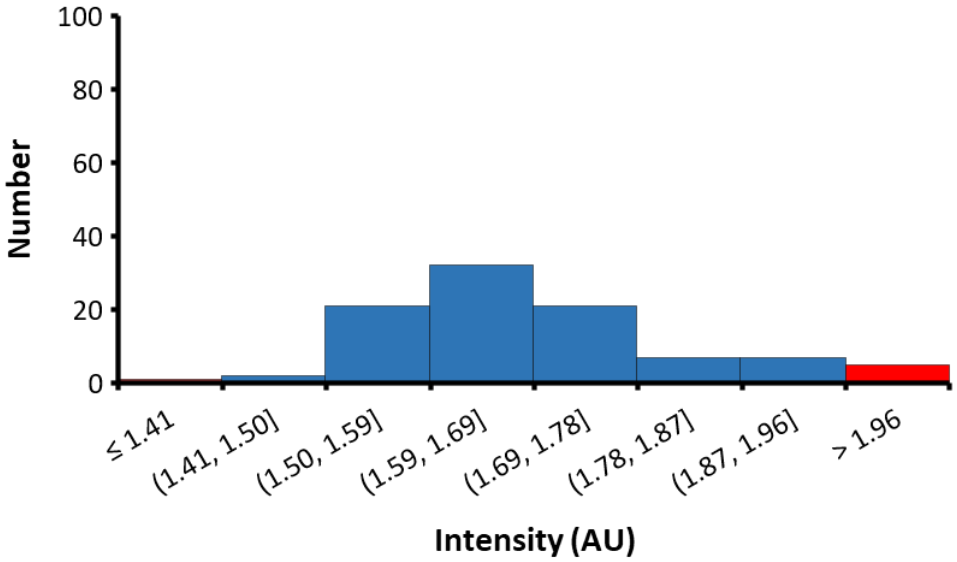

Figure S543 – Standard deviation (σ) data of the mean (μ) taken from Abs.$_{450}$ measurements of **72** (1.5 mg/mL), in aqueous NaCl (0.505 M) at 35 °C across the entirety of the 96-well microplate - 95 % of the data is within 2 σμ (blue).

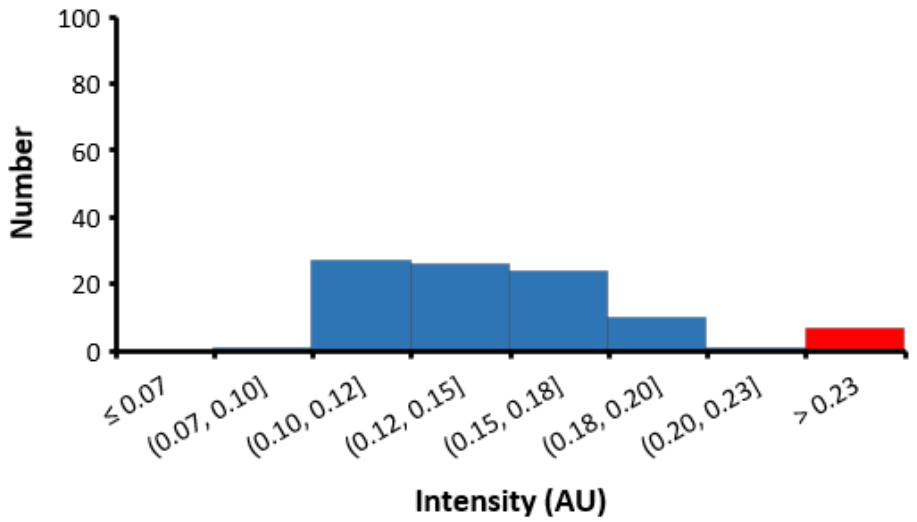

Figure S544 – Standard deviation (σ) data of the mean (μ) taken from Abs.$_{450}$ measurements of **72** (1.5 mg/mL), in H_2O at 40 °C across the entirety of the 96-well microplate - 93 % of the data is within 2 σμ (blue).

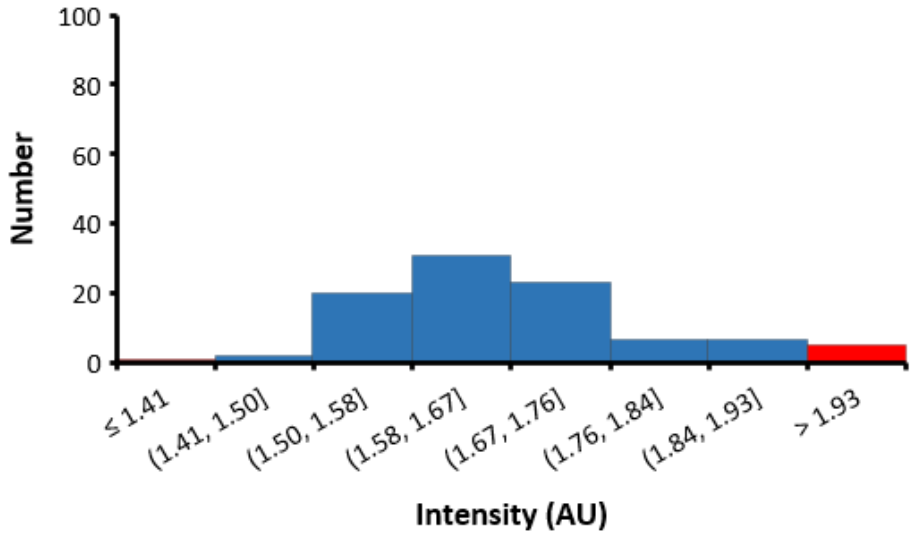

Figure S545 – Standard deviation (σ) data of the mean (μ) taken from Abs.$_{450}$ measurements of **72** (1.5 mg/mL), in aqueous NaCl (0.505 M) at 40 °C across the entirety of the 96-well microplate - 95 % of the data is within 2 σμ (blue).

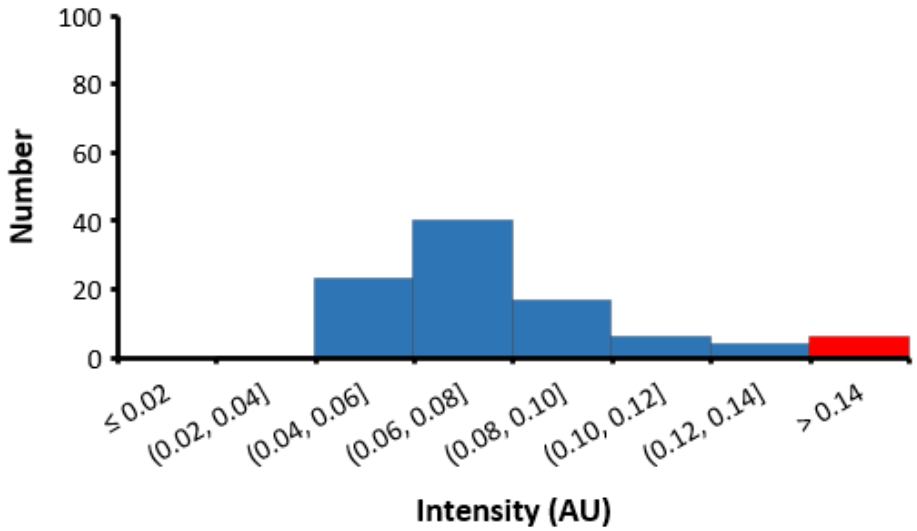

Figure S546 – Standard deviation (σ) data of the mean (μ) taken from Abs.$_{450}$ measurements of **72** (1.5 mg/mL), in H_2O at 45 °C across the entirety of the 96-well microplate - 94 % of the data is within 2 σμ (blue).

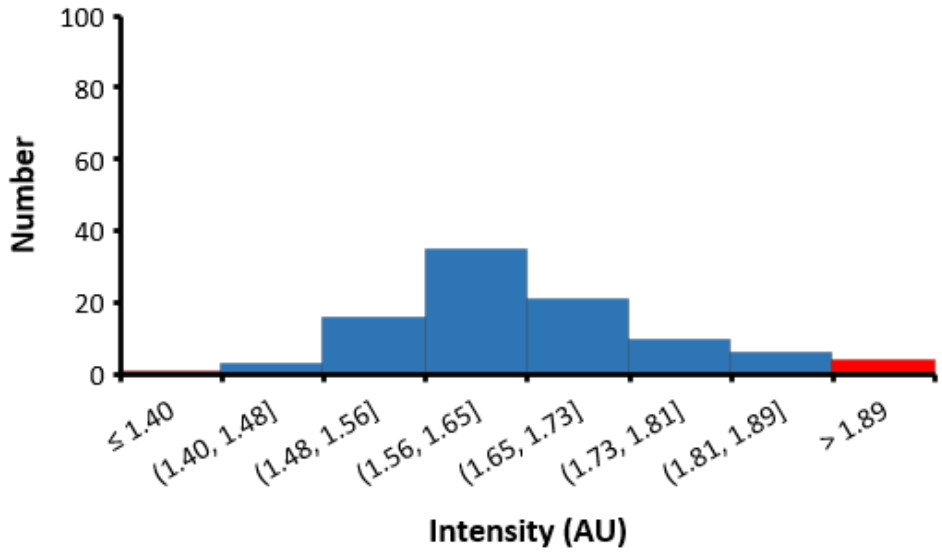

Figure S547 – Standard deviation (σ) data of the mean (μ) taken from Abs.$_{450}$ measurements of **72** (1.5 mg/mL), in aqueous NaCl (0.505 M) at 45 °C across the entirety of the 96-well microplate - 95 % of the data is within 2 σμ (blue).